

Physics and Kinematics of the Parsec Scale Jet of the Quasar 3C 345

INAUGURAL-DISSERTATION

zur
Erlangung des Doktorgrades
der Mathematisch-Naturwissenschaftlichen Fakultät
der Universität zu Köln



vorgelegt von

Frank Schinzel

aus Würzburg, Deutschland

Köln 2011

Berichterstatter: Prof. Dr. J. Anton Zensus
Prof. Dr. Andreas Eckart

Tag der letzten mündlichen Prüfung: 19. Oktober 2011

Abstract

The quasar 3C 345 is one of the archetypical examples of an active galactic nucleus (AGN) featuring a complex parsec-scale jet with a pronounced helical morphology and a range of distinct emitting regions moving at apparent superluminal speeds. Over the past 30 years, it has been followed closely from radio to gamma-ray wavebands with a special focus on Very Long Baseline Interferometry (VLBI) observations in the range of 1-100 GHz, providing milliarcsecond (mas) resolution. The results from this monitoring have made important contributions to the understanding of the physics of relativistic outflows and dynamics of the central regions in AGN.

The thesis at hand presents results from a study of the long-term jet evolution, with a particular focus on the evolution of trajectories, kinematics, and emission in more than 20 distinct regions embedded in the jet. Unique insights into the long-term evolution of the parsec-scale radio emission were gained from the formation of an unprecedented database comprising over 300 archival and new observations. The effect of frequency dependent opacity has been investigated, providing evidence for position variability of the observed origin of the jet, relating to changes in the viewing angle and to the activity state of the jet. A "closeup" on physical properties of individual features implied that shocks dissipate at distances of about 2 mas (150 pc de-projected distance) and the outer jet is most likely dominated by Kelvin-Helmholtz instabilities. Studies of general trends in properties of those features provide certain evidence for their apparent trajectories to result from an underlying (slowly evolving) pattern lit up by passages of plasma condensations ejected during high activity states. The long-term evolution of this pattern indicates its possible relation to the elliptical mode of Kelvin-Helmholtz instability.

In the present work, special attention is paid to the onset of a new period of high activity in the source that began in 2008, which has been observed from radio through gamma-rays. The relation between the radio/optical emission and the production of high energy photons in 3C 345 has been investigated. This provided the first identification of gamma-ray emission from 3C 345 and the nearby quasar NRAO 512, based on 20 months of Fermi-LAT and multi-wavelength data. The Fermi-LAT data of 3C 345, covering an energy range of 0.1-300 GeV, have been combined with 32 Very Long Baseline Array (VLBA) observations of the object made at 43.2 GHz in the period of January 2008 - March 2010. The VLBA data reveal morphology and kinematics of the flow on scales of up to approximately 5 mas (de-projected linear distances of 380 pc). Evolution of the gamma-ray, optical, and parsec-scale radio emission indicated similar physical origins based on long-term trends and on a shock-shock interaction scenario for short events. All short gamma-ray events are explained in a single framework, directly connecting moving features observed in the radio jet with high energy emission. The observations indicate that both the quiescent and flaring components of the gamma-ray emission are produced in a region of the jet of about 25 pc in extent. This region marks the Compton-loss dominated zone of the flow and its large extent may favor the synchrotron self-Compton mechanism for gamma-ray production in the relativistic jet of the quasar 3C 345.

Zusammenfassung

Der Quasar 3C 345 ist einer der urtypischsten Vertreter eines aktiven galaktischen Kerns (AGN). Seine Eigenschaften lassen sich besonders gut auf Skalen in der astronomischen Längenmaßeinheit Parsec erkennen. Auf solchen Parsec-Skalen besitzt der Quasar einen komplexen "Jet" (Teilchenstrahl) mit einer ausgeprägten spiralförmigen Struktur und einer Reihe von klar unterteilten, elektromagnetische Strahlung aussendenden Regionen, die sich scheinbar mit Überlichtgeschwindigkeit bewegen.

Der Jet wurde innerhalb der letzten 30 Jahre engmaschig vom Bereich der Radiowellenlängen bis hin zu Gammastrahlen verfolgt. Dabei lag ein besonderer Augenmerk auf Beobachtungen mittels Interferometrie auf langen Basislinien (VLBI) im Frequenzbereich von 1 bis 100 GHz, womit Auflösungen im Millibogensekundenbereich erzielt werden. Die Basislinie ist dabei die Entfernung zwischen den Beobachtungspunkten, die auf der Erde bis zu 12 000 km betragen kann. Die Resultate dieser kontinuierlichen Beobachtungen leisteten wichtige Beiträge zum Verständnis der Physik relativistischer Jets und zur Beurteilung der Dynamik in den innersten Regionen von AGN.

Die vorliegende Arbeit präsentiert die Ergebnisse einer Untersuchung der Langzeitentwicklung des Jets des Quasars 3C 345, mit besonderem Augenmerk auf die Entwicklung der Trajektorien (Bahnkurven) sowie der Kinematik und Emission von mehr als 20 im Jet eingebetteten, ausgeprägten Regionen. Die Erstellung einer noch nie dagewesenen Datenbank von VLBI-Beobachtungen, bestehend aus über 300 Archiv- und teilweise selbst vorgenommenen Neubeobachtungen, ermöglichte einmalige Einblicke in die Langzeitentwicklung der Radioemissionen auf Parsec-Skalen.

Der Effekt der frequenzabhängigen Opazität (Durchlässigkeit) wurde erforscht. Er weist auf Anzeichen für eine scheinbare zeitliche Veränderlichkeit der Position des Jetursprungpunktes hin, die mit einer Änderung des Sichtwinkels und des Aktivitätszustandes des Jets im Zusammenhang steht. Ein näherer Blick auf die physikalischen Eigenschaften einzelner herausragender Regionen deutete an, dass Schocks auf Distanzen von ungefähr 2 Millibogensekunden (150 Parsec de-projezierte Entfernung) sich aufzulösen beginnen und dass der äußere Jet sehr wahrscheinlich von Kelvin-Helmholtz-Instabilitäten dominiert wird.

Untersuchungen des allgemeinen Trends dieser Regionen lieferten sichere Beweise für ein sich langsam entwickelndes Muster, welches durch Plasmakondensationen – die durch dieses Muster wandern – aufleuchtet. Die Plasmakondensationen werden während der aktiven Phasen des Jets ausgestoßen. Die Langzeitentwicklung des Musters weist auf einen möglichen Zusammenhang mit der elliptischen Mode einer Kelvin-Helmholtz-Instabilität hin.

In den Untersuchungen wird besondere Aufmerksamkeit dem Beginn einer neuen Aktivitätsphase der Quelle geschenkt, die im Jahr 2008 begann und die vom Radio- bis zum Gammastrahlenbereich beobachtet wurde. Der Zusammenhang zwischen radio/optischer Emission und der Produktion von hochenergetischen Photonen in 3C 345 wurde erforscht. Dies führte zur ersten Identifikation von Gammastrahlung von 3C 345 und vom benachbarten Quasar NRAO 512, basierend auf 20 Monate Beobachtungsdaten des Weltraumobservatoriums Fermi Large Area Telescope (Fermi-LAT) und Multiwellenlängenbeobachtungen.

Die Fermi-LAT Daten von 3C 345 umfassten einen Energiebereich von 0,1-300 GeV und wurden mit 32 Very Long Baseline Array (VLBA) Beobachtungen bei 43,2 GHz im Zeitraum zwischen Januar 2008 und März 2010 kombiniert. Die VLBA Daten zeigten Struktur und Kinematik des Jets auf Skalen bis ungefähr 5 Millibogensekunden (deprojeziert auf eine lineare Distanz von 380 Parsec). Die Entwicklung von Gamma, optischer und Radiostrahlung auf Parsec-Skalen weist darauf hin, dass die Herkunft der Strahlung gleichen physikalischen Ursprungs ist – basierend auf Langzeittrends und eines Schock-Schock Wechselwirkungsszenarios für kurze Ereignisse.

Alle kurzen Gammastrahlungsereignisse konnten in einem einzigen Rahmen erklärt werden, welcher die Hochenergiesstrahlung direkt mit wandernden Regionen im Jet verbindet. Die Beobachtungen zeigen, dass beide, der ruhige und der aufleuchtende Anteil der Gammastrahlung, in einer Region des Jets produziert werden, die über eine Distanz von 25 Parsec reicht. Diese Region ist dominiert von Compton-Emissionsstrahlungsverlusten (Wechselwirkung von elektromagnetischer Strahlung mit freien Elektronen) und die Größe dieser Region läßt auf den Synchrotron-selbst-Compton Strahlungsmechanismus für die Produktion von Gammastrahlung im relativistischen Jet von 3C 345 schliessen.

Mit der vorliegenden Arbeit soll insgesamt ein weiterer Beitrag zur Verdeutlichung und zum Verständnis der komplexen Zusammenhänge um den besonders betrachtenswerten Quasar 3C 345 geleistet werden.

Contents

Preface	xxi
1 Introduction to Flat Spectrum Radio Quasars (FSRQ)	1
1.1 Active Galaxies and Quasars	2
1.2 Relativistic Outflows – Jets	3
1.3 Multi-wavelength Emission	4
Synchrotron Emission (Radio, Optical, X-rays)	4
Inverse-Compton Emission (X-rays, Gamma-rays, TeV)	4
2 Physical Theory of Jets	7
2.1 Formation and Structure of Jets	7
2.2 Shocks and Plasma Instability	9
2.3 Opacity and Magnetic Field	11
2.4 Flow Kinematics	14
2.5 Flares and Quasi-Periodic activity	16
3 The FSRQ 3C 345	17
3.1 Radio Properties	17
3.2 Optical Properties	20
3.3 High-Energy Emission	21

4	Multi-wavelength Observations, Data Reduction and Techniques	23
4.1	Very Long Baseline Interferometry	23
4.1.1	Observations	26
4.1.2	Data Reduction	32
4.1.3	Analysis Techniques	35
4.1.4	Nomenclature of Gaussian Components	38
4.1.5	Database of Observations	39
4.2	Swift Satellite	39
4.2.1	Observations	40
4.2.2	UVOT	41
4.2.3	XRT	43
4.3	Fermi Satellite	44
	Large Area Telescope	46
4.4	Millimeter Radio and Optical Observations	47
5	31 Years of High Angular Resolution Observations of 3C 345	49
5.1	The Nuclear Region (“core”)	49
5.2	Long-term Kinematics	59
	C1	67
	C2	68
	C3	70
	C3a	71
	C4	73
	C5	74
	C6	76
	C7	77
	C8	79
	C9	80
	C10	82
	C11	83
	C12	85

C13	86
C14	88
C15	88
C15a	89
C16	92
C17, C18, and C19	92
C20, C21, C22, and C23	94
5.3 Structural Variability of the Jet	96
5.4 Physical Properties of the Jet	100
5.4.1 Opening Angles	100
5.4.2 Kinematics	104
5.4.3 Magnetic Field and Distance to the Central Engine	111
5.5 Summary and Conclusions	112
6 First Identification of Gamma-ray Emission from 3C 345	115
6.1 Localization of Gamma-ray emission	116
6.2 Long-term Gamma-ray Variability	117
6.3 Short-term Gamma-ray Variability	120
6.4 Identification of Gamma-ray Counterpart	120
6.5 Multi-wavelength Variability	124
6.6 Conclusions	126
7 Relativistic Outflow Drives γ-ray Emission	131
7.1 Evolution of Radio Emission in the Nuclear Region	132
7.1.1 Kinematics	134
7.1.2 Flux Density	138
7.2 Radio- γ -ray Correlation	140
7.2.1 Long-term Trends	141
7.2.2 Individual Events	143
7.3 Discussion	146
7.4 Conclusions	148

8	Summary and Concluding Remarks	151
A	Historic VLBI Observations	155
B	Modelfit Parameters of Reanalyzed Observations	161
C	GASP-WEBT/SAO monitoring data of 3C 345	211
	Bibliography	225
	Acknowledgement	235
	Erklärung	237
	Lebenslauf	239

List of Figures

1.1	Illustration of an AGN and the viewing angle dependent sub-classes following the unification scheme. <i>Image credit: NASA/Aurore Simonnet, Sonoma State University.</i>	2
1.2	The scheme of a radio-loud AGN jet (not to scale).	3
1.3	Spectral energy distribution of 3C 345.	5
2.1	Schematic diagram of the required ingredients, a rotating compact object with accretion disk, to form relativistic outflows.	8
2.2	The basic outline of a simplistic relativistic jet model of a radio-loud AGN. The scale is logarithmic beyond 10 Schwarzschild radii (R_g). <i>Image credit: Lobanov (2007).</i>	10
2.3	Kelvin-Helmholtz instability acting on a cylindrical jet. (a) Example for pinch modes of K-H instability (Perucho et al. 2004). (b) Example for helical modes K-H instability (upper panel volumetric rendering, lower panel illustration of the interaction between body and surface modes (Xu et al. 2000).	11
2.4	Shift of the observed, frequency dependent VLBI core positions. The core is seen at the location of the jet where its opacity to synchrotron self-absorption is $\tau = 1$. At greater distances, the emission is optically thin ($\tau < 1$), the position of the superluminal feature does not change with frequency and can be used as reference point. The distance r_∞ corresponds to the distance of the footpoint of the jet, observed at infinite frequency. The distances r_0 and $r_{\text{core}}(\nu)$ can be estimated from the measured offsets $r_5 \dots r_{22}$. The figure is adopted from Lobanov (1996).	12
2.5	Schematic diagram for de-projecting superluminal motions.	14

3.1	(a) Flux density (open circles) and flux per logarithmic bandwidth (filled circles) are shown for the multi-frequency spectrum of 3C 345 of 1983 May (Bregman et al. 1986). (b) Radio spectrum of 3C 345 compiled from archival data and simultaneous RATAN observations. <i>Plot courtesy of the MOJAVE program and RATAN (Kovalev et al. 1999).</i>	18
3.2	Observations presented in Kollgaard et al. (1989). (a) C array VLA map from 1988.18, with a dynamic range of 25 000:1. (b) A/B array VLA map from 1983.93 with a dynamic range of 75 000:1, showing the appearance of a counter jet. (c) A array VLA map from 1985.13, with a dynamic range of 19 000:1.	19
3.3	Map of 3C 345 at milliarcsecond scales, observed at 15.4 GHz.	20
3.4	(a) <i>Swift</i> /XRT raw photon count map in the energy range of 0.3–10 keV, observed on July 26th, 2009. (b) EGRET γ -ray likelihood contours for energies above 100 MeV and observing period 5190. The contours represent confidence levels of 50%, 68%, 95%, and 99%. The cross is the revised EGRET catalog position, the plus sign is the position with maximum likelihood, the black dots mark the radio positions of 3C 345, Mrk 501, and 4C +38.41. (Casandjian & Grenier 2008)	21
4.1	(a) VLBA station at Maunaea Kea, Hawaii. (b) Location of the 10 Very Long Baseline Array antenna stations distributed across North America. Image courtesy of NRAO/AUI.	25
4.2	(a) Read-out devices for correlation at the array operations center (now the Pete V. Domenici Science Operations Center) in Socorro, New Mexico. (b) Library of observations stored on disk packs awaiting to be correlated.	26
4.3	Distribution in frequency and time of the over 300 VLBI observations used in this thesis.	27
4.4	Block schedule of VLBA data calibration and reduction procedure, providing an overview of the main AIPS tasks that were applied.	34
4.5	Exemplary VLBA “clean” image of the total brightness distribution of 3C 345 at 15.4 GHz made from observations on March 16th, 2009. The shaded ellipse in the lower left corner represents the FWHM of the restoring beam. The image peak flux density is 5.1 Jy beam^{-1} . The contour levels correspond to (-0.05 0.05 0.1 0.2 0.4 0.8 1.6 3.2 6.4 13 26 51) % of the peak flux density. Negative contours are indicated by dashed contour lines.	35

- 4.6 Exemplary VLBA image of the total brightness distribution of 3C 345 at 15.4 GHz made from observations on March 16th, 2009. The shaded ellipse in the lower left corner represents the FWHM of the restoring beam. The image peak flux density is 5.1 Jy beam^{-1} . The contour levels correspond to $(-0.1 \ 0.1 \ 0.2 \ 0.4 \ 0.8 \ 1.6 \ 3.2 \ 6.4 \ 13 \ 26 \ 51) \%$ of the peak flux density. Negative contours are indicated by dashed contour lines. Open crossed circles show the FWHM of the Gaussian components found to best represent the structure observed. The image was reconstructed using the modelfit components together with the observed calibrated visibilities. 36
- 4.7 An artist's rendering of the Swift spacecraft with a gamma-ray burst going off in the background and the Swift Mission Logo in the lower right corner. Credit: NASA EPO, Sonoma State University, Spectrum Astro. 40
- 4.8 (a) *Fermi* LAT cut-away, showing the instrument with the dimensions $1.8 \times 1.8 \times 0.72 \text{ m}$, weighting 2.8 metric tons alone and requiring a power of 650 W to operate (Atwood et al. 2009). (b) The GLAST (now *Fermi*) satellite sitting ontop of the payload attachment. The square ontop is the LAT, with the GBM detectors visible on the left side. *Image courtesy NASA/Kim Shiflett*. 45
- 4.9 Photograph of the Sub-millimeter Array on Mauna Kea, Hawaii USA. 48
- 5.1 Distribution of core-shifts of simultaneously observed frequency pairs. The core-shifts are shifted for readability by constant values of +0.5, +1.0, +1.5, and +2.0 mas, for the pairs of 15.4 – 22.2, 8.4 – 15.4, 5.0 – 8.4, and 1.6 – 5.0 GHz respectively. Points with downward arrows are 1σ upper limits. Vertical lines are drawn in corresponding colors for the particular frequency pairs 1.6 – 5.0, 5.0 – 8.4, 8.4 – 15.4, 15.4 – 22.2, 22.2 – 43.2 GHz, indicating the respective weighted averages of the core-shifts listed in Table 5.2 50
- 5.2 Time variability of the direction of the core-shifts of simultaneously observed frequency pairs. Different symbols and colors indicate the corresponding group of frequency pairs (1.6 – 5.0, 5.0 – 8.4, 8.4 – 15.4, 15.4 – 22.2, and 22.2 – 43.2 GHz). A horizontal, dashed line at -102.5° indicates the weighted average value of the direction. The solid line indicates a fitted trend (using equal weights) to all position angle values, with a slope of $(0.84 \pm 1.5)^\circ \text{ year}^{-1}$ 54
- 5.3 The average position angles of the reference components, used to calculate the core-shift between two frequencies, is compared to the obtained position angles of the core-shifts. 55
- 5.4 Time variability of the core-shift measure $\Omega_{r\nu}$. The dashed horizontal line indicates the global weighted average of $\Omega_{r\nu} = (19.16 \pm 0.81) \text{ pc GHz}$. The blue solid line indicates a long-term trend fitted to the data points, using equal weights, providing a slope of $(1.44 \pm 0.67) \text{ pc GHz year}^{-1}$ 57

- 5.5 Plot comparing the detrended (see Fig. 5.4) core-shift measure $\Omega_{r\nu}$ to the corresponding core flux densities at 43.2 GHz. Core flux densities for values with a positive core spectral index (see Figure 5.6(a)) between 22.2 and 43.2 GHz are re-calculated using the 22.2 GHz flux densities and an index of $\alpha = -0.72$ ($S_\nu \propto \nu^\alpha$), see the discussion provided in the text. These values are indicated by orange points, using dashed errorbars, two of which correspond to the outliers around 2.7 Jy. The solid blue curve represents the relationship of $\Omega_{r\nu} \propto S_\nu^{2/3}$ 58
- 5.6 (a) The time variability of core spectral indices α between 22.2 and 43.2 GHz. The three points with positive spectral indices correspond to the observations on 1997-08-15, 1999-02-11, and 1999-07-30. The average value of α for the non-positive values is -0.72. (b) Plot of the detrended core-shift measure against FWHM of the circular Gaussian representing the core at 43.2 GHz. 58
- 5.7 Averaged core-shifts as a function of frequency, referenced to 15.4 GHz. The curves represent the best-fit to the function $r_{\text{shift}} = a + b\nu_{\text{obs}}^{-1/k_r}$, with a value of $k_r = 2.9 \pm 1.1$, if the shift at 1.6 GHz is included (green slope) and $k_r = 0.98 \pm 0.15$ if 1.6 GHz is excluded from the fit (blue slope). 59
- 5.8 The effect of core-shift correction on the x,y separations of C3 respectively. The open black points represent the uncorrected kinematics data, filled green points represent the core-shift corrected data. Circles refer to data in the x coordinate and boxes to the y coordinate. The blue dotted circle around an outlier, corresponds to the 2.3 GHz data point discussed in the text. 60
- 5.9 Overview of the evolution of individual jet components in radial separation from the 15.4 GHz VLBI core over a time period of 31 years (1979 – 2010). The components C21 – C23 are not shown due to their extreme proximity to the core. For these components see discussion in Chapter 7. 62
- 5.10 Evolution of individual jet components in radial separation, zoomed in on the time range between 1994 and 2010. 62
- 5.11 Relative positions $x(t)$ and $y(t)$ of C1, dotted lines are the respective polynomial fits to the relative positions. 67
- 5.12 Two-dimensional trajectory of C1. The thick black line is reconstructed from the polynomial fits in x and y direction. The white circles are spaced at intervals of 1 year, indicating the change of component position with time. 68
- 5.13 Relative positions $x(t)$ and $y(t)$ of C2, dotted lines are the respective polynomial fits to the relative positions. 69
- 5.14 Two-dimensional trajectory of C2. The thick black line is reconstructed from the polynomial fits in x and y direction. The white circles are spaced at intervals of 1 year, indicating the change of component position with time. 69

5.15	Relative positions $x(t)$ and $y(t)$ of C3, dotted lines are the respective polynomial fits to the relative positions.	70
5.16	Two-dimensional trajectory of C3. The thick black line is reconstructed from the polynomial fits in x and y direction. The white circles are spaced at intervals of 1 year, indicating the change of component position with time.	71
5.17	Relative positions $x(t)$ and $y(t)$ of C3a, dotted lines are the respective polynomial fits to the relative positions.	72
5.18	Two-dimensional trajectory of C3a. The thick black line is reconstructed from the polynomial fits in x and y direction. The white circles are spaced at intervals of 1 year, indicating the change of component position with time.	72
5.19	Relative positions $x(t)$ and $y(t)$ of C4, dotted lines are the respective polynomial fits to the relative positions.	73
5.20	Two-dimensional trajectory of C4. The thick black line is reconstructed from the polynomial fits in x and y direction. The white circles are spaced at intervals of 1 year, indicating the change of component position with time.	74
5.21	Relative positions $x(t)$ and $y(t)$ of C5, dotted lines are the respective polynomial fits to the relative positions.	75
5.22	Two-dimensional trajectory of C5. The thick black line is reconstructed from the polynomial fits in x and y direction. The white circles are spaced at intervals of 1 year, indicating the change of component position with time.	75
5.23	Relative positions $x(t)$ and $y(t)$ of C6, dotted lines are the respective polynomial fits to the relative positions.	76
5.24	Two-dimensional trajectory of C6. The thick black line is reconstructed from the polynomial fits in x and y direction. The white circles are spaced at intervals of 1 year, indicating the change of component position with time.	77
5.25	Relative positions $x(t)$ and $y(t)$ of C7, dotted lines are the respective polynomial fits to the relative positions.	78
5.26	Two-dimensional trajectory of C7. The thick black line is reconstructed from the polynomial fits in x and y direction. The white circles are spaced at intervals of 1 year, indicating the change of component position with time.	78
5.27	Relative positions $x(t)$ and $y(t)$ of C8, dotted lines are the respective polynomial fits to the relative positions.	79

5.28	Two-dimensional trajectory of C8. The thick black line is reconstructed from the polynomial fits in x and y direction. The white circles are spaced at intervals of 1 year, indicating the change of component position with time.	80
5.29	Relative positions $x(t)$ and $y(t)$ of C9, dotted lines are the respective polynomial fits to the relative positions.	81
5.30	Two-dimensional trajectory of C9. The thick black line is reconstructed from the polynomial fits in x and y direction. The white circles are spaced at intervals of 1 year, indicating the change of component position with time.	81
5.31	Relative positions $x(t)$ and $y(t)$ of C10, dotted lines are the respective polynomial fits to the relative positions.	82
5.32	Two-dimensional trajectory of C10. The thick black line is reconstructed from the polynomial fits in x and y direction. The white circles are spaced at intervals of 1 year, indicating the change of component position with time.	83
5.33	Relative positions $x(t)$ and $y(t)$ of C11, dotted lines are the respective polynomial fits to the relative positions.	84
5.34	Two-dimensional trajectory of C11. The thick black line is reconstructed from the polynomial fits in x and y direction. The white circles are spaced at intervals of 1 year, indicating the change of component position with time.	84
5.35	Relative positions $x(t)$ and $y(t)$ of C12, dotted lines are the respective polynomial fits to the relative positions.	85
5.36	Two-dimensional trajectory of C12. The thick black line is reconstructed from the polynomial fits in x and y direction. The white circles are spaced at intervals of 1 year, indicating the change of component position with time.	86
5.37	Relative positions $x(t)$ and $y(t)$ of C13, dotted lines are the respective polynomial fits to the relative positions.	87
5.38	Two-dimensional trajectory of C13. The thick black line is reconstructed from the polynomial fits in x and y direction. The white circles are spaced at intervals of 1 year, indicating the change of component position with time.	87
5.39	Relative positions $x(t)$ and $y(t)$ of C14, dotted lines are the respective polynomial fits to the relative positions.	88
5.40	Two-dimensional trajectory of C14. The thick black line is reconstructed from the polynomial fits in x and y direction. The white circles are spaced at intervals of 1 year, indicating the change of component position with time.	89

5.41	Relative positions $x(t)$ and $y(t)$ of C15, dotted lines are the respective polynomial fits to the relative positions.	90
5.42	Two-dimensional trajectory of C15. The thick black line is reconstructed from the polynomial fits in x and y direction. The white circles are spaced at intervals of 1 year, indicating the change of component position with time.	90
5.43	Relative positions $x(t)$ and $y(t)$ of C15a, dotted lines are the respective polynomial fits to the relative positions.	91
5.44	Two-dimensional trajectory of C15a. The thick black line is reconstructed from the polynomial fits in x and y direction. The white circles are spaced at intervals of 1 year, indicating the change of component position with time.	91
5.45	Relative positions $x(t)$ and $y(t)$ of C16, dotted lines are the respective polynomial fits to the relative positions.	92
5.46	Two-dimensional trajectory of C16. The thick black line is reconstructed from the polynomial fits in x and y direction. The white circles are spaced at intervals of 1 year, indicating the change of component position with time.	93
5.47	(a) Relative positions $x(t)$ and $y(t)$ of C17, dotted lines are the respective polynomial fits to the relative positions. (b) Two-dimensional trajectory of C17. The thick black line is reconstructed from the polynomial fits in x and y direction. The white circles are spaced at intervals of 1 year, indicating the change of component position with time.	93
5.48	(a) Relative positions $x(t)$ and $y(t)$ of C18, dotted lines are the respective polynomial fits to the relative positions. (b) Two-dimensional trajectory of C18. The thick black line is reconstructed from the polynomial fits in x and y direction. The white circles are spaced at intervals of 1 year, indicating the change of component position with time.	94
5.49	(a) Relative positions $x(t)$ and $y(t)$ of C19, dotted lines are the respective polynomial fits to the relative positions. (b) Two-dimensional trajectory of C19. The thick black line is reconstructed from the polynomial fits in x and y direction. The white circles are spaced at intervals of 1 year, indicating the change of component position with time.	95
5.50	(a) Relative positions $x(t)$ and $y(t)$ of C20, dotted lines are the respective polynomial fits to the relative positions. (b) Two-dimensional trajectory of C20. The thick black line is reconstructed from the polynomial fits in x and y direction. The white circles are spaced at intervals of 1 year, indicating the change of component position with time.	95
5.51	Fitted trajectories of the jet components which are traced beyond 5 mas from the core.	96
5.52	Fitted trajectories of jet components (C6–C16) at separations less than 5 mas from the core.	97

5.53	Fitted trajectories of jet components (C4–C20) at separations less than 1 mas from the core. The dashed blue lines correspond to the fitted trajectories of C4, C5, C6, C8, and C9. The red colored line corresponds to C7.	98
5.54	Trajectories of components C4 – C20 within 1 mas from the core, positions of components ejected before 1996 (C4 – C9) are plotted in black circles and positions of components ejected after 1995 (C10 – C20) are drawn in red circles.	98
5.55	Plot of position angles the jet features (C4–C19, without C15a) at a separation of 0.5 mas from the core in chronological order. In order to maximize the number of measurements at 0.5 mas, observations at 22 (point) and 43 GHz (square) are combined. A sinusoidal function with a period of 14.5 years is plotted as a guiding line for possible oscillations.	99
5.56	Residual patterns in the trajectories of features C8, C9, C10, C12, and C16 after subtraction of the respective polynomial fits.	101
5.57	FWHM of all fitted Gaussian components plotted against their respective radial distance from the core. Linear fits are indicated by orange lines, with the slopes of 0.2425 ± 0.0072 for radial separations from 0 to 4 mas and 0.555 ± 0.023 for radial separations > 4 mas.	102
5.58	Jet opening angles at 15.4 GHz plotted against radial separation from the core. The orange dashed line represents the best fit, a 4th order polynomial, to the observed scatter between 1 and 10 mas. Red triangles are weighted averages of that particular region.	103
5.59	Component size evolution of C8, C9, and C10 at 15.4 and 22.2 GHz. The dotted lines indicate the lower and upper envelope of the size expansion. The transverse brightness profiles predicted from the Kelvin-Helmholtz instability are indicated by inlets, denoting the expected shapes.	104
5.60	Distribution of kinematic parameters. The top left panel shows the distribution of the component speeds β_{app} , the top right panel the distribution of the Lorentz factors Γ_{var} , the bottom left panel the distribution of the Doppler factors δ_{var} , and the bottom right panel the distribution of the viewing angles θ_{var} . The median values for β_{app} , Γ_{var} , δ_{var} , and θ_{var} are 12.5 c, 14.1, 15.6, 3.8°.	106
5.61	Evolution of the Lorentz factors Γ for select components required to represent the observed apparent motion described by the fitted trajectories in Section 5.2, assuming a constant viewing angle $\theta = 5^\circ$. The calculations are ended when the limits listed in Table 5.5 are reached.	108
5.62	Evolution of jet kinematic parameters for the case of $\Gamma = \text{const}$ for fast (a) and slow (b) jet components. The four panels of each plot show, the Lorentz factor Γ (top left), the distance travelled in the jet frame (top right), the Doppler factor δ (bottom left), and the viewing angle θ (bottom right).	110

- 5.63 Evolution of jet kinematic parameters for the case of $\Gamma_{\min}(t)$, ie. variable Γ and θ . The four panels of each plot show, the Lorentz factor Γ (top left), the distance traveled in the jet frame (top right), the Doppler factor δ (bottom left), and the viewing angle θ (bottom right). 111
- 6.1 γ -ray counterpart localizations together with the positions of the radio counterparts of the three candidate sources. Crosses mark the radio positions of 3C 345, NRAO 512 and B3 1640+396. The large dotted orange circle denotes the 95% confidence error localization of EGR J1642+3940 (Casandjian & Grenier 2008). The dashed blue ellipse denotes the 95% confidence error localization of 1FGL J1642.5+3947 (Abdo et al. 2010a). The two solid green ellipses denote the 95% confidence error localization of 3C 345 and NRAO 512 presented here. The confusing source Mrk 501 is 2.5° east (left) and 4C +38.41 is 2.1° southwest of the field center. 118
- 6.2 Twenty-month γ -ray spectra of 3C 345 and NRAO 512. The red curve represents the obtained respective average power-law fits. The red dots correspond to the pivot energies listed in Table 6.2. 118
- 6.3 γ -ray light curves of 3C 345 and NRAO 512 for the first 20 months of *Fermi*-LAT monitoring, obtained through fitting two point-source model components with power-law spectra to the region of interest placed at the respective counterpart positions. Values were determined from integrating observations over 30 days within an energy range of 0.1 – 300 GeV. Blue filled circles are values obtained for 3C 345, red open circles are values for NRAO 512. Values with downward arrows represent 2σ upper limits shown in place of detections with low significance ($TS < 5$). The dashed lines plot the respective 20-month average γ -ray source flux. Errors are statistical only. 119
- 6.4 Multi-wavelength light curves of 3C 345 for the 20-month period discussed here, from top to bottom for: a) γ rays observed by *Fermi* LAT between 0.1 and 300 GeV, values (filled circles) are five-day integrated, 2σ upper limits for five-day integrations are shown as light-blue crosses with downward arrows where $TS < 5$. Dark-blue filled circles have a $TS > 25$, the others are in the range $5 < TS \leq 25$. In contrast to Figure 6.3, the γ -ray emission was fitted by a single power-law component placed at the position of 3C 345. b) X-rays observed by *Swift* XRT between 0.3 and 10 keV. c) optical (R-band) observations performed by GASP and SAO. d) millimeter radio observations by the SMA at 230 GHz. The two orange downward arrows on top indicate the observation epoch for which a new feature was detected in the pc-scale radio jet of 3C 345, see Section 6.4 and Schinzel et al. (2010). Three dominant flare events of high significance observed on two-day time scales were labeled with I, II, and III. Several weaker events were identified and labeled with numbers from 1 – 6. 121

- 6.5 Correlation between the five-day integrated γ -ray light curve and the optical (top) and radio (bottom) light curves of 3C 345. The correlation is obtained by calculating the discrete correlation function (DCF) with ten-day binning. A positive time-lag corresponds to the γ -ray variations preceding the variations in the other two bands. The significance of the correlation is illustrated by 3σ (99.7%) significance contours calculated from simulated, uncorrelated data with different slopes, β , of the power spectral density (PSD). The contours are drawn for the PSD slopes $\beta = 1.0, 1.5, 2.0,$ and 2.5 (indicated by progression of colors, from light gray to black). For the simulated data, values of the correlation coefficient exceeding ± 1 are an inherent feature of the method, resulting from differences in overlap of the time series at different time lags (cf. Edelson & Krolik 1988; Timmer & Koenig 1995, and the description of the applied method in Section 6.5). 127
- 6.6 Raw power-spectral densities for the γ -ray, optical, and radio light curves. The corresponding slopes have a value of β of, -1.1 ± 0.3 (γ -ray), -0.71 ± 0.36 (optical), and 0.29 ± 0.29 (radio). 128
- 7.1 VLBA image of the total brightness distribution of 3C 345 at 43.2 GHz made from observations on Nov. 30, 2009. Open crossed circles show the FWHM of eight Gaussian components applied to fit the structure observed. The shaded ellipse, in the lower left corner, represents the FWHM of the restoring beam. The image peak flux density is 2.1 Jy beam^{-1} and the RMS noise is 1 mJy beam^{-1} . The contour levels are $(-0.15, 0.15, 0.3, 0.6, 1.2, 2.4, 4.8, 9.6, 19, 38, 77) \%$ of the peak flux density. Here the nuclear region is modeled by two circular Gaussian components (D, C22) identified as the best representation of the observed brightness distribution. 132
- 7.2 Reduced χ^2 parameters of the modelfit representations of the core region. The top panel shows the resulting χ_{reduced}^2 values of 1E, 2C and 3C Gaussian models normalized to the value of the 1C Gaussian representation. The two horizontal lines mark the limit below which, for the corresponding model, a significant improvement (68% confidence) over 1C is given (0.77, 0.82). Similarly the middle panel shows the χ_{reduced}^2 values for 2C and 3C normalized to that of 1E. The horizontal line marks the significant improvement level compared to 2C (0.91). The bottom panel normalizes the χ^2 values to that of 2C. The dashed line plots the significant improvement limit for 3C (0.86). 135
- 7.3 Evolution of the radial separations from the core of components C23, C22, C21, C20 and C19. C23-C20 are related to the radio variability since 2008, C19 is related to a previous radio flare observed in 2007. The lines are the results of polynomial fits to $x(t)$ and $y(t)$ directions separately. The dashed lines are the results of linear fits to $x(t)$ and $y(t)$ to determine ejection epochs and speeds for the two cases discussed. . . 136

- 7.4 Component brightness temperatures against radial separation from the VLBI core (D), representing the emission intensity gradient along the jet. Points with arrows are 1σ upper limits. Two lines are fitted to the data to determine the power law indices ϵ ($T_b \propto d_{\text{jet}}^{-\epsilon}$) from the data, the fit from 0.1 to 0.3 mas yields $\epsilon_1 = 0.95 \pm 0.69$ and 0.3 – 0.65 mas yields $\epsilon_2 = 4.11 \pm 0.85$ 139
- 7.5 *top: Fermi* LAT 7-day binned γ -ray light curve of 3C 345 for the energy range of 0.1-300 GeV. *bottom: VLBA* 7 mm component flux densities for the model-fitted VLBI core and inner jet, represented by up to five circular Gaussian (D, C23, C22, C21, C20). The component labeled D is the east-most component (see Figure 7.1) and represents the compact “core” or base of the jet. The black curve plots the sum of the flux densities of all four components. 140
- 7.6 Long-term trends of the radio jet, radio core flux densities, optical R band flux (Schinzel et al. 2010) and the γ -ray flux relative to their respective mean values (radio jet: 3.6 Jy, radio core: 1.5 Jy, optical R: 16.6^m ($7.7 \cdot 10^{-4}$ Jy), γ -ray: $1.8 \cdot 10^{-7}$ ph cm $^{-2}$ s $^{-1}$). The trend was extracted fitting cubic splines with 0.4 year bins. The relative radio flux density was scaled by a factor of 2:1 with respect to the relative γ -ray flux, the optical flux density was scaled by a factor of 4:1, and the data points match the sampling of the original light curves. 142
- 7.7 *Top panel (a):* The γ -ray light curve of 3C 345 for the energy range of 0.1-300 GeV, each data point is integrated over a period of 7 days. *Bottom panel (b):* Evolution of the radial separations from the core of newly appeared components since 2008. The orange dashed lines are linear fits to the data, representing the radial motion of the components. The red dashed line, passing the core around 2010 is indicating a new component not yet observed. The gray horizontal lines indicate the suggested positions of standing features (the center line is the average value, with one line each on top and below, indicating the obtained spread. Thick upward arrows indicate the times at which a feature passes 0.1 mas. Thin arrows indicate times at which features pass the first and second standing features, following the proposed scheme discussed in the text. 143
- 7.8 Distances calculated under the assumption of interaction of moving with a standing feature, producing γ -ray flares during passage. The errors on the positions are determined by the statistical uncertainty of the speed and time between flares. The uncertainty of the standing feature at 0.1 mas, used as reference, is ignored. The numbers refer to the γ -ray event labels in Figure 7.7. The grayscale boxes visualize the scatter of the calculated values. The dashed arrows indicate the radial motion of the individual moving features. The red dotted line indicates the predicted radial motion of a new jet component. 144

- 7.9 Global 3mm-VLBI array image of the total brightness distribution of 3C 345 at 86.2 GHz made from observations around May 7th, 2010. Open crossed circles show the FWHM of five Gaussian components fitting the structure observed. The parameters of these components are listed in Table 7.3. The shaded circle in the lower left corner represents the FWHM of the restoring beam and the map was reconstructed using uniform weighting. The image peak flux density is $0.38 \text{ Jy beam}^{-1}$. The contour levels are (-6, 6, 12, 24, 48, 96)% of the peak flux density. Negative contours are indicated by dashed lines. The bar in the lower left corner indicates an apparent size scale of 0.7 pc. *Courtesy of Marscher, Marti-Vidal, Krichbaum, et al., providing the calibrated GMVA dataset.* 145
- B.1 VLBA maps of the total brightness distribution of 3C 345 obtained from observations at 5.0 GHz between 1995 and 2004. Red open crossed circles/ellipses show the FWHM of Gaussian components fitting the structure observed. The parameters of these components are listed in Table B.1. The contour levels correspond to (-0.1, 0.1, 0.2, 0.4, 0.8, 1.6, 3.2, 6.4, 13, 26, 51)% of the peak flux density. Negative contours are indicated by dashed lines. The grey shaded ellipse on the left of each map represents the FWHM of the restoring beam. 187
- B.2 VLBA maps of the total brightness distribution of 3C 345 obtained from observations at 8.4 GHz between 1995 and 2004. Red open crossed circles/ellipses show the FWHM of Gaussian components fitting the structure observed. The parameters of these components are listed in Table B.1. The contour levels correspond to (-0.2 0.2 0.4 0.8 1.6 3.2 6.4 13 26 51)% of the peak flux density. Negative contours are indicated by dashed lines. The grey shaded ellipse on the left of each map represents the FWHM of the restoring beam. 189
- B.3 VLBA maps of the total brightness distribution of 3C 345 obtained from observations at 15.4 GHz between 1994 and 2010. Red open crossed circles/ellipses show the FWHM of Gaussian components fitting the structure observed. The parameters of these components are listed in Table B.1. The contour levels correspond to (-0.2 0.2 0.4 0.8 1.6 3.2 6.4 13 26 51)% of the peak flux density. Negative contours are indicated by dashed lines. The grey shaded ellipse on the left of each map represents the FWHM of the restoring beam. 191
- B.4 VLBA maps of the total brightness distribution of 3C 345 obtained from observations at 22.2 GHz between 1995 and 2010. Red open crossed circles/ellipses show the FWHM of Gaussian components fitting the structure observed. The parameters of these components are listed in Table B.1. The contour levels correspond to (-0.3 0.3 0.6 1.2 2.4 4.8 9.6 19 38 77)% of the peak flux density. Negative contours are indicated by dashed lines. The grey shaded ellipse on the left of each map represents the FWHM of the restoring beam. 200

-
- B.5 VLBA maps of the total brightness distribution of 3C 345 obtained from observations at 23.8 GHz between 2009 and 2010. The contour levels correspond to (-0.2 0.2 0.4 0.8 1.6 3.2 6.4 13 26 51)% of the peak flux density. Negative contours are indicated by dashed lines. The grey shaded ellipse on the left of each map represents the FWHM of the restoring beam. 203
- B.6 VLBA maps of the total brightness distribution of 3C 345 obtained from observations at 43.2 GHz between 1997 and 2010. Red open crossed circles/ellipses show the FWHM of Gaussian components fitting the structure observed. The parameters of these components are listed in Table B.1. The contour levels correspond to (-0.3 0.3 0.6 1.2 2.4 4.8 9.6 19 38 77)% of the peak flux density. Negative contours are indicated by dashed lines. The grey shaded ellipse on the left of each map represents the FWHM of the restoring beam. 204

List of Tables

4.1	Overview and basic characteristics of newly analyzed VLBA observations in chronological order.	27
4.2	Radio positions and redshifts of candidate γ -ray counterparts for 0FGL J1641.4+3939 in October 2009 (Reyes & Cheung 2009).	41
4.3	UV/optical observations of 3C 345, NRAO 512 and B3 1640+396 conducted by <i>Swift</i> UVOT and the 200-mm telescope of Tzec Maun observatory.	42
4.4	Overview and results of <i>Swift</i> / <i>XRT</i> observations.	43
5.1	Selected observations and jet components for core-shift analysis and their corresponding core-shift values.	51
5.2	Weighted averages of relative core-shifts for each group of frequency pairs, calculated from the values listed in Table 5.1.	56
5.3	Polynomial fits to the component trajectories.	64
5.4	Measured and derived physical parameters for radio emission regions in the jet of 3C 345.	107
5.5	Limits of constant component values.	109
5.6	Derived estimates for the core magnetic field and distance to the central engine.	112
6.1	Localization summary of different energy cuts for single a point source 1FGL J1642.5+3947.	116
6.2	The unbinned spectral likelihood results for the point-source localizations and spectra of 3C 345 and NRAO 512.	119

6.3	Characteristics of prominent γ -ray events during the first 20 months of the <i>Fermi</i> -LAT observations.	122
6.4	<i>Swift</i> -XRT observations after the reported flare in October 2009 of the three candidate sources (3C 345, NRAO 512 and B3 1640+396).	123
6.5	Quasi-simultaneous optical observations of 3C 345, NRAO 512 and B3 1640+396 conducted by <i>Swift</i> UVOT and the 200-mm telescope of Tzec Maun observatory.	123
7.1	Summary of VLBA Observations to investigate the recent activity of 3C 345 at 43.2 GHz.	133
7.2	Measured and derived physical parameters for radio emission regions in the inner jet ≤ 0.7 mas (4.6 pc).	137
7.3	Model components for global 3mm-VLBI array (GMVA) image from 2010-05-07, shown in Figure 7.9.	146
A.1	Historic Observations.	155
B.1	Historic Observations.	161
C.1	GASP optical R band observations of 3C 345 between 2008 and 2010.	211
C.2	SMA 1 mm (230 GHz) observations of 3C 345 between 2008 and 2010.	220
C.3	Multiband photometry of 3C 345, using the Zeiss-1000 telescope of the Special Astrophysical Observatory, Russia.	221

Preface

The quasar 3C 345 is one of the best and most closely monitored extragalactic radio sources, with its milliarcsecond structure studied over the past decades, with very long baseline interferometry (VLBI). This thesis project started with an objective to combine all VLBI observations from the past three decades, in order to create a consistent database uniquely suitable for studying the long-term evolution of its parsec-scale jet and broadening our understanding of relativistic jets and central regions of active galactic nuclei.

However, in 2008, the scope of the project was broadened to the opportunity to monitor the beginning of a new active period of 3C 345. As a consequence of this, a total of 120 hours of VLBA telescope time have been obtained and used for this thesis. These observations were successfully combined with the public release of the first year γ -ray monitoring data of *Fermi*/LAT. This provided a unique framework for identification of γ -ray emission from 3C 345 and lead to the investigation of a relation between the evolution of the radio jet and production of high-energy emission in 3C 345. The radio and γ -ray observations have been complemented by optical, UV, and X-ray observations, including the *Swift* satellite, providing additional information about the non-thermal emission processes.

As a result of all those efforts a much better understanding of physical processes in the parsec-scale jet of 3C 345 was achieved, addressing in particular the question of production of high-energy continuum emission and the long-term evolution of the relativistic jet. The following discussion is structured as follows:

- Chapter 1 provides a brief introduction to active galaxies, relativistic jets, introducing their taxonomy and general observational properties.
- Chapter 2 presents the basic ideas for a physical theory of relativistic jets, discussing their formation, structure, and evolution; introducing the concepts of shocks and instabilities, as well as opacity and quasi-periodic activity.
- Chapter 3 introduces the target object, flat spectrum radio quasar 3C 345 and its radio, optical, and high-energy properties.
- Chapter 4 provides background information on the multi-wavelength observations performed in the course of this dissertation and on archival data processing. It

discusses the instruments used and data reduction techniques applied.

- Chapter 5 presents results of 31 years of high angular resolution observations of 3C 345, where long-term variability of the parsec-scale jet is investigated, with a particular focus on core-shifts, kinematics, instabilities, and physical parameters of the jet.
- Chapter 6 presents the results that lead to the first identification of γ -ray emission from 3C 345, combining 20 months of γ -ray monitoring data with that of simultaneous multi-wavelength monitoring.
- Chapter 7 completes the picture, with an investigation of the origin of the observed high energy emission from 3C 345, identifying the parsec-scale jet as the main driver of multi-wavelength variability and establishing a working phenomenological scenario for the production of γ -ray flares.
- Chapter 8 provides a summary of the here presented results and gives some thoughts on possible future investigations.

CHAPTER 1

Introduction to Flat Spectrum Radio Quasars (FSRQ)

The most powerful and persistent (typical activity time: 10^8 - 10^9 years) energy sources in the Universe are active galaxies. They are responsible for a major fraction of non-thermal continuum emission produced in the Universe. They are the most significant extragalactic foreground sources of the diffuse cosmic microwave background (Planck Collaboration et al. 2011) and are the main contributors to the extragalactic γ -ray sky (Abdo et al. 2010b). At their centers, all galaxies harbor at least one super massive black hole (SMBH), which are the most massive objects known in the entire Universe. Typically, SMBH of AGN have a mass of $10^6 - 10^{10}$ solar masses (eg. Eisenhauer et al. 2005). They accrete material from a surrounding debris disk, providing the required energy for the formation of relativistic outflows perpendicular to the plane of the disk. Some fraction of this outflowing material is accelerated up to relativistic speeds (close to the speed of light) and becomes strongly collimated. These outflows are commonly referred to as jets and are introduced in more detail in Section 1.2.

In the following, a brief summary on the classification and observational properties of active galaxies, their relativistic outflows and multi-wavelength emission are given. More detailed discussions of the current state of affairs regarding active galaxies are provided by a range of excellent textbooks. A detailed overview on active galaxies, their taxonomy and unified models is given by Peterson (1997) and Krolik (1999). Hughes (1991) discusses the properties of astrophysical jets and a good overview on the emission mechanisms with a particular focus on high energy astrophysics is found in Longair (2011).

1.1 Active Galaxies and Quasars

The emission from a typical active galaxy is dominated by a very compact region at its center, which in observations at all wavelengths is contributing a similar or larger amount of emission than is produced by its stars and dust. These regions are referred to as active galactic nuclei (AGN). The entire population of AGN can be divided phenomenologically into two general subgroups, Seyfert galaxies and quasars. In Seyfert galaxies, the emission from all stars equals the emission from its nuclei, whereas the nuclei of quasars outshine the emission of stars by at least a factor of 100. Seyfert galaxies were discovered before quasars and provided the first evidence for galaxies to harbor an extremely heavy and dense region at their centers (Burbidge et al. 1963).

Quasars are highly variable star-like objects and were initially mistaken to be variable stars. However, soon after it was discovered that many of those were in fact bright objects at radio wavelengths it became clear that these objects were of extragalactic origin. The name “quasar” was coined in the 1960s and is an abbreviation for “quasi-stellar radio source”. Quasars are found at almost all distance scales, which makes them especially suited for cosmological studies. However, it soon became clear that not all quasars were radio bright objects, in fact there seems to be a subclass of “radio-quiet quasars” which makes $\sim 90\%$ of the initially identified total quasar population (Sandage 1965; Peterson 1997). Generally, the class of radio-loud quasars are also called “blazars” (blazing quasi-stellar objects) and form the extreme upper end of the quasar population. They are divided into the group of optically violent variables, also called flat spectrum radio quasars (FSRQs), and BL Lac type objects. Separating intrinsically powerful FSRQs from the intrinsically weak BL Lac type objects.

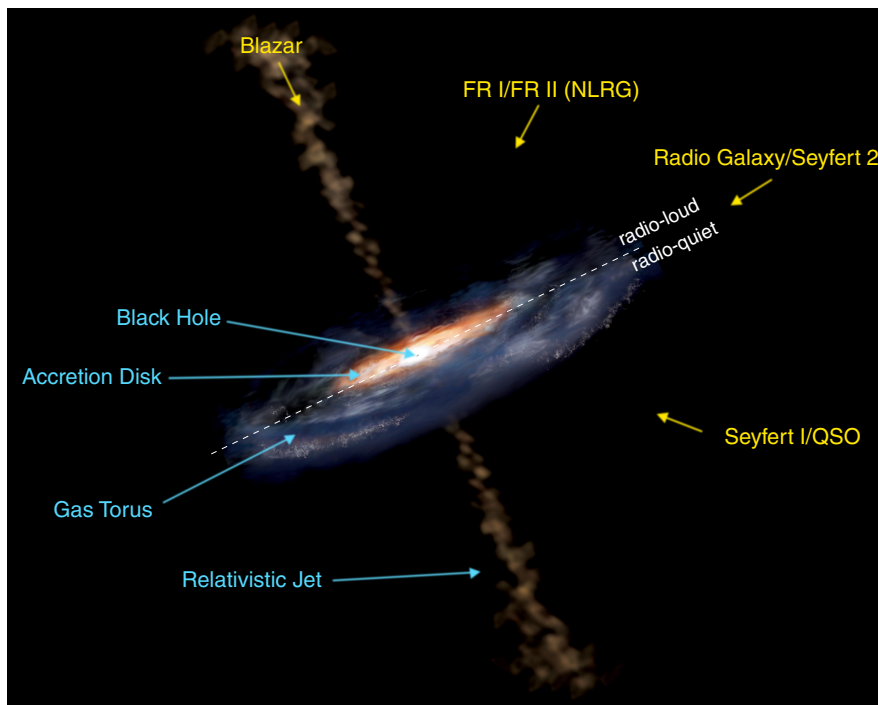


Figure 1.1: Illustration of an AGN and the viewing angle dependent sub-classes following the unification scheme. *Image credit: NASA/Aurore Simonnet, Sonoma State University.*

Eventually, with the definition of additional subclasses of AGN and the discovery of superluminal motion, it was realized that intrinsically they are not very different from each other, but the orientation at which the AGN is seen plays a very important role. This led to the proposition of a unification scheme for AGN, illustrated in Figure 1.1 (Antonucci 1993; Lobanov & Zensus 2007).

1.2 Relativistic Outflows – Jets

AGN are powered by a central engine, a black hole in combination with an accretion disk, providing an efficient mechanism ($\sim 10\%$ of the rest energy of infalling matter; Peterson 1997) to convert potential and kinetic energy from in-falling matter into radiation and leading to the formation of bi-polar relativistic outflows, jets. The formation of jets is not limited to AGN, at smaller scales, stellar mass black holes and neutron stars form jets as well. Jets are predominantly observed at radio wavelengths, where high angular resolution observations at the milliarcsecond scale are routine, but jets have also been observed in a few cases of nearby objects at optical and X-ray wavelengths.

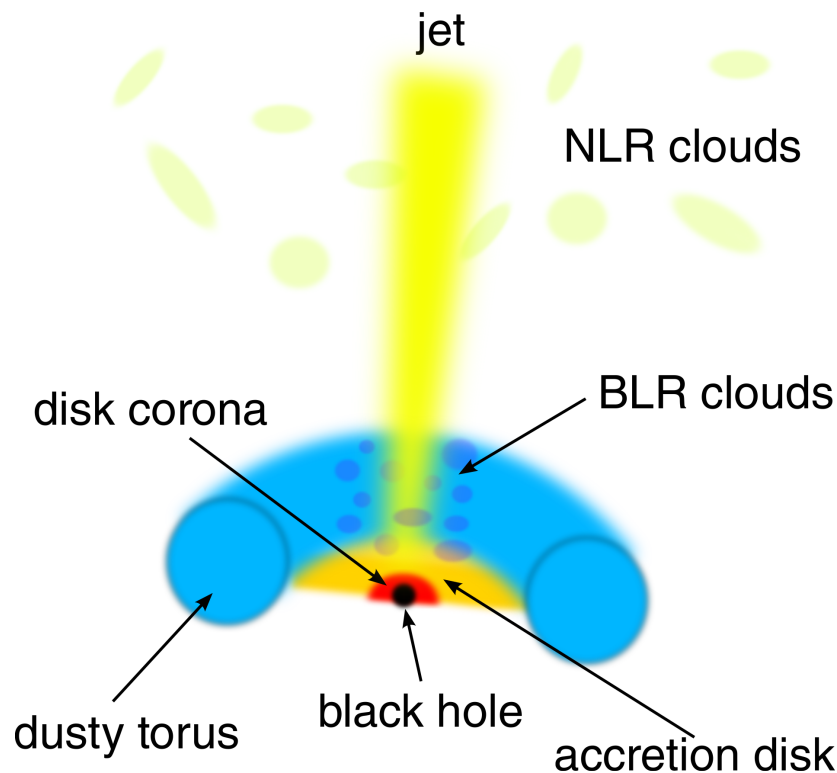


Figure 1.2: The scheme of a radio-loud AGN jet (not to scale).

The inner structure of AGN jets is illustrated in Figure 1.2. The accretion disk is surrounded by a thick dusty torus, which obscures the accretion disk if seen from the side. The jet is launched from the accretion disk and passes through the disk corona and the thick broad line region (BLR) clouds, named after broad emission lines observed from this region. After it has exited the broad line and torus region it reaches the narrow line region (NLR) clouds, which in comparison to the BLR have a much lower density. Each of these regions has characteristic observational and physical

properties. The transition region between the BLR and NLR is most likely the origin for most of the observed relativistically beamed, highly variable emission observed predominantly at NIR, optical and high energies. This zone is sometimes also referred to as the “Blazar zone”. The exact location, dimensions and basic properties of this region are very uncertain. Knowledge of the location and mechanism of the observed continuum emission from AGN is of utmost importance in high energy astrophysics, providing insights into the powerful physical processes at work.

1.3 Multi-wavelength Emission

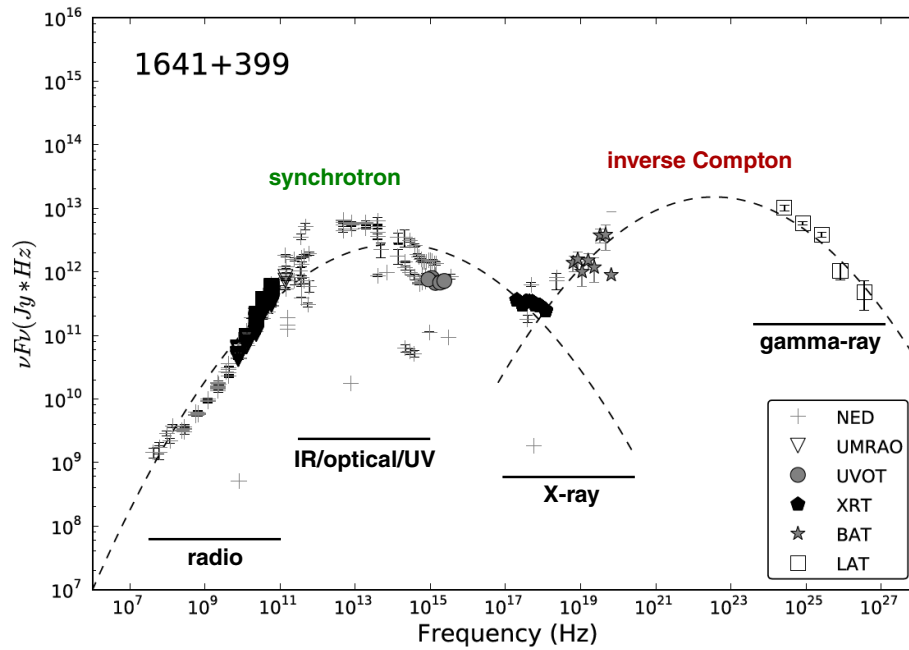
AGNs are one of the few types of objects that truly emit across the entire electromagnetic spectrum, providing complementary information about its inner workings at each wavelength. The broad band spectral energy distribution from radio to γ -rays for the blazar 3C 345 is shown in Figure 1.3. The non-thermal emission from blazar jets dominates the apparent spectral energy distribution (SED). The SED of a blazar consists of two broad components: one showing a peak between far-IR and X-ray wavelengths and the other peaks at γ -ray energies. The low energy component is due to synchrotron radiation produced by the electrons spiraling along the magnetic field lines in the jet, the high energy peak is most likely produced by inverse Compton emission, where relativistic electrons in the jet up-scatter lower energy photons.

Synchrotron Emission (Radio, Optical, X-rays)

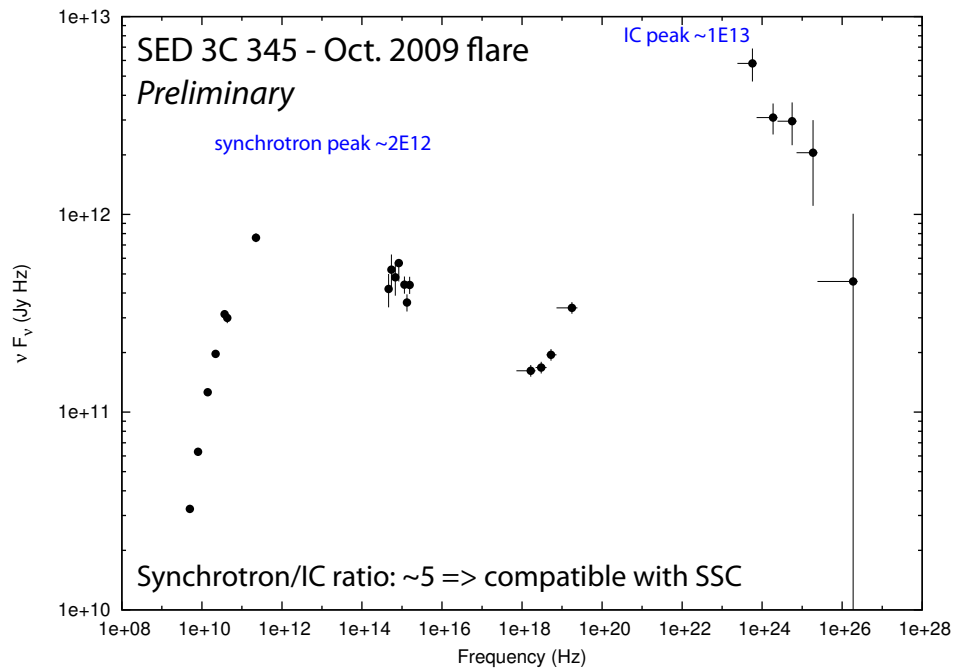
The low energy peak of the multi-wavelength emission of blazars is due to synchrotron emission. The observed synchrotron emission is generated within the jet, typically at the outer edge or outside of the BLR. The shape of the observed spectrum and the wavelength of the synchrotron peak provide information about the energy output of the jet and provide a tool to classify blazars. FSRQs typically have a synchrotron peak frequency of $< 10^{14.5}$ Hz, whereas BL Lacs can span the entire range from radio to X-rays. They are usually separated in three different groups, the low (LSP/LBL), intermediate (ISP/IBL), and high (HSP/HBL) synchrotron peak BL Lacs (eg. Meyer et al. 2011). The connection between synchrotron peak frequency and the power of the jet is usually referred to as the Blazar sequence (Fossati et al. 1998), however its interpretation in the context of the unified model and radio-loud vs. radio-quiet AGN is still debated.

Inverse-Compton Emission (X-rays, Gamma-rays, TeV)

The physical origin of the high energy component of the AGN continuum is not entirely settled yet. The most likely explanation for this component is inverse Compton scattering of low-energy photons by the same relativistic electrons that are responsible for the lower energy synchrotron emission. In the case of this “leptonic” model, the main controversy surrounds the origin of the seed photons and the site of the γ -ray emission. Possible sources of seed photons are the broad line region (Sikora et al. 1994), accretion disk (Dermer & Schlickeiser 1993), dust torus (Błażejowski et al. 2004) or



(a) SED of 3C 345 from archival observations combined with almost simultaneous radio, UV/optical, X-ray, and γ -ray observations, obtained from Chang (2010).



(b) SED of 3C 345 from a high activity state in October 2009 (also see Chapter 7). The data were collected simultaneously, involving radio, optical, UV, X-ray and γ -ray observatories.

Figure 1.3: Spectral energy distribution of 3C 345.

synchrotron radiation of the jet itself (Jones et al. 1974; Ghisellini 1989). In addition to this, “hadronic” models were proposed, where relativistic protons interact with photons initiating particle decay cascades, which are able to reproduce similar emission spectra to what is observed in blazars (Mücke & Protheroe 2001; Böttcher et al. 2002).

The biggest difficulty leading to the rejection of some of the suggested models lies in the number of free parameters required to fit the observed SEDs. In order to be able to improve our understanding of the observed high energy emission from AGNs, additional information is needed, providing limits for the parameter space of proposed models. For example through localization of the high energy emission sites and/or improving constraints on physical parameters of the emission regions, such as lower and upper limits on kinematics (Lorentz/Doppler factors) and emission power.

CHAPTER 2

Physical Theory of Jets

This chapter provides a brief review of the basic physical principles forming the foundation for a physical theory of relativistic jets. Section 2.1 discusses briefly the physical conditions leading to the formation of jets. Section 2.2 provides a brief account of shock theory and discusses possible types of jet instabilities. Section 2.3 presents an introduction to opacity effects in the nuclear regions of AGN. Section 2.4 discusses measurements and interpretation of superluminal motions observed in jets. Section 2.5 gives a brief account of factors leading to quasi-periodic variations of continuum emission in AGN.

2.1 Formation and Structure of Jets

It is understood that jets are formed as a consequence of rapidly spinning black holes surrounded by accretion disks. The jets are powered by the accretion process, which extracts energy via magnetic torque as Poynting flux (Sikora et al. 2005). The jets are collimated by the magnetic field and accelerated through conversion of magnetic energy to bulk kinetic energies. The jet emission can be driven by the kinetic energy, e.g. the dissipation of shocks and/or reconnection events of magnetic field lines, similar to what is observed at our Sun (Blandford & Znajek 1977; Blandford & Rees 1978; Blandford & Königl 1979). Figure 2.1 illustrates these main ingredients leading to the formation of relativistic outflows within a region of ~ 200 Schwarzschild radii.

Black holes alone are not able to support the magnetic fields required to form such powerful outflows. The black hole magnetospheres have to be anchored in the accretion flow (Blandford & Znajek 1977; Punnsly & Coroniti 1990), either through open (eg. Garofalo 2009) or closed (eg. Uzdensky 2005) magnetic field lines. However, only a magnetosphere with open magnetic field lines is expected to form jets, extracting angular momentum from the black hole through a Poynting flux jet (energy flux dom-

inated), whereas conditions for jet formation with a closed magnetosphere are more restrictive. It seems that closed magnetospheres are most likely to form relativistic outflows only if the spin of the black hole were opposite to the rotation of the accretion disk, so called retrograde black hole systems. If jets were mainly driven by closed magnetic field lines, then the power of jets would mainly depend on the spin of the black hole (Meier 2011).

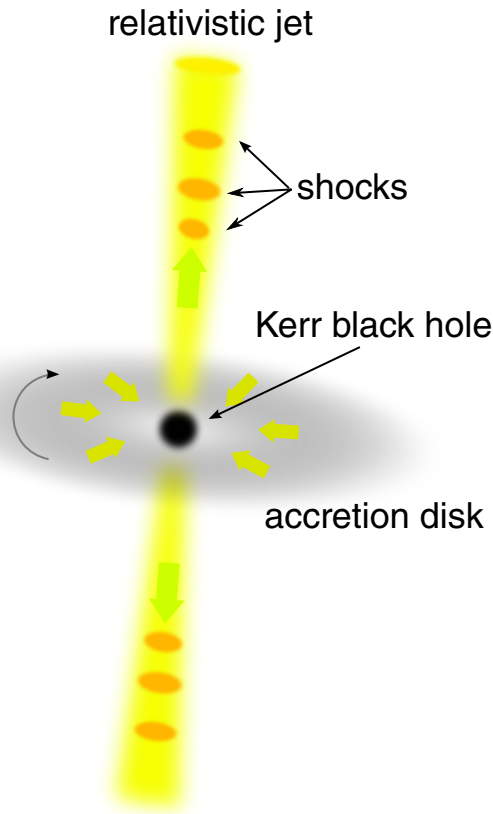


Figure 2.1: Schematic diagram of the required ingredients, a rotating compact object with accretion disk, to form relativistic outflows.

The role of the magnetized rotating accretion disk is somewhat unclear. It could provide the required conditions to form relativistic outflows if magnetic field lines passing through the accretion disk couple to the plasma in the accretion disk and, through magnetic stress, is able to transfer angular momentum from the disk to the jet (Blandford & Payne 1982; Vlahakis et al. 2000; Vlahakis & Königl 2003). The powering of a jet solely by the accretion disk is still highly debated, especially in respect to stellar size black holes, where spin coupling does not seem to be effective (Meier 2011).

The relativistically moving jet plasma itself is most likely dominated by electrons and positrons (Wardle et al. 1998; Hirotani 2005), with protons not entirely ruled out (Celotti & Fabian 1993). After the formation of the plasma flow close to the central engine, it will be collimated and accelerated in the presence of strong magnetic fields. The collimation zone spans a distance scale of $\sim 10^3$ Schwarzschild radii, for which magnetic fields play a dominant role (cf. Komissarov et al. 2007; Porth & Fendt 2010). Blandford & Payne (1982) outlines the basic principles of magneto-hydrodynamic (MHD) jet launching. New more realistic general relativistic MHD simulations, compared to observational results, are going to provide deeper insights into the acceleration and collimation mechanisms of relativistic jets (McKinney 2006; McKinney & Blandford

2009). For a brief review of recent developments in the area of magnetic acceleration, see Lobanov (2010) and Komissarov (2011).

Beyond the magnetosonic horizon, the jet becomes causally disconnected from the central engine responsible for its creation (eg. Polko et al. 2010). At these distances the jets of many quasars are observable at milliarcsecond scales, which translate to parsec scales. Theoretical models (Clarke et al. 1986; Lind et al. 1989; Komissarov 1999) predict that around the disconnection point, the jet forms (re)collimation shock features, for which observational evidence is growing (eg. Cheung et al. 2007; Arshakian et al. 2010; León-Tavares et al. 2010; also see Chapter 6 and 7 of this thesis). In addition to these standing features, relativistically moving enhanced emission regions have been found and were followed in many AGN jets. A more detailed account of shocks and instabilities found in extended jets of quasars is given in Section 2.2.

2.2 Shocks and Plasma Instability

Early on in the theoretical studies of jets, relativistic shocks propagating down in a conical jet were proposed to explain the properties observed (Blandford & Rees 1978). The basic idea of such a jet model is depicted in Figure 2.2. For most extragalactic objects, the magnetosonic surface is beyond the reach of our observational instruments. At some distance from the magnetosonic surface, the jet becomes optically thin, depending on the observing frequency, and emission from the jet can be observed. The transition point from optically thick to optically thin is usually referred to as the radio core. The apparent location of the core depends on the observing frequency (Königl 1981). Enhanced emission regions observed downstream from the core are in most cases superluminally moving features of shocked, overdense plasma, most likely injected at the jet origin.

After the jet is launched, the flow accelerates, converting internal relativistic particle energy γ_e to bulk kinetic energy γ_j , following a powerlaw dependency $\gamma_j \propto \gamma_e \propto r^\epsilon$ ($\epsilon = \text{const.}$), where r is the distance from the central engine. The particle energy density distribution can also be approximated by a power law dependence,

$$N(\gamma_e) \approx N_0 \gamma_e^{-s}. \quad (2.1)$$

The parameter s is the particle energy spectral index. With a constant jet Lorentz factor of γ_j , and a jet viewing angle to the line of sight of θ , the jet geometry can be estimated by a conical expansion, with the radius following the same powerlaw as the bulk kinetic energy. Under the assumption of a constant jet opening angle, the magnetic field and particle density decrease with r following a power-law with the indices m and n (cf. Königl 1981; Marscher & Gear 1985; Lobanov 1996, 1998b). Königl (1981) determines a combination of $m = 1, n = 2$ to best describe the observed X-ray and synchrotron emission, which corresponds to the equipartition regime of jet particle and magnetic field energy densities.

The observed radio emission from the core of a compact jet is similar to that of an inhomogeneous synchrotron emitter. An excellent review of synchrotron radiation and synchrotron self-absorption is provided by Longair (2011). From synchrotron theory it can be shown that the synchrotron spectrum of a power-law distribution of electrons in

a plasma will have a maximum frequency ν_m , where the optical depth τ_m depends on the observed spectral index $S_\nu \propto \nu^\alpha$. Further discussion on the implications of opacity and magnetic field is provided in Section 2.3. Perturbations propagating through a steady jet lead to the formation of shocks. Particles crossing these shocks gain kinetic energy and the observed enhanced emission from these shocks is expected to be dominated by the plasma interacting with the shock front. The emission from these shocks evolves while propagating through the jet, passing through three fundamental evolutionary stages, which can be related to the dominating cooling process. These are the Compton, synchrotron and adiabatic stage and as a consequence of which ν_m evolves with time (see eg., Marscher & Gear 1985; Lobanov & Zensus 1999).

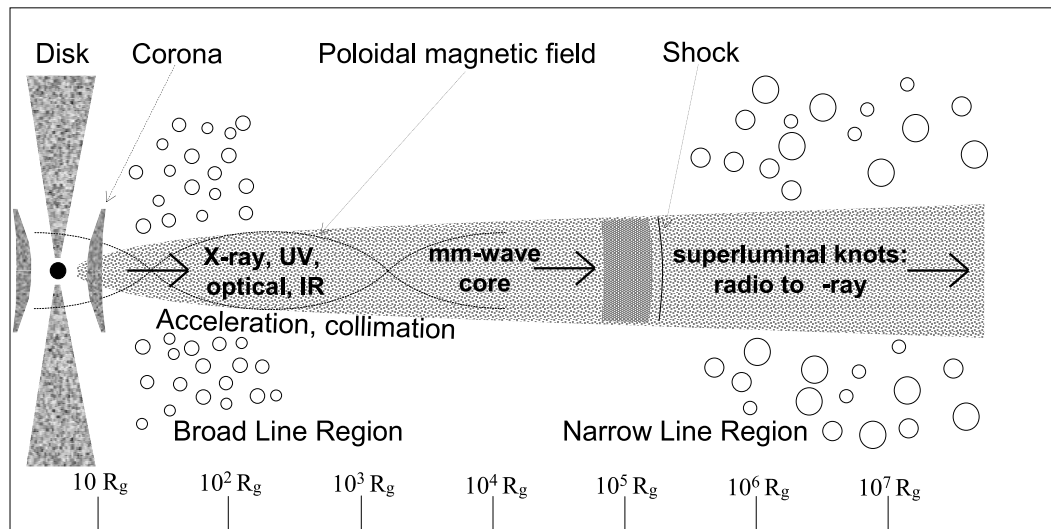


Figure 2.2: The basic outline of a simplistic relativistic jet model of a radio-loud AGN. The scale is logarithmic beyond 10 Schwarzschild radii (R_g). *Image credit: Lobanov (2007).*

Hydrodynamic simulations of a shock front passing through a steady relativistic flow (Agudo et al. 2001), revealed the formation of the shock front with a rarefaction (lower particle density) following it. The disturbances of the steady jet caused by the propagating shock leads to the formation of multiple conical shocks trailing the main shock front and even shocks that are able to travel in reverse direction to the original shock. These trailing shocks should manifest with different emission characteristics and large variations in observed velocities, compared to the perturbing shock (Agudo et al. 2001).

Close to the jet launching site, strong magnetic fields dominate and current driven instabilities are most likely to form. These instabilities form so called “kinks” in the flow or can constrict the flow. An axial magnetic field is able to prevent the growth of these, which can lead to the disruption of the jet. From recent simulations, Kink instabilities were shown to develop at distances over a few hundred R_g (McKinney & Blandford 2009), which is too small to be observable at VLBI scales. In the collimation and acceleration region, the relativistic jet begins to interact with the surrounding medium and in addition to current driven instabilities, Kelvin-Helmholtz (K-H) instabilities can form due to a contact discontinuity between the fast jet and the slow ambient medium, at parsec scales the K-H instabilities dominate. Perturbations in a cylindrical jet can be represented by a 2D wave equation. The azimuthal wave number n then describes the different modes of this wave, with $n = 0$ corresponding to the pinch mode,

$n = 1$ to helical, $n = 2$ to elliptical, $n = 3$ to the triangular mode, etc. (Hardee 1979, 2000). Figure 2.3 shows examples for the pinch and helical modes using hydrodynamic simulations. Depending on the type of boundary between the jet and the surrounding equal pressure medium, the observed waves consist of one fundamental, also called “surface” and multiple “body” modes having different radial structures, as depicted in the bottom panel of Figure 2.3(b). The naming of the modes already indicates, the surface mode usually manifests itself toward the surface of the flow, whereas body modes are found in the jet’s interior, forming threads. A thorough review on the stability of astrophysical jets was given by Hardee (2011).

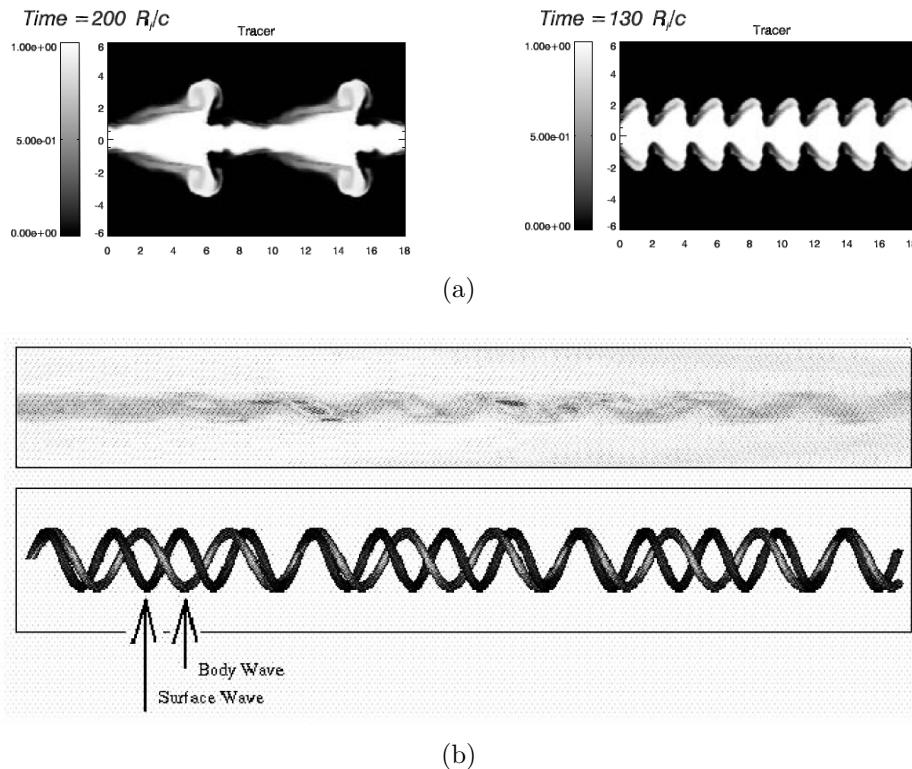


Figure 2.3: Kelvin-Helmholtz instability acting on a cylindrical jet. (a) Example for pinch modes of K-H instability (Perucho et al. 2004). (b) Example for helical modes K-H instability (upper panel volumetric rendering, lower panel illustration of the interaction between body and surface modes (Xu et al. 2000).

2.3 Opacity and Magnetic Field

In the previous section, the core was introduced as an inherent feature of the observed jet, corresponding to the $\tau = 1$ surface. It is usually the most compact (often unresolved) region of the jet, with a high flux density and flat spectrum in the radio regime. Towards higher observing frequencies, the separation r_0 of the core from the central engine becomes smaller (Königl 1981). This is illustrated in Figure 2.4. This opacity driven core is a commonly observed feature in most compact extragalactic jets (Lobanov 1996, 1998b; Kovalev et al. 2008).

For sources with little frequency dependence of r_{core} , the observed region may alternatively signify a bright, stationary emission region in close vicinity, but downstream

from the $\tau = 1$ surface. As described in the previous section, the jet is not a smooth flow, but also contains multiple bright emission features and some of which are possibly related to apparently stationary re-collimation shocks. In this case, and especially at higher frequencies, the observed narrow end of the jet may be represented by one of such stationary features (hence not changing its position depending on the observation frequency). For the remainder of this section, the opacity driven frequency dependence of r_{core} and its physical implications for the structure of the jet are discussed.

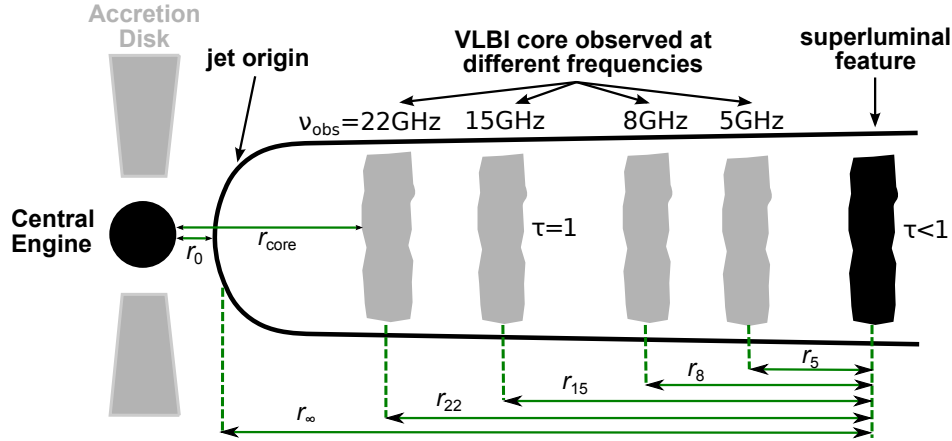


Figure 2.4: Shift of the observed, frequency dependent VLBI core positions. The core is seen at the location of the jet where its opacity to synchrotron self-absorption is $\tau = 1$. At greater distances, the emission is optically thin ($\tau < 1$), the position of the superluminal feature does not change with frequency and can be used as reference point. The distance r_{∞} corresponds to the distance of the footpoint of the jet, observed at infinite frequency. The distances r_0 and $r_{\text{core}}(\nu)$ can be estimated from the measured offsets $r_5 \dots r_{22}$. The figure is adopted from Lobanov (1996).

In the standard setting of the Königl (1981) jet model, the intrinsic relativistic particle energy is converted to bulk kinetic energy, leading to an increase of the bulk Lorentz factor γ_{kin} . The bulk Lorentz factor then reaches its maximum value most likely at the position of the VLBI core, due to the intrinsic deceleration to non-relativistic speeds of the jet particles in the rest-frame of the source (Marscher 1995).

Following the discussion of Lobanov (1996, 1998b), the magnetic field and distance of the core from the central engine are derived. The optical depth of synchrotron self-absorption is defined as:

$$\tau_s(r) = C(\alpha) N_1 \left(\frac{eB_1}{2\pi m_e} \right) \frac{\delta^\epsilon \phi_0}{r^{\epsilon m + n - 1} \nu^{\epsilon + 1}}, \quad (2.2)$$

with the electron mass m_e , $\epsilon = 3/2 - \alpha$, where α is the spectral index of the inhomogeneous synchrotron spectrum, ϕ_0 is the observed jet opening angle and δ is the Doppler factor. A description of $C(\alpha)$ can be found in Blumenthal & Gould (1970), for $\alpha = -0.5$ ($S_\nu \propto \nu^\alpha$), $C(\alpha) = 9.4 \cdot 10^{18}$. B_1 and N_1 are the magnetic field and electron density at a distance of $r_1 = 1$ pc, where the magnetic field goes as $B(r) = B_1(r_1/r)^m$ and the particle density decreases with $N(r) = N_1(r_1/r)^n$.

If τ_s is set to unity, the distance from the core in parsec, r_{pc} , to the central engine can be determined:

$$r_{\text{pc}} = F_s^{1/k_r} \nu_s^{-1/k_r} B_1^{k_b/k_r}, \quad (2.3)$$

where ν_s is the observed frequency. F_s is given by:

$$F = (1 + z)^{-1} [6.2 \cdot 10^{18} C(\alpha) \delta_j^\epsilon N_1 \phi_0]^{1/(\epsilon+1)}. \quad (2.4)$$

The factors k_r and k_b follow from Equation 2.2,

$$k_r = \frac{(3 - 2\alpha)m + 2n - 2}{5 - 2\alpha} \quad \text{and} \quad (2.5)$$

$$k_b = \frac{3 - 2\alpha}{5 - 2\alpha}. \quad (2.6)$$

For typical values of $m = 1$, $n = 2$ and $\alpha = -0.5$, $k_r = 1$ and $k_b = 2/3$. Note, with this particular choice of m and n , k_r does not depend on α .

To obtain a frequency independent measure of the apparent core positions observed between two different frequencies ν_1 , ν_2 (in units of Hz), where $\nu_1 < \nu_2$, the frequency independent measure of the core position offset $\Omega_{r\nu}$, is introduced as

$$\Omega_{r\nu} = 4.85 \cdot 10^{-9} \frac{\Delta r_{\text{mas}} D_L}{(1 + z)^2} \cdot \frac{\nu_1^{1/k_r} \nu_2^{1/k_r}}{\nu_2^{1/k_r} - \nu_1^{1/k_r}} \quad [\text{pc GHz}], \quad (2.7)$$

where Δr_{mas} is the difference of core positions between ν_1 and ν_2 in the scale of mas and D_L is the luminosity distance to the sources in units of Gpc.

If $\Omega_{r\nu}$ is measured, using Equation 2.3, the magnetic field at $r = 1$ pc can be determined

$$B_1 = \left(\frac{\Omega_{r\nu}}{\sin \theta} \right)^{k_r/k_b} F^{-1/k_b}, \quad (2.8)$$

and thus the distance from the central engine to the core

$$r_{\text{core}}(\nu) = \Omega_{r\nu} (\nu^{1/k_r} \sin \theta)^{-1}, \quad (2.9)$$

with θ being the angle between the jet axis and the line of sight. Actually, r_{core} represents the distance from the core to the point of the jet, where the pressure drops below 4/9 of its original value and the flow becomes supersonic (r_c). However since it can be assumed that $r_{\text{core}} \ll r_c$, r_{core} should be a good estimate for the distance to the central engine in most cases (Lobanov 1998b).

Finally combining Equations 2.8 and 2.9 and using the relation $B = B_1(r_1/r_{\text{core}})^m$, the magnetic field in the core as observed at frequency ν can be estimated by

$$B_{\text{core}}(\nu) \approx \nu^{m/k_r} \left(\frac{\Omega_{r\nu}}{(1 + z) \sin \Theta} \right)^{(k_r/k_b)-m} F^{-1/k_b}. \quad (2.10)$$

In the equipartition case of jet particle and magnetic field energy densities, $k_r = 1$ (with $m = 1$ and $n = 2$; Blandford & Königl 1979), the total (kinetic + magnetic field) power of the jet L_t can be estimated, using $\Omega_{r\nu}$ defined in Equation 2.7 and

$$L_t \approx 2.03 \cdot 10^{29} [\Omega_{r\nu} (1 + z) \phi_0]^{3/2} \frac{\Theta(3 + 2k_e \Lambda) \gamma_j^2 \beta_j}{k_e^{1/2} \delta_j \sin \theta}, \quad (2.11)$$

where $\Theta = \ln(r_{\max}/r_c)$, $\Lambda = \ln(\gamma_{\max}/\gamma_{\min})$, with γ_j being the jet bulk Lorentz factor, $\beta_j = \sqrt{1 - 1/\gamma_j^2}$, $r_c < r < r_{\max} - \sim 100\text{-}1000 r_c$ and γ_{\min} , γ_{\max} refers to the bulk kinetic energy of the relativistic particles (cf. Lobanov 1998b).

Following L_t , B_1 can be derived to

$$B_1 \approx 2.92 \cdot 10^{-9} \left[\frac{\Omega_{rv} (1+z)^3}{k_e \delta_j^2 \phi \sin^5 \theta} \right]^{1/4} \quad (2.12)$$

and similarly to Equation 2.10, B_{core} can be derived for the equipartition case as follows:

$$B_{\text{core}}(\nu) \approx 3.05 \cdot 10^{-3} \frac{\nu}{\delta_j} \sqrt{\frac{\Delta r_{\text{mas}} D_L (1+z)}{N_1 \phi} \frac{\nu_1 \nu_2}{\nu_2 - \nu_1}}, \quad (2.13)$$

where $N_1 \approx 10^2 \text{ cm}^{-2}$. If D_L is in units of Mpc, all frequencies in units of GHz, the resulting unit of the magnetic field is Gauss (cf. Lobanov 1996).

A prediction of the core-offset can be made, using equipartition and granted the synchrotron luminosity L_{syn} is known, then the expected shift of the core position between two frequencies is

$$\Delta r_{\text{mas}} \approx \frac{C_r (1+z)}{D_L \gamma^2 \phi_0} \frac{\nu_2 - \nu_1}{\nu_1 \nu_2} \left[\frac{L_{\text{syn}} \sin \theta}{\beta (1 - \beta \cos \theta) \Theta} \right]^{2/3}, \quad (2.14)$$

where $C_r = 4.56 \cdot 10^{-12}$ (cf. Blumenthal & Gould 1970; Lobanov 1998b).

2.4 Flow Kinematics

The observed jet structures at parsec scales reveal superluminal motion of features within the jet. The origin of which was debated in the early days of its discovery (Schraml et al. 1981), but soon it was realized that this can be explained by a geometrical projection effect, where relativistic motion due to small angles to the line of sight lead to apparent superluminal motions in the observers frame, illustrated in Figure 2.5.

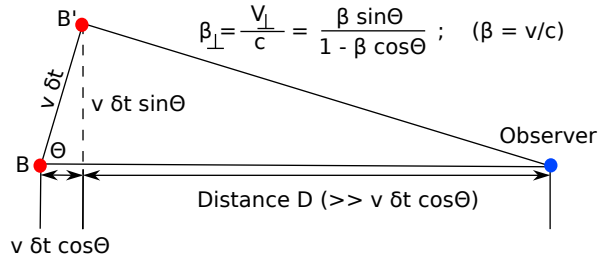


Figure 2.5: Schematic diagram for de-projecting superluminal motions.

Calculation of the intrinsic speeds β is later used to investigate jet kinematic scenarios, in order to learn more about the intrinsic behavior of the observed motions. At first the case of a constant viewing angle, $\theta = \text{const.}$ can be investigated, which implies a straight jet or at least rotational symmetry. In this case the instantaneous speed $\beta(t)$ becomes,

$$\beta(t) = \frac{\beta_{\text{app}}(t)}{\sin \theta + \beta_{\text{app}}(t) \cos \theta}, \quad (2.15)$$

and the Doppler factor becomes:

$$\frac{d\delta(t)}{dt} = \frac{\beta - 2\beta^2 \cos \theta + \cos \theta}{\sqrt{1 - \beta^2} (1 - \beta \cos \theta)^2} \frac{d\beta}{dt}. \quad (2.16)$$

In the case of a curved jet, β becomes

$$\beta = \frac{\beta_{\text{app}}(t)}{\sin \theta(t) + \beta_{\text{app}}(t) \cos \theta(t)} = \text{const.}, \quad (2.17)$$

solving for $\theta(t)$,

$$\theta(t) = \cos^{-1} \left[\frac{\beta_{\text{app}}^2(t) \pm \sqrt{\beta^2 (\beta_{\text{app}}^2(t) + 1) - \beta_{\text{app}}^2(t)}}{\beta (\beta_{\text{app}}^2(t) + 1)} \right]. \quad (2.18)$$

The solution with the '+' in front of the square-root is the "small angle" solution. Using the '-' produces the result for the "large angle" solution. These two cases were investigated by (Lobanov 1996), concluding that the "small angle" solution provides a more reasonable range of viewing angles, whereas the large angle case produces large variations in the viewing angles and values of θ as large as 100° . It is difficult to imagine the jet could stay as collimated as it is observed with such large viewing angles.

With β and θ determined, they can be used to derive the change in the Doppler factors similar to above,

$$\frac{d\delta(t)}{dt} = - \frac{\sqrt{1 - \beta^2} \beta \sin \theta}{(1 - \beta \cos \theta)^2} \frac{d\theta}{dt}. \quad (2.19)$$

The motion in the rest frame of the jet is derived including cosmological corrections, relativistic time dilation and aberration, following Lobanov (1996). The traveled distance in the rest frame of the jet can be expressed by,

$$R(t) = (1 + z)^{-1} \int_{t_0}^t \frac{\beta(t)}{1 - \beta(t) \cos \theta(t)} dt. \quad (2.20)$$

The time difference in the jet rest frame can be obtained by calculating,

$$\Delta t' = (1 + z)^{-1} \int_{t_0}^t \delta t dt. \quad (2.21)$$

The effect of aberration is corrected for, using standard aberration defined as,

$$\cos \theta'(t) = \frac{\beta(t) - \cos \theta(t)}{1 - \beta(t) \cos \theta(t)}. \quad (2.22)$$

Due to these relativistic projection effects the interpretation of the observed jet motions becomes a bit more tricky. Small changes of the viewing angle already have a significant impact on the observed emission. However, if helical motions due to K-H instabilities were present in the jet, the changes that could be seen should resemble fast oscillations, not compatible with changes in the viewing angle, whereas large scale changes of the general direction of the flow can easily be explained by a changing viewing angle. In addition to this, if the jet were slowly rotating, observed patterns should change, disappearing and reappearing depending on the phase of rotation.

2.5 Flares and Quasi-Periodic activity

Quasars caught the attention of astronomers particularly due to their fast and very pronounced flaring activity manifesting rapid changes of the observed flux at all wavelengths. The factors leading to these changes of emission are manifold. One important aspect that comes at play is the very strong relativistic beaming of any kind of emission from quasars, especially seen at small viewing angles. Constant intrinsic emission of perturbations in a twisting flow cause variation in the observed emission depending on the degree of beaming toward the observer. This is a purely geometrical effect and can explain why certain sections of a jet always appear brighter than others when imaged.

However, the assumption that intrinsic jet emission is constant is unrealistic. Most of the shorter time scale variability likely depends on the activity of perturbed regions in the jet, interacting with the steady jet or with other shocks in the jet. This causes variations in the jet emission observed, with different time scales depending on the observing frequency. In the past, faster variability was associated with high observing frequencies and distances closer to the central engine than variability at lower frequencies, under the assumption of a conical jet, the jet emission fills the entire width of the jet and the speed of light is not violated. However, recent observations and also results presented in later chapters challenge these assumptions (at least the first two).

Some objects show quasi-periodic flaring activity, with flaring “seasons” appearing at more or less regular time intervals, during which an unusually strong activity is observed in the jet. This quasi-periodic activity must be tightly connected to perturbations in the relativistic flow, either due to instabilities or due to injection cycles at the origin of the jet, influenced by the accretion behavior of the central engine. This recurring activity in AGN jets and its connection to the jet are poorly understood, since activity cycles in AGN usually last for many years. This requires decade long monitoring efforts in order to obtain information about multiple activity cycles, in order to make statistically significant statements and to provide reliable predictions on the activity state of sources.

CHAPTER 3

The FSRQ 3C 345

The focus of this thesis work is an in depth study of the parsec-scale jet in the quasar 3C 345, observed at high angular resolution in the radio regime and at other wavelengths spread over most of the observable electromagnetic spectrum. The quasar 3C 345 is known as a prominent variable source in the radio- through X-ray bands (≤ 10 keV). It is particularly bright at radio wavelengths and has an extended radio structure that is observable from sub-pc to kpc scales, which is archetypical for a relativistic blazar jet (e.g. Lobanov & Zensus 1999; Kollgaard et al. 1989). The object was first listed in the Third Cambridge catalogue of radio sources (3C catalog; Edge et al. 1959; Bennett 1962) and thus is commonly denoted as such in the literature.

At a redshift of $z = 0.593$ (Marziani et al. 1996) and with a flat Λ CDM cosmology, assuming $H_0 = 71 \text{ km s}^{-1} \text{ Mpc}^{-1}$ and $\Omega_M = 0.27$, a luminosity distance of $D_L = 3.47 \text{ Gpc}$ is derived, which corresponds to a linear scale of 6.64 pc mas^{-1} and a proper motion scale of 1 mas year^{-1} corresponding to $34.5c$. Throughout this thesis these values are used.

3.1 Radio Properties

The archetypical quasar 3C 345 is one of the best studied “superluminal” radio sources, with its parsec-scale radio emission monitored over the past 30 years, in particular by very long baseline interferometry (VLBI; *e.g.*: Biretta et al. 1986; Bååth et al. 1992; Lobanov 1996; Zensus et al. 1995; Ros et al. 2000; Klare 2003; Jorstad et al. 2007). It was first reported as superluminal source by Cohen et al. (1977) among one of the first four quasars claimed to show superluminal motions. However, due to its complex jet structure, the “superluminal” nature was not certain (Schraml et al. 1981) and only when imaging became possible at milliarcsecond scales was it confirmed. On parsec scales, it exhibits a remarkably complex, highly variable structure around

a compact unresolved radio core, commonly contributing 50 – 90% of the total flux density. Especially during high activity states, emission from the extended parsec scale jet dominates the observed flux levels. The spectrum of 3C 345 is relatively flat and steepens toward higher energies > 10 GHz following a spectral index α of -0.9 to -1.4 (with $S \propto \nu^\alpha$; Bregman et al. 1986). The radio spectrum compiled from archival and RATAN data (Kovalev et al. 1999) is shown in Figure 3.1.

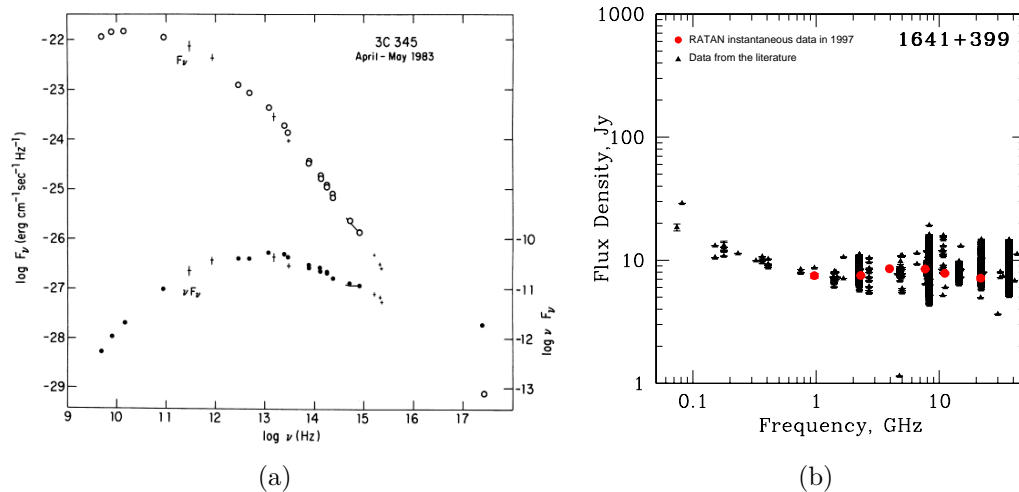


Figure 3.1: (a) Flux density (open circles) and flux per logarithmic bandwidth (filled circles) are shown for the multi-frequency spectrum of 3C 345 of 1983 May (Bregman et al. 1986). (b) Radio spectrum of 3C 345 compiled from archival data and simultaneous RATAN observations. *Plot courtesy of the MOJAVE program and RATAN (Kovalev et al. 1999).*

The large, arcsecond-scale structure of 3C 345 was investigated using the Very Large Array (VLA) at 5 GHz to produce high dynamic range images of 3C 345, shown in Figure 3.2 (Kollgaard et al. 1989), and by the Multi-Element Radio-Linked Interferometer Network (MERLIN; Browne et al. 1982). One of the VLA maps shows evidence for a weak counter jet to the northeast of the main structure of the jet. It was noted by Kollgaard et al. (1989) that this structure has been observed but was not resolved by Schilizzi & de Bruyn (1983). It was also mentioned by Browne (1987), where a structure Northeast of the core was observed, but did not connect to the core itself.

At high angular resolution, the radio emission of 3C 345 has been closely monitored since 1979 (cf. Biretta et al. 1986; Unwin & Wehrle 1992; Matveenko et al. 1992; Zensus et al. 1995; Lobanov 1996; Ros et al. 2000; Klare 2003; Lobanov & Roland 2005). Figure 3.3 shows a recently obtained map of 3C 345 at milliarcsecond scales. Between 1979 and 1994, most of the observations were primarily performed at 5, 10.7, and 22.3 GHz with some observations at 1.3, 2.3, 8.3, 43, and 89 GHz. After the VLBA became operational in 1994 the observing frequencies shifted to 1.6, 5.0, 8.4, 15.4, 22.2/23.8, 43.2 and 86 GHz, with observations primarily conducted at 15.4 and 43.2 GHz.

Over the past three decades, the radio variability has also been followed using single-dish radio telescopes by two main groups, the University of Michigan radio observatory (UMRAO) with their 26 m radio antenna (cf. Aller et al. 1985; Hughes et al. 1991; Aller et al. 2010) and the Metsähovi radio observatory with a 14 m antenna (cf. Teräsanta

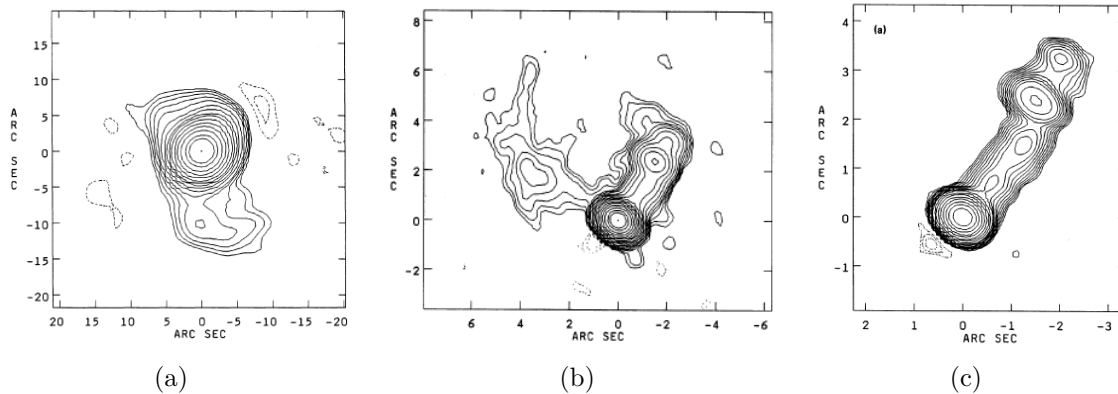


Figure 3.2: Observations presented in Kollgaard et al. (1989). (a) C array VLA map from 1988.18, with a dynamic range of 25 000:1. (b) A/B array VLA map from 1983.93 with a dynamic range of 75 000:1, showing the appearance of a counter jet. (c) A array VLA map from 1985.13, with a dynamic range of 19 000:1.

et al. 1998). The monitoring at UMRAO includes frequent flux and polarization measurements at 5, 8, and 15 GHz, whereas the Metsähovi monitoring focused on 22 and 37 GHz and since 2005 only on 37 GHz. Between 1979 and 1987, the Green Bank Interferometer provided also daily flux monitoring of 46 compact radio sources at 2.7 and 8.1 GHz, among which was 3C 345 (Waltman et al. 1991).

First major results from single dish monitoring programs were published in Hughes et al. (1992), investigating the origin and observed timescales of the variability and comparing it with the different source classes of the sample, concluding that the variability observed in BL Lacs and quasi stellar objects must have similar origins and are emanating from the observed jet structures at VLBI scales. Teräsranta et al. (1998) presented results from the first 15 years of monitoring with the Metsähovi telescope. Recently, the study of six AGN were presented, including 3C 345, using data from the IRAM calibrator monitoring between 86 and 267 GHz, suggesting the existence of “flaring states” in these sources (Trippe et al. 2011). Quasi-periodicity was observed in the radio (Aller et al. 1996; Teräsranta et al. 1998; Lobanov & Zensus 1999) regimes with a possible period of 3.5–4.5 years and major flares occurring every 8–10 years. A new cycle of such enhanced nuclear activity began in early 2008 (Larionov et al. 2009).

The kinematics of the jet of 3C 345 from multiple VLBI programs was discussed in the past by eg. Zensus et al. (1995); Lobanov (1996); Jorstad et al. (2005). Based on previous observations, spectral index and turnover frequency distributions were obtained (Lobanov 1996, 1998a; Ros et al. 2000), the spectral evolution of the jet was studied (Lobanov & Zensus 1999), properties of radio and X-ray emission were related (Unwin et al. 1997; Lobanov & Roland 2005), the dynamics of the central region was investigated (Lobanov & Roland 2005) and opacity in the nuclear region was used to determine the physical properties and matter composition of the compact jet (Lobanov 1998b; Hirotani 2005). Blandford & Rees (1978) introduced the relativistic jet model, which was later refined (cf. Hughes et al. 1991; Marscher 1987; Valtaoja et al. 1992) and applied to explain enhanced emission regions in the jet of 3C 345. Various studies followed applying a helical magnetic field (Steffen et al. 1995) to the observed emission, and strong relativistic shocks were found causing the observed flux, kinematic and polarization properties (Rabaça & Zensus 1994; Brown et al. 1994; Wardle et al. 1994).

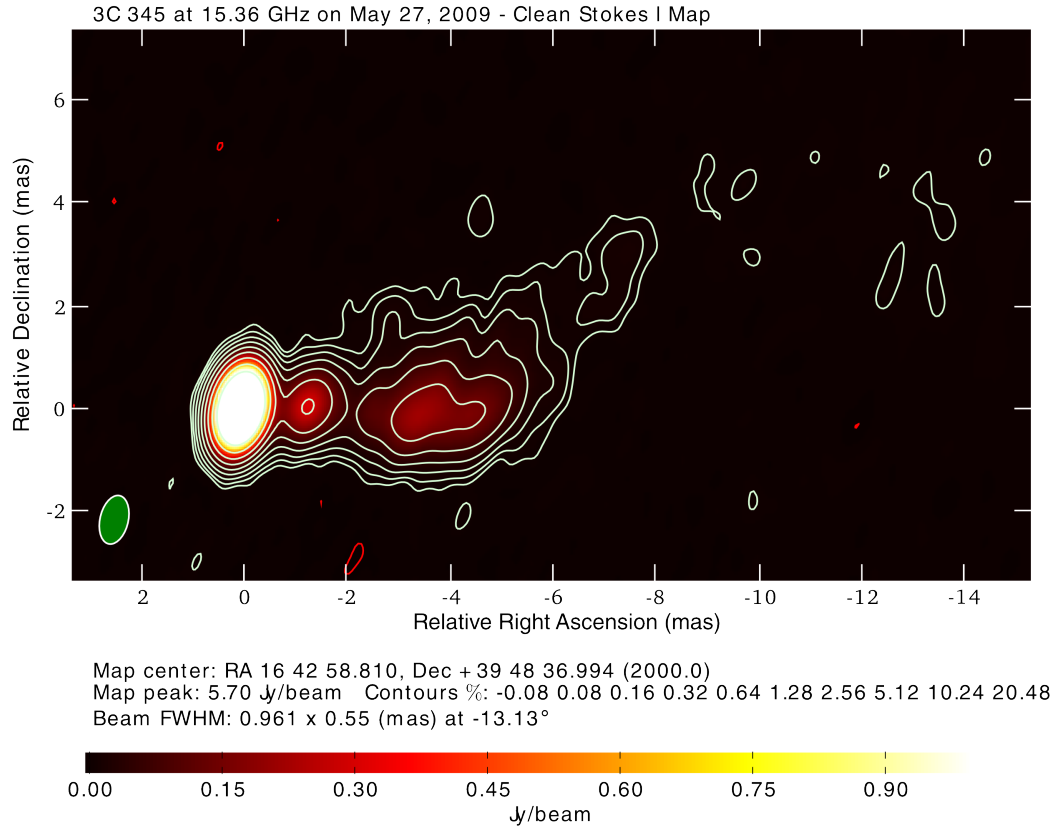


Figure 3.3: Map of 3C 345 at milliarcsecond scales, observed at 15.4 GHz.

3.2 Optical Properties

The radio source 3C 345 was first identified with its optical counterpart through a survey conducted using the Palomar Observatory Sky Survey plates. A blue star like object was reported 10" west of the position from the 3C revised catalog with a magnitude of ~ 16.3 (Bennett 1962; Wyndham 1965). Based on this identification, the first redshift was determined for this object. The observation of a broad emission feature identified as Mg II (λ 2798) and weaker emission features identified as [Ar IV], [Ne V], [Ne III], made it possible to determine a redshift of 0.595 for 3C 345 (Burbidge 1965). Later the redshift was refined by observations from Calar Alto observatory in 1994, for which a redshift of $z = 0.5928 \pm 0.0004$ was obtained (Marziani et al. 1996).

Optical variability of 3C 345 was first discovered by Goldsmith & Kinman (1965), who observed variability of a few tenths of magnitude. Later it was shown that 3C 345 exhibits variability of up to 2.9 magnitudes in B band and is highly polarized, reaching 22% (Babadzhanyants & Belokon 1984). In 1990, an unusually deep decline of optical emission was observed, with high variability down to a few minutes (Kidger & Takalo 1990). The observed optical variability shows similar time scales to that observed in the radio, following similar periodicities. It was first classified as a high-polarization quasar by Moore & Stockman (1981) and as a blazar by Impey & Neugebauer (1988). The quasi-periodicity of the optical variations with a period of ~ 4.3 years was claimed by Babadzhanyants & Belokon (1984); Kidger (1989), alternatively it has been suggested that this variability may be the result of a red noise process (Vio et al. 1991).

3.3 High-Energy Emission

The first quasar discovered to emit at X-ray energies (1–10 keV) was 3C 273, together with the other two galaxies Cen A and M87, during a rocket-borne experiment (Bowyer et al. 1970). Faint soft X-ray emission was first observed from 3C 345 by the Einstein Observatory (Ku et al. 1980). The high energy (X-ray) emission was investigated by Unwin et al. (1994), who concluded that the observed high-energy emission of this source is caused by inverse Compton up-scattering of lower energy photons by relativistic electrons of the pc-scale radio jet. However, it remained a puzzle why 3C 345 was not detected at energies above 20 MeV, while 3C 279 with similar apparent properties is a prominent source at γ -ray energies. Figure 3.4(a) presents a recent map of X-ray emission observed around 3C 345 by *Swift*/XRT.

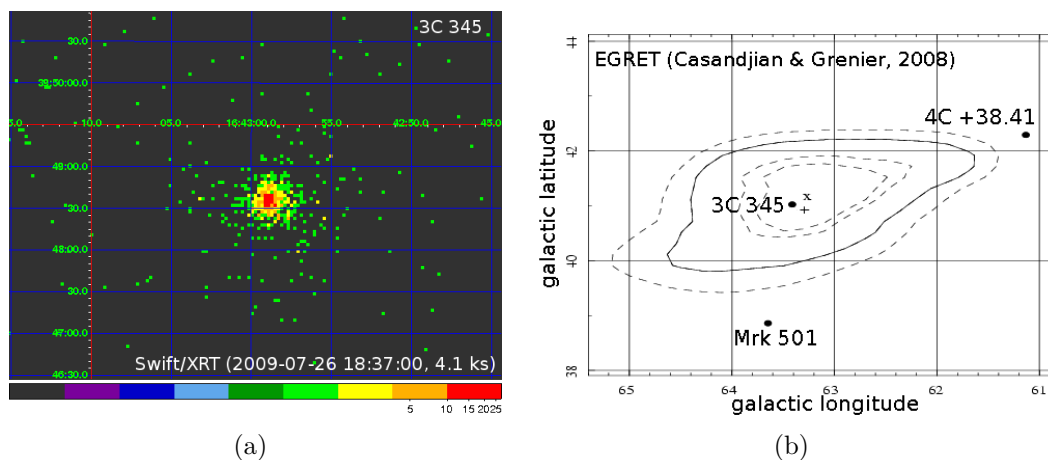


Figure 3.4: (a) *Swift*/XRT raw photon count map in the energy range of 0.3–10 keV, observed on July 26th, 2009. (b) EGRET γ -ray likelihood contours for energies above 100 MeV and observing period 5190. The contours represent confidence levels of 50%, 68%, 95%, and 99%. The cross is the revised EGRET catalog position, the plus sign is the position with maximum likelihood, the black dots mark the radio positions of 3C 345, Mrk 501, and 4C +38.41. (Casandjian & Grenier 2008)

The Energetic Gamma-Ray Experiment Telescope (EGRET; Thompson et al. 1993) on board the *Compton Gamma Ray Observatory* (CGRO) spacecraft did not observe a significant excess of γ -ray photons consistent with 3C 345 (3EG; Hartman et al. 1999), covering the first four phases of the CGRO mission (1991-1995). This lack of detectable flux of γ -rays above 20 MeV from 3C 345 was attributed to the high detection threshold of EGRET. A source consistent with the position of 3C 345, labeled as EGR J1642+3940, was found by Casandjian & Grenier (2008, also see Figure 3.4). This source was seen almost entirely in a single two-week viewing period with an excess of $\sim 5.8\sigma$, from April 23rd - May 7th, 1996 (vp5190), which was after the data used for the 3EG. Unfortunately, the angular resolution of EGRET was too poor to distinguish contributions from two nearby candidates NRAO 512 and B3 1640+396. Between October 1st and October 4th, 1993, a similar source was marginally detected by EGRET ($\sim 2.1\sigma$), but its centroid was localized closer to Mrk 501. In exactly the same viewing period, Kataoka et al. (1999) claimed EGRET detected a flare from Mrk 501, which lies 2.5° east of 3C 345. This would then be the only time that either of those sources was seen by EGRET – a strange coincidence that led Casandjian & Grenier to note that the EGR J1642+3940 source association with 3C 345 is “not clear”.

Multi-wavelength Observations, Data Reduction and Techniques

A range of observations was performed in the course of this thesis and combined with archival data, forming a large dataset that covers most of the electromagnetic spectrum, from high angular resolution observations at radio wavelengths up to observations at the highest energies. In addition to very long baseline interferometry at radio wavelengths, observations were performed involving the Submillimeter Array (SMA), the optical observatories Abastumani, Calar Alto, Crimean, Lowell, Lu-lin, Sabadell, St. Petersburg, Tjarafe, and Tzec Maun, the UV/optical (UVOT), X-ray (XRT), and the Large Area (LAT) telescopes aboard the *Swift* and *Fermi* satellites.

High angular resolution observations using the technique of very long baseline interferometry (VLBI) comprises data from a dedicated observing campaign conducted for this thesis and combined with over three decades of monitoring observations of 3C 345, covering a frequency range from 1.6 to 100 GHz and a time period from 1979 to 2010. A brief review of the observational methods, calibration and analysis techniques, as well as an introduction of the dataset are provided in Section 4.1. Observational data obtained from space instruments are introduced in Section 4.2 and 4.3. In Section 4.4, additional observations with other telescopes which have been used in this thesis are introduced.

4.1 Very Long Baseline Interferometry

The technique of interferometry and consequently very long baseline interferometry (VLBI) is driven by the quest for achieving ever higher angular resolution in astronomical observations. Cosmic electromagnetic radiation carries most of the information about the distant universe, far outside the reach of humans, covering a frequency range of $(10^6 - 10^{17})$ Hz. In the past, the study of the universe was limited to the range

of the visible light, though things changed with the advent of radar technology, which opened up a new “window” to the sky.

At radio wavelengths ($10^{-4} - 10^2$ meters), the angular resolution of a single antenna is typically of the order of 1 arcmin, which is mainly limited by the mechanics of building large structures. Currently, the largest structure of a single radio antenna is the Arecibo radio telescope with a diameter of 305 m and a collecting area of 73 000 m². Even at this scale the highest resolution that is achieved is only 0.5 arcmin. However, the angular resolution of radio astronomical observations can be dramatically improved by applying the technique of interferometry, which has been revolutionized by A.A. Michelson (Michelson & Pease 1921).

With the advent of radio astronomy and technological advances coming thereof, it became possible to connect two radio telescopes, forming a simple two-element interferometer. The distance between these telescopes is the baseline, with a length of d . If both antennas receive radiation at the same wavelength, λ , and their signals are combined and multiplied, then their products show a regular pattern of maxima and minima, so called “fringes”. These fringes are only observed if the signals from both antennas are coherent. They are observed as a consequence of changing relative path lengths while Earth rotates and they are carriers of information about the original structure of the collected radiation. The amplitude of which is an expression of the degree of coherence of the received signals, also called “visibility”. These visibilities are a complex representation of the brightness distribution of the radiating source in the Fourier plane. The resolution of such an interferometer is then of the order of λ/d (cf. Cohen et al. 1968). A more detailed review of the technique of interferometry and synthesis imaging, the method of reconstructing the original source brightness distribution, is provided in Taylor et al. (1999), and is summarized in Schinzel (2008) as well.

In the early days of radio interferometry, the baseline length and thus the resolution of observations was limited to a few hundred kilometers, with angular resolutions at the arcsecond scale (eg. Anderson et al. 1965; Adgie et al. 1965). It was soon realized that even at these baseline lengths, the angular resolution was not sufficient to observe structures that are considerably smaller, which was hinted in the particular case of bright quasars. At that time it was concluded, based on low frequency cut-offs seen in radio-frequency spectra (Slysh 1963; Williams 1963), fast variations in flux (Dent 1965), and interplanetary scintillations caused by the solar wind (Little & Hewish 1966; Cohen et al. 1966), that structures at smaller scales must be present. From this the need for longer baselines was clear, which started the development of interferometers that did not share the same local oscillator reference signal.

Important steps on the way to long (hundreds of km) and very long baselines (thousands of km) were the availability of frequency standards arising from the need of independent local oscillators and the means to record the signals at the telescopes and later to reprocess, combine, and multiply them at a “correlator”. A good review about the efforts and developments in the early days of VLBI are given by Cohen (2000) and Porcas (2010), including references therein. These efforts lead to the routine operation of “ad-hoc” VLBI arrays with existing radio telescopes, mainly distributed across Northern America and Eurasia, improving the achievable angular resolution to the milli-arcsecond scales. Eventually, this led to the construction of dedicated VLBI arrays.

The first of such efforts was the Network User Group (NUG) in the US, which coordinated six VLBI observations per year, a week every two months, with a network of seven existing telescopes. The NUG was formed in 1975 and was complemented by the Consortium for VLBI in 1979 (Cohen 2000). The formation of such an organization made it possible to start regular monitoring of radio jets, giving the possibility to spatially resolve the regions from which observed radio and optical variability originates. Thanks to the efforts of this network and scientists making use of it, I am able to present a dataset of VLBI observations of 3C 345 dating back to 1979.

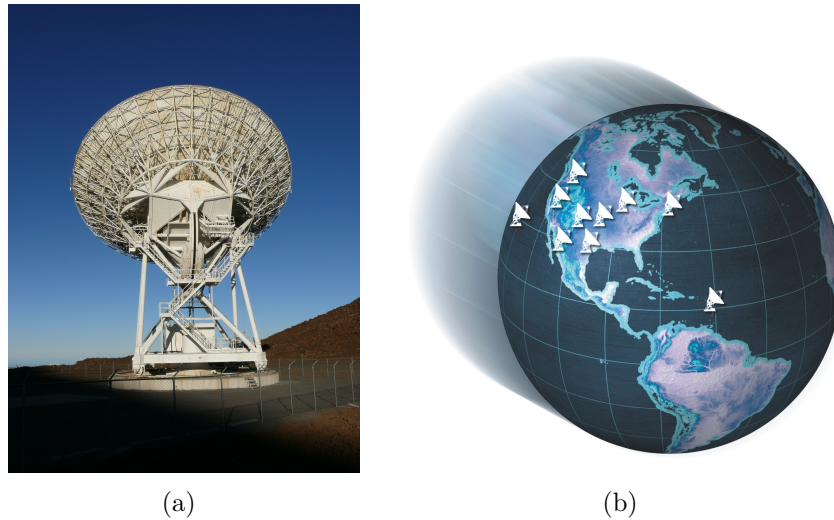


Figure 4.1: (a) VLBA station at Mauna Kea, Hawaii. (b) Location of the 10 Very Long Baseline Array antenna stations distributed across North America. Image courtesy of NRAO/AUI.

In 1993, the Very Long Baseline Array (VLBA) operated by the National Astronomical Radio Observatory (NRAO), which also operates the Very Large Array (now: Expanded Very Large Array) and the Green Bank Observatory, was dedicated. The first purpose built VLBI array that theoretically is able to perform 24 hours per day, 7 days per week long baseline interferometric observations. It consists of 10 antennas spread over North America with the longest baseline between Mauna Kea, Hawaii and Saint Croix, U.S. Virgin Islands (8611 km). The locations of all the VLBA antennas is pictured in Figure 4.1, together with a photograph of the VLBA antenna at Hawaii. These antennas are controlled centrally from Socorro, New Mexico, forming a coherently operating array. The VLBA provided improved (u, v) -coverage (sampling of the visibilities in the Fourier plane), higher sensitivity and multiple observing frequencies. The data collected at the individual antennas in the past were recorded on magnetic tapes, today are recorded on hard-disks, and are shipped to the correlator facility, which is situated in Socorro, New Mexico. Figure 4.2 shows images of the disk packs used for storage of the observational data at the telescopes and the wall of read-out devices used to read-in the telescope data to be processed by the correlator. Originally, the VLBA correlator was a custom built hardware correlator (Benson 1995) and in 2009 was replaced by the VLBA-DiFX software correlator (Deller et al. 2011), running on conventional PC hardware. After correlation of the observational data are completed, the data are archived and provided to the principal investigator of the project proposal.



Figure 4.2: (a) Read-out devices for correlation at the array operations center (now the Pete V. Domenici Science Operations Center) in Socorro, New Mexico. (b) Library of observations stored on disk packs awaiting to be correlated.

4.1.1 Observations

In this thesis the data of VLBI observations from the days of the US VLBI network up to the construction and operation of the VLBA are combined with archival and new VLBA observations of 3C 345, between 1.6 and 86 GHz. Observations between 1979 and 1994 were analyzed and presented by Lobanov (1996). Klare (2003) focused on the time period between 1997 and 1999 with a particular interest in the application of space-VLBI, providing higher angular resolution in particular at lower frequencies. For this thesis, the entire database of VLBA observations of 3C 345 was analyzed, which amounts to over 1000 observations between 1994 and 2010. Out of those the ~ 200 best VLBA observations were selected to be analyzed in order to form the largest, consistently analyzed, database of VLBI observations for a single source, surpassing the database of observations on 3C 279 collected by the MOJAVE survey. The selection criteria were mainly based on the provided (u, v) -coverage (sampling of the Fourier space needed for imaging) and integration time.

In addition to the archival observations, a new monitoring program was designed and conducted in the course of this thesis. Following the onset of a new period of flaring activity in 2008, a dedicated monthly monitoring campaign was initiated, using the VLBA to monitor the radio emission of 3C 345 at 43.2, 23.8, and 15.4 GHz (VLBA project codes: BS193, BS194). The observations were made with a bandwidth of 32 MHz (total recording bit rate 256 Mbits s^{-1}). A total of 12 VLBA observations were completed, with about 4.5 hours at 43.2 GHz spent on 3C 345 during each observation. Scans on 3C 345 were interleaved with observations of J1310+3233 (amplitude check, EVPA calibrator), J1407+2827 (D-term calibrator), and 3C 279 (amplitude check, EVPA calibrator). The VLBA data were correlated at the NRAO VLBA hardware correlator and starting from December 2009, the new VLBA-DiFX correlator was employed. The whole project was granted the initially requested total observing time of 120 hours, split in a target of opportunity proposal covering the time period until the following regular proposal deadline and a regular proposal covering a monitoring period until February 2010. Multiple proposals were submitted in an attempt to continue this monitoring campaign in order to cover the entire flaring period from the rising, through the flaring,

to the falling stage, which would have lasted until the end of 2011. Unfortunately, the proposal reviewers doubted the identification of γ -ray emission from 3C 345, which was given as the main argument to reject all subsequent proposals, despite generally positive remarks on the merits of such a project. Fortunately, the Boston University group is continuing frequent monitoring of 3C 345 at 43.2 GHz throughout 2011, providing some information on the evolution of the jet structure during that time.

The distribution of all here included observations across time and frequency is shown in Figure 4.3. A list of all historic observations together with related characteristic parameters extracted from those are provided in Appendix A. The newly analyzed observations are summarized in Table 4.1 together with characteristic parameters about image fidelity and resolution expressed by the beam size.

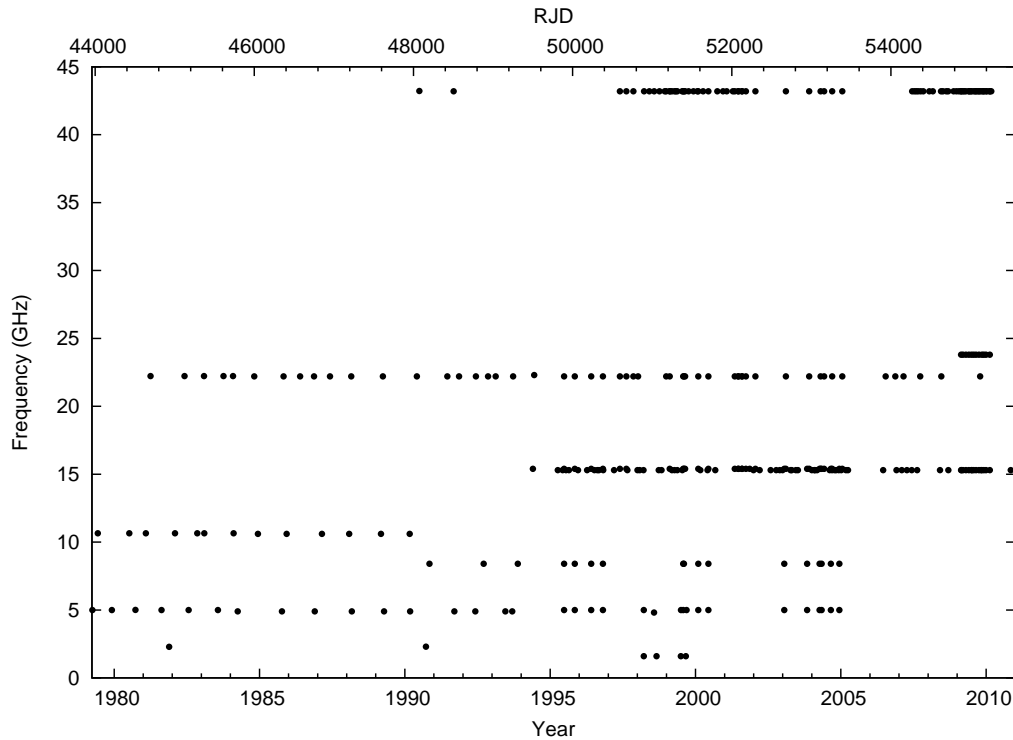


Figure 4.3: Distribution in frequency and time of the over 300 VLBI observations used in this thesis.

Table 4.1: Overview and basic characteristics of newly analyzed VLBA observations in chronological order.

Date	Code	ν_{obs} (GHz)	S_{tot} (Jy)	S_{peak} ($\frac{\text{Jy}}{\text{beam}}$)	σ_{rms} ($\frac{\text{Jy}}{\text{beam}}$)	D	b_{maj} (mas)	b_{min} (mas)	$b_{\text{p.a.}}$ ($^{\circ}$)	(*)
1994-05-28	GZ011	15.4	7.6	4.1	4.33e-04	9540:1	0.80	0.58	-15.9	
1995-04-07	BK016	15.3	8.2	4.6	7.15e-04	6377:1	0.94	0.47	-10.7	M
1995-06-06	TA003	15.3	9.5	4.3	1.09e-03	3997:1	1.17	0.44	-23.8	
1995-06-24	BL019	5.0	7.6	4.8	2.49e-04	19078:1	2.27	1.62	-7.2	
1995-06-24	BL019	8.4	9.0	5.0	5.60e-04	8903:1	1.35	0.94	-9.1	
1995-06-24	BL019	15.4	9.9	5.0	6.68e-04	7434:1	0.74	0.51	-11.9	
1995-06-24	BL019	22.2	5.9	2.5	5.53e-04	4500:1	0.52	0.36	-11.2	
1995-07-18	TA004	15.3	9.9	6.3	1.26e-03	5037:1	1.33	0.89	-34.7	
1995-08-24	TA006	15.3	19.0	0.0	0.00e+00	0:1	1.20	0.40	-1.8	F
1995-11-05	BZ017	5.0	7.2	4.6	6.32e-04	7219:1	2.65	1.66	-16.4	R

Continued on next page ...

Table 4.1 – *continued from previous page*

Date	Code	ν_{obs}	S_{tot}	S_{peak}	σ_{rms}	D	b_{maj}	b_{min}	$b_{\text{p.a.}}$	(*)
1995-11-05	BZ017	8.4	8.4	4.8	5.85e-04	8221:1	1.25	0.73	2.9	R
1995-11-05	BZ017	15.4	7.7	3.9	3.97e-04	9782:1	0.78	0.53	-6.8	R
1995-11-05	BZ017	22.2	6.3	2.7	6.80e-04	4034:1	0.48	0.33	-15.0	R
1995-12-15	BK037	15.3	8.4	3.8	5.09e-04	7475:1	0.99	0.58	-3.7	M
1996-04-09	TA013	15.3	8.3	4.0	5.54e-04	7286:1	1.46	0.51	18.8	
1996-05-30	BZ017	5.0	7.2	4.4	2.45e-04	17971:1	1.97	1.32	-9.5	R
1996-05-30	BZ017	8.4	7.2	3.9	3.28e-04	11920:1	1.14	0.81	-7.9	R
1996-05-30	BZ017	15.4	6.5	2.9	3.66e-04	7970:1	0.79	0.56	-8.3	R
1996-05-30	BZ017	22.2	4.3	1.8	6.96e-04	2609:1	0.43	0.32	-3.1	R
1996-07-10	BK037	15.3	8.2	3.6	6.60e-04	5482:1	0.92	0.51	0.0	M
1996-08-15	TA014	15.3	8.3	3.2	3.76e-04	8600:1	1.01	0.44	-7.4	
1996-09-04	TA015	15.3	6.7	2.9	3.63e-04	7919:1	1.04	0.49	-20.3	
1996-10-25	BZ017	5.0	7.1	4.3	3.38e-04	12575:1	1.86	1.53	-15.3	R
1996-10-25	BZ017	8.4	7.1	3.7	3.95e-04	9408:1	1.13	0.89	-16.8	R
1996-10-25	BZ017	15.4	5.8	2.7	4.64e-04	5924:1	0.69	0.54	-13.6	R
1996-10-25	BZ017	22.2	4.3	2.1	8.53e-04	2483:1	0.45	0.32	-15.5	R
1996-10-27	BK037	15.3	5.9	2.8	7.35e-04	3861:1	0.75	0.42	-2.1	M
1997-03-13	BK048	15.3	5.5	2.6	6.13e-04	4239:1	0.89	0.53	-9.1	M
1997-05-26	BM082	15.4	5.7	2.6	3.30e-04	8018:1	0.84	0.56	-10.8	
1997-05-26	BM082	22.2	5.4	2.5	7.63e-04	3263:1	0.60	0.38	-8.5	
1997-05-26	BM082	43.2	3.1	1.4	8.42e-04	1674:1	0.31	0.21	-4.1	
1997-08-15	BM082	15.4	6.7	2.8	4.68e-04	5912:1	0.84	0.50	-10.8	
1997-08-15	BM082	22.2	5.5	2.3	7.07e-04	3301:1	0.57	0.36	-12.1	
1997-08-15	BM082	43.2	3.7	1.6	1.00e-03	1594:1	0.30	0.19	-17.6	
1997-08-28	BK052	15.3	6.1	2.8	2.05e-03	1383:1	0.94	0.52	3.2	M
1998-01-03	BH045	15.3	6.1	2.4	3.01e-04	7842:1	0.97	0.49	-10.0	
1998-01-29	BL062	15.3	7.5	3.0	3.84e-04	7800:1	0.81	0.56	-3.8	
1998-03-19	BK052	15.3	5.6	2.2	4.10e-04	5374:1	1.03	0.55	-11.1	M
1998-03-25	BM095	43.2	4.5	2.5	9.76e-04	2547:1	0.28	0.19	-13.8	B
1998-05-31	BM0095	43.2	5.7	3.4	9.50e-04	3548:1	0.30	0.22	-12.4	B
1998-07-31	BM0095	43.2	6.6	4.3	1.10e-03	3941:1	0.29	0.22	-21.9	B
1998-09-26	BR056	15.3	8.4	4.4	3.06e-04	14469:1	1.09	0.58	-31.0	
1998-10-30	BK0052	15.3	7.7	4.0	1.60e-03	2518:1	0.93	0.39	-3.2	M
1999-02-11	BL0078	15.4	8.2	4.1	1.08e-03	3790:1	1.15	0.44	-2.3	
1999-02-11	BL0078	22.2	7.1	3.6	1.58e-03	2283:1	0.84	0.31	-3.5	
1999-02-11	BL0078	43.2	4.9	2.4	2.21e-03	1086:1	0.41	0.16	-3.0	
1999-02-13	BM0095	43.2	4.9	2.8	9.86e-04	2884:1	0.30	0.21	-10.4	B
1999-03-11	BL0078	15.3	8.7	4.5	5.45e-04	8259:1	1.25	0.53	0.4	
1999-04-12	BL0078	15.3	9.6	4.5	8.34e-04	5401:1	1.18	0.50	-15.3	
1999-04-29	BM095	43.2	6.9	4.4	1.70e-03	2611:1	0.28	0.24	-17.7	B
1999-05-18	BL078	15.3	10.6	5.3	1.15e-03	4589:1	1.27	0.45	-14.7	
1999-07-17	BM095	43.2	9.5	5.1	1.47e-03	3504:1	0.31	0.21	-11.9	B
1999-07-19	BK068	15.3	9.0	4.9	4.71e-04	10378:1	1.23	0.52	-15.9	M
1999-07-30	BL080	5.0	8.6	5.1	5.29e-04	9572:1	2.58	1.66	-8.3	
1999-07-30	BL080	8.4	9.0	4.3	7.34e-04	5803:1	1.48	1.02	-10.6	
1999-07-30	BL080	15.4	9.7	5.0	9.63e-04	5175:1	0.85	0.62	-15.8	
1999-07-30	BL080	22.2	6.2	3.6	1.21e-03	2999:1	0.58	0.43	-15.8	
1999-07-30	BL080	43.2	5.8	3.3	1.96e-03	1693:1	0.41	0.22	-22.2	
1999-08-08	BR057	8.4	9.1	4.1	2.91e-04	13958:1	1.65	0.96	-13.4	
1999-08-08	BR057	15.4	8.8	4.7	3.95e-04	11933:1	0.97	0.53	-19.2	
1999-08-08	BR057	22.2	5.9	3.3	4.11e-04	8090:1	0.66	0.36	-17.8	
1999-08-08	BR057	43.2	7.5	3.9	7.23e-04	5433:1	0.44	0.20	-24.8	
1999-08-23	BL078	15.4	8.7	4.7	6.48e-04	7225:1	1.18	0.47	-22.7	
1999-08-23	BL078	22.2	5.0	3.1	1.12e-03	2760:1	0.83	0.35	-24.5	
1999-08-23	BL078	43.2	5.6	2.5	2.92e-03	866:1	0.47	0.16	-28.3	
1999-10-06	BM092	43.2	5.5	3.0	6.80e-04	4423:1	0.33	0.33	0.3	B

Continued on next page ...

Table 4.1 – *continued from previous page*

Date	Code	ν_{obs}	S_{tot}	S_{peak}	σ_{rms}	D	b_{maj}	b_{min}	$b_{\text{p.a.}}$	(*)
1999-12-05	BM092	43.2	6.2	3.6	1.04e-03	3464:1	0.39	0.24	-23.5	B
2000-01-24	BM092	43.2	5.8	2.7	1.04e-03	2650:1	0.27	0.18	14.0	B
2000-02-04	BL0080	5.0	8.7	5.4	4.11e-04	13181:1	2.40	1.80	-20.8	
2000-02-04	BL0080	8.4	8.4	4.3	4.11e-04	10446:1	1.44	1.08	-21.4	
2000-02-04	BL0080	15.4	7.5	4.2	4.19e-04	9991:1	0.82	0.61	-24.9	
2000-02-04	BL080	22.2	6.1	2.9	5.96e-04	4912:1	0.55	0.42	-25.3	
2000-02-04	BL0080	43.2	5.0	2.5	9.35e-04	2627:1	0.29	0.22	-24.1	
2000-03-02	BL086	15.3	9.3	4.5	6.19e-04	7289:1	1.32	0.45	-18.4	
2000-04-05	BM092	43.2	5.9	2.6	6.75e-04	3861:1	0.30	0.20	-7.6	B
2000-05-31	BL086	15.3	9.6	4.5	7.64e-04	5906:1	1.20	0.43	-18.4	
2000-06-10	BL080	5.0	9.7	6.2	4.21e-04	14745:1	2.49	1.70	-22.8	
2000-06-10	BL080	8.4	9.6	4.7	5.19e-04	9044:1	1.39	1.00	-18.8	
2000-06-10	BL080	15.4	8.2	4.0	4.78e-04	8426:1	0.76	0.57	-20.0	
2000-06-10	BL080	22.2	4.6	2.3	6.81e-04	3419:1	0.52	0.40	-20.2	
2000-06-10	BL080	43.2	6.0	2.8	1.46e-03	1888:1	0.27	0.20	-19.6	
2000-09-06	BL086	15.3	9.7	4.4	6.98e-04	6353:1	1.15	0.45	-17.1	
2000-10-01	BM092	43.2	7.6	3.2	9.32e-04	3399:1	0.31	0.20	-12.4	B
2000-12-11	BM092	43.2	6.7	3.1	8.36e-04	3712:1	0.34	0.23	31.1	B
2001-01-28	BM092	43.2	6.3	2.2	2.20e-03	1018:1	0.26	0.18	-1.1	B
2001-04-14	BM092	43.2	6.1	1.5	7.34e-04	2026:1	0.29	0.20	0.4	B
2001-05-08	BL086	15.4	11.4	3.7	5.13e-04	7238:1	1.41	0.45	-20.1	
2001-05-08	BL086	22.2	8.4	2.5	1.03e-03	2439:1	0.99	0.31	-21.9	
2001-05-08	BL086	43.2	7.3	1.8	1.72e-03	1052:1	0.59	0.15	-24.0	
2001-06-19	BL104	15.4	10.9	3.3	4.10e-04	8064:1	1.10	0.45	-2.8	
2001-06-19	BL104	22.2	8.1	2.5	8.84e-04	2772:1	0.77	0.32	-3.9	
2001-06-19	BL104	43.2	5.9	1.4	9.94e-04	1364:1	0.39	0.16	-6.7	
2001-06-25	BL086	15.4	10.8	3.3	9.65e-04	3375:1	1.29	0.43	-17.6	
2001-06-25	BL086	22.2	7.6	2.2	1.12e-03	1982:1	0.86	0.32	-19.0	
2001-06-25	BL086	43.2	5.2	1.2	1.38e-03	900:1	0.51	0.17	-24.3	
2001-08-07	BL104	15.4	11.1	3.3	4.65e-04	7137:1	1.33	0.54	-9.0	
2001-08-07	BL104	22.2	8.3	2.5	8.39e-04	2921:1	0.73	0.30	-3.6	
2001-08-07	BL104	43.2	7.3	1.5	1.09e-03	1411:1	0.39	0.16	-7.4	
2001-08-08	BL0086	15.4	12.0	3.6	1.13e-03	3162:1	1.21	0.43	-19.1	
2001-08-08	BL0086	22.2	8.0	2.5	1.35e-03	1816:1	0.84	0.32	-21.4	
2001-08-08	BL086	43.2	5.6	1.5	1.73e-03	861:1	0.46	0.16	-24.6	
2001-09-24	BL0104	15.4	10.7	3.3	3.73e-04	8891:1	1.10	0.44	-2.5	
2001-09-24	BL104	22.2	8.2	2.6	8.64e-04	3039:1	0.77	0.33	-3.8	
2001-09-24	BL0104	43.2	6.8	1.4	9.51e-04	1502:1	0.40	0.16	-5.4	
2001-11-11	BL104	15.4	10.4	3.0	3.93e-04	7720:1	1.10	0.41	-4.2	
2001-12-30	BR077	15.3	8.2	2.6	1.21e-03	2107:1	0.93	0.54	3.2	M
2002-01-24	BL104	15.4	8.8	2.6	3.74e-04	6992:1	1.18	0.43	-9.1	
2002-01-24	BL104	22.2	6.9	2.3	7.05e-04	3221:1	0.79	0.31	-8.9	
2002-01-24	BL104	43.2	3.1	0.9	7.56e-04	1144:1	0.47	0.17	-15.3	
2002-03-18	BL104	15.3	8.1	2.7	9.22e-04	2972:1	1.09	0.42	7.4	
2002-08-02	BR077	15.3	6.7	2.9	7.31e-04	3930:1	0.90	0.52	-13.2	M
2002-10-11	BL104	15.3	6.6	2.6	3.45e-04	7550:1	1.21	0.47	-4.2	
2002-11-23	BL111	15.3	7.1	2.9	3.07e-04	9432:1	0.82	0.59	-14.9	M
2002-12-29	BL104	15.3	7.3	2.0	5.28e-03	386:1	1.62	0.44	-11.5	
2003-01-20	BL105	5.0	8.5	4.4	2.69e-04	16342:1	3.10	1.54	-3.7	
2003-01-20	BL105	8.4	6.4	2.1	4.04e-04	5186:1	1.75	0.88	-9.8	
2003-01-20	BL105	15.4	7.3	3.0	4.78e-04	6179:1	1.00	0.54	-8.8	
2003-02-10	BL104	15.4	6.7	2.7	2.80e-04	9777:1	1.14	0.46	-2.2	
2003-02-10	BL104	22.2	6.1	2.4	4.69e-04	5022:1	0.79	0.33	-3.9	
2003-02-10	BL104	43.2	5.2	1.6	8.88e-04	1852:1	0.48	0.19	-12.9	
2003-04-09	BB153	15.3	6.3	2.4	4.00e-04	6090:1	1.14	0.50	-6.5	
2003-04-23	BL104	15.3	6.8	2.7	3.23e-04	8281:1	1.09	0.44	-2.0	

Continued on next page ...

Table 4.1 – *continued from previous page*

Date	Code	ν_{obs}	S_{tot}	S_{peak}	σ_{rms}	D	b_{maj}	b_{min}	$b_{\text{p.a.}}$	(*)
2003-06-14	BL104	15.3	7.0	2.7	2.82e-04	9714:1	1.16	0.45	-0.6	
2003-07-10	BL104	15.3	6.9	2.7	2.98e-04	9175:1	1.14	0.45	-1.5	
2003-11-02	BL105	5.0	7.1	3.3	3.66e-04	8889:1	2.54	1.36	-7.5	
2003-11-02	BL105	8.4	6.3	1.9	3.51e-04	5516:1	1.50	0.79	-9.1	
2003-11-02	BL105	15.4	6.2	2.9	5.71e-04	5014:1	0.82	0.43	-10.2	
2003-11-28	BL104	15.4	6.1	2.8	3.42e-04	8272:1	1.15	0.46	-0.8	
2003-11-28	BL104	22.2	6.0	2.7	5.21e-04	5172:1	0.82	0.33	-2.4	
2003-11-28	BL104	43.2	4.8	2.4	8.75e-04	2768:1	0.44	0.18	-5.3	
2004-01-02	BL104	15.3	6.3	3.1	3.34e-04	9163:1	1.19	0.47	-1.4	
2004-02-02	BB168	15.3	5.8	2.9	2.44e-04	11959:1	0.91	0.60	-12.8	
2004-02-11	BL0111	15.3	6.4	3.2	3.83e-04	8258:1	0.86	0.54	-4.0	M
2004-03-07	BL104	15.3	6.9	3.4	2.83e-04	12101:1	1.13	0.46	-1.8	
2004-04-08	BL105	5.0	7.3	3.2	3.20e-04	10011:1	2.61	1.36	-13.1	
2004-04-08	BL105	8.4	7.0	2.5	5.14e-04	4948:1	1.58	0.84	-12.4	
2004-04-08	BL105	15.4	6.6	3.3	4.77e-04	6862:1	0.85	0.45	-13.6	
2004-04-21	BL104	15.4	7.0	3.4	2.88e-04	11758:1	1.12	0.45	-2.0	
2004-04-21	BL104	22.2	6.2	2.9	4.84e-04	5930:1	0.77	0.31	-4.4	
2004-04-21	BL104	43.2	5.2	1.9	9.22e-04	2080:1	0.41	0.17	-7.4	
2004-05-03	BL105	5.0	7.7	3.4	2.24e-04	15334:1	2.83	1.50	-11.0	
2004-05-03	BL105	8.4	7.5	2.8	2.38e-04	11559:1	1.75	0.95	-13.0	
2004-05-03	BL105	15.4	6.5	3.2	3.57e-04	9092:1	1.10	0.55	-22.2	
2004-06-04	BL104	15.4	6.8	3.2	3.00e-04	10629:1	1.13	0.45	-3.3	
2004-06-04	BL104	22.2	5.7	2.5	5.04e-04	5023:1	0.77	0.32	-4.3	
2004-06-04	BL104	43.2	4.9	1.7	9.45e-04	1807:1	0.44	0.18	-10.6	
2004-08-12	BL104	15.3	6.9	3.1	3.21e-04	9572:1	1.12	0.46	-0.6	
2004-08-27	BL105	5.0	7.7	3.5	3.78e-04	9163:1	3.37	1.52	-23.7	
2004-08-27	BL105	8.4	7.8	2.8	4.09e-04	6967:1	2.01	0.91	-24.2	
2004-08-27	BL105	15.4	6.6	3.0	4.78e-04	6258:1	1.12	0.50	-25.1	
2004-09-11	BL111	15.3	6.6	3.0	4.27e-04	7000:1	0.81	0.56	-7.6	M
2004-09-12	BL104	15.4	6.5	2.8	4.27e-04	6611:1	1.16	0.47	-6.1	
2004-09-12	BL104	22.2	5.2	2.0	8.38e-04	2420:1	0.83	0.31	-9.2	
2004-09-12	BL104	43.2	4.2	1.5	1.15e-03	1333:1	0.44	0.20	-13.5	
2004-10-13	BL104	15.3	6.2	2.8	4.09e-04	6858:1	1.09	0.58	9.6	
2004-11-01	BG152	15.3	5.3	2.3	5.95e-04	3940:1	0.81	0.57	-11.3	
2004-12-05	BL104	15.3	5.7	2.3	3.32e-04	6825:1	1.15	0.40	-3.1	
2004-12-12	BL0105	5.0	7.2	3.2	2.42e-04	13144:1	2.87	1.54	-14.8	
2004-12-12	BL0105	8.4	7.0	2.3	2.05e-04	11342:1	1.71	0.92	-11.8	
2004-12-12	BL105	15.4	5.8	2.4	3.21e-04	7513:1	0.95	0.53	-17.1	
2005-01-06	BL0123	15.3	5.6	2.4	6.08e-04	4015:1	0.73	0.52	0.4	M
2005-01-19	BL0104	15.4	5.1	2.1	3.30e-04	6389:1	1.21	0.46	-3.7	
2005-01-19	BL104	22.2	4.9	1.8	5.12e-04	3496:1	0.81	0.32	-3.8	
2005-01-19	BL0104	43.2	3.0	1.2	7.94e-04	1517:1	0.46	0.18	-3.8	
2005-03-05	BL104	15.3	5.8	2.6	3.13e-04	8184:1	1.18	0.47	4.0	
2005-03-31	BL104	15.3	5.5	2.4	6.16e-04	3861:1	1.12	0.50	2.1	
2006-06-15	BL137	15.3	5.2	2.8	4.90e-04	5806:1	0.84	0.59	0.1	M
2006-07-17	BA082	22.2	4.2	2.4	6.88e-04	3483:1	0.65	0.32	-9.2	A
2006-11-16	BA082	22.2	5.4	3.4	5.73e-04	5904:1	0.70	0.35	-10.4	A
2006-11-30	BB230	15.3	4.6	3.0	1.09e-03	2770:1	1.09	0.56	-16.2	
2007-02-05	BL137	15.3	6.6	4.4	3.79e-04	11725:1	0.94	0.61	-23.0	M
2007-02-26	BA082	22.2	6.3	4.0	6.96e-04	5769:1	0.73	0.34	-7.6	A
2007-04-10	BB230	15.3	6.7	4.3	8.49e-04	5013:1	1.38	0.51	-17.8	
2007-06-10	BL149	15.3	5.6	3.7	4.06e-04	9123:1	0.79	0.60	-7.3	M
2007-06-14	BM256	43.2	4.0	3.1	1.23e-03	2510:1	0.46	0.28	-88.8	B
2007-07-13	BM256	43.2	4.0	2.4	1.16e-03	2107:1	0.34	0.24	-14.2	B
2007-08-06	BM256	43.2	2.6	1.5	6.24e-04	2445:1	0.31	0.21	-31.7	B
2007-08-16	BL149	15.3	5.7	3.6	3.27e-04	10888:1	0.80	0.59	-15.8	M

Continued on next page ...

Table 4.1 – *continued from previous page*

Date	Code	ν_{obs}	S_{tot}	S_{peak}	σ_{rms}	D	b_{maj}	b_{min}	$b_{\text{p.a.}}$	(*)
2007-08-30	BM256	43.2	3.4	1.9	9.66e-04	2007:1	0.33	0.25	-28.0	B
2007-09-23	BA082	22.2	4.9	2.9	5.12e-04	5648:1	0.84	0.40	-19.8	A
2007-09-29	BM256	43.2	3.3	1.8	9.98e-04	1836:1	0.40	0.25	-35.4	B
2007-11-01	BM256	43.2	2.5	1.4	5.24e-04	2680:1	0.40	0.18	-31.3	B
2008-01-17	BM256	43.2	1.9	1.0	6.32e-04	1577:1	0.31	0.19	-27.2	B
2008-02-29	BM256	43.2	2.0	1.0	7.51e-04	1367:1	0.37	0.21	-29.1	B
2008-05-30	BL149	15.3	4.2	2.2	2.95e-04	7444:1	0.84	0.56	-16.7	M
2008-06-12	BM256	43.2	2.9	1.4	1.71e-03	820:1	0.34	0.16	-28.6	B
2008-06-15	BA082	22.2	3.8	1.9	4.93e-04	3797:1	0.80	0.31	-10.6	A
2008-07-06	BM256	43.2	2.7	1.3	2.81e-03	474:1	0.28	0.15	-10.6	B
2008-08-16	BM256	43.2	3.8	2.2	7.58e-04	2936:1	0.37	0.19	-28.7	B
2008-09-10	BM256	43.2	3.8	2.2	1.55e-03	1405:1	0.35	0.19	-31.2	B
2008-09-12	BL149	15.3	4.8	2.7	3.25e-04	8317:1	0.82	0.56	-10.5	M
2008-11-16	S1136	43.2	4.5	3.1	1.68e-03	1868:1	0.32	0.28	2.0	B
2008-12-21	S1136	43.2	3.0	1.8	3.06e-03	576:1	0.34	0.18	-11.5	B
2009-01-24	S1136	43.2	5.2	3.0	2.99e-03	998:1	0.30	0.18	-16.3	B
2009-02-19	BS193	15.3	5.9	4.1	2.16e-04	19094:1	0.93	0.57	-5.2	S
2009-02-19	BS193	23.8	4.5	4.1	4.82e-04	8578:1	0.64	0.37	-12.5	S
2009-02-19	BS193	43.2	2.8	2.5	3.89e-04	6544:1	0.31	0.21	-5.5	S
2009-02-22	S1136	43.2	4.8	2.6	1.18e-03	2228:1	0.30	0.17	-15.5	B
2009-02-25	BL149	15.3	6.8	4.8	2.75e-04	17448:1	0.83	0.57	-2.3	M
2009-03-16	BS193	15.3	7.0	5.1	1.90e-04	26625:1	1.05	0.79	11.1	S
2009-03-16	BS193	23.8	6.7	5.3	5.31e-04	10028:1	0.71	0.53	9.6	S
2009-03-16	BS193	43.2	6.0	4.7	4.67e-04	9957:1	0.39	0.27	20.8	S
2009-04-01	S1136	43.2	5.8	3.2	3.07e-03	1037:1	0.29	0.17	-15.1	B
2009-04-21	BS193	15.3	7.2	5.1	2.21e-04	22861:1	0.94	0.58	-12.6	S
2009-04-21	BS193	23.8	7.1	5.0	4.48e-04	11118:1	0.64	0.36	-14.7	S
2009-04-21	BS193	43.2	5.7	3.7	3.89e-04	9549:1	0.30	0.24	8.0	S
2009-05-27	BS193	15.3	7.9	5.7	2.36e-04	24136:1	0.96	0.55	-13.7	S
2009-05-27	BS193	23.8	7.5	5.1	5.97e-04	8488:1	0.59	0.33	-11.3	S
2009-05-27	BS193	43.2	6.9	3.9	3.95e-04	9965:1	0.32	0.18	-10.2	S
2009-05-30	S1136	43.2	8.6	4.7	1.43e-03	3248:1	0.32	0.15	-19.8	B
2009-06-21	S1136	43.2	4.9	2.6	1.32e-03	1950:1	0.29	0.15	-16.0	B
2009-06-29	BS194	15.3	8.6	6.4	3.04e-04	21063:1	0.88	0.55	-6.0	S
2009-06-29	BS194	23.8	7.8	5.7	9.73e-04	5842:1	0.55	0.34	-7.5	S
2009-06-29	BS194	43.2	5.8	3.2	7.51e-04	4265:1	0.33	0.20	-20.5	S
2009-07-05	BL149	15.3	9.2	6.9	3.32e-04	20733:1	0.83	0.55	-10.4	M
2009-07-27	BS194	15.3	8.9	6.7	3.79e-04	17762:1	0.89	0.53	-17.5	S
2009-07-27	BS194	23.8	7.9	5.4	5.09e-04	10541:1	0.56	0.31	-18.4	S
2009-07-27	BS194	43.2	7.1	3.9	5.26e-04	7365:1	0.37	0.19	-31.5	S
2009-08-16	BM303	43.2	5.8	2.7	9.91e-04	2748:1	0.30	0.16	-20.4	B
2009-08-26	BS194	15.3	9.2	6.7	5.85e-04	11528:1	0.88	0.52	-10.4	S
2009-08-26	BS194	23.8	7.3	4.8	8.04e-04	5983:1	0.54	0.31	-13.6	S
2009-08-26	BS194	43.2	6.1	3.1	5.29e-04	5791:1	0.18	0.30	-16.0	S
2009-09-16	BM303	43.2	6.8	3.1	1.14e-03	2725:1	0.35	0.19	-18.3	B
2009-10-01	BS194	15.3	8.6	6.4	6.01e-04	10598:1	0.92	0.62	-22.2	S
2009-10-01	BS194	23.8	7.4	4.6	6.27e-04	7277:1	0.57	0.30	-14.4	S
2009-10-01	BS194	43.2	6.1	2.6	6.40e-04	4076:1	0.27	0.17	-19.5	S
2009-10-16	BA082	43.2	6.8	3.0	9.59e-04	3176:1	0.41	0.17	-30.5	A
2009-10-27	BL194	15.3	8.4	6.0	3.59e-04	16727:1	0.83	0.58	-14.7	M
2009-11-07	BS194	15.3	8.2	5.8	4.22e-04	13632:1	1.15	0.54	-18.9	S
2009-11-07	BS194	23.8	7.4	4.4	5.33e-04	8325:1	0.72	0.31	-21.9	S
2009-11-07	BS194	43.2	5.7	2.2	7.60e-04	2932:1	0.30	0.18	-16.5	S
2009-11-28	BM303	43.2	5.3	2.2	1.14e-03	1942:1	0.28	0.16	-24.6	B
2009-11-30	BS194	15.3	7.7	5.2	6.24e-04	8377:1	0.90	0.49	-11.9	S
2009-11-30	BS194	23.8	6.9	3.9	5.98e-04	6565:1	0.55	0.29	-16.3	S

Continued on next page ...

Table 4.1 – *continued from previous page*

Date	Code	ν_{obs}	S_{tot}	S_{peak}	σ_{rms}	D	b_{maj}	b_{min}	$b_{\text{p.a.}}$	(*)
2009-11-30	BS194	43.2	5.5	2.2	5.83e-04	3763:1	0.29	0.16	-16.9	S
2009-12-28	BS194	15.3	6.7	4.4	4.66e-04	9547:1	0.89	0.52	-8.5	S
2009-12-28	BS194	23.8	5.0	2.8	9.08e-04	3044:1	0.56	0.30	-10.1	S
2009-12-28	BS194	43.2	4.9	2.0	6.40e-04	3060:1	0.31	0.16	-8.1	S
2010-01-10	BM303	43.2	4.3	2.1	9.61e-04	2142:1	0.33	0.20	-8.8	B
2010-02-11	BM303	43.2	5.6	2.9	1.65e-03	1731:1	0.27	0.15	-17.0	B
2010-02-15	BS194	15.3	7.1	4.7	7.58e-04	6199:1	1.02	0.54	-12.0	S
2010-02-15	BS194	23.8	6.3	4.0	4.01e-04	10032:1	0.59	0.35	-11.5	S
2010-02-15	BS194	43.2	5.1	2.5	4.82e-04	5124:1	0.31	0.20	-6.4	S
2010-03-06	BM303	43.2	5.4	3.0	7.07e-04	4205:1	0.39	0.28	-12.1	B
2010-11-04	BL149	15.3	7.0	3.8	3.75e-04	10059:1	0.85	0.55	-8.6	M

Notes:

Date – observing date; **Code** – legacy code pointing to the related observing proposal; ν_{obs} – center frequency of the observation; S_{tot} – total “clean” map flux density; S_{peak} – peak flux density of the “clean” map; σ_{rms} – observed RMS noise; b_{maj} – beam major axis; b_{min} – beam minor axis; $b_{\text{p.a.}}$ – beam major axis position angle (North through East); (*) – indicator to which observing campaign the particular datasets belongs, which also indicates observations for which calibrated datasets were provided (except for S), M = MOJAVE survey, B = Boston University blazar monitoring program, R = Ros et al. (2000, priv. comm.), A = Agudo et al. (priv. comm.), S = this thesis.

4.1.2 Data Reduction

For some of the archival VLBA data it was possible to obtain calibrated (u,v) -datasets, as indicated in Table 4.1. The MOJAVE (Monitoring Of Jets in Active galactic nuclei with VLBA Experiments) program provided 24 calibrated datasets, observed at 15.4 GHz, (Lister et al. 2009a) and its predecessor, the VLBA 2cm survey (1995–2002; eg. Zensus et al. 2002). Another 40 calibrated observations, pre-dominantly at 43.2 GHz, were provided by the Boston University blazar group (Marscher et al.), covering a time period of 1998 – 2001 (Jorstad et al. 2005) and from 2007 onward¹. In addition to this, calibrated datasets from dedicated observing programs have been provided by Eduardo Ros (Ros et al. 2000, 3 observations with 4 frequencies each in 1995 and 1996; project code BZ017) and Ivan Agudo (6 observations at 22.2 and 43.2 GHz each, project code BA084; 2006–2009).

All other VLBA datasets were first calibrated using the Astronomical Image Processing System (AIPS; Greisen 2003) in the versions 31DEC09 and 31DEC10. Figure 4.4 shows schematically the most important data processing steps within AIPS. After read-in of the data, using the task FITLD, the data were first sorted and properly indexed, if not provided in proper chronological order. If calibration files are not yet present, these have to be processed and read into AIPS in a specific format at this stage. Calibration tables refer to data tables providing system temperatures of all antennas, elevation dependent gain curves (usually in polynomial format), flagged time intervals and weather station information. In a final preparatory step, if the observation included multiple frequencies, the data were split into separate files, containing one frequency only.

Next, if the observing frequency were 8 GHz or less, the data were corrected for the ionosphere, provided that proper IONEX data were available from NASA’s archive of

¹<http://www.bu.edu/blazars/research.html>

space geodesy data, which contains information about the total electron content along the line of sight of the telescopes and correcting for it, introducing additional phase offsets and delays. After this the task **ACCOR** was run, as required for the output of the VLBA correlators (old and new), which does not correct amplitudes in cross-correlation spectra introduced by the digitization using the four level quantization scheme (Kogan 1995). This effect potentially introduces systematic errors to the visibility amplitudes, especially for bright sources like 3C 345, hence requiring a correction to be applied. Additional amplitude correction was performed by the task **APCAL**, which uses the system temperature and gain curve calibration information and applies it to the amplitudes. Also for high frequencies >40 GHz, opacity correction was applied using the same task, based on the information provided in the weather station data table. After this the task **VLBAPANG** was run to apply phase corrections due to parallactic angle effects, basically the parallactic angle at each antenna contributes to the phase, which can be removed by rotating the observed visibilities in the (u, v) -plane. In the next step, the pulse calibration information injected into the signal path at each antenna was used to correct for additional instrumental phases and delays. After this the task **VLBAFRNG** was used to compensate for group delay and calibrate the phase for each antenna (fringe fitting). This task runs **FRING** and applies the found solutions to the target and calibrators using the task **CLCAL**. As a last step the task **BPASS** was used to determine the bandpass response function of each individual antenna, using observations of 3C 345. Finally, all calibrations were combined and applied to the actual data and written out to a new multi-source dataset using the task **SPLAT**. Then the sources contained in the dataset were separated using the task **SPLIT** and exported into FITS files for analysis with external tools, using the task **FITTP**.

For imaging, Caltech's Difmap (Shepherd et al. 1995) software was used. This software was used to flag remaining "bad" data, due to glitches in the observations or bad weather at particular antennas. After this, the data were averaged and statistical weights were calculated for each complex visibility. After all the calibration and editing steps, the resulting phases of the target source still contain residual variations due to remaining station-based atmospheric effects, or a bad representation of the source model during fringe fitting, where a point source was assumed in this case. Images of the original source structure are reconstructed using deconvolution. The deconvolution method implemented in Difmap is that of the "Clean" algorithm, which was introduced by Högbom (1974), and refined by Clark (1980) and Schwab & Cotton (1983). Detailed discussions of the clean algorithm can be found in Taylor et al. (1999) and references therein. In addition, the iterative process of self-calibration was applied, which tries to minimize the difference between the observed phases and phases of a trial model. This allows to correct for instrumental phases and gains. This comes at the price of loss of absolute position information in the obtained images (Cornwell 1995; Cornwell & Fomalont 1999). A typical 15.4 GHz "clean" image obtained following this method is shown in Figure 4.5. The "clean" images for all re-analyzed VLBA observations are provided in Appendix B.

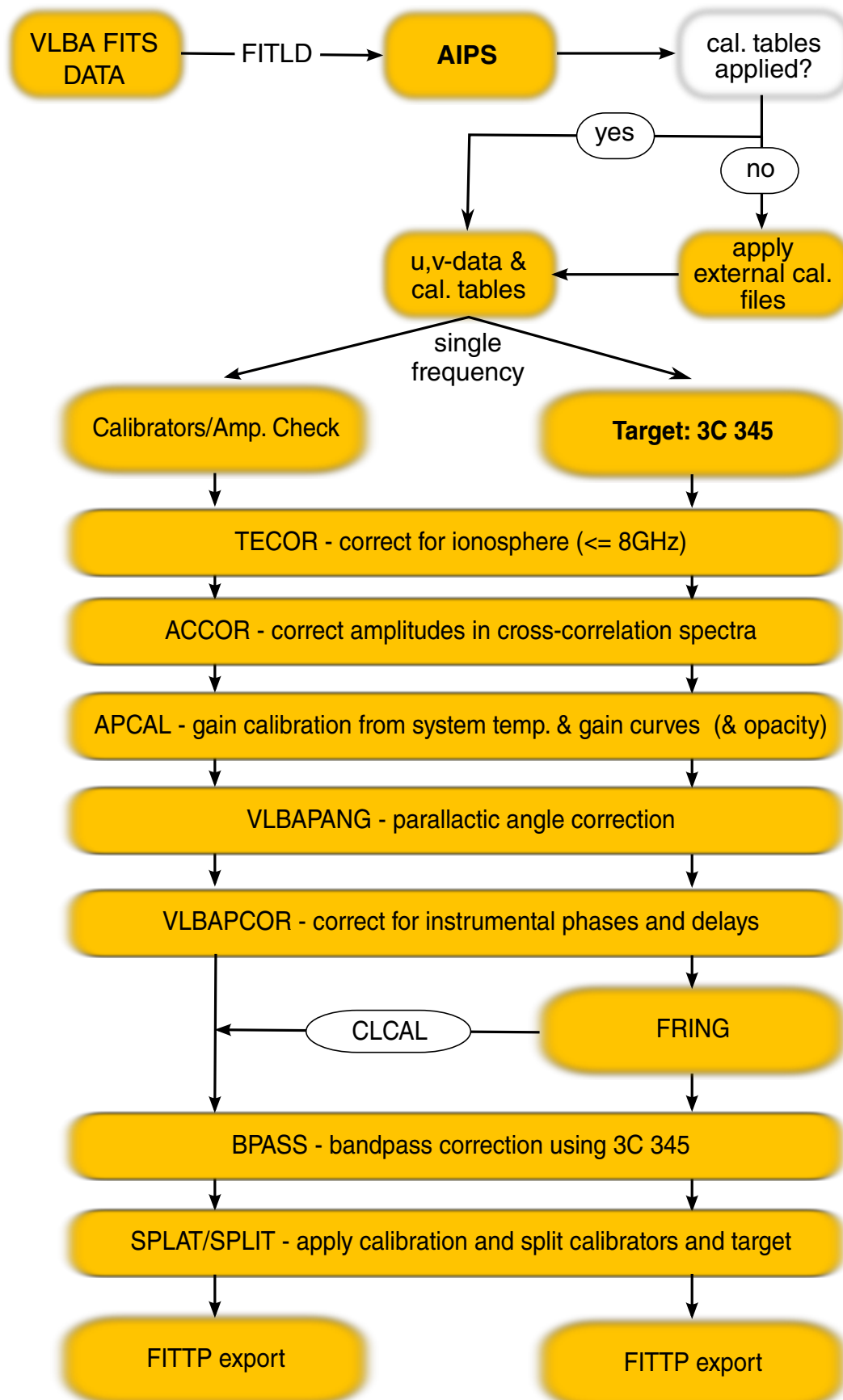


Figure 4.4: Block schedule of VLBA data calibration and reduction procedure, providing an overview of the main AIPS tasks that were applied.

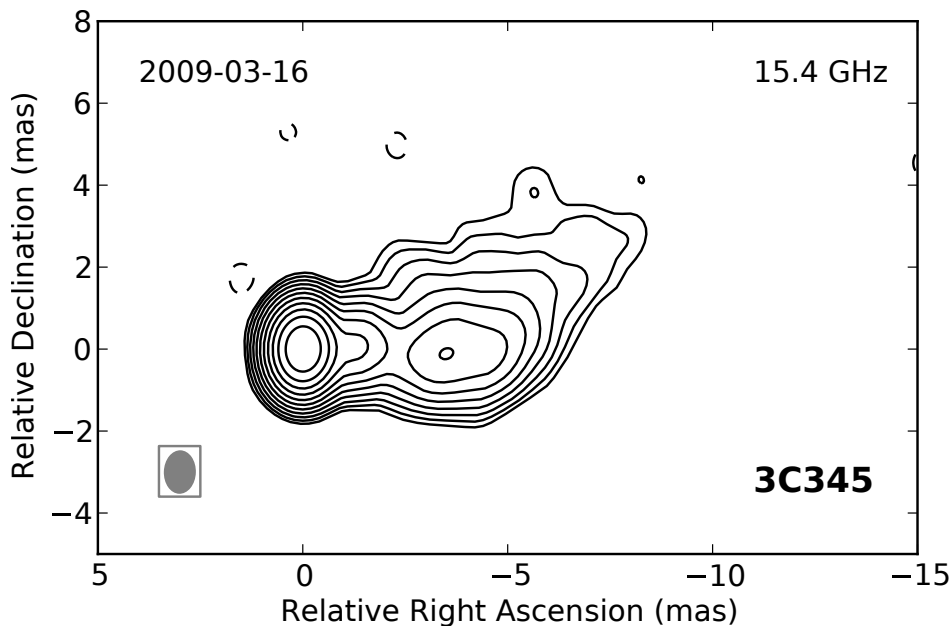


Figure 4.5: Exemphary VLBA “clean” image of the total brightness distribution of 3C345 at 15.4 GHz made from observations on March 16th, 2009. The shaded ellipse in the lower left corner represents the FWHM of the restoring beam. The image peak flux density is 5.1 Jy beam^{-1} . The contour levels correspond to $(-0.05 \ 0.05 \ 0.1 \ 0.2 \ 0.4 \ 0.8 \ 1.6 \ 3.2 \ 6.4 \ 13 \ 26 \ 51) \%$ of the peak flux density. Negative contours are indicated by dashed contour lines.

4.1.3 Analysis Techniques

In the early days of VLBI, the visibility data were not well sampled in the (u, v) -plane, which in many cases made it impossible to obtain images using the above described deconvolution method. However, one can directly inspect the distribution of visibilities in the (u, v) -plane in order to interpret the observed data directly. The method of fitting the observed visibility data with a model (model fitting), provides a parametric description of the observed source brightness distribution. Brightness peaks in the obtained images are represented by 2D-Gaussian components, which are Fourier transformed and fitted to the observed visibility data. Their parameters, flux density, size, position, and ellipticity are varied, minimizing the χ^2 using a least squares implementation of the maximum likelihood method. An excellent review of this method is given by Pearson (1999).

This resulted in a database, providing model fit parameters for more than 300 VLBI observations, corresponding to over 2000 individual Gaussian components. Their values are listed in the tables provided in Appendices A and B. A similar example map as above is provided in Figure 4.6, but instead of showing the brightness distribution obtained by the method of deconvolution, here the image is reconstructed using the modelfit components indicated by open crossed circles. The reconstructed brightness distribution is similar to what was obtained using the deconvolution method, although the root-mean-square (rms) noise is a bit higher for the map reconstructed using the model fitting approach.

The errors of modelfit parameters are estimated from the image plane, following analytical approximations introduced by Fomalont (1999) and Lobanov (2005) with mod-

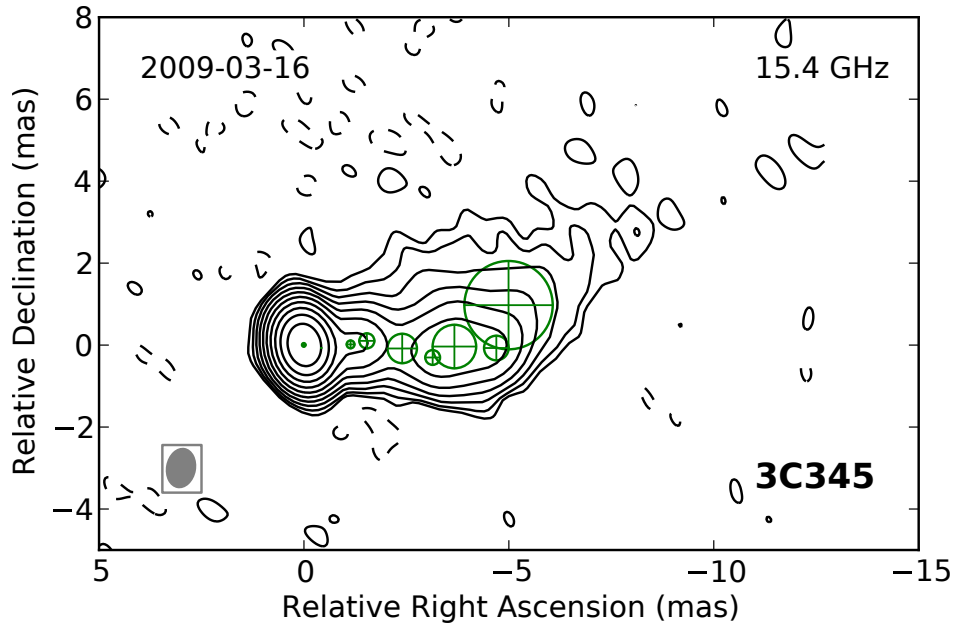


Figure 4.6: Exemplary VLBA image of the total brightness distribution of 3C 345 at 15.4 GHz made from observations on March 16th, 2009. The shaded ellipse in the lower left corner represents the FWHM of the restoring beam. The image peak flux density is 5.1 Jy beam^{-1} . The contour levels correspond to $(-0.1 \ 0.1 \ 0.2 \ 0.4 \ 0.8 \ 1.6 \ 3.2 \ 6.4 \ 13 \ 26 \ 51)$ % of the peak flux density. Negative contours are indicated by dashed contour lines. Open crossed circles show the FWHM of the Gaussian components found to best represent the structure observed. The image was reconstructed using the model fit components together with the observed calibrated visibilities.

ifications to account for the strong side-lobe case inherent to VLBI observations. For each component in the model, the root-mean-square (rms) noise (σ_p) was determined measuring around its position in the residual image. Then the respective component was removed from the Gaussian model and the modified model was subtracted from the data, yielding an image that contained only the contribution from the component investigated. The flux density (S_p) at the peak position of the Gaussian was taken. Further input values were, observation beam size ($b = \sqrt{b_{\text{maj}} \cdot b_{\text{min}}}$), component total flux density (S_t), component distance (r), position angle (Φ), and size (d). The errors for the model fit parameters were calculated in the following way:

$$SNR = \frac{S_p}{\sigma_p} \quad (SNR > 1) \quad (4.1)$$

$$\sigma_t = \left(\sigma_p \cdot \sqrt{1 + SNR} \right) \sqrt{1 + \left(\frac{S_t^2}{S_p^2} \right)} \quad (4.2)$$

$$d_{\text{lim}} = \frac{4}{\pi} \cdot \sqrt{\pi \ln(2.0) \cdot b \cdot \ln \left(\frac{SNR}{SNR - 1} \right)}; \quad (4.3)$$

$$\text{if } (d_{\text{lim}} > d) \text{ else } (d_{\text{lim}} = d) \quad (4.4)$$

$$\sigma_d = \frac{\sigma_p \cdot d_{\text{lim}}}{S_p} \quad (4.5)$$

$$\sigma_r = 0.5 \cdot \sigma_d \quad (4.6)$$

$$\text{if } (r > 0) : \sigma_\Phi = \arctan \left(\frac{\sigma_r}{r} \cdot \frac{180}{\pi} \right). \quad (4.7)$$

These error estimates only reflect the statistical image errors and are assumed uncorrelated. No additional systematic errors were taken into account, such as errors of the amplitude calibration that could add an additional uncertainty to the determined flux density values.

Modelfit components are re-referenced to the VLBI core at the particular observation frequency, which in case of 3C 345 is always the east-most component in the image plane. The re-referencing is performed in Cartesian coordinates for those cases where the obtained core position is not located at the phase center, additionally most of the subsequent analysis is performed in a 2D polar coordinate system, with the core component as origin. In order to perform a correct error propagation, it is important to note that the errors on the polar coordinates are not independent, thus a covariance matrix needs to be computed to account for this dependence. For the transformation from Cartesian (x, y) to polar coordinates (r, ϕ) ,

$$r = r(x, y) = \sqrt{x^2 + y^2} \quad (4.8)$$

$$\phi = \phi(x, y) = \tan \left(\frac{y}{x} \right). \quad (4.9)$$

In this case the error propagation is straight-forward, since x and y are assumed uncorrelated, the respective errors σ_x and σ_y are uncorrelated as well. This way the errors are obtained, with the knowledge of the errors for r (σ_r) and ϕ (σ_ϕ), using

$$\sigma_r^2 = \left(\frac{dr}{dx} \sigma_x \right)^2 + \left(\frac{dr}{dy} \sigma_y \right)^2 = \frac{x^2 \sigma_x^2 + y^2 \sigma_y^2}{x^2 + y^2} \quad (4.10)$$

$$\sigma_\phi^2 = \left(\frac{d\phi}{dx} \sigma_x \right)^2 + \left(\frac{d\phi}{dy} \sigma_y \right)^2 = \frac{y^2 \sigma_x^2 + x^2 \sigma_y^2}{(x^2 + y^2)^2}. \quad (4.11)$$

If there were a correlation between x and y , the term

$$2 \cdot \left[\frac{dr}{dx} \frac{dr}{dy} \cdot \text{cov}(x, y) \right] \quad (4.12)$$

needs to be added, where $\text{cov}(x, y)$ corresponds to the covariance between x and y . For the reverse transformation, the assumption of uncorrelated variables cannot be made, since the errors of r and ϕ will be correlated. Thus, the error propagation has to take the covariance into account and the errors for σ_x and σ_y can be calculated as follows,

$$x = x(r, \phi) = r \sin \phi; \quad y = y(r, \phi) = r \cos \phi \quad (4.13)$$

$$\sigma_x^2 = \left(\frac{dx}{dr} \sigma_r \right)^2 + \left(\frac{dx}{d\phi} \sigma_\phi \right)^2 + 2 \left(\frac{dx}{dr} \right) \left(\frac{dx}{d\phi} \right) \cdot \text{cov}(r, \phi) \quad (4.14)$$

$$= [(\sin \phi) \sigma_r]^2 + [r (\cos \phi) \sigma_\phi]^2 + 2 r (\sin \phi) (\cos \phi) \text{cov}(r, \phi) \quad (4.15)$$

$$\sigma_y^2 = \left(\frac{dy}{dr} \sigma_r \right)^2 + \left(\frac{dy}{d\phi} \sigma_\phi \right)^2 + 2 \left(\frac{dy}{dr} \right) \left(\frac{dy}{d\phi} \right) \cdot \text{cov}(r, \phi) \quad (4.16)$$

$$= [(\cos \phi) \sigma_r]^2 + [r (-\sin \phi) \sigma_\phi]^2 - 2 r (\sin \phi) (\cos \phi) \text{cov}(r, \phi) \quad (4.17)$$

with the covariance defined as,

$$\text{cov}(r, \phi) = \frac{dr}{dx} \frac{d\phi}{dx} \sigma_x^2 + \frac{dr}{dy} \frac{d\phi}{dy} \sigma_y^2 + \text{cov}(x, y) \left(\frac{dr}{dy} \frac{d\phi}{dx} + \frac{dr}{dx} \frac{d\phi}{dy} \right) \quad (4.18)$$

$$= \frac{\text{cov}(x, y) - \left(\frac{dx}{dy} \frac{dy}{dr} \sigma_r^2 + \frac{dx}{d\phi} \frac{dy}{d\phi} \sigma_\phi^2 \right)}{\frac{dx}{d\phi} \frac{dy}{dr} + \frac{dx}{dr} \frac{dy}{d\phi}} \quad (4.19)$$

$$= \frac{\text{cov}(x, y) - \frac{1}{2} (\sin 2\phi) (\sigma_r^2 + r^2 \sigma_\phi^2)}{r \cos 2\phi}, \quad (4.20)$$

if x, y are assumed uncorrelated, then $\text{cov}(x, y) = 0$. An additional systematic correlation is introduced due to $\sigma_\phi = \arctan(\sigma_r/r \cdot 180/\pi)$. The upper limit of the additionally introduced covariance $\text{cov}_{\text{sys}}(r, \phi)$ between r and ϕ is then determined to be

$$\text{cov}_{\text{sys}}(r, \phi) \leq \sqrt{\sigma_r^2 \sigma_\phi^2} = \sqrt{\sigma_r^2 \cdot \arctan^2 \left(\frac{\sigma_r}{r} \frac{180}{\pi} \right)}. \quad (4.21)$$

For typical errors of $\sigma_r = 0.1 \text{ mas}$ and $\sigma_\phi = 5^\circ$, $\text{cov}_{\text{sys}}(r, \phi) \leq 0.5$. Compared to the covariance introduced by the coordinate transformation, $\text{cov}(r, \phi) \gg \text{cov}_{\text{sys}}(r, \phi)$, thus in regards of the error propagation between the spherical and the Cartesian coordinate systems, the systematic correlation between r and ϕ is.

In practice, for this particular case, the linearized approach of the error propagation can be further simplified. The ratios of σ_x and σ_y reflect the eccentricity of the shape of the reconstructed interferometric beam. For the VLBA, the eccentricity of the beam is small and in some cases it is even circular. In addition, $\sigma_r \propto d_{\text{lim}}$, where the observation beam-size is used in the form $b = \sqrt{b_{\text{maj}} b_{\text{min}}}$, therefore it is safe to assume $\sigma_x \approx \sigma_y$, which simplifies the error propagation to $\sigma_r \approx \sigma_x, \sigma_y$. This assumption is used throughout this thesis when dealing with transformations between Cartesian and polar coordinates or vice versa.

4.1.4 Nomenclature of Gaussian Components

Jet components are labeled following the naming scheme developed for 3C 345 in the early analysis of the Caltech group (Biretta et al. 1986; Zensus et al. 1995) and continued by Lobanov (1996). In 3C 345 the VLBI core (origin of the jet) is the Eastern-most component, which exhibits a flat or inverted spectrum. This component is labeled with the letter “D” and is assumed to be stationary for the analysis of jet kinematics. Superluminally moving components are labeled with the letter “C”. A trailing number is added in the order of appearance, e.g. C1, C2, C3, etc. The identification of components was accomplished following different strategies based on consistency of kinematics. The dense sampling and the knowledge of typical component speeds make it possible to follow the evolution of individual features from one observations to the next. In cases of doubt about the identification, component sizes, flux densities and brightness temperatures are examined and checked for consistency. In Chapter 5 the properties of individual components, their kinematics and physical interpretation are found.

4.1.5 Database of Observations

The established database of observations and modelfit parameters was stored in a relational online database (MySQL²), following an approach similar to the one adopted in the MOJAVE program. The data are split in one table describing characteristics of each observation, such as date, frequency, observation code, total flux density, beam size, etc. A second table contains all modelfit information, listing the key modelfit parameters together with their errors, component label, related observation, etc. Additional tables were created for specific analysis, *eg.*, for core-shifts. All the relevant database table contents is listed in the Appendices A and B. A suite of Python scripts was developed to interact with this database, providing facilities to add new data using Difmap output files, to automatize the calculation of errors and many other tasks, and provide outputs supporting the cross-identification of components and analysis.

4.2 Swift Satellite

The *Swift* Gamma Ray Burst Explorer (Gehrels et al. 2004) is part of NASA's medium class "Explorer" spacecraft series (MIDEX), one of their longest running spacecraft series, with highly durable and long-lasting spacecrafts, probing a wide range of scientific areas. It was launched on November 20th, 2004 from Cape Canaveral and is since successfully operating in a nearly circular low Earth orbit of ~ 600 km altitude. *Swift* unites three instruments covering the optical (UVOT), soft X-ray (XRT) and hard X-ray/soft γ -ray (BAT) regimes. An artists conception of *Swift* is shown in Figure 4.7. The three instruments, the UV/Optical Telescope (UVOT), X-ray Telescope (XRT), and the Burst Alert Telescope (BAT) were constructed and operated under the lead of the State College Pennsylvania (Penn State) and NASA, with a strong collaboration both in England and Italy. The instruments are co-aligned, providing the unique capability to observe the same area of the sky with all three instruments simultaneously. The main mission goal of *Swift* is to detect gamma ray bursts (GRBs) and observe their afterglows within seconds after the detection. The BAT continuously scans a large fraction of the sky, watching out for sudden bursts of γ -ray radiation. During the times at which *Swift* is not detecting or following up on GRBs, the XRT and UVOT instruments are used to observe interesting targets, which can be proposed in a Target of Opportunity mode or through regular science proposals. This provides an excellent opportunity for AGN science to obtain simultaneous observations in the spectral region where the synchrotron emission dominated part connects to the inverse Compton dominated one.

The BAT instrument, designed and constructed by NASA's Goddard Space Flight Center, uses a coded aperture mask placed at some distance from the γ -ray detector, making it possible to reconstruct the direction of the γ -ray emission with an accuracy of 1-3 arcminutes within 10s after its detection, to alert the GRB community about a possible GRB and to re-point the spacecraft to observe the afterglow of the burst. BAT data is also used to compile an all-sky hard-X-ray survey, while it scans the entire sky. Results of it related to AGN science are published in Burlon et al. (2011). For a more detailed description of the BAT instrument, the Swift BAT software guide

²<http://www.mysql.com/>

provides a technical review of the instrument and instructions on how to analyze its data (Markwardt et al. 2007). For this thesis no data from BAT were used, due to its limited spatial resolution and sensitivity. A description of the other instruments, UVOT and XRT, are provided within the appropriate sections below.

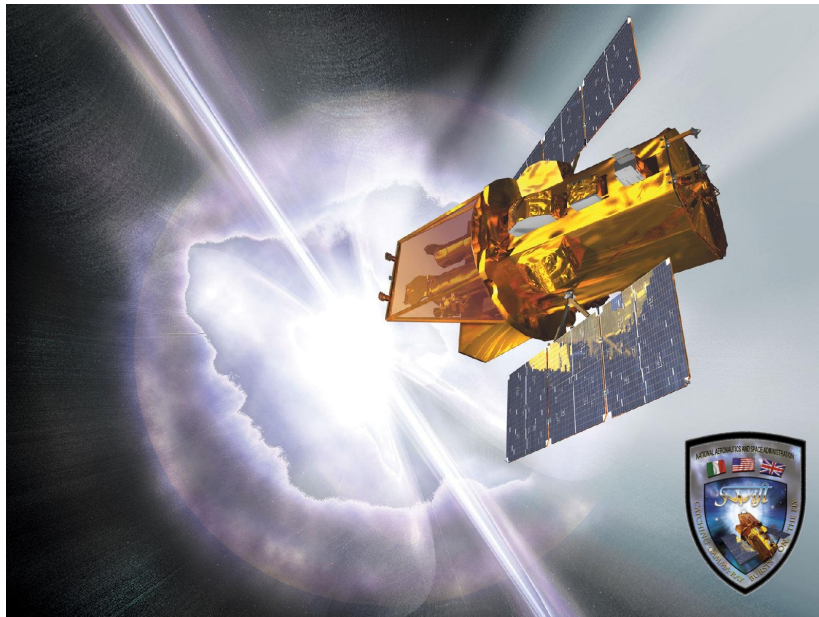


Figure 4.7: An artist's rendering of the Swift spacecraft with a gamma-ray burst going off in the background and the Swift Mission Logo in the lower right corner. Credit: NASA EPO, Sonoma State University, Spectrum Astro.

4.2.1 Observations

All *Swift* observations are immediately public after their data were down-linked and processed by the mission control center. They can be accessed from the quick look data archive and about a week after the observation is available in the global *Swift* data archive³. *Swift* observed NRAO 512 for the first time in January 2007 and 3C 345 in February 2007, their values are included for comparison with the current activity. For 3C 345, a dedicated target of opportunity program was proposed in the course of this thesis, in order to complement the ongoing VLBI observations during the second half of the monitoring period. The proposal was submitted and approved on July 22nd, 2009, requesting medium priority observations of 3C 345 every two weeks until the end of 2009 with an integration time of 4 ks each and all 6 narrow band optical filters provided by UVOT. The first pointing triggered by this proposal was on July 26th, 2009.

Additionally, triggered by the reported γ -ray flare of 0FGL J1641.4+3939 in October 2009 (Reyes & Cheung 2009), observations of three candidate counterpart sources, listed in Table 4.2, were performed. Another low priority target of opportunity proposal was submitted on August 13th, 2010, to observe 3C 345 and NRAO 512 simultaneously in order to determine the high energy state of each source at that time. A list of all *Swift*/XRT observations together with the spectral fit results is reported in Table 4.4. Results of simultaneous *Swift*/UVOT observations are listed in Table 4.3.

³<http://heasarc.gsfc.nasa.gov/>

Table 4.2: Radio positions and redshifts of candidate γ -ray counterparts for 0FGL J1641.4+3939 in October 2009 (Reyes & Cheung 2009).

Name(s)	3C 345	NRAO 512	B3 1640+396 CLASS J1641+3935
R.A.	16 ^h 42 ^m 58 ^s 810	16 ^h 40 ^m 29 ^s 633	16 ^h 41 ^m 47 ^s 540
Dec.	+39°48'36.99"	+39°46'46.03"	+39°35'03.33"
z	0.5928	1.666	0.540
Refs.	(1, 3)	(1, 4)	(2, 5)

Refs. – The numerals in the references row translate to:

(1) Fey et al. (2004); (2) Myers et al. (2003); (3) Marziani et al. (1996); (4) Stickel et al. (1989); (5) Brinkmann et al. (1995)

Notes: **Name(s)** – common source names; **R.A./Dec.** – right ascension/declination (J2000) of the radio source localization; **z** – source redshift.

4.2.2 UVOT

Observations of 3C 345 and NRAO 512 were performed with the Ultraviolet/Optical Telescope (UVOT) on board the *Swift* spacecraft. UVOT is a modified Ritchey-Chrétien optical telescope using a 30 cm primary mirror. The collected light is passed to two redundant detectors lying behind an identical 11-position filter wheel at each. The filters provided, cover a wavelength range of 51 – 600 nm, however for practical reasons only 6 of the 11 filters are used in observations described here, covering the UV/optical bands UVM2 (51 nm), UVW1 (70 nm), UVW2 (76 nm), V (75 nm), U (87.5 nm), and B (98 nm). The detectors are micro-channel plate intensified charged-coupled devices, which image the incoming photons using photon counting mode. In space, UVOT provides a comparable imaging sensitivity than 4-m class telescopes on the ground (Roming et al. 2005).

The optical photometry of UVOT data (V,U,B bands) was calibrated using comparison stars from Smith et al. (1985). Calibration of the UV data (UVW1,UVM2,UVW2 bands) were performed following the method of Poole et al. (2008). Comparison stars in the vicinity of 3C 345 could not be used to calibrate optical photometry of NRAO 512 with *Swift* UVOT because of its narrow field of view. Instead, the magnitude scale was calibrated using Sloan Digital Sky Survey (SDSS; Abazajian et al. 2009) stars in the field and transformations between the SDSS and Johnson photometric systems from Smith et al. (2002). The resulting magnitudes for 3C 345 and NRAO 512 in all the observed UV and optical bands are listed in Table 4.3.

Table 4.3: UV/optical observations of 3C 345, NRAO 512 and B3 1640+396 conducted by *Swift* UVOT and the 200-mm telescope of Tzec Maun observatory.

Target	Obs. date (*)	U	B	V	R	UVW1	UVW2	UVM2
3C 345:	2008-11-10 (4781)	16.886 ± 0.035				16.69 ± 0.03		
	2009-01-26 (4858)				16.48 ± 0.02			
	2009-02-13 (4876)				16.92 ± 0.03			
	2009-05-12 (4967)					16.19 ± 0.01		
	2009-06-09 (4992)					16.47 ± 0.01		
	2009-07-26 (5039)	16.808 ± 0.036	17.637 ± 0.035	17.194 ± 0.013		16.40 ± 0.03	16.35 ± 0.02	16.14 ± 0.03
	2009-08-09 (5053)	16.669 ± 0.063	17.487 ± 0.043	16.982 ± 0.062		16.38 ± 0.03	16.32 ± 0.02	15.96 ± 0.02
	2009-08-10 (5054)	16.694 ± 0.072	17.598 ± 0.043	17.057 ± 0.059				
	2009-08-23 (5067)	16.634 ± 0.081	17.508 ± 0.036	16.909 ± 0.045				
	2009-09-11 (5086)	16.221 ± 0.025	17.054 ± 0.026	16.451 ± 0.061		16.07 ± 0.02	16.04 ± 0.02	
NRAO 512:	2009-10-04 (5109)	16.053 ± 0.038	16.874 ± 0.022	16.374 ± 0.033				
	2009-10-06 (5111)	16.415 ± 0.053	17.139 ± 0.035	16.700 ± 0.078		15.88 ± 0.02	15.94 ± 0.02	15.80 ± 0.02
	2009-10-08 (5113)	16.447 ± 0.054	17.295 ± 0.040	16.747 ± 0.057		16.28 ± 0.03	16.20 ± 0.02	16.08 ± 0.04
	2009-10-10 (5115)	16.486 ± 0.032	17.322 ± 0.033	16.819 ± 0.090		16.29 ± 0.03	16.24 ± 0.03	15.88 ± 0.04
	2010-08-18 (5427)					16.47 ± 0.02		
	2007-01-18 (4119)	18.00 ± 0.04	18.74 ± 0.04	18.29 ± 0.06		18.28 ± 0.04		
	2007-01-26 (4127)	18.06 ± 0.06	18.83 ± 0.07	18.49 ± 0.10		18.27 ± 0.03	18.26 ± 0.05	
	2007-01-28 (4129)	17.49 ± 0.06	18.68 ± 0.07	18.50 ± 0.11			18.80 ± 0.07	
	2009-04-16 (4938)						19.41 ± 0.06	
	2009-10-08 (5113)	18.61 ± 0.04						
B3 1640+396:	2009-10-15 (5120)					19.02 ± 0.06		
	2010-08-06 (5415)	17.71 ± 0.05				18.07 ± 0.02		
	2009-01-26 (4858)				18.57 ± 0.13			
	2009-02-13 (4876)				> 18.6 [†]			

Notes:

Target – target source; **Obs. Date** (*) – Date of *Swift*-XRT observation (*=JD-2450000); **U,B,V,R,UVW1,UVW2,UVM2** – corresponding UV/optical filter bands; Observed optical magnitudes in given filter band are not corrected for Galactic extinction; † no detection.

4.2.3 XRT

The X-ray Telescope (XRT) has the shape of a long tube, at one end is the opening with a grazing incidence Wolter I telescope with a focal length of 3.5 m to focus X-rays onto a thermoelectrically cooled charge-coupled-device (CCD). The CCD consists of an array of 600×600 pixels and can be used in image, photo diode, window timing, and photon counting mode. The energy range that can be probed ranges from 0.2 to 10 keV, with a sensitivity of $2 \cdot 10^{-14}$ erg cm $^{-2}$ s $^{-1}$ reached within 10 ks (Burrows et al. 2005). For the XRT data used in this thesis, observations were only performed in photon counting mode, since the target sources are weak enough that no significant charge built-up would affect the measurements.

The XRT data were processed with standard procedures (`xrtpipeline` v0.12.4) to calibrate the observations. The filtering and screening criteria were applied by means of the FTOOLS in the *Heasoft* package version 6.8⁴. Given the low fluxes of the sources during observations (< 0.5 counts s $^{-1}$ in the 0.2–10 keV range), only photon counting (PC) data were considered for the analysis with XRT grades 0–12 selected (according to *Swift* nomenclature, see Burrows et al. 2005). The source events were extracted in a circle of radius 15–20 pixels (covering 85–90% of the XRT point spread function, PSF, at 1.5 keV) around the source, depending on its intensity. The background was estimated from a nearby source-free circular region of 40-pixel radius. Ancillary response files were generated with `xrtmkarf` to account for different extraction regions, vignetting and PSF corrections. The spectral redistribution matrices v011 in the calibration database maintained by HEASARC were used.

The adopted energy range for spectral fitting is 0.3–10 keV. All data were rebinned with a minimum of 20 counts per energy bin to use the χ^2 minimization fitting technique, except when the statistics were poor (< 200 counts), in which case the Cash statistic (Cash 1979) was used and the data were binned to 1 counts bin $^{-1}$. The Cash statistic is based on a likelihood ratio test and is widely used for parameter estimation in photon counting experiments. *Swift*-XRT uncertainties are given at 90% confidence level for each parameter, unless stated otherwise.

Spectral fitting was performed using *XSPEC* version 12.5.1 with an absorbed power law model. For the Galactic absorption a fixed HI column density n_{H} of $1.14 \cdot 10^{20}$ cm $^{-2}$ was used for 3C 345, $1.17 \cdot 10^{20}$ cm $^{-2}$ for B3 1640+396 and $1.07 \cdot 10^{20}$ cm $^{-2}$ for NRAO 512, obtained from the Leiden/Argentine/Bonn Galactic HI survey (Kalberla et al. 2005). The resulting unabsorbed fluxes for each observation are listed in Table 4.4.

Table 4.4: Overview and results of *Swift*/*XRT* observations.

Target	Obs. date	Exp	Rate	Index	Flux _{0.3–10}	Flux _{2–10}	χ^2/dof
3C 345:	2007-02-07	9.5	1.93	1.52 ± 0.05	9.70 ± 0.44	6.42 ± 0.30	1.07/78
	2008-11-09	2.0	1.03	1.76 ± 0.17	5.32 ± 0.71	6.0 ± 3.0	0.70/8
	2009-05-12	1.7	1.70	1.63 ± 0.16	9.1 ± 1.0	10.1 ± 4.5	0.82/12
	2009-06-09	2.4	1.68	1.81 ± 0.13	7.97 ± 0.73	4.33 ± 0.40	0.52/18
	2009-07-26	4.1	1.43	1.76 ± 0.10	7.21 ± 0.54	4.04 ± 0.30	0.76/26
	2009-08-09	3.9	1.41	1.77 ± 0.10	6.41 ± 0.50	3.58 ± 0.28	0.85/24

Continued on next page ...

⁴`xrtpipeline` and FTOOLS are part of the *Heasoft* software package: <http://heasarc.gsfc.nasa.gov/lheasoft/>; a detailed discussion on XRT data analysis can be found in the XRT User's Guide: http://heasarc.gsfc.nasa.gov/docs/swift/analysis/xrt_swguide_v1_2.pdf

Table 4.4 – *continued from previous page*

Target	Obs. date	Exp	Rate	Index	Flux _{0.3–10}	Flux _{2–10}	χ^2/dof
	2009-08-23	3.3	1.10	1.72 ± 0.13	5.82 ± 0.56	3.37 ± 0.32	0.83/15
	2009-09-11	4.2	1.42	1.83 ± 0.10	6.28 ± 0.46	3.36 ± 0.25	0.99/27
	2009-09-20	2.4	1.29	1.62 ± 0.16	6.58 ± 0.76	4.08 ± 0.47	1.21/13
	2009-10-04	4.2	1.39	1.68 ± 0.11	6.79 ± 0.53	4.05 ± 0.31	0.87/26
	2009-10-06 ^a	1.9	0.94	1.66 ± 0.17	$4.68^{+0.66}_{-0.62}$	$2.82^{+0.39}_{-0.37}$	
	2009-10-08	2.1	1.40	1.75 ± 0.16	7.11 ± 0.77	4.03 ± 0.44	1.26/12
	2009-10-09	2.2	1.27	1.62 ± 0.15	6.37 ± 0.73	3.95 ± 0.46	0.73/12
	2009-10-18	3.9	1.25	1.67 ± 0.12	6.15 ± 0.53	3.70 ± 0.32	0.85/21
	2009-11-01	4.1	1.23	1.77 ± 0.11	5.54 ± 0.45	3.09 ± 0.25	0.91/23
	2009-11-15	4.0	1.25	1.88 ± 0.11	5.87 ± 0.48	2.99 ± 0.24	0.73/22
	2009-11-29	4.1	1.21	1.71 ± 0.12	5.73 ± 0.49	3.35 ± 0.28	0.91/22
	2010-03-06/07	2.6	1.09	1.84 ± 0.15	5.64 ± 0.62	2.97 ± 0.33	0.55/12
	2010-03-09 ^a	1.4	1.22	1.78 ± 0.18	$5.57^{+0.80}_{-0.26}$	$3.09^{+0.45}_{-0.40}$	
	2010-04-09 ^a	2.0	1.12	1.88 ± 0.16	$5.48^{+0.65}_{-0.59}$	$2.80^{+0.45}_{-0.33}$	
	2010-08-18	4.3	0.99	1.54 ± 0.11	5.39 ± 0.49	3.53 ± 0.32	0.94/19
NRAO 512:	2007-01-18 ^a	8.1	0.16	1.45 ± 0.18	$8.6^{+1.5}_{-1.4}$	$5.9^{+1.0}_{-1.5}$	10.0σ
	2007-01-26/28 ^a	5.9	0.13	1.58 ± 0.30	$7.7^{+1.9}_{-1.7}$	$4.9^{+1.2}_{-1.1}$	7.3σ
	2009-04-16 ^a	3.0	0.06	1.60 ± 0.60	$3.6^{+1.8}_{-1.4}$	$2.24^{+1.1}_{-0.87}$	4.1σ
	2009-10-08 ^a	2.1	0.11	1.49 ± 0.54	$5.5^{+3.0}_{-2.3}$	$3.7^{+2.0}_{-1.6}$	4.3σ
	2009-10-15 ^a	2.1	0.12	2.18 ± 0.64	$4.6^{+2.0}_{-1.8}$	$3.7^{+2.0}_{-1.6}$	4.6σ
	2010-08-06/07 ^a	5.5	0.16	2.02 ± 0.28	7.3 ± 1.3		7.5σ
B3 1640+396:	2009-12-01 ^a	1.1	0.15	1.83 ± 0.71	$6.8^{+3.7}_{-2.6}$	$3.61^{+1.8}_{-1.4}$	3.6σ

Notes:

Target – observed target source in the field; **Obs. data** – Observation date, could include data from multiple passes during the specified dates, the ^a flag defines the type of statistic used in the analysis, χ^2 (if no flag is given) or Cash (with ^a flag), depending if the number of photons is higher or lower than 200 counts; **Exp** – effective exposure in photon counting mode; **Rate** – net count rate in units of 10^{-1} counts s^{-1} ; **Index** – power law spectral index; **Flux_{0.3–10}/Flux_{2–10}** – unabsorbed X-ray flux for the energy range of 0.3–10 keV and 2–10 keV, calculated from the fitted spectrum in units of 10^{-12} erg cm^{-2} s^{-1} ; **χ^2/dof** – if χ^2 statistics was used, then the χ^2 value of the fit and corresponding degrees of freedom are given, if Cash statistics was used, the signal to noise ratio of the detection of the source is provided.

4.3 Fermi Satellite

The *Fermi* Gamma-ray Space Telescope, formerly called Gamma-ray Large Area Space Telescope (GLAST), carries two major instruments, the Gamma-ray Burst Monitor (GBM) and the Large Area Telescope (LAT). It was launched on June 11th, 2008 from Cape Canaveral. Its orbit is similar to that of the *Swift* satellite, with a low Earth orbit at an altitude of ~ 550 km. It has an expected life time of at least 5 years.

The GBM is constructed to be used to detect short bursts of γ -ray emission from GRBs or solar flares. Recently, it has also been used to detect terrestrial γ -ray flashes produced in thunderstorms. It is mounted on the side of the spacecraft (see Figure 4.8), providing a view of the entire sky, except when it is blocked by the Earth. The main partners operating the GBM are the Marshall Space Flight Center, in Florida USA and the Max-Planck-Institut für Extraterrestrische Physik in Germany.

The LAT is a pair conversion telescope designed to cover the energy band from 20 MeV to greater than 300 GeV. It is the product of an international collaboration between NASA and DOE in the U.S. and many scientific institutions across France, Italy, Japan, Sweden, and Germany. The major scientific goals to be addressed by

the LAT are the determination of the nature of unidentified γ -ray sources and the diffuse γ -ray emission, to understand the principles of particle acceleration in particular in AGN, pulsars, supernova remnants and the Sun, to probe the early universe at high redshifts and to probe for dark matter annihilation signatures. The general construction of LAT is depicted in Figure 4.8. It consists of 16 “towers”, with each tower containing multiple thin metal plates that convert the incident γ -ray photons to a shower of electrons and positrons, these plates are interleaved by position sensitive silicon detectors which record the passage of the shower, providing the information to reconstruct the directions of the incident photons. A heavy calorimeter at the end of each tracker consists of multiple CsI crystals that is able to measure the energies of the charged particles resulting from the incident photon. It is able to detect energies up to a hundred GeV, enough to enable measuring incident photon energies up to one TeV. The entire calorimeter weighs 1.8 metric tons, which corresponds to $\sim 64\%$ of the total weight of LAT. To avoid measuring back-scattering events or to reject other background particles, an anti-coincidence detector made of plastic scintillators is fixed all around LAT, enabling the detection of stray charged particles, in order to reject measurements with which they could interfere (Atwood et al. 2009). The LAT instrument has a field of view of 2.4 steradian which corresponds to $\sim 20\%$ of the sky. In default operating mode it continuously observes the entire sky every 3 hours (~ 2 orbits). For the subsequent analysis and discussion, only LAT data were used.

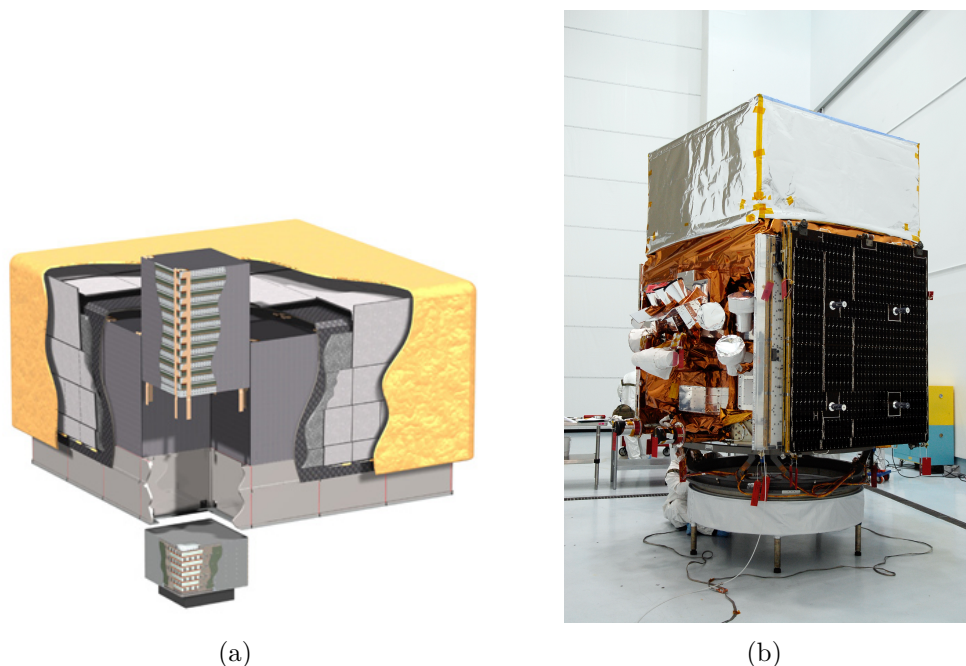


Figure 4.8: (a) *Fermi* LAT cut-away, showing the instrument with the dimensions $1.8 \times 1.8 \times 0.72$ m, weighting 2.8 metric tons alone and requiring a power of 650 W to operate (Atwood et al. 2009). (b) The GLAST (now *Fermi*) satellite sitting on top of the payload attachment. The square on top is the LAT, with the GBM detectors visible on the left side. *Image courtesy NASA/Kim Shiflett.*

Large Area Telescope

The *Fermi*-LAT data on the field in which 1FGL J1642.5+3947 (Abdo et al. 2010a) is located were processed and analyzed using the *Fermi* Science Tools software package (version: v9r15p2⁵; Abdo et al. 2010a). 1FGL J1642.5+3947 is the γ -ray source reported closest to 3C 345 in 2010. The photons were extracted from a region of interest (ROI) centered on the radio position of 3C 345 within a radius of 15° and a time range of 20 months, August 4th, 2008, to April 4th, 2010 (in MET⁶ 239557417 - 292088627 s). The general data processing procedures applied were similar to those described in Abdo et al. (2009b) and Abdo et al. (2010a).

To ensure that the collected events considered in this analysis have a high probability of being photons, the “diffuse class” selection was applied. Furthermore, events above the zenith angle 105° were removed to avoid a significant contamination by γ rays produced from cosmic-ray interactions in Earth’s atmosphere⁷ (Abdo et al. 2009c). The P6_V3_DIFFUSE instrument response functions (IRF) were used (see Rando et al. 2009).

The remaining γ -ray-like events were analyzed using a maximum-likelihood approach (Mattox et al. 1996) to localize γ -ray sources and extract their spectra. As in the analysis of 1FGL, two sets of standard LAT analysis tools were used, and their results compared for consistency. The first set, based on `gtfindsrc` and `gtlike` tools, employs an unbinned likelihood analysis in which the expected response of the LAT is evaluated separately for each photon, given its energy and direction with respect to the detector axes. The second toolset, `pointlike`, uses a simpler, binned analysis methodology, where photons are binned spatially and in energy, and an averaged set of response functions is applied. The two packages give very similar results, with the `pointlike` package running much more quickly.

In both likelihood methodologies the γ -ray emission in the ROI is assumed to arise from two diffuse components and a number of point sources. Each point source is modeled spatially as a delta function and spectrally as a power law. The statistical significance of a potential source is estimated by forming a “test statistic” (TS),

$$TS = 2(\ln L_1 - \ln L_0), \quad (4.22)$$

where L_1 is the value of the likelihood obtained in the “source” hypothesis, with the source present in the model of the ROI and L_0 is the value in the alternate, “null” hypothesis, that the source is not real (and hence not included in the ROI model). If the null hypothesis is true, and assuming certain applicability conditions are met, Wilks’ theorem (Wilks 1938) states that TS is distributed as $\chi^2(N)$, where N is the number of additional parameters optimized in the source model leading to L_1 . Because each point source has four free parameters (two for its position and two for its spectrum), we expect that $TS \sim \chi^2(4)$, from which its significance can be evaluated. A source-detection threshold of $TS=25$ was adopted in 1FGL, which corresponds to a false detection probability of 5×10^{-5} if $TS \sim \chi^2(4)$.

The `gtlike` model used for localization in this paper includes the 1FGL J1642.5+3947

⁵<http://fermi.gsfc.nasa.gov/ssc/data/analysis/documentation/Cicerone/>

⁶Mission Elapsed Time (MET) is measured in seconds from 2001.0 UT, including leap seconds.

⁷The Earth’s limb lies at a zenith angle of $\sim 113^\circ$ at the 565 km nearly circular orbit of *Fermi*. The zenith angle is defined as the angle of a photon’s apparent origin to the Earth-spacecraft vector.

point-source component and all other point sources from the 1FGL catalog (Abdo et al. 2010b) within a 20° radius around the radio position of 3C 345. Further analysis was performed using two point-source components instead of one to fit the observed data. The model parameters for sources outside the 15° ROI were fixed to their respective 1FGL values. The model included 20 or 21 point sources with free parameters (flux and spectral index), depending on whether a single point source was fitted for 1FGL J1642.5+3947 (20 point sources) or whether two source components were added to take into account the separate contributions of 3C 345 and NRAO 512 (21 point sources). The background component of Galactic diffuse emission (`gll_iem_v02.fit`) and an isotropic component (`isotropic_iem_v02.txt`), both of which are the standard models available from the *Fermi* Science Support Center (FSSC)⁸, were added as well. The isotropic component includes both the contribution from the extragalactic diffuse emission and from the residual, charged particle backgrounds.

To produce light curves, the standard tool `gtlike` was used, applying an unbinned spectral likelihood analysis as described above. A `gtlike` input source model was constructed based on the improved 20-month spectral fits obtained from the localization analysis. Only sources that were detected with a $TS > 25$ in the 20-month integration were included in the final `gtlike` input source model to construct a light curve. The data were split into regular time intervals, each integrating over periods of 2, 5, 7 and 30 days. Then an unbinned spectral likelihood analysis was performed on each integrated dataset with photon indices fixed to the 20-month average values. For time periods with a significance of the detection of $TS < 5$ on 5- and 30-day scales, 2σ upper limits were calculated following the likelihood profile (Rolke et al. 2005), where the upper limit is determined by increasing the flux from the maximum likelihood value until the log likelihood decreases by 2.0 (for the particular implementation in case of LAT data see Abdo et al. 2010a). All light curves make use of the collected data in the energy range of 0.1-300 GeV. Different time binnings were chosen to study different aspects of the time evolution of the source flux. To study the longer term behavior, 30-day bins were used, monthly bins being relatively standard for *Fermi* analysis. To assess faster flaring behavior, and in particular to estimate when the peak flaring occurs, a two-day time binning was selected. Finally, the best compromise between short and long time bins is the light curve with five-day integration periods. The interpretation of the results from this analysis is provided in Chapter 6 and 7.

4.4 Millimeter Radio and Optical Observations

In the case of 3C 345, a dense optical monitoring was performed by the GLAST-AGILE Support Program (GASP) of the Whole Earth Blazar Telescope (WEBT) collaboration. The GASP-WEBT is performing long-term monitoring of 28 γ -ray loud blazars in the optical, near-infrared, mm, and radio bands (Villata et al. 2008, 2009). The GASP has been closely following a strong optical outburst in 3C 345 reported during the second half of 2009 (Larionov et al. 2009). The optical GASP data for this thesis were acquired at the following observatories: Abastumani (Georgia), Calar Alto (Spain, within the MAPCAT program), Crimean (Ukraine), Lowell (Perkins, USA), Lu-lin (SLT, Taiwan), Sabadell (Spain), St. Petersburg (Russia), and Tjarafe (Spain).

⁸ <http://fermi.gsfc.nasa.gov/ssc/data/access/lat/BackgroundModels.html>



Figure 4.9: Photograph of the Sub-millimeter Array on Mauna Kea, Hawaii USA.

Optical magnitude calibration was performed with respect to a common choice of reference stars in the field of the source obtained from the photometric sequence by González-Pérez et al. (2001). In addition to the GASP monitoring data, optical observations performed by the Special Astrophysical Observatory (SAO) of the Russian Academy of Sciences, using the SAO Zeiss 1-m telescope in BVR bands were included. The observational strategy and calibration procedures applied were described in detail by Bychkova et al. (2004). In Chapter 6 and 7 of this thesis, the R band magnitudes were converted to the linear flux density scale to compare light curves between wavelengths. The magnitudes were corrected for a Galactic extinction of 0.036 mag, for the magnitude to flux conversion the zero magnitude fluxes of Bessell et al. (1998) were used.

Two R-band observations of 3C 345 and B3 1640+396 were conducted on January 26th, 2009 (14x180 s exposure), and on February 13th, 2009 (13x180 s exposure) by K. Sokolvosky on my behalf, using a robotic 200-mm telescope of the Tzec Maun observatory (Mayhill, NM, USA). Magnitude calibration was performed in a manner similar to the GASP observations.

Table 4.3 lists the relevant results of UV/optical observations of 3C 345, NRAO 512 and B3 1640+396 performed at Tzec Maun observatory and *Swift* UVOT. The resulting R magnitudes and SMA flux densities are listed in Appendix C. The Galactic extinction in the direction of these sources is between $E(B-V) = 0.010$ mag and 0.014 mag according to the tables of Schlegel et al. (1998). Using the extinction law by Cardelli et al. (1989) and coefficients describing the UVOT filters (Romíng et al. 2009), the following extinctions (in magnitudes) were obtained for the individual bands: 0.03–0.04 (V), 0.04–0.06 (B), 0.05–0.07 (U), 0.07–0.09 (W1), 0.09–0.13 (M2) and 0.08–0.12 (W2).

The source 3C 345 was monitored also at mm wavelengths (230 GHz) by the Submillimeter Array (SMA) on Mauna Kea, shown in Figure 4.9, for the GASP and in separate private communication with M. Gurwell. Additionally, a program conducted by Ann Wehrle (*private communication*) provided the data collected by the SMA for NRAO 512 and B3 1640+396. In general the SMA provides regular monitoring of bright blazars through their calibrator monitoring program.

31 Years of High Angular Resolution Observations of 3C 345

An unprecedented database of high angular resolution observations of 3C 345 is established, covering a frequency range from 1 – 43 GHz and a time range of 31 years (1979 – 2010). The general properties of this dataset are summarized in the previous chapter. In the following, the frequency and time dependence of core-shifts are investigated (Sec. 5.1), the long-term kinematics (Section 5.2) and structural variability (Section 5.3) of the parsec scale jet are studied and physical properties of the jet itself are derived (Section 5.4).

5.1 The Nuclear Region (“core”)

The base of the jet, i.e. the “core”, in images obtained with very long baseline interferometry (VLBI) observations at any given frequency is usually the most compact feature identified in jets. For many blazars it is believed to be the optically thick region of the jet with $\tau = 1$. The absolute position of the core to the true foot-point of the jet depends on the observing frequency ν_{obs} , which was introduced in Section 2.3. The frequency dependent position shifts have to be taken into account when multi-wavelength observations are combined to study the kinematics of components in this chapter.

Here, the time and frequency dependence of the absolute core position is investigated using the database of observations established for this thesis. Suitable observations are selected based on availability of simultaneous multi-frequency coverage and presence of well defined, optically thin jet features. The distance of optically thin feature(s) to the VLBI core is compared between two frequencies. This way a total of 71 frequency pair values from 99 observations are obtained. In cases of multiple, reference components per frequency pair, the weighted average is computed. The resulting values and characteristics of the frequency pairs are summarized in Table 5.1. To illustrate the

distribution of obtained core-shifts, the absolute value of the core-shift (r_{shift}) for each frequency pair is plotted against time in Figure 5.1.

The directions of the core-shift (ϕ_{shift}), for which a significant shift is obtained, are plotted in Figure 5.2. The average direction of the shift is $(-102.5 \pm 2.0)^\circ$, which is consistent with the general direction of the flow of the jet. No significant frequency dependence is found for the direction of the shifts (see Table 5.2). The position angles of the shift scatter around the average value at the 1σ level. The significance of a deviation from the weighted average of the position angles is estimated using the standard χ^2 test. A $\chi^2 = 600$ is obtained, which corresponds to an extremely small chance probability, less than 0.1% (with 62 degrees of freedom). This implies that no significant deviation of the values from the mean value is obtained. A linear slope is fitted to the position angle dataset, resulting in a slope of $(0.84 \pm 1.5)^\circ \text{ year}^{-1}$, this slope is shown in Fig. 5.2 as well. This clearly demonstrates that no long-term trend is observed for the direction of the shift.

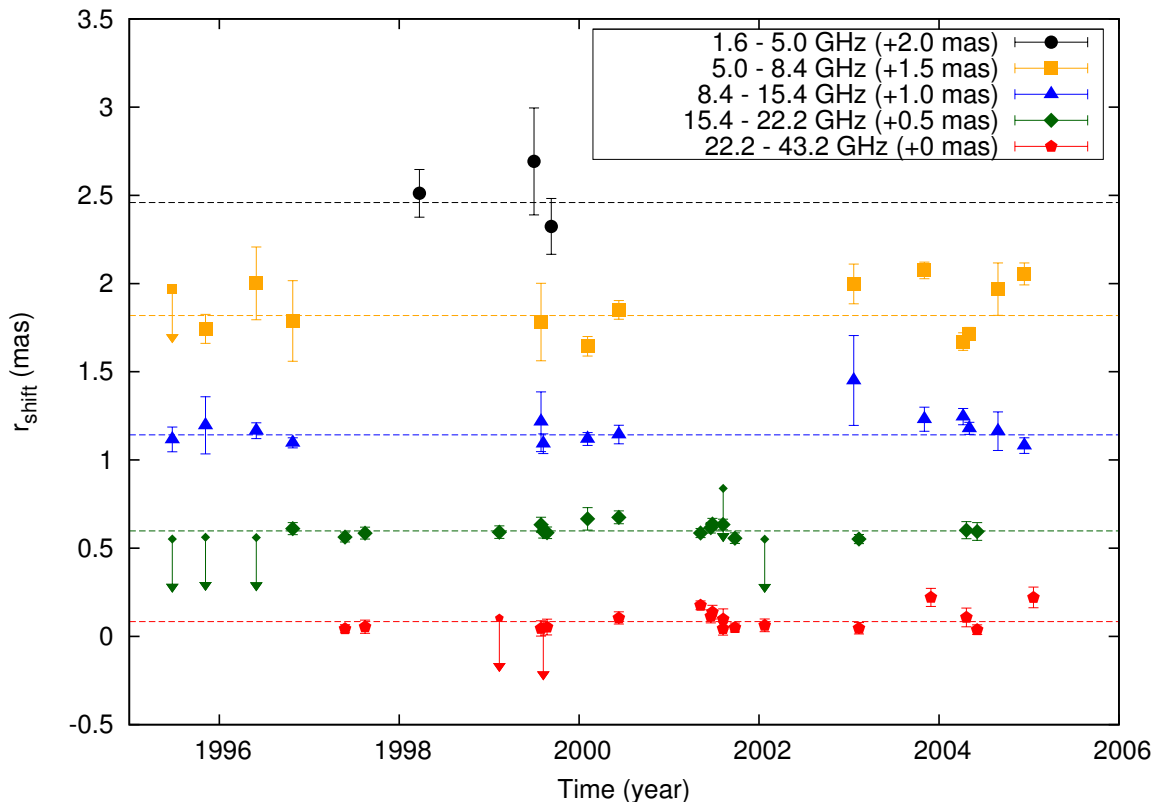


Figure 5.1: Distribution of core-shifts of simultaneously observed frequency pairs. The core-shifts are shifted for readability by constant values of +0.5, +1.0, +1.5, and +2.0 mas, for the pairs of 15.4 – 22.2, 8.4 – 15.4, 5.0 – 8.4, and 1.6 – 5.0 GHz respectively. Points with downward arrows are 1σ upper limits. Vertical lines are drawn in corresponding colors for the particular frequency pairs 1.6 – 5.0, 5.0 – 8.4, 8.4 – 15.4, 15.4 – 22.2, 22.2 – 43.2 GHz, indicating the respective weighted averages of the core-shifts listed in Table 5.2

Table 5.1: Selected observations and jet components for core-shift analysis and their corresponding core-shift values.

Date	ν_1 - ν_2 (GHz)	C	\bar{x}_{shift} (mas)	\bar{y}_{shift} (mas)	r_{shift} (mas)	ϕ_{shift} ($^\circ$)	$\Omega_{r\nu}$ (pc GHz)
1995-06-24	5-8	5	-0.10 ± 0.36	-0.034 ± 0.36	≤ 0.47	-	≤ 38
	8-15	5,7	-0.062 ± 0.070	-0.099 ± 0.070	0.117 ± 0.070	-146 ± 34	14.3 ± 8.6
	15-22	7,8	-0.012 ± 0.036	-0.010 ± 0.036	≤ 0.052	-	≤ 17
1995-11-05	5-8	7	-0.233 ± 0.082	-0.071 ± 0.082	0.243 ± 0.082	-107 ± 19	19.9 ± 6.7
	8-15	5	-0.110 ± 0.16	0.0098 ± 0.16	0.110 ± 0.16	-87 ± 47	24 ± 20
	15-22	5,7	-0.022 ± 0.039	0.0097 ± 0.039	≤ 0.062	-	≤ 21
1996-05-30	5-8	3,4,5	-0.50 ± 0.21	0.017 ± 0.21	0.50 ± 0.21	-88 ± 24	41 ± 17
	8-15	7	-0.142 ± 0.045	-0.086 ± 0.045	0.166 ± 0.045	-121 ± 15	20.3 ± 5.5
	15-22	7,8	-0.0079 ± 0.041	-0.017 ± 0.041	≤ 0.0510	-	≤ 20
1996-10-25	5-8	5	-0.16 ± 0.23	-0.24 ± 0.23	0.29 ± 0.23	-144 ± 45	24 ± 19
	8-15	7,8	-0.087 ± 0.029	-0.044 ± 0.029	0.097 ± 0.029	-117 ± 17	11.9 ± 3.5
	15-22	7,8	-0.092 ± 0.034	-0.061 ± 0.034	0.111 ± 0.034	-123 ± 18	37 ± 11
1997-05-26	15-22	8,9	-0.059 ± 0.028	-0.022 ± 0.028	0.063 ± 0.028	-110 ± 25	21.1 ± 9.3
	22-43	8,9	-0.041 ± 0.023	-0.014 ± 0.023	0.043 ± 0.023	-108 ± 30	13.2 ± 7.0
1997-08-15	15-22	8,9	-0.085 ± 0.034	-0.0060 ± 0.034	0.085 ± 0.034	-94 ± 23	28 ± 11
	22-43	9	-0.033 ± 0.037	-0.044 ± 0.037	0.055 ± 0.037	-143 ± 39	17 ± 11
1998-03-24	2-5	4,5,7	-0.50 ± 0.13	0.099 ± 0.13	0.51 ± 0.13	-77 ± 15	8.0 ± 2.1
1999-02-11	15-22	8,9	-0.085 ± 0.035	0.033 ± 0.035	0.091 ± 0.035	-68 ± 22	30 ± 12
	22-43	8,9	-0.042 ± 0.061	0.0022 ± 0.061	≤ 0.10	-	≤ 31
1999-07-01/02	2-5	4,5	0.36 ± 0.30	-0.59 ± 0.30	0.69 ± 0.30	31 ± 25	10.8 ± 4.7
1999-07-30	5-8	7	-0.24 ± 0.22	-0.16 ± 0.22	0.28 ± 0.22	-123 ± 45	23 ± 18
	8-15	9	-0.12 ± 0.17	0.18 ± 0.17	0.22 ± 0.17	-31 ± 45	27 ± 21
	15-22	9,10	-0.132 ± 0.042	-0.013 ± 0.042	0.133 ± 0.042	-94 ± 18	44 ± 14
	22-43	9	-0.00110 ± 0.043	-0.045 ± 0.043	0.045 ± 0.043	-177 ± 55	14 ± 13
1999-08-08	8-15	9	-0.054 ± 0.056	-0.075 ± 0.056	0.092 ± 0.056	-144 ± 35	11.3 ± 6.8
	15-22	9	-0.095 ± 0.039	-0.015 ± 0.039	0.096 ± 0.039	-97 ± 23	32 ± 13
	22-43	8,9	-0.0050 ± 0.035	-0.0110 ± 0.035	≤ 0.056	-	≤ 17
1999-08-23	15-22	7,8,9	-0.086 ± 0.033	-0.015 ± 0.033	0.087 ± 0.033	-98 ± 22	29 ± 11
	22-43	7,9	-0.023 ± 0.045	-0.047 ± 0.045	0.053 ± 0.045	-152 ± 49	16 ± 14
1999-09-09/10	2-5	7	-0.32 ± 0.16	-0.059 ± 0.16	0.32 ± 0.16	-100 ± 28	5.1 ± 2.5
2000-02-04	5-8	7,8	-0.144 ± 0.055	-0.0059 ± 0.055	0.144 ± 0.055	-92 ± 22	11.8 ± 4.5

Continued on next page ...

Table 5.1 – continued from previous page

Date	$\nu_1 - \nu_2$ (GHz)	C	\bar{x}_{shift} (mas)	\bar{y}_{shift} (mas)	r_{shift} (mas)	ϕ_{shift} ($^\circ$)	Ω_{rv} (pc GHz)
	8-15	8,9	-0.117 ± 0.036	-0.020 ± 0.036	0.119 ± 0.036	-98 ± 17	14.6 ± 4.5
	15-22	9,10	-0.133 ± 0.064	-0.100 ± 0.064	0.166 ± 0.064	-125 ± 22	55 ± 21
2000-06-10	5-8	5,7,8	-0.332 ± 0.053	-0.113 ± 0.053	0.351 ± 0.053	-108.8 ± 8.7	28.7 ± 4.4
	8-15	8,9	-0.137 ± 0.052	0.047 ± 0.052	0.144 ± 0.052	-71 ± 21	17.7 ± 6.4
	15-22	9,10	-0.168 ± 0.037	-0.048 ± 0.037	0.175 ± 0.037	-104 ± 12	58 ± 12
2001-05-08	22-43	10,11	-0.105 ± 0.034	-7.789 ± 0.034	0.105 ± 0.034	-90 ± 19	32 ± 10
	15-22	12	-0.083 ± 0.026	-0.024 ± 0.026	0.086 ± 0.026	-106 ± 17	28.7 ± 8.5
	22-43	9,10,12	-0.176 ± 0.025	-0.0085 ± 0.025	0.176 ± 0.025	-92.6 ± 8.1	53.3 ± 7.5
2001-06-19	15-22	9,10,11	-0.106 ± 0.030	-0.047 ± 0.030	0.116 ± 0.030	-114 ± 15	39 ± 10
	22-43	11	-0.113 ± 0.037	0.013 ± 0.037	0.114 ± 0.037	-83 ± 19	34 ± 11
2001-06-25	15-22	9,10,11	-0.134 ± 0.032	-0.026 ± 0.032	0.137 ± 0.032	-101 ± 14	46 ± 11
	22-43	10,11	-0.135 ± 0.039	-0.025 ± 0.039	0.138 ± 0.039	-99 ± 16	42 ± 12
2001-08-07	15-22	9,10,11	-0.130 ± 0.030	-0.034 ± 0.030	0.134 ± 0.030	-103 ± 13	44.8 ± 10.0
	22-43	12	-0.039 ± 0.037	-0.021 ± 0.037	0.044 ± 0.037	-116 ± 48	13 ± 11
2001-08-08	15-22	7	-0.053 ± 0.29	0.0035 ± 0.29	≤ 0.34	-	≤ 113
	22-43	11	-0.092 ± 0.058	0.034 ± 0.058	0.098 ± 0.058	-68 ± 34	30 ± 18
2001-09-24	15-22	10,12	-0.032 ± 0.030	-0.047 ± 0.030	0.057 ± 0.030	-146 ± 30	18.9 ± 10.0
	22-43	12,13	-0.049 ± 0.026	0.010 ± 0.026	0.050 ± 0.026	-78 ± 29	15.3 ± 7.7
2002-01-24	15-22	9,10	-0.00410 ± 0.039	-0.011 ± 0.039	≤ 0.051	-	≤ 17
	22-43	10,12	-0.063 ± 0.036	0.0064 ± 0.036	0.063 ± 0.036	-84 ± 33	19 ± 11
2003-01-20	5-8	9	-0.30 ± 0.11	-0.310 ± 0.11	0.410 ± 0.11	-141 ± 13	40.8 ± 9.2
	8-15	7	-0.33 ± 0.25	0.31 ± 0.25	0.45 ± 0.25	-46 ± 32	55 ± 31
2003-02-10	15-22	10,12,14	-0.051 ± 0.026	-0.0086 ± 0.026	0.052 ± 0.026	-98 ± 29	17.3 ± 8.6
	22-43	10,12,14	-0.046 ± 0.033	-0.0072 ± 0.033	0.046 ± 0.033	-97 ± 41	14.0 ± 9.9
2003-11-02	5-8	8,9	-0.550 ± 0.047	-0.163 ± 0.047	0.574 ± 0.047	-106.5 ± 4.7	47.0 ± 3.8
	8-15	8,9	-0.225 ± 0.068	-0.051 ± 0.068	0.231 ± 0.068	-101 ± 17	28.3 ± 8.4
2003-11-28	22-43	12,14	-0.222 ± 0.051	-0.00083 ± 0.051	0.222 ± 0.051	-90 ± 13	67 ± 16
2004-04-08	5-8	8,10	-0.160 ± 0.050	0.059 ± 0.050	0.171 ± 0.050	-68 ± 17	14.0 ± 4.1
	8-15	12	-0.217 ± 0.046	-0.115 ± 0.046	0.246 ± 0.046	-116 ± 11	30.1 ± 5.7
2004-04-21	15-22	9,10	-0.081 ± 0.049	-0.062 ± 0.049	0.102 ± 0.049	-127 ± 27	34 ± 16
	22-43	10,12	-0.107 ± 0.053	-0.0087 ± 0.053	0.108 ± 0.053	-93 ± 28	33 ± 16
2004-05-03	5-8	5,8,10	-0.206 ± 0.035	0.065 ± 0.035	0.216 ± 0.035	-72.2 ± 9.4	17.7 ± 2.9

Continued on next page ...

Table 5.1 – continued from previous page

Date	ν_1 - ν_2 (GHz)	C	\bar{x}_{shift} (mas)	\bar{y}_{shift} (mas)	r_{shift} (mas)	ϕ_{shift} ($^\circ$)	$\Omega_{r\nu}$ (pc GHz)
2004-06-04	8-15	10,12	-0.174 ± 0.034	-0.042 ± 0.034	0.179 ± 0.034	-103 ± 11	22.0 ± 4.2
	15-22	9,13	-0.088 ± 0.050	-0.035 ± 0.050	0.094 ± 0.050	-110 ± 31	31 ± 17
2004-08-27	22-43	16	-0.016 ± 0.027	-0.035 ± 0.027	0.038 ± 0.027	-153 ± 41	11.6 ± 8.2
	5-8	6,9	-0.47 ± 0.15	-0.013 ± 0.15	0.47 ± 0.15	-90 ± 18	38 ± 12
2004-12-12	8-15	9,12	-0.12 ± 0.11	-0.11 ± 0.11	0.16 ± 0.11	-132 ± 38	20 ± 13
	5-8	9	-0.527 ± 0.062	-0.173 ± 0.062	0.555 ± 0.062	-108.2 ± 6.4	45.4 ± 5.1
2005-01-19	8-15	8,9,10	-0.081 ± 0.044	0.013 ± 0.044	0.082 ± 0.044	-81 ± 31	10.0 ± 5.4
	22-43	12,13	-0.190 ± 0.058	-0.113 ± 0.058	0.221 ± 0.058	-119 ± 15	67 ± 18

Notes:

Date – Observations data;

 ν_1 - ν_2 – Observation frequency pair (low–high);

C – Component label (see Section 4.1);

 $\bar{x}_{\text{shift}}, \bar{y}_{\text{shift}}$ – Values (in case of multiple components) of the position shifts in relative right ascension (x) and declination (y); r_{shift} – Magnitude of the core-shift vector, in cases where the error is larger than the value, the 1σ upper limit is given; ϕ – Angle (to the North–South axis) indicating the direction of the shift; $\Omega_{r\nu}$ – Core-shift measure as defined in Section 2.3.

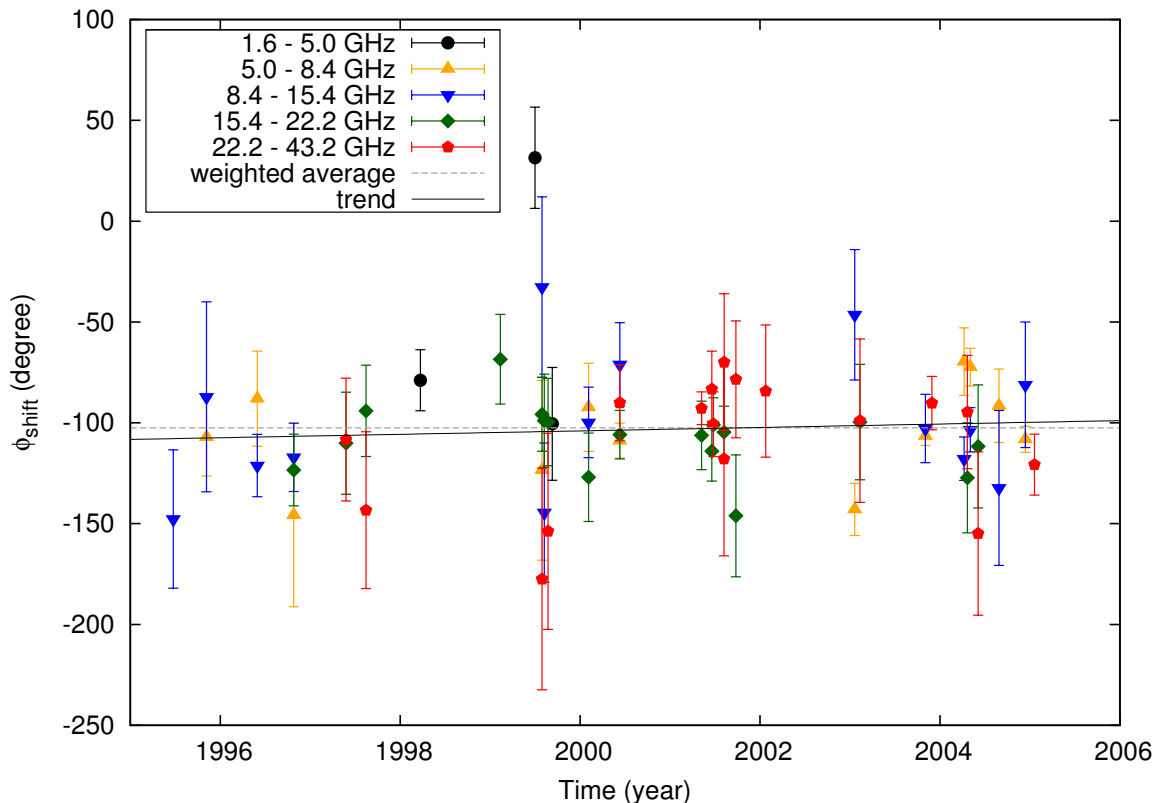


Figure 5.2: Time variability of the direction of the core-shifts of simultaneously observed frequency pairs. Different symbols and colors indicate the corresponding group of frequency pairs (1.6 – 5.0, 5.0 – 8.4, 8.4 – 15.4, 15.4 – 22.2, and 22.2 – 43.2 GHz). A horizontal, dashed line at -102.5° indicates the weighted average value of the direction. The solid line indicates a fitted trend (using equal weights) to all position angle values, with a slope of $(0.84 \pm 1.5)^\circ \text{ year}^{-1}$.

To further investigate the observed variability in the position angle of the core-shifts, the values of ϕ_{shift} are compared to the position angles of the reference components. The respective position angles are plotted in Figure 5.3, from which no correlation is evident. However, to quantify whether these values are weakly correlated or just random, the formal linear correlation estimate, using the Pearson product-moment correlation coefficient (Fisher 1944; Wall & Jenkins 2003), is determined:

$$r = \frac{\sum_{i=1}^N (X_i - \bar{X})(Y_i - \bar{Y})}{\sqrt{\sum_{i=1}^N (X_i - \bar{X})^2 \sum_{i=1}^N (Y_i - \bar{Y})^2}}. \quad (5.1)$$

This results in a value of $r = -0.22$. The significance of a non-zero value of r can be tested calculating:

$$t = \frac{r\sqrt{N-2}}{\sqrt{1-r^2}}, \quad (5.2)$$

where $(N - 2)$ corresponds to the degrees of freedom, here corresponding to 61 degrees of freedom. The parameter t follows the distribution of the Student's t statistic¹. A

¹“[Named] after its discoverer W.S. Gosset (1876–1937), who developed the test while working on quality control sampling for Guinness. For reasons of industrial secrecy Gosset was required to publish under a pseudonym” (Wall & Jenkins 2003, p. 62).

value of $t = -1.8$ is obtained, which corresponds to a critical value of $p < 0.077$ ($> 92\%$ probability of making a correct statement), using the percent point function. This indicates (at most) a weak, direct correlation between the position angles of the shift and the related position angles of the reference components.

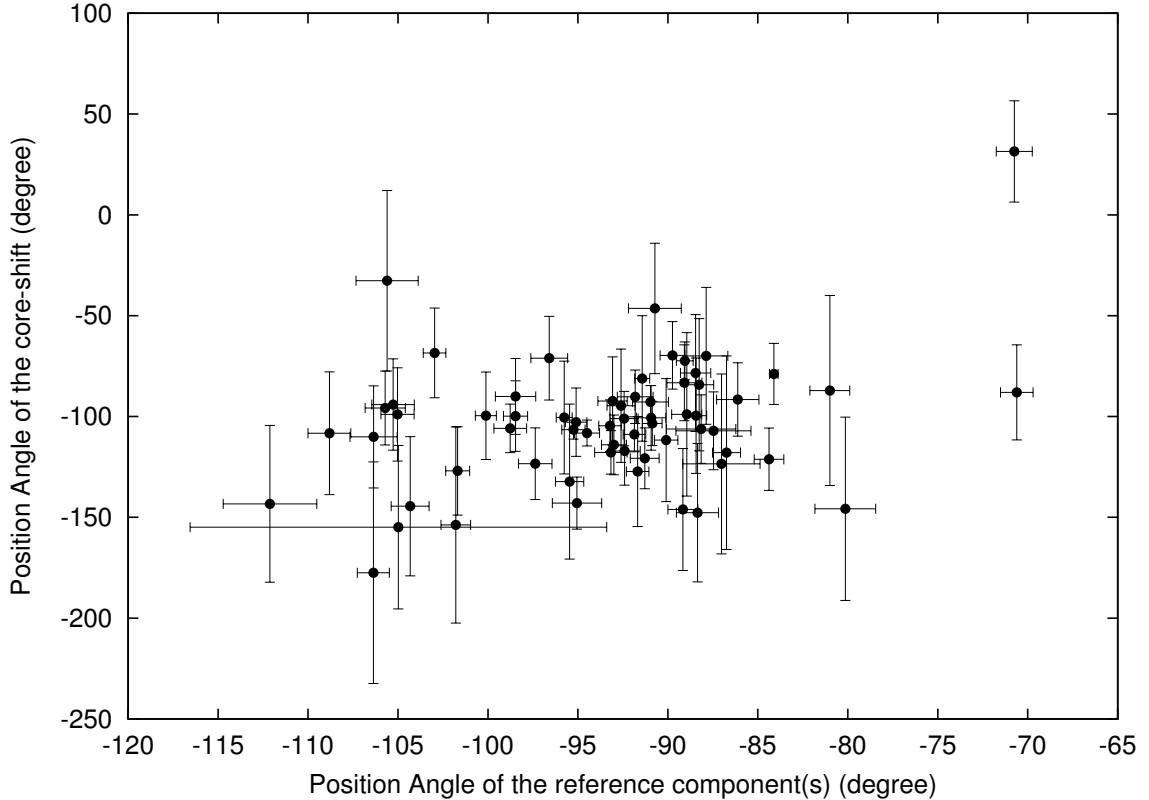


Figure 5.3: The average position angles of the reference components, used to calculate the core-shift between two frequencies, is compared to the obtained position angles of the core-shifts.

The core-shift measure $\Omega_{r\nu}$, introduced in Section 2.3 (Equation 2.7), provides a frequency independent expression for the core-shift r_{shift} . Also, the value of $\Omega_{r\nu}$ should remain constant in time, if $\Omega_{r\nu} = (B_1^{k_b} F)^{1/k_r} \sin \theta = \text{const.}$, where B_1 is the magnetic field at a distance of 1 pc from the central engine, F , k_r and k_b are defined in Section 2.3, θ is the viewing angle of the jet axis to the line of sight. The values of $\Omega_{r\nu}$ are computed for the equipartition case and are listed in Table 5.1, weighted averages for each group of frequency pairs are listed in Table 5.2. The 1.6–5.0 GHz pairs clearly disagree with values obtained at the other frequency pairs, which points toward an underestimation of the core-shift. The direction of the shift is $\sim 40^\circ$ more toward the North than for the other frequency pairs and the shift at 1.6 GHz is based on only three frequency pair values (see Table 5.2). The typical beam size at 1.6 GHz is a factor of ~ 3 higher than for 5.0 GHz, which is significantly higher than for the other frequency pairs. In the case of the lowest frequency pair, most of the reference components used for calculation of the core-shift are within, or close to, the beam size at 1.6 GHz, leading to a blending of the components and a systematic offset from the true core-shift. The remaining frequency pairs agree well with each other and their weighted average, excluding 1.6–5.0 GHz, is $\Omega_{r\nu} = (23.80 \pm 0.94) \text{ pc GHz}$. The time variability of $\Omega_{r\nu}$ is shown in Figure 5.4. Similar to the core-shift direction, a large scatter of the values is observed toward both sides of the long-term trend, but it does not appear random in all the cases, which

Table 5.2: Weighted averages of relative core-shifts for each group of frequency pairs, calculated from the values listed in Table 5.1.

$\nu_1 - \nu_2$ (GHz)	#	\bar{r}_{shift} (mas)	$\bar{\phi}_{\text{shift}}$ ($^\circ$)	$\Omega_{r\nu}$ (pc GHz)
1.6–5.0	3	0.459 ± 0.097	-59 ± 12	7.2 ± 1.5
5.0–8.4	12	0.319 ± 0.018	-103.8 ± 3.0	26.1 ± 1.5
8.4–15.4	14	0.142 ± 0.013	-106.7 ± 5.1	17.4 ± 1.6
15.4–22.2	17	0.0978 ± 0.0081	-106.4 ± 4.5	32.6 ± 2.7
22.2–43.2	17	0.0841 ± 0.0084	-97.8 ± 4.8	25.5 ± 2.5

Notes:

$\nu_1 - \nu_2$ – frequency pair (low – high) frequency;

– number of pairs used for the weighted average;

\bar{r}_{shift} – average absolute value of the core-shift;

$\bar{\phi}_{\text{shift}}$ – average direction of the core-shift, the angle is measured to the North-South axis.

could mean that errorbars are slightly over-predicted. As a consequence of this, the linear trend is obtained using equal weights for fitting data points, note, this produces an offset of the trend from the weighted average of $\Omega_{r\nu}$. Similar to the direction of the core-shift, the core-shift measure shows a mild long-term trend with a change in its value from ~ 20 to ~ 30 pc GHz.

In the case of constant jet particle and magnetic field energy densities (equipartition), the only plausible cause for a change of $\Omega_{r\nu}$ is a change in the viewing angle θ . This is supported by a possible weak connection found between the core-shift direction and the reference components, which would indicate a connection between the structure of the jet and the core-shift measurement. However, if the variation in $\Omega_{r\nu}$ is not purely geometrical, then an increase in the magnetic field and/or particle density can cause an increase in the core-shift, as well. In Section 2.3, for the equipartition case, it was shown that the synchrotron luminosity L_{syn} can be related to the observed core-shift, $r_{\text{shift}} \propto L_{\text{syn}}^{2/3}$.

The observed scatter of $\Omega_{r\nu}$ could be related to the activity state of the source. Since the luminosity is directly proportional to the core flux density ($L_{\text{syn}} \propto S_\nu$), the obtained values of $\Omega_{r\nu}$ are compared to the core flux densities. In order to avoid systematics from the combination of frequency pairs at different frequency ranges, one of the most frequently observed frequency pair (22.2 – 43.2 GHz) is selected. No matter whether the long-term trend is subtracted from the values, a weak direct correlation is found between $\Omega_{r\nu}$ and the core flux density at 43.2 GHz with a significance of $\sim 90\%$ ($r = 0.43$, $t = 1.66$ and 12 degrees of freedom), if the three outliers with positive core spectral index are ignored. No significant correlation is found if the outliers are included (see Figure 5.5). Also, the data points follow the expected relationship $\Omega_{r\nu} \propto S_\nu^{2/3}$, however due to the large errorbars and scatter it is not possible to establish this relationship from the data.

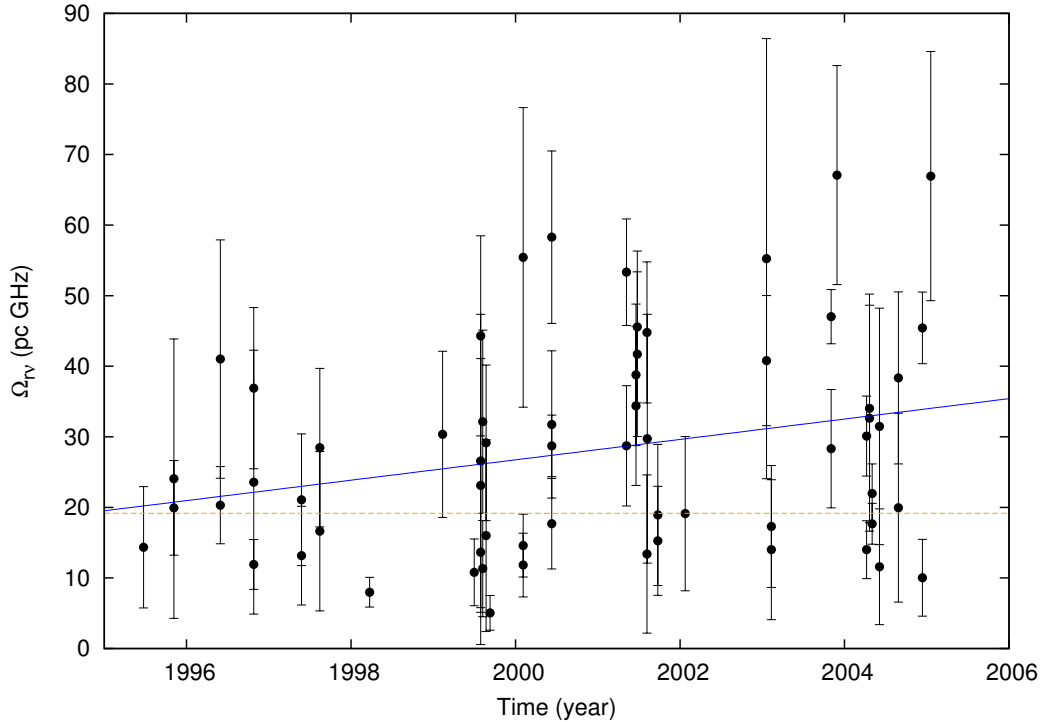


Figure 5.4: Time variability of the core-shift measure $\Omega_{r\nu}$. The dashed horizontal line indicates the global weighted average of $\Omega_{r\nu} = (19.16 \pm 0.81)$ pc GHz. The blue solid line indicates a long-term trend fitted to the data points, using equal weights, providing a slope of (1.44 ± 0.67) pc GHz year $^{-1}$.

The values of $\Omega_{r\nu}$ compared to the core flux densities at 43.2 GHz shown in Fig. 5.5 have the observed long-term trend subtracted. The two outliers at core flux densities around 2.7 Jy correspond to the observations on 1999-02-11 and 1999-07-30, where the core spectral index α ($S_\nu \propto \nu^\alpha$) between 22.2 and 43.2 GHz is positive, indicating blending of a new moving feature with the core, predominantly at the high frequency, whereas the average spectral index for the remaining epochs is $\alpha = -0.72$. This implies the cores between 22.2 and 43.2 GHz are dominated by optically thin synchrotron emission. This is surprising, the core-regions of VLBI jets are expected to have a flat spectrum, since the core represents the transition region between optically thick and optically thin emission. The average resolution limit at 43.2 GHz, d_{lim} , calculated from Equation 4.3 in Section 4.1, is ~ 0.1 mas. Fig. 5.6(b) shows that the core at 43.2 GHz is smaller than the resolution limit and can be considered unresolved in all cases. The core sizes are uncorrelated with the detrended $\Omega_{r\nu}$. In summary, except in the case of the outlier values with high values of α , blending of optically thin moving features with the core can be ruled out.

For the entire analysis and discussion of core-shifts, the equipartition case between the magnetic field and the particle energy densities was assumed. However it has to be shown that the assumption of $k_r = 1$ is consistent with the observed data. The average core-shifts listed in Table 5.2 are now used to produce the plot shown in Figure 5.7. Here, the core-shifts relative to the core position at 15.4 GHz are plotted. The relationship $r_{\text{core}} \propto \nu_{\text{obs}}^{-1/k_r}$ is used to fit the observed core-shifts, which results in $k_r = 2.9 \pm 1.1$ and $k_r = 0.98 \pm 0.19$, depending on whether the value at 1.6 GHz is included. Clearly the fit of $k_r = 2.9$ through the point at 1.6 GHz does not provide a

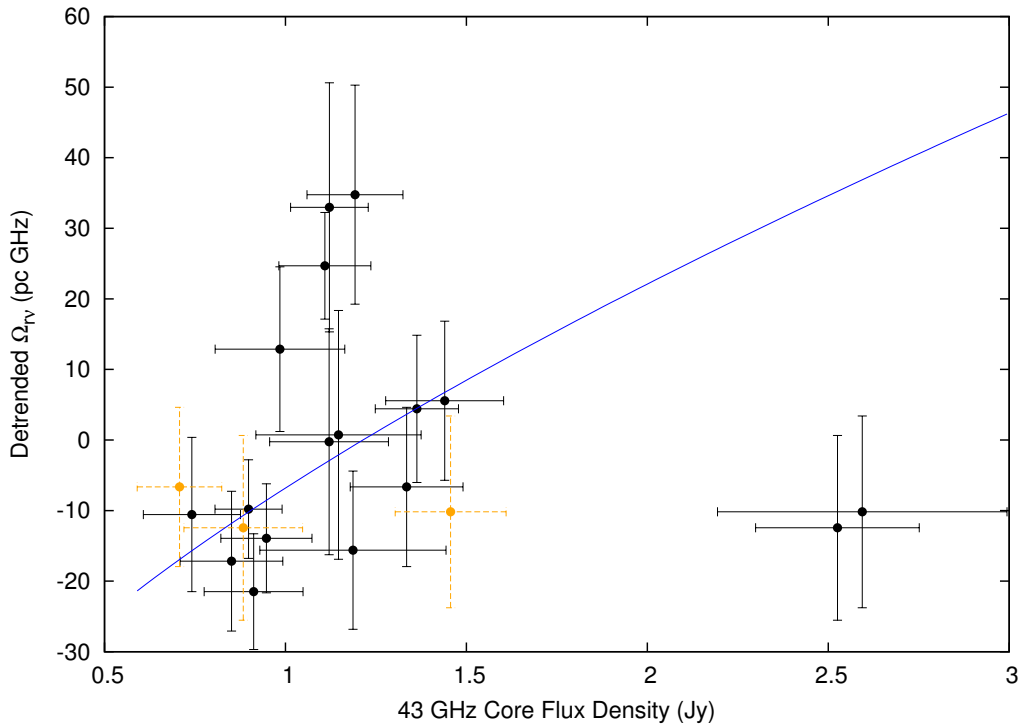


Figure 5.5: Plot comparing the detrended (see Fig. 5.4) core-shift measure $\Omega_{r\nu}$ to the corresponding core flux densities at 43.2 GHz. Core flux densities for values with a positive core spectral index (see Figure 5.6(a)) between 22.2 and 43.2 GHz are recalculated using the 22.2 GHz flux densities and an index of $\alpha = -0.72$ ($S_{\nu} \propto \nu^{\alpha}$), see the discussion provided in the text. These values are indicated by orange points, using dashed errorbars, two of which correspond to the outliers around 2.7 Jy. The solid blue curve represents the relationship of $\Omega_{r\nu} \propto S_{\nu}^{2/3}$.

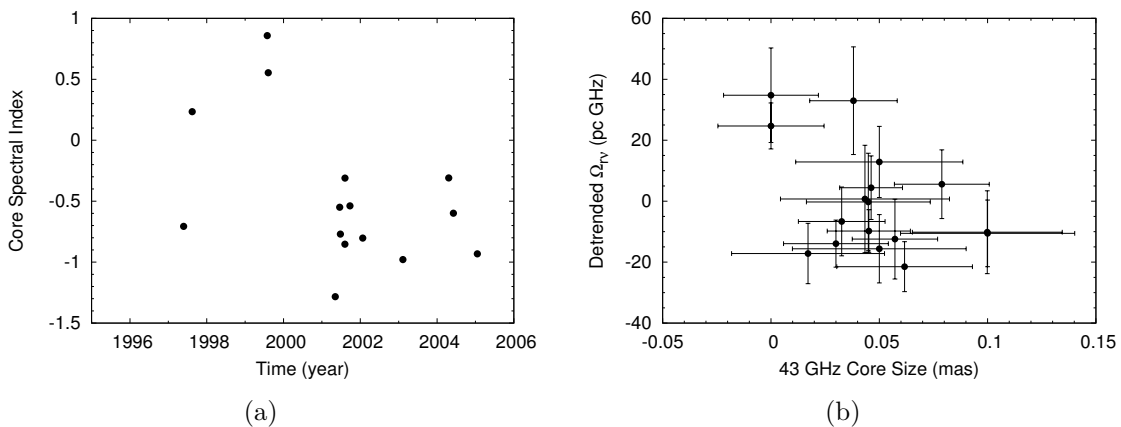


Figure 5.6: (a) The time variability of core spectral indices α between 22.2 and 43.2 GHz. The three points with positive spectral indices correspond to the observations on 1997-08-15, 1999-02-11, and 1999-07-30. The average value of α for the non-positive values is -0.72. (b) Plot of the detrended core-shift measure against FWHM of the circular Gaussian representing the core at 43.2 GHz.

good fit through the remaining data points compared to $k_r = 0.98$. Also, a $k_r = 2.9$ is physically implausible (Lobanov 1998b) and the χ^2 value for this fit is of times 8 higher than for the fit excluding the 1.6 GHz data point.

It was already noted earlier that the measured core-shift at 1.6 GHz is most likely affected by blending. Thus for subsequent analysis, the fit yielding a $k_r = 2.9$ is discarded due to this systematic effect. In conclusion, a $k_r = 1$ is consistent with the here presented observations and is used for further discussions of physical parameters in Section 5.4.

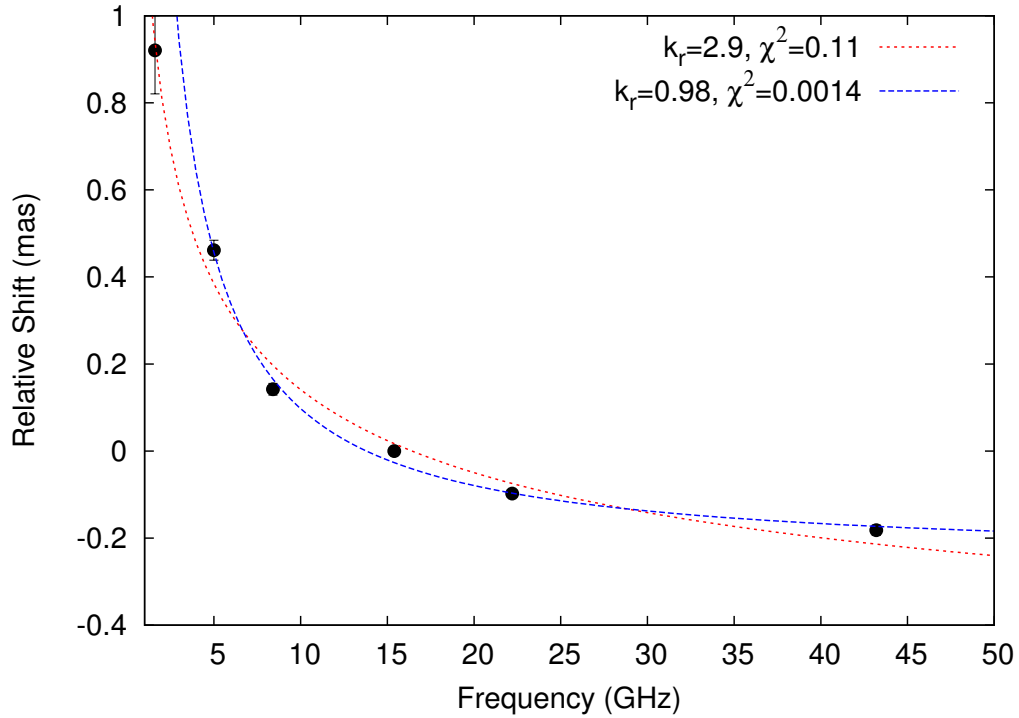


Figure 5.7: Averaged core-shifts as a function of frequency, referenced to 15.4 GHz. The curves represent the best-fit to the function $r_{\text{shift}} = a + b\nu_{\text{obs}}^{-1/k_r}$, with a value of $k_r = 2.9 \pm 1.1$, if the shift at 1.6 GHz is included (green slope) and $k_r = 0.98 \pm 0.15$ if 1.6 GHz is excluded from the fit (blue slope).

5.2 Long-term Kinematics

The full dataset of high resolution multi-wavelength observations of the parsec scale jet of 3C 345 is now combined to study the variability of the jet structure, covering a time range of 31 years (1979 – 2010). In Section 5.1, it was demonstrated that the position of the core is frequency dependent. Since the component positions are measured at each frequency with respect to the core position, the core-shift effect needs to be taken into account. Most of the observations are around 15.4 GHz, thus the positions of features in the jet are re-referenced to that of the core at 15.4 GHz (cf. Fig. 5.7). The variability of the core-shifts and direction of the shift is small compared to the magnitude of the shift and the position accuracy of the observations. The fit on the average coreshifts, from the previous chapter for a value of $k_r = 1$,

$$r_{\text{shift},15.4\text{ GHz}}(\nu_{\text{obs}}) = (3.55 \pm 0.15) \nu_{\text{obs}}^{-1} - (0.257 \pm 0.017), \quad (5.3)$$

and the direction of the shift along the axis of the jet -102.5° , are applied to all observations at frequencies other than 15.4 GHz. The typical contribution of the core-shift correction to the error in R.A./Dec is $\lesssim 15\%$. Since the error on the core-shift is different in x than in y , the full error propagation using covariances, as described in Section 4.1, would be required. However, since this additional error on the error is small, it is neglected for the subsequent analysis.

For most components and especially for those pre-dating the VLBA, many multi-wavelength observations are combined to increase the sampling of the trajectories. In particular, for these observations, subtraction of the core-shift effect and re-referencing of the component positions to the main observing frequency (15.4 GHz) is expected to improve the determination of kinematics for this period. A good example, where the scatter in the data is clearly reduced after applying the core-shift, is that of the component C3. In Figure 5.8, its original core-separations measured for the x (relative right ascension) and y (relative declination) directions separately are compared to the core-shift corrected position offsets. Also note, after core-shift correction, around 1982, one data point becomes an outlier. This point was obtained from a 2.3 GHz observations and is marked with a dotted blue circle in Figure 5.8. In Section 5.1 it was shown that at this frequency, due to blending, the core position cannot be determined accurately. For subsequent kinematic analysis, data from observations at frequencies < 5.0 GHz are not included. The scatter both in x and y direction, after the correction, is greatly reduced and even a consistent variation in the y direction becomes evident, which was not evident before.

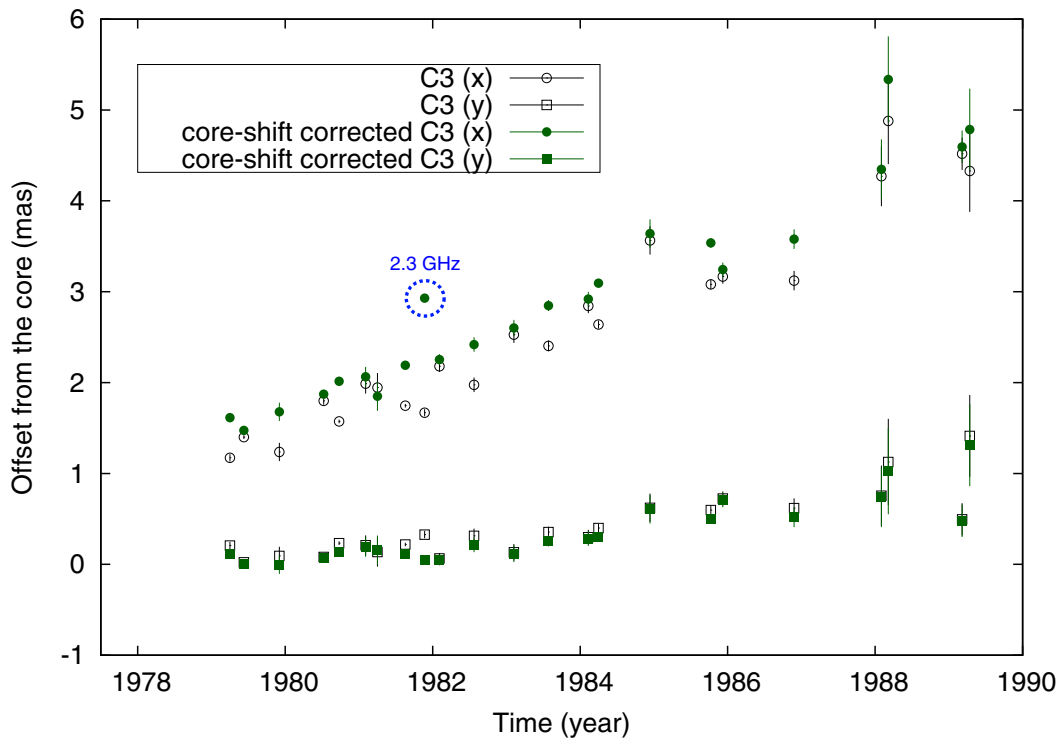


Figure 5.8: The effect of core-shift correction on the x,y separations of C3 respectively. The open black points represent the uncorrected kinematics data, filled green points represent the core-shift corrected data. Circles refer to data in the x coordinate and boxes to the y coordinate. The blue dotted circle around an outlier, corresponds to the 2.3 GHz data point discussed in the text.

The jet kinematics of 3C 345 for the time period between 1979 and 2000 was summarized and studied by Lobanov (1996) and Klare (2003). This thesis combines the previous works with the analysis of additional ~ 200 observations between 1995 and 2010. This combined dataset provides the exceptional opportunity to follow structure in the parsec scale jet of 3C 345 over a period of 30 years. Figure 5.9 provides an impression of the evolution of all individual emission regions identified over the past 31 years, with the exception of the latest features observed at 43.2 GHz in 2008 and 2009 (C21, C22, and C23). The newest features did not cover enough distance in the jet to be included in the long-term kinematic analysis. Their kinematics and relation to multi-wavelength emission are discussed at a later stage in Chapter 7.

Figure 5.10 provides a zoomed-in view on the time period that is added by this thesis. During the first 15 years, the evolution of eight components was observed, whereas during the second 16 years, the evolution of a total of 14 new components was observed. Comparing the properties of components between the first and second half of the dataset, a difference in flux density levels is observed. On average, during the first half, components were observed at higher flux density levels than during the second half. This implies a change in the flaring behavior of the source, which can also be inferred from single dish light curves at 37 GHz. After two ~ 15 Jy flares around 1982 and 1992, the peaks of high states thereafter reached only levels of about 10 Jy and the duration of the high-states get prolonged, especially visible between 1998 and 2003 (Teräsranta et al. 1998; Léon-Tavares et al. 2010). This could have the effect that even though the total energy output of the flares remains similar, the output energy is distributed over more weaker components, compared to flares before 1995. An additional observational bias could have been introduced by the advent of the VLBA after 1995, which provided a higher sampling rate and a greatly improved dynamic range. Due to this improvement it is possible to pick-up features in the jet that would have been missed otherwise. Also, the standard observation frequencies moved from mainly 5.0–10.6 GHz, to predominantly 15.4 GHz or even higher, providing a slightly higher resolution thereafter.

The kinematics of the jet in 3C 345 is investigated using the relative right ascension and declination (x , y) positions of the identified jet components relative to the core component (D), fitting them separately using polynomials of different order:

$$\{x(t), y(t)\} = \sum_i^N a_i (t - t_0)^i, \quad (5.4)$$

where t_0 refers to the midpoint in time of the dataset ($t_0 = (t_1 + t_N)/2$; cf. Zensus et al. 1995) and applying the following procedure:

1. The first order polynomial is fitted to the trajectory using the nonlinear least-squares Marquardt-Levenberg algorithm (as implemented by *gnuplot*).
2. The second order polynomial is fitted to the trajectory and if the condition of a statistically significant improvement of the reduced χ^2 is satisfied, the fit is accepted.
3. The order of the fit polynomial is increased until no statistically significant improvement according to the χ^2 statistics is achieved.

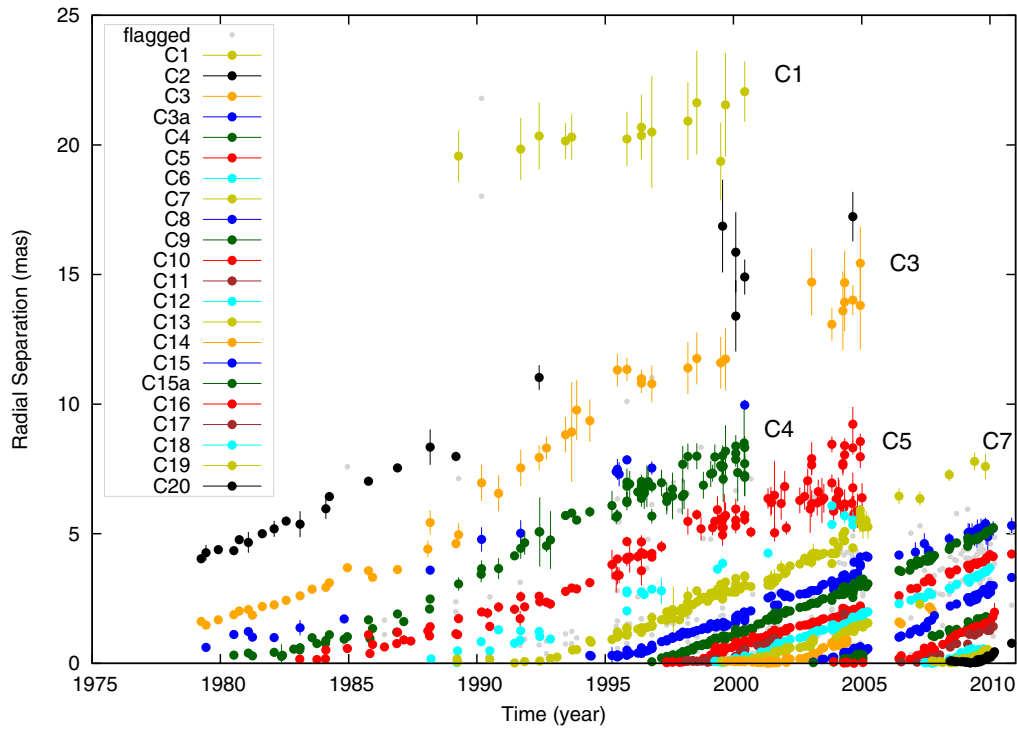


Figure 5.9: Overview of the evolution of individual jet components in radial separation from the 15.4 GHz VLBI core over a time period of 31 years (1979 – 2010). The components C21 – C23 are not shown due to their extreme proximity to the core. For these components see discussion in Chapter 7.

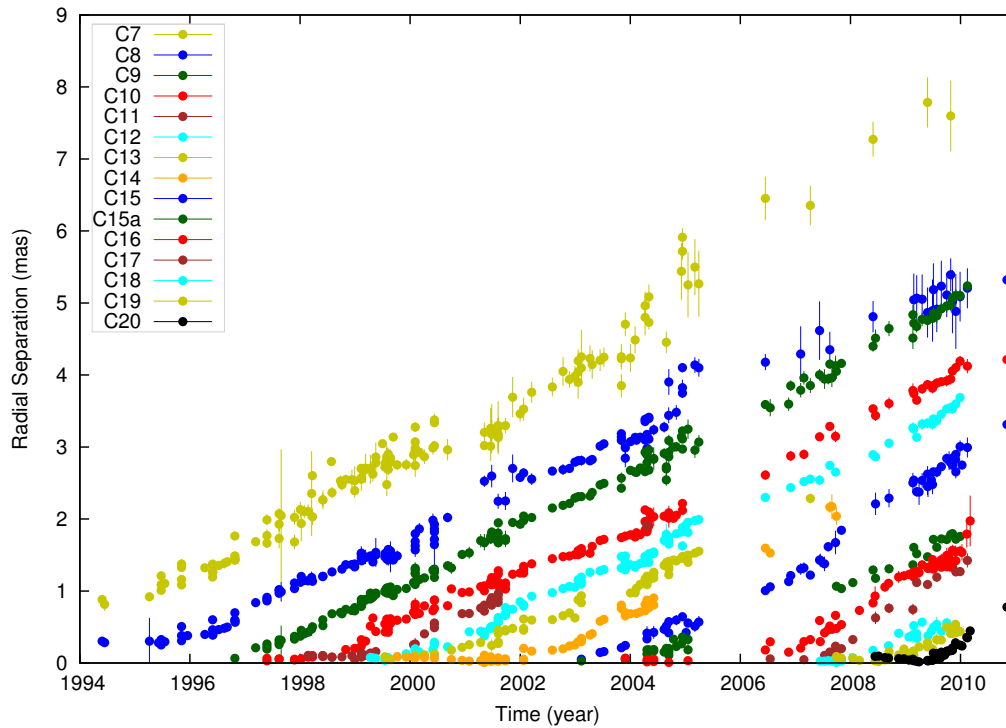


Figure 5.10: Evolution of individual jet components in radial separation, zoomed in on the time range between 1994 and 2010.

The fitted polynomial coefficients for each component in both x and y directions are listed in Table 5.3 together with the corresponding reduced χ^2 value, indicating the quality of the fit. From these fits the radial separations $r(t) = \sqrt{x(t)^2 + y(t)^2}$ are derived. For each component, the average proper motion, mean angular speed $\langle\mu\rangle$ and the average direction of motion $\langle\Phi\rangle$ can be calculated,

$$\langle\mu\rangle = \sqrt{\langle\mu_x\rangle^2 + \langle\mu_y\rangle^2} \quad (5.5)$$

$$\langle\Phi\rangle = \tan^{-1} \frac{\langle\mu_x\rangle}{\langle\mu_y\rangle} \quad (5.6)$$

$$\text{with } \langle\mu_{\{x,y\}}\rangle = \int_{t_1}^{t_N} \frac{\{\dot{x}, \dot{y}\}}{t_N - t_1} dt. \quad (5.7)$$

The time at which the component passes the 15.4 GHz VLBI core, τ_e (ejection epoch), is determined using a linear fit to the radial separation of the component with time. This assumes the observed jet emission is optically thin all the way to the core and the features already travel at the observed average speed while passing through the core. This approach provides reasonable estimates for τ_e of non-accelerating features. For features with a significant acceleration, the ejection epoch is determined from a linear fit to the initial time period, up an epoch at which the acceleration becomes statistically significant, this provides good estimates for some cases. Components for which no good fit is obtained, τ_e remains undetermined.

In the following, the individual components and their respective fits are discussed in detail, providing comparative plots of the observed trajectories with the obtained fits. The kinematic parameters and derived physical quantities are summarized in Section 5.4.

Table 5.3: Polynomial fits to the component trajectories.

Comp.		a_0	a_1	a_2	a_3	χ^2_{red}
C1	# 14	$t_{\text{mid}} = 1995.0$				
	$x(t)$	-17.21 ± 0.13	-0.078 ± 0.043			0.19
	$y(t)$	10.92 ± 0.10	0.153 ± 0.033			0.11
C2	# 22	$t_{\text{mid}} = 1992.0$				
	$x(t)$	-9.42 ± 0.13	-0.436 ± 0.014			1.7
	$y(t)$	3.39 ± 0.14	0.194 ± 0.015			2.0
C3	# 48	$t_{\text{mid}} = 1992.0$				
	$x(t)$	-6.49 ± 0.13	-0.532 ± 0.024	-0.0111 ± 0.0014		5.3
	$y(t)$	1.545 ± 0.073	0.211 ± 0.014	0.00727 ± 0.00082		1.8
C3a	# 17	$t_{\text{mid}} = 1990.0$				
	$x(t)$	-3.70 ± 0.13	-0.462 ± 0.020	-0.0158 ± 0.0020		10.8
	$y(t)$	0.92 ± 0.17	0.21 ± 0.0248	0.0097 ± 0.0026		17.1
C4	# 86	$t_{\text{mid}} = 1990.5$				
	$x(t)$	-2.958 ± 0.076	-0.415 ± 0.020	-0.0129 ± 0.0016		54
	$y(t)$	0.360 ± 0.054	0.105 ± 0.011	0.0135 ± 0.0015	$0.97\text{e-}3 \pm 0.14\text{e-}3$	14
C5	# 113	$t_{\text{mid}} = 1994.0$				
	$x(t)$	-2.746 ± 0.057	-0.357 ± 0.014	-0.0101 ± 0.0011		35
	$y(t)$	-0.069 ± 0.022	0.1255 ± 0.0055	$12.96\text{e-}3 \pm 0.43\text{e-}3$		5.1
C6	# 27	$t_{\text{mid}} = 1996.4$				
	$x(t)$	-2.557 ± 0.084	-0.351 ± 0.016			16
	$y(t)$	-0.131 ± 0.088	0.042 ± 0.014	0.0109 ± 0.0028		11
C7	# 136	$t_{\text{mid}} = 1996.6$				
	$x(t)$	-1.3423 ± 0.0031	-0.4116 ± 0.0054	-0.0203 ± 0.0013	0.00160 ± 0.00026	23
	$y(t)$	-0.0532 ± 0.0019	-0.01932 ± 0.00084			9.9

Continued on next page ...

Table 5.3 – continued from previous page

Comp.	\mathbf{a}_0	\mathbf{a}_1	\mathbf{a}_2	\mathbf{a}_3	χ^2_{red}
C7	# 18	$t_{\text{mid}} = 2006.9$	(2004 – 2010)		
$x(t)$	-6.20 ± 0.18	-0.507 ± 0.080			4.3
$y(t)$	1.77 ± 0.22	0.572 ± 0.097			6.4
C8	# 147	$t_{\text{mid}} = 2002.6$			
$x(t)$	-2.653 ± 0.028	-0.3754 ± 0.0045			16
$y(t)$	-0.074 ± 0.013	0.0483 ± 0.0052	$4.41\text{e-}3 \pm 0.80\text{e-}3$		3.6
C9	# 163	$t_{\text{mid}} = 2003.5$			
$x(t)$	-2.4560 ± 0.0096	-0.3804 ± 0.0022			3.5
$y(t)$	-0.301 ± 0.011	0.0098 ± 0.0027	$5.72\text{e-}3 \pm 0.58\text{e-}3$		3.7
C10	# 132	$t_{\text{mid}} = 2004.1$			
$x(t)$	-1.902 ± 0.013	-0.3356 ± 0.0036	$-5.13\text{e-}3 \pm 0.67\text{e-}3$		7.3
$y(t)$	-0.0166 ± 0.0075	-0.0052 ± 0.0017			3.0
C11	# 37	$t_{\text{mid}} = 2001.2$			
$x(t)$	-0.705 ± 0.022	-0.487 ± 0.026	-0.0721 ± 0.0085		15
$y(t)$	0.056 ± 0.011	0.0046 ± 0.0046			4.2
C12	# 112	$t_{\text{mid}} = 2004.6$			
$x(t)$	-1.598 ± 0.011	-0.3422 ± 0.0035	$-5.10\text{e-}3 \pm 0.73\text{e-}3$		7.2
$y(t)$	-0.0633 ± 0.00633	-0.0431 ± 0.0021	$-4.36\text{e-}3 \pm 0.44\text{e-}3$		4.9
C13	# 60	$t_{\text{mid}} = 2003.4$			
$x(t)$	-0.9109 ± 0.0097	-0.3064 ± 0.0062	-0.0133 ± 0.0022		4.3
$y(t)$	-0.0019 ± 0.0074	0.0210 ± 0.0047	0.0100 ± 0.0017		4.0
C14	# 57	$t_{\text{mid}} = 2003.75$			
$x(t)$	-0.558 ± 0.017	-0.320 ± 0.011	-0.0322 ± 0.0038	0.0024 ± 0.0010	5.7
$y(t)$	0.0426 ± 0.0083	0.0258 ± 0.0053	0.0020 ± 0.0019	$-1.45\text{e-}3 \pm 0.50\text{e-}3$	1.4

Continued on next page ...

Table 5.3 – continued from previous page

Comp.	a_0	a_1	a_2	a_3	χ^2_{red}
C15	# 58	$t_{\text{mid}} = 2007.0$			
$x(t)$	-1.287 ± 0.018	-0.4359 ± 0.0043	-0.0319 ± 0.0023		2.0
$y(t)$	-0.0705 ± 0.0064	-0.0225 ± 0.0021			0.75
C15a	# 38	$t_{\text{mid}} = 2006.55$			
$x(t)$	-0.622 ± 0.022	-0.2712 ± 0.0046	-0.0236 ± 0.003451		3.3
$y(t)$	-0.0500 ± 0.013	0.0147 ± 0.0026	0.0110 ± 0.0020		1.1
C16	# 59	$t_{\text{mid}} = 2007.0$			
$x(t)$	-0.306 ± 0.018	-0.2675 ± 0.0050	-0.0542 ± 0.0032		4.2
$y(t)$	0.0190 ± 0.0036	0.0042 ± 0.0016			0.53
C17	# 19	$t_{\text{mid}} = 2008.3$			
$x(t)$	-0.365 ± 0.021	-0.422 ± 0.023	-0.130 ± 0.015		8.0
$y(t)$	-0.0430 ± 0.0096	-0.0247 ± 0.0099			1.8
C18	# 23	$t_{\text{mid}} = 2008.7$			
$x(t)$	-0.260 ± 0.013	-0.258 ± 0.013			3.0
$y(t)$	-0.0238 ± 0.0058	-0.0193 ± 0.0059			0.62
C19	# 30	$t_{\text{mid}} = 2008.7$			
$x(t)$	-0.0480 ± 0.010	-0.203 ± 0.011	-0.081 ± 0.017		3.9
$y(t)$	-0.0277 ± 0.0042	-0.0289 ± 0.0062			1.3
C20	# 36	$t_{\text{mid}} = 2009.6$			
$x(t)$	-0.357 ± 0.017	-0.550 ± 0.039	-0.173 ± 0.020		5.0
$y(t)$	-0.0592 ± 0.0054	-0.0350 ± 0.0052			1.6

Notes:

Comp. – Component label, $x(t), y(t)$ indicate the corresponding parameters of the polynomial fit $x(t), y(t) = \sum_i a_i t^i$;
 χ^2_{red} – Lists the value of the reduced χ^2 providing a measure of the quality of the fit.

C1

The component C1 was first identified in 1981 at 2.2 and 1.6 GHz (Biretta et al. 1986; Waak et al. 1988) and was the outermost component at that time. Observations at this frequency are not included, thus the first data point in the kinematic analysis corresponds to a 5.0 GHz measurement on 1989-04-14, where C1 is identified with the outermost component as well. At this time its radial distance to the core is ~ 19.6 mas.

The component is identified in 14 observations at 5.0 GHz between 1989 and 2000. The polynomial fits to the relative positions in $x(t)$ and $y(t)$ are shown in Figure 5.11. The two-dimensional trajectory of C1 is presented in Figure 5.12. The trajectory can be represented linearly, with no evidence for curvature, acceleration or deceleration, as suggested by Lobanov (1996). The average speed of the component is (0.17 ± 0.30) mas year $^{-1}$ with an average direction of the motion of $(-26 \pm 13)^\circ$ measured along the north-south axis. The scatter of the position measurements of C1 is large, which makes this component not very well suited for further kinematic analysis.

Historically, this component was claimed to show a change in the direction of the component motion by 10° within 13 years, with C1 being consistent with the large-scale jet position angle, and a component speed deceleration from 0.52 to 0.36 mas year $^{-1}$ (Lobanov 1996), with similar component speeds reported by Unwin & Wehrle (1992).

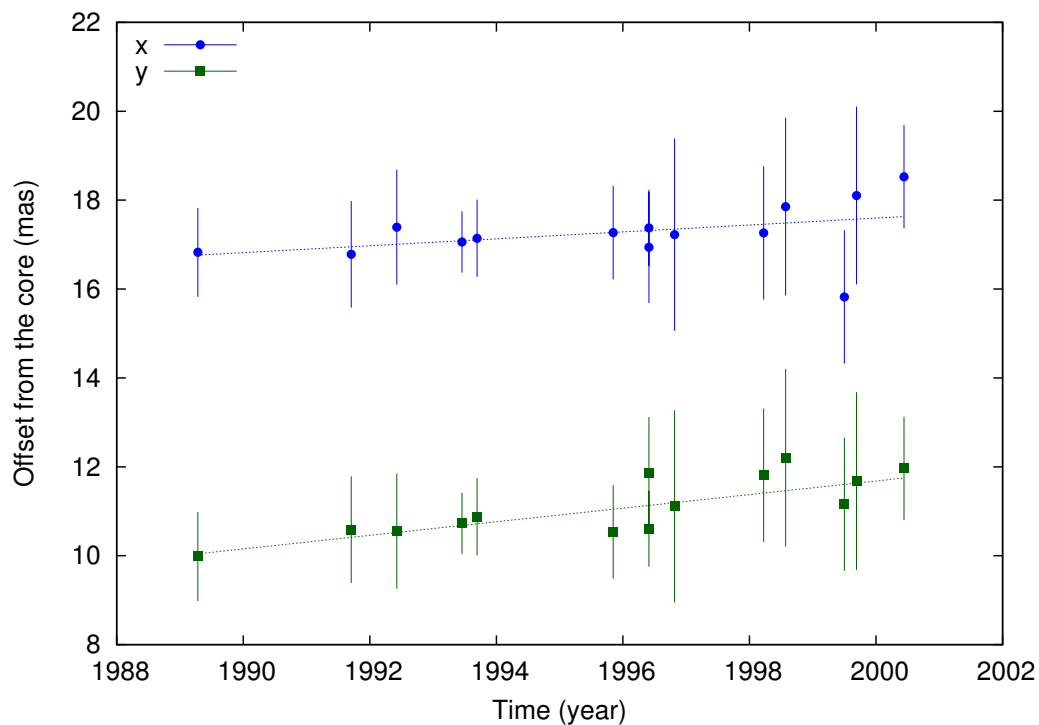


Figure 5.11: Relative positions $x(t)$ and $y(t)$ of C1, dotted lines are the respective polynomial fits to the relative positions.

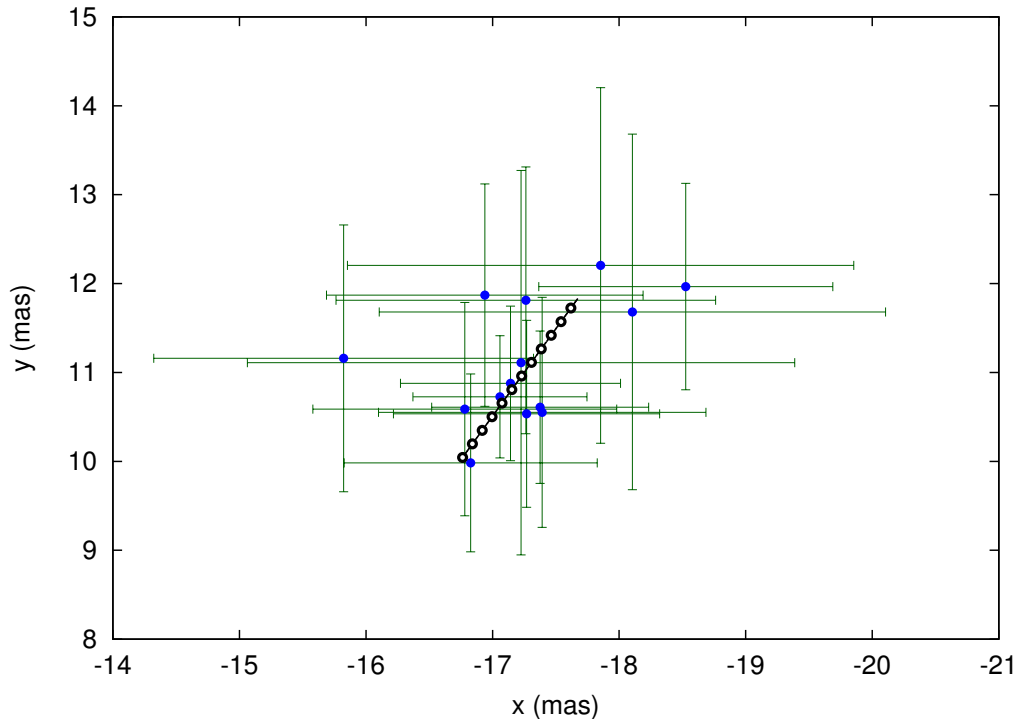


Figure 5.12: Two-dimensional trajectory of C1. The thick black line is reconstructed from the polynomial fits in x and y direction. The white circles are spaced at intervals of 1 year, indicating the change of component position with time.

C2

The component C2 was observed already in the first epoch of the database, 1979-04-02, reported in Biretta et al. (1986) and references therein. It was regularly detected at the frequencies of 2.2 – 10.6 GHz until 1992, after which it was detected at 5.0 and 8.4 GHz only, leading to a more sparse sampling of component positions. It was already noted by Unwin & Wehrle (1992) and Lobanov (1996) that the region of the jet within ~ 9 – 12 mas distance from the core shows a decreased level of emission, which was suggested to be the result of an increased viewing angle or jet decollimation. This could explain why the detection thereafter becomes scarce and is limited to lower observing frequencies, also due to the spectral evolution of the component emission and a higher observational sensitivity to large scale structures.

The component is reliably identified in 22 observations between 5.0 GHz and 10.6 GHz between 1979 and 2004. The polynomial fits to the relative positions in $x(t)$ and $y(t)$ are shown in Figure 5.13. The two-dimensional trajectory of C2 is presented in Figure 5.14. The trajectory can be represented linearly, with no strong evidence for curvature or change in component speed. However, the detections around 2000 suggest a possible slight acceleration or change in direction of the component motion, but cannot be significantly established. The average speed of the component is (0.48 ± 0.25) mas year $^{-1}$ with a general direction of the motion of $(-66 \pm 10)^\circ$ measured along the north-south axis.

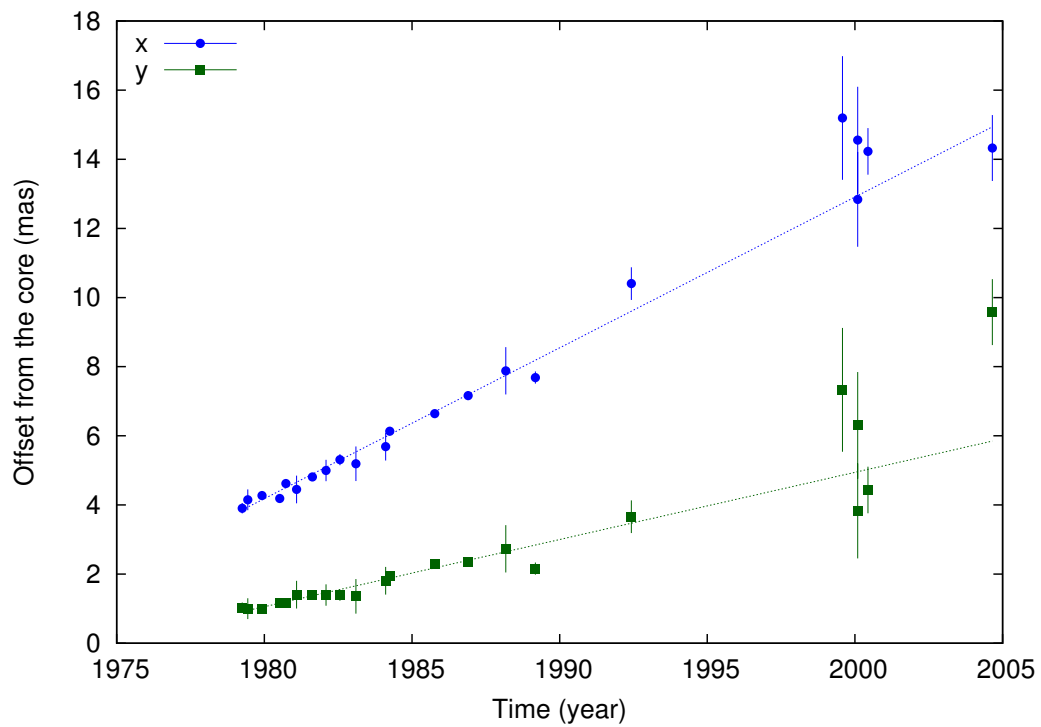


Figure 5.13: Relative positions $x(t)$ and $y(t)$ of C2, dotted lines are the respective polynomial fits to the relative positions.

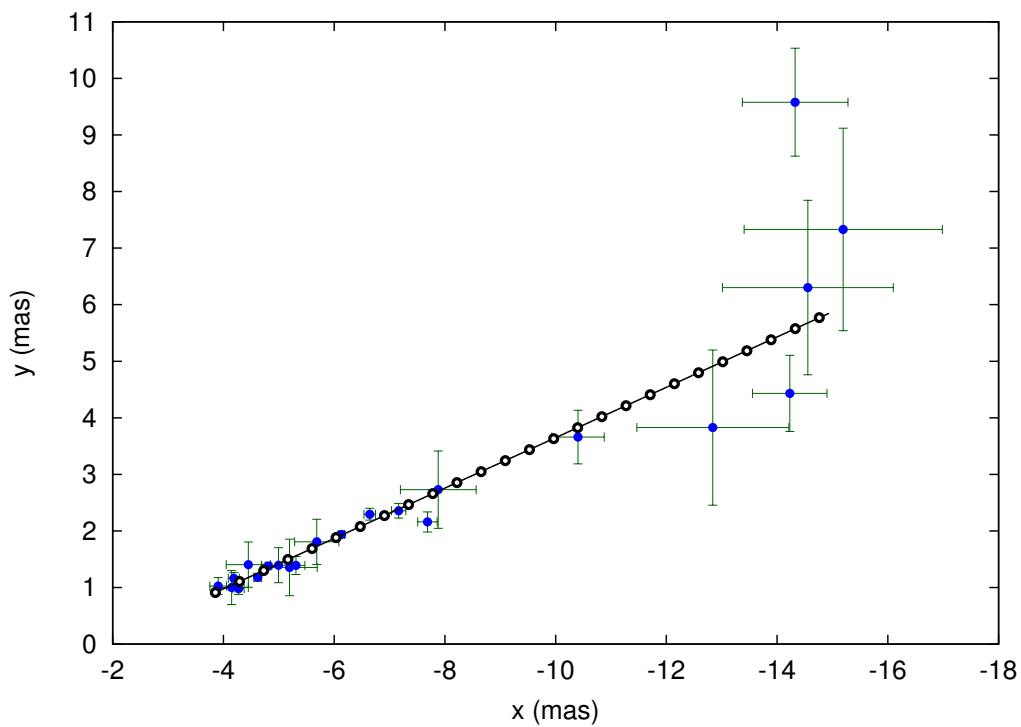


Figure 5.14: Two-dimensional trajectory of C2. The thick black line is reconstructed from the polynomial fits in x and y direction. The white circles are spaced at intervals of 1 year, indicating the change of component position with time.

C3

Similar to C2, the component C3 was observed already in the first epoch of the database and was continuously detected up to 2004-12-12, where it was last detected at a distance of ~ 13 mas. At the beginning it was mainly detected between 1.6 and 10.6 GHz, while during the second half, the component was only reliably detected between 5.0 and 8.4 GHz.

The component is identified in 48 observations in a frequency range of 5.0 GHz to 15.4 GHz, between 1979 and 2005. The polynomial fits to the relative positions in $x(t)$ and $y(t)$ are shown in Figure 5.15. The two-dimensional trajectory of C3 is presented in Figure 5.16. The full fit to the trajectory is best represented by a second order polynomial in both x and y direction, indicating an acceleration in the component motion. The average speed of the component is (0.57 ± 0.45) mas year $^{-1}$ with an average direction of the motion of $(-68 \pm 15)^\circ$ measured along the north-south axis. The direction of the jet motion clearly changed from -73 to -66° within 20 years (1980 – 2000). During the same time period the component speed increased from 0.42 to 0.68 mas year $^{-1}$.

Giving a closer look to the smaller scale variability, in particular that in the y direction (see Figure 5.15), the jet seems to wiggle around the average motion represented by the polynomial fit. This wiggling could be a result of an underlying precession pattern in the jet, as suggested by Lobanov & Roland (2005). Underlying patterns and the variability of the jet structure are further investigated in Section 5.3.

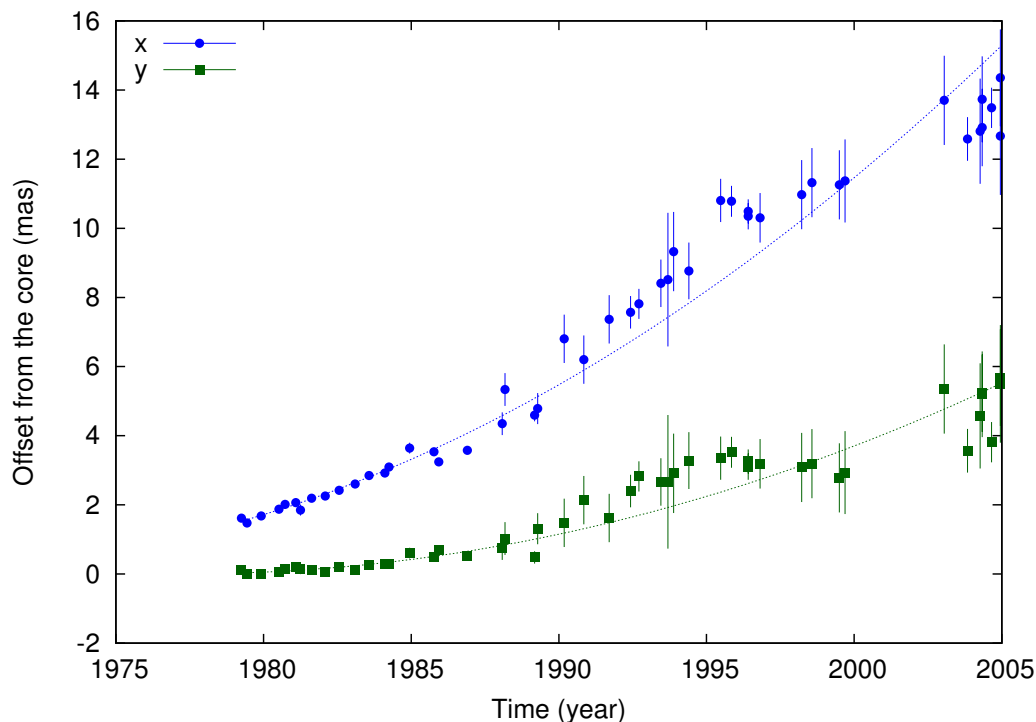


Figure 5.15: Relative positions $x(t)$ and $y(t)$ of C3, dotted lines are the respective polynomial fits to the relative positions.

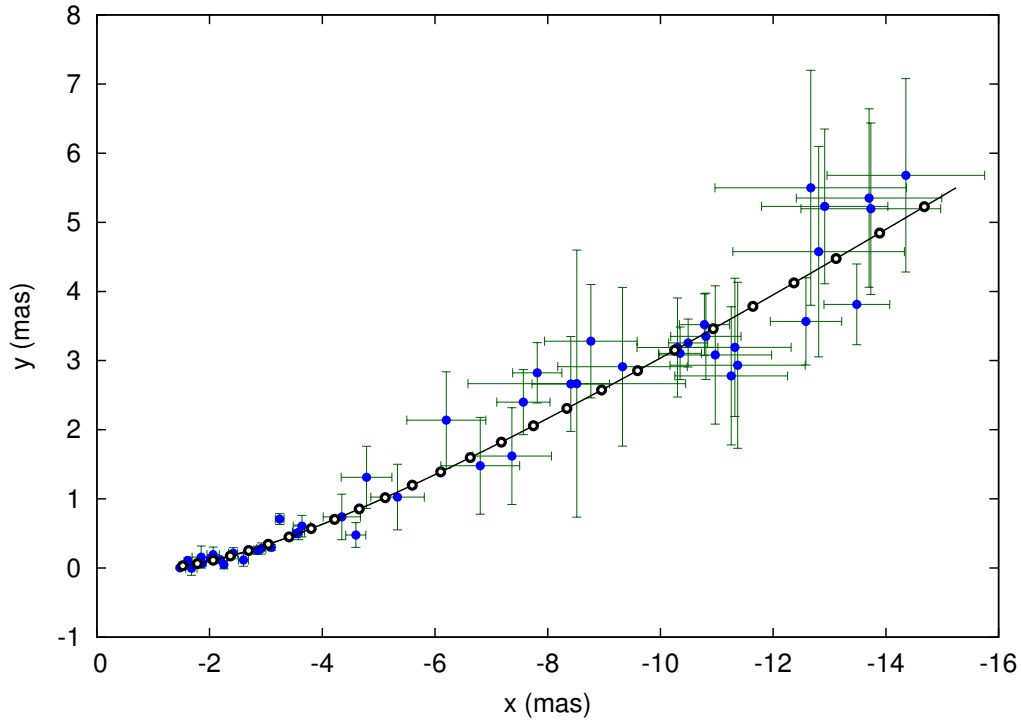


Figure 5.16: Two-dimensional trajectory of C3. The thick black line is reconstructed from the polynomial fits in x and y direction. The white circles are spaced at intervals of 1 year, indicating the change of component position with time.

C3a

This component was introduced after a weaker feature was detected between C3 and C4 related to the outburst in 1979. Following the historic naming scheme, this weak component is labeled C3a (see Lobanov 1996). The highest flux density of this feature was recorded at a level of 1.4 Jy at 10.6 GHz in 1979. It quickly decayed thereafter to a level of < 0.5 Jy by 1981. The component was last detected in 2000, but during the whole observing period its detection was mostly limited to lower observing frequencies which were sampled less frequently, leading to a very patchy detection. It is possible that C3a is related to the subsequent feature C4, which is always very close to C3a. The fast decay and weak emission of C3a supports this suspicion. Lobanov (1996) argues that C3a may originate from a splitting of C4 due to the passage through a recollimation shock.

In total, the component is identified in 17 observations, between 1979 and 2000. The polynomial fits to the relative positions in $x(t)$ and $y(t)$ are shown in Figure 5.17. The two-dimensional trajectory of C3a is presented in Figure 5.18. The full fit to the trajectory is best represented by a second order polynomial in both x and y direction, indicating an acceleration in the component motion. Due to the sparse sampling of the data the fit is forced to go toward the measurements clustering around 1995. Nevertheless, the fitted acceleration is consistent with the remaining data points. The average speed of the component is (0.51 ± 0.49) mas year $^{-1}$ with an average direction of motion of $(-66 \pm 21)^\circ$ measured along the north-south axis. From this fit, a change in the direction of the motion is inferred, going from -84 to -69° while accelerating from 0.15 to 0.36 mas year $^{-1}$ between 1980 and 1986.

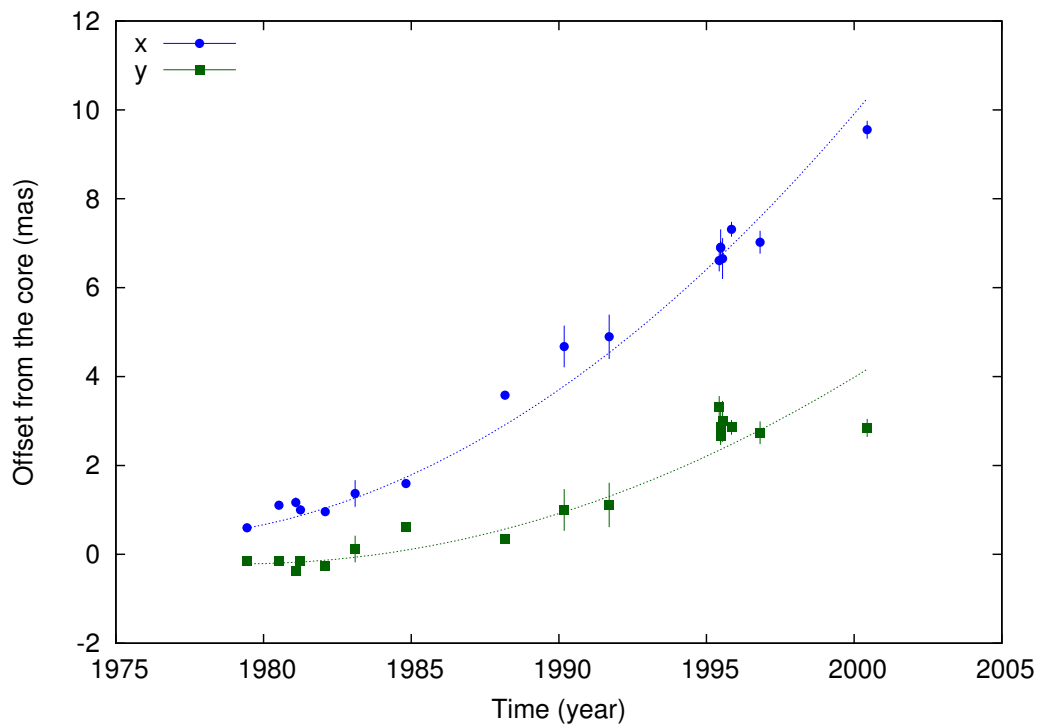


Figure 5.17: Relative positions $x(t)$ and $y(t)$ of C3a, dotted lines are the respective polynomial fits to the relative positions.

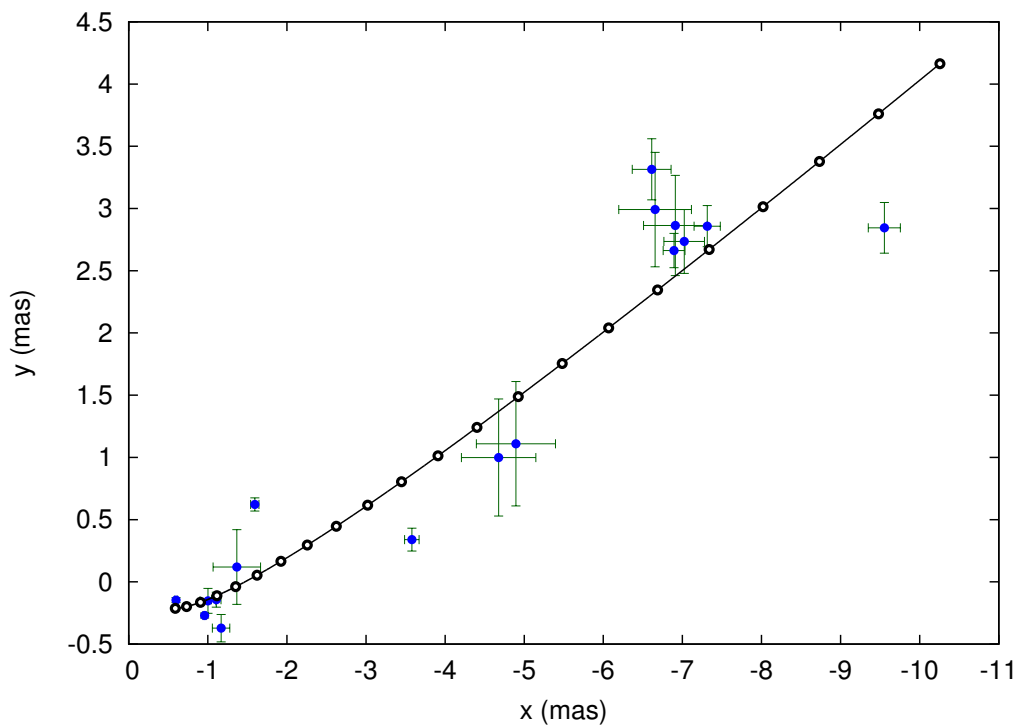


Figure 5.18: Two-dimensional trajectory of C3a. The thick black line is reconstructed from the polynomial fits in x and y direction. The white circles are spaced at intervals of 1 year, indicating the change of component position with time.

C4

The component C4 was first identified in the 10.6 GHz observation on 1980-07-09 by Biretta et al. (1986). It is one of the brightest features observed at its time, with a flux density of up to 8 Jy, observed at 10.6 and 22.2 GHz in 1982 and 1983. Even 10 years after its emission, in 1990, it was detected with a flux density of 1 Jy at 5.0 GHz and even after 20 years it is detected at a flux density of ~ 0.3 Jy at 5.0 GHz. After 2000, C4 is not detected anymore. The trajectory of this dominant feature was studied in detail by Steffen et al. (1995), where it was modeled by a helix and Rabaça & Zensus (1994) discussed its emission properties. Lobanov & Zensus (1999) investigated the shock evolution of jet components, including C4.

In total, the component is reliably identified in 86 observations, between 1980 and 2000. The polynomial fits to the relative positions in $x(t)$ and $y(t)$ are shown in Figure 5.19. The two-dimensional trajectory of C4 is presented in Figure 5.20. The full fit to the trajectory is best represented by a second order polynomial in x and by a third order polynomial in y direction, indicating an acceleration in the component motion and a higher complexity in y direction. The average speed of the component is (0.46 ± 0.34) mas year $^{-1}$ with an average direction of the motion of $(-64 \pm 13)^\circ$ measured along the north-south axis. The direction of the motion starts out with -57° in 1981, turns to -77° by 1990 and then twists upward ending with an angle of -47° by 2000. During this time period the component accelerates from 0.20, through 0.41 up to 0.91 mas year $^{-1}$.

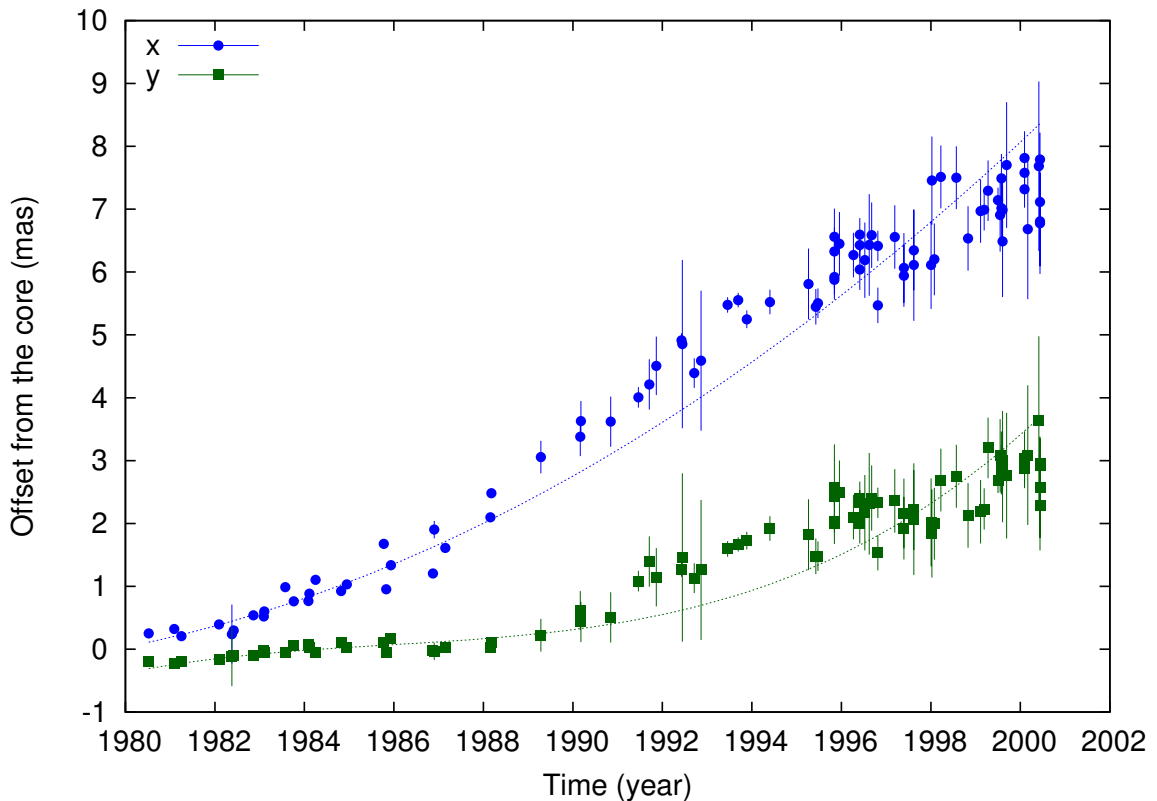


Figure 5.19: Relative positions $x(t)$ and $y(t)$ of C4, dotted lines are the respective polynomial fits to the relative positions.

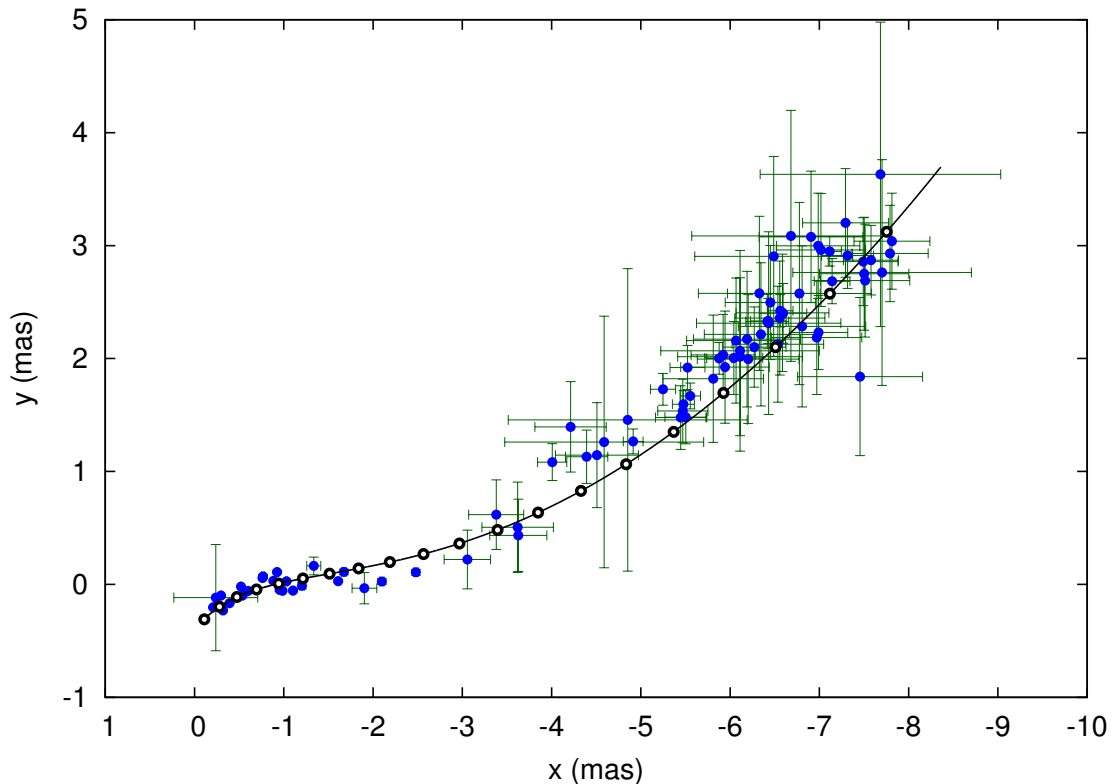


Figure 5.20: Two-dimensional trajectory of C4. The thick black line is reconstructed from the polynomial fits in x and y direction. The white circles are spaced at intervals of 1 year, indicating the change of component position with time.

C5

The component C5 was first detected on 1983-02-03 at 22.2 GHz (Biretta et al. 1986) and was observed regularly until 2005. Its flux density at a distance of 1.1 mas from the core, was 1.5 Jy (10.6 GHz), which is a bit less than for component C4. However comparing peak flux densities, C5 reached only levels half as bright than C4. In the context of shock evolution C5 was studied by Lobanov & Zensus (1999).

In total, the component is reliably identified in 113 observations, between 1983 and 2005. The polynomial fits to the relative positions in $x(t)$ and $y(t)$ are shown in Figure 5.21. The two-dimensional trajectory of C5 is presented in Figure 5.22. The full fit to the trajectory is best represented by a second order polynomial in both x and y directions, indicating an acceleration in the component motion. The average speed of the component is (0.38 ± 0.22) mas year⁻¹ with an average direction of $(-70.5 \pm 5.9)^\circ$ measured along the north-south axis. Between 2000 and 2005, the polynomial fit systematically underestimates the observed data. This is most likely due to a blending with components C6 and C7.

The direction of the motion starts out with -122° in 1985. At ~ 1 mas it flattens and begins to turn upward, with a change in direction from -85° in 1990 to -68° by 1995. Between 1985 and 1995 the component accelerates from 0.21 to 0.41 mas year⁻¹ and reaches a speed of 0.71 mas year⁻¹ by 2005.

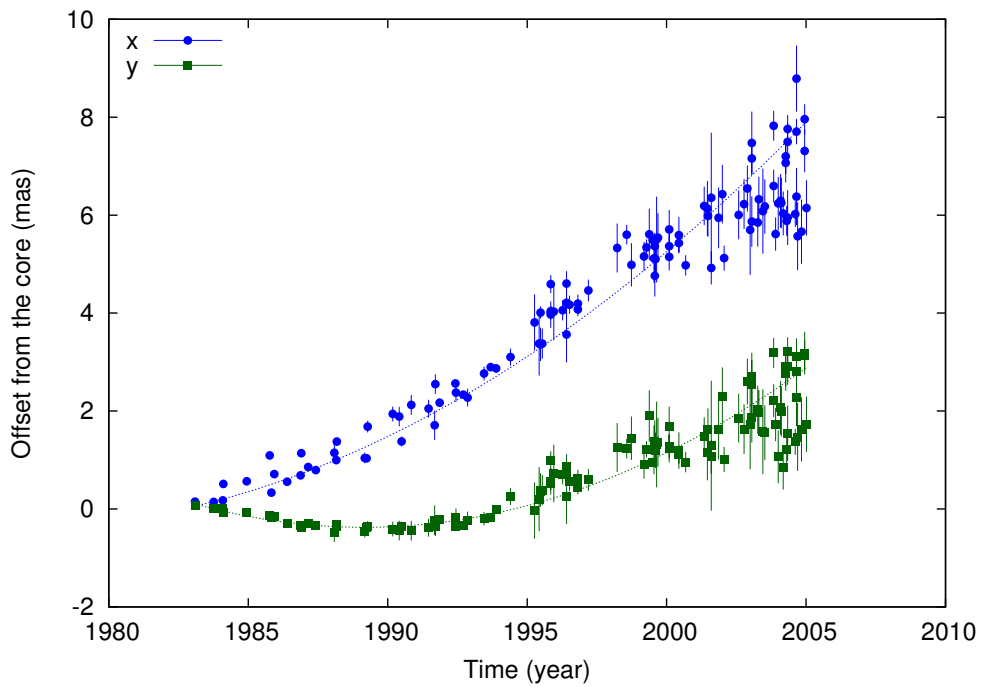


Figure 5.21: Relative positions $x(t)$ and $y(t)$ of C5, dotted lines are the respective polynomial fits to the relative positions.

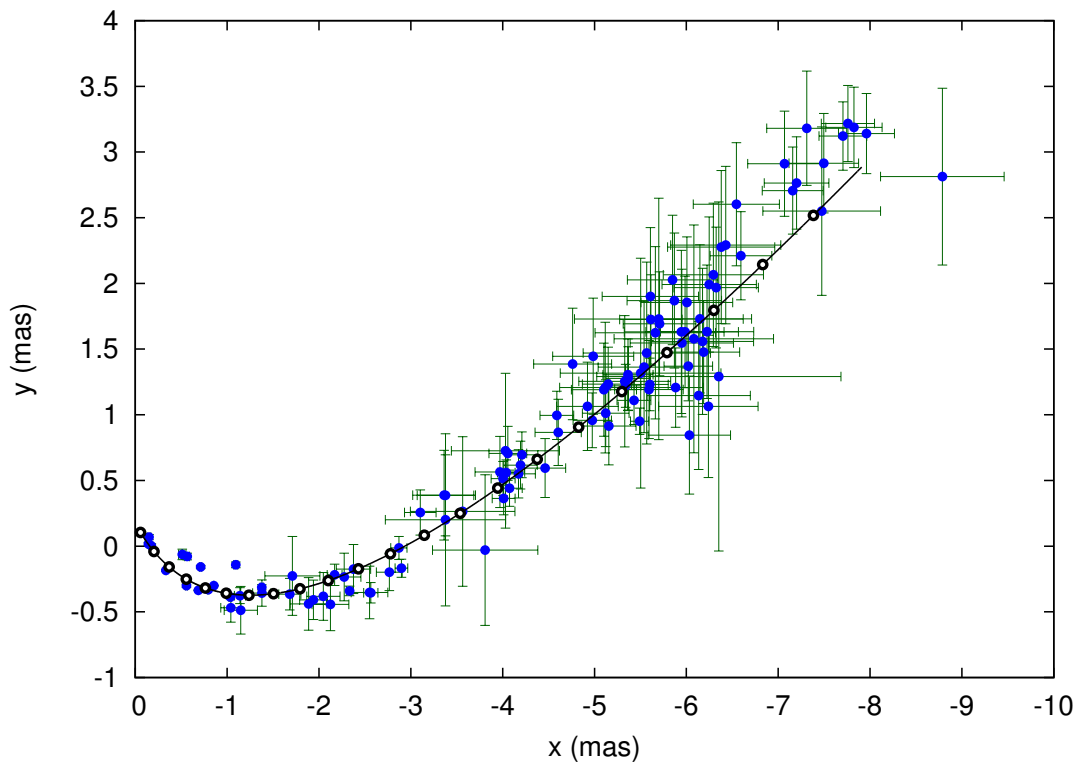


Figure 5.22: Two-dimensional trajectory of C5. The thick black line is reconstructed from the polynomial fits in x and y direction. The white circles are spaced at intervals of 1 year, indicating the change of component position with time.

C6

The component C6 is the first feature detected after a quiescent period of 5 years. C6 was first detected on 1988-03-18 at 100 GHz (Bååth et al. 1992), the first detection at 22 GHz was made a year later on 1989-03-31 (Lobanov 1996). The component is reliably identified in only 27 observations between 1988 and 2005. The polynomial fits to the relative positions in $x(t)$ and $y(t)$ are shown in Figure 5.23. The two-dimensional trajectory of C6 is presented in Figure 5.24.

The path of C6 is highly curved, however the component was not detected continuously between 1988 and 2005 and was mainly picked up in observations at lower frequencies (i.e. 5.0 – 8.4 GHz). The highest flux densities for this component were reported at 43.2 GHz, with a flux density of 1.25 Jy and 4.4 Jy for VLBI observations on 1990-07-02 and 1991-09-06 (Krichbaum & Witzel 1992; Krichbaum et al. 1993). Flux density levels reported at 22.2 GHz were between 0.1–0.3 Jy during the same time period (Lobanov 1996). Most of the other times when C6 was identified it remained a very weak feature. It was discussed that C6 decelerated from 1991 onward, which is confirmed by the fit in y direction here. Also, it showed an unusually rapid flux density decay, either due to an intrinsic weakness of the feature or due to a larger viewing angle, leading to a reduced relativistic beaming (Lobanov 1996). The highly curved trajectory supports a strong change in the viewing angle while it propagates down the jet. In 1990 the component speed was $0.36 \text{ mas year}^{-1}$, by 1996 it has remained relatively constant and had a speed of $0.35 \text{ mas year}^{-1}$, with a re-acceleration afterwards, reaching a speed of $0.41 \text{ mas year}^{-1}$ by 2004, while the direction of the motion changed from -105° , through -85° , to -59° .

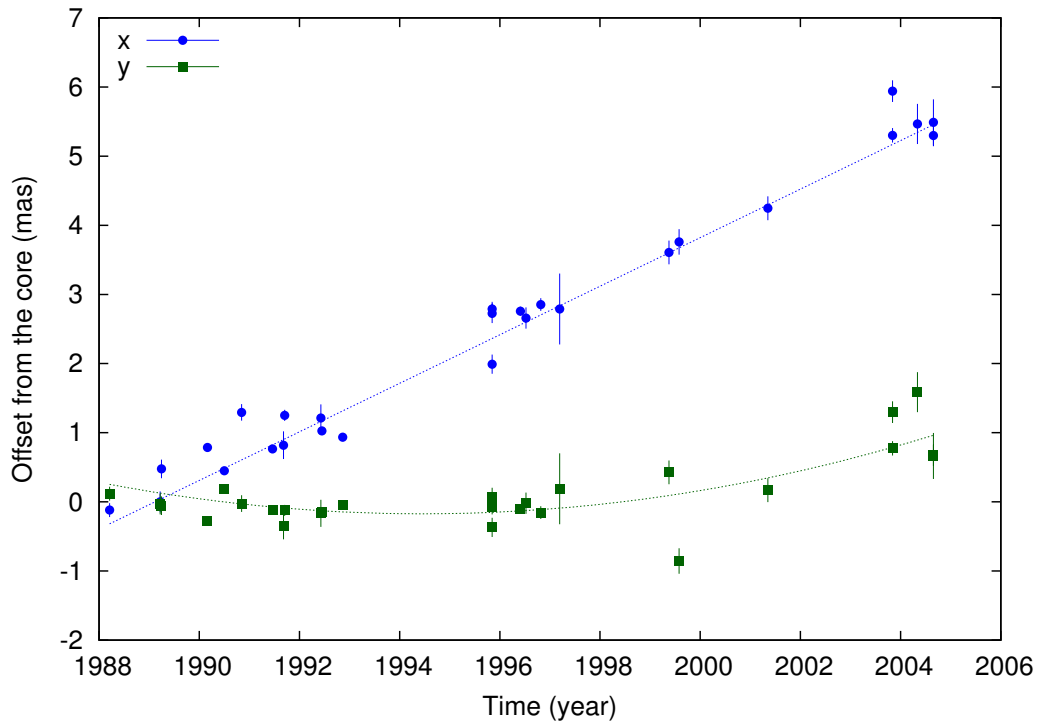


Figure 5.23: Relative positions $x(t)$ and $y(t)$ of C6, dotted lines are the respective polynomial fits to the relative positions.

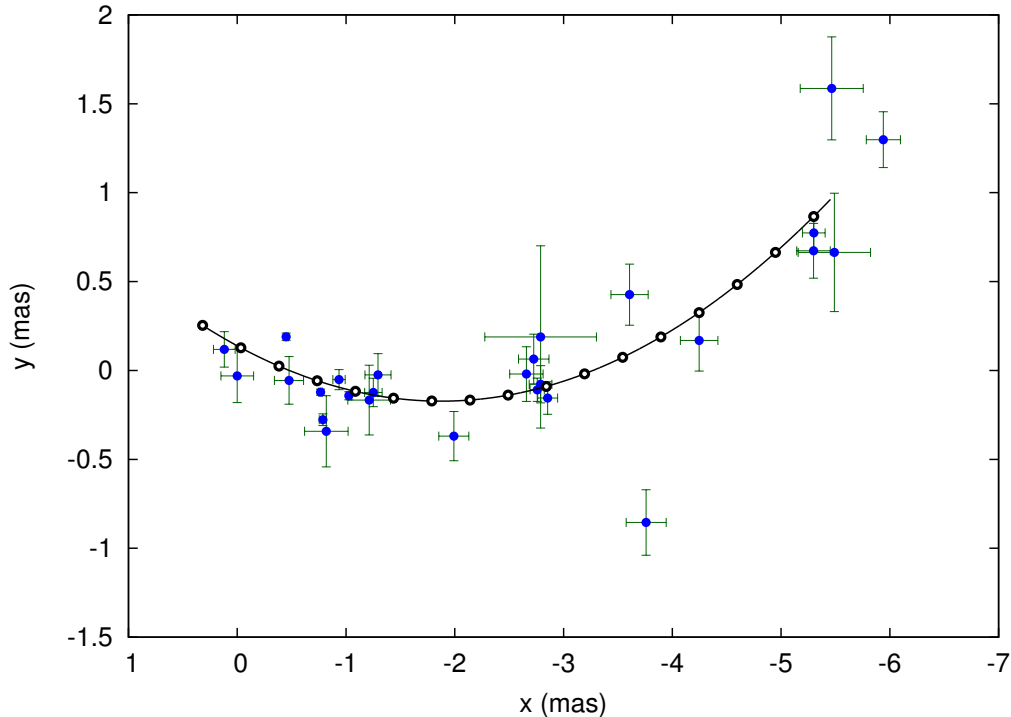


Figure 5.24: Two-dimensional trajectory of C6. The thick black line is reconstructed from the polynomial fits in x and y direction. The white circles are spaced at intervals of 1 year, indicating the change of component position with time.

C7

The component C7 was first detected on 1989-03-22 at 100 GHz (Bååth et al. 1992) and 1989-03-31 at 22 GHz (Lobanov 1996). It is also the last component discussed by Lobanov (1996). Lobanov & Roland (2005) discussed the kinematics and flux of C7 in the context of a binary black hole model.

It reached its peak flux density at 22.2 GHz in 1992 with a value of 6.2 Jy, which is considerably brighter than C6. The component is reliably identified in a total of 154 observations between 1989 and the end of 2009. The polynomial fits to the relative positions in $x(t)$ and $y(t)$ are shown in Figure 5.25. The two-dimensional trajectory of C7 is presented in Figure 5.24.

At first the component follows a trajectory similar to the previous features, with an initial speed that stayed relatively constant until the peak flux density at 22.2 GHz was reached in mid-1992. It accelerates thereafter with a general direction of the motion along the jet axis of $\sim -90^\circ$. After ~ 4 mas the motion of the component seems to turn sharply upward, following an angle of -42° . After this its speed remained constant at a value of (0.76 ± 0.36) mas year $^{-1}$. In order to represent this behavior with polynomial fits, the trajectory had to be fitted in two steps, first for the time period prior the sharp turn (1989 – 2004) and then for the time after the turn (2004 – 2010). The polynomial coefficients of both fits are listed in Table 5.3 and their trajectories are indicated in Figure 5.25 and Figure 5.24. An explanation for the sudden change in speed and direction of the component motion could be a significant change in the direction of the jet flow and, as a consequence of which, produce a significant change in the viewing angle. An alternate explanation for the sudden change in direction could be a blending

with C6 and C5. Especially around 2004, when the locations of components C5, C6, and C7 were difficult to determine (see Figure 5.9). After 2005, C7 is the outermost component in the jet.

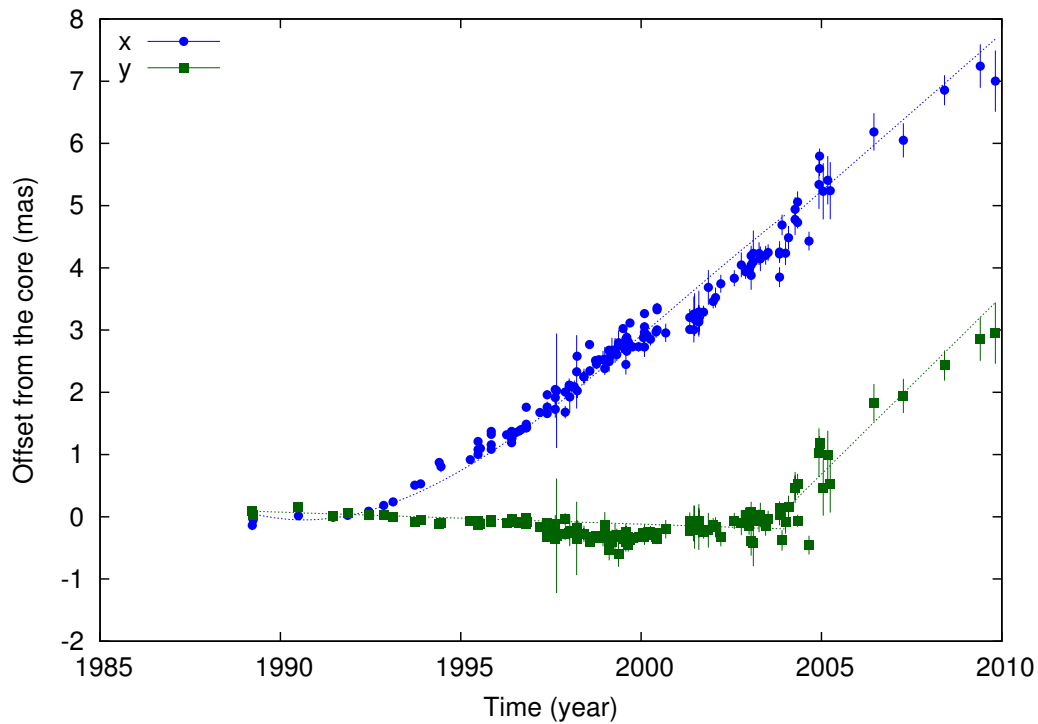


Figure 5.25: Relative positions $x(t)$ and $y(t)$ of C7, dotted lines are the respective polynomial fits to the relative positions.

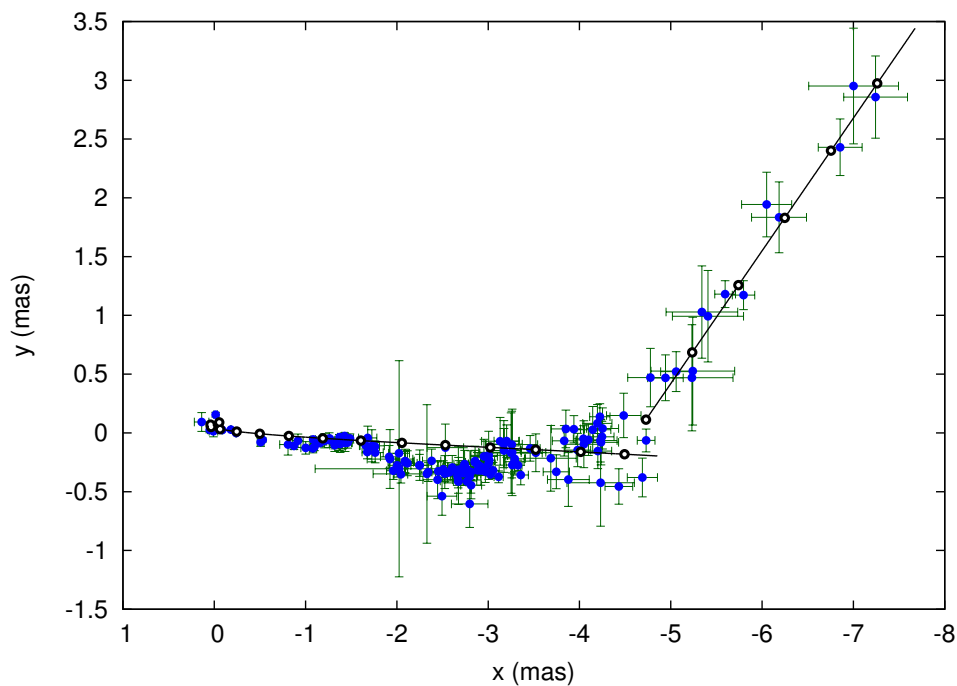


Figure 5.26: Two-dimensional trajectory of C7. The thick black line is reconstructed from the polynomial fits in x and y direction. The white circles are spaced at intervals of 1 year, indicating the change of component position with time.

C8

This component was first detected on 1994-05-28 at 15.4 GHz, which is the first new component identified in the jet of 3C 345 after the VLBA became operational. and was first noted by Jorstad et al. (2005) and Klare (2003). It reached a peak brightness of 3.4 Jy at 15.4 GHz by mid 1995, followed by a slow decay, still having a flux density of ~ 0.5 Jy by the end of 1998. The component is reliably identified in 147 observations, between 1994 and 2010. The polynomial fits to the relative positions in $x(t)$ and $y(t)$ are shown in Figure 5.27. The two-dimensional trajectory of C8 is presented in Figure 5.28. The full fit to the trajectory is best represented by a first order polynomial in x and a second order polynomial in y direction, indicating a weak acceleration in that coordinate. The average speed of the component is (0.379 ± 0.078) mas year $^{-1}$ with an average direction of the motion of $(-82.6 \pm 3.9)^\circ$ measured along the north-south axis.

The first acceleration phase of C8 seen between 1994 and 1996 is not represented by the polynomial. This is not dramatic, since in this section the interest lies on the large-scale, long-term kinematics. The sub-mas scales are investigated in Chapter 7 for the most recent features identified in 2008 and 2009. Around 2006, the polynomial fit in y direction starts to deviate significantly from the observed positions. This appears to occur at a distance of ~ 4 mas, similarly to the distance at which a sharp turn was observed in the previous component C7, which is also observed in other components, but is less pronounced. It seems at this distance the curvature of the jet plays a dominant role, which is most likely due to a change in viewing angle rather than a systematic observational effect.

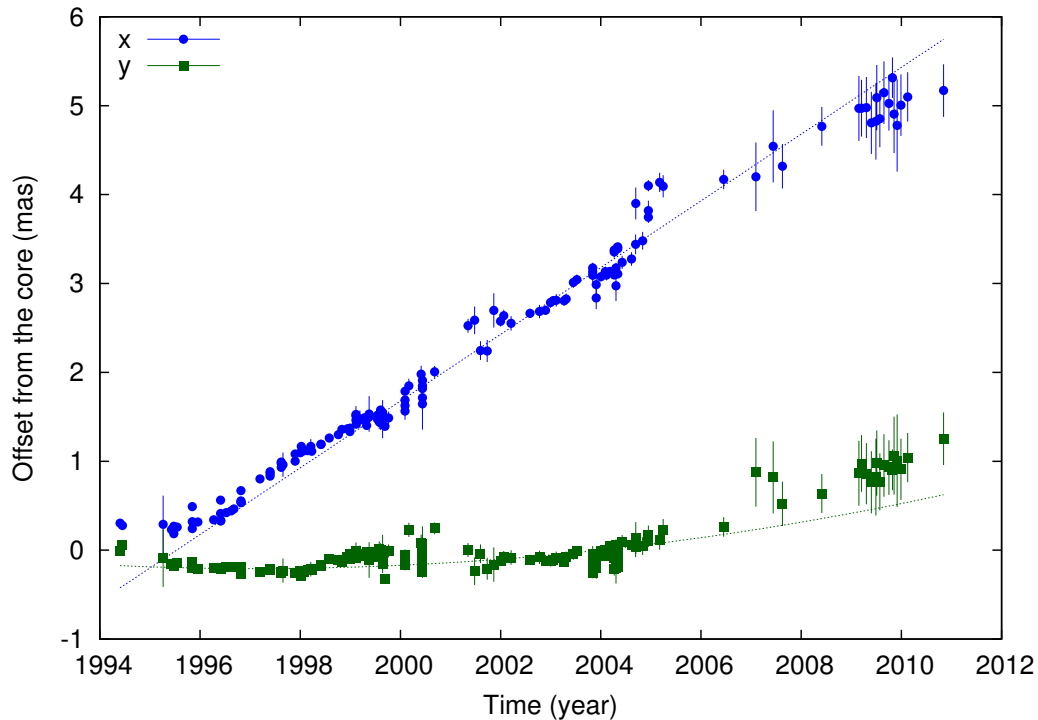


Figure 5.27: Relative positions $x(t)$ and $y(t)$ of C8, dotted lines are the respective polynomial fits to the relative positions.

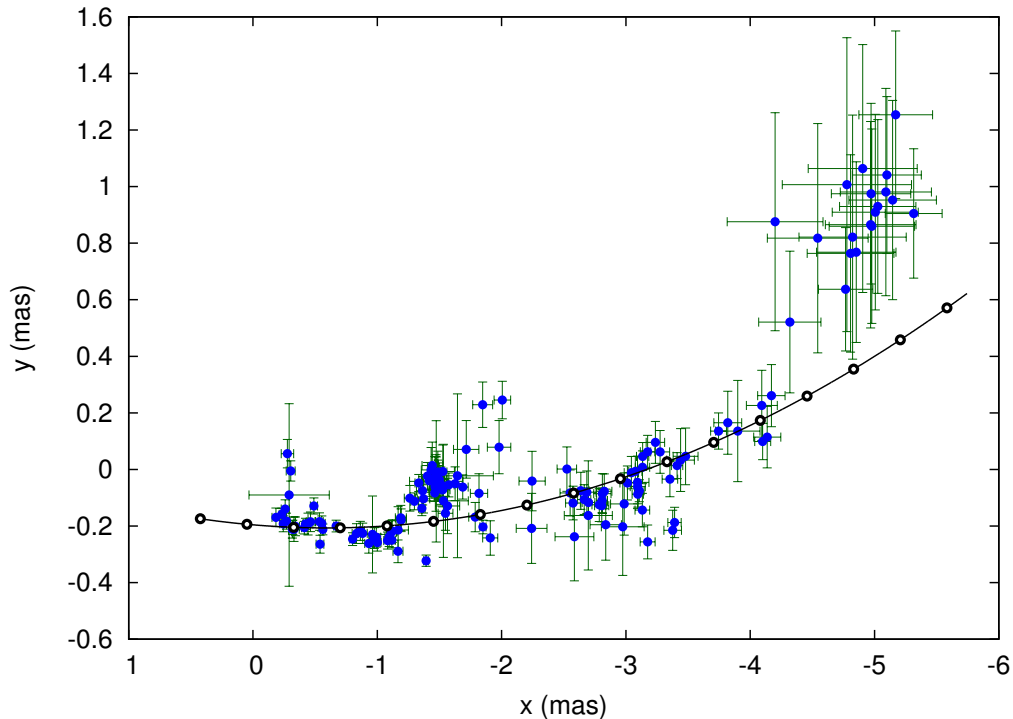


Figure 5.28: Two-dimensional trajectory of C8. The thick black line is reconstructed from the polynomial fits in x and y direction. The white circles are spaced at intervals of 1 year, indicating the change of component position with time.

C9

The component C9 was first detected on 1996-10-25 at 22.2 GHz and was discussed by Klare (2003) and Jorstad et al. (2005). It is a weaker feature than C8, with a peak flux density of ~ 1.6 Jy at 15.4 and 22.2 GHz. The component is reliably identified in 157 observations, between 1996 and 2010. The polynomial fits to the relative positions in $x(t)$ and $y(t)$ are shown in Figure 5.29. The two-dimensional trajectory of C9 is presented in Figure 5.30. The full fit to the trajectory is best represented by a first order polynomial in x and a second order polynomial in y direction. The trajectory of C9 is strongly curved and shows a small initial deceleration until about 2002, after which it then re-accelerated. It looks almost like an exact copy of component C6, with the difference that C9 is much better sampled. Looking at the scatter around the general fit of the trajectory of C9, an oscillating motion can be seen. Such an underlying pattern is also seen in C3 at larger scales, however it is much less pronounced compared to C9.

The average speed of the component is (0.381 ± 0.034) mas year $^{-1}$ with an average direction of the motion of $(-88.6 \pm 1.8)^\circ$ measured along the north-south axis. In 1997 the component speed was 0.386 mas year $^{-1}$, by 2002 it has remained relatively constant and had a speed of 0.380 mas year $^{-1}$, with a re-acceleration afterwards, reaching a speed of 0.39 mas year $^{-1}$ by 2010, while the direction of the motion changed from -100° , through -91° , to -78° .

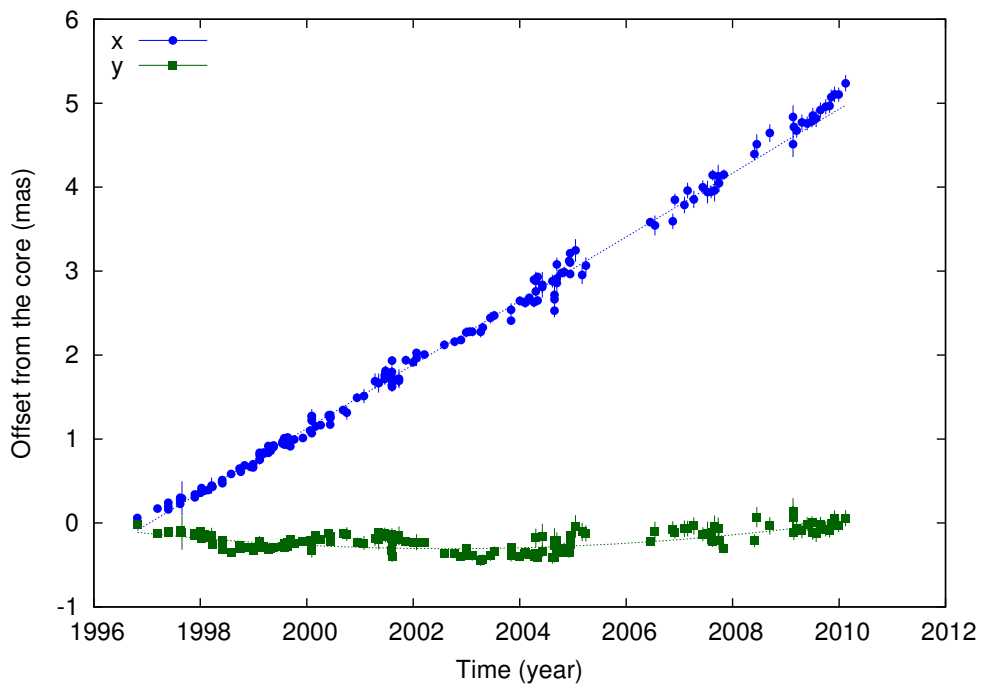


Figure 5.29: Relative positions $x(t)$ and $y(t)$ of C9, dotted lines are the respective polynomial fits to the relative positions.

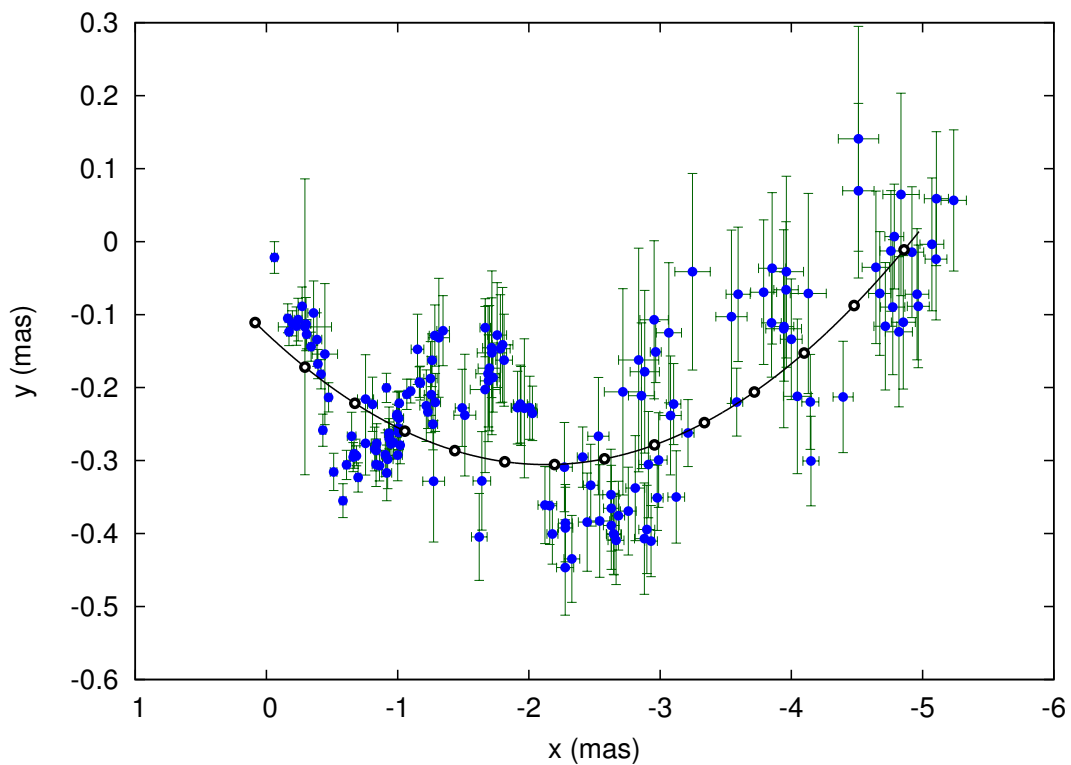


Figure 5.30: Two-dimensional trajectory of C9. The thick black line is reconstructed from the polynomial fits in x and y direction. The white circles are spaced at intervals of 1 year, indicating the change of component position with time.

C10

The component C10 was first detected on 1997-05-26 at 22.2 GHz, which is about 7 months after C9 and was included in the kinematic discussion of Jorstad et al. (2005). Its brightness is comparable to C9, with a value of ~ 1 Jy during the peak brightness at 22.2 GHz. The component is identified in 132 observations, and was reliably detected between 1997 and 2010. The polynomial fits to the relative positions in $x(t)$ and $y(t)$ are shown in Figure 5.31. The two-dimensional trajectory of C10 is presented in Figure 5.32. The full fit to the trajectory is best represented by a second order polynomial in x and a first order polynomial in y direction. No significant acceleration is observed in the general direction of the component motion. Even though there is no indication of blending with another feature in the jet, after mid-2001, the trailing component C11 disappeared from the jet. It either decayed away or has merged with C10 thereafter. Since C10 continued to follow its general path, there is no indication of a significant impact on the identification and motion of C10.

The average speed of the component is (0.336 ± 0.041) mas year $^{-1}$ with an average direction of motion of $(-90.89 \pm 0.65)^\circ$ measured along the north-south axis. Although the general direction of the trajectory is well represented by the polynomial fits, it is not able to represent the additional oscillation around the general direction of the component motion. These oscillations are similar to those seen in components C9 and C3 and are investigated further in the next section.

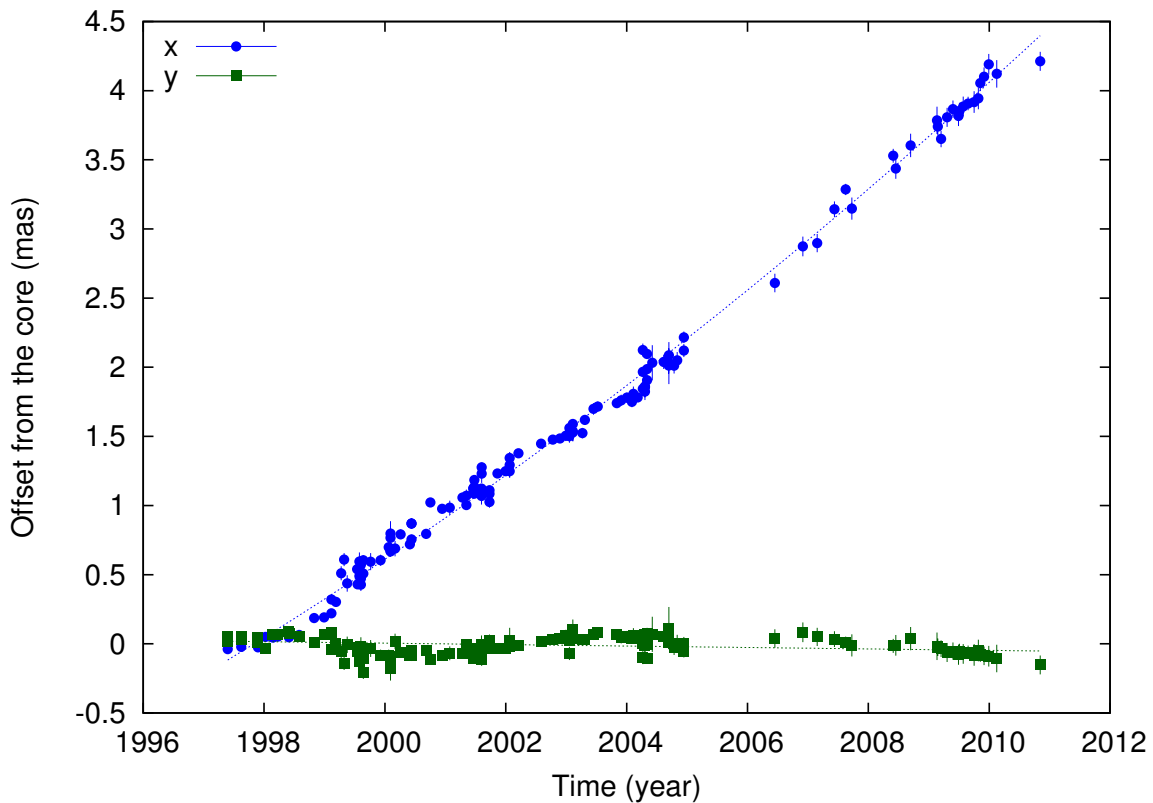


Figure 5.31: Relative positions $x(t)$ and $y(t)$ of C10, dotted lines are the respective polynomial fits to the relative positions.

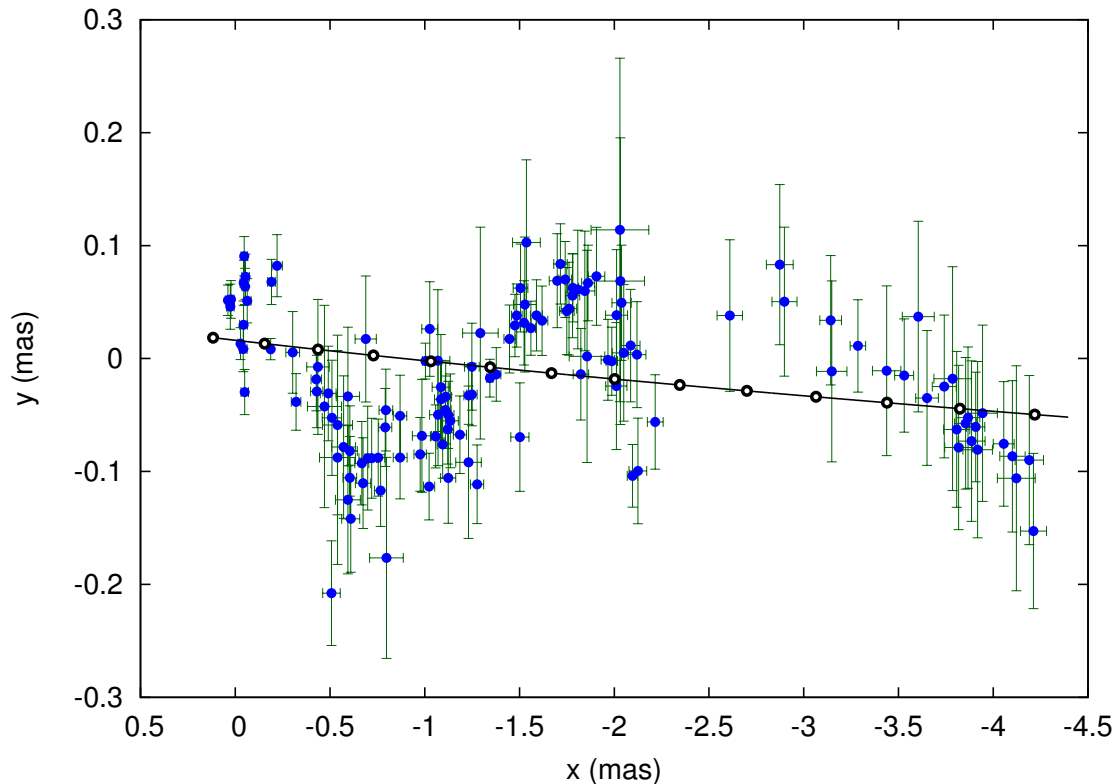


Figure 5.32: Two-dimensional trajectory of C10. The thick black line is reconstructed from the polynomial fits in x and y direction. The white circles are spaced at intervals of 1 year, indicating the change of component position with time.

C11

Nine months after the first detection of C10, the component C11 was first identified on 1998-02-23 at 43.2 GHz. Initially, it had a flux density of 1–2 Jy at 22.2 GHz, which decayed only very slowly. It was identified as individual feature until mid-2001, after which it either merged with component C10 or has faded away. The identification of a feature on 2004-04-21, with a flux density of 200 mJy at 22.2 GHz, could be related to C11, but was not confirmed by subsequent observations. Its kinematics was investigated by Jorstad et al. (2005) using a bi-weekly 43.2 GHz monitoring.

The component is identified in 37 observations, and was detected between 1998 and mid-2001. The polynomial fits to the relative positions in $x(t)$ and $y(t)$ are shown in Figure 5.33. The two-dimensional trajectory of C11 is presented in Figure 5.34. The full fit to the trajectory is best represented by a second order polynomial in x and a first order polynomial in y direction. The average speed of the component is $(0.49 \pm 0.12) \text{ mas year}^{-1}$ with an average direction of the motion of $(-89.46 \pm 0.82)^\circ$ measured along the north-south axis.

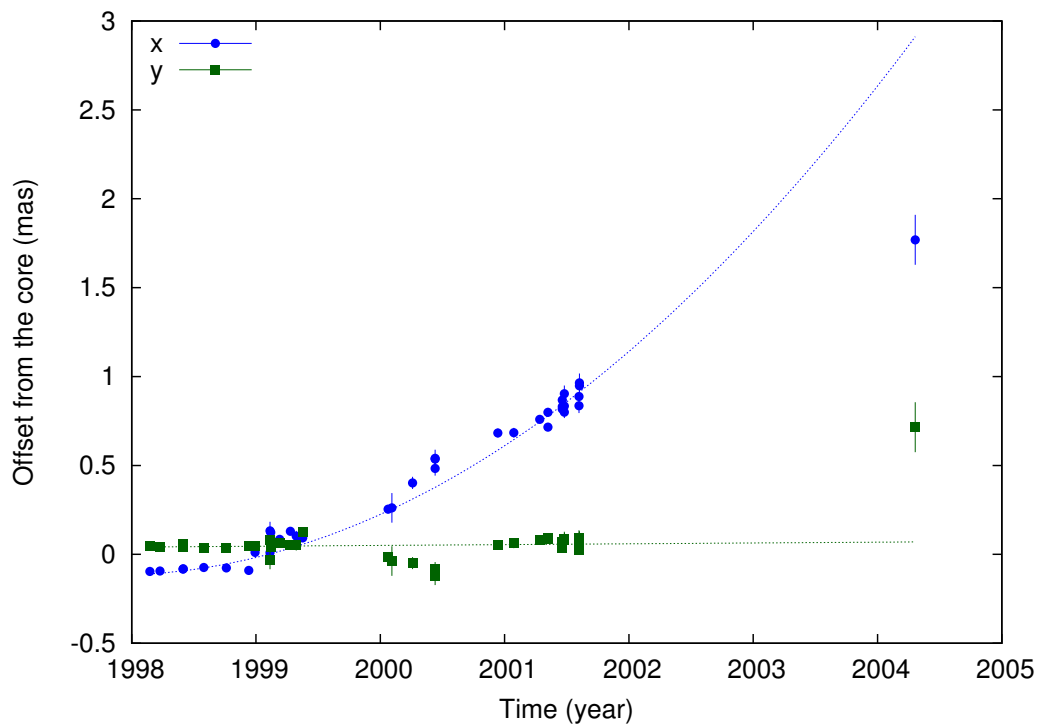


Figure 5.33: Relative positions $x(t)$ and $y(t)$ of C11, dotted lines are the respective polynomial fits to the relative positions.

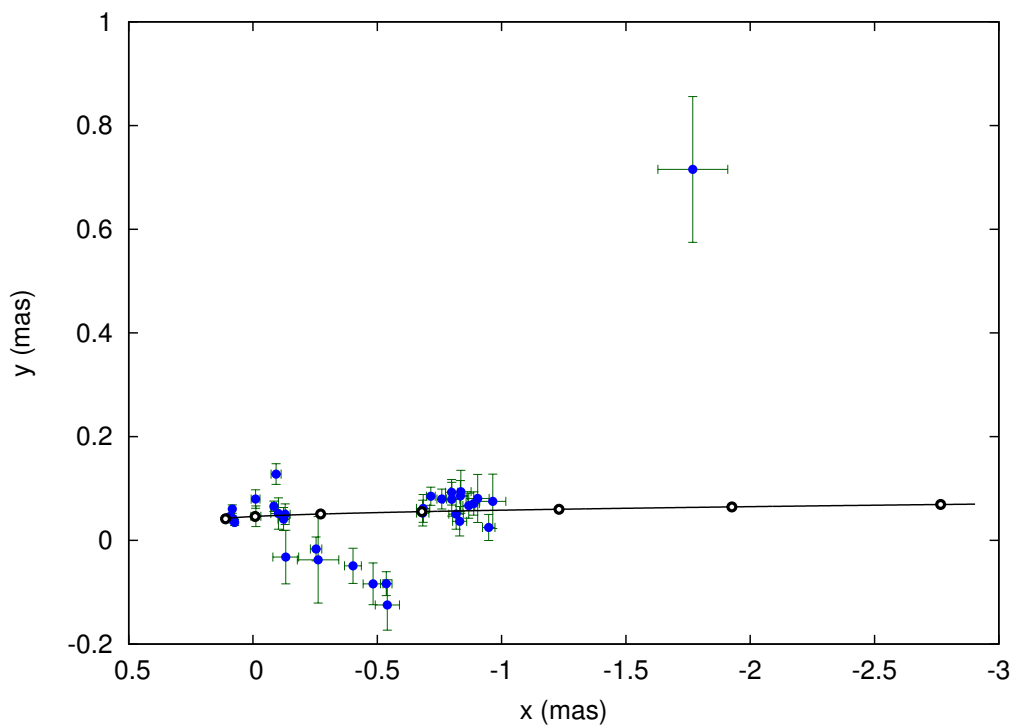


Figure 5.34: Two-dimensional trajectory of C11. The thick black line is reconstructed from the polynomial fits in x and y direction. The white circles are spaced at intervals of 1 year, indicating the change of component position with time.

C12

Component C12 was first identified on 1999-02-11 at 43.2 GHz, but its position was still a blend with the core. The first observation at which C12 was clearly separated from the core, was two months later. It reached a peak flux density of ~ 2.8 Jy at 15.4 GHz and was continuously detected between 1999 and 2010. Its early kinematics was investigated by Jorstad et al. (2005).

The component is identified in 37 observations and the polynomial fits to the relative positions in $x(t)$ and $y(t)$ are shown in Figure 5.35. The two-dimensional trajectory of C12 is presented in Figure 5.36. The full fit to the trajectory is best represented by a second order polynomial in both x and y directions. The average speed of the component is (0.345 ± 0.032) mas year $^{-1}$ with an average direction of the motion of $(-97.22 \pm 0.98)^\circ$ measured along the north-south axis. Within the observation period the component accelerated from 0.30 to 0.41 mas year $^{-1}$, and the direction of motion changed from -91 to -103° . The underlying oscillating pattern observed at previous components is also visible here, although not as pronounced.

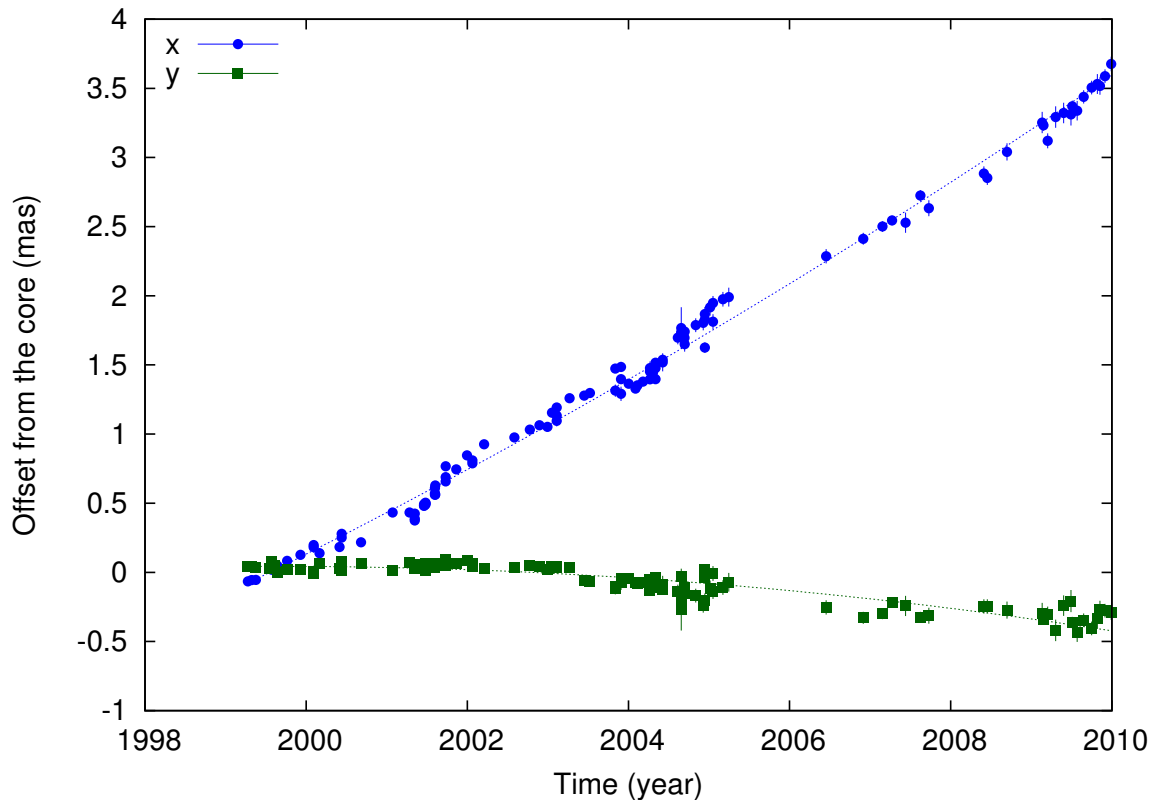


Figure 5.35: Relative positions $x(t)$ and $y(t)$ of C12, dotted lines are the respective polynomial fits to the relative positions.

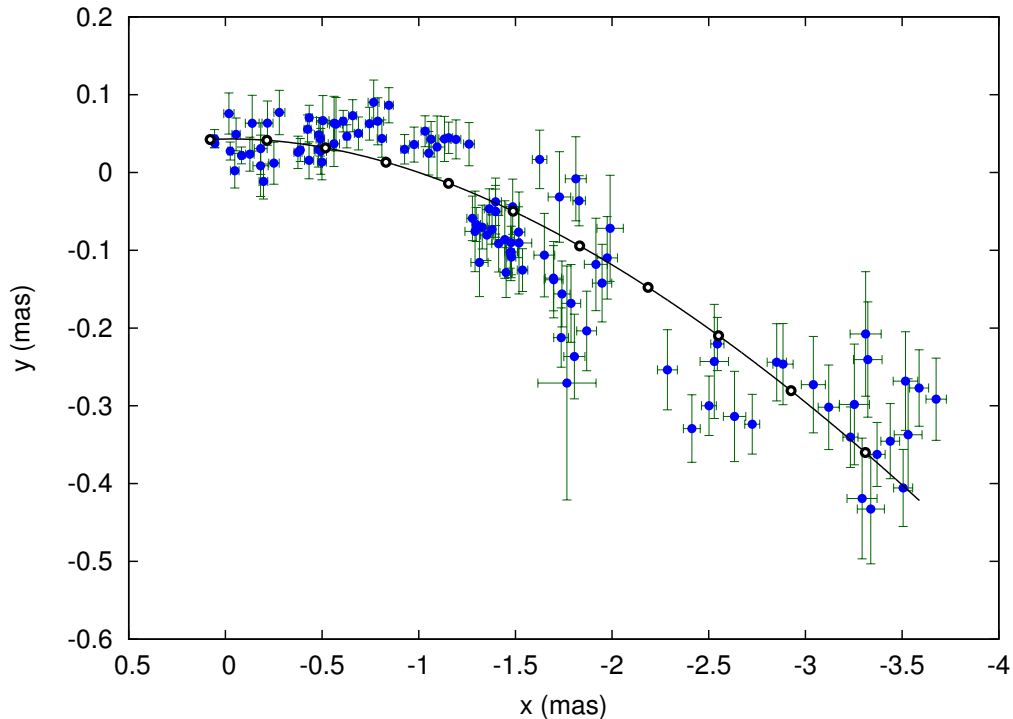


Figure 5.36: Two-dimensional trajectory of C12. The thick black line is reconstructed from the polynomial fits in x and y direction. The white circles are spaced at intervals of 1 year, indicating the change of component position with time.

C13

The component C13 is the one of the last components that emerged within the high state period that lasted from 1998 to 2001, the previously discussed features C10, C11, and C12 were all ejected during that time period. On 1999-07-17, C13 was first detected at 43.2 GHz. It reached similar peak flux density levels than C12 and was continuously observed between 1999 and 2003. Between 2003 and 2004 it became difficult to identify C13 as individual component due to strong blending with the equally bright close component C12, which caused a shift in the observed position of C13 closer toward C12. In 2004, the two components C12 and C13 were clearly separated again. Its early kinematics was investigated by Jorstad et al. (2005).

The component is identified in a total of 60 observations and the polynomial fits to the relative positions in $x(t)$ and $y(t)$ are shown in Figure 5.37. The two-dimensional trajectory of C13 is presented in Figure 5.38. The full fit to the trajectory is best represented by a second order polynomial in both x and y directions. The average speed of the component is (0.307 ± 0.051) mas year⁻¹ with an average direction of motion of $(-86.1 \pm 1.8)^\circ$ measured along the north-south axis. The component traces a strongly curved path, initially with a constant speed and a mild acceleration after a distance of 0.6 mas. The trajectory only traces up to a distance of 1.6 mas, thus only the inner jet is probed. Looking at the trajectory of component C10 (Figure 5.32), what is fit in C13 is not the average long-term direction of the motion, but the underlying pattern as seen in C10. If the trajectory of C13 were sampled to greater distances, the trajectory is expected to turn down to smaller angles again.

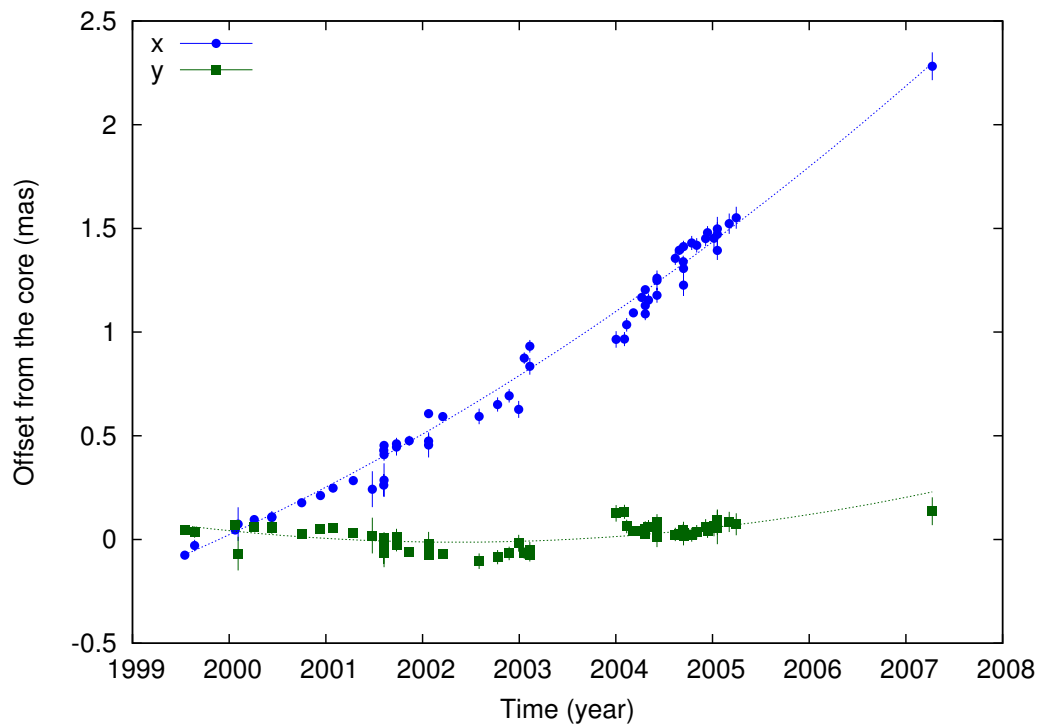


Figure 5.37: Relative positions $x(t)$ and $y(t)$ of C13, dotted lines are the respective polynomial fits to the relative positions.

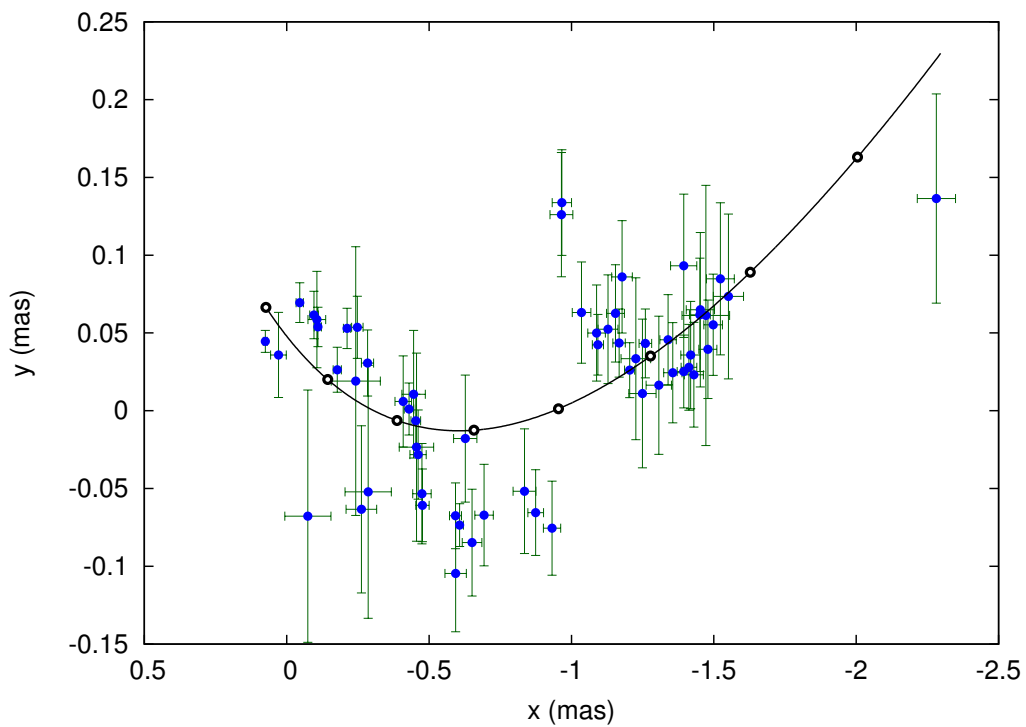


Figure 5.38: Two-dimensional trajectory of C13. The thick black line is reconstructed from the polynomial fits in x and y direction. The white circles are spaced at intervals of 1 year, indicating the change of component position with time.

C14

Component C14 was first identified on 1999-10-06 at 43.2 GHz and is the last component ejected during the flaring period 1999 – 2002. It had a similar brightness than the previous features C12 and C13. The component is identified in a total of 57 observations between 1999 and 2010. The polynomial fits to the relative positions in $x(t)$ and $y(t)$ are shown in Figure 5.39. The two-dimensional trajectory of C14 is presented in Figure 5.40. The full fit to the trajectory is best represented by a third order polynomial in x and y directions. The average speed of the component is (0.28 ± 0.11) mas year⁻¹ with an average direction of motion of $(-89.4 \pm 2.8)^\circ$ measured along the north-south axis. The component shows a fast acceleration between 1999 and 2003, with a constant bulk speed observed afterwards. The trajectory is highly curved, with a sharp bend at the beginning of the trajectory, which could have been caused by a highly curved intrinsic trajectory, causing a viewing angle change.

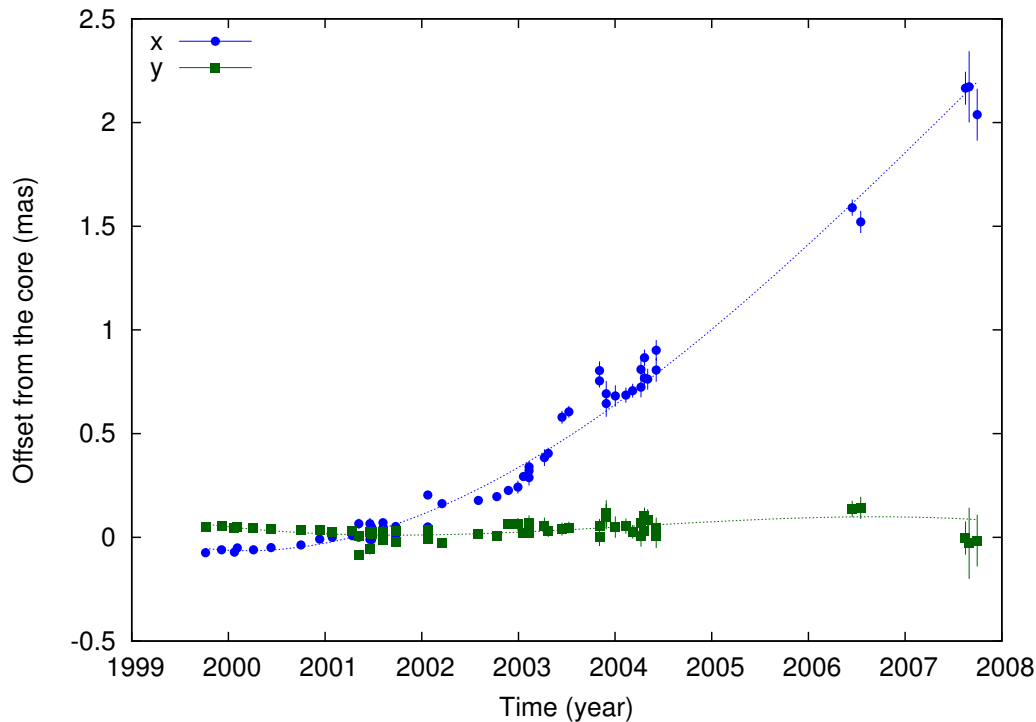


Figure 5.39: Relative positions $x(t)$ and $y(t)$ of C14, dotted lines are the respective polynomial fits to the relative positions.

C15

The component was first detected on 2003-02-10 at 22.2 GHz. Compared to previous components, the flux density of C15 decayed very fast from a peak value of 1.8 Jy on 2003-06-14 at 15.4 GHz to ~ 0.2 Jy a year later. The component was ejected during a period of low total flux density and low activity state of the jet. The polynomial fits to the relative positions in $x(t)$ and $y(t)$ are shown in Figure 5.41. The two-dimensional trajectory of C15 is presented in Figure 5.42. It was frequently detected in a total of 58 observations between 2003 and 2010 at predominantly 15.4 and 22.2 GHz. The obtained trajectory traces the path of the component up to a distance of ~ 3.0 mas

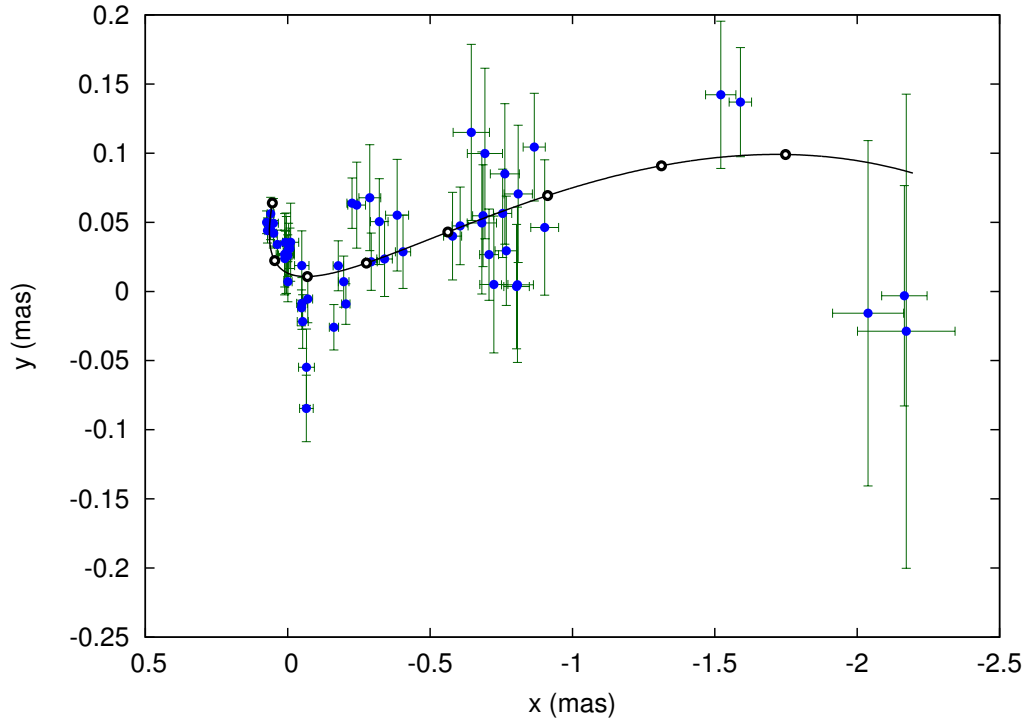


Figure 5.40: Two-dimensional trajectory of C14. The thick black line is reconstructed from the polynomial fits in x and y direction. The white circles are spaced at intervals of 1 year, indicating the change of component position with time.

and the full fit to the trajectory is best represented by a second order polynomial in x and a first order polynomial in y direction. The average speed of the component is $(0.435 \pm 0.039) \text{ mas year}^{-1}$ with an average direction of motion of $(-92.97 \pm 0.49)^\circ$ measured along the north-south axis.

C15a

Similar to C15, this component was first detected in the same observation on 2003-02-10 and shows similar properties than C15. To express the connection in the naming scheme, this component is labeled C15a. The polynomial fits to the relative positions in $x(t)$ and $y(t)$ are shown in Figure 5.43. The two-dimensional trajectory of C15a is presented in Figure 5.44. It was frequently detected in a total of 38 observations between 2003 and 2010 at predominantly 15.4 and 22.2 GHz. The observational gap seen in C15 and C15a between 2005 and 2006 is due to a lack of observations during that time period. However, C15a was only picked up in 2007 again. Due to the short time period it was monitored, the obtained trajectory only traces the path of the component at $0 - 0.4 \text{ mas}$ and $1.0 - 1.8 \text{ mas}$. The full fit to the trajectory is best represented by second order polynomials in x and y directions. The average speed of the component is $(0.272 \pm 0.050) \text{ mas year}^{-1}$ with an average direction of motion of $(-86.9 \pm 1.4)^\circ$ measured along the north-south axis.

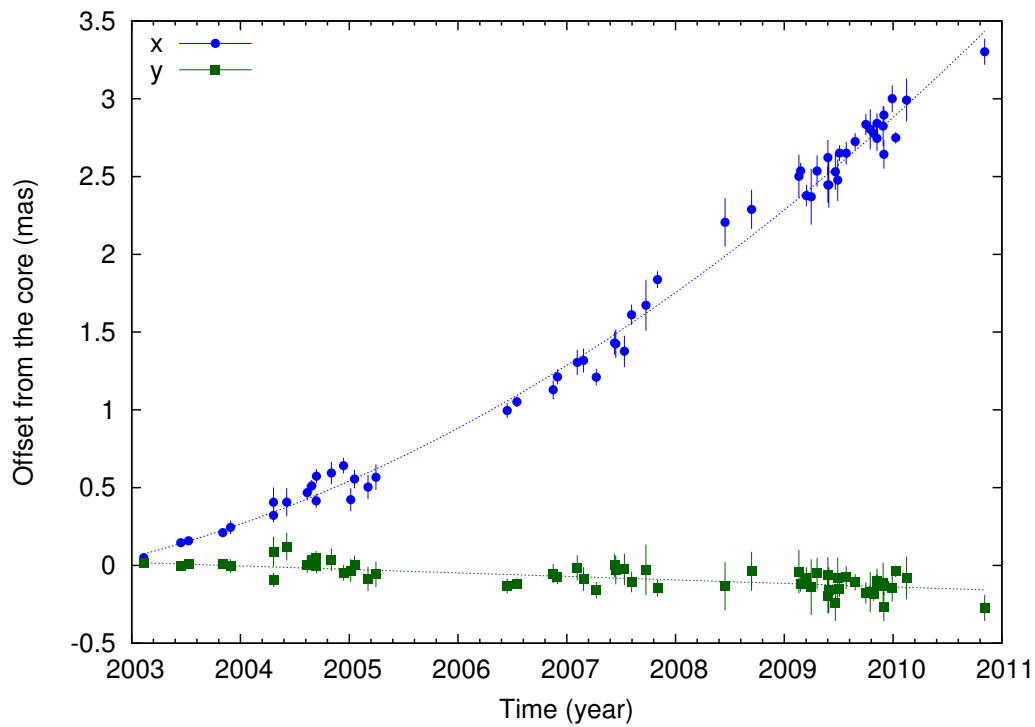


Figure 5.41: Relative positions $x(t)$ and $y(t)$ of C15, dotted lines are the respective polynomial fits to the relative positions.

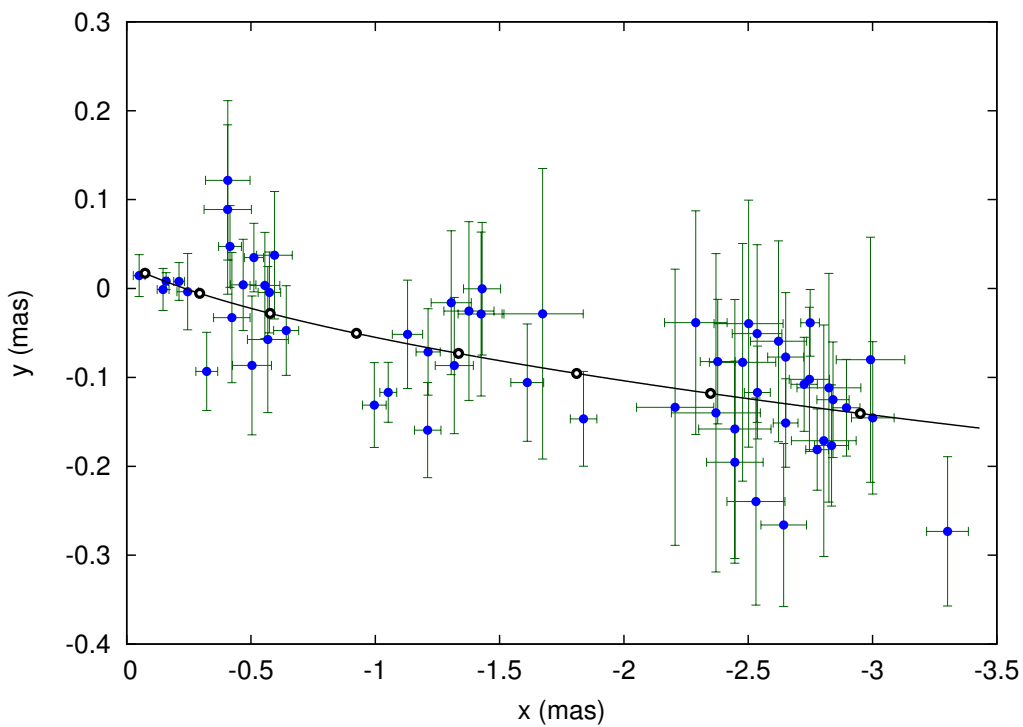


Figure 5.42: Two-dimensional trajectory of C15. The thick black line is reconstructed from the polynomial fits in x and y direction. The white circles are spaced at intervals of 1 year, indicating the change of component position with time.

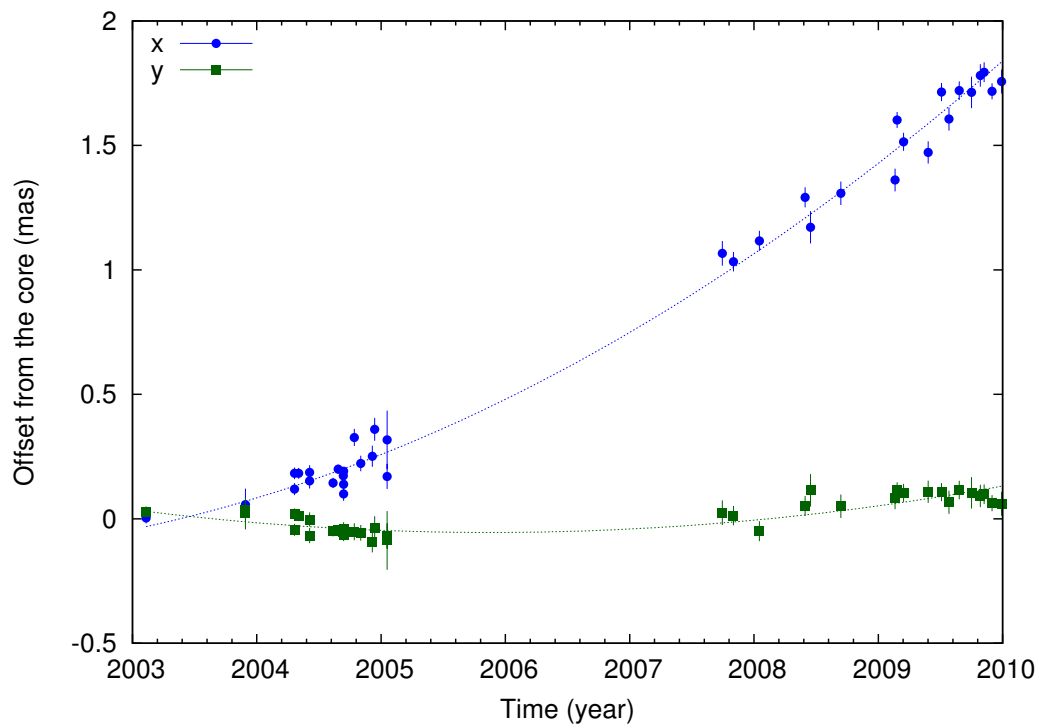


Figure 5.43: Relative positions $x(t)$ and $y(t)$ of C15a, dotted lines are the respective polynomial fits to the relative positions.

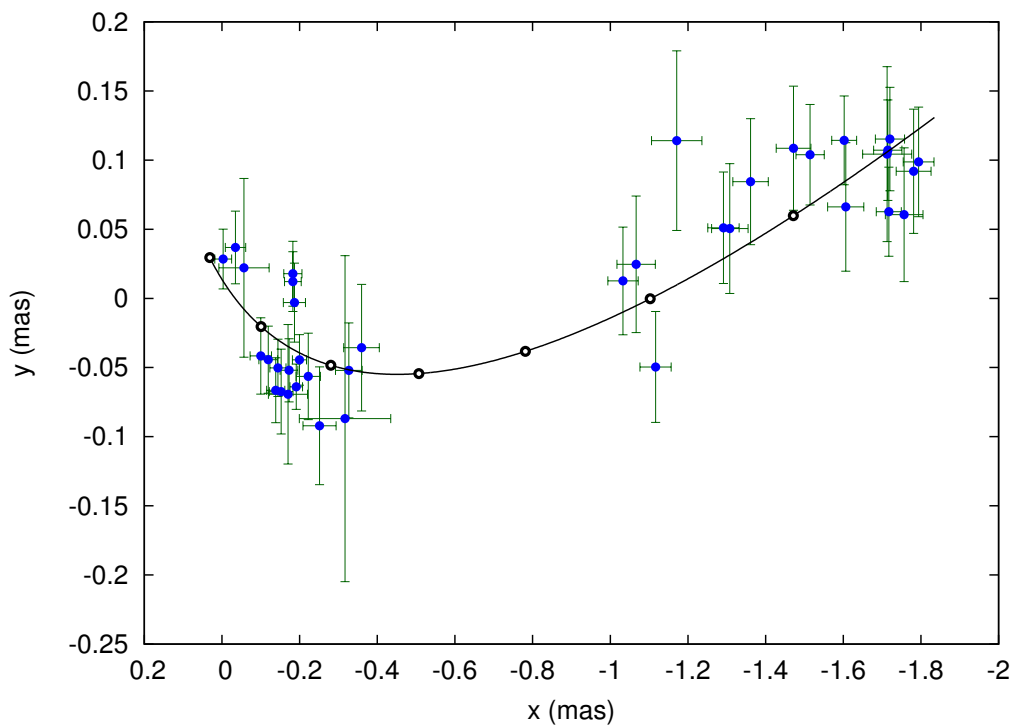


Figure 5.44: Two-dimensional trajectory of C15a. The thick black line is reconstructed from the polynomial fits in x and y direction. The white circles are spaced at intervals of 1 year, indicating the change of component position with time.

C16

Component C16 was first detected on 2003-11-28 at 43.2 GHz. It is a weaker feature than C15/C15a, with a peak flux density of ~ 1 Jy. In contrast to C15a, it was continuously detected in 59 observations between 2003 and 2010, besides the monitoring gaps in between. The polynomial fits to the relative positions in $x(t)$ and $y(t)$ are shown in Figure 5.45. The two-dimensional trajectory of C16 is presented in Figure 5.46. The full fit to the trajectory is best represented by a second order polynomial in x and a first order polynomial in y direction. The trajectory within 1.5 mas from the core is straight along the general jet axis, with an average direction of motion of $(-89.11 \pm 0.30)^\circ$. The average speed of the component is (0.272 ± 0.037) mas year $^{-1}$, however the component accelerated between 2005 and 2008 from 0.051 to 0.38 mas year $^{-1}$.

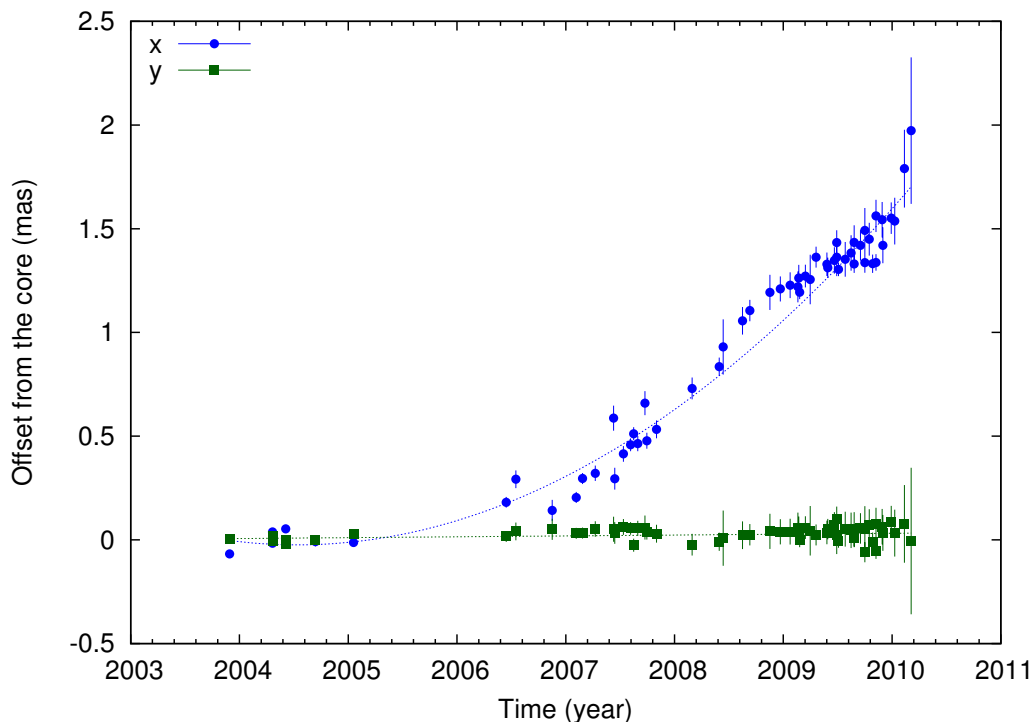


Figure 5.45: Relative positions $x(t)$ and $y(t)$ of C16, dotted lines are the respective polynomial fits to the relative positions.

C17, C18, and C19

The three components C17, C18, and C19 are the most recent features in the jet observed at 15.4 GHz. Due to the limited time period, these components are only sampled to distances of ≤ 1.2 mas.

C17 was first detected on 2006-07-17 at 22.2 GHz. It was detected in 19 observations between 2006 and 2010. The polynomial fits to the relative positions in $x(t)$ and $y(t)$ and the two-dimensional trajectory of C17 are shown in Figure 5.47. The full fit to the trajectory is best represented by a second order polynomial in x and a first order polynomial in y direction. The trajectory is slightly curved, with an average direction of the motion of $(-93.3 \pm 1.1)^\circ$. The average speed of the component is (0.431 ± 0.068) mas year $^{-1}$.

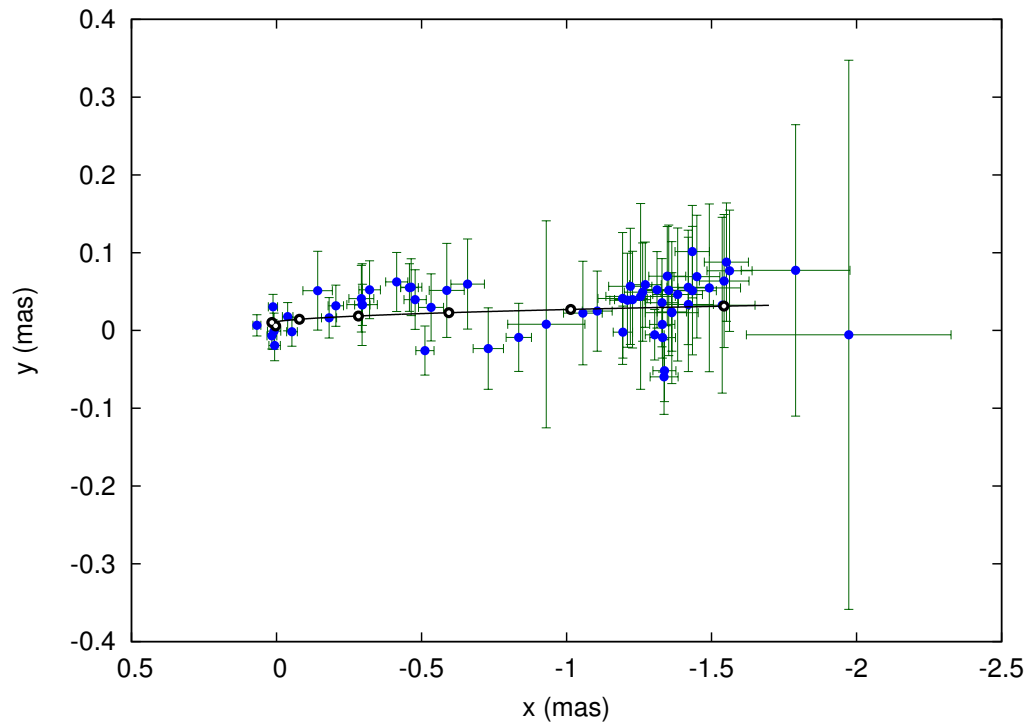


Figure 5.46: Two-dimensional trajectory of C16. The thick black line is reconstructed from the polynomial fits in x and y direction. The white circles are spaced at intervals of 1 year, indicating the change of component position with time.

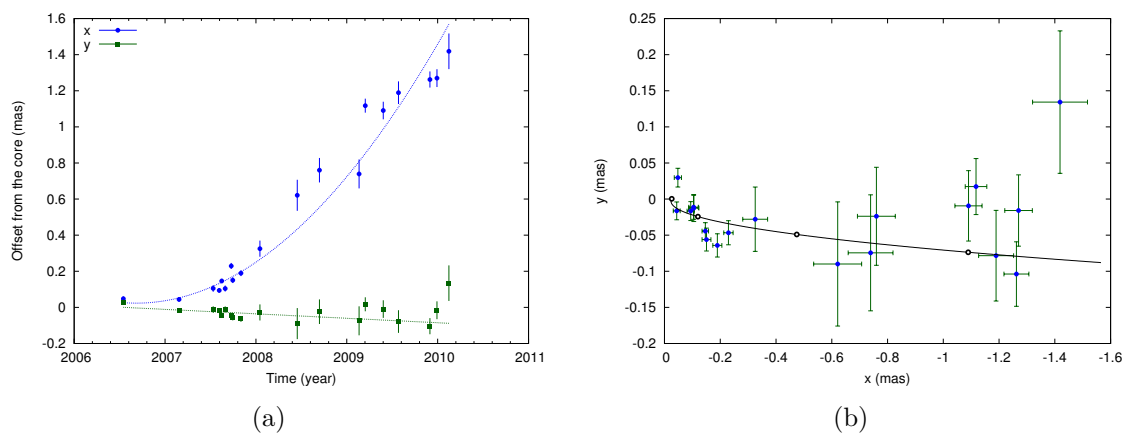


Figure 5.47: (a) Relative positions $x(t)$ and $y(t)$ of C17, dotted lines are the respective polynomial fits to the relative positions. (b) Two-dimensional trajectory of C17. The thick black line is reconstructed from the polynomial fits in x and y direction. The white circles are spaced at intervals of 1 year, indicating the change of component position with time.

C18 was first detected on 2007-06-14 at 43.2 GHz. It was identified in 23 observations between 2007 and 2010, however only in 2009 it became reliably detected in all subsequent observations. The polynomial fits to the relative positions in $x(t)$ and $y(t)$ and the two-dimensional trajectory of C18 are shown in Figure 5.48. The full fit to the trajectory is best represented by a first order polynomial in both x and y direction. The trajectory within 0.6 mas from the core is straight, with an average direction of the motion of $(-94.28 \pm 0.36)^\circ$. The average speed of the component is (0.259 ± 0.015) mas year $^{-1}$.

C19 was first detected on 2007-09-29 at 43.2 GHz. It was detected in 30 observations between 2007 and 2010. The polynomial fits to the relative positions in $x(t)$ and $y(t)$ and the two-dimensional trajectory of C19 are shown in Figure 5.49. The full fit to the trajectory is best represented by a second order polynomial in x and a first order polynomial in y direction. The trajectory within 0.6 mas from the core is slightly curved, with an average direction of the motion of $(-97.16 \pm 0.50)^\circ$. The average speed of the component is (0.232 ± 0.032) mas year $^{-1}$. At distances > 0.3 mas from the core the scatter of the determined positions increases significantly.

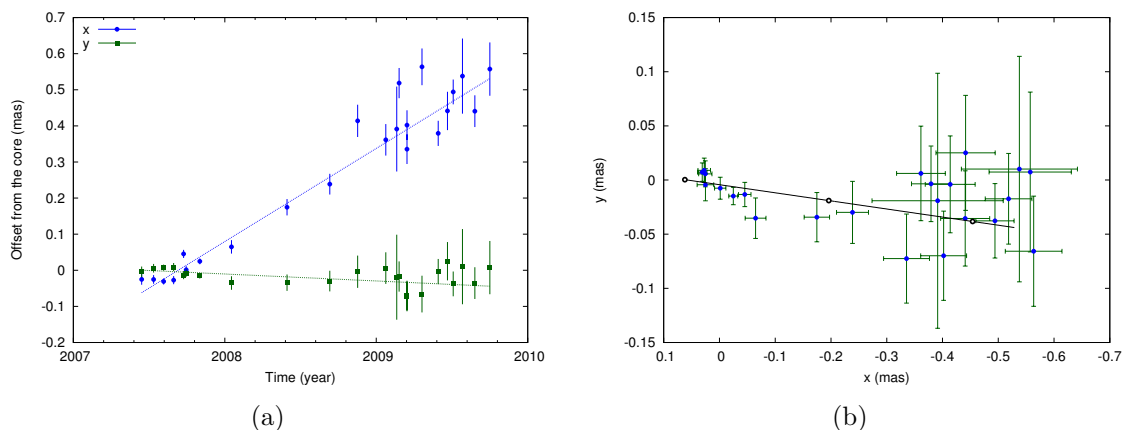


Figure 5.48: (a) Relative positions $x(t)$ and $y(t)$ of C18, dotted lines are the respective polynomial fits to the relative positions. (b) Two-dimensional trajectory of C18. The thick black line is reconstructed from the polynomial fits in x and y direction. The white circles are spaced at intervals of 1 year, indicating the change of component position with time.

C20, C21, C22, and C23

New observations were obtained for this thesis which revealed four new moving components between 2008 and 2010 that are related to an increase in emission at other wavelengths, in particular γ -rays. By the end of 2010 these features have traveled ≤ 0.4 mas, with the exception of C20. Thus, trajectories of the features C21, C22, and C23 are not included in this analysis. C21 was observed in a total of 22 observations, up to a distance of ~ 0.4 mas. C22 was observed in a total of 14 observations, up to a distance of ~ 0.2 mas. C23 was observed only in a total of 7 observations, up to a distance of ~ 0.1 mas. A detailed discussion of the kinematics and emission properties of these features is provided in Chapter 7.

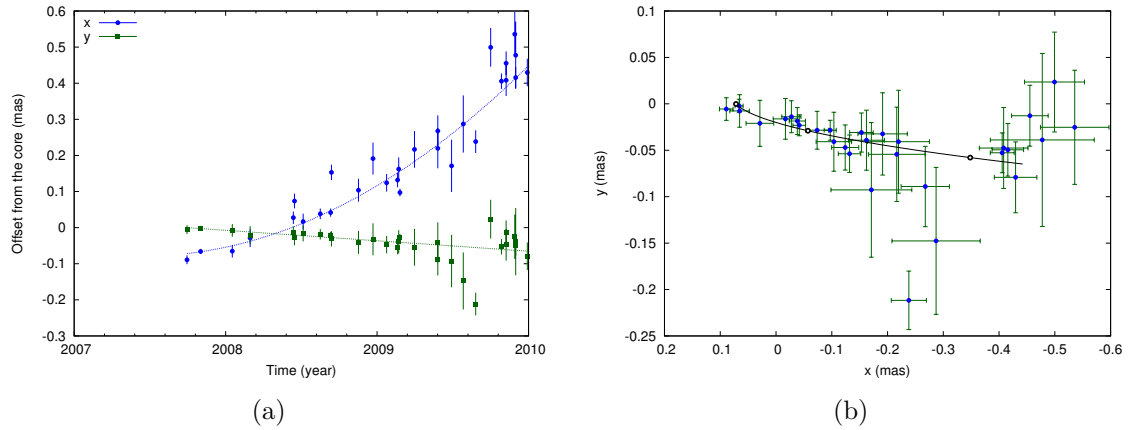


Figure 5.49: (a) Relative positions $x(t)$ and $y(t)$ of C19, dotted lines are the respective polynomial fits to the relative positions. (b) Two-dimensional trajectory of C19. The thick black line is reconstructed from the polynomial fits in x and y direction. The white circles are spaced at intervals of 1 year, indicating the change of component position with time.

C20 was first detected on 2008-06-12 at 43.2 GHz and is the first jet feature of a new cycle of increased activity of 3C 345. It was detected in 36 observations between 2008 and 2010. The polynomial fits to the relative positions in $x(t)$ and $y(t)$ and the two-dimensional trajectory of C20 are shown in Figure 5.50. The full fit to the trajectory is best represented by a second order polynomial in x and a first order polynomial in y direction. The trajectory within 0.4 mas from the core is curved, with an average direction of the motion of $(-93.54 \pm 0.42)^\circ$. The dense monitoring of 3C 345 stopped at the beginning of 2010, the data point at the end of 2011 was obtained from a 15.4 GHz observation of the MOJAVE survey. The average speed of the component is $(0.567 \pm 0.058) \text{ mas year}^{-1}$.

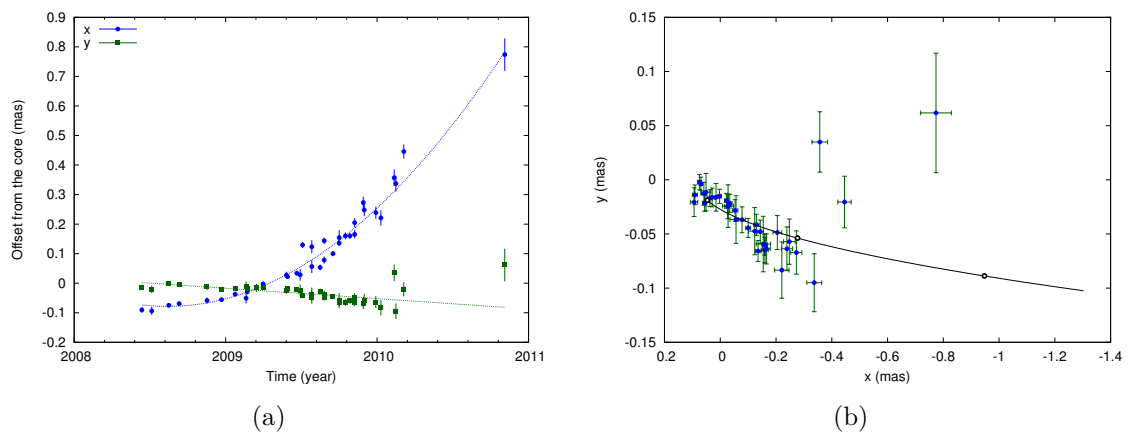


Figure 5.50: (a) Relative positions $x(t)$ and $y(t)$ of C20, dotted lines are the respective polynomial fits to the relative positions. (b) Two-dimensional trajectory of C20. The thick black line is reconstructed from the polynomial fits in x and y direction. The white circles are spaced at intervals of 1 year, indicating the change of component position with time.

5.3 Structural Variability of the Jet

With the parametrized trajectories of the jet components, the structural variability of the whole jet, as traced by the jet components is investigated. The two dimensional trajectories of those components that trace the jet beyond distances of 5 mas are plotted together in Figure 5.51. The spread of the fitted trajectories provide an insight in the variation of motion along the jet. At 4 mas from the core, the fitted trajectories have a spread of ~ 0.5 mas (3.3 pc), at 10 mas from the core this spread is ~ 1 mas (6.6 pc), which corresponds to an opening angle of $\alpha \approx 2.4^\circ$ at these distances. Remarkably, the trajectories of different components trace a similar path even at these distances, indicating a well collimated outflow even to distances as far as 15 mas from the core (~ 100 pc), which corresponds to a linear de-projected distance of 1.2 kpc, assuming an initial viewing angle of $\theta \approx 5^\circ$. Lobanov (1996) pointed out that C1 outlines the transition from the compact jet to to the large scale one. The features at < 16 mas outline the general direction of the flow of $\approx -70^\circ$, whereas C1 points toward $\approx -30^\circ$, consistent with the $\approx -40^\circ$ found by Kollgaard et al. (1989). Note, the maps of 5.0 GHz observations provided in Appendix B show two turning points in the jet at distances ~ 5 and ~ 15 mas from the core, consistent with the observed trajectories.

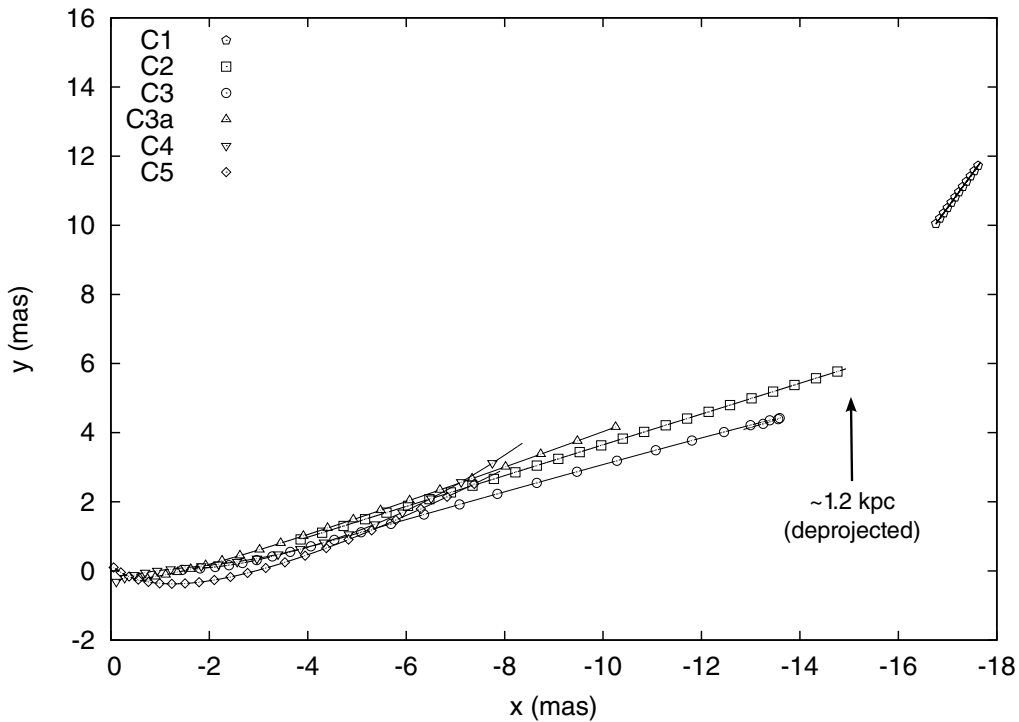


Figure 5.51: Fitted trajectories of the jet components which are traced beyond 5 mas from the core.

At intermediate distances, 1 – 5 mas from the core (Figure 5.52), the trajectories follow even more closely the same general path. At distances less than ~ 3 mas from the core the general direction of the flow is around -90° and only at larger distances it turns upward to larger angles. At 1 mas from the core the spread of trajectories is ~ 0.34 mas (2.3 pc) and increases to ~ 0.49 mas (3.3 pc) at 2 mas. This corresponds to an apparent opening angle of $\approx 4.3^\circ$.

At distances ≤ 1 mas, which are shown in Figure 5.53, the trajectories of many

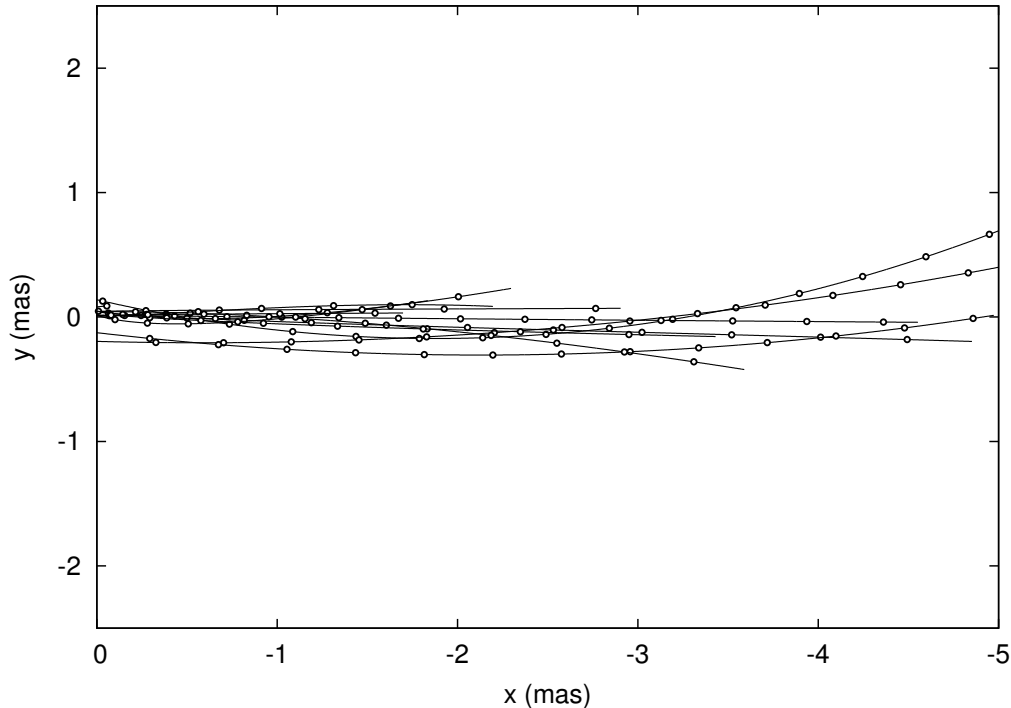


Figure 5.52: Fitted trajectories of jet components (C6–C16) at separations less than 5 mas from the core.

features seem to cluster around the same general direction, along $y = 0$ mas. The spread of these component trajectories is 0.074 mas (0.50 pc) extrapolated to the core and 0.12 mas (0.80 pc) at 0.5 mas from the core, which corresponds to an opening angle of the spread of $\sim 2.6^\circ$. If we take the difference in spread between 0.5 and 1 mas (here 0.17 mas) from the core, then a consistent opening angle of ~ 2.9 mas is obtained.

However, as indicated by blue dashed lines in Figure 5.53, some of the fitted trajectories do not follow the general direction, but seem to congregate along $y = -0.2$ mas, with the exception of the trajectory of C6. Out of the trajectories of components C4 to C9, which are all ejected in the time period between 1980 and 1996, only C7 (marked in red) follows the general path outlined around $y = 0$. Systematics introduced by pre-VLBA observations can be ruled out, since components C8 and C9 are among these outliers, which have been monitored by the VLBA at all frequencies ranging from 5.0 to 43 GHz. Figure 5.54 provides a comparison between component positions of C4 – C9 and C10 – C20.

Lobanov (1996) already pointed out that interestingly the features indicated by blue lines seem to get very close to each other and even cross around 0.4 – 0.6 mas from the core. After the end of a flare in 1997, clearly visible in the Metsähovi monitoring data (Teräsanta et al. 1998, A. Lahteenmaki *priv. comm.*), subsequent components starting with C10 follow the general path along $y = 0$ mas with no exceptions. This sudden change in general component trajectories is curious and no clear explanation exists for this. A possible reason for this could be a difference of the injection point of perturbations into the jet, which lead to the formation of the observed and model-fitted features in the jet. This difference of injection could either be due to a second central engine (ie. binary black hole) or a change in the accretion behavior of the central object. This should be further investigated, possibly by using numerical simulations to

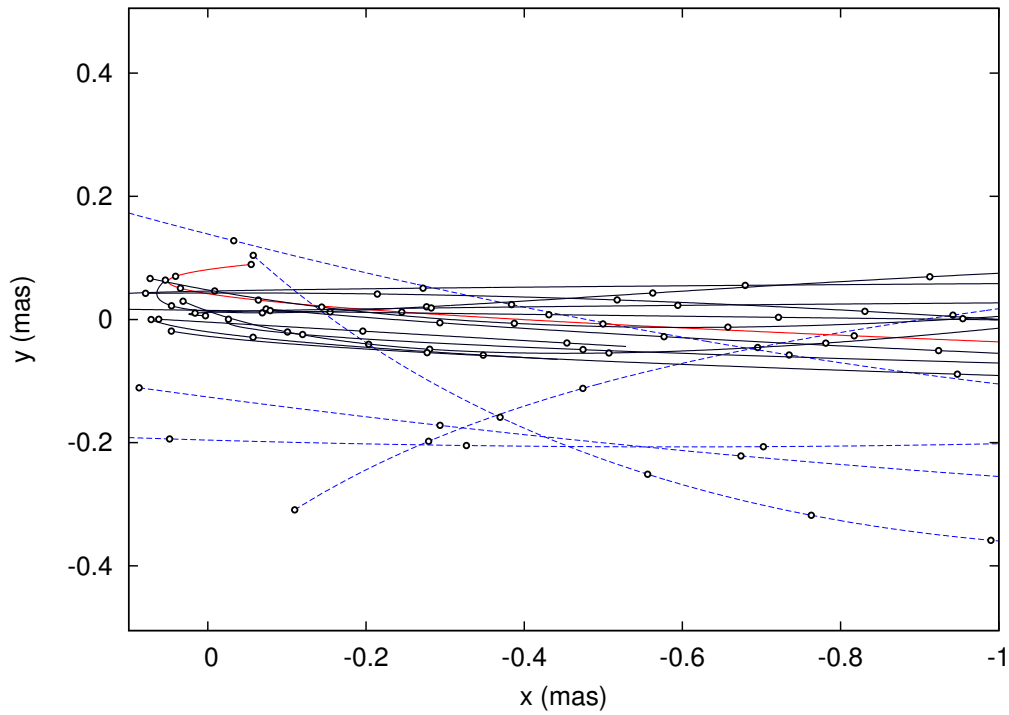


Figure 5.53: Fitted trajectories of jet components (C4–C20) at separations less than 1 mas from the core. The dashed blue lines correspond to the fitted trajectories of C4, C5, C6, C8, and C9. The red colored line corresponds to C7.

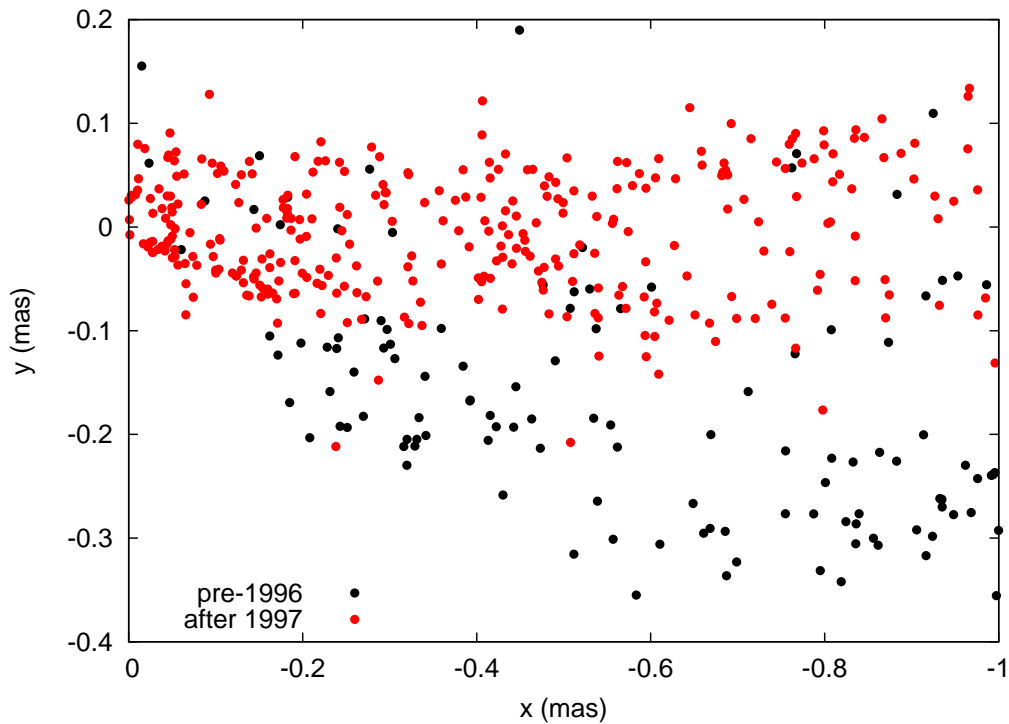


Figure 5.54: Trajectories of components C4 – C20 within 1 mas from the core, positions of components ejected before 1996 (C4 – C9) are plotted in black circles and positions of components ejected after 1995 (C10 – C20) are drawn in red circles.

test different scenarios.

The component position angles measured at 0.5 mas radial distance from the core offer a way to represent time dependent variations of the observed trajectories of the jet features C4–C19 (1983 – 2010), as shown in Figure 5.55. Pre-1995 the position angles of C4–C7 seem to be randomly distributed, after 1995, a clear increasing trend peaking around 2005 and followed by a falling trend is observed. The amplitude of the increase is highly significant and ranges from -120° to -70° . Lobanov & Roland (2005) and Klare et al. (2003) describe in their work a short-term periodicity of 8–10 years with an underlying long-term trend of $0.4 - 2.6^\circ \text{ year}^{-1}$. No clear periodic trends are evident from the determined position angles here, with no visible trend prior 1995. However, to illustrate a possible oscillation of position angles, a sinusoidal function is plotted in Figure 5.55. If the observed variation were due to a precession in the jet, from the time difference between the lowest and highest position angle value between 1998 and 2005, a short-time scale period of ~ 14.5 years could be inferred, which is 5.0 years longer than the 9.5 ± 0.1 years period suggested by Lobanov & Roland (2005). A closer inspection of the position angles of C4 and C5 gives the impression that, if there is an oscillating pattern, the period of the oscillation must have been shorter at earlier times.

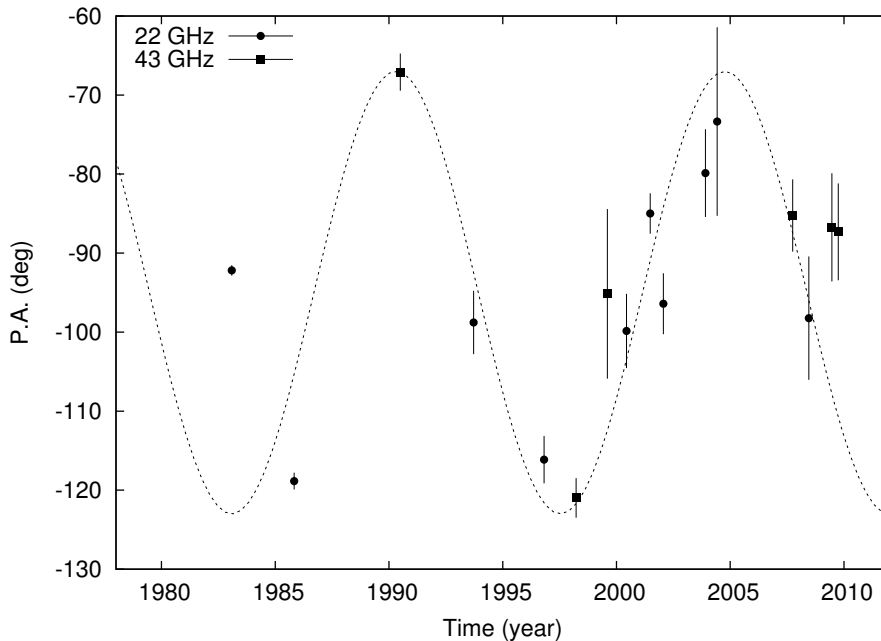


Figure 5.55: Plot of position angles the jet features (C4–C19, without C15a) at a separation of 0.5 mas from the core in chronological order. In order to maximize the number of measurements at 0.5 mas, observations at 22 (point) and 43 GHz (square) are combined. A sinusoidal function with a period of 14.5 years is plotted as a guiding line for possible oscillations.

An alternate explanation for the oscillating behavior reflected in the time variability of the component position angle of the jet could be an underlying pattern that is introduced at the injection point where matter is brought into the jet, which then causes variations in the observed jet pattern. The component trajectories of C9 (Figure 5.29) and C10 (Figure 5.31) show this underlying pattern very clearly. This pattern is not represented in the polynomial fits discussed in the previous section. Variations of this

pattern could be the root cause for the observed oscillation in the position angles. To investigate this pattern, components that exhibit this underlying pattern are selected, their general direction of motion (i.e. the respective polynomial fits) is subtracted and the residual pattern is compared between them, by plotting each of these components on top of each other in Figure 5.56. The trajectory patterns of C8, C9, and C10 agree reasonably well with each other showing an oscillation with similar amplitudes. This is in contrast to components C12 and C16, where the amplitude of the residual pattern is almost zero. A closer comparison between C12 and C16 reveals that the residual pattern of C12 seems to be positively curved, whereas C16 is almost a straight line, see Figure 5.56(b). In summary, what is observed is a standing, oscillating pattern that changes its amplitude with time. This also explains, why an oscillation is seen in Figure 5.55, which is the effect of a change in amplitude of the underlying jet patterns. The overall evolution of this pattern resembles a rotation of the inner structure of the jet, hence the observation of a straight curve (C16), where the pattern is seen edge on.

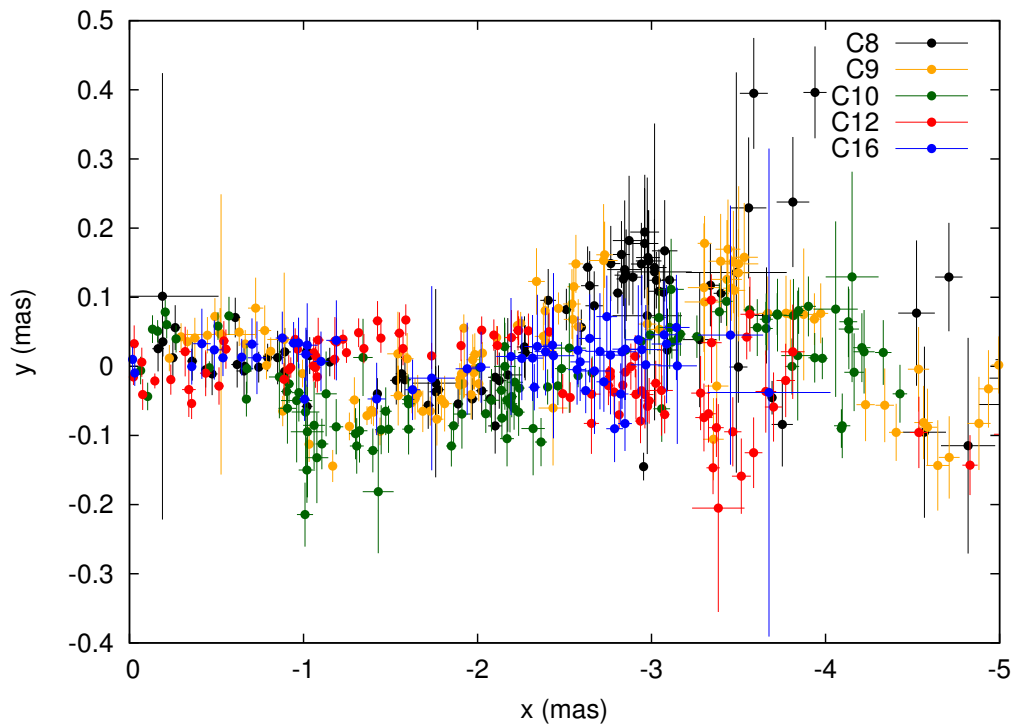
The origin of the underlying jet pattern is unclear with various scenarios or even, a combination of those possible. As suggested by Lobanov & Roland (2005), it could be the signature of jet precession, like it might be expected from a binary black hole system. However, jet precession is expected to undergo much slower changes than it is observed in this case. Alternatively, it could also be the signature of Kelvin-Helmholtz instabilities in the internal structure of the jet (Perucho et al. 2006), as a consequence of a fast spine/slow sheath jet structure or a variation in the injection properties into the jet. In this case, similar to 3C 273 (Lobanov & Zensus 2001), the observed regular patterns in the component trajectories may reflect the presence of helical and elliptical surface modes of Kelvin-Helmholtz instabilities.

5.4 Physical Properties of the Jet

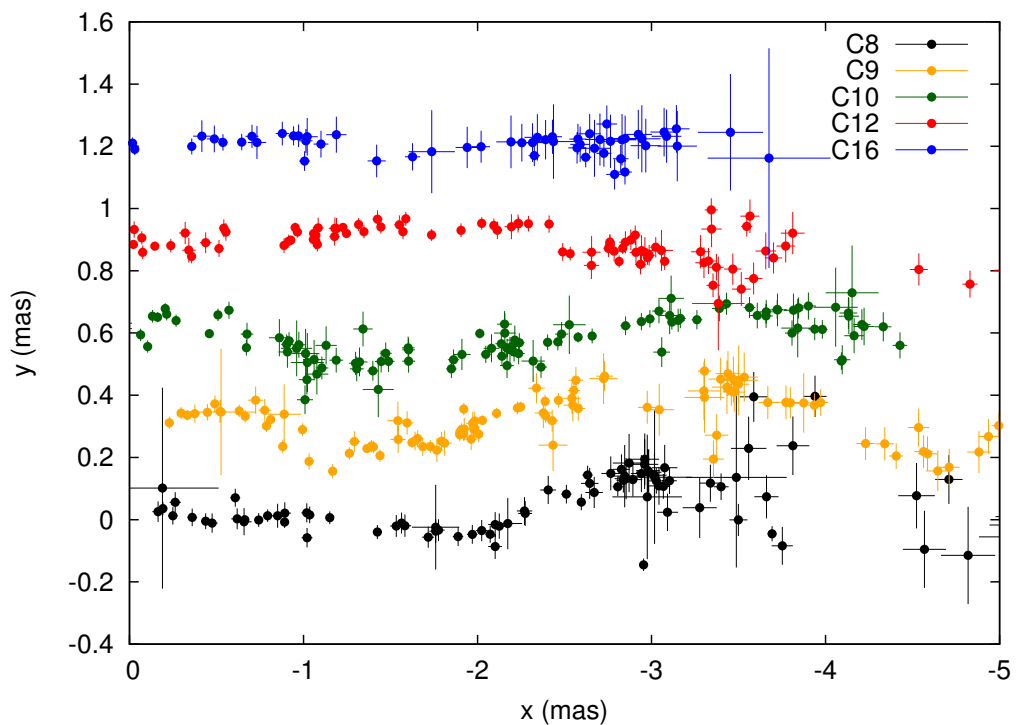
The information gathered on the jet features are now combined to derive physical parameters of the jet flow, including Doppler and Lorentz factors of the relativistically moving regions, as well as average magnetic field strength or the actual separations of the core from the jet base.

5.4.1 Opening Angles

In some approximation, a combination of all component sizes provides an estimate on the overall opening angle of the channel of the jet through which the individual components pass. In Figure 5.57, the sizes of all components, for which the trajectories were determined, are plotted together with the corresponding radial separation from the core. The jet size with distance is estimated by making a linear fit to the data ($d_{\text{fit}}(r)$). Since the general jet direction is turning at a distance of 4 mas, a break in the component size increase is observed. Due to this, two jet opening angles are determined, one for a distance up to 4 mas and a separate one for distances > 4 mas. The linear fit provides the value for the average FWHM of the components, $d_{\text{FWHM}}(r) \propto d_{\text{fit}}(r)$, with which the apparent (α_{app}) and intrinsic (α_{int}) jet opening angles can be determined



(a) The residual jet patterns of C8 (1994), C9 (1996), C10 (1997), C12 (1999), and C16 (2003) plotted on top of each other.



(b) The residual jet patterns spread for readability, adding in y direction 0.3 mas for C9, 0.6 mas for C10, 0.9 mas for C12, and 1.2 mas for C16.

Figure 5.56: Residual patterns in the trajectories of features C8, C9, C10, C12, and C16 after subtraction of the respective polynomial fits.

calculating,

$$\alpha_{\text{app}} = 2 \tan^{-1} \left(\frac{d_{\text{FWHM}}}{r_{\text{jet}}} \right); \quad \alpha_{\text{int}} = \alpha_{\text{app}} \sin \theta, \quad (5.8)$$

where d_{FWHM} is the deconvolved angular size, r_{jet} is the distance in the jet at which d_{eff} is measured and θ is the viewing angle of the jet axis to our line of sight. This way the average opening angle of the jet is determined to be $\alpha_{\text{app}} = (33.8 \pm 1.0)^\circ$ for 0–4 mas and $(49.2 \pm 3.5)^\circ$ for >4 mas. The average opening angles for individual components are listed in Table 5.4 together with other physical parameters of the jet. Pushkarev et al. (2009) determined $\alpha_{\text{app}} = 12.9^\circ$, with no error estimates provided, using the general direction of the jet brightness distribution at 15.4 GHz and fitting the observed deconvolved jet profiles.

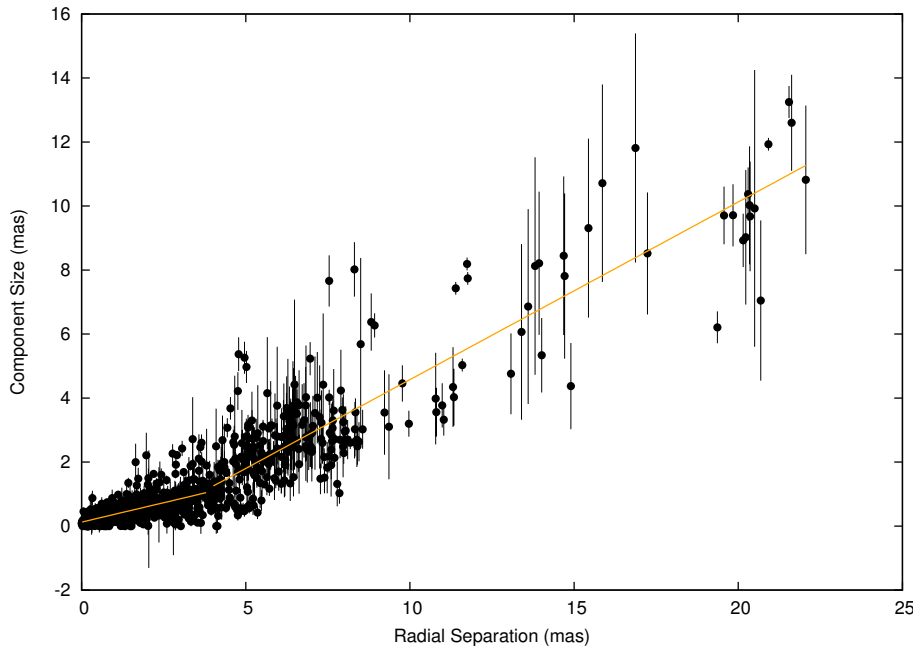


Figure 5.57: FWHM of all fitted Gaussian components plotted against their respective radial distance from the core. Linear fits are indicated by orange lines, with the slopes of 0.2425 ± 0.0072 for radial separations from 0 to 4 mas and 0.555 ± 0.023 for radial separations > 4 mas.

A different way to look at jet opening angles is to calculate a jet opening angle value for each modelfit component in the dataset. Most of the monitoring observations were performed at 15.4 GHz, for which 622 value pairs can be determined. Choosing a single observing frequency removes the effect of beam size from the dataset, especially if including lower frequency observations (i.e. larger beam size). The distribution of α_{app} at 15.4 GHz is shown in Figure 5.58. A polynomial fit is applied, similar to the representation of trajectories in the previous section. Only values at distances > 1 mas from the core are used, because of a decreased measurement accuracy at $\lesssim 1$ mas due to blending, unresolved jet components, and unknown distance to the jet base lead to overestimation of α_{app} at small distances r . Nevertheless, the fit indicates a decreasing trend of α_{app} between the core and 2 mas. Beyond 2 mas, α_{app} remains relatively constant with a slight increasing trend, which is picking up at around 4 mas, the distance at which a change in the jet direction is observed. These trends become even more dramatical when calculating the weighted averages for selected distances. This results in values of α_{app} of $(35.43 \pm 0.22)^\circ$, $(23.53 \pm 0.15)^\circ$, $(19.97 \pm 0.23)^\circ$, and

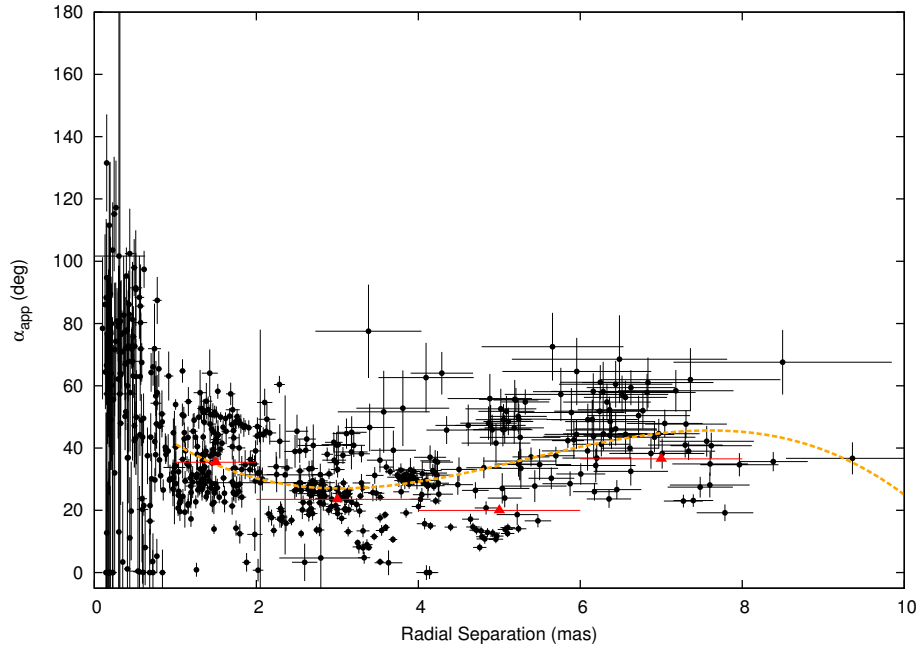


Figure 5.58: Jet opening angles at 15.4 GHz plotted against radial separation from the core. The orange dashed line represents the best fit, a 4th order polynomial, to the observed scatter between 1 and 10 mas. Red triangles are weighted averages of that particular region.

$(36.55 \pm 0.58)^\circ$ for distances of 1–2, 2–4, 4–6, 6–8 mas respectively. These points are indicated by red triangles in Figure 5.58. These observed changes of α_{app} indicate a possible recollimation of the jet between the core and 2 mas (13.3 pc), with a slowly increasing opening angle thereafter.

An interesting discovery was made during the analysis of the size evolution of individual components. The component size evolution observed at 15.4 and 22.2 GHz for the components C8, C9, and C10 is shown in Figure 5.59, which resembles a step-like function size evolution (C10) or in the cases of C8 and C9 an oscillations. Two steps are clearly visible with a rising stage between 0 and 0.5 mas going from an unresolved component size to ~ 0.5 mas, a plateau between 0.5 and ~ 1.4 mas in distance (C10), then a second increase in component size ~ 0.3 mas and a second plateau from 1.5 mas separation onward. Beyond, C9 shows a significant drop in component size, followed by a rising stage again, the other components are becoming too scattered to clearly see the continuation of a step-like/oscillating pattern. The times at which the first two steps occur (0.4 and 1.5 mas) match perfectly with one oscillation period observed at these distances in the trajectories of C8 (Figure 5.28), C9 (Figure 5.30), and C10 (Figure 5.32). Such a pattern is expected if the jet is changing its position angle to our line of sight, possibly caused by Kelvin-Helmholtz type instabilities, briefly mentioned in the previous Section. The observed size resolution resembles two threads resulting from the elliptical surface mode of a Kelvin-Helmholtz instability. During maxima, the threads are apart and a double humped (edge brightened) transverse profile of the jet at this position should be observed, during minima the threads overlap (in projection) leading to a single peaked transverse jet profile, which is indicated in Figure 5.59.

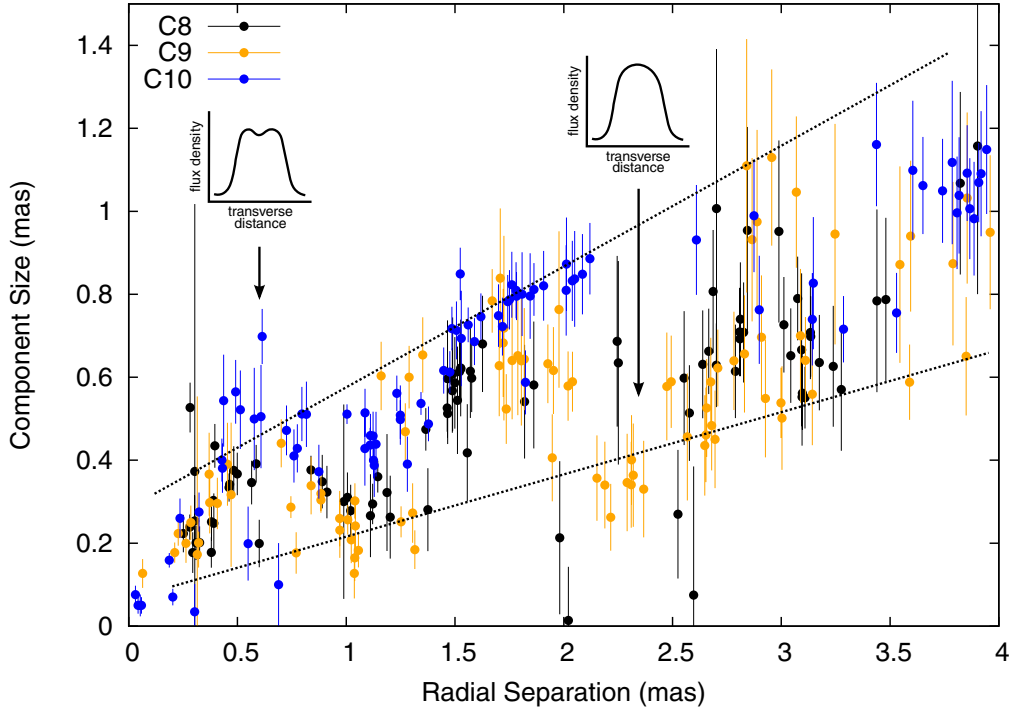


Figure 5.59: Component size evolution of C8, C9, and C10 at 15.4 and 22.2 GHz. The dotted lines indicate the lower and upper envelope of the size expansion. The transverse brightness profiles predicted from the Kelvin-Helmholtz instability are indicated by inlets, denoting the expected shapes.

5.4.2 Kinematics

The polynomial fits to the trajectories of individual jet components provide not only information about the temporal evolution of the general jet flow, but also give insights into the actual dynamics of each of the superluminal features. The obtained average speeds and the direction of the flow are listed in Table 5.4 together with derived quantities, which are discussed in the following.

Using $\langle \mu \rangle$, the average apparent speed $\bar{\beta}_{\text{app}}$, the speed in the source frame (deprojected) $\bar{\beta}$ can be derived through,

$$\bar{\beta}_{\text{app}} = \langle \mu \rangle \frac{D_L}{(1+z)} \quad (5.9)$$

and

$$\bar{\beta} = \frac{\bar{\beta}_{\text{app}}}{\bar{\beta}_{\text{app}} \cos \theta + \sin \theta} \quad (5.10)$$

where D_L is the luminosity distance, z is the redshift and θ is the jet angle to the line of sight (viewing angle).

The physical parameters like Doppler factor δ , Lorentz factor Γ and viewing angle θ can be derived for most of the components. For these calculations, the jet emission is assumed to be dominated by radiative losses (cf. Jorstad et al. 2005; Lobanov & Zensus 1999, and Chapter 7 of this thesis) and consists of optically thin shocked gas, $\alpha = -0.7$ (i.e. $S_\nu \propto R^{-1.633} \cdot \nu^{+\alpha}$, where R is the size of the emitting region in the

rest-frame of the jet and ν the frequency in the observer's frame, Marscher & Gear 1985). The variability Doppler factor is then derived as,

$$\delta_{\text{var}} = \frac{d_{\text{eff}} D_{\text{L}}}{c \Delta t_{\text{var}} (1+z)}, \quad (5.11)$$

where D_{L} is the luminosity distance and d_{eff} is the effective angular size of a spherical region (i.e. the measured FWHM of the component multiplied by a factor of 1.8; cf. Pearson 1999). The flux variability time scale is defined as $\Delta t_{\text{var}} = dt / \ln(S_1/S_2)$. The value of S_1 is the measured maximum component flux density, while S_2 represents the minimum component flux density selected at the time of maximum absolute value of the time derivative of the flux density. Δt_{var} is determined from observations at ~ 15 GHz only. It is then possible to calculate bulk Lorentz factors by combining the derived δ_{var} with β_{app} ,

$$\Gamma_{\text{var}} = \frac{\beta_{\text{app}}^2 + \delta_{\text{var}}^2 + 1}{2\delta_{\text{var}}}. \quad (5.12)$$

Combining the derived values for all components for which kinematic parameters are derived, a median Lorentz factor of 14.1 and a median Doppler factor of 15.6 are obtained (see Figure 5.60 and Table 5.4).

An upper limit for the viewing angle θ can immediately be determined using the median apparent component speed $\bar{\beta}_{\text{app}}$, with a value of $12.5c$, and the relation $\delta_{\text{min}} = \sqrt{1 + \beta_{\text{app}}^2}$. This combined with the equation

$$\theta = \arctan \frac{2\beta_{\text{app}}}{\beta_{\text{app}}^2 + \delta^2 - 1}, \quad (5.13)$$

yields $\theta \leq 4.6^\circ$. Using the variability time scale argument and the derived values of δ_{var} from above, the values θ_{var} for each component are obtained, which together have a median value of $\theta = 3.8^\circ$, consistent with the afore determined upper limit. Pushkarev et al. (2009) obtained a slightly larger value of $\theta = 5.1^\circ$, which was determined by combining the component speeds at 15 GHz and variability Doppler factors derived from single-dish observations at 37 GHz. Earlier, Jorstad et al. (2005) obtained a smaller viewing angle of $2.7^\circ \pm 0.9^\circ$ using VLBI data at 43.2 GHz alone. In the remainder of the text, a conservative $\theta = 5^\circ$ is adopted.

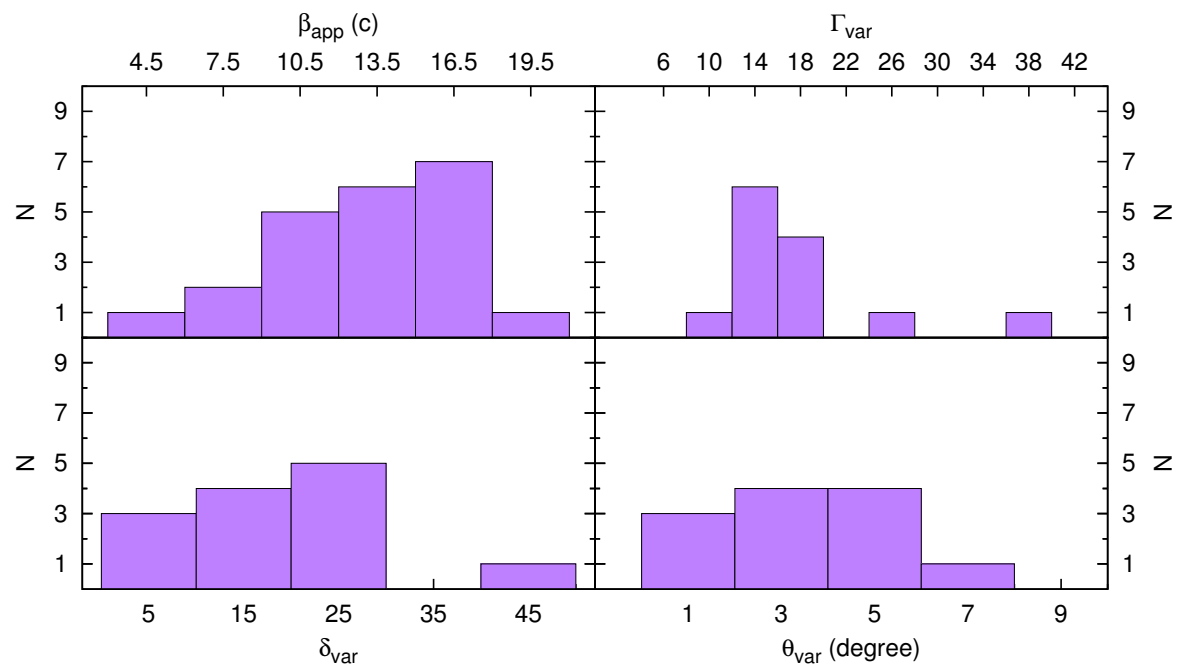


Figure 5.60: Distribution of kinematic parameters. The top left panel shows the distribution of the component speeds β_{app} , the top right panel the distribution of the Lorentz factors Γ_{var} , the bottom left panel the distribution of the Doppler factors δ_{var} , and the bottom right panel the distribution of the viewing angles θ_{var} . The median values for β_{app} , Γ_{var} , δ_{var} , and θ_{var} are 12.5 c, 14.1, 15.6, 3.8°.

Table 5.4: Measured and derived physical parameters for radio emission regions in the jet of 3C 345.

Comp.	$\langle\mu\rangle(\beta_{\text{app}})$	$\langle\Phi\rangle$	τ_e	Δt_{var}	δ_{var}	Γ_{var}	Θ_{var}	α_{app}	α_{int}
C1	0.17 ± 0.30 (5.9)	-27 ± 13	-	-	-	-	-	49 ± 70	4.3 ± 4.3
C2	0.48 ± 0.25 (17)	-66 ± 10	1972.5	-	-	-	-	52.2 ± 8.4	4.5 ± 0.7
C3	0.47 ± 1.3 (16)	-70 ± 45	1975.3	1.67 ± 0.33	$26.1^{+5.5}_{-7.1}$	$17.8^{+45}_{-6.6}$	$2.0^{+0.27}_{-2.0}$	56.0 ± 5.2	4.9 ± 0.5
C3a	0.50 ± 0.49 (17)	-65 ± 21	1977.9	2.1 ± 2.0	29^{+12}_{-29}	$17.1^{+20}_{-8.3}$	$3.02^{+0.55}_{-3.02}$	46 ± 17	4.0 ± 1.5
C4	0.46 ± 0.34 (16)	-64 ± 13	1980.1	-	-	-	-	48.9 ± 4.4	4.3 ± 0.4
C5	0.38 ± 0.22 (13)	-70.5 ± 5.9	1983.0	2.37 ± 0.66	$7.4^{+3.8}_{-2.9}$	16^{+11}_{-12}	$6.8^{+0.97}_{-3.0}$	46.4 ± 3.8	4.3 ± 0.1
C6	0.35 ± 0.26 (12)	-83 ± 13	1988.7	3.27 ± 0.44	$14.8^{+4.7}_{-4.2}$	$12.4^{+6.5}_{-6.0}$	$3.8^{+0.8}_{-2.6}$	25.9 ± 7.4	2.3 ± 0.6
C7 ₂₀₀₄	0.33 ± 0.13 (11)	-93.41 ± 0.58	-	-	-	-	-	29.7 ± 2.0	2.6 ± 0.2
C7 ₂₀₀₉	0.76 ± 0.37 (26)	-41 ± 15	-	-	-	-	-	-	-
C8	0.379 ± 0.078 (13)	-82.6 ± 3.9	1994.9	1.12 ± 0.15	$13.2^{+2.3}_{-2.5}$	13.1 ± 2.7	4.37 ± 0.81	37.6 ± 3.0	3.3 ± 0.3
C9	0.381 ± 0.034 (13)	-88.6 ± 1.8	1997.0	0.61 ± 0.18	$20.3^{+8.4}_{-7.1}$	$14.1^{+2.4}_{-1.4}$	$2.8^{+1.3}_{-1.2}$	21.2 ± 1.6	1.8 ± 0.1
C10	0.347 ± 0.039 (12)	-90.73 ± 0.55	1998.1	1.09 ± 0.72	$15.6^{+8.2}_{-10}$	$12.0^{+2.4}_{-1.1}$	$4.7^{+2.0}_{-1.8}$	38.2 ± 1.7	3.3 ± 0.1
C11	0.49 ± 0.12 (17)	-89.46 ± 0.82	1998.9	0.314 ± 0.077	45^{+13}_{-12}	$25^{+6.0}_{-4.5}$	$0.89^{+0.41}_{-0.44}$	34.5 ± 5.0	3.0 ± 0.1
C12	0.345 ± 0.033 (12)	-97.22 ± 0.98	1999.2	0.128 ± 0.023	-	-	-	17.7 ± 1.9	1.5 ± 0.2
C13	0.307 ± 0.051 (11)	-86.1 ± 1.8	1999.3	0.74 ± 0.22	$24.8^{+7.7}_{-7.9}$	$14.1^{+2.7}_{-2.6}$	$1.84^{+0.84}_{-0.83}$	36.9 ± 4.1	3.2 ± 0.4
C14	0.28 ± 0.11 (10)	-89.4 ± 2.8	2002.0	1.14 ± 0.57	-	-	-	39.6 ± 3.4	3.5 ± 0.3
C15	0.435 ± 0.039 (15)	-92.97 ± 0.49	2003.0	0.277 ± 0.070	$28.2^{+8.3}_{-7.3}$	$17.8^{+2.4}_{-2.2}$	$1.78^{0.61}_{-0.67}$	34.0 ± 3.9	3.0 ± 0.3
C15a	0.272 ± 0.050 (9.4)	-86.9 ± 1.4	2003.3	0.061 ± 0.012	-	-	-	46.5 ± 5.7	4.1 ± 0.5
C16	0.272 ± 0.037 (9.4)	-89.11 ± 0.30	2003.9	1.86 ± 0.68	$4.3^{+2.4}_{-2.2}$	$13.2^{+6.0}_{-4.7}$	$10.2^{+1.7}_{-1.5}$	51.3 ± 7.2	4.5 ± 0.6
C17	0.431 ± 0.068 (15)	-93.3 ± 1.1	2007.2	0.490 ± 0.049	-	-	-	44.8 ± 9.2	3.9 ± 0.8
C18	0.259 ± 0.015 (8.9)	-94.28 ± 0.36	2007.5	0.651 ± 0.077	-	-	-	41 ± 13	3.6 ± 1.1
C19	0.232 ± 0.032 (8.0)	-97.16 ± 0.50	2008.5	0.430 ± 0.033	$12.0^{+2.5}_{-2.1}$	$8.7^{+1.1}_{-0.85}$	4.5 ± 1.2	42 ± 12	3.7 ± 1.0
C20	0.567 ± 0.058 (20)	-93.54 ± 0.42	2009.4	1.00 ± 0.82	$7.4^{+0.3}_{-4.5}$	39^{+16}_{-15}	$5.44^{+0.39}_{-0.75}$	73 ± 10	6.4 ± 0.9

Notes:

Comp. – Component label, C7₂₀₀₄ refers to the time period up to 2004.0 and C7₂₀₀₉ refers to the time period 2004–2009; $\langle\mu\rangle(\beta_{\text{app}})$ – apparent speed in mas year⁻¹ in the case of $\langle\mu\rangle$ and in units of β_{app} ; τ_e , Δt_{var} , δ , Γ , Θ – estimated ejection epoch, flux variability time scale, variability Doppler factor, variability Lorentz factor, and jet viewing angle to our line of sight in units of degrees; α_{app} , α_{int} – apparent and intrinsic (using $\theta = 5^\circ$) jet opening angles in degrees.

The intrinsic component speeds β , described in Section 2.4, are now investigated. Components showing little observed apparent acceleration, such as C2, C8, C9, and C10 are well represented by a constant viewing angle, and their values of Γ are relatively constant at a value of ~ 11 . However, for most of the other components a dramatic increase in Γ , as shown in Figure 5.61, is required to reproduce the observed motion, which in some cases is not even possible to be represented beyond a certain distance, like in the case of C3, C3a, C11 and C17, because the values leave the parameter space beyond which no valid solutions are found. This parameter space is described by,

$$0 \leq \sin \theta \leq \frac{2\beta_{\text{app}}}{1 + \beta_{\text{app}}^2}. \quad (5.14)$$

The possible values of a constant θ for each of the components is listed in Table 5.5, calculated using the average component speeds. Note, for accelerating components, the maximum speed needs to be used to determine the limit of θ . The required changes of the Lorentz factors in about half of the tested cases are too big to be deemed physical, therefore a scenario with a purely constant θ is rejected.

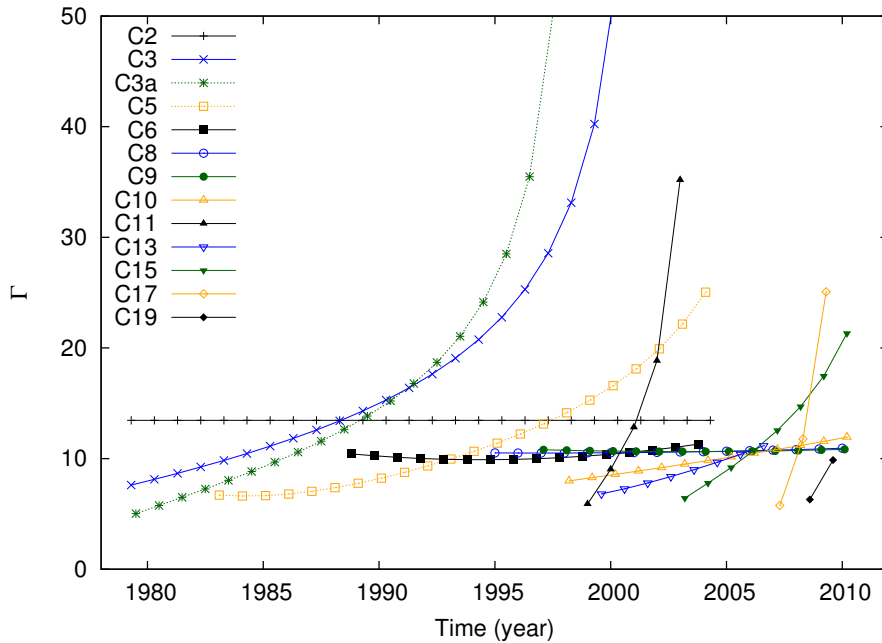


Figure 5.61: Evolution of the Lorentz factors Γ for select components required to represent the observed apparent motion described by the fitted trajectories in Section 5.2, assuming a constant viewing angle $\theta = 5^\circ$. The calculations are ended when the limits listed in Table 5.5 are reached.

A second case to investigate is the possibility of a curved jet, which seems more likely based on what is observed. The large angle solution fails to explain subluminal speeds and the rapid changes of component trajectories observed in the cases of C8, C9, or C10. For the remainder of this discussion the “small” angle solution is preferred and applied as described in Section 2.4.

In the case of a constant Lorentz factor, the observed curvature in the component motions is obtained by time variability of the viewing angle θ . However, similar to the $\theta = \text{const}$ case the parameter space of Γ is limited by the inequality,

$$\Gamma \geq \sqrt{1 + \beta_{\text{app}}^2}, \quad (5.15)$$

in order to be able to describe the observed trajectories. The limits of Γ for each component investigated are listed in Table 5.5 as well.

Table 5.5: Limits of constant component values.

Comp.	$\theta = \text{const.}$	$\Gamma = \text{const.}$
C2	$0 \leq \theta \leq 6.7^\circ$	$\Gamma \geq 17.0$
C3	$0 \leq \theta \leq 4.5^\circ$	$\Gamma \geq 25.5$
C3a	$0 \leq \theta \leq 3.8^\circ$	$\Gamma \geq 30.3$
C5	$0 \leq \theta \leq 4.7^\circ$	$\Gamma \geq 24.5$
C6	$0 \leq \theta \leq 7.9^\circ$	$\Gamma \geq 14.5$
C8	$0 \leq \theta \leq 8.1^\circ$	$\Gamma \geq 14.1$
C9	$0 \leq \theta \leq 8.5^\circ$	$\Gamma \geq 13.5$
C10	$0 \leq \theta \leq 8.1^\circ$	$\Gamma \geq 14.1$
C11	$0 \leq \theta \leq 5.5^\circ$	$\Gamma \geq 20.7$
C13	$0 \leq \theta \leq 8.5^\circ$	$\Gamma \geq 13.5$
C15	$0 \leq \theta \leq 4.0^\circ$	$\Gamma \geq 28.6$
C17	$0 \leq \theta \leq 2.7^\circ$	$\Gamma \geq 42.4$
C19	$0 \leq \theta \leq 4.8^\circ$	$\Gamma \geq 23.8$

Notes: The limits of θ and Γ are calculated using the maximum speed reached by the end of the monitoring period.

The observed Lorentz factors Γ_{obs} , determined through variability time scales (see Figure 5.60) mainly fall within the range of $12 \leq \Gamma_{\text{obs}} \leq 20$, comparing these with the limits listed in Table 5.5, the required Lorentz factors are of course much higher than those obtained from average kinematics, since the largest β_{app} is used here. If a constant Γ , which is similar for all components were used, the Lorentz factor would be required to have at least a value of 42.4, as determined for C17. One could split the components in two general categories, fast components with a minimum $\Gamma = 42.4$ (C3, C3a, C5, C11, C15, C17, C19) and slow ones with a $\Gamma = 17.0$ (C2, C6, C8, C9, C10, C13). The evolution of Γ , δ , θ , and the radial distance in the source frame, are plotted in Figure 5.62 for both the fast and slow component cases. The fast component case is difficult to imagine, having such high component speeds, which lead to extremely large distances traveled in the jet frame, almost out to the kpc scales. Also the viewing angles need to be very small $< 0.5^\circ$ in order to explain the observed trajectories. In the case of the slow components, the results are more realistic, with reasonable distances traveled, but a still rather small viewing angle of $0.5 - 1.6^\circ$ needed. It is also difficult to imagine to have features with this large difference in Lorentz factors, which would in the end produce a chaotic appearance of the jet in the source rest frame. On the other hand it is also clear that Lorentz factors do not appear to be the same from one feature to another.

Obviously, the scenario of a constant Lorentz factor does not yield satisfying results as well. One can imagine a combination of both varying opening angles paired with an accelerating flow, thus increasing Lorentz factor. This implies that significant acceleration of either the bulk flow or the shocked emission region is also present at larger scales, not only close to the core. As proposed by Lobanov (1996) the minimal jet kinetic power is used, as expressed by the minimum allowed Lorentz factor, shown in

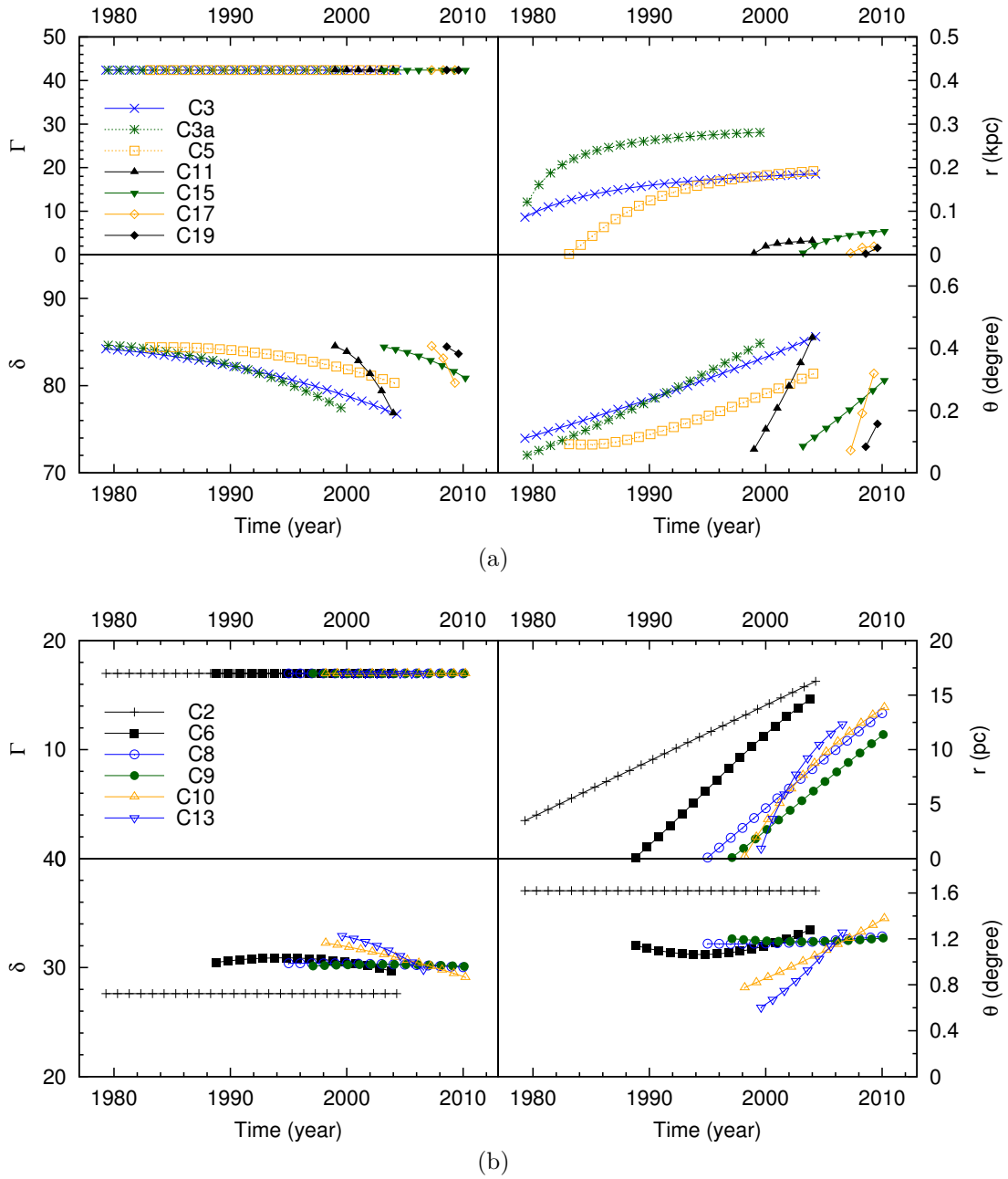


Figure 5.62: Evolution of jet kinematic parameters for the case of $\Gamma = \text{const}$ for fast (a) and slow (b) jet components. The four panels of each plot show, the Lorentz factor Γ (top left), the distance travelled in the jet frame (top right), the Doppler factor δ (bottom left), and the viewing angle θ (bottom right).

Equation 5.15. The resulting evolution for Γ , δ , r in the jet frame, and θ are shown in Figure 5.63. The component tracks in the jet rest frame are following the same ordered evolution. The required change in Γ to obtain such an evolution is relatively large, but remains in a plausible range of 4 – 24, whereas especially for the fast components the viewing angle is initially at a relatively large value and decreases rapidly, whereas most of the slow features show slow, smooth changes around a viewing angle of 5° . Altogether it appears that the combination of acceleration and viewing angle change produces the best results and provides a satisfactory interpretation of the observed component motion. The case of a linear increase of $\Gamma(r)$ was also considered in Lobanov & Zensus (1996, 1999); Lobanov & Roland (2005) and magnetohydrodynamic acceleration was applied to 3C 345 by Vlahakis & Königl (2004).

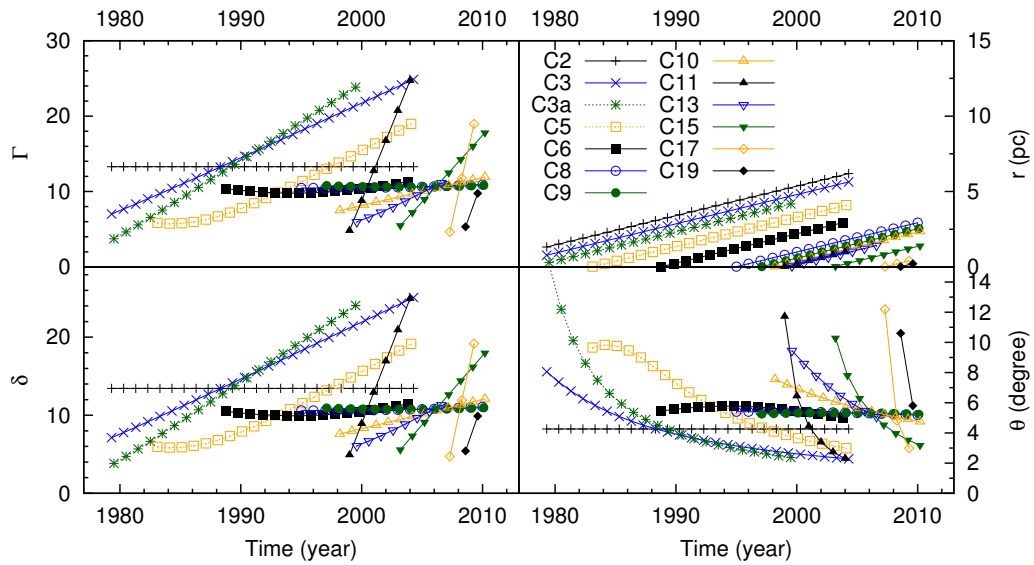


Figure 5.63: Evolution of jet kinematic parameters for the case of $\Gamma_{\min}(t)$, i.e. variable Γ and θ . The four panels of each plot show, the Lorentz factor Γ (top left), the distance traveled in the jet frame (top right), the Doppler factor δ (bottom left), and the viewing angle θ (bottom right).

5.4.3 Magnetic Field and Distance to the Central Engine

In the beginning of this chapter the frequency dependent core-shift was investigated, which can be used to determine the magnetic field at the VLBI core and the distance of the core to the central engine (also see Section 2.3). In this and the previous sections an average core-shift measure of $\Omega_{r\nu} = (23.80 \pm 0.94) \text{ pc GHz}$, a jet opening angle (within 4 mas of the core) of $\alpha_{\text{int}} = (2.95 \pm 0.09)^\circ$, a median Doppler factor of $\delta = 15.6$ and viewing angle $\theta = 5^\circ$ are obtained. It was also shown that $k_r = 1$ thus the core-shift relative to 15.4 GHz can be determined using Equation 5.3. With these values, the magnetic field and distance to the central engine are calculated for each of the observing frequencies. The resulting values listed in Table 5.6 are within a reasonable range and are comparable with those previously derived by Lobanov (1998b) for 22.2 GHz.

Table 5.6: Derived estimates for the core magnetic field and distance to the central engine.

Freq. [GHz]	B_{core} [G]	r_{core} [pc]
1.6	0.011	171
5.0	0.035	55
8.4	0.058	33
15.4	0.11	18
22.2	0.15	12
43.2	0.30	6.3
86.0	0.60	3.2

5.5 Summary and Conclusions

The dataset presented here is a result of the efforts of many scientists over the past three decades that were monitoring the evolution of the parsec-scale jet in 3C 345 using VLBI. In the course of this thesis the dataset was systematically analyzed forming an unprecedented database of jet kinematics for a single object.

A significant variation of the core-shift is observed, with a long-term trend that is attributed to a change in the viewing angle and in the brightness of the VLBI core, corresponding to additional core-shift variability introduced during different activity states of the jet. The average core-shift is consistent with a $k_r = 1$, the equipartition case between the jet particle and magnetic field energy densities.

The pattern of motion of components propagating in the jet apparent superluminal speeds is well repeated between subsequent features. The jet opening angles determined from the size evolution of the components is $\sim 3^\circ$ in the jet rest frame, with even smaller values obtained if the jet cross-section profile is used instead of Gaussian components (Pushkarev et al. 2009). A fundamentally different generation of component motion is observed before 1997, suspecting that what is observed as the radio jet is only a subset of the true flow, ie. the inner fast structure of the total jet. A different generation of jet motion could be explained by fundamental changes of the injection pattern at the base of the jet.

These observations require the jet to be a highly collimated and stable relativistic outflow up to distances of ~ 750 pc (deprojected with $\theta = 5^\circ$) and possibly going beyond. The observed also supports the proposed and simulated theoretical scenario of a fast spine, slow sheath jet flow structure (eg. Hardee et al. 2007). Such a jet structure, under the right conditions, at parsec scales leads to the formation of Kelvin-Helmholtz instabilities (eg. Perucho et al. 2006), which would perturb the jet flow. In fact looking at small scale changes in component motion of the best sampled features, an oscillating standing pattern is observed both in the motion and in the size evolution. The pattern resembles small changes in the viewing angle and a rotation of the internal structure of the jet.

The the jet opening angle seems to vary along the jet and shows an apparent decrease

with the distance from the VLBI core up to the point at which the large scale motion of the jet turns northward, at a distance of ~ 300 pc (deprojected) from core, after which the jet opening angle increases again slightly. This could be interpreted as a recollimation of the jet at very large distances. Conversely, if the jet opening angle were constant, the viewing angle of the jet would be required to decrease and increase again, a possibly more realistic scenario than recollimation at hundreds of pc.

Physical interpretation of the observed kinematics supports the afore mentioned interpretation of change of the viewing angle and intrinsic acceleration of the flow. Neither an accelerating flow moving at a constant viewing angle or a constant speed in a curved jet with a changing viewing angle are compatible with the observed trajectories. Acceleration up to hundreds of pc for most of the components and a change of the viewing angle are required to reproduce the observed component motions without producing extreme results.

The magnetic field strength at the VLBI core is calculated combining the collected knowledge from the kinematics and the core-shifts. This results in the magnetic field values ranging from a few mG to a few hundreds of mG at distances between 171 to 3 pc from the central engine, corresponding to the observing frequencies 1.6 – 86.0 GHz.

The here presented results coming of this dataset are just a small fraction of what it might be able to provide in the future. In particular a spectral analysis, analysis of polarization or determination of evolution of ridge lines from the observed brightness distributions could provide further insights into the physics of the jet. Only the surface has been scratched with this dataset with further new results expected, possibly even ground breaking. A deeper investigation of absolute motions in the jet, in particular core-shift variabilities or jumps in the trajectories of features could provide a systematic phase-referenced multi-frequency VLBI monitoring. However, such a monitoring would require a sustained time period going beyond the scope of a single PhD thesis and could be envisioned as embedded in a long-term jet monitoring program of multiple sources like the MOJAVE survey.

First Identification of Gamma-ray Emission from 3C 345

On June 11th, 2008, the *Fermi* Gamma-ray Space Telescope (short *Fermi*) was launched, equipped with the Large Area Telescope (LAT) instrument (Atwood et al. 2009) providing continuous all-sky monitoring of γ -ray emission as a default mode of operation. It is one of *Fermi*'s major science goals related to AGN to perform more individual source studies, trying to understand what makes some blazars brighter in γ -rays than others and in particular to answer the question why is that 3C 345 was not detected by EGRET? The LAT, compared with EGRET, has an improved sensitivity by a factor of ~ 25 and an improved point-source localization. After 20 months of LAT operation within the region around 3C 345, a localization improvement (comparing radii of 95% error circles) of a factor of ~ 14 was reached compared to EGRET. These improvements provided a new opportunity to probe 3C 345 for γ -ray emission above 100 MeV.

The three-month bright *Fermi* source list (0FGL) for the dataset collected between August and October 2008 reported a γ -ray source (0FGL J1641.4+3939) near the position of 3C 345. It was then associated with the quasar B3 1640+396 (CLASS J1641+3935) at low confidence (Abdo et al. 2009b). The bright 0FGL source was listed in the first *Fermi*-LAT source catalog (1FGL) as 1FGL J1642.5+3947 (Abdo et al. 2010a), further constraining its localization. An association with 3C 345 was still not possible with high confidence based on *Fermi*-LAT data alone, nevertheless, 1FGL J1642.5+3947 was listed in the catalog as being affiliated with its most likely counterpart 3C 345 (Abdo et al. 2010b).

In October 2009 a GeV flare was detected from the vicinity of 0FGL J1641.4+3939 (Reyes & Cheung 2009). Simultaneously, the GASP-WEBT collaboration reported on increased optical and radio activity of 3C 345 (Larionov et al. 2009). This event triggered additional observations at different frequencies, which made it possible to establish an identification through correlated multi-wavelength activity.

Table 6.1: Localization summary of different energy cuts for single a point source 1FGL J1642.5+3947.

Energy (GeV)	Flux (10^{-7} ph cm $^{-2}$ s $^{-1}$)	Index	TS	R.A. (degree)	Dec. (degree)	r68 (degree)
0.1–300	1.797 ± 0.079	2.448 ± 0.031	2854	250.6	39.8077	0.0234
0.1–100	1.774 ± 0.079	2.442 ± 0.031	2821	250.6	39.8077	0.0234
0.3–10	0.365 ± 0.014	2.464 ± 0.048	2194	250.589	39.8141	0.0270
1–10	0.0644 ± 0.0040	2.68 ± 0.12	1036	250.571	39.8049	0.0338
1–100	0.0658 ± 0.0040	2.68 ± 0.10	1086	250.595	39.7969	0.0293
0.3–100	0.368 ± 0.014	2.484 ± 0.044	2240	250.606	39.8034	0.0251

Notes:

Energy – energy range the power-law was fitted to; **Flux** – integrated γ -ray flux for the particular energy range; **Index** – Power-law spectral index Γ ; **TS** – test statistics; **R.A.** – right ascension coordinate of the localization; **Dec.** – declination coordinate of the localization; **r68** – 68% confidence circle around the position of the localization.

In this chapter, 20 months of monitoring observations by *Fermi* LAT of the region around 3C 345, NRAO 512 and B3 1640+396 are presented, as well as radio, optical, UV, and X-ray observations of these sources. The observations and data reduction methods applied to obtain calibrated datasets for the subsequent analysis are described in Chapter 4. In Section 6.1 the results of the *Fermi*-LAT observations, in particular the localization of γ -ray emitters in the field of interest are discussed. The short and long-term variability of γ -ray emission from 3C 345 and NRAO 512 are presented in Sections 6.2 and 6.3. The identification of γ -ray counterparts through multi-wavelength observations and through multi-wavelength variability are made in Sections 6.4 and 6.5. Section 6.6 discusses and summarizes the presented results in this chapter.

6.1 Localization of Gamma-ray emission

An unbinned spectral likelihood analysis was performed using integrated 20-month *Fermi*-LAT monitoring data in the energy range of 0.1–100 GeV. This energy range was chosen after a series of different energy cuts were compared, to minimize the error on the localization, see Table 6.1. In the 1FGL catalog, γ -ray sources are typically localized with a 95% position error radius of $0.02^\circ - 0.07^\circ$ for sources with $TS \approx 1000$, but $0.06^\circ - 0.5^\circ$ for $TS \approx 30$ (Abdo et al. 2010a). In cases of faint γ -ray emitters it is difficult to obtain well-constrained localizations to make statistically significant associations, even more so for two faint γ -ray emitters in close vicinity of each other.

A single point-source, 1FGL J1642.5+3947, is listed in the 1FGL catalog around the analyzed region. Assuming a single point-source, the best-fit position using the 20-month LAT dataset is R.A. $16^{\text{h}}42^{\text{m}}24^{\text{s}}$, Dec. $+39^\circ48'27''$, with a 95% error circle radius of 0.037° . This procedure also provided the following characteristic source parameters: photon index¹: $\Gamma = 2.44 \pm 0.03$, integrated flux: $(1.78 \pm 0.08) \cdot 10^{-7}$ ph cm $^{-2}$ s $^{-1}$, TS value of 2825. The estimated systematic uncertainty of the integrated flux is 10% at

¹The photon spectral index Γ is defined as $N(E) \propto E^{-\Gamma}$, where $N(E)$ is the γ -ray photon flux as a function of energy E .

100 MeV, 5% at 500 MeV and 20% at 10 GeV. After 20 months of data the localized position is shifted by 0.042° from its 1FGL position toward NRAO 512, separated by 0.13° (east) from 3C 345 and by 0.48° (west) from NRAO 512. This suggested a significant contribution of excess photons from the direction west of 3C 345.

The unbinned spectral likelihood analysis was complemented by a `pointlike` analysis, similar to the method applied to determine positions and error ellipses for the 1FGL catalog. The approach of `pointlike` is described in Section 4.2 of Abdo et al. (2010a). This analysis revealed that a significant number of excess γ -ray photons were detected from the vicinity of NRAO 512 after November 2009 (15 month). A fit with two point-source models in which source positions were not fixed, representing contributions by 3C 345 and NRAO 512, yielded significant detections for the 20-month period (see Table 6.2). Figure 6.1 shows the radio positions of the three candidate sources together with the EGRET and 1FGL localizations, as well as the improved localizations for the two γ -ray sources found in the 20-month dataset. B3 1640+396 is $19.3'$ and $16.5'$ separated from the respective localizations of 3C 345 and NRAO 512. Both γ -ray counterparts of 3C 345 and NRAO 512 now coincide with their respective radio positions (within the 95% error ellipse). This suggests that both sources may be γ -ray emitters. This is firmly established in Section 6.4 using the broadband temporal characteristics of the sources. There is no evidence for significant γ -ray emission from the third candidate source, B3 1640+396. The results of `pointlike` were cross-checked with an iterative use of `gtlike` and `gtfindsrc`, which confirm the `pointlike` results within errors, see Table 6.2. A 2σ upper limit was calculated for B3 1640+396 by fixing each of the three candidate sources to their radio positions and assuming a $\Gamma = 2.3$ spectral shape for B3 1640+396 and using the previously fitted Γ for 3C 345 and NRAO 512. This resulted in a 20-month upper limit for the integrated flux of $7.4 \cdot 10^{-9}$ ph cm $^{-2}$ s $^{-1}$. Figure 6.2 shows the observed binned spectra of the two sources together with their respective power-law fits. The `pointlike` best-fit parameters are listed in Table 6.2. In Figure 6.3 the respective 30-day binned γ -ray light curves of the two localized sources are shown and are discussed below in more detail.

6.2 Long-term Gamma-ray Variability

To study the long-term variability, light curves were produced for the γ -ray counterparts associated with 3C 345 and NRAO 512 with 30-day binning. The 30-day binned light curve is shown in Figure 6.3. For most of the data points NRAO 512 did not reach above a TS of 25, except for the last five months of the 20-month period. This led to the conclusion that NRAO 512 did not produce a significant excess of γ -ray emission over the local background during the first 15 months of LAT operation; thus it did not appear in the 1FGL catalog. After 15 months the amount of excess photons from the vicinity of NRAO 512 slowly increased, making a detection over the integrated 20-month period possible. The average *Fermi*-LAT flux for the first 15-months of the monitoring period was $(0.42 \pm 0.07) \cdot 10^{-7}$ ph cm $^{-2}$ s $^{-1}$ compared to $(1.1 \pm 0.1) \cdot 10^{-7}$ ph cm $^{-2}$ s $^{-1}$ for the last quarter of the monitoring period (months 15-20).

The observed γ -ray flux values reveal variability on timescales from days to months. To quantify this variability, the variability index (V) as defined through the χ^2 distribution (see Abdo et al. 2010a) was determined. It is computed from the 30-day

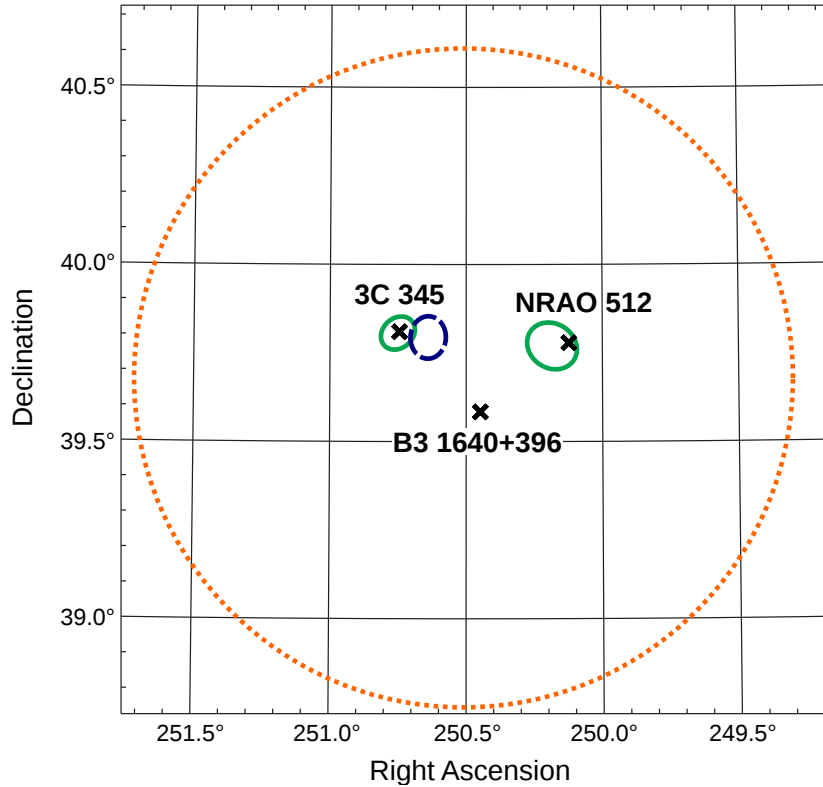


Figure 6.1: γ -ray counterpart localizations together with the positions of the radio counterparts of the three candidate sources. Crosses mark the radio positions of 3C 345, NRAO 512 and B3 1640+396. The large dotted orange circle denotes the 95% confidence error localization of EGR J1642+3940 (Casandjian & Grenier 2008). The dashed blue ellipse denotes the 95% confidence error localization of 1FGL J1642.5+3947 (Abdo et al. 2010a). The two solid green ellipses denote the 95% confidence error localization of 3C 345 and NRAO 512 presented here. The confusing source Mrk 501 is 2.5° east (left) and 4C +38.41 is 2.1° southwest of the field center.

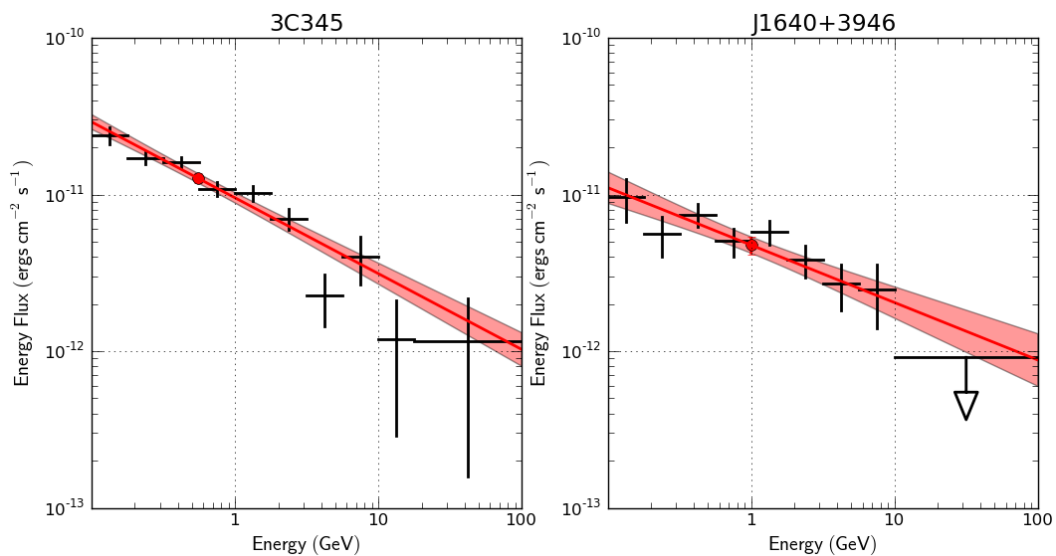


Figure 6.2: Twenty-month γ -ray spectra of 3C 345 and NRAO 512. The red curve represents the obtained respective average power-law fits. The red dots correspond to the pivot energies listed in Table 6.2.

Table 6.2: The unbinned spectral likelihood results for the point-source localizations and spectra of 3C 345 and NRAO 512.

	3C 345	NRAO 512
R.A. (J2000)	16 ^h 43 ^m 0.24 ^s	16 ^h 40 ^m 44.4 ^s
Dec. (J2000)	+39°48'22.7"	+39°46'12.0"
Δr	0.35'	2.9'
a (95%)	0.0490°	0.0735°
b (95%)	0.0442°	0.0626°
Φ	41.6	-33.2
Γ (pl)	2.49 \pm 0.02	2.37 \pm 0.04
Γ (gt)	2.45 \pm 0.05	2.41 \pm 0.08
Flux (pl)	1.22 \pm 0.10	0.51 \pm 0.23
Flux (gt)	1.13 \pm 0.13	0.67 \pm 0.13
Pivot Energy	949	1598
TS	1076	246

Notes:

R.A./Dec. – Right ascension/declination of the γ -ray localization; Δr – distance to respective radio source position; a (95%) – major axis of 95% localization error ellipse; b (95%) – minor axis of 95% localization error ellipse; Φ – Rotation angle of the error ellipse East of North (degrees); Γ – spectral index of power-law fit, (pl) are the values obtained from the `pointlike` fit and (gt) are values from the `gtlike` fit; Flux – 20-month average flux (0.1-100 GeV) determined from the power-law spectral fit in units of 10^{-7} ph cm $^{-2}$ s $^{-1}$; Pivot Energy – in MeV, this is the energy for which there is no correlation between the flux or normalization and spectral index uncertainties; TS – Likelihood test statistic value.

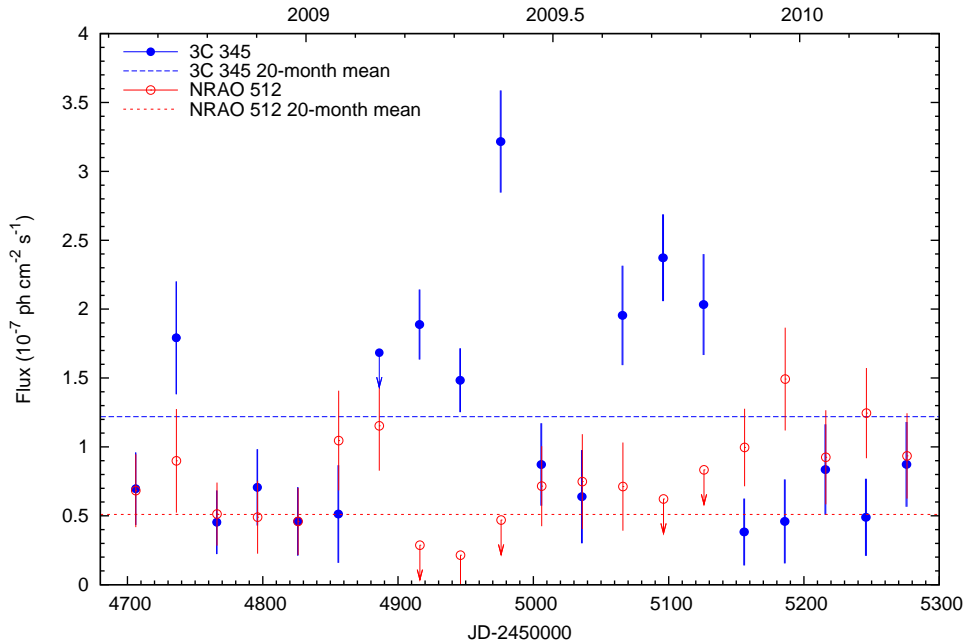


Figure 6.3: γ -ray light curves of 3C 345 and NRAO 512 for the first 20 months of *Fermi*-LAT monitoring, obtained through fitting two point-source model components with power-law spectra to the region of interest placed at the respective counterpart positions. Values were determined from integrating observations over 30 days within an energy range of 0.1 – 300 GeV. Blue filled circles are values obtained for 3C 345, red open circles are values for NRAO 512. Values with downward arrows represent 2σ upper limits shown in place of detections with low significance (TS<5). The dashed lines plot the respective 20-month average γ -ray source flux. Errors are statistical only.

integrated light curve data shown in Figure 6.3. Whenever $TS < 5$ the 2σ upper limit was computed and its error estimate for that interval was replaced with half the difference between that upper limit and its value determined through the unbinned spectral likelihood analysis. In the absence of variability, V is expected to follow a χ^2 distribution with 19 ($= N_{\text{int}} - 1$) degrees of freedom. At the 99% confidence level the light curve is significantly different from a flat one if $V > 36.2$. For 3C 345 a V of 115.3 was obtained, for NRAO 512 it was 37.7. Both sources are variable according to the 99% confidence interval with higher variability observed from 3C 345.

In the shorter binned light curve of NRAO 512, $\sim 63\%$ of the derived values had a $TS < 5$ (i.e. non-detections) compared to $\sim 48\%$ for 3C 345. Because NRAO 512 did not show a significant flux for most of the time on integrations of five days or less and with the observation that the flux of 3C 345 dominates, the model component of NRAO 512 was removed and light curves were produced with a single component fixed at the position of the γ -ray localization of 3C 345 listed in Table 6.2. This reduced the amount of noise in the light curve of 3C 345 and the number of values with a $TS < 5$ was only 14%. The same results were obtained if instead placing the γ -ray component at the radio position of 3C 345.

6.3 Short-term Gamma-ray Variability

For the remainder of this chapter the discussion is based on light curves produced with a single point-source model component. The five-day binned light curve of 3C 345 is shown in Figure 6.4 together with observations at other wavelengths.

To investigate shorter term variability in the observed γ -ray emission of 3C 345, several prominent light curve “flare events” were identified and parameters such as rise time, fall time and time of the peak were extracted using the five-day and two-day integrated light curves. These parameters can be used to constrain the size of emission regions and cooling-times. Table 6.3 summarizes these results, listing characteristic parameters for all γ -ray flare events for which the peak had a significance of $TS > 25$ in the two-day light curve. This corresponded to a flux greater than $3.0 \cdot 10^{-7}$ ph cm $^{-2}$ s $^{-1}$. The time of onset and end of an individual flare event was determined through a change in the sign of the gradient at the rising and declining slope of the light curve around the peak of a flare event.

Three dominant flare events of at least $5.0 \cdot 10^{-7}$ ph cm $^{-2}$ s $^{-1}$ and a significance of above 7σ were observed on two-day time scales, one during 2008 and two during 2009. They were labeled with I, II and III in Figure 6.4. Several weaker flares were identified and labeled with numbers from 1 to 6. On average, the flares had a duration of 38 days a slightly faster rise than fall time and an average peak flux of $(5.0 \pm 0.5) \cdot 10^{-7}$ ph cm $^{-2}$ s $^{-1}$ (two-day integrations centered on the peak).

6.4 Identification of Gamma-ray Counterpart

Following the γ -ray outburst on October 2nd, 2009, *Swift* observations were triggered on the candidate sources 3C 345, NRAO 512 and B3 1640+396. X-ray spectra and

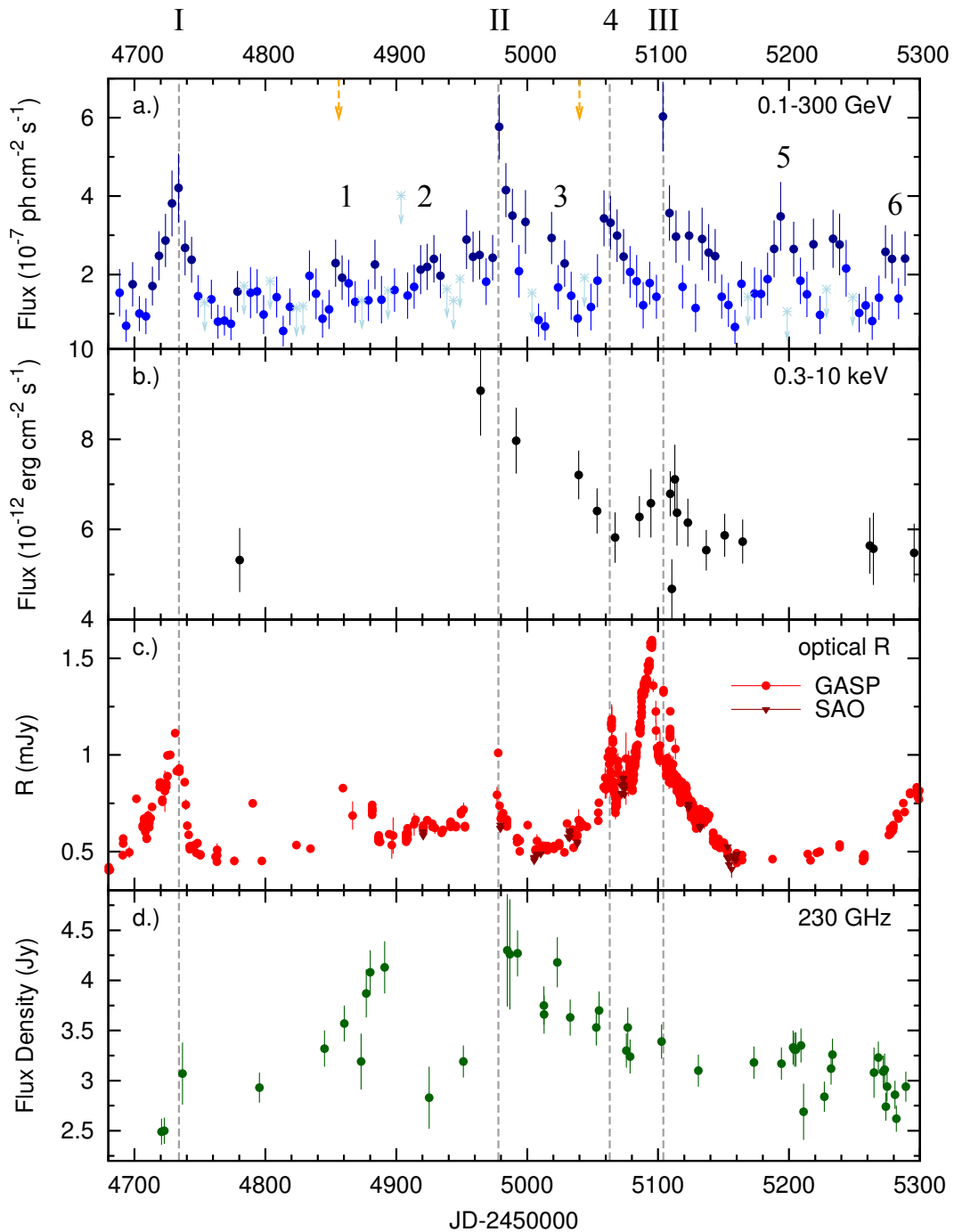


Figure 6.4: Multi-wavelength light curves of 3C 345 for the 20-month period discussed here, from top to bottom for: a) γ rays observed by *Fermi* LAT between 0.1 and 300 GeV, values (filled circles) are five-day integrated, 2σ upper limits for five-day integrations are shown as light-blue crosses with downward arrows where $TS < 5$. Dark-blue filled circles have a $TS > 25$, the others are in the range $5 < TS \leq 25$. In contrast to Figure 6.3, the γ -ray emission was fitted by a single power-law component placed at the position of 3C 345. b) X-rays observed by *Swift* XRT between 0.3 and 10 keV. c) optical (R-band) observations performed by GASP and SAO. d) millimeter radio observations by the SMA at 230 GHz. The two orange downward arrows on top indicate the observation epoch for which a new feature was detected in the pc-scale radio jet of 3C 345, see Section 6.4 and Schinzel et al. (2010). Three dominant flare events of high significance observed on two-day time scales were labeled with I, II, and III. Several weaker events were identified and labeled with numbers from 1 – 6.

Table 6.3: Characteristics of prominent γ -ray events during the first 20 months of the *Fermi*-LAT observations.

t_{peak} JD(†)	t_{start} JD(†)	t_{stop} JD(†)	Δt days	Δt_{rise} days	Δt_{fall} days	S_{γ}^{max} $10^{-7} \frac{\text{ph}}{\text{cm}^2 \text{s}}$	(*)
4734	4709	4754	45	25	20	5.5 ± 1.5	I
4856	4844	4874	30	12	18	3.6 ± 1.1	1
4916	4904	4944	40	12	28	4.0 ± 1.2	2
4978/4998	4969	5014	45	9	16	$5.7 \pm 1.3/5.4 \pm 1.5$	II
5020	5014	5044	30	6	24	4.5 ± 1.2	3
5056/5070	5044	5089	45	12	19	$4.4 \pm 1.4/4.5 \pm 1.2$	4
5104	5099	5119	20	5	15	9.1 ± 1.6	III
5194	5169	5214	45	25	20	4.7 ± 1.4	5
5278	5264			14		3.6 ± 1.1	6
Average values:			38	13	20	5.0 ± 0.5	

Notes: t_{peak} – in units of JD(†) = JD-2450000, peak value was obtained from the two-day integrated light curve, all values have an error of ± 1 day;

$t_{\text{start}}, t_{\text{stop}}$ – in units of JD(†) = JD-2450000, all values have an error of ± 3 days;

$\Delta t, \Delta t_{\text{rise}}, \Delta t_{\text{fall}}$ – in units of days, all values with error of ± 4 days;

S_{γ}^{max} – two-day integrated flux value of the γ -ray event peak value;

(*) Labels are split into two sub-categories according to their peak flux and significance of detection, denoted by Roman and Arab numbers, see Figure 6.4 for details.

optical magnitudes were obtained from these observations. A summary of relevant measurements is listed in Tables 6.4 and 6.5. The X-ray data was combined with dedicated bi-weekly *Swift* monitoring observations triggered in the course of this thesis work, pre-dating the October 2nd flare and are shown in Figure 6.4. The values and properties of all XRT observations are provided in Chapter 4.

The brightest source of the three candidates in X-ray as well as in optical is 3C 345. On January 26th, 2009, 3C 345 and B3 1640+396 were detected in the optical R-band at respective magnitudes of 16.48 ± 0.02 and 18.6 ± 0.1 . On October 8th, 2009, observations of 3C 345 and NRAO 512 showed respective optical U-band magnitudes of 16.45 ± 0.08 and 18.64 ± 0.04 . Both NRAO 512 and B3 1640+396 were a factor of 7-8 fainter than 3C 345 at optical wavelengths. At X-ray energies, as seen from Table 6.4, NRAO 512 and B3 1640+396 had similar fluxes, which were a factor of 8-9 fainter than 3C 345. Archival *Swift*-UVOT and XRT data from observations of NRAO 512 made in January 2007 have an average optical U magnitude of 18.0 ± 0.1 and an X-ray flux of $(8.3 \pm 2.3) \cdot 10^{-13} \text{ erg cm}^{-2} \text{ s}^{-1}$, which are consistent with the recently observed values. Quasi-simultaneous mm observations between October and December 2009 determined the fluxes of 3C 345, NRAO 512 and B3 1640+396 to be ~ 3.0 , ~ 0.4 and $\sim 0.1-0.3$ Jy. The respective flux ratios are consistent with the ones in the optical/UV and X-rays. The mm radio flux density of 3C 345 was at least a factor of 7 higher than for NRAO 512 and B3 1640+396.

No significant excess of γ -ray emission from NRAO 512 was observed during the first 15-months of the *Fermi*-LAT operation. At the end of 2009, NRAO 512 showed an increasing trend in its 15 GHz VLBI radio flux observed by the MOJAVE team (Lister

Table 6.4: *Swift*-XRT observations after the reported flare in October 2009 of the three candidate sources (3C 345, NRAO 512 and B3 1640+396).

Source	Obs. Date (*)	Exp.	Flux	Index
3C 345:	2009-10-04 (5109)	4.2	6.8 ± 0.5	1.68 ± 0.11
	2009-10-06 ^a (5111)	1.9	4.7 ± 0.7	1.66 ± 0.17
	2009-10-08 (5113)	2.1	7.1 ± 0.8	1.75 ± 0.16
	2009-10-09 (5114)	2.2	6.4 ± 0.7	1.62 ± 0.15
	2009-10-18 (5123)	3.9	6.2 ± 0.5	1.67 ± 0.12
	2009-11-01 (5137)	4.1	5.5 ± 0.5	1.77 ± 0.11
	2009-11-15 (5151)	4.0	5.9 ± 0.5	1.88 ± 0.11
	2009-11-29 (5165)	4.1	5.7 ± 0.5	1.71 ± 0.12
	2010-03-06/07 (5262/3)	2.6	5.6 ± 0.6	1.84 ± 0.15
	2010-03-09 ^a (5265)	1.4	5.6 ± 0.8	1.78 ± 0.18
	2010-04-09 ^a (5296)	2.0	5.5 ± 0.7	1.88 ± 0.16
	2010-08-18 (5427)	4.3	5.4 ± 0.5	1.54 ± 0.11
	NRAO 512:	2009-10-08 ^a (5113)	2.1	$0.6^{+0.3}_{-0.2}$
2009-10-15 ^a (5120)		2.1	0.5 ± 0.2	2.2 ± 0.6
2010-08-06/07 ^a (5415/6)		5.5	0.7 ± 0.1	2.0 ± 0.3
B3 1640+396:	2009-12-01 ^a (5167)	1.1	$0.7^{+0.4}_{-0.3}$	1.8 ± 0.7

Notes: Obs. Date (*) – Date of *Swift*-XRT observation (*=JD-2450000).

Exp. – *Swift*-XRT effective exposure time in ks.

Flux – Integrated unabsorbed photon flux 0.3-10 keV in units of 10^{-12} erg cm⁻² s⁻¹.

^a Cash statistic used for observations with less than 200 photons.

Table 6.5: Quasi-simultaneous optical observations of 3C 345, NRAO 512 and B3 1640+396 conducted by *Swift* UVOT and the 200-mm telescope of Tzec Maun observatory.

Source	Obs. Date (*)	Band	Magnitude
3C 345:	2009-01-26 (4858)	R	16.48 ± 0.02
	2009-02-13 (4876)	R	16.92 ± 0.03
	2009-10-08 (5113)	U	16.44 ± 0.06
	2009-10-08 (5113)	UVW1	16.28 ± 0.03
	2010-08-18 (5427)	UVW1	16.47 ± 0.02
NRAO 512:	2009-10-08 (5113)	U	18.61 ± 0.04
	2010-08-06 (5415)	U	17.71 ± 0.05
	2010-08-06 (5415)	UVW1	18.07 ± 0.02
B3 1640+396:	2009-01-26 (4858)	R	18.57 ± 0.13
	2009-02-13 (4876)	R	$> 18.6^\dagger$

Notes: Obs. Date (*) – Date of *Swift*-XRT observation (*=JD-2450000).

Band – Optical filter used for photometric observations

Magnitude – Observed optical magnitude in given filter band. The magnitudes are not corrected for Galactic extinction.

† no detection

et al. 2009a)². Indeed, the radio flux density reached a low activity level around May 2009 and more than doubled until about July 2010 with the mm-radio flux density reaching a peak value of over 0.6 Jy in August 2010. A similar trend was observed in optical emission. Within one year, the optical flux increased by a factor of ~ 2.2 (see Table 6.5). In X-rays a flux increase of at least 20-30% was observed, but because of the low statistics (less than 200 photons) it is difficult to compare the observations. An increased number of γ -ray photons was detected spatially consistent with NRAO 512 during the last quarter of the 20-month period. The excess is not high enough to affect the short-term bins of the light curve of 3C 345 significantly, however, as was shown in Section 6.1, the integrated 20-month dataset made it possible to detect a second point source west of 1FGL J1642.5+3947, which is consistent with the radio position of NRAO 512 (see Figure 6.1). Altogether this identifies NRAO 512 as a γ -ray source.

6.5 Multi-wavelength Variability

During 2009 nine optical observatories, introduced in Section 4.4, regularly monitored 3C 345, mainly as part of the GASP-WEBT program. This provided a densely sampled optical R-band light curve (Figure 6.4). Visual comparison of the γ -ray and optical light curves indicates a likely correspondence between at least four γ -ray/optical flare events: Flare I, II, 4 and III. With the addition of X-ray and mm-radio monitoring data, the following aspects are of particular interest:

1. A possible fast optical brightening of at least 0.3 mag with a duration of only a few days (Figure 6.4) was observed (JD 2454978), coincident with the peak of Flare II. Unfortunately, the optical monitoring had a gap between JD 2454953 and JD 2454977. At the same time the mm radio light curve showed a maximum of around 4.3 Jy. Moreover, a high X-ray flux was observed in the same period of the Flare II, followed by a decrease similar to what was observed in γ and radio bands. Even if the maximum X-ray flux was observed two weeks before Flare II, the γ -ray event lacks strictly simultaneous X-ray observations, thus we cannot exclude that a simultaneous X-ray flare was missed.
2. The broad optical flaring episode observed around September/October 2009 had a total duration of about five months, with shorter timescale sub-structures that correspond to activity variations observed also at γ - and X-rays. The peak in the optical was observed on September 19th, 2009 (JD 2455094), and had no similarity in profile with events at other wavelengths (see Figure 6.4).
3. Ten days after the peak of the optical light curve, the strong γ -ray Flare III was observed. The optical peak was followed by fast optical variability at a significant amplitude of 0.3–0.5 mag, with an elevated magnitude observed on September 29th on the same day as γ -ray Flare III.
4. Flares 1 and 3 can be related to the appearance of new features in the pc-scale radio jet of 3C 345 at 43 GHz (see Schinzel et al. 2010 and Chapter 7, Section 7.2 of this thesis).

²<http://www.physics.purdue.edu/MOJAVE/sourcepages/1638+398.shtml>

5. All but Flares 5 and 6 occur before the significant excess of γ -ray emission was observed near NRAO 512. However, at least for Flare 6, a correspondence in optical variability was found for 3C 345; unfortunately, a lack of multi-wavelength data around Flare 5 makes it impossible to identify it with either 3C 345 or NRAO 512.

To quantify the cross-correlation between light curves, a discrete correlation was calculated (DCF; Edelson & Krolik 1988) using the 20-month *Fermi*-LAT light curve and the optical R-band light curve between JD 2454680 (August 1st, 2008) and 2455299 (April 12th, 2010), as well as the radio SMA light curve between JD 2454721 (September 11th, 2008) and 2455289 (April 2nd, 2010). Figure 6.5 (top) plots the resulting DCF comparing optical and γ -ray light curves using a five-day γ -ray integration and a ten-day timelag binning. This yields a number of distinct correlation peaks, of which the two most significant are discussed. In the first peak the optical leads the γ -ray flux by (15 ± 10) days with a correlation coefficient of 0.44 ± 0.05 . The second peak corresponds to the optical flux lagging the γ -rays by 110 ± 5 days with a correlation coefficient of 0.77 ± 0.06 . To test the robustness of these peaks in the DCF, we artificially removed the points corresponding to the peak γ -ray flux from Flares II and III and recalculated the DCF. The same behavior was observed, with the γ -ray flux leading the optical by 20 days and lagging by 110 days. This shows that the results obtained do not solely depend on these two events. Finally, the DCF between the γ -ray and the SMA light curve of 3C 345 was calculated, which yielded a noisy distribution of correlation peaks (also see Figure 6.5). The strongest peak indicates that the radio emission leads the γ rays by 120 ± 5 days with a correlation coefficient of 0.83 ± 0.30 .

The statistical significance of the cross-correlation peaks was investigated using Monte Carlo simulations, following Chatterjee et al. (2008) and Max-Moerbeck et al. (2010) and assuming that the noise properties of the light curves can be described by a power-law power spectral density (PSD; $\propto 1/f^{-\beta}$) with an exponent that depends on the particular energy band of the emission.

In order to estimate the significance of the γ -ray/optical cross correlation, an attempt was made to calculate and characterize the PSD shape from the presented data directly, despite the limited length (20 months) and sampling (> 1 day) of the light curves. For the optical and γ -ray data, the light curves available support a range of time scales corresponding to about one decade in the frequency domain. The respective range is even smaller for the more sparsely sampled radio data. The PSDs were calculated following Section 3.1 in Uttley et al. (2002). The resulting power-law slopes, β , are in the range of 1.2–0.7 (Figure 6.6). Values of $\beta \gg 2.0$ are not consistent with the calculated PSD shapes and can be ruled out. However, Uttley et al. (2002) demonstrated that aliasing effects add to the power spectral slopes and could potentially flatten the observed power spectrum. The relatively high noise and short time span of the data makes this range of β rather unreliable. Monte Carlo simulations for these values of β yield extremely high cross-correlation significances of $>99.999\%$ for the γ -ray/optical light curves and $>99.98\%$ for the γ -ray/radio case. It should be noted that a reliable determination of the PSD from observational data is usually done with a much larger dynamic range (ie. covering 4–5 orders of magnitude in frequency), which is also the case in Uttley et al. (2002). The radio, optical and γ -ray data discussed here do not provide such an extended coverage in the frequency space. Therefore a more cautious approach exploring a range of power-law indices based on published values.

In the γ -ray regime $\beta_\gamma = 1.7 \pm 0.3$ for BL Lacs and $\beta_\gamma = 1.4 \pm 0.1$ for flat spectrum radio quasars (Abdo et al. 2010c). Instead, for 3C 279, it has been found that $\beta_{\text{radio}} = 2.3 \pm 0.5$ at 14.5 GHz and $\beta_{\text{optical}} = 1.7 \pm 0.3$ in the R-band (Chatterjee et al. 2008). More recently Chatterjee et al. (2011) found an average optical power-law index of $\beta_{\text{optical}} = 1.6 \pm 0.3$ for a sample of six blazars in the R-band. Simulated light curves with PSD power-law indices in these ranges can provide reliable estimates on the significance of the cross-correlations. The simulations use light curves of the same length as the data and simulated up to a maximum frequency of 1 day^{-1} using the method described by Timmer & Koenig (1995). Each case uses 10000 pairs of light curves, which are sampled and cross-correlated in the same fashion as the observed light curves. From these simulated data the distribution of correlation coefficients for each time bin can be obtained for the case of non correlated time series. Figure 6.5 presents the 3σ (99.7%) significance levels for all tested PSD shape combinations.

The γ -ray/optical correlation has a significance of higher than 3σ (99.7%) for the peak at a timelag of 110 days in most of the tested cases. It is the most significant peak in the DCF and it has a moderately high confidence level ($> 98.5\%$) even for the least significant case ($\beta_\gamma = 2.5$ and $\beta_{\text{optical}} = 2.5$; highest dashed line in the top panel of Figure 6.5) among the β values considered. The γ -ray/optical peak at a timelag of about -20 days has a much lower confidence level ($> 67.6\%$) in the least significant case and it remains below the 3σ level at all times. The γ -ray/radio cross-correlation at timelag -120 days has a confidence level of $> 90.7\%$ in the least significant case ($\beta_\gamma = 2.5$ and $\beta_{\text{radio}} = 3.0$).

The source 3C 345 is by far the brightest of the three quasars in the γ -ray region studied during the presented time period. In all bands it was consistently brighter than NRAO 512 and B3 1640+396. The improved *Fermi* position combined with multi-wavelength activity and a moderate significance of correlated optical/ γ -ray variability, using a plausible range of β in the γ -ray and optical PSDs, strongly suggest an identification of 3C 345 as γ -ray source and the main contributor to the observed γ -ray flux in 1FGL J1642.5+3947.

6.6 Conclusions

Properties of the γ -ray emitting region reported in the first three-month Bright Source List (Abdo et al. 2009a) as well as in the first 11-month *Fermi*-LAT source catalog (Abdo et al. 2010a,b) were compared to the 20-month dataset presented here. Localizations of the sources in this region were improved over the previously reported values, leading to the detection of two γ -ray point sources, one consistent with 1FGL J1642.5+3947 and a new γ -ray source $\sim 0.4^\circ$ west of it. 3C 345 and NRAO 512 were identified as the counterparts for these γ -ray sources. Their γ -ray spectra have a spectral slope of $\Gamma = 2.4$ – 2.5 typical for that of flat spectrum radio quasars (Abdo et al. 2010b). No significant spectral break was observed in the spectrum of either source, unlike in the case of 3C 454.3 (Ackermann et al. 2010), however, the statistics at the highest energies are poor, and the presence of a spectral break at $E > 10 \text{ GeV}$ is not ruled out.

The γ -ray emission from 3C 345 was identified based on an improved γ -ray counterpart localization and multi-wavelength activity including correlations of moderate significance found between the optical and radio variability, using a plausible range

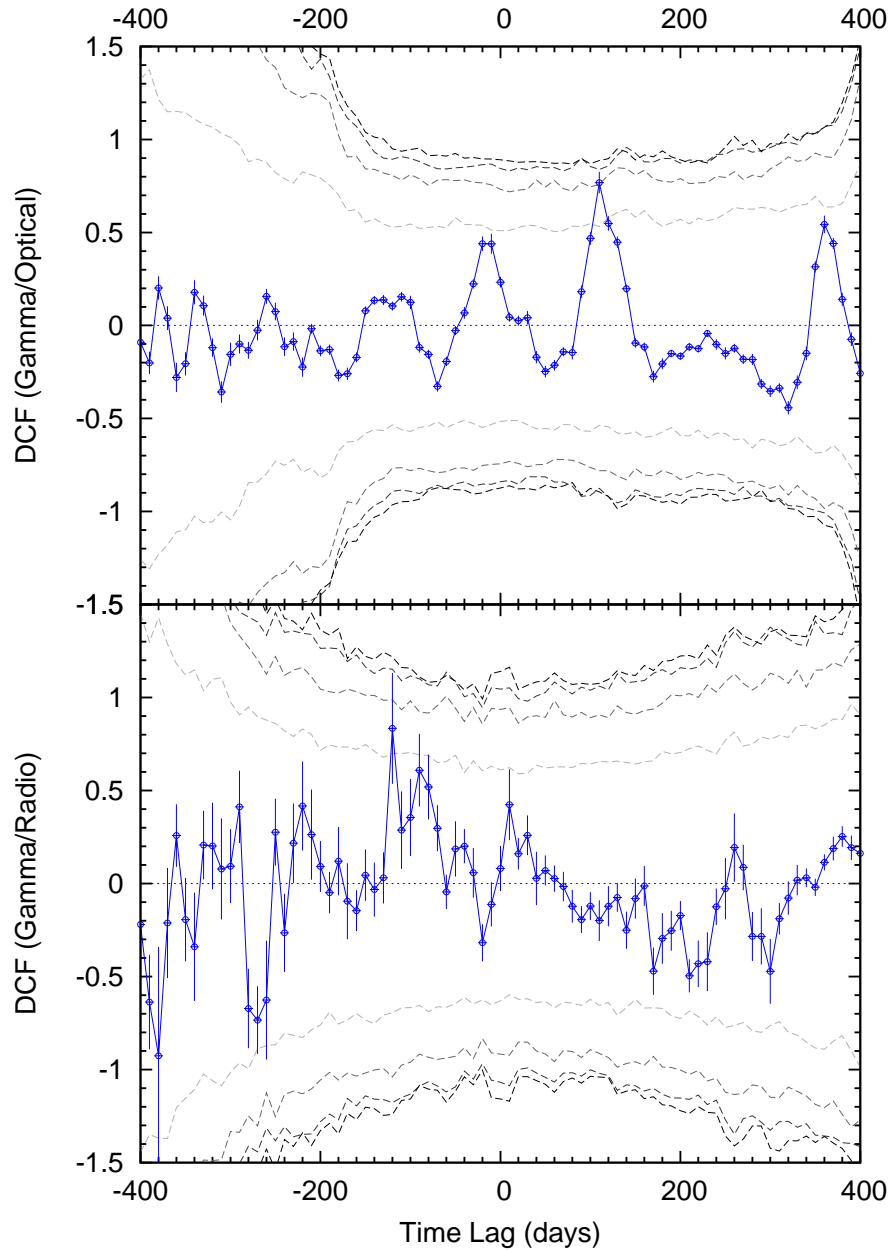


Figure 6.5: Correlation between the five-day integrated γ -ray light curve and the optical (top) and radio (bottom) light curves of 3C 345. The correlation is obtained by calculating the discrete correlation function (DCF) with ten-day binning. A positive time-lag corresponds to the γ -ray variations preceding the variations in the other two bands. The significance of the correlation is illustrated by 3σ (99.7%) significance contours calculated from simulated, uncorrelated data with different slopes, β , of the power spectral density (PSD). The contours are drawn for the PSD slopes $\beta = 1.0, 1.5, 2.0,$ and 2.5 (indicated by progression of colors, from light gray to black). For the simulated data, values of the correlation coefficient exceeding ± 1 are an inherent feature of the method, resulting from differences in overlap of the time series at different time lags (cf. Edelson & Krolik 1988; Timmer & Koenig 1995, and the description of the applied method in Section 6.5).

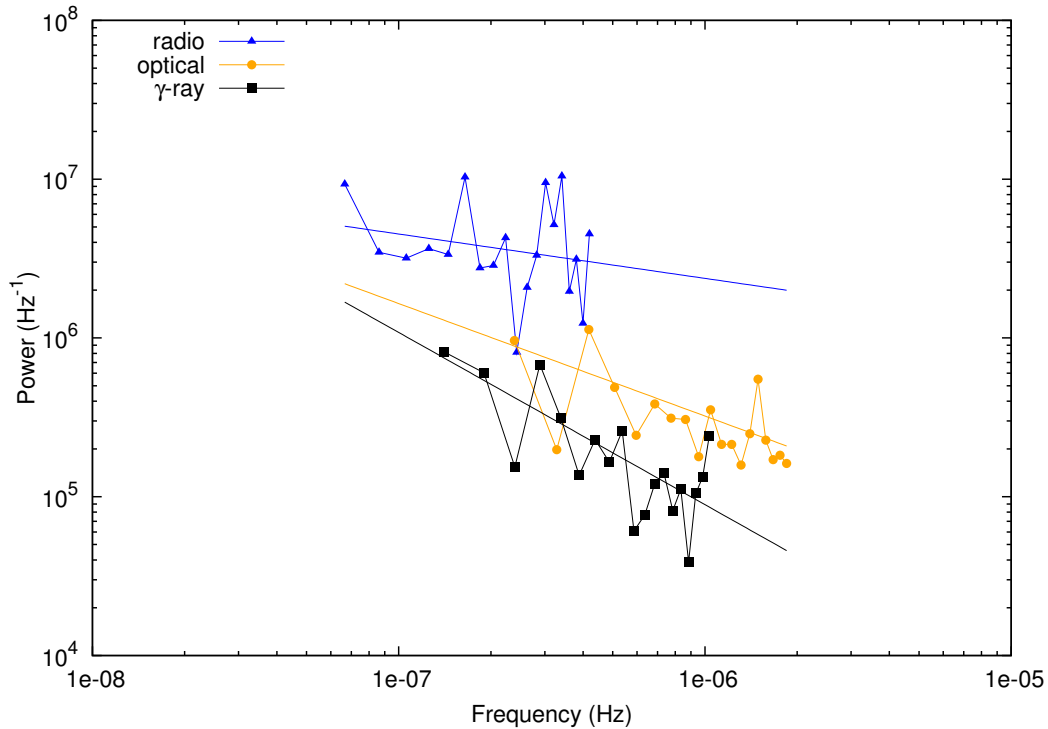


Figure 6.6: Raw power-spectral densities for the γ -ray, optical, and radio light curves. The corresponding slopes have a value of β of, -1.1 ± 0.3 (γ -ray), -0.71 ± 0.36 (optical), and 0.29 ± 0.29 (radio).

of β in the γ -ray and optical PSDs, and major γ -ray events observed by *Fermi* LAT during its first 20 months of operation. EGRET observed 3C 345 between 1991 and 1994 during a time of enhanced radio activity. An upper limit of $2.5 \cdot 10^{-7}$ $\text{ph cm}^{-2} \text{s}^{-1}$ for the viewing period September 12th - 19th, 1991, was reported (Fichtel et al. 1994). However, Casandjian & Grenier (2008) report the detection of a γ -ray source that could be consistent with 3C 345 in the period April 23rd - May 7th, 1996 with a γ -ray flux of $(3.5 \pm 0.8) \cdot 10^{-7}$ $\text{ph cm}^{-2} \text{s}^{-1}$, but it was noted that the association with 3C 345 remains unclear because of a possible confusion with Mrk 501. In the *Fermi*-era, with an increased sensitivity and the possibility of long-term integrations, 3C 345 was already detected during the first three months of operation at a level of $\sim 18\sigma$ and after 20 months it reached over 30σ . However, owing to the unclear association of 3C 345 with EGR J1642+3940, the three-month data were falsely associated with CLASS J1641+3035 (B3 1640+396), which, as shown in this chapter, did not produce a significant excess of γ -ray emission above the detection threshold of *Fermi*-LAT. Thus the simplest explanation for the previous non-detection of 3C 345 is that its emission was just below or at the detection limit of EGRET.

These findings end the decade-long debate whether 3C 345 is γ -ray loud (Unwin et al. 1997). The identification of 1FGL J1642.5+3947 with 3C 345 is further supported by the connection of radio-emission of the parsec-scale jet with the observed γ -ray emission (Schinzel et al. 2010), which is presented in the next chapter.

The cross-correlation found between γ -ray and optical light curves at 110 days had a moderate confidence level of $> 98.5\%$, whereas the lag at -20 days had a confidence level of only $> 67.6\%$ using a plausible range of β in the γ -ray and optical PSDs. If typical values for the power spectral density (PSD) shapes are assumed ($\beta_\gamma = 1.5$ and

$\beta_{\text{optical}} = 1.5$; second to lowest dashed line in the top panel of Figure 6.5), the confidence level remains low at $> 89.3\%$. The weak correlation found between the γ -ray and 230 GHz radio light curves had a worst-case confidence level of $> 89.3\%$. Assuming a possibly more typical combination of PSD shapes ($\beta_{\gamma} = 1.5$ and $\beta_{\text{radio}} = 2.0$), a confidence level of $> 96.1\%$ is obtained. If this weak correlation holds, it could suggest a connection between the radio emission and production of γ -rays. A timelag of ~ 120 days suggests the mm-radio emission precedes the γ -rays. Pushkarev et al. (2010) showed for a larger sample of radio-loud quasars that on average the 15 GHz radio emission lags ~ 1.2 months behind γ -rays. The result presented here indicates that between 15 GHz and 230 GHz it is possible to directly observe the γ -ray emitting region, as already implied by Unwin et al. (1997), which supports the argument of γ -ray production in the relativistic jet on pc scales. However, in contrast to these, a more confident cross-correlation result of γ -rays leading by ~ 80 and ~ 50 days was recently obtained for two prominent BL Lac type objects, OJ 287 (Agudo et al. 2011a) and AO 0235+164 (Agudo et al. 2011b), respectively. Doubts on the indicated radio/ γ -ray correlation of 3C 345 remain in this problem and should be investigated more thoroughly with a longer and denser sampled lightcurve at mm wavelengths.

The γ -ray emission from NRAO 512, a high-redshift quasar, was identified based on a correlated increase in multi-wavelength emission from radio up to GeV energies between 2009 and 2010. At monthly timescales the source started to be significant around November 2009. This increase of γ -ray flux led to the first detection of the now identified new γ -ray counterpart west of 3C 345. The LAT flux quoted in this chapter, for the first 15 months was below the EGRET detection threshold, offering a plausible explanation of why EGRET did not see emission from NRAO 512, except possibly during a γ -ray flare event.

The radio, optical and X-ray flux ratios between 3C 345, NRAO 512 and B3 1640+396 could be used to gauge their individual γ -ray photon contributions and might be able to provide an indication of false associations for γ -ray photons from this part of the sky. Multi-wavelength monitoring, in addition to the continuous all-sky monitoring by *Fermi* LAT, will help to improve the localization of γ -ray emission from this region and is necessary for a deeper variability study for any of these sources in the future. Ultimately this might lead to the detection of γ -ray emission from B3 1640+396 as well.

As a consequence of the work presented in this chapter, the two objects 3C 345 and NRAO 512 are now listed in the LAT 2-year point source catalog (2FGL) which uses 24 months of LAT monitoring data. They are listed at the positions of 2FGL J1642.9+3949 and 2FGL J1640.7+3945 and are properly associated with 3C 345 and NRAO 512 respectively. At the time of writing of this thesis only a draft version of the 2FGL has been made available, pending the submission of a descriptive paper.

Relativistic Outflow Drives γ -ray Emission

Observations of high-energy emission (keV – TeV range) provide important insights into the physical properties of Active Galactic Nuclei (AGN), in particular for the subgroup of quasars. However, high energy production scenarios are still heavily debated with many possibilities discussed (e.g., Böttcher et al. 2009; Dermer et al. 2009; Błażejowski et al. 2004). Most of these physical models depend on the emission site, mainly its distance to the central engine. A connection between cm-/mm-radio and high energy emission of quasars was already suggested by Valtaoja & Teraesranta (1996), Jorstad et al. (2001) and references therein. To investigate this connection, variability of AGN are studied in coordinated multi-wavelength observation campaigns covering radio to γ -ray wavelengths. Their results, especially on archetypal sources, are essential for the physical understanding of the emission processes in AGN up to the highest energies (cf. Longair 2011). These observations, in particular simultaneous high-resolution very long baseline interferometry (VLBI) observations at mm-wavelengths, provide new limits on the parameter space of proposed emission models, placing constraints on size, energetics and locations of emission regions.

This chapter presents results from a coordinated observational campaign performed for this thesis, targeting 3C 345 and combining the 20-month *Fermi*-LAT γ -ray monitoring data (Chapter 6) with monthly VLBI observations made at 43.2 GHz (7 mm wavelength) at the VLBA. In Section 7.1, the kinematics of the pc-scale radio jet, its flux density evolution, and a possible connection with the high energy γ -ray emission are presented. Section 7.2.1 discusses long-term properties of the radio and γ -ray emission, comparing them with each other. In Section 7.2.2 an interpretation scheme is proposed that is able to explain all of the short-time scale variability observed in the γ -ray light curve.

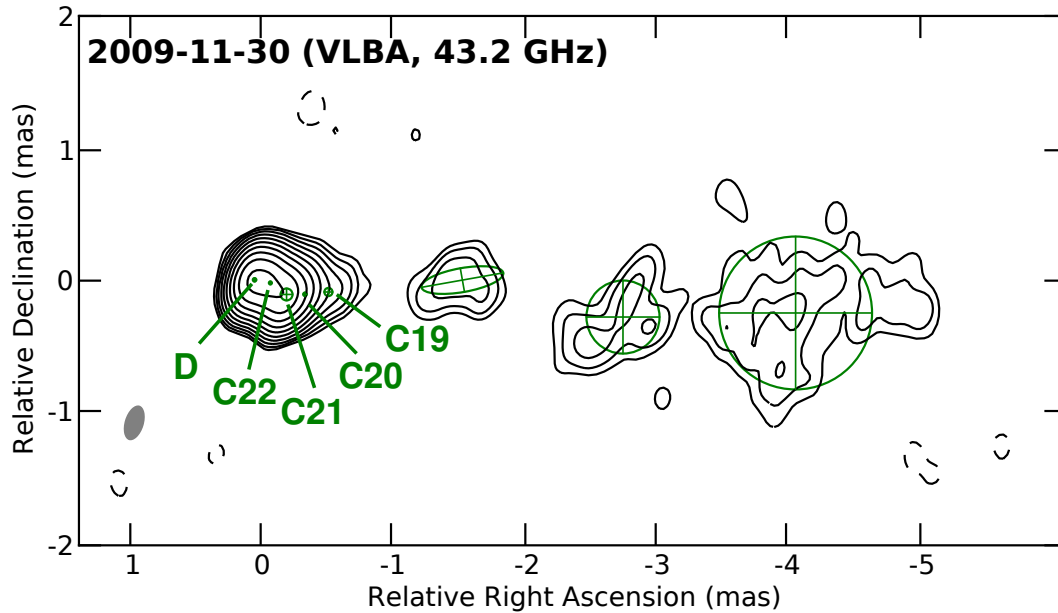


Figure 7.1: VLBA image of the total brightness distribution of 3C 345 at 43.2 GHz made from observations on Nov. 30, 2009. Open crossed circles show the FWHM of eight Gaussian components applied to fit the structure observed. The shaded ellipse, in the lower left corner, represents the FWHM of the restoring beam. The image peak flux density is 2.1 Jy beam^{-1} and the RMS noise is 1 mJy beam^{-1} . The contour levels are $(-0.15, 0.15, 0.3, 0.6, 1.2, 2.4, 4.8, 9.6, 19, 38, 77)$ % of the peak flux density. Here the nuclear region is modeled by two circular Gaussian components (D, C22) identified as the best representation of the observed brightness distribution.

7.1 Evolution of Radio Emission in the Nuclear Region

Following the onset of a new period of flaring activity in 2008, a dedicated monthly monitoring campaign was initiated, using the VLBA to monitor the radio emission of 3C 345 at 43.2, 23.8, and 15.4 GHz (VLBA project codes: BS193, BS194). In this chapter, only the 43.2 GHz observations are used, combined with some observations from the blazar monitoring program of Marscher et al. (VLBA project codes BM256, S1136) available online¹. The combined data (see Table 7.1) cover a period from January 2008 to March 2010, with observations spaced roughly at monthly intervals or shorter and overlap with *Fermi*-LAT γ -ray monitoring observations. Their brightness distribution was model-fitted by multiple Gaussian components providing positions, flux densities and sizes of distinct emitting regions in the jet, as described in Chapter 4. Figure 7.1 illustrates the observed radio structure and the Gaussian model-fit representation for a typical 43.2 GHz observation during this active period.

Variability of the region close to the VLBI core is of special interest here. In order to find the best description of the observed brightness distribution, compact emission in the nuclear region ($\leq 0.15 \text{ mas}$ from D) was modeled using four different approaches: 1) single circular Gaussian, 2) single elliptical Gaussian, 3) two circular Gaussians, 4) three circular Gaussians. In the following discussion, these model-fitting approaches are designated 1C, 1E, 2C and 3C, respectively.

¹<http://www.bu.edu/blazars/VLBAproject.html>

Table 7.1: Summary of VLBA Observations to investigate the recent activity of 3C 345 at 43.2 GHz.

Date	S_{tot} (Jy)	D	Beam (bpa) (mas) \times (mas) ($^\circ$)	Ref.
2008-01-17	1.90	2300	0.31 \times 0.19 (-27.2)	1
2008-02-29	2.02	1600	0.37 \times 0.21 (-29.1)	1
2008-06-12	2.44	2100	0.38 \times 0.16 (-28.2)	1
2008-07-06	2.23	800	0.33 \times 0.15 (-16.6)	1
2008-08-16	3.78	2700	0.41 \times 0.19 (-30.2)	1
2008-09-10	3.67	4300	0.37 \times 0.19 (-32.5)	1
2008-11-16	4.43	300	0.37 \times 0.33 (-1.49)	1
2008-12-21 [†]	2.91	5500	0.39 \times 0.17 (-16.9)	1
2009-01-24	5.04	8900	0.31 \times 0.17 (-20.5)	1
2009-02-19 [†]	3.55	2200	0.37 \times 0.20 (-19.0)	2
2009-02-22	4.63	8800	0.35 \times 0.15 (-19.1)	1
2009-03-16	6.01	2400	0.43 \times 0.30 (9.31)	2
2009-04-01	5.67	8000	0.33 \times 0.16 (-18.7)	1
2009-04-21	5.78	2600	0.33 \times 0.22 (-16.7)	2
2009-05-27	7.00	3500	0.33 \times 0.18 (-15.2)	2
2009-05-30	8.65	6900	0.32 \times 0.16 (-19.8)	1
2009-06-21	5.04	6500	0.28 \times 0.16 (-10.9)	1
2009-06-29	6.43	2600	0.29 \times 0.16 (-11.6)	2
2009-07-27	7.63	2900	0.38 \times 0.16 (-30.8)	2
2009-08-16	5.80	4300	0.30 \times 0.16 (-20.4)	1
2009-08-26	6.58	2000	0.32 \times 0.17 (-24.8)	2
2009-09-16	6.75	4600	0.35 \times 0.19 (18.3)	1
2009-10-01	6.67	2300	0.22 \times 0.18 (-21.6)	2
2009-10-16	6.80	4800	0.41 \times 0.17 (-30.5)	1
2009-11-07	6.38	1400	0.32 \times 0.16 (-15.3)	2
2009-11-28	5.31	4900	0.28 \times 0.16 (-24.6)	1
2009-11-30	5.53	2000	0.29 \times 0.16 (-16.9)	2
2009-12-28	4.95	2400	0.31 \times 0.16 (-8.14)	2
2010-01-10	4.25	2400	0.33 \times 0.20 (-8.75)	1
2010-02-11	5.57	2100	0.27 \times 0.15 (-17.0)	1
2010-02-15	5.11	1300	0.31 \times 0.20 (-6.37)	2
2010-03-06	5.38	3300	0.39 \times 0.28 (-12.1)	1

Notes: S_{tot} – total flux density recovered in VLBA image;

D – dynamic range measured as a ratio of the image peak flux density to the RMS noise;

Beam (bpa) – beam size, major axis vs minor axis with position angle of ellipse in parentheses;

References: 1 – blazar monitoring Marscher et al. (VLBA project codes BM256, S1136); 2 – dedicated monitoring (VLBA project codes BS193, BS194).

[†] – not used for the flux density analysis due to gain calibration problems and bad weather conditions on some of the VLBA antennas.

The criterion for significant improvement between two modelfits was developed using a ratio of reduced χ^2 parameters

$$\frac{\chi_1^2}{\chi_2^2} \geq \frac{x_{0.68;2}}{x_{0.68;1}}, \quad (7.1)$$

where the subscripts refer to the two modelfits compared. The order is defined by the number of degrees of freedom n of the individual modelfits with the condition $n_1 < n_2$. The parameter $x_{0.68}$ is obtained by solving the equation of the cumulative distribution function (CDF) of the χ^2 distribution,

$$0.68 = \frac{1}{\Gamma\left(\frac{n}{2}\right)} \gamma\left(\frac{n}{2}, \frac{x_{0.68}}{2}\right), \quad (7.2)$$

where Γ denotes Euler's Gamma function and γ represents the lower incomplete Gamma function. The number of degrees of freedom, n , depends on the number of modelfit parameters, since $\chi_\alpha^2 = \chi_{\min}^2 + x_\alpha(n, \alpha)$, with α describing the significance level ($\alpha = 0.68$, in our case). The proof and application of this property are discussed in Avni (1976).

Figure 7.2 compares the χ^2 parameters of each modelfit, normalized to the χ^2 values of the 1C (top panel), 1E (middle panel) and 2C (bottom panel). The horizontal lines in the plots represent the upper thresholds for significant improvement over the labeled Gaussian model. The 1C models compared to the 1E and 2C models have the respective threshold values of 0.77 and 0.82. 1E models compared to 2C models have a threshold value of 0.91, and 2C compared to 3C models needs to have an improvement of 0.86 or less. For some of the observations, the representation of the nuclear region by 1E is comparable to 2C. However, in order to form a consistent dataset, the representation by 2C providing the optimal ratio of χ^2 to the number of model parameters for all epochs is adopted.

Comparisons of the component positions, flux densities and sizes determined from the Gaussian modelfits revealed a new moving emission region, labeled C20, first detected in the VLBA image from June 16, 2008, followed by detections of another new component on January 24, 2009 (C21), a third one on July 27, 2009 (C22), and a fourth on November 28, 2009 (C23). In the following, components C20, C21, C22, and C23 (Figure 7.1) observed within a distance of 0.5 mas from the core D are referred to as the "jet".

7.1.1 Kinematics

The kinematics of individual features are determined from their relative positional offsets with respect to D. The temporal evolution of the measured offsets is plotted in Figure 7.3. The component C19, which was first observed in 2007, is also included for comparative purposes. The motions in the jet of 3C 345 are investigated using the right ascension, declination (x, y) positions of a jet component, relative to the core component (D) over the observed time period, fitting them separately using polynomials of different order, following the procedure described in Chapter 5.

Using this approach, it is sufficient to represent the trajectories of components C19, C22 and C23 by linear fits in both the x and y directions. In the case of components C20 and C21, a second order polynomial represents the best fit to the observed data

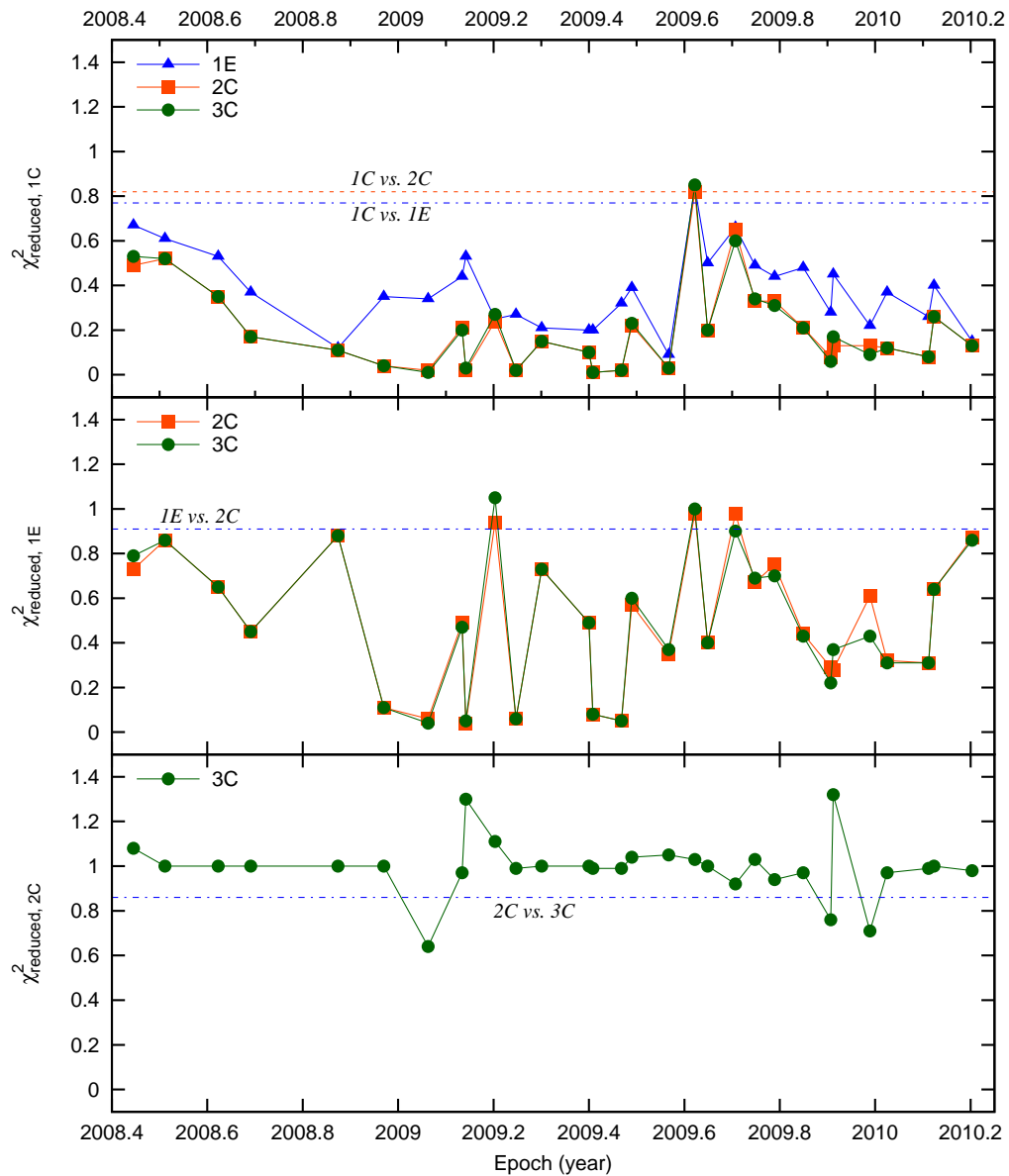


Figure 7.2: Reduced χ^2 parameters of the modelfit representations of the core region. The top panel shows the resulting χ^2_{reduced} values of 1E, 2C and 3C Gaussian models normalized to the value of the 1C Gaussian representation. The two horizontal lines mark the limit below which, for the corresponding model, a significant improvement (68% confidence) over 1C is given (0.77, 0.82). Similarly the middle panel shows the χ^2_{reduced} values for 2C and 3C normalized to that of 1E. The horizontal line marks the significant improvement level compared to 2C (0.91). The bottom panel normalizes the χ^2 values to that of 2C. The dashed line plots the significant improvement limit for 3C (0.86).

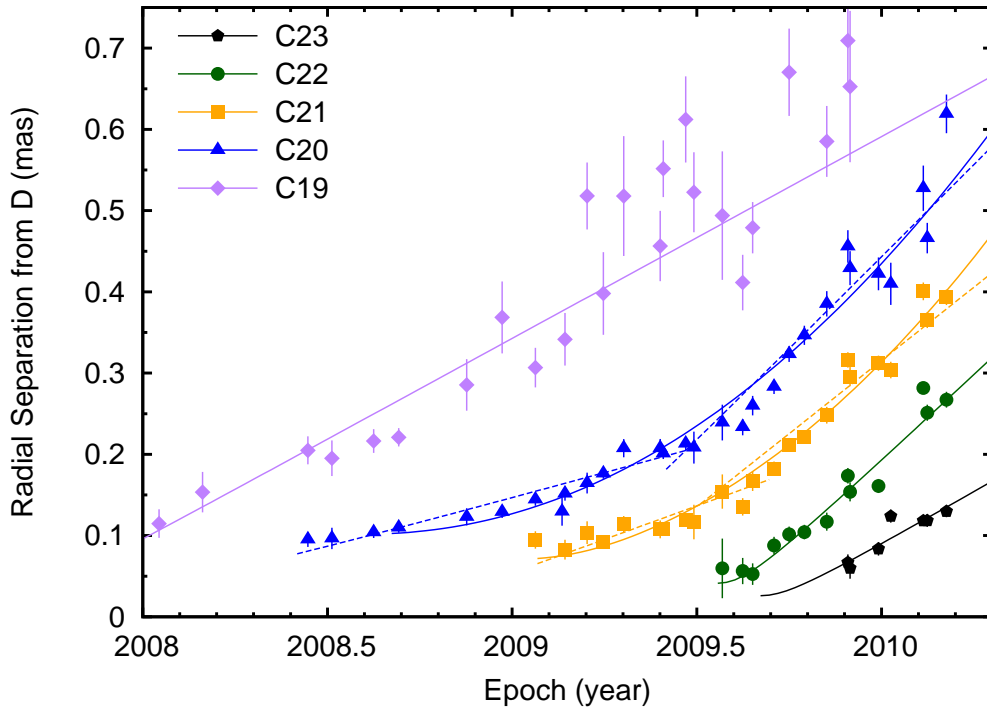


Figure 7.3: Evolution of the radial separations from the core of components C23, C22, C21, C20 and C19. C23-C20 are related to the radio variability since 2008, C19 is related to a previous radio flare observed in 2007. The lines are the results of polynomial fits to $x(t)$ and $y(t)$ directions separately. The dashed lines are the results of linear fits to $x(t)$ and $y(t)$ to determine ejection epochs and speeds for the two cases discussed.

in the x direction, implying apparent acceleration. In the y direction a linear fit is sufficient in all cases. The resulting fitted radial separations, $r(t)$, are drawn in Figure 7.3. For each component, the fits yield average proper motion, mean angular speed $\langle\mu\rangle$ and the average direction of motion $\langle\Phi\rangle$. The kinematic properties derived for the jet components indicate that C20 and C21 underwent a clear phase of apparent acceleration over a period of 1.5 years and over a distance of ~ 0.3 mas (2 pc). No statistically significant acceleration was observed for C19, C22 and C23. The observed values for $\langle\mu\rangle$ are in the range of $0.25 - 0.42$ mas year $^{-1}$ and for $\langle\Phi\rangle$ in the range of -96 to -120° . Using $\langle\mu\rangle$, the average apparent speed $\bar{\beta}_{\text{app}}$ and the speed in the source frame (deprojected) $\bar{\beta}$ are derived, also see Table 7.2. Jorstad et al. (2005) previously reported apparent jet component speeds of $0.29 - 0.69$ mas year $^{-1}$ and a jet position angle of $-66 - -95^\circ$. As a final step the physical parameters, Doppler factor δ , Lorentz factor Γ and viewing angle Θ of each jet component are derived, as described in Chapter 5. Combining the derived values for all components, a mean Lorentz factor of 12.5 and a mean Doppler factor of 14.4 are obtained. Which is consistent with the values obtained from the long-term kinematics, where median values for the Lorentz and Doppler factors of 14.1 and 15.6 respectively were obtained. Also, the derived viewing angles using the variability timescale argument are consistent with the observed long-term properties. Here, a Θ_{var} of $4.7_{-0.51}^{+0.65}$ degrees is obtained, which is comparable to the 3.8° from Chapter 5.

Table 7.2: Measured and derived physical parameters for radio emission regions in the inner jet ≤ 0.7 mas (4.6 pc).

Label	C19	C20	C21	C22	C23
#	26	30	23	13	7
$\langle \mu \rangle$ (β_{app})	0.248 ± 0.022 (8.5c)	0.277 ± 0.012 (9.5c)	0.300 ± 0.011 (10c)	0.427 ± 0.020 (15c)	0.272 ± 0.027 (9.0c)
$\langle \mu \rangle_{\text{lower}} >$	-	0.1260 ± 0.0088	0.165 ± 0.016	-	-
$\langle \mu \rangle_{\text{upper}} >$	-	0.458 ± 0.089	0.360 ± 0.049	-	-
$\langle \Phi \rangle$	$-100.0^\circ \pm 2.9^\circ$	$-96.3^\circ \pm 1.1^\circ$	$-114.3^\circ \pm 1.8^\circ$	$-120.5^\circ \pm 3.5^\circ$	$-117.8^\circ \pm 5.4^\circ$
$\langle \Phi \rangle_{\text{lower}} >$	-	$-97.0^\circ \pm 1.0^\circ$	$-109.7^\circ \pm 3.2^\circ$	-	-
$\langle \Phi \rangle_{\text{upper}} >$	-	$-96.2^\circ \pm 1.6^\circ$	$-112.3^\circ \pm 2.1^\circ$	-	-
τ_e	2007.62 ± 0.12	2006.91 ± 0.11	2009.055 ± 0.025	2009.544 ± 0.018	2009.651 ± 0.042
τ_{lower}	-	2007.834 ± 0.083	2008.674 ± 0.073	-	-
τ_{upper}	-	2009.00 ± 0.16	2009.11 ± 0.11	-	-
S ₁	0.73 ± 0.12	3.44 ± 0.16	2.301 ± 0.072	1.489 ± 0.086	2.01 ± 0.11
S ₂	0.257 ± 0.078	0.311 ± 0.038	0.816 ± 0.044	0.786 ± 0.057	-
d ₁	0.114 ± 0.038	0.1115 ± 0.0088	0.1012 ± 0.0067	0.0620 ± 0.0094	-
d ₂	0.244 ± 0.094	0.232 ± 0.036	0.170 ± 0.016	0.06 ± 0.011	-
dt	1.33	0.715	0.385	0.204	-
Δt_{var}	1.27 ± 0.42	0.297 ± 0.016	0.371 ± 0.022	0.319 ± 0.046	-
δ_{var}	5.6 ± 2.2	23.3 ± 2.2	16.9 ± 1.4	11.9 ± 2.5	-
Γ_{var}	9.8 ± 1.4	13.61 ± 0.93	11.6 ± 0.5	15.1 ± 1.0	-
Θ_{var}	$9.4_{-1.9}^{+2.4}$	$1.70_{-0.23}^{+0.34}$	$2.97_{-0.32}^{+0.42}$	$4.66_{-0.69}^{+0.81}$	-
(*)	<i>no</i>	<i>yes</i>	<i>yes</i>	<i>no</i>	<i>no</i>

Notes: # – number of data points;

$\langle \mu \rangle$ (β_{app}), $\langle \mu \rangle_{\text{lower}} >$, $\langle \mu \rangle_{\text{upper}} >$ – average component speed in mas year^{-1} , in parentheses the apparent speed β_{app} , for C21 and C22 lower and upper limits of the component speeds;

$\langle \Phi \rangle$, $\langle \Phi \rangle_{\text{lower}} >$, $\langle \Phi \rangle_{\text{upper}} >$ – average position angle of the component motion in degree, for C21 and C22 lower and upper limit;

τ_e (τ_{lower} , τ_{upper}) – Ejection epoch/time of zero separation from component labeled D, determined through linear extrapolation using the average component speed and component position at the midpoint, $t_{\text{mid}} = 0.5 \cdot (t_{\text{max}} - t_{\text{min}})$, of the respective dataset, for C21 and C22 lower and upper limits;

S₁, S₂ – maximum, minimum (at the time of maximum absolute value of the time derivative) component flux density in units of Jy;

d₁, d₂ – circular Gaussian model fit component FWHM in units of mas at the time of S₁, S₂;

dt – time between S_{max} and S_{min} in units of years; Δt_{var} – time variability factor in units of years;

δ_{var} , Γ_{var} , Θ_{var} – derived quantities in order of the variability Doppler and Lorentz factors, and the viewing angle to the line of sight in degrees

(*) – indicator whether component was accelerating (*yes*) or not (*no*)

The asymptotic standard errors for the fits are statistical only, obtained using an implementation of the nonlinear least-squares Marquardt-Levenberg algorithm with position errors as weights. Errors of the derived parameters are 68% confidence limits determined through Monte-Carlo simulations.

With the kinematics determined, it is possible to estimate the time at which a moving jet feature passes the VLBI core at 43 GHz. These passages are referred to as ejection epochs. The ejection epoch also marks the time at which a new jet feature begins to contribute to the observed radio emission.

As a first approach to determine the ejection epochs, we assume that the jet is optically thin all the way to the core and the features already travel at the observed average speed while passing through the VLBI core. Under these assumptions the ejection epoch is determined by back tracing the fitted linear trajectories. The resulting ejection epochs for all features are listed in Table 7.2, as well. This approach provides reasonable estimates of the ejection epochs for non-accelerating features, while for the apparently accelerating components C20 and C21 a different approach is required.

Looking at the radial separations of C20 and C21 in Figure 7.3, the acceleration is most evident for the time before 2009.6. An upper limit on the ejection epoch can be determined using a linear fit to the data points after 2009.5 for C20 and 2009.4 for C21 (τ_{upper} in Table 7.2). Similarly, lower limits, τ_{lower} , on the ejection epochs of C20 and C21 are obtained by considering only data points before 2009.5 and 2009.4 respectively.

7.1.2 Flux Density

In flat spectrum radio quasars (FSRQs), such as 3C 345, the component flux decay is commonly driven by radiative losses (Marscher & Gear 1985; Lobanov & Zensus 1999; Jorstad et al. 2005), which was assumed in the previous section and also in Chapter 5 without further justification. To test this, the maximum component brightness temperature needs to be calculated as a measure for the emission intensity of each component, using:

$$T_{\text{b}} = 1.22 \cdot 10^{12} \cdot \frac{S_{\text{comp}} \cdot (1+z)}{d_{\text{comp}}^2 \cdot \nu^2}, \quad (7.3)$$

where S_{comp} is the component flux density in Jansky, z the redshift of the source, d_{comp} the FWHM size of the circular Gaussian in mas and ν the observing frequency in GHz. In Figure 7.4 the brightness temperatures for components C20, C21 and C22 are plotted as a function of the radial separation from the core.

In the common picture of the shock-in-jet model, a relativistic shock propagates down a conical jet, slowly expanding adiabatically albeit maintaining shock conditions. In this scenario the assumption of a power-law electron energy distribution ($N(E) dE \propto E^{-s} dE$), a power-law magnetic field evolution ($B \propto r_{\text{jet}}^{-a}$) and a constant jet opening angle with the jet transverse size proportional to the distance along the jet ($d_{\text{jet}} \propto r_{\text{jet}} \sin \Theta$) can be made. While the shock continues to travel down the jet, it undergoes three major evolutionary stages dominated by Compton, synchrotron and adiabatic energy losses (Marscher et al. 1992). From this it follows that the brightness temperature decays as a power-law, $T_{\text{b,jet}} \propto r_{\text{jet}}^{-\epsilon}$, where r_{jet} is the distance in the jet at which $T_{\text{b,jet}}$ is measured. The value of ϵ can be derived from spectral evolution of radio emission (Lobanov & Zensus 1999), assuming $T_{\text{b}} \propto S_{\text{comp}}/(r_{\text{jet}}^2 \nu^2)$ and the Doppler factor $\delta = \text{const}$.

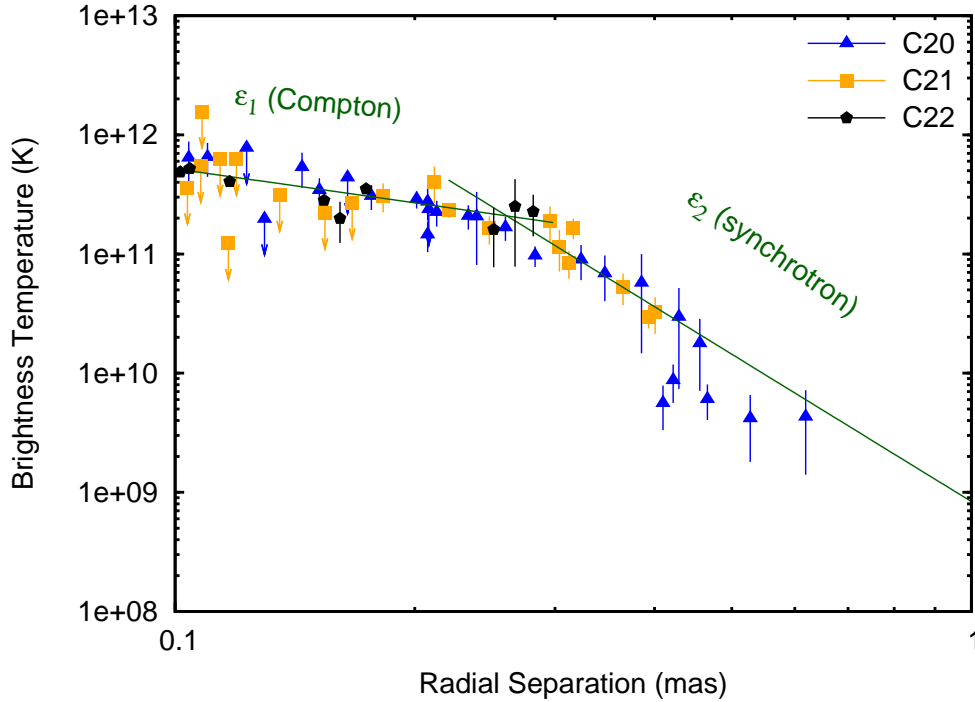


Figure 7.4: Component brightness temperatures against radial separation from the VLBI core (D), representing the emission intensity gradient along the jet. Points with arrows are 1σ upper limits. Two lines are fitted to the data to determine the power law indices ϵ ($T_b \propto d_{\text{jet}}^{-\epsilon}$) from the data, the fit from 0.1 to 0.3 mas yields $\epsilon_1 = 0.95 \pm 0.69$ and 0.3 – 0.65 mas yields $\epsilon_2 = 4.11 \pm 0.85$.

For Compton (ϵ_c), synchrotron (ϵ_s) and adiabatic (ϵ_a) losses, ϵ are calculated as follows,

$$\epsilon_c = [(s + 5) + a(s + 1)] / 8, \quad (7.4)$$

$$\epsilon_s = [4(s + 2) + 3a(s + 1)] / 6 \quad (7.5)$$

$$\epsilon_a = [2(2s + 1) + 3a(s + 1)] / 6 \quad (7.6)$$

with a typical value of $s = 2.0$ (corresponding to a synchrotron spectral index $\alpha = -0.5$; $S_\nu \propto \nu^{+\alpha}$) and $a = 1$ (dominant transverse magnetic field), $\epsilon_c = 10/8 = 1.25$, $\epsilon_s = 25/6 \approx 4.17$ and $\epsilon_a = 25/6 \approx 3.17$. For the slopes to be shallower than these derived values, acceleration resulting in increasing Doppler factors of $\delta \propto r_{\text{jet}}^b$ may be considered. For a moderate acceleration (i.e. $b = 0.1 - -0.2$), a value $\epsilon_c \approx 0.13$ is obtained assuming $s = 2$ and with a longitudinal magnetic field ($a = 2$).

The observed brightness temperature gradient along the jet, shown in Figure 7.4, reveals a possible broken power-law behavior of the jet intensity gradient with a break distance of ~ 0.3 mas and the two slopes $\epsilon_1 = 0.95 \pm 0.69$ and $\epsilon_2 = 4.11 \pm 0.85$. The value of ϵ_1 is consistent with ϵ_c , with the possible indication of a mild change in δ , and ϵ_2 is consistent with the derived ϵ_s . Note that, using the spectral evolution of a jet component, Lobanov & Zensus (1999) found evidence for a change from the synchrotron to the adiabatic stage at a distance of 1.2–1.5 mas from the core.

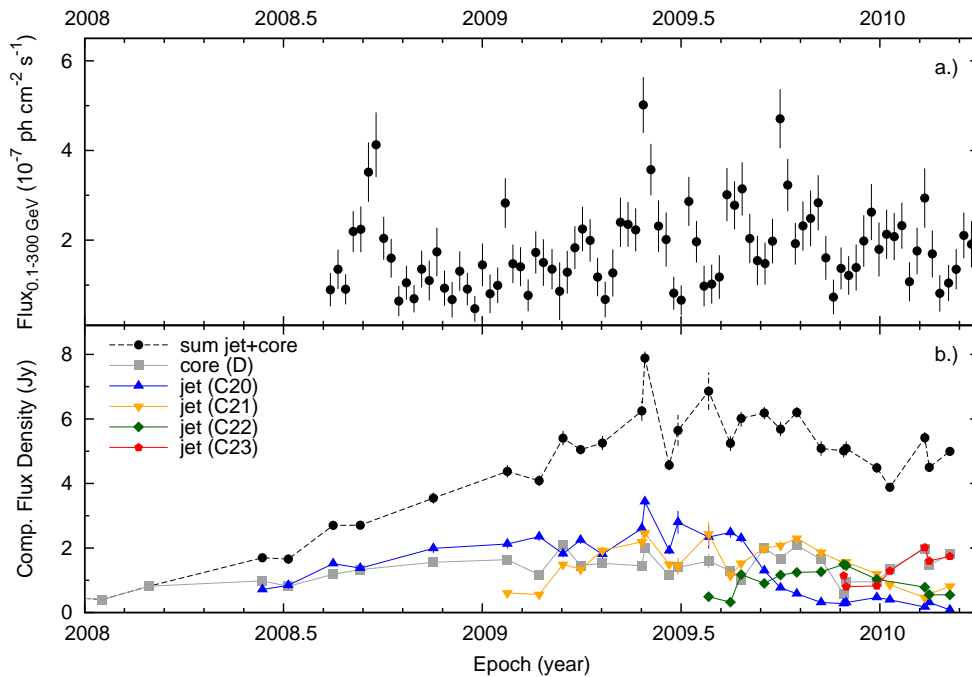


Figure 7.5: *top*: *Fermi* LAT 7-day binned γ -ray light curve of 3C 345 for the energy range of 0.1-300 GeV. *bottom*: VLBA 7 mm component flux densities for the model-fitted VLBI core and inner jet, represented by up to five circular Gaussian (D, C23, C22, C21, C20). The component labeled D is the east-most component (see Figure 7.1) and represents the compact “core” or base of the jet. The black curve plots the sum of the flux densities of all four components.

7.2 Radio- γ -ray Correlation

The γ -ray emission of 3C 345 was identified based on correlations found between the optical variability and major γ -ray events observed by *Fermi* LAT between August 2008 and April 2010 (see Chapter 6). For this analysis a light curve for which the γ -ray monitoring data was split into regular time intervals, each integrating over periods of 7 days and an energy range of 0.1-300 GeV, was obtained in the fashion described in Chapter 4. The position of the γ -ray counterpart was fixed to the radio localization of 3C 345. For the spectral shape of the γ -ray emission of 3C 345 a power-law was used with the spectral index fixed to its 20 month average value of $\Gamma = 2.45$. The particular time binning of 7 days in this case provides the best trade-off between time resolution and signal to noise. This yielded a light curve with 81 significant detections and five 2σ upper limit time intervals (JD 2454756, 2454826, 2454903, 2454945, 2455155), in total this covers a time period of 602 days (20 months). In order to homogenize the light curve, 2σ upper limits were used as values with their error estimate for that interval replaced with half the difference between that upper limit and its value determined through the unbinned spectral likelihood analysis. This method was applied for the calculation of the variability index in Chapter 6 and Abdo et al. (2010a). The top panel in Figure 7.5 shows the resulting γ -ray light curve.

The correlation between γ -ray, radio and optical emission was investigated in Chapter 6 for identification of γ -ray emission from 3C 345. Here, the connection between the

synchrotron radio emission and γ -ray emission is investigated. To quantify a possible connection, the correlation between the γ -ray and the radio light curve is calculated. For this we used the discrete correlation function presented by Edelson & Krolik (1988), which works well for unevenly sampled data. No statistically significant correlation is found, although around 2009.4, a rapid change in VLBI flux densities by ~ 1.5 Jy within only 4 days coincided well with a γ -ray flare (also see Figure 7.5).

7.2.1 Long-term Trends

The top panel of Figure 7.5 plots the weekly averaged γ -ray light curve of 3C 345. From it a seemingly long-term trend is seen, most evident between 2008.7 and 2009.4. After 2009.4 an increase in short-time variability is observed, followed by a slightly decreasing trend after 2009.8. The measured γ -ray flux increases by a factor of 2-3 between 2008.6 and 2009.5. Even more evident is a long-term trend in the light curve of the radio jet features (bottom panel of Figure 7.5), following from the sum of the flux density of individual jet components. The optical R band data presented in Figure 6.4 in Chapter 6 similarly showed a rising trend for the same time period. Here, the optical dataset is added for comparison as well.

To quantify this relation, the light curves are first rescaled with the zero flux representing their respective mean value. The radio flux density of the jet has a mean value of 3.60 Jy and corresponds to the emission from the jet of an apparent size of ≤ 2 pc (excluding the core). The core has a mean flux density of 1.5 Jy and an apparent size of ~ 0.3 pc. Note, the jet flux density is by a factor of 2.4 stronger than that of the core. The average γ -ray flux is $1.8 \cdot 10^{-7}$ ph cm $^{-2}$ s $^{-1}$. Observations at optical R band have an average magnitude of 16.6, which corresponds to a flux density of $7.7 \cdot 10^{-4}$ Jy.

In the final step, the rescaled light curves are de-trended using cubic spline interpolations over 0.4 year bins (Press et al. 1992). The extracted long-term trends are shown in Fig 7.6. From these it is immediately evident that a similar trend is obtained for the radio jet and the γ -rays, whereas the core does not show a significant trend. The discrepancy of the first 0.4 year is caused by the lack of γ -ray monitoring before 2008.6 and a flare immediately after 2008.6 (see Figure 7.5). The trend of the optical emission shows a similar behavior compared to the γ -ray and radio trends, however it is more peaked. Comparing trend amplitudes, the amplitude of the variation in the optical is 4 times greater than in the γ -rays. The radio shows a factor of 2 higher amplitude of the variation than γ -rays. Based on the peak values of these trends, the radio leads the γ -ray trend by 31_{-11}^{+29} days and optical leads the γ -ray trend by $1.1_{-7.7}^{+11.3}$ days. Altogether this is consistent with an almost zero time lag between the observed long-term trends.

The observed emission from the radio jet showing the matching trend is most of the time dominated by the jet component closest to the core. At the beginning of the monitoring period this is C20 & C21 and by the end of 2010 they are replaced by C22 & C23. This connects the emission from the radio jet with that observed at optical and γ -ray energies and places the site of the underlying multi-wavelength emission within the resolved 43 GHz radio jet. The very region that was shown to be Compton loss dominated in the previous section.

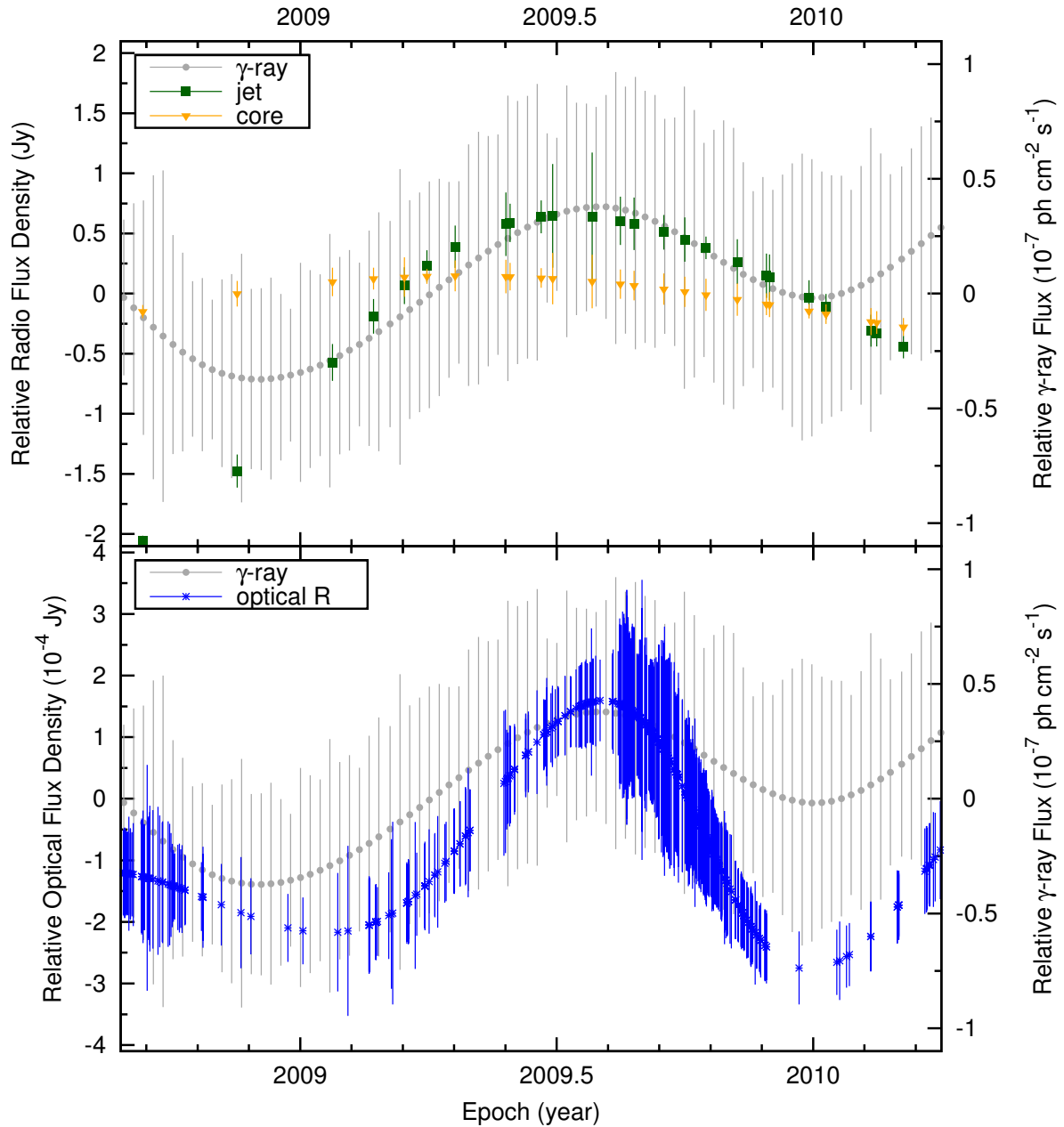


Figure 7.6: Long-term trends of the radio jet, radio core flux densities, optical R band flux (Schinzel et al. 2010) and the γ -ray flux relative to their respective mean values (radio jet: 3.6 Jy, radio core: 1.5 Jy, optical R: 16.6^m ($7.7 \cdot 10^{-4}$ Jy), γ -ray: $1.8 \cdot 10^{-7}$ ph cm $^{-2}$ s $^{-1}$). The trend was extracted fitting cubic splines with 0.4 year bins. The relative radio flux density was scaled by a factor of 2:1 with respect to the relative γ -ray flux, the optical flux density was scaled by a factor of 4:1, and the data points match the sampling of the original light curves.

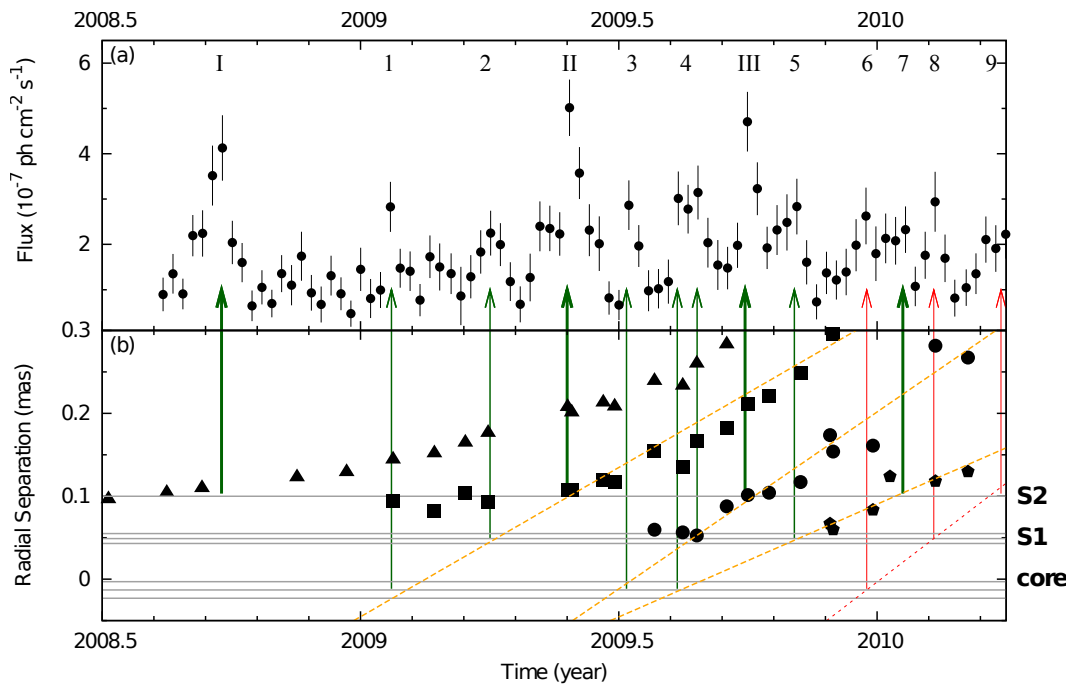


Figure 7.7: *Top panel (a)*: The γ -ray light curve of 3C 345 for the energy range of 0.1-300 GeV, each data point is integrated over a period of 7 days. *Bottom panel (b)*: Evolution of the radial separations from the core of newly appeared components since 2008. The orange dashed lines are linear fits to the data, representing the radial motion of the components. The red dashed line, passing the core around 2010 is indicating a new component not yet observed. The gray horizontal lines indicate the suggested positions of standing features (the center line is the average value, with one line each on top and below, indicating the obtained spread). Thick upward arrows indicate the times at which a feature passes 0.1 mas. Thin arrows indicate times at which features pass the first and second standing features, following the proposed scheme discussed in the text.

7.2.2 Individual Events

The long-term trends observed in the γ -ray and radio emission are firmly connected by similar long-term trends, indicating a common origin and emission mechanism. In this context however, an interpretation of faster variability observed in γ -rays is lacking. In the following few paragraphs an attempt is made to combine the gained knowledge from these observations in order to interpret the origin of faster variability observed at high energies.

Combining the above information on the jet structural and γ -ray variability, three strong γ -ray flares can be related to jet features passing through the region (labeled S2) at a distance of around 0.1 mas. This is indicated by thick arrows pointing toward the events labeled with roman numerals in Figure 7.7. If the excess of the observed γ rays is an intrinsic feature of the structure of the relativistic flow, then it might be possible to identify distinct regions in the jet at which this excess is produced. Knowing the speeds of respective jet features and the time between subsequent γ -ray events, positions of these regions can be obtained. In Figure 7.8 the results are visualized.

Despite different speeds and time differences between γ -ray events, the positions line

up and form a repeating pattern. For the investigated timerange the calculated distances cluster around the radial distances of (-0.013 ± 0.010) and (0.049 ± 0.006) mas. Note, the errors only take into account the uncertainties on the speeds and γ -ray flares. The first value is consistent with a zero separation, thus the radio core. Together with the indication of a second standing feature between the core and 0.1 mas, the presence of a triple structure of standing features is suggested. Triple structures seem to be a common occurrence and were first observed in the case of 3C 454.3 (Pauliny-Toth et al. 1987). To aid comparison between radial motion of features and the observed γ -ray variability, the suggested interaction zones are indicated by horizontal lines in Figure 7.7.

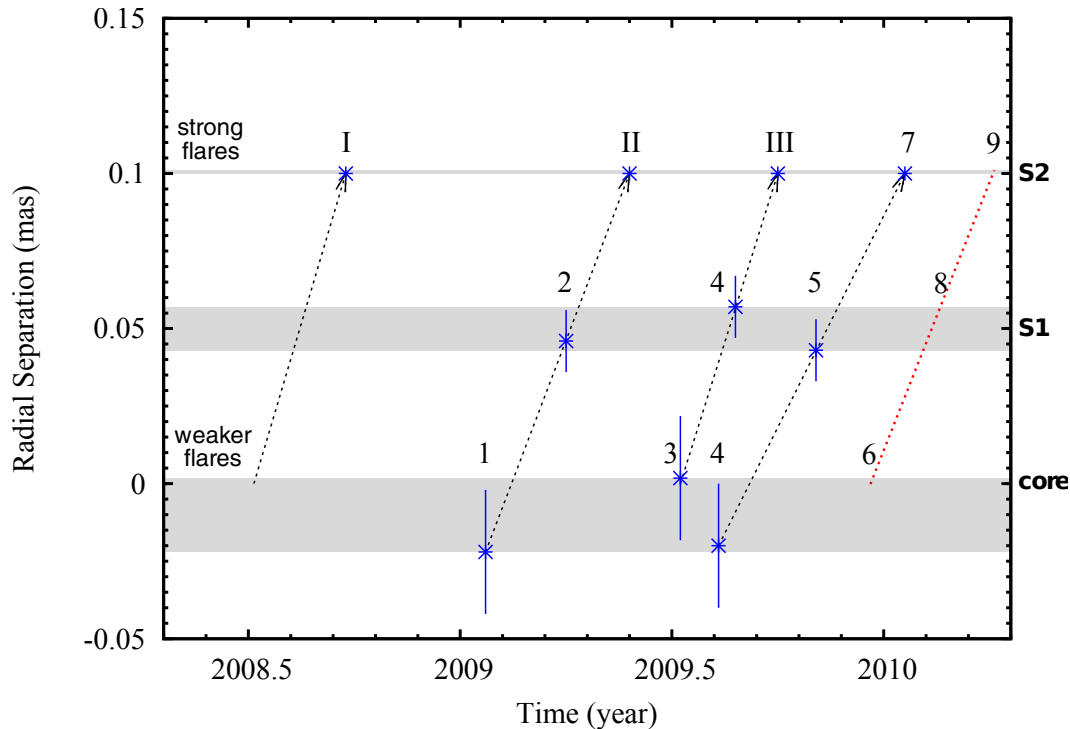


Figure 7.8: Distances calculated under the assumption of interaction of moving with a standing feature, producing γ -ray flares during passage. The errors on the positions are determined by the statistical uncertainty of the speed and time between flares. The uncertainty of the standing feature at 0.1 mas, used as reference, is ignored. The numbers refer to the γ -ray event labels in Figure 7.7. The grayscale boxes visualize the scatter of the calculated values. The dashed arrows indicate the radial motion of the individual moving features. The red dotted line indicates the predicted radial motion of a new jet component.

This scenario matches the γ -ray variability extremely well and is even able to explain the peculiar double peaked γ -ray event labeled “4” shown in Figure 7.7. The first peak is produced when the latest feature (“4”) passes the core, the second peak coincides with the previous feature (“3”) passing the second standing feature of the triple structure. Additionally, the γ -ray events 6, 8, and 9 show a similar triple pattern, indicating a new but not yet detected jet feature propagating through the triple structure. A radio observation on May 19th, 2010 provided by the Boston University blazar monitoring program shows evidence for changes in the structure of the compact jet, consistent with the appearance of a new feature.

3C 345 was also observed at the currently highest possible resolution using the Global 3mm-VLBI array (GMVA). The GMVA was formed to improve accessibility of regular 3mm (86.2 GHz) observations to the astronomical community. The array regularly observes in two blocks per year, connecting most of the mm radio telescopes in the Northern hemisphere to one big array using VLBI. In most GMVA experiments, the following stations are participating: the VLBA (with 8 antennas), the IRAM 30-m at Pico Veleta, the Plateau de Bure interferometer, the 100-m Effelsberg telescope, the Onsala 20 m telescope, and the Metsähovi 14 m telescope. In Figure 7.9 the resulting map of the brightness distribution of 3C 345 at 86.2 GHz is shown. It is the result of the observations performed by the GMVA during the May 2010 block, as part of a larger project monitoring γ -ray-loud AGN leader by the Boston group (P.I. A. Marscher).

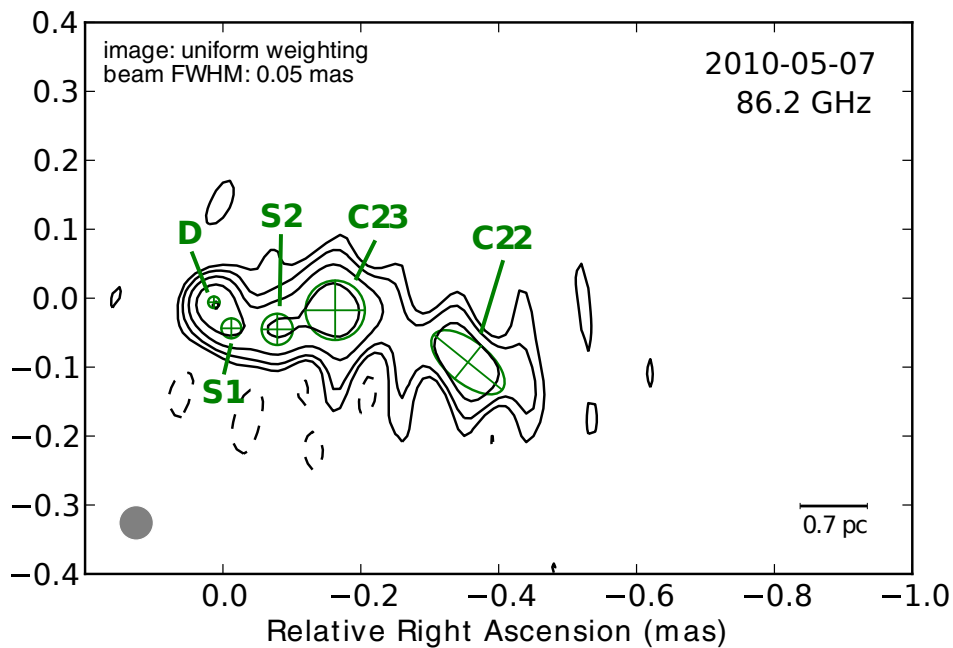


Figure 7.9: Global 3mm-VLBI array image of the total brightness distribution of 3C 345 at 86.2 GHz made from observations around May 7th, 2010. Open crossed circles show the FWHM of five Gaussian components fitting the structure observed. The parameters of these components are listed in Table 7.3. The shaded circle in the lower left corner represents the FWHM of the restoring beam and the map was reconstructed using uniform weighting. The image peak flux density is $0.38 \text{ Jy beam}^{-1}$. The contour levels are (-6, 6, 12, 24, 48, 96)% of the peak flux density. Negative contours are indicated by dashed lines. The bar in the lower left corner indicates an apparent size scale of 0.7 pc. *Courtesy of Marscher, Marti-Vidal, Krichbaum, et al., providing the calibrated GMVA dataset.*

The (u, v) -dataset was modelfitted using Gaussian components (cf. Chapter 4). The resulting component parameters are shown in Table 7.3 and are indicated by open crossed circles/ellipses in Figure 7.9. The core component and the component next to the core, labeled “S1”, are both unresolved. The two most distant components from the core are identified as C22 and C23, which were also identified in 43.2 GHz observations, presented above. Interestingly, two additional features in the jet are observed between C23 and the core D. One with a separation from the core of $(0.045 \pm 0.021) \text{ mas}$ (“S1”) and $(0.10 \pm 0.01) \text{ mas}$ (“S2”). Surprisingly, the component between S2 and D is compatible with the found γ -ray production region. Altogether this provides strong

evidence for a connection of these emission regions in the radio jet with that of high energy emission, which means not only long-term trends in γ -ray and optical emission are connected to the observed radio emission, but also short time scale emission.

Table 7.3: Model components for global 3mm-VLBI array (GMVA) image from 2010-05-07, shown in Figure 7.9.

label	S (Jy)	r (mas)	ϕ ($^\circ$)	d (mas)	ratio	cpa ($^\circ$)
D	0.343 ± 0.098	0.0144 ± 0.0098	114 ± 34	0.017 ± 0.020	1	0
S1	0.268 ± 0.092	0.045 ± 0.019	-164 ± 22	0.029 ± 0.037	1	0
S2	0.278 ± 0.089	0.091 ± 0.020	-120 ± 10	0.045 ± 0.034	1	0
C23	1.02 ± 0.17	0.1637 ± 0.0087	-96.1 ± 3.0	0.086 ± 0.017	1	0
C22	0.74 ± 0.20	0.367 ± 0.019	-104.7 ± 2.9	0.127 ± 0.037	0.48	51

Notes:

label – component label, following the scheme used here; S – component flux density; r – distance of component center to the phase center (0,0 position) of the map; ϕ – angle of the component to the phase center of the map (North through West); d – FWHM of the component; ratio – in case of an elliptical Gaussian component, this number provides the axial ratio between the major and minor axis; cpa – is then the rotation angle of the ellipse (North through West).

7.3 Discussion

Monitoring of the fine structure of the jet in 3C 345 reveals a wealth of morphological and kinematic features of the flow. In particular, compelling evidence for two stationary feature in the parsec-scale radio jet of 3C 345 are found. This stationary feature is located at a distance of ~ 0.1 mas (~ 0.7 pc) from the core. The kinematics of a large sample of relativistic jets, obtained through the MOJAVE survey, revealed stationary features as a frequent occurrence (Lister et al. 2009b). In particular, in the jets of γ -ray blazars, observed at 22 and 43 GHz, stationary features within 2 pc (projected) from the core are commonly observed (Jorstad et al. 2001). Stationary jet features were investigated in more detail in the cases of 3C 390.3 (Arshakian et al. 2010), a nearby double-peaked radio galaxy at $z = 0.0561$, and the Seyfert galaxy 3C 120 ($z = 0.033$; León-Tavares et al. 2010). For these two sources, stationary features were found at distances of ~ 0.4 pc (3C 390.3) and ~ 1.3 pc (3C 120) from the core at 15 GHz. Their physical origin was associated with that of standing shocks.

The moving plasma condensations (components) are most likely generated near the nucleus of the jet of 3C 345, but can only be reliably monitored after they pass through the location of the stationary feature. After this passage, the superluminal components in 3C 345 undergo an apparent acceleration from ~ 5 to ~ 15 c over a distance of 0.3 mas in extent (~ 23 pc deprojected). This acceleration seems to be a commonly observed feature of many objects in the MOJAVE sample, where a statistically significant tendency for acceleration in the base of jets is found (Homan et al. 2009). Previously, Lobanov & Roland (2005) discussed the observed acceleration of a different component in 3C 345, testing the case of a substantially curved three-dimensional path, causing the observed dramatic change of the apparent component speed. They concluded that the observed acceleration is not likely to be a geometrical effect, but should reflect

physical acceleration of plasma. The possibility of intrinsic acceleration of jet features on parsec scales was discussed by Vlahakis & Königl (2004). There it was specifically argued that the acceleration observed in 3C 345 is not purely hydrodynamic, but can be attributed to magnetic driving. They showed that the observed acceleration is consistent with an acceleration from $\Gamma \sim 5$ to $\Gamma \sim 10$ over a linear distance of ~ 3 to ~ 20 pc. The results presented here are consistent with these findings.

The times of passage of knots C20, C21, and C22 through the 43 GHz VLBI core coincide with short-term increases in the γ -ray flux (see Figure 7.5, with times listed in Table 7.2). In a similar case, PKS 1510-089 showed, in addition to the appearance of a new VLBI component, a rapid rotation in the optical linear polarization just prior the components passage through the core. This was explained by the feature following a spiral path through a toroidal field until it crosses a standing shock in the 43 GHz core (Marscher et al. 2010).

A γ -ray flare centered on 2009.4 may be related to the brightening of radio structure at distances of 0.12 – 0.20 mas from the core (0.8 – 1.3 pc), corresponding to a deprojected distance of ~ 9 -15 pc. Interestingly, this includes the region for which the presence of a standing shock is suggested by the observations presented here. Radio flares in the compact jet downstream of the VLBI core are known to occur (e.g., Wehrle et al. 2001). Furthermore, Jorstad et al. (2001, 2010) have found that γ -ray flares often occur after superluminal knots have separated from the VLBI core. The results presented here support the inference that γ -ray emission still occurs parsecs downstream of the central engine, contrary to conclusions based on theoretical arguments (e.g., Tavecchio et al. 2010; Poutanen & Stern 2010). These arguments place the γ -ray emission zones within the broad-line region (BLR) at distances of $\lesssim 1$ pc from the central engine. Within this region a high number of optical–UV photons are produced (e.g. Kaspi et al. 2007), providing ideal conditions for inverse Compton scattering with relativistic electrons from the jet (e.g. Arshakian et al. 2011; Dermer et al. 1997). In addition, the observed variability time scales place constraints on the size of the emitting region due to causality arguments. Usually this size is related to the jet cross section, implying that the emission region is located close to the black hole. However, these standard assumptions do not necessarily need to be true.

In Section 7.2.1 it was shown that long-term trends observed at γ -ray and optical energies correlate with those of the radio emission at VLBI scales, which imply a common emission region. This emission region is related to the inner jet, extending over a distance of up to 23 pc from the VLBI core, which is at a distance of >1 pc from the central engine, well beyond the BLR. Additionally, it was found above, that the properties of the emission in this region are consistent with the Compton-loss stage of a shock (Section 7.1.2). Altogether, this contradicts the common theoretical high energy production scenario described in the previous paragraph. Recent observations of TeV emission from FSRQs (e.g. Aleksić et al. 2011) should not have been possible if the high energy emission site were within the BLR, which is expected to be opaque to γ -rays at TeV energies due to $\gamma\gamma$ interactions.

Agudo et al. (2011a) have reported on the location of a γ -ray flare in OJ 287, which was placed at a distance of more than 14 pc from the central engine. They proposed a model for the multi-wavelength emission where the high energy emission could be explained by the synchrotron self-Compton process or inverse Compton scattering of infrared radiation from a hot dusty torus, although it was concluded that the hot dusty

torus scenario is less likely. In the case of 3C 345 it seems to be clear that multiple compact emission features are responsible for the observed variability and what seems to be a reasonable model for the case of OJ 287, could apply for 3C 345 as well. A new plasma disturbance passes through a first conical shock in the core and produces a fast rise in high energy emission; as it continues to propagate down the jet it continues to produce high energy emission.

The short time scale variability of γ -ray emission is localized to a region between the VLBI core at 86.2 GHz and 0.1 mas. This corresponds to a deprojected region of 7.6 pc, which refers to a distance of up to 11 pc from the central engine, using the estimated distance of the core to the central engine at 86 GHz, derived from core-shift measurements presented in Chapter 5. In this scheme, γ -ray flares are shown to be produced in different but discrete regions of the jet and are related to relativistically moving features that pass through these regions.

The existence of a triple structure in relativistic jets are physically explained through the nature of collimated plasma flows. The physical properties of the jet flow are mainly determined through the initial flow speed (Lorentz factor) and the ratio between external and internal jet pressure. With the right conditions, an over-pressured jet and steep pressure gradients, leads to the formation of a standing shock. If the flow does not expand after this standing shock, e.g. due to the presence of a strong magnetic field, a series of so called re-collimation shocks is possible Daly & Marscher (1988). However, the formation of a series of standing shocks always requires steep pressure gradients between the jet and the external medium, which puts heavy constraints on the feasibility of this scenario.

An alternate interpretation for the formation of a triple structure could be provided by Kelvin-Helmholtz (K-H) surface instabilities Hardee (1983); Perucho et al. (2007). As above, this requires a pressure and velocity difference between the external medium and the interior of the jet, with the “shear” layer being the separation zone. This leads to the manifestation of instabilities in the form of waves, which are easily able to explain recurring patterns observed in relativistic jets. In particular at the transition from stratified to turbulent flows, these instabilities are very likely to be present. In addition, in contrast to the re-collimation scenario, the physical constraints leading to a repeating pattern of apparently standing features are more relaxed.

7.4 Conclusions

Based on 32 VLBA observations of 3C 345 at 43.2 GHz, the structure and evolution of the radio emission were investigated and was related to variations of the γ -ray and optical emission observed 2008–2010 by *Fermi*-LAT and a number of optical observatories. Four new moving emission features (jet components) were identified in the radio jet of 3C 345 and their evolution was analyzed. These regions were found to move at apparent speeds of 9–15 c , with the corresponding Doppler and Lorentz factors in the ranges of 12–23 and 12–15, respectively. The kinematic data strongly favor a viewing angle of 4.7° between the jet axis and the line of sight.

Evidence was brought forth for the γ -ray emission to be produced not in a compact region near the central engine of the AGN, but in the Compton-loss dominated zone

of the parsec-scale jet extending up to $r \approx 0.3$ mas, corresponding to a deprojected linear extent of ≈ 23 pc (accounting for the source distance and jet orientation). This zone is further marked by a break in the evolution of the brightness temperature, T_b , of the radio emission, with $T_b \propto r^{-(0.95 \pm 0.69)}$ at $r \leq 0.3$ mas and $T_b \propto r^{-(4.11 \pm 0.85)}$ at larger separations. Ejections of new superluminally moving and apparently accelerating features in the jet are linked to the flaring component of the γ -ray and optical emission.

It was demonstrated that the γ -ray emission region is barely resolved by VLBI observations at 43 GHz, but can be imaged at 86 GHz. The observed connection of radio kinematics with γ -ray variability shows strong, highly variable γ -ray emission to be produced in three discrete emission regions within the pc-scale jet. This is in contrast to the production within a few Schwarzschild radii to the central engine. Individual γ -ray events were connected with passages through features identified in the radio jet at 86 GHz, which could be a consequence of re-collimation shocks or K-H instabilities. For the first time, a working scheme is found that is able to explain all the observed γ -ray emission of a blazar in a consistent manner.

Altogether, these findings favor the synchrotron self-Compton mechanism of the high-energy emission production, while questioning the entire class of models that place the high energy emission site within 1 pc from the central engine of AGN, with external seed photons for inverse Compton scattering from the accretion disk or broad-line-region. They also imply that a significant part of the γ -ray emission is generated by highly-relativistic electrons propagating at a large bulk speed in the jet. In the context of newly emerging results, stimulated by Fermi data, more detailed analytical and numerical descriptions of such a scenario are clearly needed in order to explain the observed connection between radio and γ -ray variability. At the same time, continued monitoring and more densely sampled VLBI observations of well studied, bright blazar radio jets represent an essential requirement for improving the degree of detail and statistical accuracy of the correlation reported and further improving the spatial localization of individual flares in relativistic jets.

Summary and Concluding Remarks

Continuing the work started by Lobanov (1996) and Klare (2003), published, archival and new data of many different VLBI monitoring campaigns were combined to form a consistent database from which new insights into the physics of the jet of 3C 345 can be gained. This database covers over three decades of VLBI observations of the quasar 3C 345, forming one of the largest observational datasets of high angular resolution observations of a single quasar. In this work many of the results published on 3C 345 over the past thirty years have been reproduced and were used as a starting basis to expand and solidify our knowledge about the inner workings of the jet of 3C 345.

Simultaneous, multi-wavelength VLBI observations, covering a frequency range of 1.6 to 43.2 GHz, were used to investigate the frequency dependent position of the bright, narrow end of the jet (“core” of the jet). Not only frequency dependence (core-shift) but also time dependence of the position of the core was found, which was connected to a long-term change in the jet viewing angle and on short time scales to the brightness of the VLBI core. The average magnitude of the core-shift was shown to be consistent with equipartition between the jet particle and magnetic field energy densities. Magnetic field strengths obtained by combining the core-shift measurement with the kinematic properties of the jet are within a range of 0.011 and 0.60 Gauss at VLBI scales.

The kinematics of 22 jet components was determined, adding eight new components for which no kinematics have been obtained yet. From these the average values for the apparent component speed, Lorentz factor, Doppler factor and viewing angle were derived to be 12.5 c , 14.1, 15.6, and 3.8° respectively. However, most of the jet components showed significant variation in their apparent speeds and direction of motion. Further investigation of different scenarios showed that a changing intrinsic speed and changing viewing angle can reproduce the observed trajectories, while assumed parameters remain within physical limits. This shows that besides a change in the jet direction, leading to a change in the viewing angle, intrinsic acceleration is present.

The overall jet traced by the individual components has an intrinsic opening angle of $< 5^\circ$ and is extremely stable and well collimated up to deprojected distances of more than 750 pc. Patterns in the jet flow that were not well represented by the long-term fits to the trajectories revealed a standing oscillating pattern observed both in the motion and in the size evolution of individual jet components. These patterns resemble a perturbation in the jet flow and a slow rotation of the jet structure around the direction of the flow, which produces variations in the amplitudes of the observed pattern. These observations, together with the kinematics, support the theoretical scenario of a fast spine, slow sheath jet flow, which forms Kelvin-Helmholtz instabilities, perturbing the jet flow at parsec-scale distances. The instability pattern found, if being a result of Kelvin-Helmholtz instabilities, paired with simulations, could be used to obtain a measure for the jet particle densities and possibly provide insights into the matter composition of the jet, one of the major remaining questions on relativistic extragalactic jets.

The quasar 3C 345 was unequivocally identified as γ -ray emitting object, combining multi-wavelength localizations and variability. This sets the record straight on the so far lacking identification of high energy emission from this prominent blazar. Continuous monitoring at γ -ray, optical and radio energies since 2008 revealed a connection between the radio jet within 30 pc from the central engine. This particular region of the jet was found to be Compton loss dominated with a transition to synchrotron loss dominance observed beyond a distance of 30 pc.

Underlying emission at optical and γ -ray energies were shown to match that of newly observed jet features at 43.2 GHz. This implies that not a single emission region is responsible for the observed emission, but multiple interaction zones and multiple simultaneously emitting regions. This questions the simplification to a single homogeneous emission region found in many γ -ray emission models. Short term γ -ray flares were connected to the propagation of multiple moving features in the jet interacting with something in the general jet flow at distinct distances. These interaction zones form a triple structure at distances of 6.3, 10, and 14 pc from the central engine. This exact structure was found as brightness enhanced regions in the jet emission observed at 86.2 GHz, confirming the predicted interaction zones and directly imaging the γ -ray emission sites. Altogether, these findings provide proof beyond any doubt that most if not all of the high energy emission that is observed in this case is produced at parsec scales and not only in regions within a few Schwarzschild radii of the central engine, questioning most of the established theoretical γ -ray emission scenarios. The triple structure itself could be the consequence of multiple recollimation shocks and/or sharp bends in the jet that lead to a fast variation in the intrinsic Doppler factor within these particular regions.

What remains to be verified is whether what has been found to be valid for 3C 345 would apply also to other well known and frequently observed blazars such as 3C 454.3, 3C 279 or 3C 273. Major observing campaigns are underway studying multi-wavelength emission from those objects, which will very likely provide similar conclusions to what has been found for 3C 345 and is going to provide a more general statement on the properties of the whole class of flat spectrum radio quasars. Further analysis of the database of the VLBI observations of 3C 345 is going to provide deeper insights into the spectral evolution of different components, polarization properties, etc. With the application of novel analysis methods, going beyond representation of source struc-

ture by two-dimensional Gaussian patterns, even more information could be extracted from this very unique dataset. The potential insights that would be gained from further, more detailed investigations are truly ground-breaking, making this database an invaluable asset.

This database will be continued, broadened and enhanced, benefiting from a continuation of Fermi/LAT observations beyond 2012 and from new observational capabilities by the sensitivity upgrade of the VLBA and the Expanded Very Large Array. New dimensions will be added to this study by the planned inclusion of observations at the Panoramic Survey Telescope & Rapid Response System (PanStarrs), the Atacama Large Millimeter Array (ALMA), and VLBI observations at 1 mm and with orbiting antennas. Extending and expanding this truly unique observational program will surely provide key answers to the outstanding issues and questions about the formation and propagation of relativistic flows as well as their connection to intricate processes in the vicinity of supermassive black holes and in the central regions of active galaxies.

APPENDIX A

Historic VLBI Observations

In this appendix the characteristics of historic VLBI observations described in the literature and used for the thesis work from which published modelfit values were obtained and used. The modelfit parameters and characteristics of those observations, including references to the literature are provided in Table A.1

Table A.1: Historic Observations.

Date	ν_{obs}	S_{tot}	L	S	r	Φ	d	ratio	cpa	Ref.
1979-04-02	5.0	7.5	D	4.30 ± 0.3	0.000 ± 0.0	0.0 ± 0.0	1.50 ± 0.2	1.0	-	(1)
			C3	2.30 ± 0.2	1.190 ± 0.04	-80.0 ± 3.0	0.90 ± 0.4	1.0	-	
			C2	0.90 ± 0.2	3.640 ± 0.15	-72.0 ± 2.0	1.40 ± 0.6	1.0	-	
1979-06-10	10.7	8.5	D	4.45 ± 0.45	0.000 ± 0.0	0.0 ± 0.0	0.52 ± 0.07	1.0	-	(1)
			C3a	1.43 ± 0.65	0.540 ± 0.02	-104.0 ± 3.0	0.64 ± 0.26	1.0	-	
			C3	1.95 ± 0.13	1.400 ± 0.02	-89.1 ± 0.9	0.85 ± 0.05	1.0	-	
1979-12-02	5.0	6.5	C2	0.70 ± 1.0	4.200 ± 0.3	-76.0 ± 6.0	1.40 ± 1.2	1.0	-	
			D	2.66 ± 0.14	0.000 ± 0.0	0.0 ± 0.0	1.14 ± 0.16	1.0	-	(1)
			C3	2.62 ± 0.12	1.240 ± 0.1	-85.7 ± 1.1	0.99 ± 0.17	1.0	-	
1980-07-09	10.7	10.5	C2	1.20 ± 0.12	3.980 ± 0.1	-74.3 ± 1.1	1.72 ± 0.17	1.0	-	
			D	4.40 ± 1.4	0.000 ± 0.0	0.0 ± 0.0	0.24 ± 0.12	1.0	-	(1)
			C4	3.40 ± 1.3	0.250 ± 0.02	-135.0 ± 4.0	0.32 ± 0.13	1.0	-	
			C3a	0.86 ± 0.15	1.040 ± 0.06	-97.0 ± 4.0	0.98 ± 0.12	1.0	-	
1980-09-24	5.0	7.4	C3	1.02 ± 0.11	1.800 ± 0.04	-87.4 ± 0.8	0.79 ± 0.09	1.0	-	
			C2	0.80 ± 0.18	4.280 ± 0.1	-74.0 ± -2.0	2.00 ± 1.2	1.0	-	
			D	4.28 ± 0.08	0.000 ± 0.0	0.0 ± 0.0	1.10 ± 0.05	1.0	-	(1)
			C3	2.25 ± 0.1	1.590 ± 0.02	-81.6 ± 0.7	1.30 ± 0.08	1.0	-	
1981-02-03	10.7	12.8	C2	0.87 ± 0.08	4.370 ± 0.07	-73.0 ± 0.8	1.70 ± 0.2	1.0	-	
			D	6.60 ± 0.5	0.000 ± 0.0	0.0 ± 0.0	0.06 ± 0.06	1.0	-	(1)
			C4	3.60 ± 0.4	0.325 ± 0.01	-131.0 ± 2.0	0.20 ± 0.09	1.0	-	
			C3a	0.52 ± 0.23	1.150 ± 0.11	-108.0 ± 9.0	0.80 ± 0.4	1.0	-	
1981-04-02	22.2	13.9	C3	1.11 ± 0.26	2.000 ± 0.11	-84.0 ± 2.0	1.17 ± 0.36	1.0	-	
			C2	1.00 ± 1.0	4.600 ± 0.4	-72.0 ± 4.0	2.80 ± 1.9	1.0	-	
			D	9.80 ± 0.2	0.000 ± 0.0	0.0 ± 0.0	0.14 ± 0.02	1.0	-	(1)
			C4	3.22 ± 0.16	0.377 ± 0.0	-126.5 ± 1.2	0.26 ± 0.03	1.0	-	
1981-08-18	5.0	9.9	C3a	0.30 ± 0.1	1.110 ± 0.1	-99.0 ± -5.0	0.30 ± 0.2	1.0	-	
			C3	0.55 ± 0.13	1.950 ± 0.16	-86.0 ± 4.0	0.80 ± 0.2	1.0	-	
			D	6.57 ± 0.08	0.000 ± 0.0	0.0 ± 0.0	1.08 ± 0.05	1.0	-	(1)
1981-11-21	2.3	6.3	C3	1.99 ± 0.07	1.760 ± 0.02	-82.9 ± 0.8	1.63 ± 0.08	1.0	-	
			C2	1.33 ± 0.13	4.610 ± 0.05	-71.3 ± 0.7	2.80 ± 0.2	1.0	-	
1981-11-21	2.3	6.3	D	1.54 ± 0.25	0.000 ± 0.0	0.0 ± 0.0	1.60 ± 0.6	1.0	-	(1)
			C3	2.42 ± 0.25	1.700 ± 0.04	-78.9 ± 1.4	1.90 ± 0.5	1.0	-	

Continued on next page ...

Table A.1 – *continued from previous page*

Date	ν_{obs}	S_{tot}	L	S	r	Φ	d	ratio	cpa	Ref.
1999-05-18	43.2	5.6	C9	1.03 ± 0.05	0.865 ± 0.02	-113.4 ± 2.0	0.18 ± 0.05	1.0	-	
			C8	0.60 ± 0.1	1.472 ± 0.05	-94.9 ± 2.0	0.28 ± 0.1	1.0	-	
			C7	0.50 ± 0.1	2.630 ± 0.2	-93.2 ± 3.0	0.81 ± 0.1	1.0	-	
			D	1.47 ± 0.3	0.000 ± 0.0	0.0 ± 0.0	0.06 ± 0.01	1.0	-	(9)
			C12	2.60 ± 0.2	0.116 ± 0.01	-90.3 ± 1.0	0.12 ± 0.01	1.0	-	
			C11	0.22 ± 0.02	0.278 ± 0.02	-71.1 ± 1.0	0.07 ± 0.01	1.0	-	
1999-07-01	1.6	7.4	C9	0.88 ± 0.02	1.126 ± 0.03	-107.0 ± 1.0	0.30 ± 0.02	0.61	-13.2	
			C8	0.24 ± 0.04	1.709 ± 0.2	-95.0 ± 2.0	0.47 ± 0.12	0.57	-2.3	
			C7	0.17 ± 0.04	3.037 ± 0.2	-102.2 ± 9.0	0.88 ± 0.5	1.0	-	
			D	0.40 ± 0.3	0.000 ± 0.0	0.0 ± 0.0	0.35 ± 0.1	1.0	-	(9)
			C9	1.86 ± 0.3	0.697 ± 0.16	-98.5 ± 6.0	0.35 ± 0.1	1.0	-	
			C8	1.33 ± 0.3	1.444 ± 0.16	-90.6 ± 5.0	0.35 ± 0.1	1.0	-	
1999-07-02	5.0	7.9	C7	1.26 ± 0.05	2.614 ± 0.16	-95.1 ± 1.0	0.75 ± 0.1	1.0	-	
			C5	0.71 ± 0.1	5.455 ± 0.4	-70.4 ± 2.0	2.31 ± 0.4	1.0	-	
			C4	0.64 ± 0.1	8.024 ± 0.4	-66.9 ± 2.0	2.68 ± 0.4	1.0	-	
			C3	0.43 ± 0.2	12.819 ± 1.0	-73.4 ± 3.0	6.84 ± 0.8	0.51	-63.3	
			C1	0.48 ± 0.2	21.385 ± 2.0	-55.6 ± 3.0	12.03 ± 1.0	0.6	-76.8	
			C0	0.25 ± 0.1	44.068 ± 5.0	-52.3 ± 3.0	44.47 ± 3.0	0.53	-31.0	
			D	1.80 ± 0.03	0.000 ± 0.0	0.0 ± 0.0	0.41 ± 0.01	0.53	82.6	(9)
			C9	3.04 ± 0.03	0.823 ± 0.02	-105.3 ± 0.5	0.55 ± 0.01	0.81	51.0	
			C7a	1.21 ± 0.03	1.379 ± 0.02	-89.4 ± 0.5	0.59 ± 0.01	0.65	-84.9	
			C7	0.86 ± 0.05	2.595 ± 0.02	-95.7 ± 0.5	1.06 ± 0.04	0.61	-63.2	
1999-09-01	1.6	7.6	C5	0.16 ± 0.05	5.156 ± 0.1	-78.3 ± 2.0	1.30 ± 0.1	1.0	-	
			C4	0.45 ± 0.05	7.255 ± 0.2	-67.4 ± 2.0	2.66 ± 0.2	1.0	-	
			C3	0.19 ± 0.05	11.190 ± 1.0	-75.1 ± 2.0	5.03 ± 0.2	0.8	-88.0	
			C1	0.15 ± 0.05	19.060 ± 1.5	-53.8 ± 5.0	6.21 ± 0.5	0.72	-81.0	
			D	0.90 ± 0.3	0.000 ± 0.0	0.0 ± 0.0	0.38 ± 0.2	1.0	-	(9)
			C9	1.80 ± 0.3	0.663 ± 0.16	-92.6 ± 5.0	0.34 ± 0.2	1.0	-	
			C8	1.05 ± 0.3	1.300 ± 0.16	-85.7 ± 5.0	0.35 ± 0.2	1.0	-	
			C7	1.26 ± 0.05	2.364 ± 0.15	-95.3 ± 1.0	0.97 ± 0.1	0.82	-69.9	
			C5	0.71 ± 0.1	5.285 ± 0.4	-69.9 ± 2.0	2.31 ± 0.4	1.0	-	
			C4	0.64 ± 0.1	7.856 ± 0.4	-65.7 ± 2.0	2.59 ± 0.4	1.0	-	
1999-09-10	5.0	9.3	C3	0.47 ± 0.2	12.511 ± 1.0	-72.4 ± 2.0	7.07 ± 0.8	0.51	-60.2	
			C1	0.48 ± 0.2	21.195 ± 2.0	-54.6 ± 3.0	11.62 ± 1.0	0.61	-81.9	
			C0	0.31 ± 0.1	45.853 ± 5.0	-50.5 ± 3.0	43.34 ± 3.0	0.44	-34.5	
			D	2.17 ± 0.04	0.000 ± 0.0	0.0 ± 0.0	0.19 ± 0.01	0.6	-76.9	(9)
			C9	1.12 ± 0.04	0.482 ± 0.02	-102.2 ± 0.5	0.32 ± 0.01	1.0	-	
			C8	2.75 ± 0.03	0.977 ± 0.02	-103.3 ± 0.5	0.43 ± 0.01	0.71	5.7	
			C7b	1.24 ± 0.03	1.486 ± 0.02	-88.4 ± 0.5	0.60 ± 0.0	0.7	-54.6	
			C7	0.87 ± 0.05	2.686 ± 0.05	-95.9 ± 0.5	1.02 ± 0.04	0.57	-52.6	
			C5	0.30 ± 0.05	5.302 ± 0.5	-74.0 ± 2.0	2.22 ± 0.1	1.0	-	
			C4	0.40 ± 0.05	7.803 ± 1.0	-68.5 ± 2.0	2.60 ± 0.2	1.0	-	
			C3	0.19 ± 0.05	11.340 ± 1.2	-74.5 ± 2.0	8.19 ± 0.2	0.28	-66.0	
			C1	0.28 ± 0.05	21.230 ± 2.0	-56.3 ± 3.0	13.25 ± 0.5	0.71	-60.0	

Notes: **Date** – date of the observation; ν_{obs} – observation frequency in units of GHz; S_{tot} – sum of component flux densities in units of Jy; **L** – component label; **S** – component flux density in units of Jy; r – distance from map center in mas; Φ – position angle to the map center in $^{\circ}$; d – component FWHM size in mas; **ratio** – in case of an elliptical Gaussian component, this number provides the axial ratio between the major and minor axis; **cpa** – is then the rotation angle of the ellipse (North through West); **Ref.** – references: (0) Unwin 1992 *unpublished*; (1) Biretta et al. (1986); (2) Zensus et al. (1995); (3) Bååth et al. (1992); (4) Lobanov (1996); (5) Unwin & Wehrle (1992); (6) Unwin et al. (1994); (7) Krichbaum et al. (1993); (8) Leppänen et al. (1995); (9) Klare (2003).

APPENDIX B

Modelfit Parameters of Reanalyzed Observations

This appendix presents new images and modelfits obtained as part of this project. Modelfit parameters for all newly analyzed VLBI observations are listed in Table B.1. Figures B.1 through B.6 show the maps for the observations listed in Table 4.1. To facilitate visual comparison, the contour levels are the same within each figure, as indicated in the figure captions. The contour levels are selected so as to show the extended emission in high dynamic range maps, thus noise like features can be seen in some of the plotted maps with low dynamic range (cf. Table 4.1). Observations at 23.8 GHz were imaged, but not modelfitted, since simultaneous observations at 15.4 and 43.2 GHz provide redundant information on jet component parameters.

Table B.1: Historic Observations.

Date	ν_{obs}	S_{tot}	L	S	r	Φ	d	ratio	cpa
1994-05-28	15.4	7.6	D	3.66 ± 0.26	0.045 ± 0.02	76.7 ± 22.43	0.18 ± 0.04	1.0	-
			C8	1.31 ± 0.15	0.260 ± 0.03	-88.9 ± 6.75	0.25 ± 0.06	1.0	-
			C7	1.89 ± 0.16	0.836 ± 0.02	-96.9 ± 1.65	0.31 ± 0.05	1.0	-
			C5	0.19 ± 0.05	3.071 ± 0.17	-85.0 ± 3.19	1.28 ± 0.34	1.0	-
			C4	0.40 ± 0.07	5.809 ± 0.19	-70.6 ± 1.92	2.27 ± 0.39	1.0	-
			C3	0.10 ± 0.05	9.323 ± 0.82	-69.3 ± 5.03	3.10 ± 1.64	1.0	-
1995-04-07	15.3	8.6	D	5.69 ± 0.77	0.000 ± 0.02	0.0 ± 0.0	0.36 ± 0.04	1.0	-
			C8	0.15 ± 0.14	0.329 ± 0.32	-106.9 ± 44.42	0.37 ± 0.64	1.0	-
			C7	2.23 ± 0.5	0.944 ± 0.05	-94.4 ± 3.27	0.56 ± 0.11	1.0	-
			C5	0.21 ± 0.13	3.833 ± 0.57	-90.5 ± 8.5	1.89 ± 1.15	1.0	-
			C4	0.33 ± 0.18	6.111 ± 0.56	-72.7 ± 5.27	2.16 ± 1.13	1.0	-
1995-06-06	15.3	9.5	D	3.13 ± 0.16	0.110 ± 0.01	50.9 ± 7.72	0.22 ± 0.03	1.0	-
			C8	3.27 ± 0.17	0.195 ± 0.02	-119.1 ± 4.48	0.24 ± 0.03	1.0	-
			C7	1.91 ± 0.15	0.925 ± 0.03	-93.8 ± 1.78	0.50 ± 0.06	1.0	-
			C7a	0.36 ± 0.06	1.361 ± 0.04	-94.8 ± 1.87	0.22 ± 0.09	1.0	-
			C5	0.34 ± 0.16	3.328 ± 0.66	-85.4 ± 11.14	2.72 ± 1.31	1.0	-
			C4	0.19 ± 0.07	5.601 ± 0.28	-74.0 ± 2.88	1.53 ± 0.56	1.0	-
			C3a	0.28 ± 0.08	7.370 ± 0.25	-62.7 ± 1.91	1.51 ± 0.49	1.0	-
1995-06-24	5.0	7.4	D	2.83 ± 0.1	0.437 ± 0.02	89.8 ± 3.2	0.28 ± 0.05	1.0	-
			C8	1.89 ± 0.08	0.285 ± 0.03	-88.7 ± 6.09	0.13 ± 0.06	1.0	-
			C7	1.34 ± 0.06	0.750 ± 0.03	-94.5 ± 2.55	0.54 ± 0.07	1.0	-
			C5	0.25 ± 0.03	2.698 ± 0.1	-80.2 ± 2.15	1.36 ± 0.2	1.0	-

Continued on next page ...

Table B.1 – *continued from previous page*

Date	ν_{obs}	Stot	L	S	r	Φ	d	ratio	cpa
1999-07-17	43.2	9.6	C6	0.07 ± 0.05	3.632 ± 0.17	-84.1 ± 2.68	0.10 ± 0.34	1.0	-
			C5	0.38 ± 0.17	5.911 ± 0.52	-71.8 ± 5.07	2.31 ± 1.05	1.0	-
			D	2.50 ± 0.15	0.059 ± 0.01	97.1 ± 5.27	0.00 ± 0.01	1.0	-
			C13	2.99 ± 0.15	0.037 ± 0.0	-90.9 ± 7.1	0.05 ± 0.01	1.0	-
			C12	1.58 ± 0.16	0.138 ± 0.01	-97.3 ± 4.26	0.08 ± 0.02	1.0	-
			C10	0.60 ± 0.18	0.660 ± 0.08	-99.1 ± 6.85	0.51 ± 0.16	1.0	-
			C9	1.09 ± 0.18	1.108 ± 0.02	-106.9 ± 1.03	0.17 ± 0.04	1.0	-
1999-07-19	15.3	9.0	C8	0.60 ± 0.14	1.588 ± 0.07	-92.5 ± 2.45	0.57 ± 0.14	1.0	-
			C7	0.20 ± 0.05	2.837 ± 0.08	-97.7 ± 1.71	0.60 ± 0.17	1.0	-
			D	4.93 ± 0.2	0.022 ± 0.01	132.9 ± 28.42	0.17 ± 0.02	1.0	-
			C10	0.71 ± 0.06	0.441 ± 0.03	-96.5 ± 3.85	0.38 ± 0.06	1.0	-
			C9	1.81 ± 0.1	1.020 ± 0.02	-106.9 ± 1.0	0.26 ± 0.04	1.0	-
			C8	0.91 ± 0.08	1.530 ± 0.04	-92.9 ± 1.46	0.61 ± 0.08	1.0	-
			C7	0.35 ± 0.04	2.786 ± 0.05	-96.6 ± 0.99	0.64 ± 0.1	1.0	-
1999-07-30	5.0	8.6	C5	0.10 ± 0.04	5.261 ± 0.5	-77.0 ± 5.4	2.09 ± 0.99	1.0	-
			C4	0.23 ± 0.09	7.560 ± 0.58	-66.2 ± 4.4	2.91 ± 1.16	1.0	-
			D	2.41 ± 0.16	0.694 ± 0.05	82.3 ± 4.15	0.44 ± 0.1	1.0	-
			C9	4.04 ± 0.22	0.257 ± 0.04	-99.9 ± 9.56	0.59 ± 0.09	1.0	-
			C7	1.06 ± 0.13	1.727 ± 0.11	-91.6 ± 3.81	1.06 ± 0.23	1.0	-
			C5	0.24 ± 0.05	4.491 ± 0.27	-70.5 ± 3.41	2.06 ± 0.54	1.0	-
			C4	0.48 ± 0.11	7.053 ± 0.39	-64.4 ± 3.14	2.95 ± 0.77	1.0	-
1999-07-30	8.4	9.0	C2	0.36 ± 0.11	15.948 ± 1.79	-61.9 ± 6.4	11.81 ± 3.58	1.0	-
			D	0.28 ± 0.1	1.048 ± 0.16	64.7 ± 8.82	0.10 ± 0.33	1.0	-
			C9	4.09 ± 0.29	0.071 ± 0.03	112.6 ± 25.01	0.29 ± 0.07	1.0	-
			C8	3.17 ± 0.24	0.932 ± 0.04	-102.3 ± 2.35	0.52 ± 0.08	1.0	-
			C7	0.36 ± 0.06	1.708 ± 0.08	-84.9 ± 2.6	0.10 ± 0.16	1.0	-
			C6	0.55 ± 0.08	2.676 ± 0.09	-98.0 ± 1.84	0.77 ± 0.17	1.0	-
			C5	0.53 ± 0.15	6.733 ± 0.46	-68.2 ± 3.93	3.17 ± 0.92	1.0	-
1999-07-30	15.4	9.5	D	5.09 ± 0.32	0.028 ± 0.02	86.5 ± 31.59	0.18 ± 0.03	1.0	-
			C10	0.97 ± 0.1	0.464 ± 0.04	-93.6 ± 4.72	0.56 ± 0.08	1.0	-
			C9	1.67 ± 0.18	1.015 ± 0.03	-106.7 ± 1.73	0.24 ± 0.06	1.0	-
			C8	0.97 ± 0.14	1.498 ± 0.06	-92.7 ± 2.23	0.62 ± 0.12	1.0	-
			C7	0.37 ± 0.07	2.761 ± 0.08	-96.9 ± 1.61	0.61 ± 0.16	1.0	-
			C5	0.14 ± 0.06	4.933 ± 0.42	-73.7 ± 4.91	1.88 ± 0.85	1.0	-
			C4	0.28 ± 0.1	7.592 ± 0.5	-67.0 ± 3.77	2.83 ± 1.0	1.0	-
1999-07-30	22.2	6.1	D	1.43 ± 0.16	0.079 ± 0.02	119.2 ± 14.71	0.05 ± 0.04	1.0	-
			C12	2.56 ± 0.22	0.048 ± 0.02	-69.9 ± 19.1	0.14 ± 0.03	1.0	-
			C10	0.56 ± 0.11	0.648 ± 0.06	-106.5 ± 5.49	0.51 ± 0.12	1.0	-
			C9	0.78 ± 0.12	1.078 ± 0.03	-106.2 ± 1.61	0.13 ± 0.06	1.0	-
			C8	0.57 ± 0.12	1.494 ± 0.07	-93.3 ± 2.7	0.60 ± 0.14	1.0	-
			C7	0.24 ± 0.06	2.786 ± 0.11	-96.7 ± 2.35	0.77 ± 0.23	1.0	-
			D	2.53 ± 0.23	0.043 ± 0.01	97.8 ± 13.03	0.06 ± 0.02	1.0	-
1999-07-30	43.2	5.8	C12	1.81 ± 0.2	0.095 ± 0.01	-87.6 ± 7.77	0.10 ± 0.03	1.0	-
			C10	0.36 ± 0.12	0.681 ± 0.09	-101.1 ± 7.88	0.51 ± 0.19	1.0	-
			C9	0.64 ± 0.1	1.109 ± 0.02	-106.4 ± 1.07	0.15 ± 0.04	1.0	-
			C8	0.28 ± 0.08	1.571 ± 0.08	-91.1 ± 3.0	0.51 ± 0.16	1.0	-
			C7	0.14 ± 0.05	2.613 ± 0.16	-99.7 ± 3.53	0.85 ± 0.32	1.0	-
			D	3.95 ± 0.3	0.090 ± 0.04	102.0 ± 21.43	0.32 ± 0.07	1.0	-
			C9	3.30 ± 0.23	0.888 ± 0.04	-103.3 ± 2.31	0.52 ± 0.07	1.0	-
1999-08-08	8.4	8.9	C7a	0.48 ± 0.07	1.602 ± 0.07	-88.4 ± 2.44	0.04 ± 0.14	1.0	-
			C7	0.60 ± 0.07	2.651 ± 0.07	-96.5 ± 1.59	0.81 ± 0.15	1.0	-
			C4	0.53 ± 0.1	6.739 ± 0.35	-69.3 ± 2.94	3.61 ± 0.69	1.0	-
			D	4.80 ± 0.18	0.012 ± 0.01	77.0 ± 39.78	0.17 ± 0.02	1.0	-
			C10	0.78 ± 0.06	0.416 ± 0.03	-92.2 ± 3.56	0.40 ± 0.05	1.0	-
			C9	1.82 ± 0.13	1.028 ± 0.02	-104.6 ± 1.18	0.30 ± 0.04	1.0	-
			C8	0.82 ± 0.08	1.565 ± 0.04	-91.9 ± 1.5	0.60 ± 0.08	1.0	-
1999-08-08	15.4	8.9	C7	0.32 ± 0.06	2.815 ± 0.06	-96.8 ± 1.31	0.55 ± 0.13	1.0	-
			C5	0.14 ± 0.04	5.229 ± 0.35	-76.8 ± 3.87	2.40 ± 0.71	1.0	-
			C4	0.18 ± 0.07	7.593 ± 0.47	-66.7 ± 3.52	2.39 ± 0.93	1.0	-
			D	1.99 ± 0.16	0.066 ± 0.01	103.8 ± 11.62	0.03 ± 0.03	1.0	-
			C12	1.74 ± 0.16	0.087 ± 0.02	-81.9 ± 10.55	0.09 ± 0.03	1.0	-
			C10	0.49 ± 0.1	0.613 ± 0.06	-100.8 ± 5.74	0.50 ± 0.12	1.0	-
			C9	0.79 ± 0.11	1.078 ± 0.03	-105.7 ± 1.48	0.16 ± 0.06	1.0	-
1999-08-08	22.2	5.9	C8	0.50 ± 0.1	1.521 ± 0.07	-92.8 ± 2.57	0.61 ± 0.14	1.0	-
			C7	0.16 ± 0.03	2.805 ± 0.07	-97.3 ± 1.39	0.56 ± 0.14	1.0	-
			C4	0.22 ± 0.11	7.121 ± 0.88	-66.3 ± 7.08	3.53 ± 1.77	1.0	-
			D	2.88 ± 0.28	0.046 ± 0.01	100.1 ± 13.09	0.06 ± 0.02	1.0	-
			C12	2.50 ± 0.28	0.091 ± 0.01	-89.0 ± 8.59	0.12 ± 0.03	1.0	-
			C10	0.41 ± 0.14	0.602 ± 0.09	-98.4 ± 8.39	0.50 ± 0.18	1.0	-
			C9	0.85 ± 0.11	1.104 ± 0.02	-106.3 ± 0.92	0.17 ± 0.04	1.0	-
1999-08-08	43.2	7.1	C8	0.41 ± 0.1	1.558 ± 0.08	-91.8 ± 2.88	0.59 ± 0.16	1.0	-

Continued on next page ...

Table B.1 – *continued from previous page*

Date	ν_{obs}	S_{tot}	L	S	r	Φ	d	ratio	cpa
1999-08-23	15.4	8.8	C7	0.10 ± 0.03	2.819 ± 0.08	-98.4 ± 1.57	0.39 ± 0.15	1.0	-
			D	4.98 ± 0.26	0.038 ± 0.02	128.4 ± 21.69	0.24 ± 0.03	0.56	-73.9
			C10	1.11 ± 0.08	0.589 ± 0.03	-102.6 ± 3.23	0.70 ± 0.07	0.74	66.1
			C9	1.26 ± 0.09	1.034 ± 0.02	-107.0 ± 1.14	0.18 ± 0.04	1.0	-
			C8	0.88 ± 0.08	1.498 ± 0.04	-93.6 ± 1.41	0.62 ± 0.07	1.0	-
1999-08-23	22.2	5.0	C7	0.36 ± 0.06	2.768 ± 0.07	-97.3 ± 1.36	0.59 ± 0.13	1.0	-
			C5	0.24 ± 0.1	5.623 ± 0.88	-76.7 ± 8.85	4.15 ± 1.75	1.0	-
			D	2.35 ± 0.15	0.038 ± 0.01	78.6 ± 18.01	0.05 ± 0.03	1.0	-
			C12	1.08 ± 0.1	0.106 ± 0.02	-96.1 ± 9.89	0.05 ± 0.04	1.0	-
			C10	0.36 ± 0.08	0.607 ± 0.04	-111.4 ± 4.2	0.20 ± 0.09	1.0	-
1999-08-23	43.2	5.5	C9	0.80 ± 0.1	1.082 ± 0.03	-103.4 ± 1.49	0.21 ± 0.06	1.0	-
			C8	0.33 ± 0.07	1.615 ± 0.06	-96.0 ± 2.08	0.42 ± 0.12	1.0	-
			C7	0.11 ± 0.03	2.879 ± 0.08	-97.7 ± 1.52	0.35 ± 0.15	1.0	-
			D	2.59 ± 0.4	0.029 ± 0.02	101.7 ± 30.61	0.10 ± 0.03	1.0	-
			C13	1.39 ± 0.25	0.113 ± 0.02	-94.0 ± 10.6	0.13 ± 0.04	1.0	-
1999-10-06	43.2	5.5	C11	0.39 ± 0.11	0.446 ± 0.04	-122.9 ± 5.7	0.23 ± 0.09	1.0	-
			C9	0.71 ± 0.15	1.120 ± 0.03	-105.9 ± 1.62	0.21 ± 0.06	1.0	-
			C8	0.30 ± 0.14	1.618 ± 0.21	-93.0 ± 7.53	0.90 ± 0.43	1.0	-
			C7	0.08 ± 0.04	2.995 ± 0.11	-99.4 ± 2.17	0.38 ± 0.23	1.0	-
			D	1.72 ± 0.08	0.054 ± 0.01	94.3 ± 6.07	0.04 ± 0.01	1.0	-
1999-12-05	43.2	6.2	C14	1.52 ± 0.07	0.044 ± 0.01	-79.3 ± 7.64	0.03 ± 0.01	1.0	-
			C12	1.02 ± 0.07	0.201 ± 0.01	-95.7 ± 2.61	0.11 ± 0.02	1.0	-
			C10	0.28 ± 0.07	0.715 ± 0.06	-96.1 ± 4.88	0.42 ± 0.12	1.0	-
			C9	0.57 ± 0.06	1.145 ± 0.01	-104.2 ± 0.75	0.17 ± 0.03	1.0	-
			C8	0.29 ± 0.06	1.605 ± 0.07	-91.8 ± 2.61	0.61 ± 0.15	1.0	-
2000-01-24	43.2	5.8	C7	0.09 ± 0.02	2.872 ± 0.07	-97.7 ± 1.32	0.47 ± 0.13	1.0	-
			D	2.92 ± 0.19	0.011 ± 0.01	10.3 ± 33.72	0.08 ± 0.01	1.0	-
			C14	1.20 ± 0.1	0.113 ± 0.01	-74.9 ± 4.7	0.03 ± 0.02	1.0	-
			C12	0.73 ± 0.11	0.295 ± 0.02	-90.7 ± 3.98	0.17 ± 0.04	1.0	-
			C10	0.32 ± 0.07	0.781 ± 0.04	-98.0 ± 2.88	0.30 ± 0.08	1.0	-
2000-02-04	5.0	8.6	C9	0.52 ± 0.06	1.207 ± 0.02	-101.9 ± 0.71	0.17 ± 0.03	1.0	-
			C8	0.43 ± 0.11	1.522 ± 0.09	-92.3 ± 3.55	0.73 ± 0.19	1.0	-
			C7	0.10 ± 0.03	2.923 ± 0.08	-97.0 ± 1.53	0.46 ± 0.16	1.0	-
			D	1.28 ± 0.11	0.069 ± 0.01	93.5 ± 5.85	0.03 ± 0.01	1.0	-
			C14	1.85 ± 0.13	0.031 ± 0.01	-86.3 ± 10.55	0.03 ± 0.01	1.0	-
2000-02-04	8.4	8.4	C13	0.89 ± 0.1	0.151 ± 0.01	-79.5 ± 4.08	0.10 ± 0.02	1.0	-
			C11	0.40 ± 0.08	0.361 ± 0.02	-99.4 ± 3.48	0.13 ± 0.04	1.0	-
			C10	0.43 ± 0.1	0.811 ± 0.05	-99.2 ± 3.21	0.34 ± 0.09	1.0	-
			C9	0.40 ± 0.06	1.227 ± 0.01	-101.6 ± 0.69	0.13 ± 0.03	1.0	-
			C8	0.45 ± 0.12	1.478 ± 0.09	-94.6 ± 3.58	0.67 ± 0.19	1.0	-
2000-02-04	15.4	7.5	C7	0.10 ± 0.03	2.997 ± 0.09	-95.8 ± 1.81	0.55 ± 0.19	1.0	-
			D	2.76 ± 0.12	0.587 ± 0.03	83.2 ± 3.15	0.32 ± 0.06	1.0	-
			C9	2.36 ± 0.12	0.202 ± 0.04	-106.7 ± 10.37	0.30 ± 0.07	1.0	-
			C8	1.92 ± 0.09	0.762 ± 0.04	-90.1 ± 3.03	0.74 ± 0.08	1.0	-
			C7	0.62 ± 0.04	2.242 ± 0.06	-92.7 ± 1.52	0.75 ± 0.12	1.0	-
2000-02-04	22.2	6.0	C5	0.25 ± 0.05	4.575 ± 0.24	-71.6 ± 2.99	2.22 ± 0.48	1.0	-
			C4	0.38 ± 0.08	7.223 ± 0.31	-65.1 ± 2.43	2.70 ± 0.61	1.0	-
			C2	0.34 ± 0.1	14.996 ± 1.54	-64.4 ± 5.87	10.71 ± 3.08	1.0	-
			D	3.17 ± 0.15	0.164 ± 0.02	86.5 ± 7.53	0.19 ± 0.04	1.0	-
			C10	1.63 ± 0.11	0.355 ± 0.03	-100.5 ± 5.42	0.46 ± 0.07	1.0	-
2000-02-04	22.2	6.0	C9	1.56 ± 0.09	0.965 ± 0.03	-102.2 ± 1.63	0.37 ± 0.06	1.0	-
			C8	1.01 ± 0.06	1.362 ± 0.04	-90.7 ± 1.56	0.81 ± 0.07	1.0	-
			C7	0.44 ± 0.05	2.741 ± 0.06	-95.7 ± 1.34	0.68 ± 0.13	1.0	-
			C5	0.16 ± 0.04	4.991 ± 0.28	-75.1 ± 3.22	2.02 ± 0.56	1.0	-
			C4	0.26 ± 0.05	7.590 ± 0.29	-67.1 ± 2.19	2.70 ± 0.58	1.0	-
2000-02-04	22.2	6.0	C2	0.12 ± 0.05	13.098 ± 1.37	-72.8 ± 5.98	6.07 ± 2.74	1.0	-
			D	2.69 ± 0.14	0.073 ± 0.01	86.3 ± 10.04	0.00 ± 0.03	1.0	-
			C12	1.79 ± 0.12	0.124 ± 0.02	-93.2 ± 8.43	0.20 ± 0.04	1.0	-
			C10	1.07 ± 0.09	0.703 ± 0.03	-99.2 ± 2.37	0.43 ± 0.06	1.0	-
			C9	0.87 ± 0.06	1.180 ± 0.02	-101.2 ± 0.91	0.25 ± 0.04	1.0	-
2000-02-04	22.2	6.0	C8	0.64 ± 0.09	1.554 ± 0.06	-91.7 ± 2.14	0.68 ± 0.12	1.0	-
			C7	0.25 ± 0.04	2.908 ± 0.06	-95.9 ± 1.16	0.57 ± 0.12	1.0	-
			C5	0.13 ± 0.04	5.885 ± 0.4	-73.2 ± 3.85	2.43 ± 0.79	1.0	-
			C4	0.10 ± 0.03	8.317 ± 0.43	-68.5 ± 2.93	2.69 ± 0.85	1.0	-
			D	0.41 ± 0.09	0.232 ± 0.08	70.2 ± 18.95	0.63 ± 0.16	1.0	-
2000-02-04	22.2	6.0	C13	2.23 ± 0.18	0.051 ± 0.01	101.5 ± 15.71	0.12 ± 0.03	1.0	-
			C11	1.16 ± 0.14	0.139 ± 0.02	-81.7 ± 9.7	0.22 ± 0.05	1.0	-
			C10	0.90 ± 0.12	0.684 ± 0.04	-100.0 ± 3.3	0.51 ± 0.08	1.0	-
			C9	0.41 ± 0.05	1.182 ± 0.02	-103.2 ± 1.13	0.18 ± 0.05	1.0	-
			C8	0.56 ± 0.09	1.443 ± 0.06	-92.8 ± 2.24	0.61 ± 0.11	1.0	-
C7	0.20 ± 0.05	2.809 ± 0.1	-95.3 ± 1.96	0.73 ± 0.19	1.0	-			

Continued on next page ...

Table B.1 – *continued from previous page*

Date	ν_{obs}	Stot	L	S	r	Φ	d	ratio	cpa
2007-11-01	43.2	5.2	C10	0.17 ± 0.03	3.413 ± 0.06	-88.8 ± 0.93	0.61 ± 0.11	1.0	-
			C9	0.10 ± 0.03	4.127 ± 0.11	-93.1 ± 1.47	0.61 ± 0.21	1.0	-
			D	0.60 ± 0.03	0.101 ± 0.01	72.0 ± 3.04	0.05 ± 0.01	1.0	-
			C19	0.69 ± 0.04	0.012 ± 0.0	-135.4 ± 21.65	0.01 ± 0.01	1.0	-
			C18	0.79 ± 0.04	0.102 ± 0.01	-102.1 ± 3.37	0.10 ± 0.01	1.0	-
			C17	0.16 ± 0.02	0.274 ± 0.02	-105.0 ± 3.18	0.05 ± 0.03	1.0	-
			C16	0.08 ± 0.02	0.608 ± 0.04	-87.8 ± 4.03	0.22 ± 0.09	1.0	-
			C15a	0.04 ± 0.01	1.108 ± 0.04	-89.7 ± 2.0	0.27 ± 0.08	1.0	-
			C15	0.01 ± 0.01	1.919 ± 0.05	-94.6 ± 1.58	0.19 ± 0.11	1.0	-
			C12	0.09 ± 0.02	2.819 ± 0.05	-95.6 ± 1.07	0.44 ± 0.11	1.0	-
2008-01-17	43.2	3.9	C10	0.09 ± 0.02	3.463 ± 0.06	-89.9 ± 0.95	0.45 ± 0.11	1.0	-
			C9	0.04 ± 0.01	4.236 ± 0.06	-94.2 ± 0.83	0.32 ± 0.12	1.0	-
			D	0.40 ± 0.07	0.118 ± 0.01	69.8 ± 6.91	0.01 ± 0.03	1.0	-
			C19	0.63 ± 0.07	0.007 ± 0.01	131.4 ± 54.53	0.04 ± 0.02	1.0	-
			C18	0.53 ± 0.07	0.129 ± 0.01	-104.5 ± 5.34	0.10 ± 0.02	1.0	-
			C17	0.16 ± 0.04	0.386 ± 0.04	-93.7 ± 6.24	0.27 ± 0.08	1.0	-
			C15a	0.05 ± 0.01	1.178 ± 0.04	-92.3 ± 1.83	0.21 ± 0.08	1.0	-
			C12	0.06 ± 0.03	2.740 ± 0.19	-92.2 ± 3.89	0.80 ± 0.37	1.0	-
			C10	0.13 ± 0.07	3.649 ± 0.28	-92.1 ± 4.36	1.05 ± 0.56	1.0	-
			D	0.82 ± 0.13	0.042 ± 0.02	62.5 ± 21.22	0.06 ± 0.03	1.0	-
2008-02-29	43.2	4.1	C19	0.73 ± 0.12	0.112 ± 0.02	-110.7 ± 9.51	0.11 ± 0.04	1.0	-
			C16	0.13 ± 0.03	0.865 ± 0.05	-92.8 ± 3.3	0.36 ± 0.1	0.52	-59.8
			C15	0.06 ± 0.02	1.595 ± 0.13	-91.8 ± 4.8	0.68 ± 0.27	0.14	39.1
			C12	0.10 ± 0.03	2.781 ± 0.07	-94.5 ± 1.48	0.49 ± 0.14	1.0	-
			C10	0.23 ± 0.09	3.794 ± 0.22	-90.8 ± 3.38	1.12 ± 0.45	1.0	-
			D	1.63 ± 0.09	0.050 ± 0.01	78.0 ± 15.3	0.07 ± 0.03	1.0	-
			C18	0.77 ± 0.06	0.153 ± 0.02	-101.0 ± 6.75	0.13 ± 0.04	1.0	-
			C16	0.24 ± 0.03	0.810 ± 0.04	-90.3 ± 2.93	0.40 ± 0.08	1.0	-
			C15a	0.23 ± 0.03	1.268 ± 0.04	-87.5 ± 1.71	0.33 ± 0.08	1.0	-
			C15	0.27 ± 0.05	2.634 ± 0.14	-85.3 ± 3.03	1.45 ± 0.28	1.0	-
2008-05-30	15.3	4.2	C12	0.19 ± 0.03	2.869 ± 0.05	-94.8 ± 1.0	0.51 ± 0.1	1.0	-
			C10	0.38 ± 0.04	3.505 ± 0.05	-90.2 ± 0.79	0.76 ± 0.1	1.0	-
			C9	0.22 ± 0.04	4.375 ± 0.08	-92.7 ± 0.98	0.56 ± 0.15	1.0	-
			C8	0.24 ± 0.07	4.786 ± 0.22	-82.3 ± 2.61	1.46 ± 0.44	1.0	-
			C7	0.05 ± 0.02	7.251 ± 0.24	-70.4 ± 1.9	1.48 ± 0.48	1.0	-
			D	0.98 ± 0.07	0.044 ± 0.01	58.6 ± 7.8	0.04 ± 0.01	1.0	-
			C20	0.71 ± 0.06	0.051 ± 0.01	-124.2 ± 7.54	0.05 ± 0.01	1.0	-
			C19	0.43 ± 0.07	0.163 ± 0.02	-100.1 ± 5.63	0.13 ± 0.03	1.0	-
			C16	0.24 ± 0.07	1.063 ± 0.13	-90.4 ± 7.13	0.87 ± 0.27	0.19	-81.1
			C12	0.27 ± 0.07	3.208 ± 0.12	-90.7 ± 2.19	1.02 ± 0.25	1.0	-
2008-06-12	43.2	5.7	C10	0.22 ± 0.1	4.242 ± 0.25	-90.6 ± 3.33	1.05 ± 0.49	1.0	-
			D	1.70 ± 0.09	0.038 ± 0.01	75.6 ± 15.26	0.13 ± 0.02	1.0	-
			C19	0.65 ± 0.06	0.138 ± 0.02	-106.9 ± 7.27	0.20 ± 0.04	1.0	-
			C17	0.22 ± 0.05	0.687 ± 0.09	-98.5 ± 7.09	0.62 ± 0.17	1.0	-
			C15a	0.24 ± 0.05	1.234 ± 0.06	-85.2 ± 2.98	0.55 ± 0.13	1.0	-
			C15	0.13 ± 0.03	2.269 ± 0.16	-93.7 ± 3.91	1.13 ± 0.31	1.0	-
			C12	0.08 ± 0.02	2.921 ± 0.05	-95.0 ± 0.95	0.27 ± 0.1	1.0	-
			C10	0.52 ± 0.06	3.496 ± 0.07	-90.4 ± 1.22	1.16 ± 0.15	1.0	-
			C9	0.23 ± 0.06	4.570 ± 0.12	-89.3 ± 1.49	0.86 ± 0.24	1.0	-
			D	0.81 ± 0.11	0.055 ± 0.01	53.4 ± 9.92	0.01 ± 0.02	1.0	-
2008-06-15	22.2	3.8	C20	0.85 ± 0.1	0.042 ± 0.01	-128.1 ± 12.38	0.04 ± 0.02	1.0	-
			C19	0.42 ± 0.08	0.145 ± 0.02	-98.5 ± 7.76	0.15 ± 0.04	1.0	-
			C16	0.19 ± 0.06	1.210 ± 0.1	-89.4 ± 4.81	0.62 ± 0.2	0.42	75.5
			C12	0.25 ± 0.12	3.711 ± 0.26	-89.3 ± 4.02	1.11 ± 0.52	1.0	-
			D	1.19 ± 0.07	0.066 ± 0.01	68.6 ± 4.62	0.04 ± 0.01	1.0	-
			C20	1.52 ± 0.07	0.038 ± 0.0	-114.8 ± 6.77	0.05 ± 0.01	1.0	-
			C19	0.18 ± 0.03	0.151 ± 0.01	-102.3 ± 5.11	0.03 ± 0.03	1.0	-
			C18	0.17 ± 0.03	0.244 ± 0.03	-102.5 ± 6.22	0.25 ± 0.05	1.0	-
			C16	0.26 ± 0.05	1.165 ± 0.07	-89.6 ± 3.26	0.71 ± 0.13	0.31	-79.0
			C12	0.16 ± 0.04	3.090 ± 0.09	-92.7 ± 1.63	0.66 ± 0.18	1.0	-
2008-08-16	43.2	7.5	C10	0.29 ± 0.08	4.112 ± 0.18	-90.5 ± 2.45	1.17 ± 0.35	1.0	-
			D	1.33 ± 0.07	0.062 ± 0.01	69.1 ± 4.73	0.03 ± 0.01	1.0	-
			C20	1.38 ± 0.05	0.048 ± 0.0	-114.0 ± 4.39	0.05 ± 0.01	1.0	-
			C19	0.27 ± 0.03	0.160 ± 0.01	-104.1 ± 3.6	0.08 ± 0.02	1.0	-
			C18	0.08 ± 0.02	0.355 ± 0.03	-97.4 ± 4.55	0.20 ± 0.06	1.0	-
			C16	0.25 ± 0.04	1.219 ± 0.05	-89.6 ± 2.4	0.68 ± 0.1	0.28	-74.9
			C12	0.13 ± 0.05	3.060 ± 0.14	-94.0 ± 2.54	0.73 ± 0.27	1.0	-
			C10	0.32 ± 0.1	4.078 ± 0.2	-90.0 ± 2.85	1.25 ± 0.41	1.0	-
			D	1.99 ± 0.09	0.050 ± 0.01	76.5 ± 11.65	0.00 ± 0.02	1.0	-
			C19	0.88 ± 0.07	0.131 ± 0.02	-100.8 ± 7.97	0.09 ± 0.04	1.0	-
2008-09-10	43.2	7.5	C17	0.20 ± 0.04	0.736 ± 0.07	-91.4 ± 5.21	0.39 ± 0.13	1.0	-

Continued on next page ...

Table B.1 – *continued from previous page*

Date	ν_{obs}	S_{tot}	L	S	r	Φ	d	ratio	cpa
			C22	1.81 ± 0.16	0.102 ± 0.02	-107.1 ± 12.26	0.13 ± 0.04	1.0	-
			C21	1.02 ± 0.09	0.428 ± 0.02	-107.1 ± 3.11	0.21 ± 0.05	1.0	-
			C20	0.56 ± 0.07	0.693 ± 0.05	-82.3 ± 4.25	0.74 ± 0.1	1.0	-
			C15a	0.14 ± 0.03	2.155 ± 0.08	-90.3 ± 2.23	0.77 ± 0.17	1.0	-
			C15	0.19 ± 0.03	3.224 ± 0.08	-94.3 ± 1.45	0.80 ± 0.16	1.0	-
			C10	0.43 ± 0.06	4.127 ± 0.07	-91.7 ± 0.91	0.86 ± 0.13	1.0	-
			C9	0.23 ± 0.06	4.999 ± 0.16	-88.4 ± 1.79	1.14 ± 0.31	1.0	-
			C8	0.38 ± 0.08	5.243 ± 0.3	-75.8 ± 3.23	2.76 ± 0.59	1.0	-

Notes: **Date** – date of the observation; ν_{obs} – observation frequency in units of GHz; S_{tot} – sum of component flux densities in units of Jy; **L** – component label; **S** – component flux density in units of Jy; r – distance from map center in mas; Φ – position angle to the map center in $^{\circ}$; d – component FWHM size in mas; **ratio** – in case of an elliptical Gaussian component, this number provides the axial ratio between the major and minor axis; **cpa** – is then the rotation angle of the ellipse (North through West);

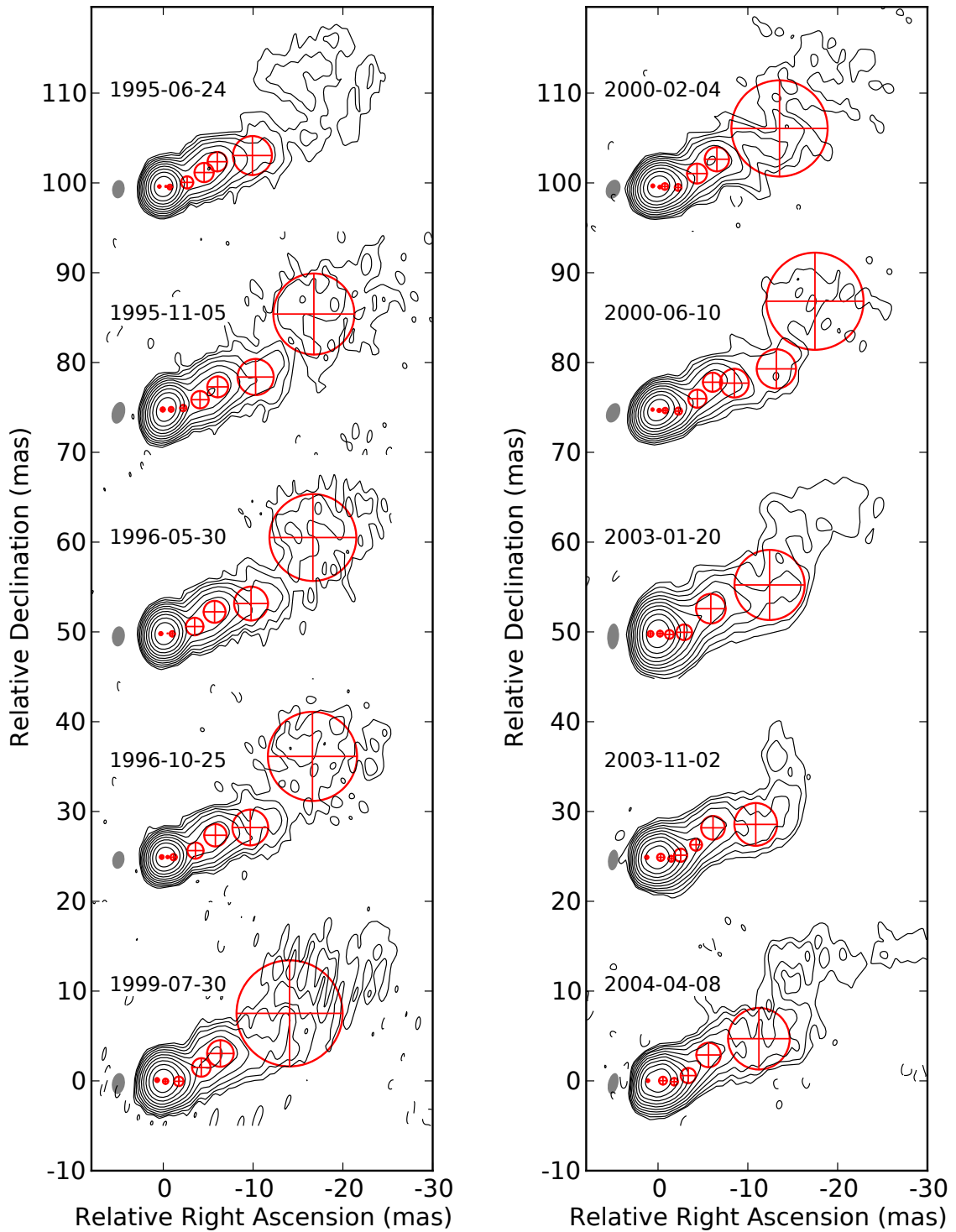


Figure B.1: VLBA maps of the total brightness distribution of 3C 345 obtained from observations at 5.0 GHz between 1995 and 2004. Red open crossed circles/ellipses show the FWHM of Gaussian components fitting the structure observed. The parameters of these components are listed in Table B.1. The contour levels correspond to $(-0.1, 0.1, 0.2, 0.4, 0.8, 1.6, 3.2, 6.4, 13, 26, 51)\%$ of the peak flux density. Negative contours are indicated by dashed lines. The grey shaded ellipse on the left of each map represents the FWHM of the restoring beam.

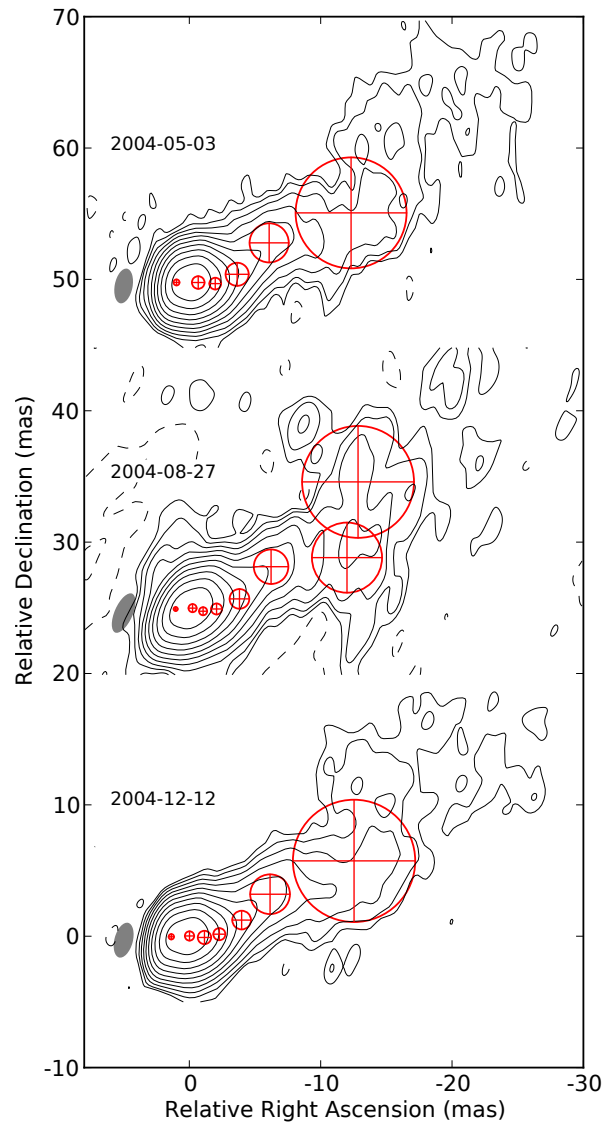


Figure B.1 5.0 GHz (continued)

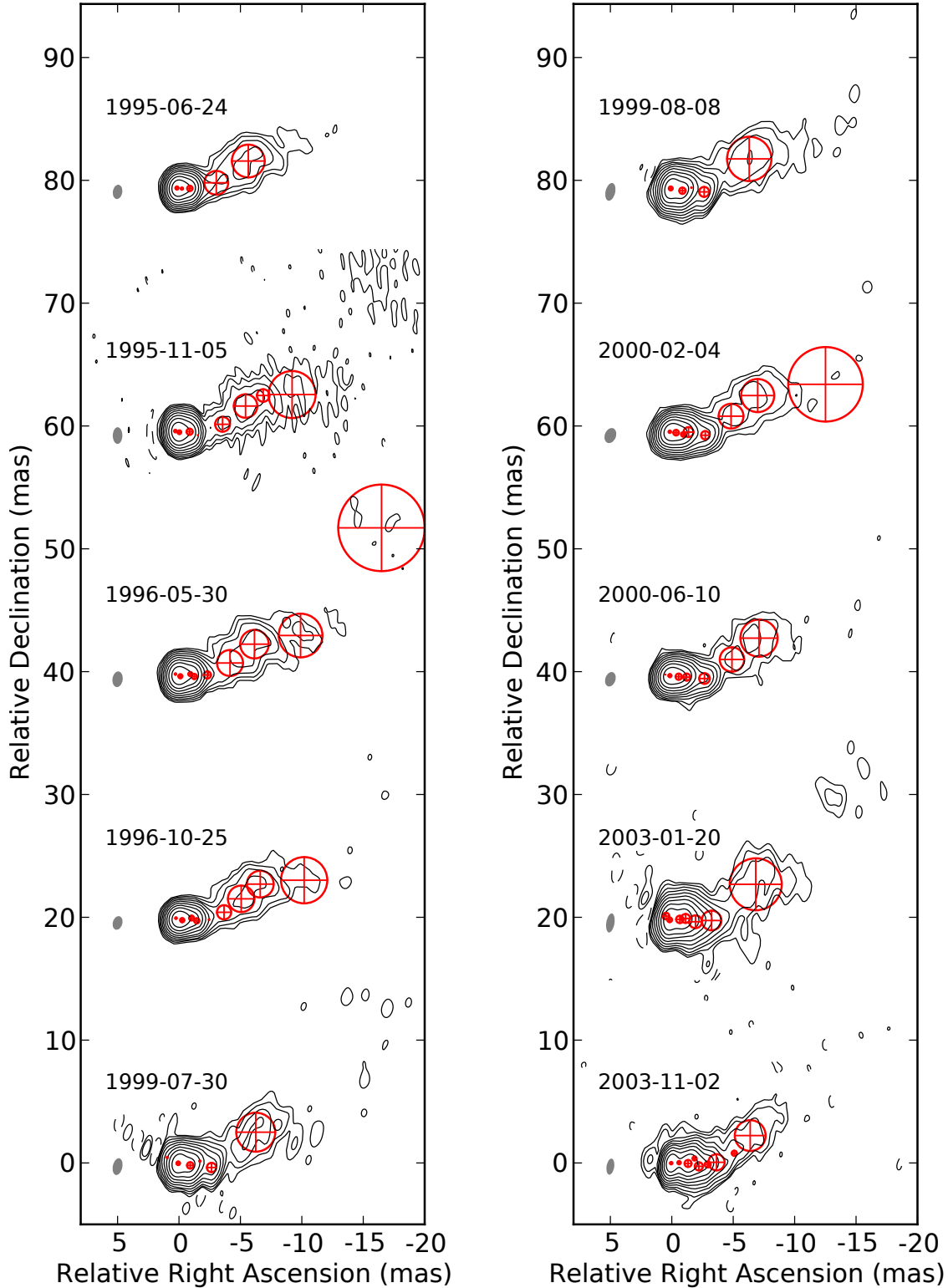


Figure B.2: VLBA maps of the total brightness distribution of 3C 345 obtained from observations at 8.4 GHz between 1995 and 2004. Red open crossed circles/ellipses show the FWHM of Gaussian components fitting the structure observed. The parameters of these components are listed in Table B.1. The contour levels correspond to (-0.2 0.2 0.4 0.8 1.6 3.2 6.4 13 26 51)% of the peak flux density. Negative contours are indicated by dashed lines. The grey shaded ellipse on the left of each map represents the FWHM of the restoring beam.

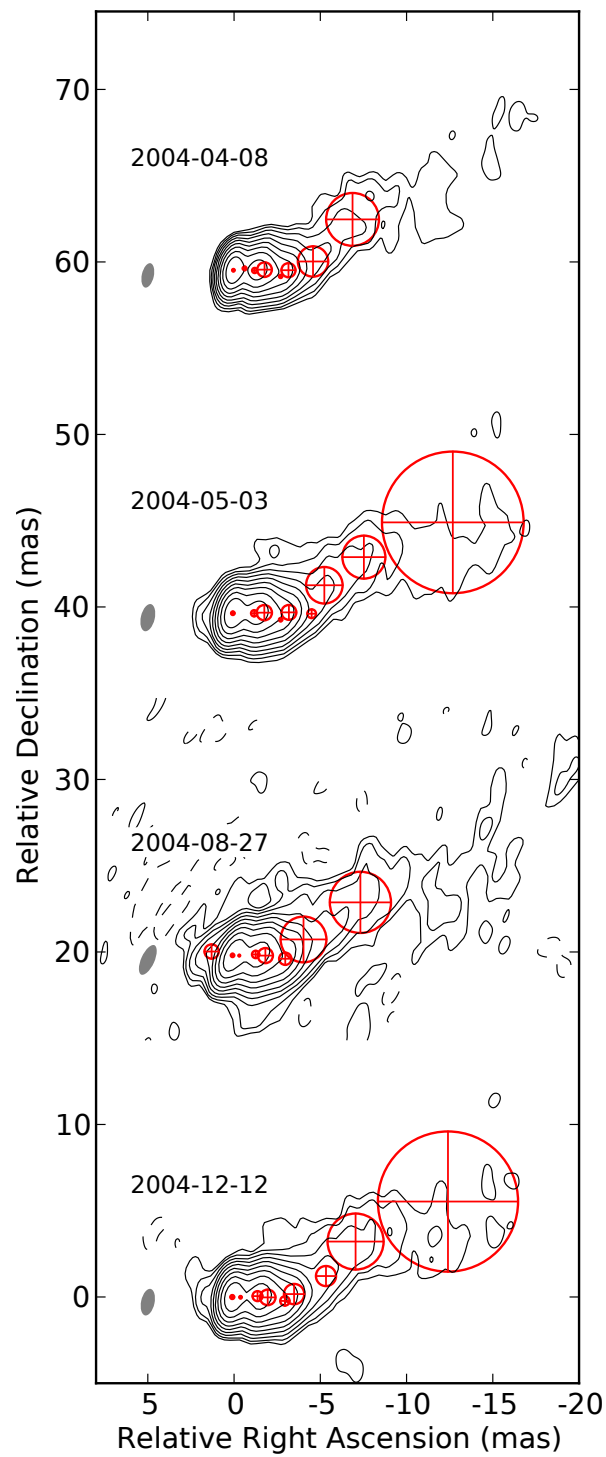


Figure B.2 8.4 GHz (continued)

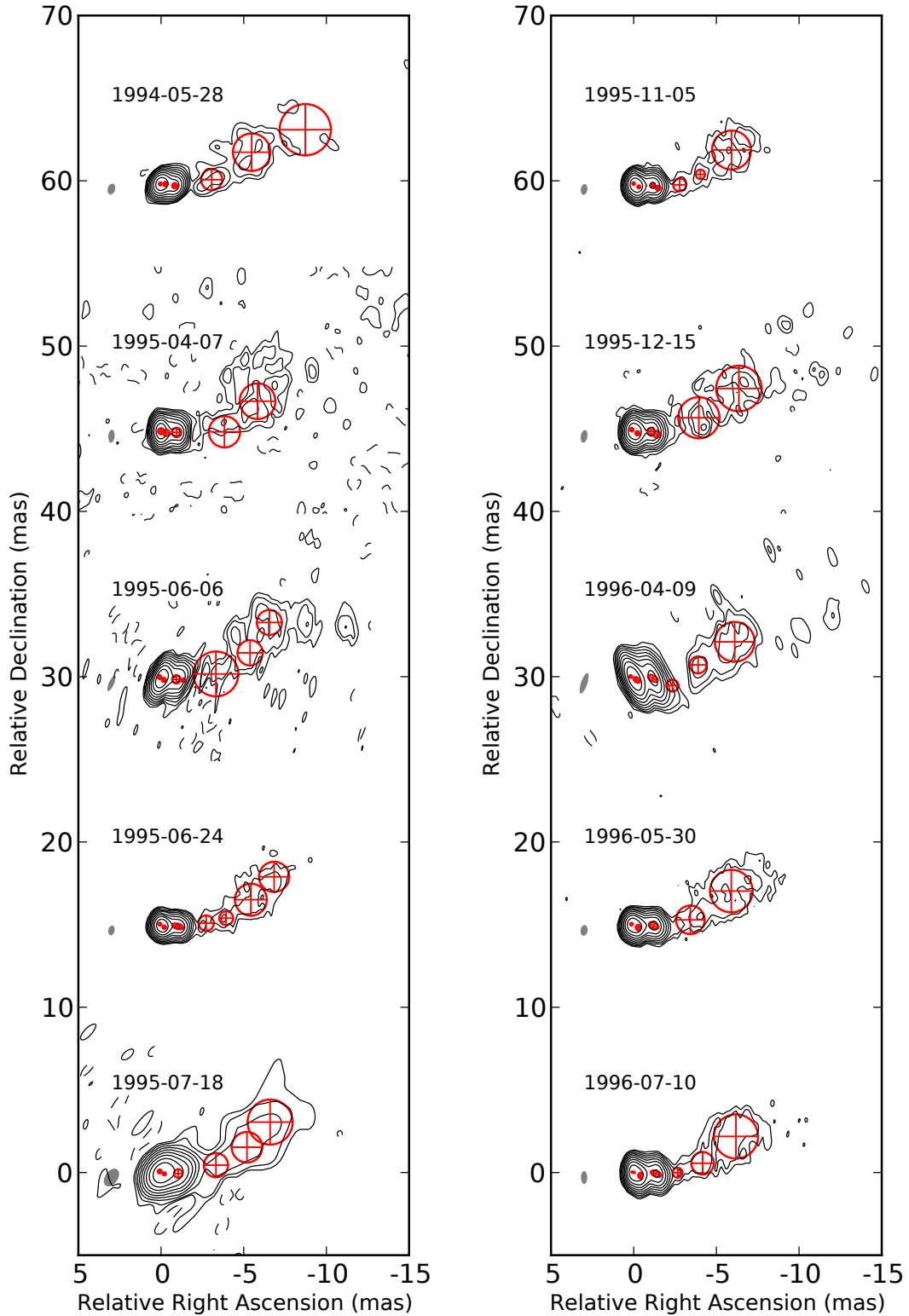


Figure B.3: VLBA maps of the total brightness distribution of 3C 345 obtained from observations at 15.4 GHz between 1994 and 2010. Red open crossed circles/ellipses show the FWHM of Gaussian components fitting the structure observed. The parameters of these components are listed in Table B.1. The contour levels correspond to $(-0.2\ 0.2\ 0.4\ 0.8\ 1.6\ 3.2\ 6.4\ 13\ 26\ 51)\%$ of the peak flux density. Negative contours are indicated by dashed lines. The grey shaded ellipse on the left of each map represents the FWHM of the restoring beam.

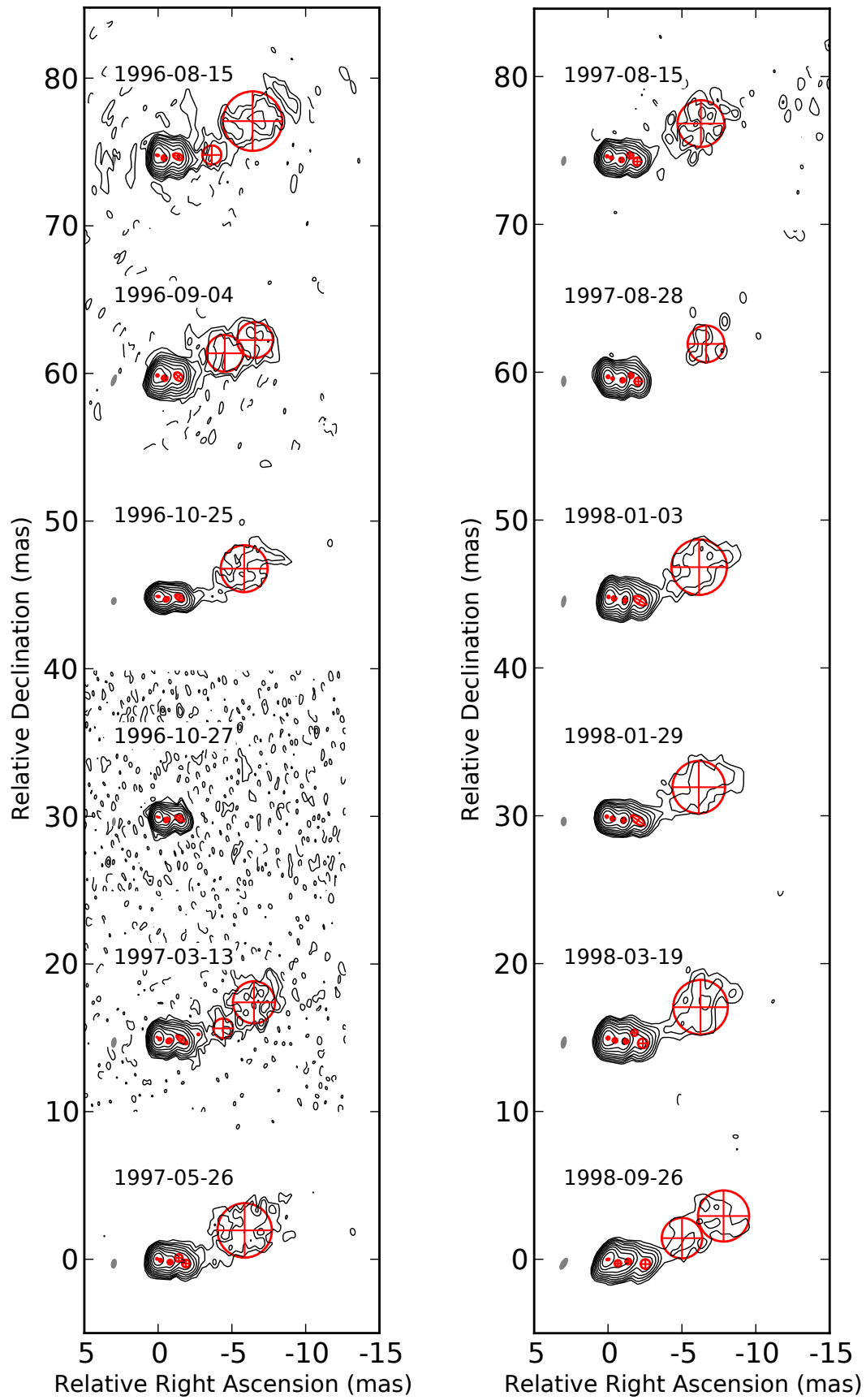


Figure B.3 15.4 GHz (continued)

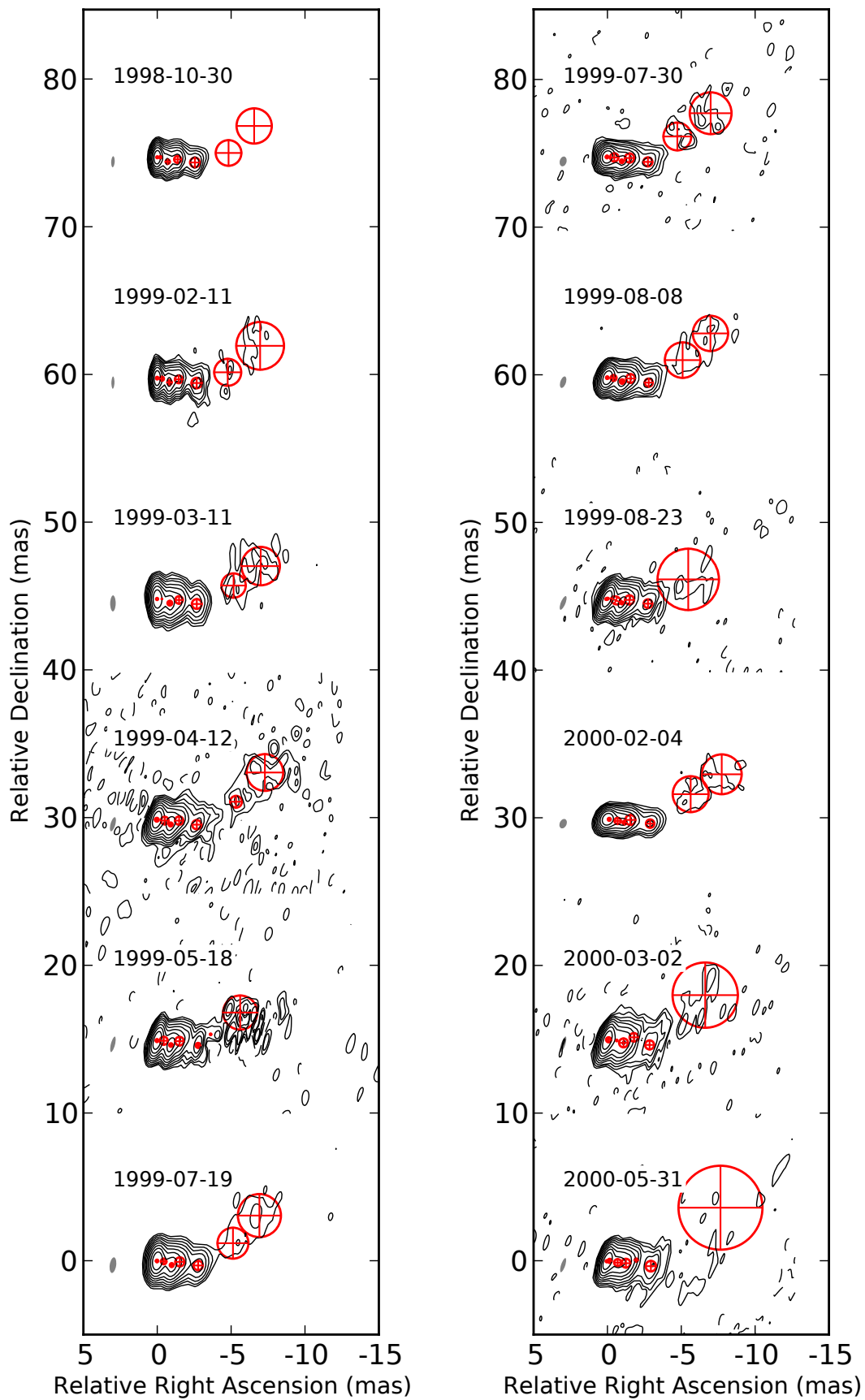


Figure B.3 15.4 GHz (continued)

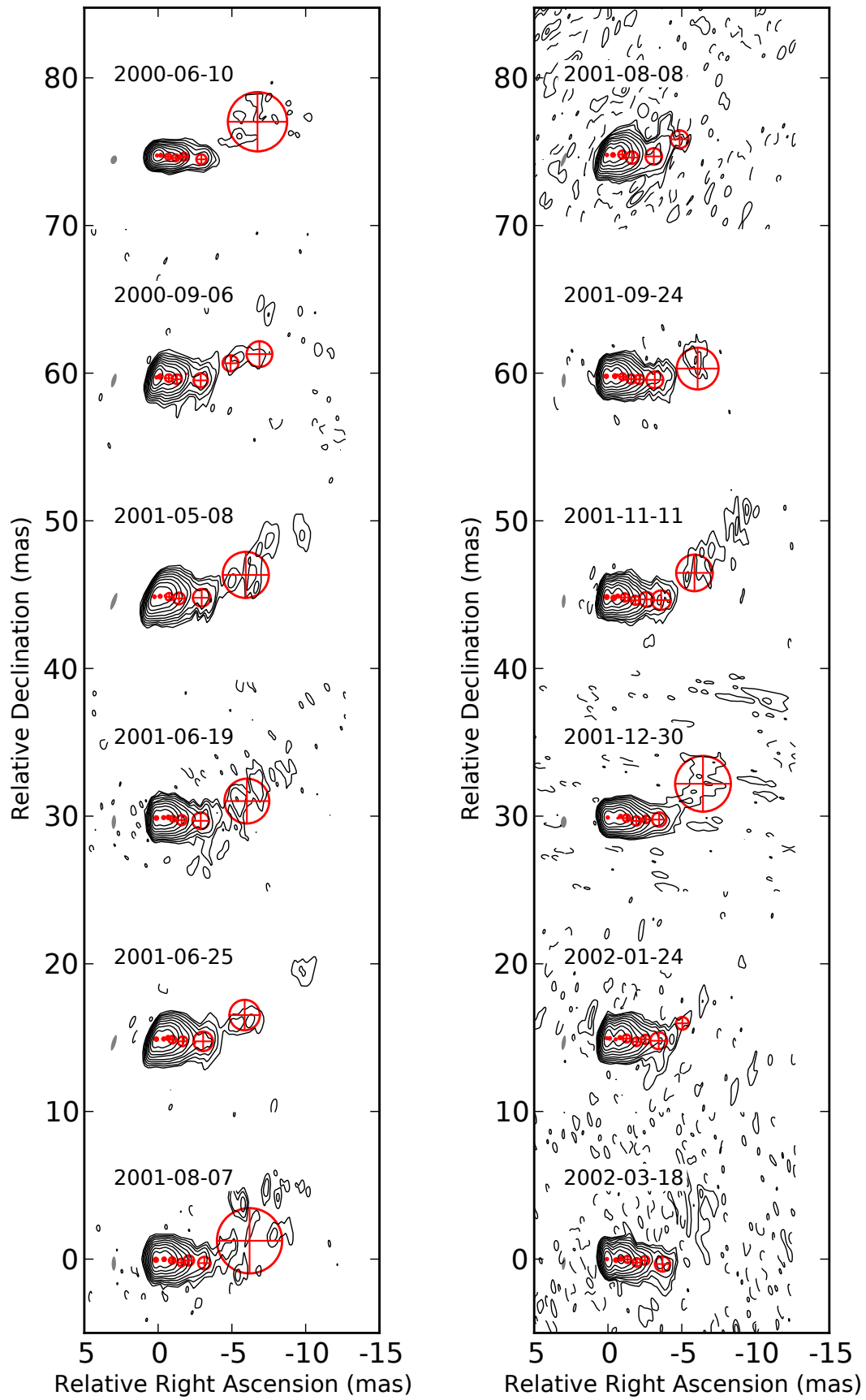


Figure B.3 15.4 GHz (continued)

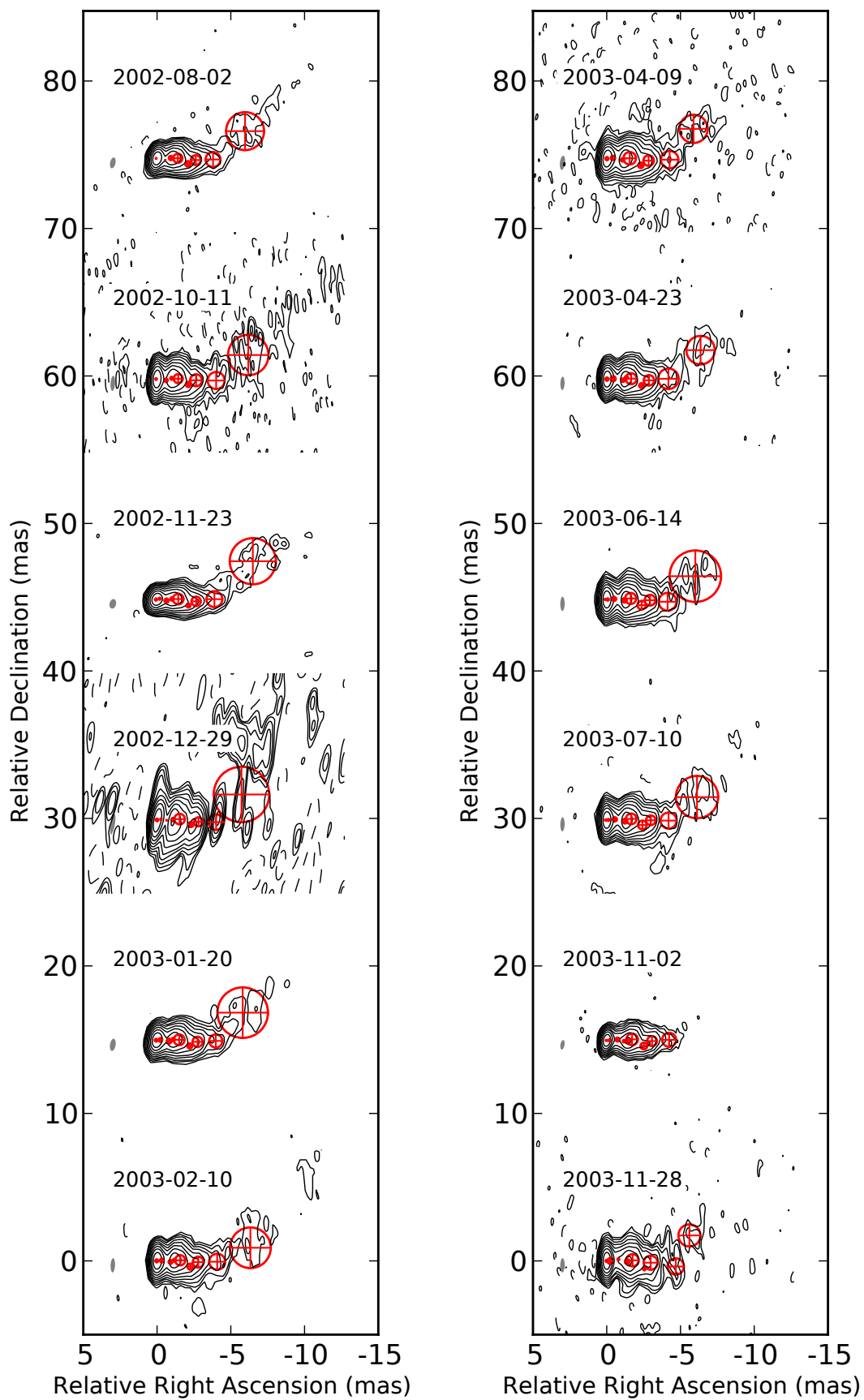


Figure B.3 15.4 GHz (continued)

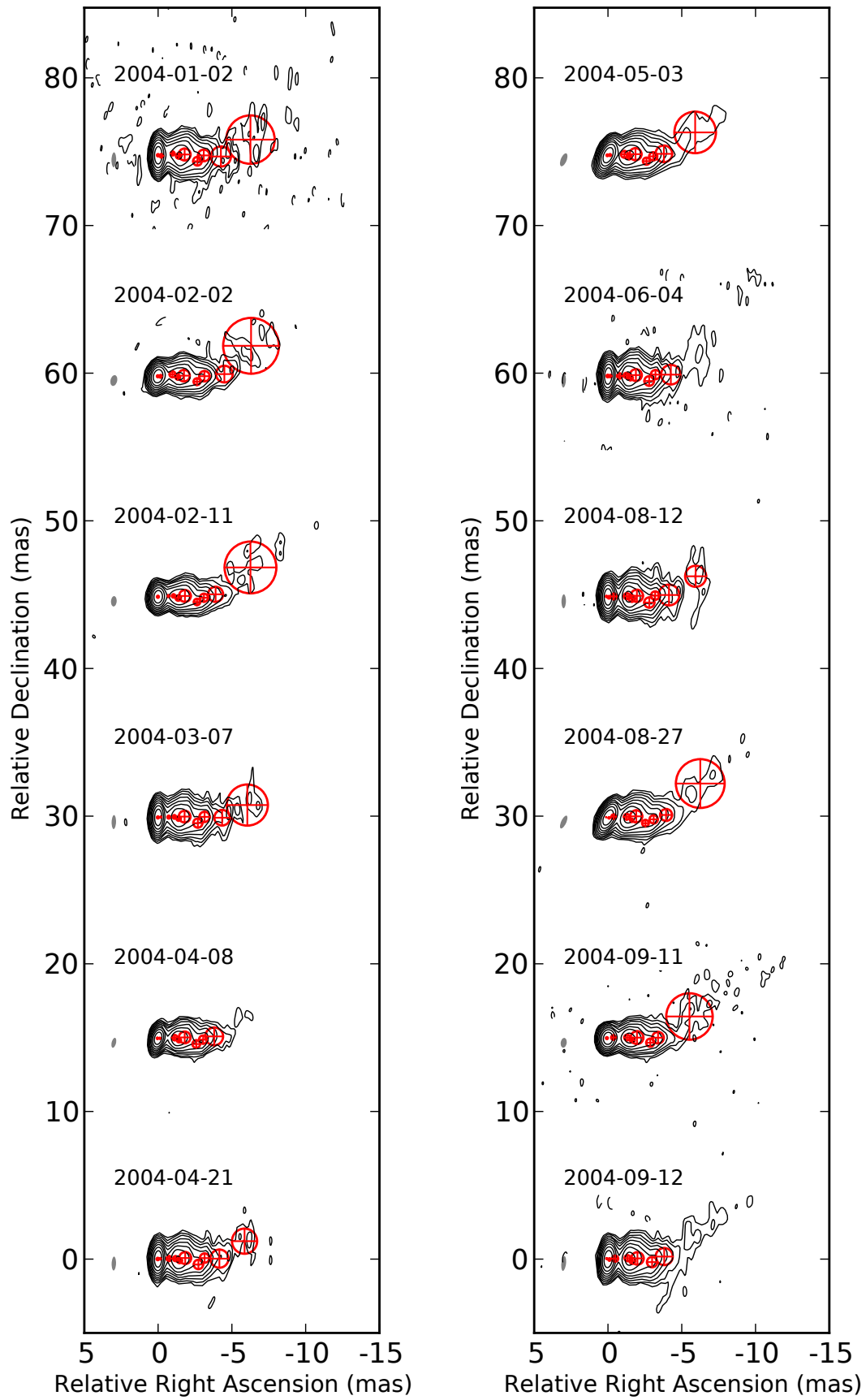


Figure B.3 15.4 GHz (continued)

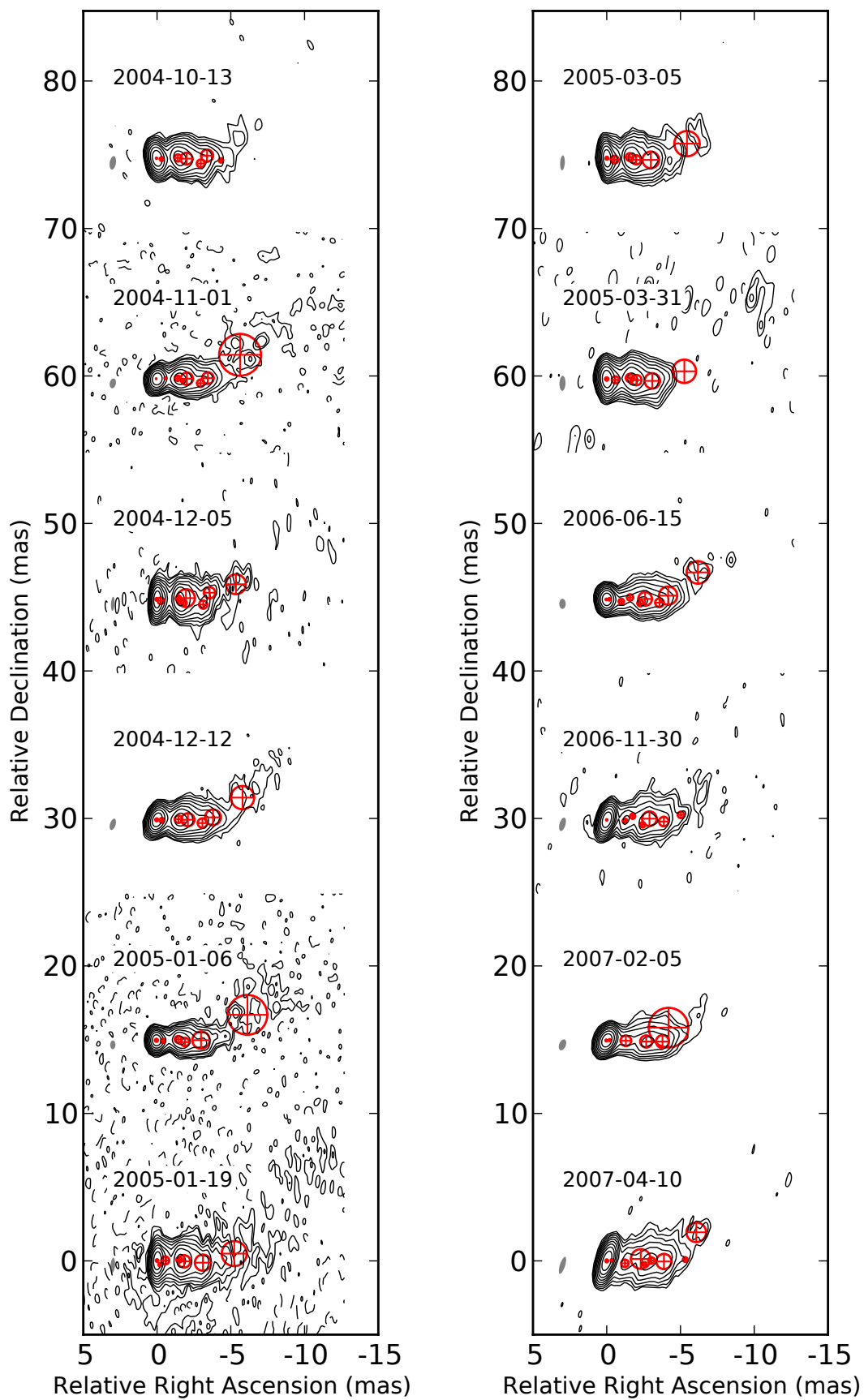


Figure B.3 15.4 GHz (continued)

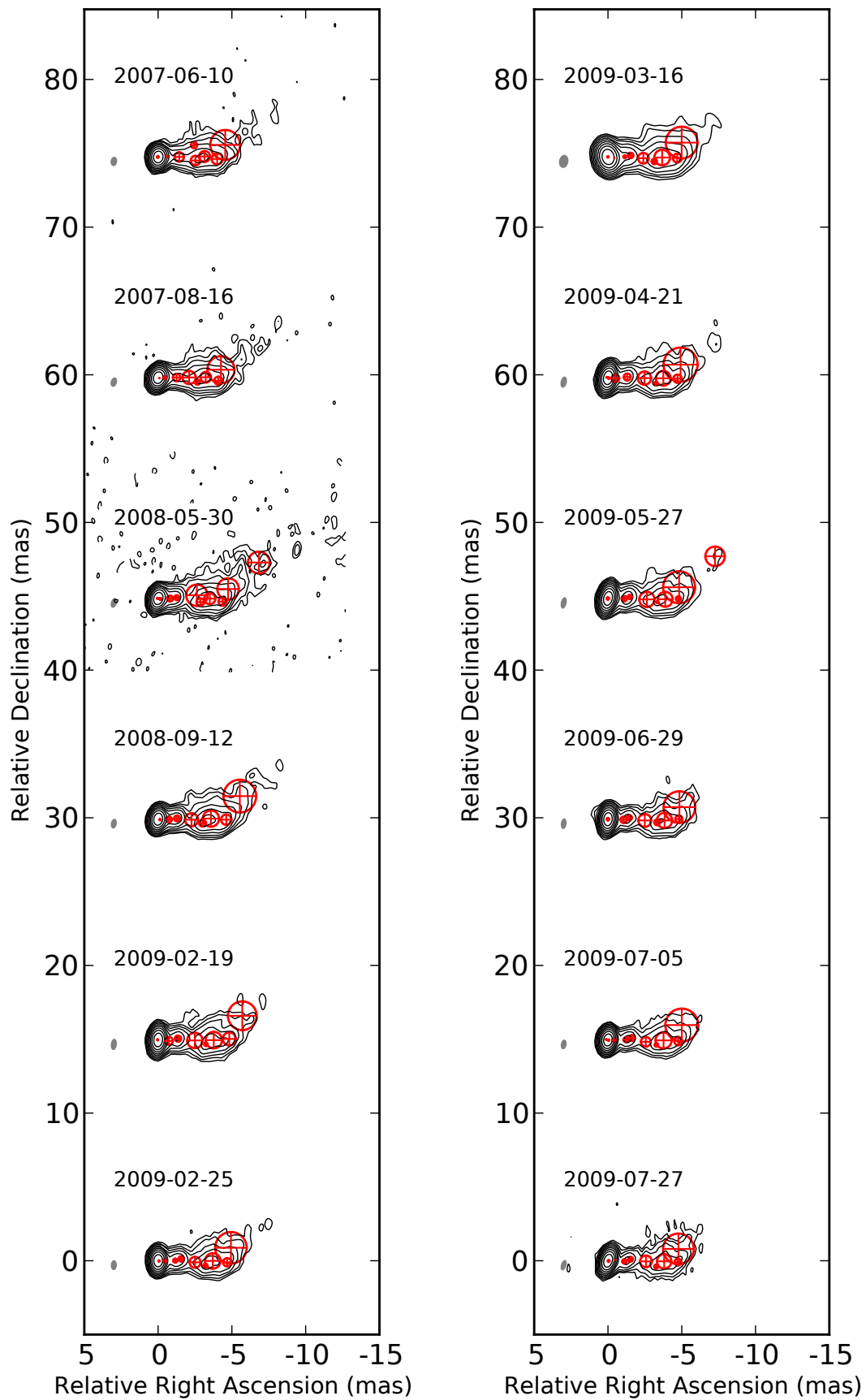


Figure B.3 15.4 GHz (continued)

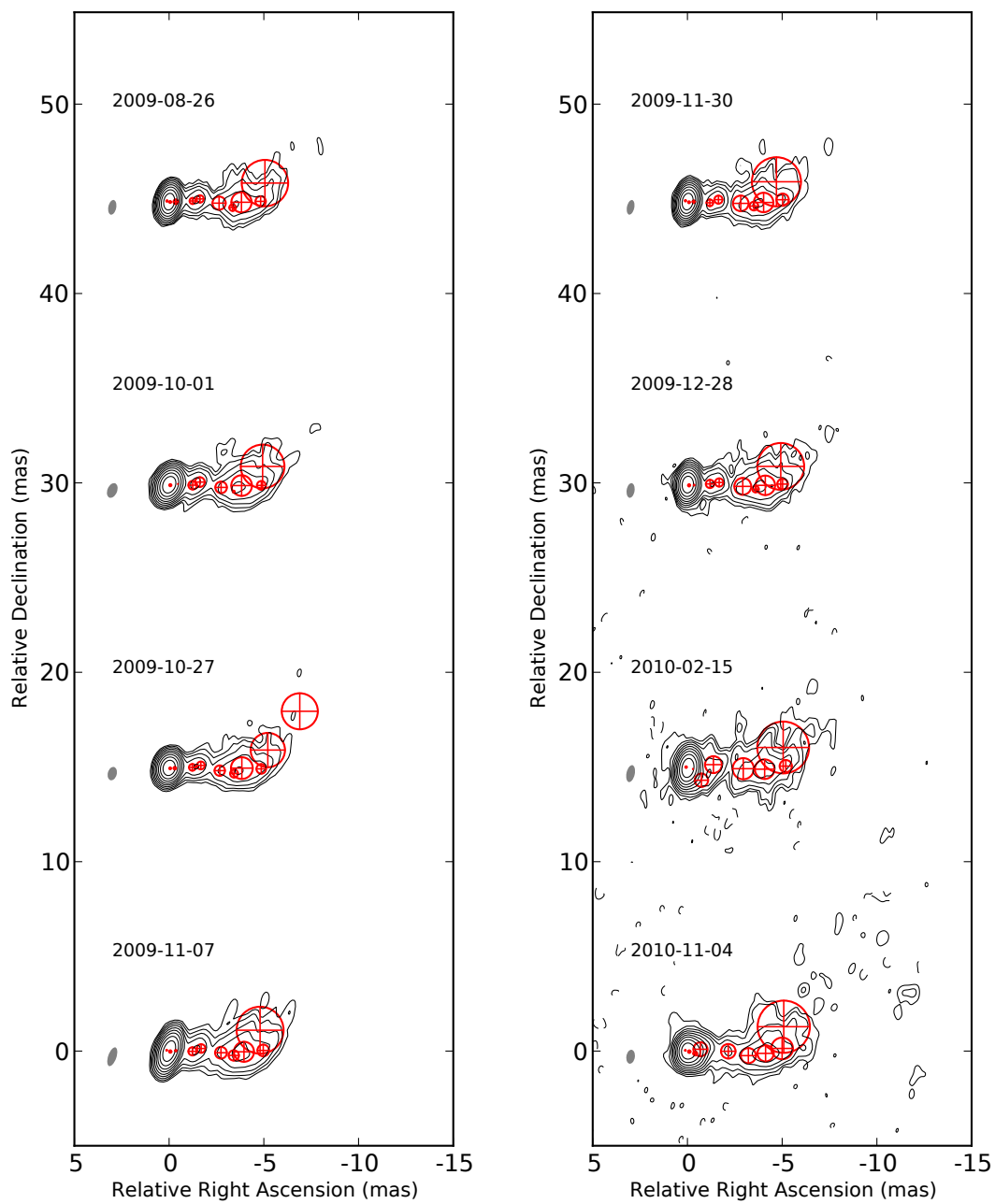


Figure B.3 15.4 GHz (continued)

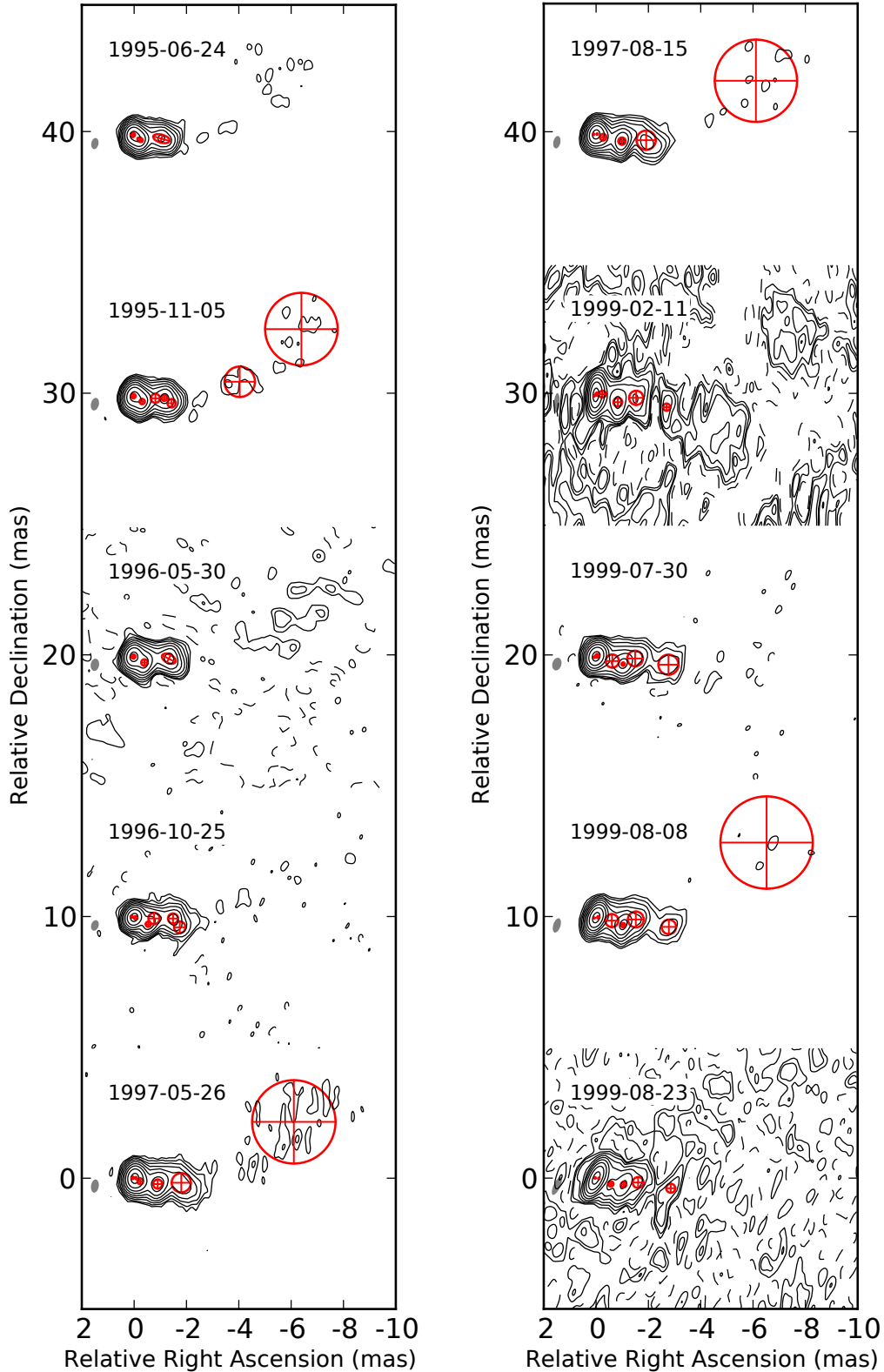


Figure B.4: VLBA maps of the total brightness distribution of 3C 345 obtained from observations at 22.2 GHz between 1995 and 2010. Red open crossed circles/ellipses show the FWHM of Gaussian components fitting the structure observed. The parameters of these components are listed in Table B.1. The contour levels correspond to $(-0.3 \ 0.3 \ 0.6 \ 1.2 \ 2.4 \ 4.8 \ 9.6 \ 19 \ 38 \ 77)\%$ of the peak flux density. Negative contours are indicated by dashed lines. The grey shaded ellipse on the left of each map represents the FWHM of the restoring beam.

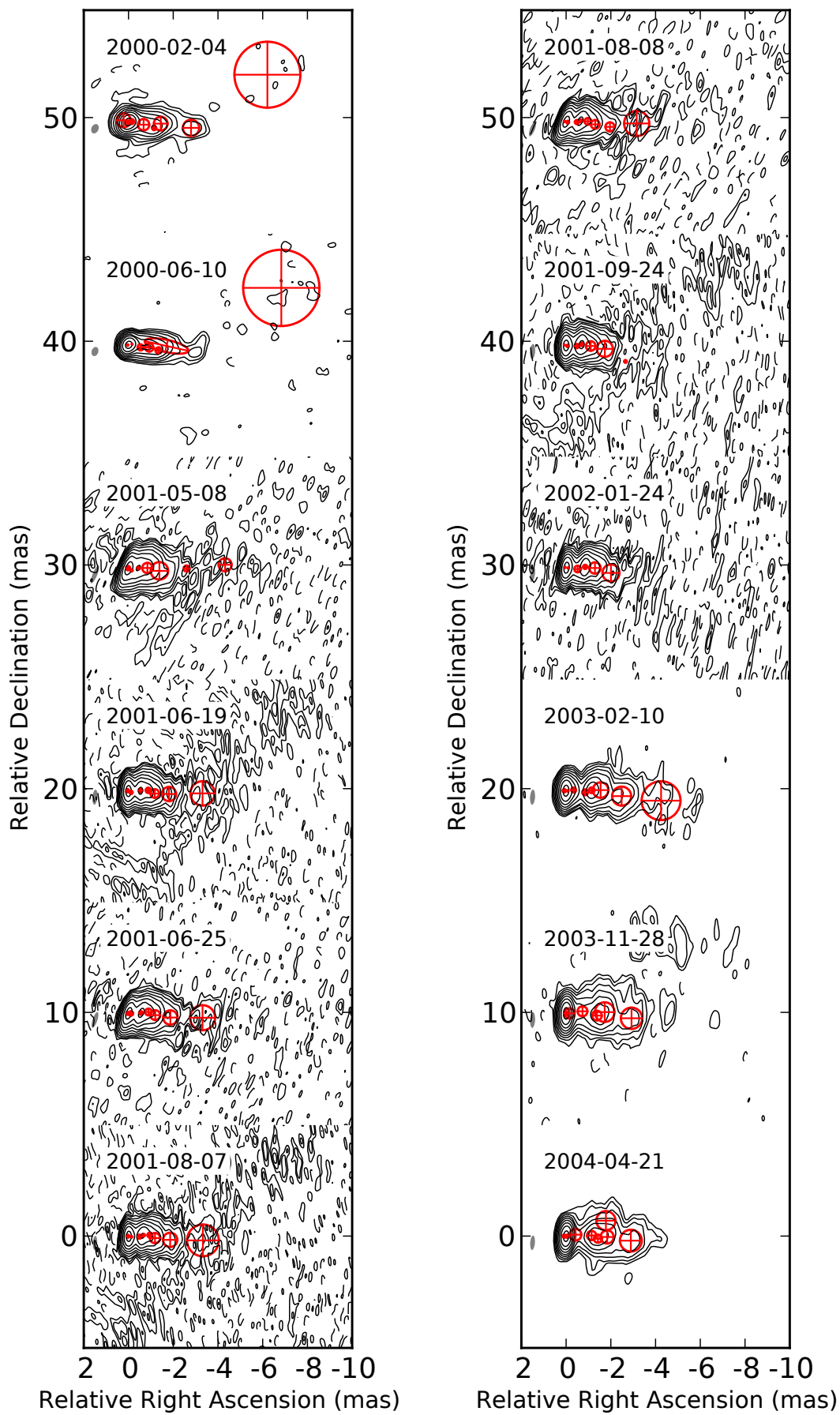


Figure B.4 22.2 GHz (continued)

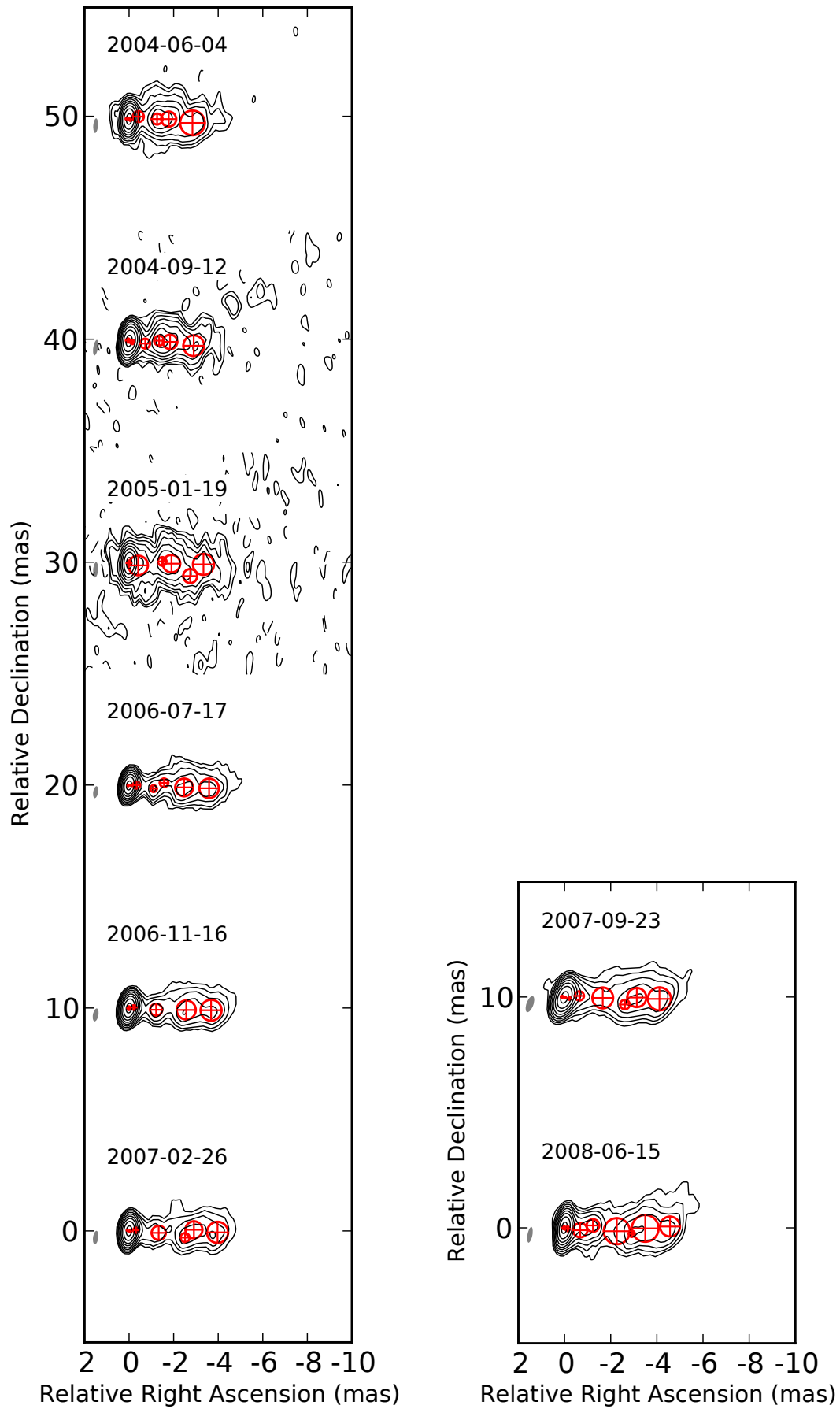


Figure B.4 22.2 GHz (continued)

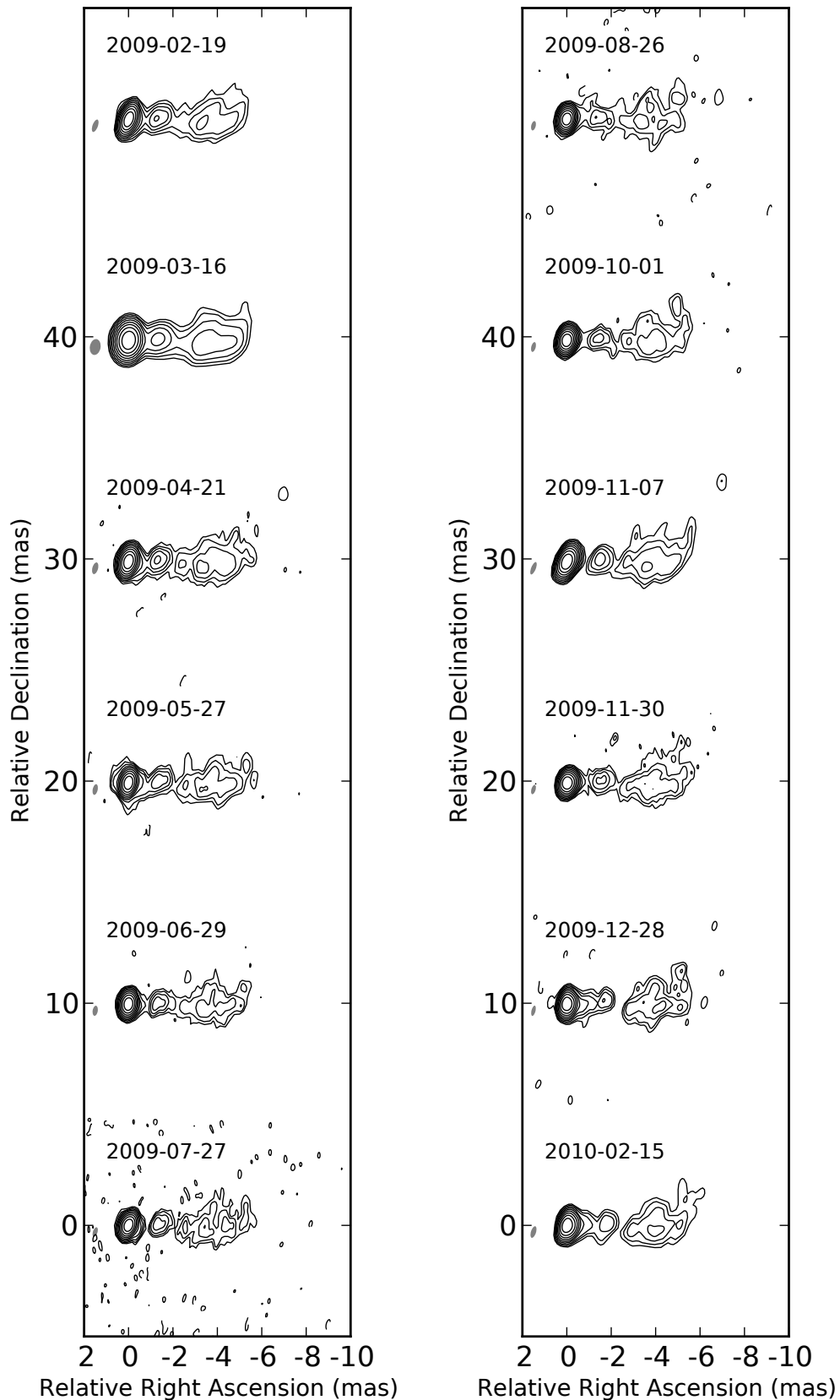


Figure B.5: VLBA maps of the total brightness distribution of 3C 345 obtained from observations at 23.8 GHz between 2009 and 2010. The contour levels correspond to (-0.2 0.2 0.4 0.8 1.6 3.2 6.4 13 26 51)% of the peak flux density. Negative contours are indicated by dashed lines. The grey shaded ellipse on the left of each map represents the FWHM of the restoring beam.

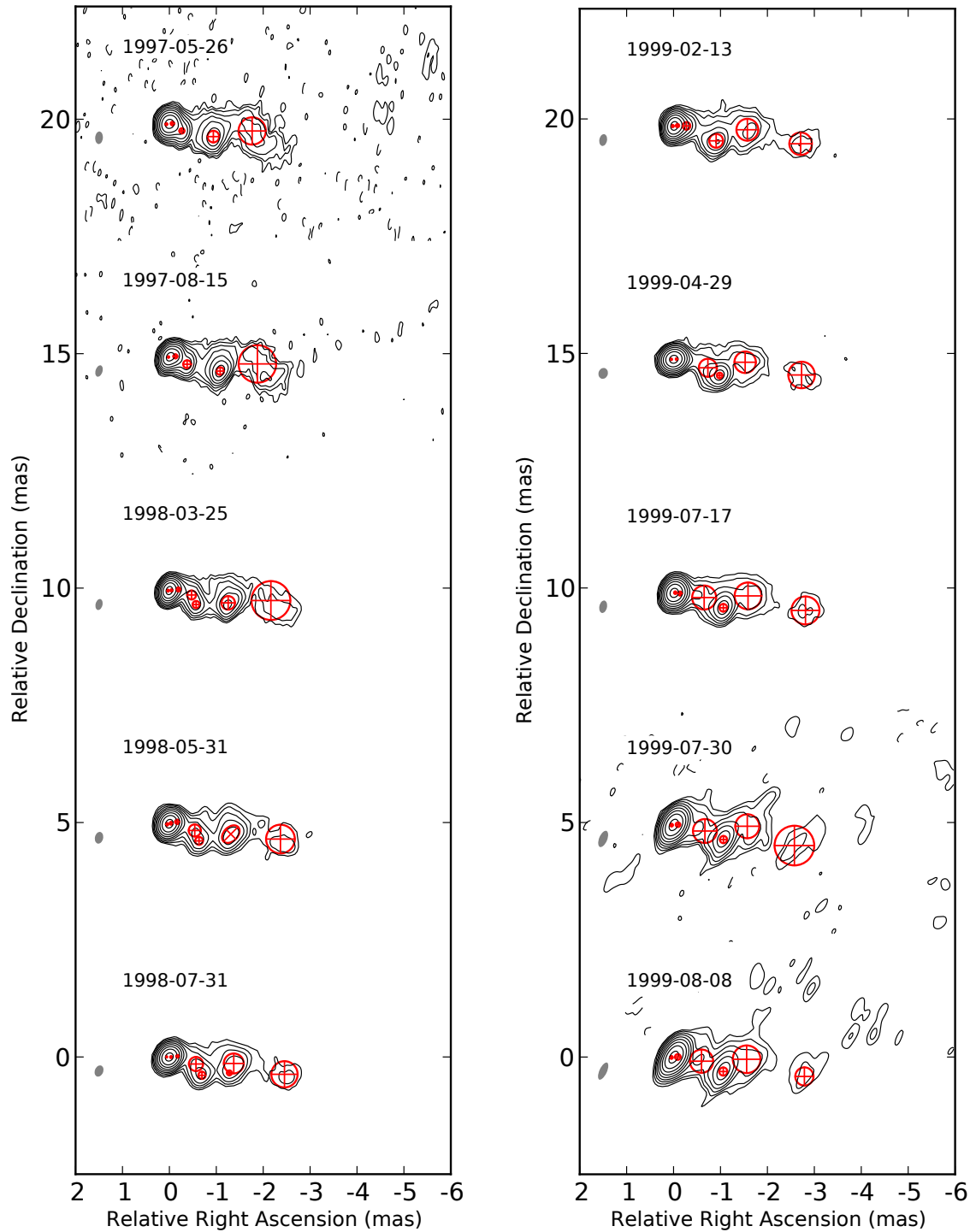


Figure B.6: VLBA maps of the total brightness distribution of 3C 345 obtained from observations at 43.2 GHz between 1997 and 2010. Red open crossed circles/ellipses show the FWHM of Gaussian components fitting the structure observed. The parameters of these components are listed in Table B.1. The contour levels correspond to $(-0.3\ 0.3\ 0.6\ 1.2\ 2.4\ 4.8\ 9.6\ 19\ 38\ 77)\%$ of the peak flux density. Negative contours are indicated by dashed lines. The grey shaded ellipse on the left of each map represents the FWHM of the restoring beam.

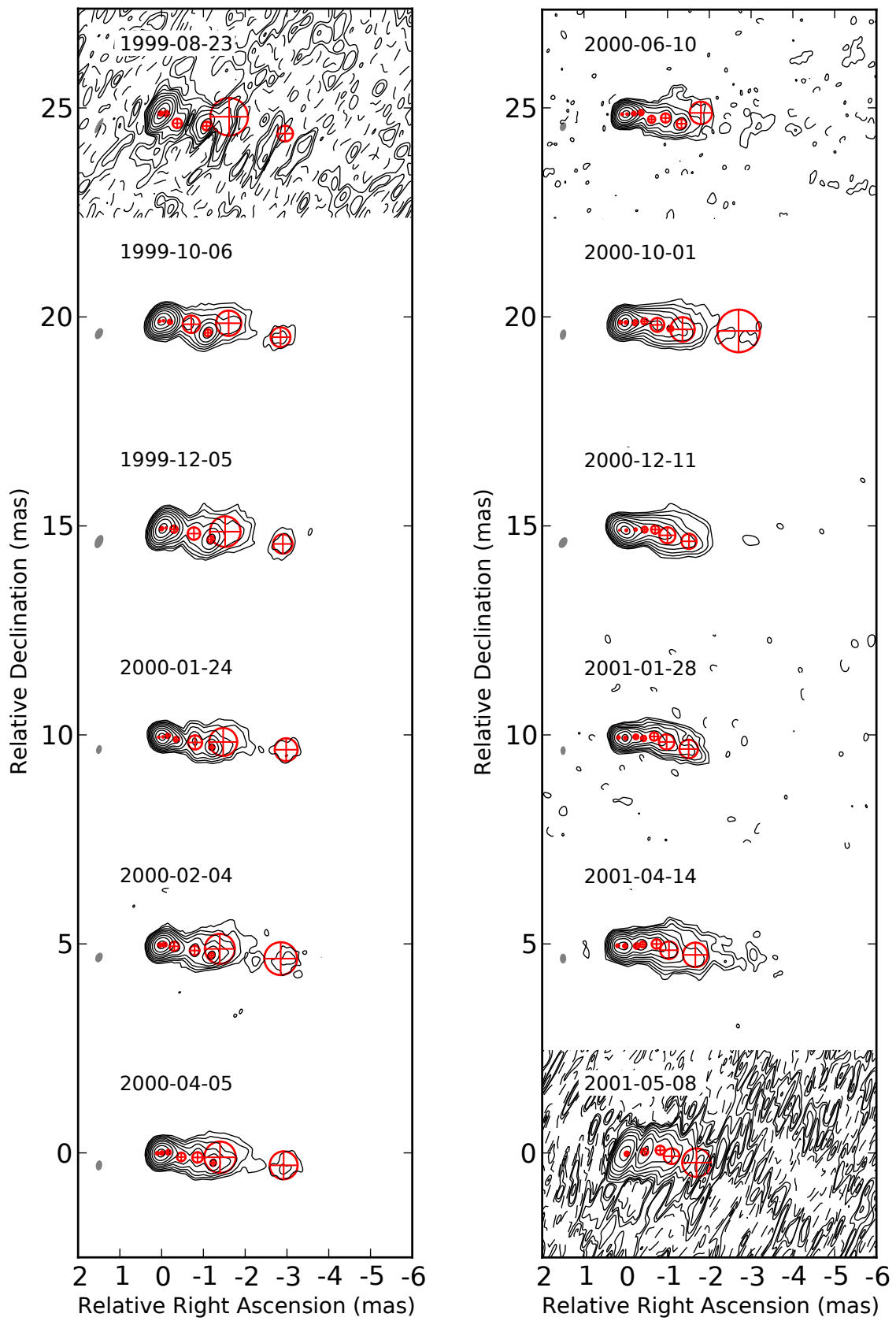


Figure B.6 43.2 GHz (continued)

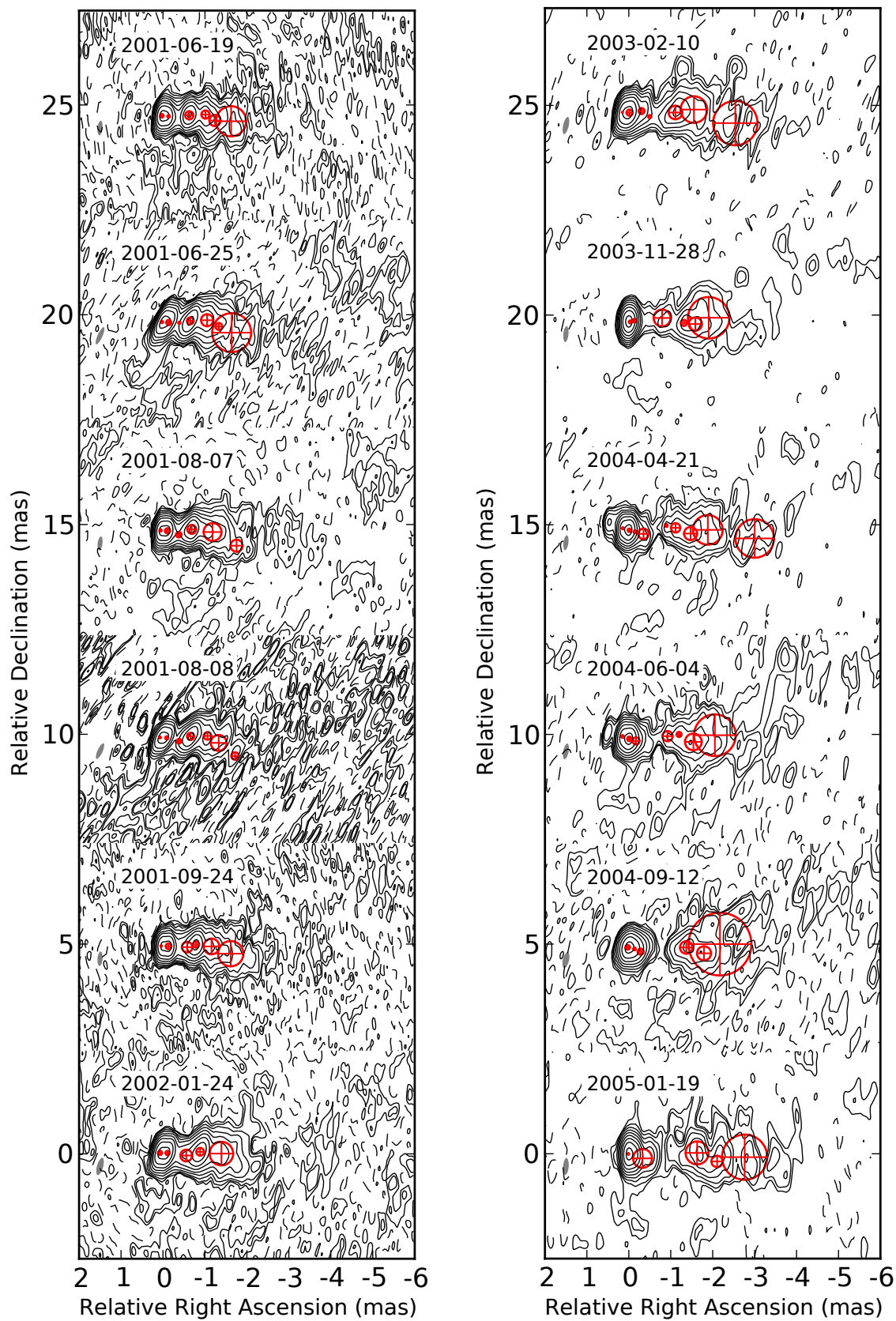


Figure B.6 43.2 GHz (continued)

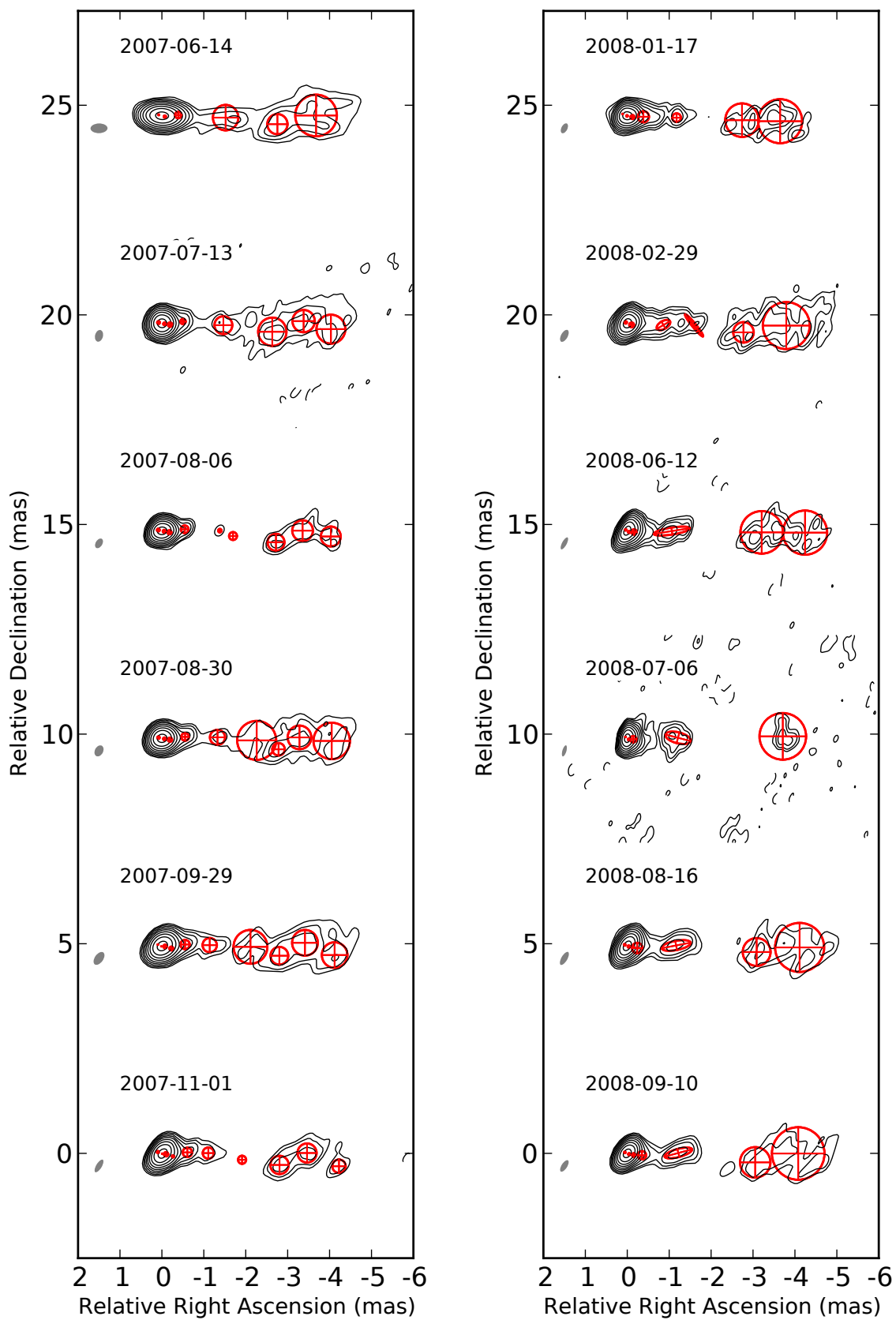


Figure B.6 43.2 GHz (continued)

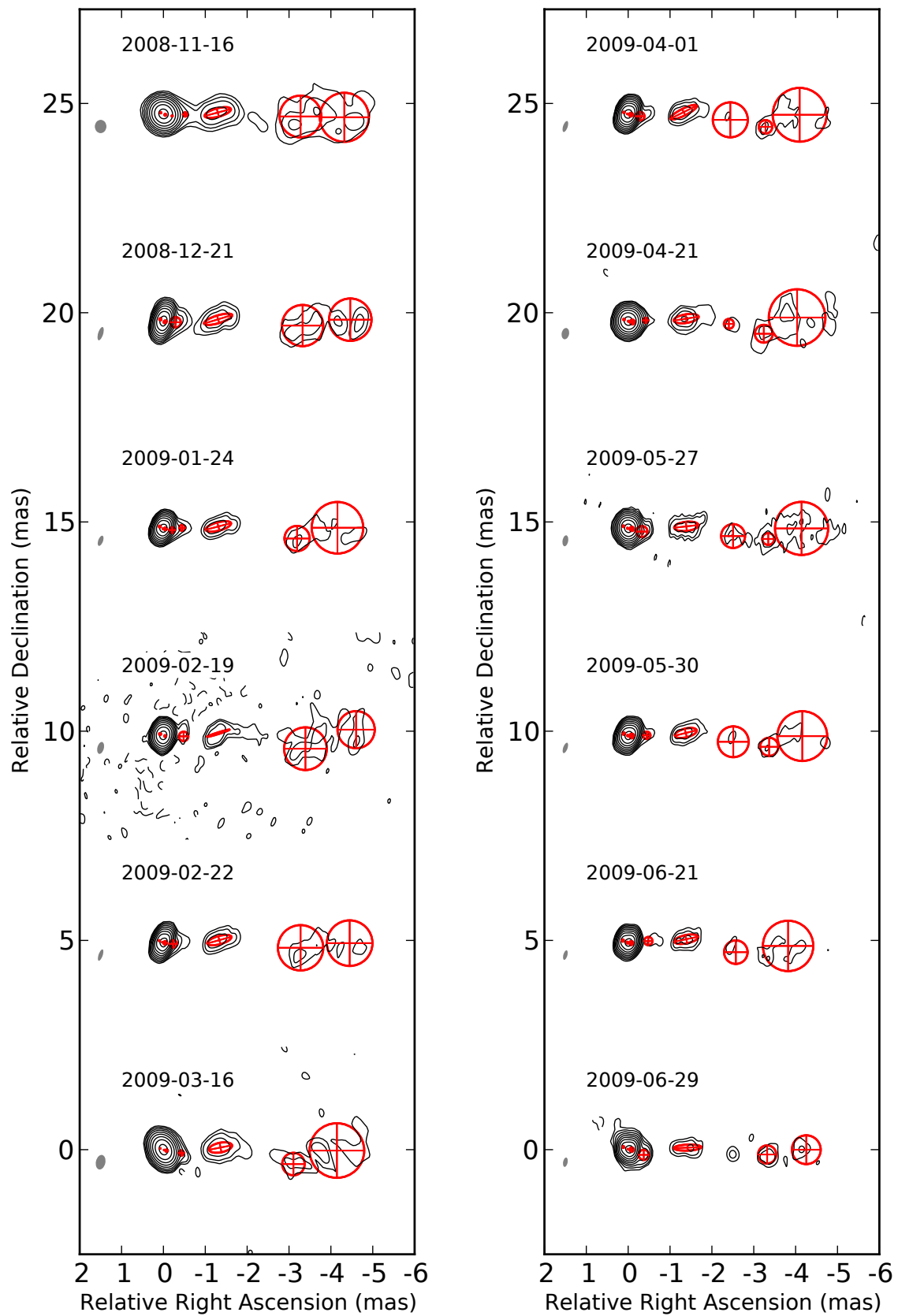


Figure B.6 43.2 GHz (continued)

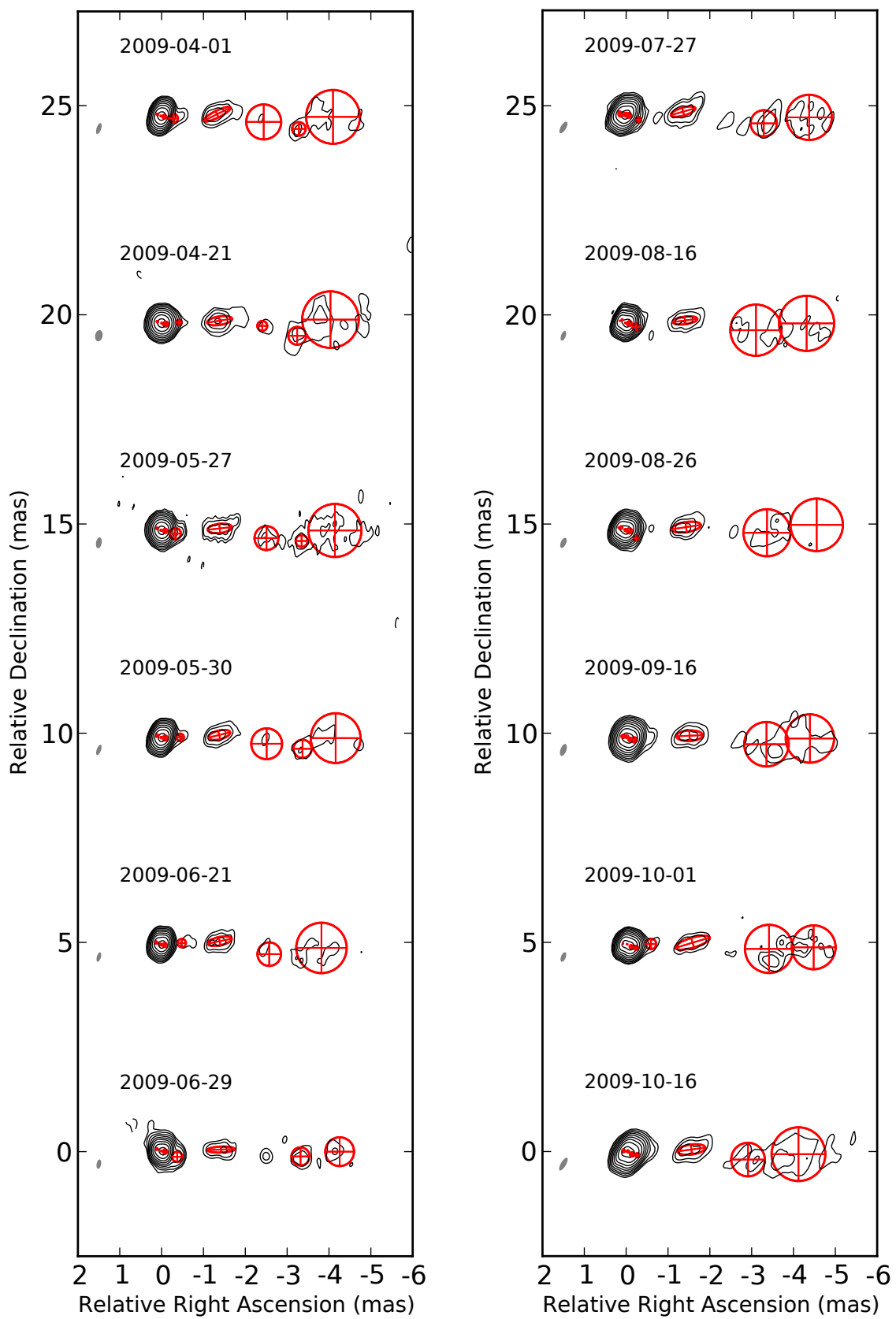


Figure B.6 43.2 GHz (continued)

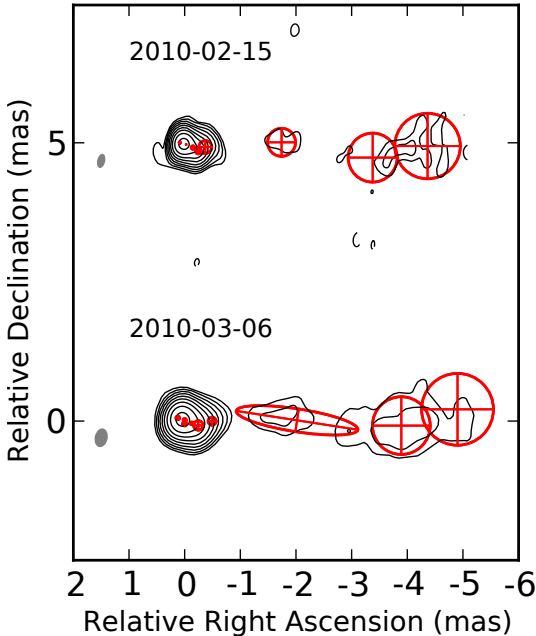


Figure B.6 43.2 GHz (continued)

APPENDIX C

GASP-WEBT/SAO monitoring data of 3C 345

Data that were provided through the GLAST/AGILE support program of the world blazar telescope consortium are presented in Table C.1 (optical R data) and Table C.2 for 1 mm radio data from the SMA. Optical multi-band data provided by O. Spiridonova et al. (*priv. comm.*) as part of ongoing monitoring by the Special Astrophysical Observatory in Russia is listed in Table C.3. The plots of these datasets are provided in Figure 6.4.

Table C.1: GASP optical R band observations of 3C 345 between 2008 and 2010.

Epoch	JD	Date	Magnitude	Observatory
2008.58425	2454680.33630	2008-08-01	17.197 ± 0.020	Crimean (70 cm; ST-7; pol)
2008.58427	2454680.34170	2008-08-01	17.241 ± 0.022	Crimean (70 cm; ST-7; pol)
2008.58649	2454681.15428	2008-08-02	17.233 ± 0.046	Lulin (SLT)
2008.61364	2454691.09119	2008-08-12	17.046 ± 0.053	Lulin (SLT)
2008.61431	2454691.33710	2008-08-12	16.867 ± 0.024	Crimean (70 cm; ST-7; pol)
2008.61432	2454691.34250	2008-08-12	16.917 ± 0.022	Crimean (70 cm; ST-7; pol)
2008.62716	2454696.03915	2008-08-17	17.013 ± 0.063	Lulin (SLT)
2008.64178	2454701.39020	2008-08-22	16.531 ± 0.029	St. Petersburg
2008.65518	2454706.29530	2008-08-27	16.745 ± 0.014	Crimean (70 cm; ST-7; pol)
2008.65519	2454706.30050	2008-08-27	16.761 ± 0.013	Crimean (70 cm; ST-7; pol)
2008.65790	2454707.28970	2008-08-28	16.685 ± 0.014	Crimean (70 cm; ST-7; pol)
2008.65791	2454707.29490	2008-08-28	16.697 ± 0.013	Crimean (70 cm; ST-7; pol)
2008.66064	2454708.29430	2008-08-29	16.775 ± 0.016	Crimean (70 cm; ST-7; pol)
2008.66066	2454708.30040	2008-08-29	16.802 ± 0.015	Crimean (70 cm; ST-7; pol)
2008.66345	2454709.32260	2008-08-30	16.863 ± 0.025	Crimean (70 cm; ST-7; pol)
2008.66348	2454709.33220	2008-08-30	16.870 ± 0.023	Crimean (70 cm; ST-7; pol)
2008.66611	2454710.29760	2008-08-31	16.661 ± 0.042	St. Petersburg
2008.66894	2454711.33150	2008-09-01	16.701 ± 0.015	Crimean (70 cm; ST-7; pol)
2008.66895	2454711.33700	2008-09-01	16.761 ± 0.024	Crimean (70 cm; ST-7; pol)
2008.66898	2454711.34710	2008-09-01	16.722 ± 0.005	Calar Alto
2008.67173	2454712.35170	2008-09-02	16.682 ± 0.005	Calar Alto
2008.67439	2454713.32536	2008-09-03	16.591 ± 0.019	Sabadell
2008.69073	2454719.30590	2008-09-09	16.419 ± 0.014	Crimean (70 cm; ST-7; pol)
2008.69074	2454719.30910	2008-09-09	16.450 ± 0.014	Crimean (70 cm; ST-7; pol)
2008.69341	2454720.28690	2008-09-10	16.421 ± 0.032	St. Petersburg
2008.69619	2454721.30620	2008-09-11	16.538 ± 0.017	Crimean (70 cm; ST-7; pol)
2008.69621	2454721.31150	2008-09-11	16.553 ± 0.017	Crimean (70 cm; ST-7; pol)
2008.70151	2454723.25260	2008-09-13	16.477 ± 0.143	St. Petersburg
2008.70423	2454724.24680	2008-09-14	16.427 ± 0.023	Crimean (70 cm; ST-7; pol)

Continued on next page ...

Table C.1 – *continued from previous page*

Epoch	JD	Date	Magnitude	Observatory
2008.70424	2454724.25200	2008-09-14	16.448 ± 0.022	Crimean (70 cm; ST-7; pol)
2008.70691	2454725.22980	2008-09-15	16.378 ± 0.027	Crimean (70 cm; ST-7; pol)
2008.70693	2454725.23500	2008-09-15	16.255 ± 0.024	Crimean (70 cm; ST-7; pol)
2008.71263	2454727.32244	2008-09-17	16.251 ± 0.017	Sabadell
2008.72277	2454731.03511	2008-09-21	16.135 ± 0.012	Lulin (SLT)
2008.72613	2454732.26490	2008-09-22	16.346 ± 0.022	St. Petersburg
2008.73145	2454734.21250	2008-09-24	16.331 ± 0.008	Crimean (70 cm; ST-7)
2008.73150	2454734.22750	2008-09-24	16.347 ± 0.010	Crimean (70 cm; ST-7; pol)
2008.73151	2454734.23270	2008-09-24	16.349 ± 0.012	Crimean (70 cm; ST-7; pol)
2008.74250	2454738.25330	2008-09-28	16.417 ± 0.024	St. Petersburg
2008.74536	2454739.30300	2008-09-29	16.575 ± 0.040	St. Petersburg
2008.74796	2454740.25310	2008-09-30	16.747 ± 0.040	St. Petersburg
2008.75086	2454741.31392	2008-10-01	16.831 ± 0.020	Sabadell
2008.75284	2454742.03870	2008-10-02	16.948 ± 0.015	Lulin (SLT)
2008.75362	2454742.32500	2008-10-02	16.978 ± 0.005	Calar Alto
2008.75557	2454743.03922	2008-10-03	16.945 ± 0.005	Lulin (SLT)
2008.76150	2454745.20770	2008-10-05	16.946 ± 0.038	St. Petersburg
2008.76433	2454746.24360	2008-10-06	16.931 ± 0.042	St. Petersburg
2008.76707	2454747.24690	2008-10-07	17.021 ± 0.036	St. Petersburg
2008.76966	2454748.19580	2008-10-08	16.914 ± 0.038	St. Petersburg
2008.77514	2454750.20290	2008-10-10	17.037 ± 0.023	Crimean (70 cm; ST-7; pol)
2008.77516	2454750.20810	2008-10-10	17.045 ± 0.023	Crimean (70 cm; ST-7; pol)
2008.77517	2454750.21360	2008-10-10	17.043 ± 0.019	Crimean (70 cm; ST-7)
2008.80731	2454761.97653	2008-10-22	17.065 ± 0.023	Lulin (SLT)
2008.81003	2454762.97246	2008-10-23	17.126 ± 0.006	Lulin (SLT)
2008.81057	2454763.16680	2008-10-23	16.984 ± 0.071	St. Petersburg
2008.81061	2454763.18220	2008-10-23	17.047 ± 0.055	St. Petersburg
2008.84621	2454776.21390	2008-11-05	17.115 ± 0.055	St. Petersburg
2008.88461	2454790.26711	2008-11-19	16.564 ± 0.026	Sabadell
2008.90366	2454797.24067	2008-11-26	17.114 ± 0.044	Sabadell
2008.97608	2454823.74610	2008-12-23	16.933 ± 0.007	Calar Alto
2009.00508	2454834.35872	2009-01-02	16.973 ± 0.009	Lulin (SLT)
2009.07318	2454859.28541	2009-01-27	16.456 ± 0.021	Lulin (SLT)
2009.09322	2454866.62030	2009-02-04	16.660 ± 0.116	St. Petersburg
2009.13419	2454881.61515	2009-02-19	16.654 ± 0.010	Abastumani (70 cm)
2009.13420	2454881.61726	2009-02-19	16.576 ± 0.010	Abastumani (70 cm)
2009.13421	2454881.61936	2009-02-19	16.621 ± 0.015	Abastumani (70 cm)
2009.13421	2454881.62147	2009-02-19	16.622 ± 0.010	Abastumani (70 cm)
2009.13422	2454881.62357	2009-02-19	16.611 ± 0.010	Abastumani (70 cm)
2009.13422	2454881.62567	2009-02-19	16.601 ± 0.010	Abastumani (70 cm)
2009.13423	2454881.62778	2009-02-19	16.619 ± 0.010	Abastumani (70 cm)
2009.14777	2454886.58351	2009-02-24	16.862 ± 0.010	Abastumani (70 cm)
2009.14777	2454886.58561	2009-02-24	16.836 ± 0.010	Abastumani (70 cm)
2009.14778	2454886.58772	2009-02-24	16.885 ± 0.010	Abastumani (70 cm)
2009.14779	2454886.58982	2009-02-24	16.870 ± 0.010	Abastumani (70 cm)
2009.14779	2454886.59192	2009-02-24	16.886 ± 0.012	Abastumani (70 cm)
2009.14780	2454886.59403	2009-02-24	16.898 ± 0.010	Abastumani (70 cm)
2009.14780	2454886.59612	2009-02-24	16.888 ± 0.010	Abastumani (70 cm)
2009.14781	2454886.59823	2009-02-24	16.860 ± 0.010	Abastumani (70 cm)
2009.14782	2454886.60034	2009-02-24	16.873 ± 0.010	Abastumani (70 cm)
2009.14782	2454886.60244	2009-02-24	16.867 ± 0.010	Abastumani (70 cm)
2009.14783	2454886.60454	2009-02-24	16.861 ± 0.010	Abastumani (70 cm)
2009.14783	2454886.60664	2009-02-24	16.854 ± 0.010	Abastumani (70 cm)
2009.14784	2454886.60875	2009-02-24	16.876 ± 0.010	Abastumani (70 cm)
2009.14784	2454886.61085	2009-02-24	16.866 ± 0.010	Abastumani (70 cm)
2009.15061	2454887.62230	2009-02-25	16.902 ± 0.005	Calar Alto
2009.17240	2454894.59771	2009-03-04	16.825 ± 0.025	Abastumani (70 cm)
2009.17779	2454896.57050	2009-03-06	16.933 ± 0.145	St. Petersburg
2009.18040	2454897.52510	2009-03-07	16.838 ± 0.175	St. Petersburg
2009.20785	2454907.57370	2009-03-17	16.829 ± 0.011	Abastumani (70 cm)
2009.20786	2454907.57580	2009-03-17	16.846 ± 0.010	Abastumani (70 cm)
2009.20786	2454907.57791	2009-03-17	16.899 ± 0.011	Abastumani (70 cm)
2009.20787	2454907.58001	2009-03-17	16.817 ± 0.010	Abastumani (70 cm)
2009.20787	2454907.58211	2009-03-17	16.869 ± 0.022	Abastumani (70 cm)
2009.21065	2454908.59648	2009-03-18	16.872 ± 0.010	Abastumani (70 cm)
2009.21065	2454908.59859	2009-03-18	16.830 ± 0.022	Abastumani (70 cm)
2009.21066	2454908.60068	2009-03-18	16.810 ± 0.017	Abastumani (70 cm)
2009.21066	2454908.60279	2009-03-18	16.769 ± 0.015	Abastumani (70 cm)
2009.22432	2454913.59950	2009-03-23	16.734 ± 0.099	St. Petersburg
2009.22712	2454914.62690	2009-03-24	16.695 ± 0.005	Calar Alto
2009.24324	2454920.52436	2009-03-30	16.771 ± 0.010	Abastumani (70 cm)

Continued on next page ...

Table C.1 – *continued from previous page*

Epoch	JD	Date	Magnitude	Observatory
2009.24324	2454920.52647	2009-03-30	16.765 ± 0.010	Abastumani (70 cm)
2009.24325	2454920.52858	2009-03-30	16.789 ± 0.010	Abastumani (70 cm)
2009.24325	2454920.53068	2009-03-30	16.764 ± 0.010	Abastumani (70 cm)
2009.24326	2454920.53278	2009-03-30	16.745 ± 0.018	Abastumani (70 cm)
2009.24326	2454920.53488	2009-03-30	16.786 ± 0.010	Abastumani (70 cm)
2009.25143	2454923.52360	2009-04-02	16.699 ± 0.034	St. Petersburg
2009.26249	2454927.57270	2009-04-06	16.757 ± 0.010	Abastumani (70 cm)
2009.26250	2454927.57479	2009-04-06	16.730 ± 0.010	Abastumani (70 cm)
2009.26788	2454929.54330	2009-04-08	16.766 ± 0.054	St. Petersburg
2009.28177	2454934.62760	2009-04-13	16.812 ± 0.011	Calar Alto
2009.28449	2454935.62450	2009-04-14	16.785 ± 0.009	Calar Alto
2009.30052	2454941.49010	2009-04-19	16.736 ± 0.010	Abastumani (70 cm)
2009.30053	2454941.49221	2009-04-19	16.719 ± 0.010	Abastumani (70 cm)
2009.30053	2454941.49432	2009-04-19	16.712 ± 0.010	Abastumani (70 cm)
2009.30054	2454941.49641	2009-04-19	16.757 ± 0.010	Abastumani (70 cm)
2009.31136	2454945.45900	2009-04-23	16.749 ± 0.013	Crimean (70 cm; ST-7; pol)
2009.31138	2454945.46630	2009-04-23	16.759 ± 0.015	Crimean (70 cm; ST-7; pol)
2009.32231	2454949.46440	2009-04-27	16.632 ± 0.018	Crimean (70 cm; ST-7; pol)
2009.32233	2454949.47110	2009-04-27	16.648 ± 0.016	Crimean (70 cm; ST-7; pol)
2009.32244	2454949.51320	2009-04-28	16.634 ± 0.006	Calar Alto
2009.32754	2454951.38082	2009-04-29	16.613 ± 0.055	Sabadell
2009.33066	2454952.52087	2009-05-01	16.761 ± 0.010	Abastumani (70 cm)
2009.33066	2454952.52298	2009-05-01	16.751 ± 0.010	Abastumani (70 cm)
2009.39722	2454976.88280	2009-05-25	16.503 ± 0.057	Lowell (Perkins)
2009.40002	2454977.90720	2009-05-26	16.240 ± 0.020	Lowell (Perkins)
2009.40264	2454978.86630	2009-05-27	16.583 ± 0.014	Lowell (Perkins)
2009.40539	2454979.87210	2009-05-28	16.685 ± 0.014	Lowell (Perkins)
2009.40819	2454980.89900	2009-05-29	16.653 ± 0.024	Lowell (Perkins)
2009.40995	2454981.54220	2009-05-30	16.642 ± 0.018	Calar Alto
2009.41789	2454984.44833	2009-06-01	16.754 ± 0.010	Abastumani (70 cm)
2009.41790	2454984.45043	2009-06-01	16.732 ± 0.010	Abastumani (70 cm)
2009.41790	2454984.45254	2009-06-01	16.694 ± 0.015	Abastumani (70 cm)
2009.41791	2454984.45464	2009-06-01	16.716 ± 0.010	Abastumani (70 cm)
2009.43956	2454992.37720	2009-06-09	16.874 ± 0.024	Crimean (70 cm; ST-7; pol)
2009.43957	2454992.38250	2009-06-09	16.864 ± 0.025	Crimean (70 cm; ST-7; pol)
2009.43958	2454992.38549	2009-06-09	16.874 ± 0.010	Abastumani (70 cm)
2009.43958	2454992.38758	2009-06-09	16.905 ± 0.010	Abastumani (70 cm)
2009.44501	2454994.37200	2009-06-11	17.003 ± 0.026	Crimean (70 cm; ST-7; pol)
2009.44502	2454994.37720	2009-06-11	16.886 ± 0.023	Crimean (70 cm; ST-7; pol)
2009.46145	2455000.39184	2009-06-17	16.742 ± 0.039	Sabadell
2009.47793	2455006.42197	2009-06-23	16.993 ± 0.010	Abastumani (70 cm)
2009.47793	2455006.42407	2009-06-23	16.980 ± 0.010	Abastumani (70 cm)
2009.48062	2455007.40830	2009-06-24	16.994 ± 0.050	Crimean (70 cm; ST-7; pol)
2009.48064	2455007.41350	2009-06-24	16.890 ± 0.067	Crimean (70 cm; ST-7; pol)
2009.49155	2455011.40730	2009-06-28	16.940 ± 0.022	Crimean (70 cm; ST-7; pol)
2009.49157	2455011.41320	2009-06-28	16.989 ± 0.037	Crimean (70 cm; ST-7; pol)
2009.49711	2455013.44330	2009-06-30	16.943 ± 0.010	Calar Alto
2009.50247	2455015.40389	2009-07-02	16.970 ± 0.010	Abastumani (70 cm)
2009.50248	2455015.40598	2009-07-02	16.945 ± 0.012	Abastumani (70 cm)
2009.50248	2455015.40809	2009-07-02	16.989 ± 0.010	Abastumani (70 cm)
2009.50249	2455015.41020	2009-07-02	16.944 ± 0.010	Abastumani (70 cm)
2009.51617	2455020.41640	2009-07-07	16.944 ± 0.028	Crimean (70 cm; ST-7; pol)
2009.51618	2455020.42170	2009-07-07	16.975 ± 0.030	Crimean (70 cm; ST-7; pol)
2009.52715	2455024.43831	2009-07-11	16.924 ± 0.010	Abastumani (70 cm)
2009.52716	2455024.44042	2009-07-11	16.941 ± 0.010	Abastumani (70 cm)
2009.52717	2455024.44252	2009-07-11	16.913 ± 0.010	Abastumani (70 cm)
2009.52717	2455024.44463	2009-07-11	16.940 ± 0.012	Abastumani (70 cm)
2009.53794	2455028.38639	2009-07-15	17.014 ± 0.034	Sabadell
2009.54350	2455030.42110	2009-07-17	16.728 ± 0.006	Calar Alto
2009.55537	2455034.76680	2009-07-22	16.782 ± 0.017	Lowell (Perkins)
2009.55706	2455035.38409	2009-07-22	16.962 ± 0.046	Sabadell
2009.55964	2455036.32910	2009-07-23	16.847 ± 0.015	Crimean (70 cm; ST-7; pol)
2009.55966	2455036.33540	2009-07-23	16.847 ± 0.017	Crimean (70 cm; ST-7; pol)
2009.56506	2455038.31180	2009-07-25	16.835 ± 0.015	Crimean (70 cm; ST-7; pol)
2009.56507	2455038.31710	2009-07-25	16.841 ± 0.018	Crimean (70 cm; ST-7; pol)
2009.56800	2455039.38825	2009-07-26	16.699 ± 0.093	Sabadell
2009.57084	2455040.42865	2009-07-27	16.708 ± 0.011	Abastumani (70 cm)
2009.57085	2455040.43075	2009-07-27	16.759 ± 0.010	Abastumani (70 cm)
2009.57085	2455040.43286	2009-07-27	16.760 ± 0.010	Abastumani (70 cm)
2009.57086	2455040.43497	2009-07-27	16.747 ± 0.014	Abastumani (70 cm)
2009.57087	2455040.43707	2009-07-27	16.742 ± 0.010	Abastumani (70 cm)

Continued on next page ...

Table C.1 – *continued from previous page*

Epoch	JD	Date	Magnitude	Observatory
2009.57622	2455042.39637	2009-07-29	16.737 ± 0.020	Sabadell
2009.58477	2455045.52460	2009-08-02	16.755 ± 0.009	Calar Alto
2009.60889	2455054.35210	2009-08-10	16.636 ± 0.016	Crimean (70 cm; ST-7; pol)
2009.60891	2455054.36120	2009-08-10	16.704 ± 0.018	Crimean (70 cm; ST-7; pol)
2009.61017	2455054.82370	2009-08-11	16.560 ± 0.017	Lowell (Perkins)
2009.62005	2455058.43970	2009-08-14	16.450 ± 0.005	Calar Alto
2009.62305	2455059.53470	2009-08-16	16.463 ± 0.066	Tijarafe (35 cm)
2009.62305	2455059.53742	2009-08-16	16.389 ± 0.067	Tijarafe (35 cm)
2009.62564	2455060.48347	2009-08-16	16.433 ± 0.062	Tijarafe (35 cm)
2009.62565	2455060.48646	2009-08-16	16.462 ± 0.064	Tijarafe (35 cm)
2009.62839	2455061.49069	2009-08-17	16.265 ± 0.063	Tijarafe (35 cm)
2009.63127	2455062.54405	2009-08-19	16.305 ± 0.059	Tijarafe (35 cm)
2009.63128	2455062.54698	2009-08-19	16.231 ± 0.055	Tijarafe (35 cm)
2009.63343	2455063.33560	2009-08-19	16.385 ± 0.010	Crimean (70 cm; ST-7; pol)
2009.63343	2455063.33650	2009-08-19	16.390 ± 0.020	St. Petersburg
2009.63345	2455063.34140	2009-08-19	16.410 ± 0.010	Crimean (70 cm; ST-7; pol)
2009.63382	2455063.47903	2009-08-19	16.348 ± 0.056	Tijarafe (35 cm)
2009.63383	2455063.48205	2009-08-19	16.444 ± 0.070	Tijarafe (35 cm)
2009.63616	2455064.33360	2009-08-20	16.091 ± 0.007	Crimean (70 cm; ST-7; pol)
2009.63617	2455064.33950	2009-08-20	16.083 ± 0.007	Crimean (70 cm; ST-7; pol)
2009.63646	2455064.44445	2009-08-20	16.095 ± 0.051	Tijarafe (35 cm)
2009.63647	2455064.44722	2009-08-20	16.111 ± 0.069	Tijarafe (35 cm)
2009.63651	2455064.46230	2009-08-20	16.100 ± 0.026	St. Petersburg
2009.63670	2455064.53193	2009-08-21	16.067 ± 0.071	Tijarafe (35 cm)
2009.63671	2455064.53479	2009-08-21	16.079 ± 0.073	Tijarafe (35 cm)
2009.63889	2455065.33200	2009-08-21	16.167 ± 0.008	Crimean (70 cm; ST-7; pol)
2009.63890	2455065.33740	2009-08-21	16.177 ± 0.008	Crimean (70 cm; ST-7; pol)
2009.63915	2455065.42750	2009-08-21	16.184 ± 0.018	St. Petersburg
2009.63922	2455065.45367	2009-08-21	16.229 ± 0.053	Tijarafe (35 cm)
2009.63923	2455065.45663	2009-08-21	16.256 ± 0.043	Tijarafe (35 cm)
2009.63939	2455065.51798	2009-08-22	16.285 ± 0.052	Tijarafe (35 cm)
2009.64170	2455066.36400	2009-08-22	16.474 ± 0.009	Crimean (70 cm; ST-7; pol)
2009.64172	2455066.36970	2009-08-22	16.481 ± 0.010	Crimean (70 cm; ST-7; pol)
2009.64198	2455066.46627	2009-08-22	16.422 ± 0.052	Tijarafe (35 cm)
2009.64199	2455066.46922	2009-08-22	16.417 ± 0.041	Tijarafe (35 cm)
2009.64215	2455066.52630	2009-08-23	16.461 ± 0.052	Tijarafe (35 cm)
2009.64216	2455066.52896	2009-08-23	16.486 ± 0.066	Tijarafe (35 cm)
2009.64442	2455067.35930	2009-08-23	16.569 ± 0.010	Crimean (70 cm; ST-7; pol)
2009.64444	2455067.36490	2009-08-23	16.605 ± 0.011	Crimean (70 cm; ST-7; pol)
2009.64461	2455067.42839	2009-08-23	16.639 ± 0.051	Tijarafe (35 cm)
2009.64462	2455067.43104	2009-08-23	16.530 ± 0.051	Tijarafe (35 cm)
2009.64476	2455067.48313	2009-08-23	16.519 ± 0.058	Tijarafe (35 cm)
2009.64477	2455067.48579	2009-08-23	16.602 ± 0.055	Tijarafe (35 cm)
2009.64702	2455068.31043	2009-08-24	16.502 ± 0.010	Abastumani (70 cm)
2009.64703	2455068.31254	2009-08-24	16.519 ± 0.012	Abastumani (70 cm)
2009.64703	2455068.31464	2009-08-24	16.526 ± 0.011	Abastumani (70 cm)
2009.64704	2455068.31674	2009-08-24	16.505 ± 0.010	Abastumani (70 cm)
2009.64707	2455068.32770	2009-08-24	16.562 ± 0.009	Crimean (70 cm; ST-7; pol)
2009.64708	2455068.33310	2009-08-24	16.554 ± 0.010	Crimean (70 cm; ST-7; pol)
2009.64710	2455068.33790	2009-08-24	16.585 ± 0.023	St. Petersburg
2009.64731	2455068.41658	2009-08-24	16.540 ± 0.091	Tijarafe (35 cm)
2009.64748	2455068.47736	2009-08-24	16.531 ± 0.096	Tijarafe (35 cm)
2009.65014	2455069.45075	2009-08-25	16.286 ± 0.044	Tijarafe (35 cm)
2009.65015	2455069.45414	2009-08-25	16.359 ± 0.052	Tijarafe (35 cm)
2009.65031	2455069.51342	2009-08-26	16.363 ± 0.061	Tijarafe (35 cm)
2009.65032	2455069.51723	2009-08-26	16.322 ± 0.057	Tijarafe (35 cm)
2009.65634	2455071.72010	2009-08-28	16.422 ± 0.021	Lowell (Perkins)
2009.65915	2455072.74820	2009-08-29	16.433 ± 0.025	Lowell (Perkins)
2009.66178	2455073.71000	2009-08-30	16.385 ± 0.051	Lowell (Perkins)
2009.66338	2455074.29550	2009-08-30	16.401 ± 0.055	St. Petersburg
2009.66345	2455074.32160	2009-08-30	16.371 ± 0.022	St. Petersburg
2009.66651	2455075.44313	2009-08-31	16.435 ± 0.131	Tijarafe (35 cm)
2009.66652	2455075.44608	2009-08-31	16.273 ± 0.150	Tijarafe (35 cm)
2009.67205	2455077.47077	2009-09-02	16.450 ± 0.061	Tijarafe (35 cm)
2009.67206	2455077.47369	2009-09-02	16.278 ± 0.050	Tijarafe (35 cm)
2009.67431	2455078.29893	2009-09-03	16.370 ± 0.010	Abastumani (70 cm)
2009.67432	2455078.30104	2009-09-03	16.399 ± 0.010	Abastumani (70 cm)
2009.67433	2455078.30315	2009-09-03	16.358 ± 0.010	Abastumani (70 cm)
2009.67433	2455078.30524	2009-09-03	16.381 ± 0.011	Abastumani (70 cm)
2009.67434	2455078.30735	2009-09-03	16.328 ± 0.010	Abastumani (70 cm)
2009.67434	2455078.30946	2009-09-03	16.318 ± 0.025	Abastumani (70 cm)

Continued on next page ...

Table C.1 – *continued from previous page*

Epoch	JD	Date	Magnitude	Observatory
2009.67435	2455078.31156	2009-09-03	16.326 ± 0.010	Abastumani (70 cm)
2009.67435	2455078.31366	2009-09-03	16.429 ± 0.026	Abastumani (70 cm)
2009.67436	2455078.31576	2009-09-03	16.369 ± 0.015	Abastumani (70 cm)
2009.67437	2455078.31787	2009-09-03	16.331 ± 0.014	Abastumani (70 cm)
2009.67437	2455078.31998	2009-09-03	16.346 ± 0.010	Abastumani (70 cm)
2009.67438	2455078.32207	2009-09-03	16.334 ± 0.010	Abastumani (70 cm)
2009.67438	2455078.32418	2009-09-03	16.326 ± 0.010	Abastumani (70 cm)
2009.67439	2455078.32629	2009-09-03	16.316 ± 0.011	Abastumani (70 cm)
2009.67439	2455078.32839	2009-09-03	16.358 ± 0.013	Abastumani (70 cm)
2009.67440	2455078.33049	2009-09-03	16.389 ± 0.012	Abastumani (70 cm)
2009.67480	2455078.47718	2009-09-03	16.350 ± 0.064	Tijarafe (35 cm)
2009.67978	2455080.29840	2009-09-05	16.387 ± 0.017	Crimean (70 cm; ST-7; pol)
2009.67979	2455080.30420	2009-09-05	16.385 ± 0.020	Crimean (70 cm; ST-7; pol)
2009.67989	2455080.34015	2009-09-05	16.373 ± 0.010	Abastumani (70 cm)
2009.67991	2455080.34646	2009-09-05	16.384 ± 0.010	Abastumani (70 cm)
2009.67992	2455080.35067	2009-09-05	16.358 ± 0.017	Abastumani (70 cm)
2009.67993	2455080.35278	2009-09-05	16.367 ± 0.010	Abastumani (70 cm)
2009.67993	2455080.35487	2009-09-05	16.363 ± 0.013	Abastumani (70 cm)
2009.67994	2455080.35698	2009-09-05	16.352 ± 0.012	Abastumani (70 cm)
2009.67994	2455080.35909	2009-09-05	16.459 ± 0.010	Abastumani (70 cm)
2009.67995	2455080.36263	2009-09-05	16.416 ± 0.011	Abastumani (70 cm)
2009.67996	2455080.36472	2009-09-05	16.473 ± 0.010	Abastumani (70 cm)
2009.67996	2455080.36683	2009-09-05	16.422 ± 0.010	Abastumani (70 cm)
2009.68248	2455081.28660	2009-09-06	16.333 ± 0.017	Crimean (70 cm; ST-7; pol)
2009.68249	2455081.29230	2009-09-06	16.333 ± 0.019	Crimean (70 cm; ST-7; pol)
2009.68266	2455081.35202	2009-09-06	16.363 ± 0.010	Abastumani (70 cm)
2009.68266	2455081.35412	2009-09-06	16.366 ± 0.017	Abastumani (70 cm)
2009.68267	2455081.35623	2009-09-06	16.404 ± 0.010	Abastumani (70 cm)
2009.68268	2455081.36044	2009-09-06	16.373 ± 0.018	Abastumani (70 cm)
2009.68268	2455081.36253	2009-09-06	16.304 ± 0.023	Abastumani (70 cm)
2009.68269	2455081.36464	2009-09-06	16.300 ± 0.026	Abastumani (70 cm)
2009.68270	2455081.36675	2009-09-06	16.278 ± 0.010	Abastumani (70 cm)
2009.68271	2455081.37095	2009-09-06	16.335 ± 0.010	Abastumani (70 cm)
2009.68500	2455082.21062	2009-09-07	16.234 ± 0.020	Abastumani (70 cm)
2009.68501	2455082.21273	2009-09-07	16.288 ± 0.010	Abastumani (70 cm)
2009.68501	2455082.21484	2009-09-07	16.316 ± 0.010	Abastumani (70 cm)
2009.68502	2455082.21693	2009-09-07	16.268 ± 0.014	Abastumani (70 cm)
2009.68502	2455082.21904	2009-09-07	16.293 ± 0.010	Abastumani (70 cm)
2009.68503	2455082.22115	2009-09-07	16.285 ± 0.015	Abastumani (70 cm)
2009.68504	2455082.22325	2009-09-07	16.303 ± 0.017	Abastumani (70 cm)
2009.68504	2455082.22535	2009-09-07	16.314 ± 0.015	Abastumani (70 cm)
2009.68505	2455082.22745	2009-09-07	16.310 ± 0.010	Abastumani (70 cm)
2009.68505	2455082.22956	2009-09-07	16.289 ± 0.016	Abastumani (70 cm)
2009.68518	2455082.27660	2009-09-07	16.293 ± 0.015	Crimean (70 cm; ST-7; pol)
2009.68520	2455082.28300	2009-09-07	16.267 ± 0.016	Crimean (70 cm; ST-7; pol)
2009.68528	2455082.31270	2009-09-07	16.267 ± 0.022	St. Petersburg
2009.68618	2455082.64020	2009-09-08	16.236 ± 0.021	Lowell (Perkins)
2009.68779	2455083.23196	2009-09-08	16.243 ± 0.010	Abastumani (70 cm)
2009.68780	2455083.23405	2009-09-08	16.268 ± 0.010	Abastumani (70 cm)
2009.68780	2455083.23616	2009-09-08	16.234 ± 0.012	Abastumani (70 cm)
2009.68781	2455083.23826	2009-09-08	16.251 ± 0.020	Abastumani (70 cm)
2009.68782	2455083.24037	2009-09-08	16.236 ± 0.010	Abastumani (70 cm)
2009.68782	2455083.24247	2009-09-08	16.213 ± 0.012	Abastumani (70 cm)
2009.68783	2455083.24457	2009-09-08	16.223 ± 0.010	Abastumani (70 cm)
2009.68783	2455083.24668	2009-09-08	16.203 ± 0.010	Abastumani (70 cm)
2009.68784	2455083.24878	2009-09-08	16.243 ± 0.011	Abastumani (70 cm)
2009.68784	2455083.25088	2009-09-08	16.259 ± 0.010	Abastumani (70 cm)
2009.68785	2455083.25299	2009-09-08	16.261 ± 0.010	Abastumani (70 cm)
2009.68786	2455083.25509	2009-09-08	16.239 ± 0.010	Abastumani (70 cm)
2009.69081	2455084.33750	2009-09-09	16.197 ± 0.024	St. Petersburg
2009.69377	2455085.41910	2009-09-10	16.115 ± 0.020	St. Petersburg
2009.69613	2455086.28460	2009-09-11	16.136 ± 0.018	St. Petersburg
2009.69614	2455086.28560	2009-09-11	16.099 ± 0.010	Abastumani (70 cm)
2009.69614	2455086.28771	2009-09-11	16.083 ± 0.010	Abastumani (70 cm)
2009.69615	2455086.28981	2009-09-11	16.114 ± 0.010	Abastumani (70 cm)
2009.69615	2455086.29191	2009-09-11	16.101 ± 0.010	Abastumani (70 cm)
2009.69616	2455086.29402	2009-09-11	16.103 ± 0.010	Abastumani (70 cm)
2009.69616	2455086.29612	2009-09-11	16.133 ± 0.016	Abastumani (70 cm)
2009.69617	2455086.29823	2009-09-11	16.106 ± 0.012	Abastumani (70 cm)
2009.69618	2455086.30032	2009-09-11	16.119 ± 0.010	Abastumani (70 cm)
2009.69887	2455087.28660	2009-09-12	15.970 ± 0.014	St. Petersburg

Continued on next page ...

Table C.1 – *continued from previous page*

Epoch	JD	Date	Magnitude	Observatory
2009.69902	2455087.34069	2009-09-12	16.037 ± 0.014	Abastumani (70 cm)
2009.69902	2455087.34279	2009-09-12	16.039 ± 0.010	Abastumani (70 cm)
2009.69903	2455087.34490	2009-09-12	16.011 ± 0.010	Abastumani (70 cm)
2009.69904	2455087.34700	2009-09-12	15.944 ± 0.010	Abastumani (70 cm)
2009.69904	2455087.34911	2009-09-12	15.954 ± 0.025	Abastumani (70 cm)
2009.69905	2455087.35120	2009-09-12	15.985 ± 0.010	Abastumani (70 cm)
2009.69905	2455087.35409	2009-09-12	16.054 ± 0.010	Abastumani (70 cm)
2009.69912	2455087.37760	2009-09-12	16.033 ± 0.036	St. Petersburg
2009.70412	2455089.20812	2009-09-14	15.909 ± 0.010	Abastumani (70 cm)
2009.70413	2455089.21023	2009-09-14	15.919 ± 0.010	Abastumani (70 cm)
2009.70413	2455089.21233	2009-09-14	15.921 ± 0.010	Abastumani (70 cm)
2009.70414	2455089.21443	2009-09-14	15.935 ± 0.010	Abastumani (70 cm)
2009.70414	2455089.21654	2009-09-14	15.932 ± 0.010	Abastumani (70 cm)
2009.70415	2455089.21865	2009-09-14	15.938 ± 0.010	Abastumani (70 cm)
2009.70416	2455089.22074	2009-09-14	15.938 ± 0.012	Abastumani (70 cm)
2009.70416	2455089.22285	2009-09-14	15.959 ± 0.010	Abastumani (70 cm)
2009.70438	2455089.30200	2009-09-14	15.948 ± 0.037	St. Petersburg
2009.70710	2455090.29880	2009-09-15	15.938 ± 0.021	St. Petersburg
2009.70714	2455090.31160	2009-09-15	15.896 ± 0.007	Crimean (70 cm; ST-7)
2009.70729	2455090.36950	2009-09-15	15.897 ± 0.033	St. Petersburg
2009.70748	2455090.43880	2009-09-15	15.892 ± 0.029	Tijarafe (35 cm)
2009.70749	2455090.44282	2009-09-15	15.917 ± 0.033	Tijarafe (35 cm)
2009.70995	2455091.34190	2009-09-16	15.899 ± 0.007	Crimean (70 cm; ST-7; pol)
2009.70997	2455091.34870	2009-09-16	15.891 ± 0.007	Crimean (70 cm; ST-7; pol)
2009.71016	2455091.41763	2009-09-16	15.900 ± 0.024	Tijarafe (35 cm)
2009.71017	2455091.42173	2009-09-16	15.901 ± 0.055	Tijarafe (35 cm)
2009.71253	2455092.28770	2009-09-17	15.860 ± 0.007	Crimean (70 cm; ST-7; pol)
2009.71255	2455092.29350	2009-09-17	15.837 ± 0.007	Crimean (70 cm; ST-7; pol)
2009.71513	2455093.23705	2009-09-18	15.839 ± 0.010	Abastumani (70 cm)
2009.71513	2455093.23916	2009-09-18	15.844 ± 0.010	Abastumani (70 cm)
2009.71514	2455093.24126	2009-09-18	15.835 ± 0.010	Abastumani (70 cm)
2009.71515	2455093.24337	2009-09-18	15.825 ± 0.010	Abastumani (70 cm)
2009.71524	2455093.27850	2009-09-18	15.822 ± 0.007	Crimean (70 cm; ST-7; pol)
2009.71526	2455093.28550	2009-09-18	15.844 ± 0.008	Crimean (70 cm; ST-7; pol)
2009.71785	2455094.23160	2009-09-19	15.755 ± 0.007	Crimean (70 cm; ST-7; pol)
2009.71786	2455094.23680	2009-09-19	15.768 ± 0.007	Crimean (70 cm; ST-7; pol)
2009.72053	2455095.21490	2009-09-20	15.772 ± 0.007	Crimean (70 cm; ST-7; pol)
2009.72055	2455095.22010	2009-09-20	15.762 ± 0.007	Crimean (70 cm; ST-7; pol)
2009.72064	2455095.25330	2009-09-20	15.745 ± 0.014	St. Petersburg
2009.72096	2455095.37210	2009-09-20	15.756 ± 0.014	St. Petersburg
2009.72341	2455096.26880	2009-09-21	15.919 ± 0.027	St. Petersburg
2009.72898	2455098.30538	2009-09-23	16.032 ± 0.050	Sabadell
2009.72930	2455098.42443	2009-09-23	16.122 ± 0.050	Tijarafe (35 cm)
2009.73184	2455099.35187	2009-09-24	16.213 ± 0.024	Tijarafe (35 cm)
2009.73185	2455099.35597	2009-09-24	16.213 ± 0.031	Tijarafe (35 cm)
2009.73413	2455100.19214	2009-09-25	16.231 ± 0.012	Abastumani (70 cm)
2009.73414	2455100.19425	2009-09-25	16.237 ± 0.025	Abastumani (70 cm)
2009.73414	2455100.19635	2009-09-25	16.258 ± 0.010	Abastumani (70 cm)
2009.73415	2455100.19845	2009-09-25	16.247 ± 0.010	Abastumani (70 cm)
2009.73415	2455100.20056	2009-09-25	16.249 ± 0.010	Abastumani (70 cm)
2009.73416	2455100.20266	2009-09-25	16.216 ± 0.010	Abastumani (70 cm)
2009.73417	2455100.20477	2009-09-25	16.246 ± 0.010	Abastumani (70 cm)
2009.73417	2455100.20686	2009-09-25	16.251 ± 0.010	Abastumani (70 cm)
2009.73428	2455100.24650	2009-09-25	16.227 ± 0.030	St. Petersburg
2009.73448	2455100.31880	2009-09-25	16.235 ± 0.017	St. Petersburg
2009.73477	2455100.42718	2009-09-25	16.263 ± 0.038	Tijarafe (35 cm)
2009.73478	2455100.43128	2009-09-25	16.243 ± 0.037	Tijarafe (35 cm)
2009.73690	2455101.20506	2009-09-26	16.262 ± 0.013	Abastumani (70 cm)
2009.73690	2455101.20716	2009-09-26	16.274 ± 0.010	Abastumani (70 cm)
2009.73691	2455101.20927	2009-09-26	16.277 ± 0.013	Abastumani (70 cm)
2009.73692	2455101.21138	2009-09-26	16.261 ± 0.016	Abastumani (70 cm)
2009.73692	2455101.21376	2009-09-26	16.271 ± 0.010	Abastumani (70 cm)
2009.73693	2455101.21586	2009-09-26	16.285 ± 0.015	Abastumani (70 cm)
2009.73743	2455101.39756	2009-09-26	16.265 ± 0.055	Tijarafe (35 cm)
2009.73744	2455101.40159	2009-09-26	16.200 ± 0.073	Tijarafe (35 cm)
2009.74516	2455104.22870	2009-09-29	15.938 ± 0.008	Crimean (70 cm; ST-7; pol)
2009.74518	2455104.23410	2009-09-29	15.947 ± 0.010	Crimean (70 cm; ST-7; pol)
2009.75055	2455106.20280	2009-10-01	16.329 ± 0.012	Crimean (70 cm; ST-7; pol)
2009.75057	2455106.20810	2009-10-01	16.305 ± 0.015	Crimean (70 cm; ST-7; pol)
2009.75076	2455106.27640	2009-10-01	16.335 ± 0.020	Crimean (70 cm; ST-7; pol)
2009.75078	2455106.28620	2009-10-01	16.377 ± 0.034	Crimean (70 cm; ST-7; pol)

Continued on next page ...

Table C.1 – *continued from previous page*

Epoch	JD	Date	Magnitude	Observatory
2009.75080	2455106.29190	2009-10-01	16.315 ± 0.023	Crimean (70 cm; ST-7; pol)
2009.75083	2455106.30290	2009-10-01	16.362 ± 0.036	Crimean (70 cm; ST-7; pol)
2009.75317	2455107.16071	2009-10-02	16.269 ± 0.010	Abastumani (70 cm)
2009.75319	2455107.16702	2009-10-02	16.329 ± 0.020	Abastumani (70 cm)
2009.75320	2455107.17123	2009-10-02	16.279 ± 0.033	Abastumani (70 cm)
2009.75321	2455107.17544	2009-10-02	16.318 ± 0.039	Abastumani (70 cm)
2009.75329	2455107.20580	2009-10-02	16.356 ± 0.014	Crimean (70 cm; ST-7; pol)
2009.75331	2455107.21110	2009-10-02	16.351 ± 0.016	Crimean (70 cm; ST-7; pol)
2009.75337	2455107.23189	2009-10-02	16.316 ± 0.010	Abastumani (70 cm)
2009.75338	2455107.23610	2009-10-02	16.316 ± 0.010	Abastumani (70 cm)
2009.75338	2455107.23821	2009-10-02	16.273 ± 0.010	Abastumani (70 cm)
2009.75339	2455107.24030	2009-10-02	16.299 ± 0.010	Abastumani (70 cm)
2009.75339	2455107.24241	2009-10-02	16.276 ± 0.010	Abastumani (70 cm)
2009.75340	2455107.24451	2009-10-02	16.289 ± 0.010	Abastumani (70 cm)
2009.75340	2455107.24570	2009-10-02	16.331 ± 0.025	St. Petersburg
2009.75341	2455107.24662	2009-10-02	16.289 ± 0.010	Abastumani (70 cm)
2009.75357	2455107.30750	2009-10-02	16.316 ± 0.032	St. Petersburg
2009.75370	2455107.35527	2009-10-02	16.315 ± 0.032	Tijarafe (35 cm)
2009.75371	2455107.35943	2009-10-02	16.361 ± 0.021	Tijarafe (35 cm)
2009.75593	2455108.16869	2009-10-03	16.311 ± 0.010	Abastumani (70 cm)
2009.75593	2455108.17080	2009-10-03	16.344 ± 0.012	Abastumani (70 cm)
2009.75594	2455108.17290	2009-10-03	16.347 ± 0.010	Abastumani (70 cm)
2009.75594	2455108.17501	2009-10-03	16.357 ± 0.010	Abastumani (70 cm)
2009.75595	2455108.17711	2009-10-03	16.363 ± 0.011	Abastumani (70 cm)
2009.75595	2455108.17921	2009-10-03	16.353 ± 0.010	Abastumani (70 cm)
2009.75644	2455108.35528	2009-10-03	16.416 ± 0.046	Tijarafe (35 cm)
2009.75659	2455108.41220	2009-10-03	16.292 ± 0.057	Tijarafe (35 cm)
2009.75867	2455109.17488	2009-10-04	16.126 ± 0.010	Abastumani (70 cm)
2009.75868	2455109.17698	2009-10-04	16.130 ± 0.010	Abastumani (70 cm)
2009.75869	2455109.17909	2009-10-04	16.141 ± 0.010	Abastumani (70 cm)
2009.75869	2455109.18119	2009-10-04	16.159 ± 0.012	Abastumani (70 cm)
2009.75870	2455109.18330	2009-10-04	16.154 ± 0.010	Abastumani (70 cm)
2009.75870	2455109.18539	2009-10-04	16.115 ± 0.010	Abastumani (70 cm)
2009.75900	2455109.29243	2009-10-04	16.031 ± 0.015	Sabadell
2009.76148	2455110.20096	2009-10-05	16.357 ± 0.010	Abastumani (70 cm)
2009.76148	2455110.20307	2009-10-05	16.399 ± 0.010	Abastumani (70 cm)
2009.76149	2455110.20516	2009-10-05	16.318 ± 0.016	Abastumani (70 cm)
2009.76150	2455110.20727	2009-10-05	16.325 ± 0.010	Abastumani (70 cm)
2009.76150	2455110.20938	2009-10-05	16.381 ± 0.016	Abastumani (70 cm)
2009.76151	2455110.21148	2009-10-05	16.336 ± 0.010	Abastumani (70 cm)
2009.76151	2455110.21358	2009-10-05	16.325 ± 0.010	Abastumani (70 cm)
2009.76152	2455110.21568	2009-10-05	16.425 ± 0.010	Abastumani (70 cm)
2009.76425	2455111.21700	2009-10-06	16.368 ± 0.021	St. Petersburg
2009.76470	2455111.38164	2009-10-06	16.364 ± 0.029	Tijarafe (35 cm)
2009.76471	2455111.38567	2009-10-06	16.305 ± 0.047	Tijarafe (35 cm)
2009.76714	2455112.27315	2009-10-07	16.386 ± 0.010	Abastumani (70 cm)
2009.76715	2455112.27526	2009-10-07	16.415 ± 0.010	Abastumani (70 cm)
2009.76715	2455112.27735	2009-10-07	16.403 ± 0.018	Abastumani (70 cm)
2009.76716	2455112.27946	2009-10-07	16.400 ± 0.010	Abastumani (70 cm)
2009.76717	2455112.28367	2009-10-07	16.363 ± 0.010	Abastumani (70 cm)
2009.76966	2455113.19600	2009-10-08	16.218 ± 0.057	St. Petersburg
2009.77250	2455114.23324	2009-10-09	16.385 ± 0.010	Abastumani (70 cm)
2009.77250	2455114.23535	2009-10-09	16.382 ± 0.010	Abastumani (70 cm)
2009.77251	2455114.23745	2009-10-09	16.410 ± 0.010	Abastumani (70 cm)
2009.77251	2455114.23956	2009-10-09	16.435 ± 0.010	Abastumani (70 cm)
2009.77253	2455114.24587	2009-10-09	16.450 ± 0.010	Abastumani (70 cm)
2009.77254	2455114.24798	2009-10-09	16.476 ± 0.010	Abastumani (70 cm)
2009.77271	2455114.31030	2009-10-09	16.475 ± 0.030	St. Petersburg
2009.77277	2455114.33560	2009-10-09	16.390 ± 0.031	St. Petersburg
2009.77544	2455115.30990	2009-10-10	16.424 ± 0.023	St. Petersburg
2009.77778	2455116.16567	2009-10-11	16.405 ± 0.010	Abastumani (70 cm)
2009.77778	2455116.16778	2009-10-11	16.404 ± 0.014	Abastumani (70 cm)
2009.77779	2455116.16988	2009-10-11	16.439 ± 0.010	Abastumani (70 cm)
2009.77779	2455116.17199	2009-10-11	16.409 ± 0.010	Abastumani (70 cm)
2009.77780	2455116.17409	2009-10-11	16.443 ± 0.029	Abastumani (70 cm)
2009.77780	2455116.17619	2009-10-11	16.505 ± 0.010	Abastumani (70 cm)
2009.77781	2455116.17830	2009-10-11	16.411 ± 0.030	Abastumani (70 cm)
2009.77782	2455116.18041	2009-10-11	16.467 ± 0.010	Abastumani (70 cm)
2009.78052	2455117.17157	2009-10-12	16.513 ± 0.010	Abastumani (70 cm)
2009.78053	2455117.17367	2009-10-12	16.554 ± 0.010	Abastumani (70 cm)
2009.78053	2455117.17577	2009-10-12	16.504 ± 0.010	Abastumani (70 cm)

Continued on next page ...

Table C.1 – *continued from previous page*

Epoch	JD	Date	Magnitude	Observatory
2009.78054	2455117.17788	2009-10-12	16.527 ± 0.010	Abastumani (70 cm)
2009.78055	2455117.17999	2009-10-12	16.560 ± 0.022	Abastumani (70 cm)
2009.78055	2455117.18208	2009-10-12	16.525 ± 0.010	Abastumani (70 cm)
2009.78056	2455117.18419	2009-10-12	16.554 ± 0.010	Abastumani (70 cm)
2009.78101	2455117.34970	2009-10-12	16.508 ± 0.037	Tijarafe (35 cm)
2009.78102	2455117.35385	2009-10-12	16.516 ± 0.045	Tijarafe (35 cm)
2009.78337	2455118.21200	2009-10-13	16.417 ± 0.009	Crimean (70 cm; ST-7; pol)
2009.78338	2455118.21770	2009-10-13	16.429 ± 0.010	Crimean (70 cm; ST-7; pol)
2009.78646	2455119.34310	2009-10-14	16.519 ± 0.035	Tijarafe (35 cm)
2009.78647	2455119.34724	2009-10-14	16.488 ± 0.035	Tijarafe (35 cm)
2009.78716	2455119.60050	2009-10-15	16.522 ± 0.011	Lowell (Perkins)
2009.78919	2455120.34210	2009-10-15	16.530 ± 0.044	Tijarafe (35 cm)
2009.78920	2455120.34613	2009-10-15	16.517 ± 0.035	Tijarafe (35 cm)
2009.78998	2455120.63420	2009-10-16	16.440 ± 0.013	Lowell (Perkins)
2009.79141	2455121.15749	2009-10-16	16.451 ± 0.010	Abastumani (70 cm)
2009.79142	2455121.15958	2009-10-16	16.438 ± 0.010	Abastumani (70 cm)
2009.79143	2455121.16169	2009-10-16	16.479 ± 0.010	Abastumani (70 cm)
2009.79143	2455121.16380	2009-10-16	16.448 ± 0.010	Abastumani (70 cm)
2009.79144	2455121.16590	2009-10-16	16.450 ± 0.010	Abastumani (70 cm)
2009.79144	2455121.16800	2009-10-16	16.498 ± 0.010	Abastumani (70 cm)
2009.79145	2455121.17010	2009-10-16	16.475 ± 0.010	Abastumani (70 cm)
2009.79145	2455121.17221	2009-10-16	16.488 ± 0.014	Abastumani (70 cm)
2009.79149	2455121.18480	2009-10-16	16.501 ± 0.044	St. Petersburg
2009.79198	2455121.36573	2009-10-16	16.459 ± 0.041	Tijarafe (35 cm)
2009.79199	2455121.36990	2009-10-16	16.491 ± 0.040	Tijarafe (35 cm)
2009.79273	2455121.64070	2009-10-17	16.458 ± 0.014	Lowell (Perkins)
2009.79416	2455122.16198	2009-10-17	16.545 ± 0.010	Abastumani (70 cm)
2009.79416	2455122.16409	2009-10-17	16.516 ± 0.010	Abastumani (70 cm)
2009.79417	2455122.16618	2009-10-17	16.504 ± 0.010	Abastumani (70 cm)
2009.79418	2455122.16829	2009-10-17	16.506 ± 0.010	Abastumani (70 cm)
2009.79418	2455122.17039	2009-10-17	16.523 ± 0.010	Abastumani (70 cm)
2009.79540	2455122.61800	2009-10-18	16.517 ± 0.015	Lowell (Perkins)
2009.79688	2455123.15690	2009-10-18	16.574 ± 0.010	Abastumani (70 cm)
2009.79688	2455123.15899	2009-10-18	16.550 ± 0.010	Abastumani (70 cm)
2009.79689	2455123.16110	2009-10-18	16.561 ± 0.010	Abastumani (70 cm)
2009.79689	2455123.16321	2009-10-18	16.563 ± 0.010	Abastumani (70 cm)
2009.79693	2455123.17600	2009-10-18	16.551 ± 0.009	Crimean (70 cm; ST-7; pol)
2009.79694	2455123.18140	2009-10-18	16.561 ± 0.010	Crimean (70 cm; ST-7; pol)
2009.79817	2455123.63160	2009-10-19	16.560 ± 0.013	Lowell (Perkins)
2009.80086	2455124.61570	2009-10-20	16.611 ± 0.014	Lowell (Perkins)
2009.80233	2455125.15207	2009-10-20	16.636 ± 0.010	Abastumani (70 cm)
2009.80233	2455125.15417	2009-10-20	16.675 ± 0.012	Abastumani (70 cm)
2009.80234	2455125.15627	2009-10-20	16.627 ± 0.010	Abastumani (70 cm)
2009.80235	2455125.15838	2009-10-20	16.622 ± 0.010	Abastumani (70 cm)
2009.80235	2455125.16049	2009-10-20	16.647 ± 0.010	Abastumani (70 cm)
2009.80236	2455125.16258	2009-10-20	16.620 ± 0.010	Abastumani (70 cm)
2009.80236	2455125.16469	2009-10-20	16.614 ± 0.010	Abastumani (70 cm)
2009.80237	2455125.16679	2009-10-20	16.626 ± 0.010	Abastumani (70 cm)
2009.80287	2455125.34922	2009-10-20	16.546 ± 0.036	Tijarafe (35 cm)
2009.80288	2455125.35332	2009-10-20	16.630 ± 0.041	Tijarafe (35 cm)
2009.80363	2455125.62790	2009-10-21	16.626 ± 0.013	Lowell (Perkins)
2009.80507	2455126.15526	2009-10-21	16.617 ± 0.011	Abastumani (70 cm)
2009.80507	2455126.15736	2009-10-21	16.619 ± 0.012	Abastumani (70 cm)
2009.80509	2455126.16156	2009-10-21	16.590 ± 0.010	Abastumani (70 cm)
2009.80509	2455126.16367	2009-10-21	16.600 ± 0.010	Abastumani (70 cm)
2009.80510	2455126.16578	2009-10-21	16.613 ± 0.010	Abastumani (70 cm)
2009.80537	2455126.26422	2009-10-21	16.579 ± 0.014	Sabadell
2009.80558	2455126.34326	2009-10-21	16.565 ± 0.030	Tijarafe (35 cm)
2009.80559	2455126.34733	2009-10-21	16.615 ± 0.032	Tijarafe (35 cm)
2009.80638	2455126.63580	2009-10-22	16.652 ± 0.016	Lowell (Perkins)
2009.80781	2455127.15712	2009-10-22	16.646 ± 0.010	Abastumani (70 cm)
2009.80782	2455127.16132	2009-10-22	16.591 ± 0.010	Abastumani (70 cm)
2009.80782	2455127.16343	2009-10-22	16.665 ± 0.011	Abastumani (70 cm)
2009.80783	2455127.16553	2009-10-22	16.599 ± 0.010	Abastumani (70 cm)
2009.80784	2455127.16764	2009-10-22	16.621 ± 0.010	Abastumani (70 cm)
2009.80904	2455127.60930	2009-10-23	16.661 ± 0.015	Lowell (Perkins)
2009.81066	2455128.20223	2009-10-23	16.712 ± 0.010	Abastumani (70 cm)
2009.81067	2455128.20434	2009-10-23	16.712 ± 0.013	Abastumani (70 cm)
2009.81067	2455128.20645	2009-10-23	16.647 ± 0.010	Abastumani (70 cm)
2009.81068	2455128.20855	2009-10-23	16.635 ± 0.010	Abastumani (70 cm)
2009.81177	2455128.60720	2009-10-24	16.674 ± 0.017	Lowell (Perkins)

Continued on next page ...

Table C.1 – *continued from previous page*

Epoch	JD	Date	Magnitude	Observatory
2009.81327	2455129.15797	2009-10-24	16.728 ± 0.010	Abastumani (70 cm)
2009.81328	2455129.16007	2009-10-24	16.744 ± 0.010	Abastumani (70 cm)
2009.81328	2455129.16218	2009-10-24	16.772 ± 0.010	Abastumani (70 cm)
2009.81329	2455129.16428	2009-10-24	16.704 ± 0.015	Abastumani (70 cm)
2009.81454	2455129.62010	2009-10-25	16.694 ± 0.016	Lowell (Perkins)
2009.81603	2455130.16544	2009-10-25	16.751 ± 0.010	Abastumani (70 cm)
2009.81603	2455130.16755	2009-10-25	16.760 ± 0.010	Abastumani (70 cm)
2009.81604	2455130.16965	2009-10-25	16.747 ± 0.010	Abastumani (70 cm)
2009.81605	2455130.17385	2009-10-25	16.746 ± 0.010	Abastumani (70 cm)
2009.81724	2455130.60860	2009-10-26	16.706 ± 0.015	Lowell (Perkins)
2009.82146	2455132.15563	2009-10-27	16.641 ± 0.010	Abastumani (70 cm)
2009.82147	2455132.15773	2009-10-27	16.608 ± 0.013	Abastumani (70 cm)
2009.82147	2455132.15984	2009-10-27	16.666 ± 0.021	Abastumani (70 cm)
2009.82148	2455132.16194	2009-10-27	16.693 ± 0.010	Abastumani (70 cm)
2009.82149	2455132.16404	2009-10-27	16.615 ± 0.018	Abastumani (70 cm)
2009.82149	2455132.16615	2009-10-27	16.658 ± 0.010	Abastumani (70 cm)
2009.82715	2455134.23750	2009-10-29	16.663 ± 0.068	St. Petersburg
2009.82723	2455134.26580	2009-10-29	16.642 ± 0.034	St. Petersburg
2009.82965	2455135.15240	2009-10-30	16.682 ± 0.026	Crimean (70 cm; ST-7; pol)
2009.82967	2455135.15770	2009-10-30	16.672 ± 0.024	Crimean (70 cm; ST-7; pol)
2009.82990	2455135.24260	2009-10-30	16.721 ± 0.053	St. Petersburg
2009.83238	2455136.15150	2009-10-31	16.648 ± 0.028	Crimean (70 cm; ST-7; pol)
2009.83240	2455136.15980	2009-10-31	16.628 ± 0.028	Crimean (70 cm; ST-7; pol)
2009.83250	2455136.19380	2009-10-31	16.682 ± 0.029	St. Petersburg
2009.83796	2455138.19470	2009-11-02	16.687 ± 0.040	St. Petersburg
2009.84055	2455139.14030	2009-11-03	16.657 ± 0.041	St. Petersburg
2009.84876	2455142.14532	2009-11-06	16.810 ± 0.010	Abastumani (70 cm)
2009.84876	2455142.14743	2009-11-06	16.900 ± 0.010	Abastumani (70 cm)
2009.84877	2455142.14954	2009-11-06	16.824 ± 0.012	Abastumani (70 cm)
2009.84877	2455142.15163	2009-11-06	16.870 ± 0.010	Abastumani (70 cm)
2009.85419	2455144.13341	2009-11-08	16.874 ± 0.010	Abastumani (70 cm)
2009.85420	2455144.13763	2009-11-08	16.896 ± 0.013	Abastumani (70 cm)
2009.85421	2455144.13973	2009-11-08	16.892 ± 0.010	Abastumani (70 cm)
2009.85421	2455144.14183	2009-11-08	16.932 ± 0.011	Abastumani (70 cm)
2009.85422	2455144.14394	2009-11-08	16.934 ± 0.010	Abastumani (70 cm)
2009.85422	2455144.14604	2009-11-08	16.931 ± 0.010	Abastumani (70 cm)
2009.85423	2455144.14815	2009-11-08	16.940 ± 0.010	Abastumani (70 cm)
2009.85967	2455146.14031	2009-11-10	16.885 ± 0.010	Abastumani (70 cm)
2009.85968	2455146.14242	2009-11-10	16.901 ± 0.020	Abastumani (70 cm)
2009.85968	2455146.14452	2009-11-10	16.882 ± 0.010	Abastumani (70 cm)
2009.85969	2455146.14663	2009-11-10	16.943 ± 0.010	Abastumani (70 cm)
2009.85970	2455146.14873	2009-11-10	16.920 ± 0.014	Abastumani (70 cm)
2009.85970	2455146.15083	2009-11-10	16.869 ± 0.010	Abastumani (70 cm)
2009.86241	2455147.14196	2009-11-11	16.963 ± 0.013	Abastumani (70 cm)
2009.86242	2455147.14406	2009-11-11	16.940 ± 0.010	Abastumani (70 cm)
2009.86242	2455147.14617	2009-11-11	16.939 ± 0.010	Abastumani (70 cm)
2009.86243	2455147.14826	2009-11-11	16.924 ± 0.010	Abastumani (70 cm)
2009.86243	2455147.15037	2009-11-11	16.918 ± 0.010	Abastumani (70 cm)
2009.86244	2455147.15248	2009-11-11	16.923 ± 0.010	Abastumani (70 cm)
2009.86513	2455148.13885	2009-11-12	16.927 ± 0.010	Abastumani (70 cm)
2009.86514	2455148.14096	2009-11-12	16.940 ± 0.010	Abastumani (70 cm)
2009.86515	2455148.14307	2009-11-12	16.930 ± 0.010	Abastumani (70 cm)
2009.86515	2455148.14516	2009-11-12	16.941 ± 0.010	Abastumani (70 cm)
2009.86516	2455148.14727	2009-11-12	16.921 ± 0.010	Abastumani (70 cm)
2009.86516	2455148.14938	2009-11-12	16.906 ± 0.010	Abastumani (70 cm)
2009.87073	2455150.18790	2009-11-14	16.909 ± 0.019	Crimean (70 cm; ST-7; pol)
2009.87075	2455150.19530	2009-11-14	16.934 ± 0.020	Crimean (70 cm; ST-7; pol)
2009.87344	2455151.17810	2009-11-15	16.960 ± 0.013	Crimean (70 cm; ST-7; pol)
2009.87346	2455151.18600	2009-11-15	16.974 ± 0.015	Crimean (70 cm; ST-7; pol)
2009.87886	2455153.16370	2009-11-17	16.987 ± 0.027	Crimean (70 cm; ST-7; pol)
2009.87888	2455153.17110	2009-11-17	17.041 ± 0.039	Crimean (70 cm; ST-7; pol)
2009.89792	2455160.13910	2009-11-24	17.140 ± 0.028	Crimean (70 cm; ST-7; pol)
2009.89794	2455160.14730	2009-11-24	17.022 ± 0.029	Crimean (70 cm; ST-7; pol)
2009.90611	2455163.13710	2009-11-27	17.089 ± 0.033	Crimean (70 cm; ST-7; pol)
2009.90613	2455163.14460	2009-11-27	17.064 ± 0.026	Crimean (70 cm; ST-7; pol)
2009.90886	2455164.14320	2009-11-28	17.104 ± 0.024	Crimean (70 cm; ST-7; pol)
2009.90888	2455164.15140	2009-11-28	17.043 ± 0.029	Crimean (70 cm; ST-7; pol)
2009.97240	2455187.39979	2009-12-21	17.092 ± 0.035	Lulin (SLT)
2010.04611	2455214.37586	2010-01-17	17.033 ± 0.013	Lulin (SLT)
2010.05163	2455216.39799	2010-01-19	17.107 ± 0.048	Lulin (SLT)
2010.06511	2455221.32932	2010-01-24	17.019 ± 0.006	Lulin (SLT)

Continued on next page ...

Table C.1 – *continued from previous page*

Epoch	JD	Date	Magnitude	Observatory
2010.07076	2455223.39827	2010-01-26	17.005 ± 0.006	Lulin (SLT)
2010.11239	2455238.63448	2010-02-11	16.928 ± 0.010	Abastumani (70 cm)
2010.11240	2455238.63659	2010-02-11	16.956 ± 0.010	Abastumani (70 cm)
2010.16408	2455256.55160	2010-03-01	17.114 ± 0.037	Crimean (70 cm; ST-7; pol)
2010.16409	2455256.55670	2010-03-01	17.061 ± 0.031	Crimean (70 cm; ST-7; pol)
2010.16682	2455257.55515	2010-03-02	17.062 ± 0.013	Abastumani (70 cm)
2010.16682	2455257.55655	2010-03-02	17.090 ± 0.027	Abastumani (70 cm)
2010.16683	2455257.55796	2010-03-02	17.055 ± 0.021	Abastumani (70 cm)
2010.16683	2455257.55938	2010-03-02	17.082 ± 0.010	Abastumani (70 cm)
2010.16683	2455257.56079	2010-03-02	17.037 ± 0.010	Abastumani (70 cm)
2010.21789	2455276.24943	2010-03-20	16.832 ± 0.024	Lulin (SLT)
2010.22058	2455277.23104	2010-03-21	16.818 ± 0.023	Lulin (SLT)
2010.22144	2455277.54789	2010-03-22	16.821 ± 0.010	Abastumani (70 cm)
2010.22145	2455277.55000	2010-03-22	16.778 ± 0.010	Abastumani (70 cm)
2010.22145	2455277.55211	2010-03-22	16.776 ± 0.017	Abastumani (70 cm)
2010.22146	2455277.55421	2010-03-22	16.770 ± 0.010	Abastumani (70 cm)
2010.22604	2455279.22914	2010-03-23	16.794 ± 0.006	Lulin (SLT)
2010.22701	2455279.58571	2010-03-24	16.747 ± 0.010	Abastumani (70 cm)
2010.22702	2455279.58781	2010-03-24	16.768 ± 0.010	Abastumani (70 cm)
2010.22702	2455279.58991	2010-03-24	16.741 ± 0.010	Abastumani (70 cm)
2010.22703	2455279.59201	2010-03-24	16.765 ± 0.012	Abastumani (70 cm)
2010.23450	2455282.32552	2010-03-26	16.645 ± 0.015	Lulin (SLT)
2010.23808	2455283.63570	2010-03-28	16.685 ± 0.011	Calar Alto
2010.24803	2455287.28037	2010-03-31	16.563 ± 0.010	Lulin (SLT)
2010.25082	2455288.30118	2010-04-01	16.632 ± 0.008	Lulin (SLT)
2010.26235	2455292.52017	2010-04-06	16.497 ± 0.010	Abastumani (70 cm)
2010.26236	2455292.52228	2010-04-06	16.494 ± 0.010	Abastumani (70 cm)
2010.26236	2455292.52439	2010-04-06	16.489 ± 0.010	Abastumani (70 cm)
2010.26237	2455292.52649	2010-04-06	16.489 ± 0.010	Abastumani (70 cm)
2010.27608	2455297.54460	2010-04-11	16.451 ± 0.006	Calar Alto
2010.27851	2455298.43550	2010-04-11	16.520 ± 0.038	St. Petersburg
2010.27870	2455298.50250	2010-04-12	16.476 ± 0.009	Crimean (70 cm; ST-7; pol)
2010.27871	2455298.50820	2010-04-12	16.501 ± 0.011	Crimean (70 cm; ST-7; pol)
2010.28079	2455299.27020	2010-04-12	16.535 ± 0.029	Lulin (SLT)
2010.28135	2455299.47340	2010-04-12	16.474 ± 0.023	St. Petersburg

Table C.2: SMA 1 mm (230 GHz) observations of 3C 345 between 2008 and 2010.

Epoch	JD	Date	Flux Density
2008.69466	2454720.74653	2008-09-11	2.486 ± 0.132
2008.70030	2454722.80833	2008-09-13	2.498 ± 0.133
2008.73816	2454736.66528	2008-09-27	3.070 ± 0.311
2008.89860	2454795.38819	2008-11-24	2.930 ± 0.151
2009.03459	2454845.15903	2009-01-13	3.322 ± 0.184
2009.07587	2454860.26944	2009-01-28	3.570 ± 0.180
2009.11102	2454873.13333	2009-02-10	3.188 ± 0.283
2009.12188	2454877.10625	2009-02-14	3.871 ± 0.241
2009.13020	2454880.15278	2009-02-17	4.078 ± 0.224
2009.15999	2454891.05694	2009-02-28	4.132 ± 0.259
2009.25585	2454925.14236	2009-04-03	2.831 ± 0.308
2009.32706	2454951.20556	2009-04-29	3.193 ± 0.165
2009.41884	2454984.79444	2009-06-02	4.296 ± 0.559
2009.42428	2454986.78472	2009-06-04	4.255 ± 0.553
2009.44049	2454992.71944	2009-06-10	4.267 ± 0.226
2009.49517	2455012.73056	2009-06-30	3.747 ± 0.194
2009.49574	2455012.94028	2009-06-30	3.665 ± 0.186
2009.52329	2455023.02361	2009-07-10	4.183 ± 0.247
2009.55026	2455032.89444	2009-07-20	3.627 ± 0.182
2009.60471	2455052.82431	2009-08-09	3.527 ± 0.177
2009.61037	2455054.89583	2009-08-11	3.700 ± 0.189
2009.66741	2455075.77083	2009-09-01	3.300 ± 0.175
2009.67028	2455076.82361	2009-09-02	3.529 ± 0.200
2009.67536	2455078.68333	2009-09-04	3.238 ± 0.172
2009.74108	2455102.73542	2009-09-28	3.390 ± 0.173
2009.81751	2455130.71042	2009-10-26	3.099 ± 0.156
2009.93381	2455173.27569	2009-12-07	3.176 ± 0.165
2009.99111	2455194.24792	2009-12-28	3.166 ± 0.159
2010.01554	2455203.18750	2010-01-06	3.331 ± 0.168
2010.01847	2455204.25972	2010-01-07	3.310 ± 0.166

Continued on next page ...

Table C.2 – *continued from previous page*

Epoch	JD	Date	Flux Density
2010.02124	2455205.27222	2010-01-08	3.307 ± 0.166
2010.03204	2455209.22708	2010-01-12	3.350 ± 0.168
2010.03727	2455211.14167	2010-01-14	2.687 ± 0.279
2010.08089	2455227.10694	2010-01-30	2.840 ± 0.147
2010.09470	2455232.16111	2010-02-04	3.124 ± 0.159
2010.09761	2455233.22361	2010-02-05	3.259 ± 0.163
2010.18711	2455264.98333	2010-03-09	3.081 ± 0.253
2010.19610	2455268.27361	2010-03-12	3.231 ± 0.163
2010.20660	2455272.11667	2010-03-16	3.090 ± 0.156
2010.20957	2455273.20417	2010-03-17	3.108 ± 0.159
2010.21173	2455273.99236	2010-03-18	2.740 ± 0.139
2010.21446	2455274.99097	2010-03-19	2.944 ± 0.149
2010.23082	2455280.97917	2010-03-25	2.861 ± 0.145
2010.23352	2455281.96944	2010-03-26	2.615 ± 0.132
2010.25341	2455289.24792	2010-04-02	2.941 ± 0.149

Flux Density – in units of Jy.

Table C.3: Multiband photometry of 3C 345, using the Zeiss-1000 telescope of the Special Astrophysical Observatory, Russia.

Epoch	JD	Date	B	V	R	*21	seeing
2009.24320	2454920.515	2009-03-29	17.54 ± 0.01			17.14 ± 0.01	1.9"
2009.24322	2454920.518	2009-03-29		17.22 ± 0.01		16.53 ± 0.01	1.8"
2009.24322	2454920.520	2009-03-29			16.83 ± 0.02	16.17 ± 0.01	1.6"
2009.24323	2454920.524	2009-03-29	17.54 ± 0.01			17.11 ± 0.01	2.0"
2009.24324	2454920.527	2009-03-29		17.24 ± 0.01		16.51 ± 0.01	1.9"
2009.24325	2454920.528	2009-03-29			16.84 ± 0.02	16.16 ± 0.01	1.7"
2009.24325	2454920.531	2009-03-29	17.56 ± 0.01			17.13 ± 0.01	1.9"
2009.24327	2454920.535	2009-03-29		17.22 ± 0.01		16.54 ± 0.01	1.7"
2009.24327	2454920.536	2009-03-29			16.80 ± 0.02	16.13 ± 0.01	1.6"
2009.40423	2454979.447	2009-05-27	17.45 ± 0.01			17.14 ± 0.01	3.7"
2009.40424	2454979.451	2009-05-27		17.16 ± 0.02		16.54 ± 0.01	3.7"
2009.40424	2454979.452	2009-05-27			16.77 ± 0.02	16.17 ± 0.01	3.1"
2009.40425	2454979.456	2009-05-27	17.41 ± 0.01			17.11 ± 0.01	3.6"
2009.40426	2454979.458	2009-05-27		17.11 ± 0.02		16.51 ± 0.01	3.2"
2009.40426	2454979.460	2009-05-27			16.74 ± 0.02	16.17 ± 0.01	2.7"
2009.40427	2454979.463	2009-05-27	17.45 ± 0.01			17.12 ± 0.01	3.3"
2009.40428	2454979.466	2009-05-27		17.10 ± 0.02		16.53 ± 0.01	2.8"
2009.40428	2454979.468	2009-05-27			16.77 ± 0.02	16.16 ± 0.01	2.9"
2009.47483	2455005.288	2009-06-22	17.72 ± 0.02			17.17 ± 0.01	3.7"
2009.47484	2455005.290	2009-06-22		17.42 ± 0.02		16.54 ± 0.01	3.3"
2009.47484	2455005.292	2009-06-22			17.08 ± 0.03	16.13 ± 0.02	3.2"
2009.47486	2455005.297	2009-06-22	17.68 ± 0.01			17.13 ± 0.01	3.3"
2009.47486	2455005.299	2009-06-22		17.38 ± 0.02		16.49 ± 0.01	3.3"
2009.47487	2455005.301	2009-06-22			17.07 ± 0.02	16.14 ± 0.01	3.2"
2009.47488	2455005.306	2009-06-22	17.64 ± 0.02			17.11 ± 0.01	3.7"
2009.47489	2455005.309	2009-06-22		17.40 ± 0.03		16.55 ± 0.02	3.4"
2009.47489	2455005.311	2009-06-22			17.11 ± 0.03	16.14 ± 0.02	2.9"
2009.48050	2455007.364	2009-06-24	17.64 ± 0.01			17.10 ± 0.01	1.8"
2009.48051	2455007.367	2009-06-24		17.42 ± 0.01		16.53 ± 0.01	1.7"
2009.48052	2455007.369	2009-06-24			17.05 ± 0.02	16.15 ± 0.01	1.5"
2009.48052	2455007.372	2009-06-24	17.65 ± 0.01			17.12 ± 0.01	1.7"
2009.48053	2455007.375	2009-06-24		17.40 ± 0.01		16.51 ± 0.01	1.5"
2009.48054	2455007.377	2009-06-24			17.03 ± 0.02	16.13 ± 0.01	1.4"
2009.48861	2455010.331	2009-06-27		17.38 ± 0.02		16.51 ± 0.01	1.6"
2009.48861	2455010.333	2009-06-27			17.03 ± 0.02	16.15 ± 0.01	1.6"
2009.54583	2455031.272	2009-07-18	17.50 ± 0.01			17.13 ± 0.01	1.9"
2009.54585	2455031.280	2009-07-18		17.22 ± 0.01		16.52 ± 0.01	1.8"
2009.54586	2455031.283	2009-07-18			16.85 ± 0.02	16.14 ± 0.01	1.7"
2009.54589	2455031.296	2009-07-18	17.46 ± 0.01			17.10 ± 0.01	2.1"
2009.54590	2455031.300	2009-07-18		17.20 ± 0.02		16.53 ± 0.01	1.8"
2009.54591	2455031.302	2009-07-18			16.85 ± 0.02	16.12 ± 0.02	1.6"
2009.54877	2455032.348	2009-07-19	17.52 ± 0.01			17.13 ± 0.01	1.9"
2009.54877	2455032.351	2009-07-19		17.20 ± 0.01		16.50 ± 0.01	1.5"
2009.54878	2455032.353	2009-07-19			16.81 ± 0.02	16.14 ± 0.01	1.4"
2009.54879	2455032.356	2009-07-19	17.50 ± 0.01			17.12 ± 0.01	1.7"
2009.54880	2455032.359	2009-07-19		17.26 ± 0.01		16.52 ± 0.01	1.7"

Continued on next page ...

Table C.3 – *continued from previous page*

Epoch	JD	Date	B	V	R	*21	seeing
2009.54880	2455032.360	2009-07-19			16.85 ± 0.02	16.17 ± 0.01	1.5''
2009.54881	2455032.364	2009-07-19	17.52 ± 0.01			17.12 ± 0.01	1.8''
2009.54882	2455032.367	2009-07-19		17.22 ± 0.02		16.55 ± 0.01	1.5''
2009.54882	2455032.369	2009-07-19			16.86 ± 0.02	16.15 ± 0.01	1.5''
2009.54887	2455032.388	2009-07-19	17.51 ± 0.01			17.12 ± 0.01	1.9''
2009.54888	2455032.391	2009-07-19		17.22 ± 0.01		16.48 ± 0.01	1.7''
2009.54889	2455032.393	2009-07-19			16.79 ± 0.02	16.16 ± 0.01	1.6''
2009.54890	2455032.396	2009-07-19	17.53 ± 0.01			17.12 ± 0.01	1.8''
2009.54890	2455032.399	2009-07-19		17.20 ± 0.01		16.51 ± 0.01	1.8''
2009.54891	2455032.401	2009-07-19			16.82 ± 0.02	16.14 ± 0.01	1.6''
2009.56511	2455038.332	2009-07-25	17.61 ± 0.01			17.14 ± 0.01	1.8''
2009.56512	2455038.335	2009-07-25		17.28 ± 0.01		16.55 ± 0.01	1.7''
2009.56513	2455038.337	2009-07-25			16.92 ± 0.02	16.16 ± 0.01	1.5''
2009.56514	2455038.340	2009-07-25	17.61 ± 0.01			17.12 ± 0.01	2.0''
2009.56514	2455038.343	2009-07-25		17.29 ± 0.01		16.53 ± 0.01	1.8''
2009.56515	2455038.345	2009-07-25			16.90 ± 0.02	16.16 ± 0.01	1.7''
2009.65777	2455072.244	2009-08-28	17.28 ± 0.01			17.10 ± 0.01	2.9''
2009.65778	2455072.247	2009-08-28		16.95 ± 0.02		16.52 ± 0.01	2.4''
2009.65778	2455072.249	2009-08-28			16.49 ± 0.02	16.12 ± 0.02	2.0''
2009.65779	2455072.251	2009-08-28	17.27 ± 0.01			17.10 ± 0.01	3.3''
2009.65780	2455072.255	2009-08-28		16.86 ± 0.02		16.51 ± 0.01	3.0''
2009.65781	2455072.257	2009-08-28			16.50 ± 0.02	16.15 ± 0.02	2.9''
2009.65781	2455072.260	2009-08-28	17.22 ± 0.01			17.08 ± 0.01	3.2''
2009.65782	2455072.263	2009-08-28		16.84 ± 0.02		16.50 ± 0.01	2.9''
2009.65782	2455072.265	2009-08-28			16.44 ± 0.02	16.14 ± 0.01	2.7''
2009.66054	2455073.258	2009-08-29	17.24 ± 0.02			17.12 ± 0.02	2.2''
2009.66055	2455073.262	2009-08-29		16.87 ± 0.02		16.55 ± 0.02	2.6''
2009.66055	2455073.263	2009-08-29			16.43 ± 0.02	16.16 ± 0.02	2.3''
2009.66057	2455073.267	2009-08-29	17.22 ± 0.02			17.09 ± 0.02	2.7''
2009.66057	2455073.269	2009-08-28		16.89 ± 0.02		16.51 ± 0.02	2.4''
2009.66058	2455073.272	2009-08-29			16.40 ± 0.02	16.17 ± 0.02	2.1''
2009.66058	2455073.274	2009-08-29	17.19 ± 0.02			17.11 ± 0.02	2.5''
2009.66059	2455073.277	2009-08-29		16.88 ± 0.02		16.52 ± 0.02	2.5''
2009.66060	2455073.279	2009-08-29			16.39 ± 0.02	16.14 ± 0.02	2.6''
2009.66314	2455074.211	2009-08-30	17.19 ± 0.02			17.09 ± 0.02	2.0''
2009.66315	2455074.214	2009-08-30		16.83 ± 0.02		16.51 ± 0.02	1.7''
2009.66316	2455074.216	2009-08-30			16.50 ± 0.02	16.13 ± 0.02	1.6''
2009.66317	2455074.219	2009-08-30	17.19 ± 0.02			17.06 ± 0.02	1.8''
2009.66317	2455074.222	2009-08-30		16.85 ± 0.02		16.52 ± 0.02	1.8''
2009.66318	2455074.224	2009-08-30			16.46 ± 0.02	16.16 ± 0.01	1.6''
2009.66319	2455074.226	2009-08-30	17.22 ± 0.02			17.06 ± 0.02	1.9''
2009.66320	2455074.230	2009-08-30		16.88 ± 0.02		16.51 ± 0.01	2.0''
2009.66320	2455074.232	2009-08-30			16.44 ± 0.02	16.14 ± 0.02	1.9''
2009.79708	2455123.232	2009-10-18	17.32 ± 0.01			17.13 ± 0.01	2.0''
2009.79709	2455123.235	2009-10-18		16.98 ± 0.02		16.49 ± 0.01	1.8''
2009.79710	2455123.237	2009-10-18			16.60 ± 0.02	16.16 ± 0.01	1.8''
2009.79710	2455123.240	2009-10-18	17.36 ± 0.01			17.12 ± 0.01	2.2''
2009.79711	2455123.243	2009-10-18		16.97 ± 0.02		16.51 ± 0.01	1.7''
2009.79712	2455123.245	2009-10-18			16.58 ± 0.02	16.15 ± 0.01	1.7''
2009.79713	2455123.249	2009-10-18	17.35 ± 0.01			17.14 ± 0.01	2.2''
2009.79714	2455123.252	2009-10-18		17.01 ± 0.03		16.51 ± 0.02	1.8''
2009.79714	2455123.253	2009-10-18			16.57 ± 0.02	16.17 ± 0.02	1.7''
2009.82130	2455132.094	2009-10-27		17.11 ± 0.03		16.53 ± 0.02	2.3''
2009.82130	2455132.096	2009-10-27			16.77 ± 0.03	16.19 ± 0.02	2.4''
2009.82131	2455132.099	2009-10-27	17.36 ± 0.03			17.14 ± 0.02	2.6''
2009.82132	2455132.102	2009-10-27		17.08 ± 0.03		16.50 ± 0.02	2.3''
2009.82132	2455132.103	2009-10-27			16.76 ± 0.03	16.16 ± 0.02	2.0''
2009.82133	2455132.107	2009-10-27	17.43 ± 0.02			17.15 ± 0.02	2.7''
2009.82134	2455132.110	2009-10-27		17.10 ± 0.03		16.51 ± 0.02	2.4''
2009.82134	2455132.112	2009-10-27			16.75 ± 0.03	16.15 ± 0.02	2.1''
2009.87880	2455153.140	2009-11-17	17.69 ± 0.02			17.12 ± 0.01	3.9''
2009.87881	2455153.144	2009-11-17		17.39 ± 0.03		16.53 ± 0.01	3.6''
2009.87881	2455153.146	2009-11-17			16.95 ± 0.03	16.17 ± 0.02	3.4''
2009.87883	2455153.152	2009-11-17	17.65 ± 0.02			17.11 ± 0.01	4.0''
2009.87884	2455153.156	2009-11-17		17.45 ± 0.02		16.53 ± 0.01	3.7''
2009.87885	2455153.158	2009-11-17			17.08 ± 0.03	16.17 ± 0.02	3.7''
2009.87887	2455153.168	2009-11-17	17.72 ± 0.03			17.11 ± 0.02	4.1''
2009.87889	2455153.172	2009-11-17		17.43 ± 0.04		16.55 ± 0.02	3.9''
2009.87889	2455153.174	2009-11-17			17.07 ± 0.04	16.19 ± 0.02	3.8''
2009.88150	2455154.128	2009-11-18			17.09 ± 0.02	16.18 ± 0.01	2.5''
2009.88151	2455154.133	2009-11-18	17.65 ± 0.02			17.10 ± 0.01	2.6''

Continued on next page ...

Table C.3 – *continued from previous page*

Epoch	JD	Date	B	V	R	*21	seeing
2009.88152	2455154.137	2009-11-18		17.34 ± 0.02		16.52 ± 0.01	3.0"
2009.88152	2455154.138	2009-11-18			17.09 ± 0.02	16.17 ± 0.01	2.6"
2009.88154	2455154.142	2009-11-18	17.69 ± 0.02			17.11 ± 0.01	2.9"
2009.88155	2455154.146	2009-11-18		17.40 ± 0.02		16.52 ± 0.01	2.7"
2009.88155	2455154.149	2009-11-18			17.16 ± 0.04	16.16 ± 0.02	2.4"
2009.88695	2455156.122	2009-11-20			17.22 ± 0.12	16.18 ± 0.06	4.8"
2009.88695	2455156.124	2009-11-20	17.74 ± 0.07			17.20 ± 0.05	4.7"
2009.88696	2455156.128	2009-11-20		17.57 ± 0.06		16.58 ± 0.04	4.5"
2009.88968	2455157.124	2009-11-21	17.72 ± 0.03			17.11 ± 0.02	4.2"
2009.88969	2455157.128	2009-11-21		17.47 ± 0.02		16.56 ± 0.01	4.1"
2009.88970	2455157.132	2009-11-21			17.07 ± 0.02	16.15 ± 0.01	3.5"
2009.88974	2455157.146	2009-11-21		17.51 ± 0.02		16.55 ± 0.01	4.0"
2009.88978	2455157.158	2009-11-21	17.77 ± 0.02			17.16 ± 0.01	4.3"
2009.88979	2455157.162	2009-11-21		17.46 ± 0.02		16.54 ± 0.01	3.8"
2009.88980	2455157.165	2009-11-21			17.05 ± 0.02	16.12 ± 0.01	3.9"
2009.89515	2455159.124	2009-11-23		17.44 ± 0.02		16.52 ± 0.01	2.1"
2009.89516	2455159.127	2009-11-23			17.07 ± 0.02	16.15 ± 0.01	1.8"
2009.89517	2455159.133	2009-11-23	17.71 ± 0.01			17.13 ± 0.01	1.9"
2009.89519	2455159.138	2009-11-23		17.45 ± 0.01		16.48 ± 0.01	1.8"
2009.89519	2455159.140	2009-11-23			17.11 ± 0.01	16.13 ± 0.01	1.7"
2009.89787	2455160.122	2009-11-24	17.71 ± 0.03			17.13 ± 0.02	2.9"
2009.89789	2455160.126	2009-11-24		17.44 ± 0.02		16.53 ± 0.01	2.8"
2009.89789	2455160.128	2009-11-24			17.03 ± 0.02	16.16 ± 0.01	2.6"
2009.89791	2455160.135	2009-11-24	17.64 ± 0.02			17.11 ± 0.01	2.8"
2009.89792	2455160.139	2009-11-24		17.46 ± 0.02		16.52 ± 0.01	2.8"

Notes: The errors are statistical only. Magnitude values may have a systematic offset of 0.02-0.04 magnitudes from the standard photometric system. **JD** – julian day; ***21** refers to the reference star magnitude, star number 21 from González-Pérez et al. (2001).

Bibliography

- Abazajian, K. N., Adelman-McCarthy, J. K., Agüeros, M. A., et al. 2009, *ApJS*, 182, 543
- Abdo, A. A., Ackermann, M., Ajello, M., et al. 2010a, *ApJS*, 188, 405
- Abdo, A. A., Ackermann, M., Ajello, M., et al. 2010b, *Astrophys. J.*, 715, 429
- Abdo, A. A., Ackermann, M., Ajello, M., et al. 2010c, *Astrophys. J.*, 722, 520
- Abdo, A. A., Ackermann, M., Ajello, M., et al. 2009a, *ApJS*, 183, 46
- Abdo, A. A., Ackermann, M., Ajello, M., et al. 2009b, *Astrophys. J.*, 700, 597
- Abdo, A. A., Ackermann, M., Ajello, M., et al. 2009c, *Phys. Rev. D*, 80, 122004
- Ackermann, M., Ajello, M., Baldini, L., et al. 2010, *Astrophys. J.*, 721, 1383
- Adams, D. 2002, *The Ultimate Hitchhiker's Guide to the Galaxy* (Del Rey)
- Adgie, R. L., Gent, H., & Slee, O. B. 1965, *Nature*, 208, 275
- Agudo, I., Gómez, J.-L., Martí, J.-M., et al. 2001, *Astrophys. J., Lett.*, 549, L183
- Agudo, I., Jorstad, S. G., Marscher, A. P., et al. 2011a, *Astrophys. J., Lett.*, 726, L13
- Agudo, I., Marscher, A. P., Jorstad, S. G., et al. 2011b, *Astrophys. J., Lett.*, 735, L10
- Aleksić, J., Antonelli, L. A., Antoranz, P., et al. 2011, *Astrophys. J., Lett.*, 730, L8
- Aller, H. D., Aller, M. F., & Hughes, P. A. 1996, in *Astronomical Society of the Pacific Conference Series*, Vol. 110, *Blazar Continuum Variability*, ed. H. R. Miller, J. R. Webb, & J. C. Noble, 208
- Aller, H. D., Aller, M. F., Latimer, G. E., & Hodge, P. E. 1985, *ApJS*, 59, 513
- Aller, M. F., Aller, H. D., & Hughes, P. A. 2010, eprint arXiv:1012.1359
- Anderson, B., Donaldson, W., Palmer, H. P., & Rowson, B. 1965, *Nature*, 205, 375
- Antonucci, R. 1993, *Ann. Rev. Astron. Astrophys.*, 31, 473

- Arshakian, T. G., León-Tavares, J., Boettcher, M., et al. 2011, eprint arXiv:1104.4946
- Arshakian, T. G., León-Tavares, J., Lobanov, A. P., et al. 2010, *MNRAS*, 401, 1231
- Atwood, W. B., Abdo, A. A., Ackermann, M., et al. 2009, *Astrophys. J.*, 697, 1071
- Avni, Y. 1976, *Astrophys. J.*, 210, 642
- Babadzhanyants, M. K. & Belokon, E. T. 1984, *Astrophysics*, 20, 461
- Bennett, A. S. 1962, *MmRAS*, 68, 163
- Benson, J. M. 1995, in *Astronomical Society of the Pacific Conference Series*, Vol. 82, *Very Long Baseline Interferometry and the VLBA*, ed. J. A. Zensus, P. J. Diamond, & P. J. Napier, 117
- Bessell, M. S., Castelli, F., & Plez, B. 1998, *A&A*, 333, 231
- Biretta, J. A., Moore, R. L., & Cohen, M. H. 1986, *Astrophys. J.*, 308, 93
- Blandford, R. D. & Königl, A. 1979, *Astrophys. J.*, 232, 34
- Blandford, R. D. & Payne, D. G. 1982, *MNRAS*, 199, 883
- Blandford, R. D. & Rees, M. J. 1978, *Phys. Scr*, 17, 265
- Blandford, R. D. & Znajek, R. L. 1977, *MNRAS*, 179, 433
- Błażejowski, M., Siemiginowska, A., Sikora, M., Moderski, R., & Bechtold, J. 2004, *Astrophys. J., Lett.*, 600, L27
- Blumenthal, G. R. & Gould, R. J. 1970, *Reviews of Modern Physics*, 42, 237
- Böttcher, M., Mukherjee, R., & Reimer, A. 2002, *Astrophys. J.*, 581, 143
- Böttcher, M., Reimer, A., & Marscher, A. P. 2009, *Astrophys. J.*, 703, 1168
- Bowyer, C. S., Lampton, M., Mack, J., & de Mendonca, F. 1970, *Astrophys. J., Lett.*, 161, L1
- Bååth, L. B., Rogers, A. E. E., Inoue, M., et al. 1992, *A&A*, 257, 31
- Bregman, J. N., Glassgold, A. E., Huggins, P. J., et al. 1986, *Astrophys. J.*, 301, 708
- Brinkmann, W., Siebert, J., Reich, W., et al. 1995, *A&AS*, 109, 147
- Brown, L. F., Roberts, D. H., & Wardle, J. F. C. 1994, *Astrophys. J.*, 437, 108
- Browne, I. W. A. 1987, in *Superluminal Radio Sources*, ed. J. A. Zensus & T. J. Pearson, 129–147
- Browne, I. W. A., Clark, R. R., Moore, P. K., et al. 1982, *Nature*, 299, 788
- Burbidge, E. M. 1965, *Astrophys. J.*, 142, 1674
- Burbidge, G. R., Burbidge, E. M., & Sandage, A. R. 1963, *Reviews of Modern Physics*, 35, 947

-
- Burlon, D., Ajello, M., Greiner, J., et al. 2011, *Astrophys. J.*, 728, 58
- Burrows, D. N., Hill, J. E., Nousek, J. A., et al. 2005, *Space Science Reviews*, 120, 165
- Bychkova, V. S., Kardashev, N. S., Vlasyuk, V. V., & Spiridonova, O. I. 2004, *Astronomy Reports*, 48, 840
- Cardelli, J. A., Clayton, G. C., & Mathis, J. S. 1989, *Astrophys. J.*, 345, 245
- Casandjian, J.-M. & Grenier, I. A. 2008, *A&A*, 489, 849
- Cash, W. 1979, *Astrophys. J.*, 228, 939
- Celotti, A. & Fabian, A. C. 1993, *MNRAS*, 264, 228
- Chang, C.-S. 2010, PhD thesis, Universität Köln/Max-Planck-Institut für Radioastronomie
- Chatterjee, R., Baily, C., Bonning, E. W., et al. 2011, e-prints arXiv:1101.3815
- Chatterjee, R., Jorstad, S. G., Marscher, A. P., et al. 2008, *Astrophys. J.*, 689, 79
- Cheung, C. C., Harris, D. E., & Stawarz, Ł. 2007, *Astrophys. J., Lett.*, 663, L65
- Clark, B. G. 1980, *A&A*, 89, 377
- Clarke, D. A., Norman, M. L., & Burns, J. O. 1986, *Astrophys. J., Lett.*, 311, L63
- Cohen, M. H. 2000, in *Radio interferometry : the saga and the science*, ed. D. G. Finley & W. M. Goss, 173
- Cohen, M. H., Gundermann, E. J., Hardebeck, H. E., et al. 1966, *Science*, 153, 745
- Cohen, M. H., Jauncey, D. L., Kellermann, K. I., & Clark, B. G. 1968, *Science*, 162, 88
- Cohen, M. H., Linfield, R. P., Moffet, A. T., et al. 1977, *Nature*, 268, 405
- Cornwell, T. 1995, in *Astronomical Society of the Pacific Conference Series, Vol. 82, Very Long Baseline Interferometry and the VLBA*, ed. J. A. Zensus, P. J. Diamond, & P. J. Napier, 39
- Cornwell, T. & Fomalont, E. B. 1999, in *Astronomical Society of the Pacific Conference Series, Vol. 180, Synthesis Imaging in Radio Astronomy II*, ed. G. B. Taylor, C. L. Carilli, & R. A. Perley, 187
- Daly, R. A. & Marscher, A. P. 1988, *ApJ*, 334, 539
- Deller, A. T., Brisken, W. F., Phillips, C. J., et al. 2011, *PASP*, 123, 275
- Dent, W. A. 1965, *Science*, 148, 1458
- Dermer, C. D., Finke, J. D., Krug, H., & Böttcher, M. 2009, *Astrophys. J.*, 692, 32
- Dermer, C. D. & Schlickeiser, R. 1993, *Astrophys. J.*, 416, 458
- Dermer, C. D., Sturmer, S. J., & Schlickeiser, R. 1997, *ApJS*, 109, 103

- Edelson, R. A. & Krolik, J. H. 1988, *Astrophys. J.*, 333, 646
- Edge, D. O., Shakeshaft, J. R., McAdam, W. B., Baldwin, J. E., & Archer, S. 1959, *MmRAS*, 68, 37
- Eisenhauer, F., Genzel, R., Alexander, T., et al. 2005, *Astrophys. J.*, 628, 246
- Fey, A. L., Ma, C., Arias, E. F., et al. 2004, *Astron. J.*, 127, 3587
- Fichtel, C. E., Bertsch, D. L., Chiang, J., et al. 1994, *ApJS*, 94, 551
- Fisher, R. 1944, *Statistical Methods for Research Workers* (Oliver & Boyd)
- Fomalont, E. B. 1999, in *Astronomical Society of the Pacific Conference Series*, Vol. 180, *Synthesis Imaging in Radio Astronomy II*, ed. G. B. Taylor, C. L. Carilli, & R. A. Perley, 301
- Fossati, G., Maraschi, L., Celotti, A., Comastri, A., & Ghisellini, G. 1998, *MNRAS*, 299, 433
- Garofalo, D. 2009, *Astrophys. J.*, 699, 400
- Gehrels, N., Chincarini, G., Giommi, P., et al. 2004, *Astrophys. J.*, 611, 1005
- Ghisellini, G. 1989, *MNRAS*, 236, 341
- Goldsmith, D. W. & Kinman, T. D. 1965, *Astrophys. J.*, 142, 1693
- González-Pérez, J. N., Kidger, M. R., & Martín-Luis, F. 2001, *Astron. J.*, 122, 2055
- Greisen, E. W. 2003, *Information Handling in Astronomy - Historical Vistas*, 285, 109
- Hardee, P., Mizuno, Y., & Nishikawa, K.-I. 2007, *Ap&SS*, 311, 281
- Hardee, P. E. 1979, *Astrophys. J.*, 234, 47
- Hardee, P. E. 1983, *ApJ*, 269, 94
- Hardee, P. E. 2000, *Astrophys. J.*, 533, 176
- Hardee, P. E. 2011, in *IAU Symposium*, Vol. 275, *IAU Symposium*, ed. G. E. Romero, R. A. Sunyaev, & T. Belloni, 41–49
- Hartman, R. C., Bertsch, D. L., Bloom, S. D., et al. 1999, *ApJS*, 123, 79
- Hirofani, K. 2005, *Astrophys. J.*, 619, 73
- Högbom, J. A. 1974, *A&AS*, 15, 417
- Homan, D. C., Kadler, M., Kellermann, K. I., et al. 2009, *Astrophys. J.*, 706, 1253
- Hughes, P. A. 1991, *Beams and jets in astrophysics*, ed. Hughes, P. A.
- Hughes, P. A., Aller, H. D., & Aller, M. F. 1992, *Astrophys. J.*, 396, 469
- Hughes, P. A., Aller, M. F., & Aller, H. D. 1991, in *Variability of Active Galactic Nuclei*, ed. H. R. Miller & P. J. Wiita, 187

- Impey, C. D. & Neugebauer, G. 1988, *Astron. J.*, 95, 307
- Jones, T. W., O'dell, S. L., & Stein, W. A. 1974, *Astrophys. J.*, 192, 261
- Jorstad, S. G., Marscher, A. P., Lister, M. L., et al. 2005, *Astron. J.*, 130, 1418
- Jorstad, S. G., Marscher, A. P., Mattox, J. R., et al. 2001, *ApJS*, 134, 181
- Jorstad, S. G., Marscher, A. P., Smith, P. A., Larionov, V. M., & I., A. 2010, in *Fermi meets Jandky - AGN in Radio and Gamma Rays*, ed. T. Savolainen
- Jorstad, S. G., Marscher, A. P., Stevens, J. A., et al. 2007, *Astron. J.*, 134, 799
- Kalberla, P. M. W., Burton, W. B., Hartmann, D., et al. 2005, *A&A*, 440, 775
- Kaspi, S., Brandt, W. N., Maoz, D., et al. 2007, *Astrophys. J.*, 659, 997
- Kataoka, J., Mattox, J. R., Quinn, J., et al. 1999, *Astrophys. J.*, 514, 138
- Kidger, M. & Takalo, L. 1990, *A&A*, 239, L9
- Kidger, M. R. 1989, *A&A*, 226, 9
- Klare, J. 2003, PhD thesis, Rheinische-Friedrich-Wilhelms-Universität Bonn
- Klare, J., Zensus, J. A., Witzel, A., et al. 2003, in *Proceedings of the Second ENIGMA Meeting*, ed. C. M. Raiteri & M. Villata, 92–103
- Kogan, L. 1995, *Effect of Digitizers Errors on the Cross and Auto Correlation Response of an FX Correlator*, Tech. rep., VLBA Scientific Memo No. 9
- Kollgaard, R. I., Wardle, J. F. C., & Roberts, D. H. 1989, *Astron. J.*, 97, 1550
- Komissarov, S. S. 1999, *MNRAS*, 308, 1069
- Komissarov, S. S. 2011, *Mem. Soc. Astron. Italiana*, 82, 95
- Komissarov, S. S., Barkov, M. V., Vlahakis, N., & Königl, A. 2007, *MNRAS*, 380, 51
- Königl, A. 1981, *Astrophys. J.*, 243, 700
- Kovalev, Y. Y., Lobanov, A. P., Pushkarev, A. B., & Zensus, J. A. 2008, *A&A*, 483, 759
- Kovalev, Y. Y., Nizhelsky, N. A., Kovalev, Y. A., et al. 1999, *A&AS*, 139, 545
- Krichbaum, T. P. & Witzel, A. 1992, in *Variability of Blazars*, ed. E. Valtaoja & M. Valtonen, 205
- Krichbaum, T. P., Witzel, A., Graham, D. A., et al. 1993, *A&A*, 275, 375
- Krolik, J. H. 1999, *Active galactic nuclei : from the central black hole to the galactic environment*, ed. Krolik, J. H.
- Ku, W. H.-M., Helfand, D. J., & Lucy, L. B. 1980, *Nature*, 288, 323
- Larionov, V. M., Villata, M., Raiteri, C. M., et al. 2009, *The Astronomer's Telegram*, 2222, 1

- Léon-Tavares, J., E., V., Tornikoski, M., Lähteenmäki, A., & Nieppola, E. 2010, in Proceedings of Fermi meets Jansky – AGN in Radio and Gamma Rays
- León-Tavares, J., Lobanov, A. P., Chavushyan, V. H., et al. 2010, *Astrophys. J.*, 715, 355
- Leppänen, K. J., Zensus, J. A., & Diamond, P. J. 1995, *Astron. J.*, 110, 2479
- Lind, K. R., Payne, D. G., Meier, D. L., & Blandford, R. D. 1989, *Astrophys. J.*, 344, 89
- Lister, M. L., Aller, H. D., Aller, M. F., et al. 2009a, *Astron. J.*, 137, 3718
- Lister, M. L., Cohen, M. H., Homan, D. C., et al. 2009b, *Astron. J.*, 138, 1874
- Little, L. T. & Hewish, A. 1966, *MNRAS*, 134, 221
- Lobanov, A. 2007, eprint arXiv:0708.4280
- Lobanov, A. & Zensus, J. A. 2007, in *Exploring the Cosmic Frontier: Astrophysical Instruments for the 21st Century*, ed. Lobanov, A. P., Zensus, J. A., Cesarsky, C., & Diamond, P. J. (Springer-Verlag), 147
- Lobanov, A. P. 1996, PhD thesis, New Mexico Institute of Mining & Technology, Socorro, NM, USA
- Lobanov, A. P. 1998a, *A&AS*, 132, 261
- Lobanov, A. P. 1998b, *A&A*, 330, 79
- Lobanov, A. P. 2005, eprint arXiv:astro-ph/0503225
- Lobanov, A. P. 2010, in *Fermi meets Jansky - AGN in Radio and Gamma-Rays*, 151–158
- Lobanov, A. P. & Roland, J. 2005, *A&A*, 431, 831
- Lobanov, A. P. & Zensus, J. A. 1996, in *Astronomical Society of the Pacific Conference Series, Vol. 100, Energy Transport in Radio Galaxies and Quasars*, ed. P. E. Hardee, A. H. Bridle, & J. A. Zensus, 109
- Lobanov, A. P. & Zensus, J. A. 1999, *Astrophys. J.*, 521, 509
- Lobanov, A. P. & Zensus, J. A. 2001, *Science*, 294, 128
- Longair, S. M. 2011, *High Energy Astrophysics* (Cambridge University Press)
- Markwardt, C. B., Barthelmy, S. D., Cummings, J. C., et al. 2007, *The Swift BAT Software Guide*
- Marscher, A. P. 1987, in *Superluminal Radio Sources*, ed. J. A. Zensus & T. J. Pearson, 280–300
- Marscher, A. P. 1995, *Proceedings of the National Academy of Science*, 92, 11439
- Marscher, A. P. & Gear, W. K. 1985, *Astrophys. J.*, 298, 114

-
- Marscher, A. P., Gear, W. K., & Travis, J. P. 1992, in *Variability of Blazars*, ed. E. Valtaoja & M. Valtonen, 85
- Marscher, A. P., Jorstad, S. G., Larionov, V. M., et al. 2010, *Astrophys. J., Lett.*, 710, L126
- Marziani, P., Sulentic, J. W., Dultzin-Hacyan, D., Calvani, M., & Moles, M. 1996, *ApJS*, 104, 37
- Mattox, J. R., Bertsch, D. L., Chiang, J., et al. 1996, *Astrophys. J.*, 461, 396
- Matveenko, L. I., Graham, D. A., Pauliny-Toth, I. I. K., Sherwood, W. A., & Baath, L. B. 1992, *Soviet Astronomy Letters*, 18, 379
- Max-Moerbeck, W., Richards, J. L., Pavlidou, V., et al. 2010, in *Fermi meets Jansky - AGN in Radio and Gamma-Rays*, ed. T. Savolainen, E. Ros, W. P. Porcas, & J. A. Zensus, 77–80
- McKinney, J. C. 2006, *MNRAS*, 368, 1561
- McKinney, J. C. & Blandford, R. D. 2009, *MNRAS*, 394, L126
- Meier, D. L. 2011, in *IAU Symposium, Vol. 275*, IAU Symposium, ed. G. E. Romero, R. A. Sunyaev, & T. Belloni, 13–23
- Meyer, E. T., Fossati, G., Georganopoulos, M., & Lister, M. L. 2011, eprint arXiv:1107.5105
- Michelson, A. A. & Pease, F. G. 1921, *Astrophys. J.*, 53, 249
- Moore, R. L. & Stockman, H. S. 1981, *Astrophys. J.*, 243, 60
- Mücke, A. & Protheroe, R. J. 2001, *Astroparticle Physics*, 15, 121
- Myers, S. T., Jackson, N. J., Browne, I. W. A., et al. 2003, *MNRAS*, 341, 1
- Pauliny-Toth, I. I. K., Porcas, R. W., Zensus, J. A., et al. 1987, *Nature*, 328, 778
- Pearson, T. J. 1999, in *Astronomical Society of the Pacific Conference Series, Vol. 180, Synthesis Imaging in Radio Astronomy II*, ed. G. B. Taylor, C. L. Carilli, & R. A. Perley, 335
- Perucho, M., Hanasz, M., Martí, J.-M., & Miralles, J.-A. 2007, *Phys Rev E*, 75, 056312
- Perucho, M., Lobanov, A. P., Martí, J.-M., & Hardee, P. E. 2006, *A&A*, 456, 493
- Perucho, M., Martí, J. M., & Hanasz, M. 2004, *A&A*, 427, 431
- Peterson, B. M. 1997, *An Introduction to Active Galactic Nuclei*, ed. Gómez de Castro, A. I. & Franqueira, M.
- Planck Collaboration, Ade, P. A. R., Aghanim, N., et al. 2011, eprint arXiv:1101.2041
- Polko, P., Meier, D. L., & Markoff, S. 2010, *Astrophys. J.*, 723, 1343
- Poole, T. S., Breeveld, A. A., Page, M. J., et al. 2008, *MNRAS*, 383, 627

- Porcas, R. 2010, in 10th European VLBI Network Symposium and EVN Users Meeting: VLBI and the new generation of radio arrays, PoS
- Porth, O. & Fendt, C. 2010, *Astrophys. J.*, 709, 1100
- Poutanen, J. & Stern, B. 2010, *Astrophys. J., Lett.*, 717, L118
- Press, W. H., Teukolsky, S. A., Vetterling, W. T., & Flannery, B. P. 1992, *Numerical recipes in FORTRAN. The art of scientific computing*, ed. Press, W. H., Teukolsky, S. A., Vetterling, W. T., & Flannery, B. P.
- Punsly, B. & Coroniti, F. V. 1990, *Astrophys. J.*, 350, 518
- Pushkarev, A. B., Kovalev, Y. Y., & Lister, M. L. 2010, *Astrophys. J., Lett.*, 722, L7
- Pushkarev, A. B., Kovalev, Y. Y., Lister, M. L., & Savolainen, T. 2009, *A&A*, 507, L33
- Rabaça, C. R. & Zensus, J. A. 1994, in *Compact Extragalactic Radio Sources*, ed. J. A. Zensus & K. I. Kellermann, 163
- Rando et al. 2009, ArXiv e-prints, arXiv:0907.0626
- Reyes, L. C. & Cheung, C. C. 2009, *The Astronomer's Telegram*, 2226, 1
- Rolke, W. A., López, A. M., & Conrad, J. 2005, *NIM A*, 551, 493
- Roming, P. W. A., Kennedy, T. E., Mason, K. O., et al. 2005, *Space Science Reviews*, 120, 95
- Roming, P. W. A., Koch, T. S., Oates, S. R., et al. 2009, *Astrophys. J.*, 690, 163
- Ros, E., Zensus, J. A., & Lobanov, A. P. 2000, *A&A*, 354, 55
- Sandage, A. 1965, *Astrophys. J.*, 141, 1560
- Schilizzi, R. T. & de Bruyn, A. G. 1983, *Nature*, 303, 26
- Schinzel, F. K. 2008, Master's thesis, University of New Mexico, Albuquerque, NM USA
- Schinzel, F. K., Lobanov, A. P., Jorstad, S. G., et al. 2010, in *Fermi meets Jansky - AGN in Radio and Gamma-Rays*, ed. T. Savolainen, E. Ros, W. P. Porcas, & J. A. Zensus, 175–178, arXiv:1012.2820
- Schlegel, D. J., Finkbeiner, D. P., & Davis, M. 1998, *Astrophys. J.*, 500, 525
- Schraml, J., Pauliny-Toth, I. I. K., Witzel, A., et al. 1981, *Astrophys. J., Lett.*, 251, L57
- Schwab, F. R. & Cotton, W. D. 1983, *Astron. J.*, 88, 688
- Shepherd, M. C., Pearson, T. J., & Taylor, G. B. 1995, in *Bulletin of the American Astronomical Society*, Vol. 27, *Bulletin of the American Astronomical Society*, ed. B. J. Butler & D. O. Muhleman, 903
- Sikora, M., Begelman, M. C., Madejski, G. M., & Lasota, J.-P. 2005, *Astrophys. J.*, 625, 72

-
- Sikora, M., Begelman, M. C., & Rees, M. J. 1994, *Astrophys. J.*, 421, 153
- Slysh, V. I. 1963, *Nature*, 199, 682
- Smith, J. A., Tucker, D. L., Kent, S., et al. 2002, *Astron. J.*, 123, 2121
- Smith, P. S., Balonek, T. J., Heckert, P. A., Elston, R., & Schmidt, G. D. 1985, *Astron. J.*, 90, 1184
- Steffen, W., Zensus, J. A., Krichbaum, T. P., Witzel, A., & Qian, S. J. 1995, *A&A*, 302, 335
- Stickel, M., Fried, J. W., & Kuehr, H. 1989, *A&AS*, 80, 103
- Tavecchio, F., Ghisellini, G., Bonnoli, G., & Ghirlanda, G. 2010, *MNRAS*, 405, L94
- Taylor, G. B., Carilli, C. L., Perley, R. A., & G. B. Taylor, C. L. Carilli, & R. A. Perley, eds. 1999, *Astronomical Society of the Pacific Conference Series*, Vol. 180, *Synthesis Imaging in Radio Astronomy II*
- Teräsraanta, H., Tornikoski, M., Mujunen, A., et al. 1998, *A&AS*, 132, 305
- Thompson, D. J., Bertsch, D. L., Fichtel, C. E., et al. 1993, *ApJS*, 86, 629
- Timmer, J. & Koenig, M. 1995, *A&A*, 300, 707
- Trippe, S., Krips, M., Pietu, V., et al. 2011, e-print arXiv:1107.5456
- Unwin, S. C. & Wehrle, A. E. 1992, *Astrophys. J.*, 398, 74
- Unwin, S. C., Wehrle, A. E., Lobanov, A. P., et al. 1997, *Astrophys. J.*, 480, 596
- Unwin, S. C., Wehrle, A. E., Urry, C. M., et al. 1994, *Astrophys. J.*, 432, 103
- Uttley, P., McHardy, I. M., & Papadakis, I. E. 2002, *MNRAS*, 332, 231
- Uzdensky, D. A. 2005, *Astrophys. J.*, 620, 889
- Valtaoja, E. & Terasraanta, H. 1996, *A&AS*, 120, C491
- Valtaoja, E., Terasraanta, H., Urpo, S., et al. 1992, *A&A*, 254, 71
- Villata, M., Raiteri, C. M., Gurwell, M. A., et al. 2009, *A&A*, 504, L9
- Villata, M., Raiteri, C. M., Larionov, V. M., et al. 2008, *A&A*, 481, L79
- Vio, R., Cristiani, S., Lessi, O., & Salvadori, L. 1991, *Astrophys. J.*, 380, 351
- Vlahakis, N. & Königl, A. 2003, *Astrophys. J.*, 596, 1080
- Vlahakis, N. & Königl, A. 2004, *Astrophys. J.*, 605, 656
- Vlahakis, N., Tsinganos, K., Sauty, C., & Trussoni, E. 2000, *MNRAS*, 318, 417
- Waak, J. A., Simon, R. S., Spencer, J. H., & Johnston, K. J. 1988, *Astron. J.*, 95, 1023
- Wall, J. V. & Jenkins, C. R. 2003, *Practical Statistics for Astronomers*, ed. Wall, J. V. & Jenkins, C. R.

- Waltman, E. B., Fiedler, R. L., Johnston, K. J., et al. 1991, *ApJS*, 77, 379
- Wardle, J. F. C., Cawthorne, T. V., Roberts, D. H., & Brown, L. F. 1994, *Astrophys. J.*, 437, 122
- Wardle, J. F. C., Homan, D. C., Ojha, R., & Roberts, D. H. 1998, *Nature*, 395, 457
- Wehrle, A. E., Piner, B. G., Unwin, S. C., et al. 2001, *ApJS*, 133, 297
- Wilks, S. S. 1938, *Ann. Math. Stat.*, 9, 60
- Williams, P. J. S. 1963, *Nature*, 200, 56
- Wyndham, J. D. 1965, *Astron. J.*, 70, 384
- Xu, J., Hardee, P. E., & Stone, J. M. 2000, *Astrophys. J.*, 543, 161
- Zensus, J. A., Cohen, M. H., & Unwin, S. C. 1995, *Astrophys. J.*, 443, 35
- Zensus, J. A., Ros, E., Kellermann, K. I., et al. 2002, *Astron. J.*, 124, 662

Acknowledgement

I am deeply grateful for the opportunity to work with Andrei Lobanov and his patience with me. Like with any advisor there have been difficult and joyful times, sometimes all at once, but there has been no time at which he let me down. I am very thankful for all the wisdoms, knowledge and advice that were passed on to me, some of it may continue to propagate. A special thank goes to Anton Zensus, for the trust, resources, and support I have received during this very intense period. I thank Richard Porcas for sharing his deep knowledge on VLBI, life experience, general thoughts about just anything, the occasional limerick, and the nagging to stay focused. I cannot even imagine how life at the MPI would have been without him.

It is difficult to summarize all the support I have received over the past three years from so many people, which makes it difficult to summarize. I will start with my former office neighbor Kirill Sokolovsky, whose enthusiasm for astronomy has been contagious, pushing me into things that I might have not pursued otherwise, in particular an active engagement in Flare Advocate business, Swift and various other interesting things to distract ourselves from doing actual work leading to a thesis. I also owe many thanks to Tuomas Savolainen, who always had a sympathetic ear for my thoughts and ideas, providing me with insights into the inner workings of data reduction and imaging, statistics, and Finnish culture. I will really miss the late nights in the pub talking about the big pictures. I am very grateful for the company of Christian Fromm, which I value very much, may it be the occasional chat during the day, having a good time in the pub, or the trip to Greece and Argentina. Together with Manolo Perucho and many others, it has been a great pleasure discussing science and life with you. Especially, the meeting in Argentina together with Phil Hardee and Petar Mimica was a memorable experience.

I also thank Eduardo Ros, who as the research school coordinator of the time has received me when I arrived in Bonn. It has been a great pleasure for me interacting with you, chatting about politics and science and getting to know you and your family as a friend. Special thanks also go to Gabi Breuer, the research school assistant of the time, who helped me with all the paperwork that was needed in order to get settled in Bonn. I am especially thankful for her insistence with the registration at the graduate office of the University of Cologne, dealing with the complications a foreign Masters degree brings.

I acknowledge the support of Alan Marscher, Svetlana Jorstad, and Iván Agudo, who provided many helpful comments and shared calibrated datasets of their observation campaigns with me. I very much valued our interactions during different meetings in 2010 and especially during my short visit to Boston. I am also very grateful for the support I have received from the Fermi-LAT collaboration. In particular that of Teddy Cheung, Filippo D'Ammando, Walter Max-Moerbeck, Gino Tosti, Benoit Lott, Ann Wehrle, Seth Digel, Dave Thompson, Toby Burnett, Peter Michelson, and many others. I am very grateful for the occasional support I have received from Greg Taylor, especially related to the VLBA campaign during 2009 and 2010. I am looking forward to the opportunity to continue working with him back in New Mexico. I am very thankful for the discussions with Iván Martí-Vidal about science and life, and for sharing his calibrated GMVA data with me.

I especially thank Manolis Angelakis and Kosmas Lazaridis for the warm, sincere company and friendship, while sharing an office with me, during the many evenings, and especially during Manolis wedding in Greece. I also would like to particularly thank Kazi Rygl, Nicola Marchili, Ioannis Nestoras, Lars Fuhrmann, Filomena Volino, Chin-Shin Chang, and many more for their friendship and company during my PhD time. It will be kept in good memory. Especially the Friday night crowd, currently and in the past driven by Richard, James, and Yuri, has been an integral part of my social life winding down the work week with discussions about Japanese toilets or Russian women in boots.

I appreciated very much the company of Mar Mezcua during the past three years, it has been very helpful knowing that we did not walk our path alone. I hope she did not resent the almost daily interruptions by my visits, it helped to keep at taps with what Andrei was currently up to.

Finally, I would like to thank everyone I have worked with over the past three years, which have not been mentioned individually and I am ruefully sorry for those I might have missed, it has been a pleasure working with you and to be able to learn from and work with the experts in radio interferometry, γ -ray and AGN science.

Last but not least, ein besonderer Dank gilt meinen Eltern, Bruder und Großeltern, für ihre kontinuierliche Unterstützung – nicht nur während der letzten drei Jahre in Bonn. Vielen Dank das ihr mir den Rücken freigehalten habt und immer ein offenes Ohr für meine Wünsche und Sorgen hattet. Man erkennt erst wirklich wie wichtig Familie ist wenn sie nicht in der Nähe ist.

Erklärung

Ich versichere, dass ich die von mir vorgelegte Dissertation selbständig angefertigt, die benutzten Quellen und Hilfsmittel vollständig angegeben und die Stellen der Arbeit, einschließlich Tabellen, Karten und Abbildungen, die anderen Werken im Wortlaut oder dem Sinn nach entnommen sind, in jedem Einzelfall als Entlehnung kenntlich gemacht habe; dass diese Dissertation noch keiner anderen Fakultät oder Universität zur Prüfung vorgelegen hat; dass sie, abgesehen von unten angegebenen Teilpublikationen – noch nicht veröffentlicht worden ist sowie, dass ich eine solche Veröffentlichung vor Abschluss des Promotionsverfahrens nicht vornehmen werde. Die Bestimmungen der Promotionsordnung sind mir bekannt. Die von mir vorgelegte Dissertation ist von Prof. Dr. J. Anton Zensus und Dr. Andrei P. Lobanov betreut worden.

Köln, den 22.08.2011

Teilpublikationen

Schinzel, F. K.; Lobanov, A. P.; Taylor, G. B.; Jorstad, S. G.; Marscher, A. P. and Zensus, J. A.: “*Relativistic Outflow Drives γ -Ray Emission in 3C 345*”, submitted to A&A, 2011

Schinzel, F. K.; Sokolovsky, K. V.; D’Ammando, F.; Burnett, T. H.; Max-Moerbeck W.; Cheung, C. C.; Fegan, S. J.; Casandjian, J. M.; Reyes, L. C.; Villata, M.; Raiteri, C. M.; Agudo, I.; Bravo Calle, O. J. A.; Carosati, D.; Casas, R.; Gómez, J. L.; Gurwell, M. A.; Hsiao, H. Y.; Jorstad, S. G.; Kimeridze, G.; Konstantinova, T. S.; Kopatskaya, E. N.; Koptelova, E.; Kurtanidze, O. M.; Kurtanidze, S. O.; Larionov, V. M.; Larionova, E. G.; Larionova, L. V.; Marscher, A. P.; Morozova, D. A.; Nikolashvili, M. G.; Roca-Sogorb, M.; Ros, J. A.; Sigua, L. A.; Spiridonova, O.; Troitsky, I. S.; Vlasyuk, V. V.; Lobanov, A. P.; Zensus, J. A.: “*Identification of γ -ray emission from 3C 345 and NRAO 512*”, A&A 2011, Vol. 532, A150

Schinzel, F. K.; Lobanov, A. P.; Zensus, J. A.; Taylor, G. B.; Jorstad, S. G.; Marscher, A. P.: “*Evolution of the Parsec-Scale Jet in 3C 345*”, Proceedings IAU Symposium No. 275, 2010 (Buenos Aires, Argentina), pp. 196–197

Schinzel, F. K.; Lobanov, A. P.; Jorstad, S. G.; Marscher, A. P.; Taylor, G. B.; Zensus, J. A.: “*Radio Flaring Activity of 3C 345 and its Connection to γ -ray Emission*”, Proceedings “Fermi meets Jansky – AGN in Radio and Gamma-Rays“ in Bonn, Germany, 2010, pp. 175–178

Schinzel, F. K.; Lobanov, A. P. and Zensus, J. A.: “*Three Decades of Very Long Baseline Interferometry Monitoring of the Parsec-Scale Jet in 3C 345*“, Proceedings Accretion and Ejection in AGN: A Global View, Como, Italy, 2009, pp. 153–158

Lebenslauf

Persönliche Daten

Name: Frank Karlheinz Schinzel
Anschrift: Max-Planck-Institut für Radioastronomie
Auf dem Hügel 69, 53121 Bonn, Deutschland
Telefon: +49 (228) 525-366
E-mail: schinzel@mpifr-bonn.mpg.de
Geburtsdatum und -ort: 24.02.1983, Würzburg, Deutschland

Ausbildung

- 2008 - 2011 Promotionsstudent an der Universität zu Köln und dem Max-Planck-Institut für Radioastronomie in Bonn
wiss. Betreuer: Dr. Andrei P. Lobanov und Prof. Dr. J. Anton Zensus
Titel: “*Physics and Kinematics of the Parsec Scale Jet of the Quasar 3C 345*”
- 2006 - 2008 Master of Science in Physics an der University of New Mexico, Albuquerque, USA
wiss. Betreuer: Prof. Dr. Gregory B. Taylor
Titel: “*Radio Interferometry Observations of SN 2001em*”
- 2003 - 2006 Diplomstudent an der Julius-Maximilians-Universität Würzburg, Vordiplom Physik (2005)
- 1994 - 2003 Allgemeine Hochschulreife am städt. Mozart- und Schönborn-Gymnasium mit Realschule Würzburg
- 2000 - 2001 High School Diploma, East High School, Rochester, NY USA

Stipendien

- 2009 - 2011 Stipendium der *International Max Planck Research School for Astronomy and Astrophysics*
- 2006 - 2007 Stipendium des Deutschen Akademischen Austausch Dienstes (DAAD)

Veröffentlichungen

26. *Identification of γ -ray emission from 3C 345 and NRAO 512*
F.K. Schinzel, K.V. Sokolovsky, F. D'Ammando, T.H. Burnett, W. Max-Moerbeck, C.C. Cheung, S.J. Fegan, J.M. Casandjian, L.C. Reyes, M. Villata, C.M. Raiteri, I. Agudo, O.J.A. Bravo Calle, D. Carosati, R. Casas, J.L. Gómez, M.A. Gurwell, H.Y. Hsiao, S.G. Jorstad, G. Kimeridze, T.S. Konstantinova, E.N. Kopatskaya, E. Koptelova, O.M. Kurtanidze, S.O. Kurtanidze, V.M. Larionov, E.G. Larionova, L.V. Larionova, A.P. Marscher, D.A. Morozova, M.G. Nikolashvili, M. Roca-Sogorb, J.A. Ros, L.A. Sigua, O. Spiridonova, I.S. Troitsky, V.V. Vlasyuk, A.P. Lobanov, J.A. Zensus
 A&A 2011, Vol. 532, A150
25. *The Discovery and Nature of Optical Transient CSS100217:102913+404220*
 A.J. Drake, S.G. Djorgovski, A. Mahabal, J. Anderson, R. Roy, V. Mohan, S. Ravindranath, D. Frail, S. Gezari, J.D. Neill, L.C. Ho, J.L. Prieto, D. Thompson, J. Thorstensen, M. Wagner, R. Kowalski, J. Chiang, J.E. Grove, **F.K. Schinzel**, D.L. Wood, L. Carrasco, E. Recillas, L. Kewley, K.N. Archana, Aritra Basu, Y. Wadadekar, B. Kumar, A.D. Myers, E.S. Phinney, R. Williams, J.M. Graham, M. Catelan, E. Beshore, S. Larson, E. Christensen
 ApJ 2011, Vol. 735, Issue 2, 106, eprint arXiv:1103.5514
24. *Fermi Large Area Telescope Detection of Bright Gamma-ray Outbursts from a Peculiar Quasar 4C +21.35*
 Y.T. Tanaka, L. Stawarz, D.J. Thompson, F. D'Ammando, S.J. Fegan, B. Lott, D.L. Wood, C.C. Cheung, J. Finke, S. Buson, L. Escande, S. Saito, M. Ohno, T. Takahashi, D. Donato, J. Chiang, M. Giroletti, **F.K. Schinzel**, G. Iafrate, F. Longo
 ApJ 2011, Vol. 733, Issue 1, 19T – eprint arXiv:1101.5339
23. *The first multifrequency campaign on BL Lac: characterizing the low activity state of the eponymous blazar*
 A.A. Abdo, M. Ackermann, M. Ajello, ..., **F.K. Schinzel**, et al. (The Fermi-LAT Collaboration)
 ApJ 2011 Vol. 730, Issue 2, 101 – eprint arXiv:1101.5905
22. *Evolution of the Parsec-Scale Jet in 3C 345*,
F.K. Schinzel, A.P. Lobanov, J.A. Zensus, G.B. Taylor, S.G. Jorstad, A.P. Marscher
 IAU Symposium No. 275, 2010 (Buenos Aires, Argentina), pp. 196–197

-
21. *Flaring blazar B2 0619+33: Swift X-ray and UV/optical observations*
D. Donato, K.V. Sokolovsky, F. D'Ammando F., **F.K. Schinzel**
2010, *Astronomer's Telegram* #2848
 20. *PKS 1329-049 revived: new gamma-ray activity observed by Fermi LAT*
K.V. Sokolovsky, **F.K. Schinzel**
2010, *Astronomer's Telegram* #2837
 19. *Fermi LAT detection of a GeV flare from B2 0619+33*
F.K. Schinzel
2010, *Astronomer's Telegram* #2829
 18. *Swift observations of the new gamma-ray quasar PKS 1915-458*
K.V. Sokolovsky, F. D'Ammando, **F.K. Schinzel**
2010, *Astronomer's Telegram* #2679
 17. *Fermi/LAT detection of a new possible high-z gamma-ray quasar PKS 1915-458*
K.V. Sokolovsky, **F.K. Schinzel**, S.E. Healey, D. Donato, E. Wallace, M. Boeck
Astronomer's Telegram #2666
 16. *Fermi and Swift observation of a GeV/X-ray/UV flare from PKS 2233-148*
K.V. Sokolovsky, D. Donato, **F.K. Schinzel**, Y.Y. Kovalev
Astronomer's Telegram #2589
 15. *Swift XRT/UVOT follow-up of blazar PKS B0906+015 after a gamma-ray flare*
K.V. Sokolovsky, **F.K. Schinzel**, F. D'Ammando, M. Kadler, C.S. Chang,
M.A. Stark, E. Ros *Astronomer's Telegram* #2582
 14. *Fermi LAT detection of a GeV flare from PKS 0906+015*
F.K. Schinzel, K.V. Sokolovsky
2010, *Astronomer's Telegram* #2543
 13. *Gamma-Ray Emission Concurrent with the Nova in the Symbiotic Binary V407 Cygni*
A.A. Abdo, M. Ackermann, M. Ajello, ..., **F.K. Schinzel**, et al. (The
Fermi-LAT Collaboration)
Science 2010 Vol. 329, Issue #5993, pp. 817-821
 12. *VLBI detection of V407 Cyg*
M. Giroletti, E. Koerding, S. Corbel, K. Sokolovsky, L. Fuhrmann,
F. Schinzel, C.C. Cheung
2010, *Astronomer's Telegram* #2536
 11. *Fermi LAT detection of a GeV flare from PKS B 1622-297*
E. Wallace, **F. Schinzel**
2010, *Astronomer's Telegram* #2531
 10. *Fermi LAT detection of increased gamma-ray activity of two blazars PKS 0420-01 and BL Lacertae*
K.V. Sokolovsky, **F.K. Schinzel**, E. Wallace
2010, *Astronomer's Telegram* #2402

9. *Fermi LAT detection of a GeV flare from OX 169 (S3 2141+17)*
K.V. Sokolovsky, **F.K. Schinzel**, Y.Y. Kovalev
2010, *Astronomer's Telegram* #2393
8. *Radio Flaring Activity of 3C 345 and its Connection to γ -ray Emission*
F.K. Schinzel, A.P. Lobanov, S.G. Jorstad, A.P. Marscher, G.B. Taylor,
J.A. Zensus,
"Fermi meets Jansky – AGN in Radio and Gamma-Rays" in Bonn, Germany, 2010,
pp. 175–178
7. *Constraints on the gamma-ray emitting region in blazars from multi-frequency VLBI measurements*
K.V. Sokolovsky, Y.Y. Kovalev, A.P. Lobanov, J.D. Finke, T. Savolainen,
A.B. Pushkarev, M. Kadler, **F.K. Schinzel**, V.H. Chavushyan, L. Carrasco,
A. Carraminana, M.A. Gurwell,
"Fermi meets Jansky – AGN in Radio and Gamma-Rays" in Bonn, Germany, 2010,
pp. 167–170
6. *Fermi LAT detection of a GeV flare from GB6 B1310+4844*
K.V. Sokolovsky, S.E. Healey, **F.K. Schinzel**, Y.Y. Kovalev
2009, *Astronomer's Telegram* #2306
5. *Three Decades of Very Long Baseline Interferometry Monitoring of the Parsec-Scale Jet in 3C 345*
F.K. Schinzel, A.P. Lobanov, J.A. Zensus,
Accretion and Ejection in AGN: A Global View, Como, Italy, 2009, pp. 153–158
4. *SN 2001em: Not So Fast*
F.K. Schinzel, G.B. Taylor, C.J. Stockdale, J. Granot, E. Ramirez-Ruiz
ApJ 2009 Vol. 691, Issue 2, pp. 1379-1385 – eprint arXiv:0810.1478
3. *SN 2001em: Evidence for a dense circumstellar environment*
F.K. Schinzel, G.B. Taylor, C.J. Stockdale, J. Granot, E. Ramirez-Ruiz,
9th EVN Symposium, Bologna, Italy 2008
2. *The Combined Radio Interferometry and COSMIC Experiment in Tomography (CRICKET) Campaign*
K.F. Dymond, C. Watts, C. Coker, S. Budzien, P. Bernhardt, N. Kassim,
J. Lazio, A. Cohen, K. Weiler, P. Crane, L.J. Rickard, G. Taylor, **F. Schinzel**,
Y. Philström, S. Close, P. Closestock, S. Myers, A. Dhatta,
IES2008
1. *Four epochs of VLBA/HSA observations of SN 2001em*
F.K. Schinzel, G.B. Taylor, C.J. Stockdale, J. Granot, E. Ramirez-Ruiz
Gamma Ray Bursts 2007, Santa Fe, pp. 509–512